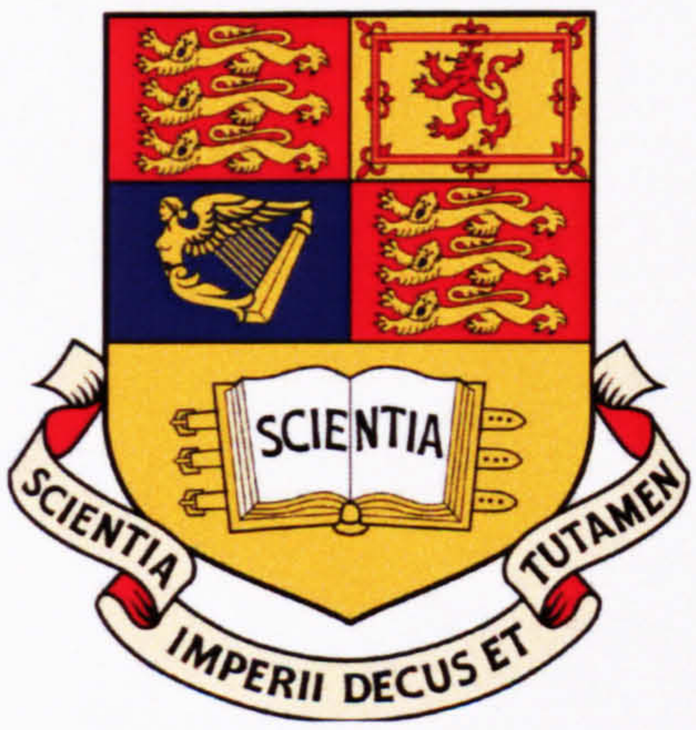
Numerical Prediction of Flow-Field Characteristics in a Hypersonic Intake

Nili Bachchan



September 2005

Thesis submitted for the degree of
Doctor of Philosophy
of the University of London
and the Diploma of Imperial College

Department of Aeronautics
Imperial College of Science, Technology and Medicine

IMPERIAL COLL. LOND. IN. UNIV

Abstract

The flow-field characteristics of a fixed-geometry hypersonic intake for high-speed propulsion have been studied using theoretical aerodynamics and CFD. An axisymmetric isentropic compression intake is examined at Mach numbers from 4 to 6. Numerical simulations have been carried out, partly as a design tool for optimisation of the intake design, and also for aerodynamic studies of high-speed intakes, in particular for the off-design conditions. Various off-design wave interactions have been considered. Parametric CFD studies conducted by varying inlet geometry have led to an understanding of the wide range of possible off-design cases. These have been found to have a significant effect on flow quality and intake performance.

Theoretical analysis has been carried out to focus on the essential detail of the shock-expansion interactions at inlet to predict the resultant inlet flow phenomena. Results obtained from parameter studies based on this analysis have found to be in good agreement with the CFD results. The problem of flow separation, particularly from shock/boundary-layer interactions has also been studied, and the findings have led to the improvement in intake design by controlling flow separation.

Numerical simulations of the intake with a simulated combustion pressure rise have also been carried out to focus on the inlet-isolator interactions. The results have shown that flow non-uniformities in the intake duct can lead to difficulties in stabilising the terminal shock system, and can deteriorate isolator performance.

For my family

Acknowledgements

Sincere gratitude to Professor Richard Hillier with whose continued guidance and support it was a privilege to persevere with this research. I am indebted to his expertise and enthusiasm in realising this project.

I gratefully acknowledge QinetiQ Ltd for sponsoring this research in particular the contract supervisors Dr Terry Cain and Dr Craig Walton for their excellent interaction during this period.

The support of the Aeronautics staff has been invaluable. Dr Letty Foulkes provided generous technical advice for all my hardware and software problems; and Sabine Grune von Steiglitz, Molly Ip and John O'Leary provided helpful assistance.

I wish to extend warmest thanks to my colleagues in the Hypersonics Group for inspiring me with their dedication to their own work. For this and friendship a special mention to Dr Abderrahmane Fiala, Dr Sean Creighton, Dr Simon Williams, Dr Wadud Miah and Charalampos Tsimis. I also wish to thank Dr Shumit Das and Dr Stefan Seefeldt for their friendship and generosity during this time.

And finally, I would like to thank my dear family and friends for their encouragement and support all along and particularly in difficult times in the final year.

Contents

Abstract 2

Acknowledgements 4

Nomenclature 8

List of Figures 26

List of Tables 28

1 Introduction 29

1.1 Hypersonic flight 29

1.2 Thesis objectives 33

2 Literature review 35

2.1 Ramjet/scramjet propulsion 35

2.1.1 Intake configuration 37

2.1.2 Intake performance 43

2.1.3 Self-starting 47

2.2 Intake flow characteristics 48

2.2.1 Shock wave systems 48

2.2.2 Spike and cowl blunting 60

2.2.3 Cowl positioning 62

2.2.4 Angle-of-attack 62

2.2.5 Oscillations (buzz) 64

2.3 Isolator flow characteristics 65

2.3.1 Shock train phenomenon 65
2.3.2 Isolator geometry 69

3 Numerical methods 79
3.1 CFD methodology 79
3.1.1 Mesh generation 80
3.1.2 Euler solver 80
3.1.3 Navier-Stokes solver 82
3.1.4 Turbulence modelling 85
3.1.5 Block-marching 88
3.2 Numerical set-up 89
3.2.1 Geometry definition 89
3.2.2 Mesh configuration 91
3.2.3 Boundary-layer refinement 93
3.2.4 Initial and boundary conditions 94
3.3 Validation and convergence 96
3.3.1 Taylor-Maccoll case 96
3.3.2 CFD and experiment 99
3.3.3 Mesh convergence (inviscid) 101
3.3.4 Mesh convergence (turbulent) 102

4 Intakes with supersonic outflow I 109
4.1 Wave system at the forebody (no cowl) 109
4.1.1 Design condition 109
4.2 Intake off-design wave interactions 111
4.2.1 Interaction types 112
4.3 Intake with shock-on-lip at Mach 4.8 115
4.3.1 Design/Off-design conditions 116
4.3.2 Intake performance 124
4.4 Intake with shock-on-lip at Mach 5.5 130
4.4.1 Design/Off-design conditions 130
4.4.2 Intake performance 136

4.4.3 Effects of cowl blunting 141
4.5 Theoretical analysis 147
4.5.1 Shock-expansion interaction analysis 147
4.5.2 Results from parameter study 154
4.5.3 Reducing the spike-termination angle 159

5 Intakes with supersonic outflow II **169**
5.1 Flow separation at inlet 169
5.1.1 Flow system (no cowl) 171
5.1.2 Off-design conditions 174
5.1.3 Flow separation process 175
5.1.4 Effects of small changes in geometry 182
5.1.5 Increasing Mach number/altitude 187
5.1.6 Effects of cowl blunting 192
5.2 Separation control at inlet 194
5.2.1 Backward step at inlet 194
5.2.2 Flow system (no cowl) 195
5.2.3 Flow system (thin-plate cowl) 197
5.3 i1533 intake analysis 203
5.4 i1530 intake analysis 217

6 Intakes with applied back pressure **231**
6.1 Flow characteristics in the isolator 231
6.2 Method for applying a back pressure 233
6.3 Effect of non-uniformity on sustainable back pressure levels 236
6.3.1 Case 1: Intake at Mach 4 (inviscid) 237
6.3.2 Case 2: Intake at Mach 6 (inviscid) 241
6.3.3 Case 3: Viscous effects 246

7 Conclusions and further work **248**
7.1 Conclusions 248
7.2 Further work 252
7.3 Publications 253

A Appendix **254**

A.1 Shock-expansion interaction analysis 254

A.2 Intake geometry definition 256

Bibliography **258**

Nomenclature

A	Area (m^2)
β	Shock angle (deg.)
C_d	Drag coefficient
$C_{d_{intake}}$	Drag coefficient for forces on intake surfaces
$C_{d_{add}}$	Additive drag coefficient
C_p	Specific heat, constant pressure
d	Diameter (m)
δ_c	Cowl angle (deg.)
δ	Boundary-layer thickness (m)
δ_1	Boundary-layer displacement thickness (m)
δ_2	Boundary-layer momentum thickness (m)
F	Thrust (N)
γ	Ratio of specific heats
H	Annulus height (m)
k	Thermal conductivity
L_1	Reattachment length (m)
λ	Second coefficient of viscosity
$\dot{m}$	Mass flow rate (kg/s)
M	Mach number
M_∞	Freestream Mach number
M_c	Surface Mach number
μ	Dynamic viscosity
μ_t	Eddy viscosity
P_∞	Freestream total pressure (KPa)
p_∞	Freestream static pressure (KPa)
p	Pressure (KPa)
p_c	Surface static pressure (KPa)
Pr	Prandtl number
p	Pressure (Pa)
q	Heat transfer (Wcm^{-2})
η_{pr}	Total pressure efficiency
η_{ke}	Kinetic energy efficiency
r	Radius (m)
R	Gas constant (J/kg/K)
Re	Reynolds number
Re_w	Reynolds number at the wall
ρ	Density (kg/m^3)

ρ_∞	Freestream density (kg/m^3)
t	Time (s)
T	Temperature (K)
$T_{0\infty}$	Freestream total temperature (K)
T_∞	Freestream static temperature (K)
θ_1	Spike termination angle (deg.)
θ_2	Centrebody angle (deg.)
U_∞	Freestream velocity (m/s)
x_c	Cowl lip x-position (m)
x_l	Length of the transition region (m)
x_{tr}	Transition onset point (m)
y_c	Cowl lip radial position (m)

Subscripts

c	Cowl lip
ke	Kinetic energy
sol	Shock-on-lip condition
∞	Freestream condition

Abbreviations

C/SiC	Carbon/Silicon-Carbide
CFD	Computational Fluid Dynamics
CIAM	Central Institute of Aviation Motors
CR	Compression Ratio
DARPA	Defense Advanced Research Projects Agency
DLR	Deutschen Zentrum fur Luft und Raumfahrt
ESA	European Space Agency
GRP	Generalised Riemann Problem
HRE	Hypersonic Research Engine
MCR	Mass Capture Ratio
MOC	Method of Characteristics
NASA	National Aeronautics and Space Administration
NASP	National Aerospace Plane
RBCC	Rocket-Based Combined Cycle
RLV	Reusable Launch Vehicle
SHYFE	Sustained Hypersonic Flight Experiment
SSTO	Single-Stage-To-Orbit
TBCC	Turbine-Based Combined Cycle

List of Figures

1.1 Conceptual picture of The Sustained Hypersonic Flight Experiment vehicle (side view). Copyright QinetiQ Ltd. Published with permission. 31

2.1 Conventional ramjet engine components (Oswatitsch 1944[22]). 36

2.2 Temperature-entropy diagram of an air-breathing engine cycle, or Brayton cycle with corresponding component station points to Figure 2.1.[115] 36

2.3 (a) 2-shock and (b) 3-shock external compression intakes. 38

2.4 Ideal inlet-cowl configuration for an external compression intake and a close-up view of the wave system after isentropic compression on the forebody. 39

2.5 Total flow turning angle for optimum two-dimensional shocks (Seddon[58]). 40

2.6 Types of hypersonic intakes: (*top*) Hypersonic Research Engine external compression intake (NASA); (*middle*) modular Busemann or waverider intake model (QinetiQ scramjet); and (*bottom*) sidewall compression intake model (DLR). 41

2.7 Airframe-propulsion system integration illustration showing an engine module that can be installed on the vehicle undersurface (Anderson et al.[9]). 42

2.8 Area definitions and mass capture spillage. 45

2.9 Impingement of an oblique shock (IS) on the stand-off shock (BS) formed at a blunt leading edge categorised into six distinct patterns I to VI by Edney.[13] 49

2.10 Type IV Edney interaction surface pressure and heat transfer distributions; comparison between numerical and experimental results (Bertin[65]). 50

2.11 (a) Comparison of shock structure with and without shock impingement from numerical prediction at Mach 5.94 (b) Comparison of surface static pressure with and without shock impingement (White et al.[60]). 51

2.12 Illustration of the reflection of a shock wave as either (a) regular reflection or (b) Mach reflection (Li and Ben-Dor[73]). 52

2.13 Transition from regular to Mach reflection according to the detachment and von Neumann criteria showing the dual-solution domain (Li and Ben-Dor[73]). 53

2.14 Illustration of a cowl shock reflecting from the centrebody and being acted on by the corner expansion fan to form a Mach reflection (Ben-Dor[73]). 54

2.15 Variation of predicted angle, from method of characteristics, for detachment from the cowl leading edge and transition between regular and Mach reflection, on the downstream surface, according to the von Neumann and detachment criteria. (Bachchan and Hillier[86]). 55

2.16 Regular reflection simulation for incident flow at 0.5 degrees below the incident angle for regular-to-Mach transition according to the detachment criterion: Mach 2.0 at 5% intervals in ρ/ρ_∞; point (c) on Figure 2.17 (Bachchan and Hillier[86]). 55

2.17 Detail in the Mach number and flow deflection plane showing the test cases corresponding to CFD simulations in the Figure 2.18 (Bachchan and Hillier[86]). 56

2.18 CFD simulation for Mach reflection for incident perturbed from the Mach 2.0 regular reflection case of Figure 2.16. (a) incidence increased by 1.0 degrees; (b) incidence maintained at original value and Mach number reduced to 1.92; (c) Mach number returned to original value; (d) Mach number held fixed and incidence reduced by 0.5 degrees; (e) further reduction by 0.5 degrees; (f) a further reduction by 0.5 degrees (Bachchan and Hillier[86]). 57

2.19 Shock/boundary-layer interaction flow physics (Shapiro[7]). 58

2.20 Shock/turbulent-boundary-layer interaction flow characteristics in (left) supersonic and (right) hypersonic flow (Knight et al.[105]). 59

2.21 Effects of leading-edge bluntness (Van Wie[112]). 61

2.22 Two operating conditions of an axisymmetric intake with a single-surface conical centrebody (a) 0 deg α (b) high value of α (Mahoney[66]). 63

2.23 Effect of angle of attack on the measured performance of an axisymmetric semi-isentropic inlet (Mahoney[66]). 63

2.24 Typical shock positions during one cycle of intake shock oscillation showing the forward and rearward movement of the shock position (Seddon[58]). 65

2.25 Normal and oblique shock trains in an isolator duct (Heiser[115]). . . . 66

2.26 Simplified representation of shock structure and comparison with pitot pressure surveys in a cylindrical duct (Waltrup and Billig[89]). . 68

2.27 Comparative sketches of a family of inlets designed in accordance with conservative practices as described in the work of Mahoney.[66] 69

2.28 Ratio of shock train axial length to duct height as a function of inlet Mach number and back pressure ratio for an isolator or constant area diffuser with typical inlet condition (Heiser and Pratt[115]). 70

2.29 Schematic diagram of the model used for parametric inlet-isolator tests at Mach 4 at NASA Langley Research Centre (Emami et al.[35]). 72

2.30 Inlet-isolator maximum back pressure with constant-area isolator length (L/H) of 2.7, 4.7, 8.7 and 16.7 for 2.5-in cowl; thin boundary-layer (Emami et al.[35]). 73

2.31 Inlet-isolator maximum back pressure with constant-area isolator length (L/H) of 2.7, 4.7, 8.7 and 16.7 for 2.5-in cowl; thick boundary-layer (Emami et al.[35]). 73

2.32 Inlet-isolator maximum back pressure with constant-area isolator length (L/H) of 2.7, 4.7, 8.7 and 16.7 for 4.4-in cowl; thick boundary-layer (Emami et al.[35]). 74

2.33 Two-dimensional mixed compression inlet-isolator model tested at Mach 4 and 5 conditions (M_{sol}=3.0) by Reinartz et al.[91] (Aachen University/DLR) 75

2.34 Waltrup-Billig empirical correlation for isolator length and computed maximum compression ratios for different isolator lengths (Reinartz et al.[91]). 75

2.35 Comparison of a schlieren picture (top) and corresponding CFD Mach contours (bottom) with a specified back pressure ratio of 7. (Reinartz et al.[91]). 76

2.36 Static pressure contours in an isolator ($M_\infty = 4$) to shows regular intersection and reflection between shocks and expansion waves (Ding et al.[26]). 77

2.37 Static pressure contours in an isolator ($M_\infty = 4$) to show irregular intersection and reflection between shocks and expansion waves (Ding et al.[26]). 77

3.1 Typical cell structure in a mesh. 80

3.2 Piecewise constant (left) and piecewise linear (right) gradient calculation. 81

3.3 The Sustained Hypersonic Flight Experiment conceptual picture, copyright QinetiQ, Farnborough (Published with permission). 89

3.4 2D Drawing of an initial variant of the Shyfe intake from the apex to the combustor entry; and a close-up view of the blunted cowl geometry. Further geometries will be explained in the thesis and also in the appendix section. 90

3.5 Methodology of the mesh block structure (close-up of the inlet). . . . 91

3.6 Intake mesh with a thin-plate cowl in the geometry from the spike leading edge up to the end of the parallel section; for illustration purposes only every second point is plotted (the full isolator and diffuser section is not shown). 91

3.7 Intake mesh with a (a) thin-plate and (b) blunt cowl in the geometry. 93

3.8 Boundary-layer meshing with stretched cells near the wall by fitting $y+$=1 in the surface cells for the full chord length using a mesh reforming method. 94

3.9 Application of CFD boundary conditions. 95

3.10 Flow model for Taylor-Maccoll flow over a cone (Zucrow[67]). 97

3.11 CFD Pressure contours from an inviscid simulation of flow over a cone with a 10 degree semi-angle at freestream Mach 5 (low resolution mesh). 98

3.12 CFD Pressure contours from an inviscid simulation of flow over a cone with a 10 degree semi-angle at freestream Mach 5 (high resolution mesh). 98

3.13 Comparison of experimental and laminar computational results for a low Reynolds number cavity flow (L/D=1) at Mach 9; (a) Surface pressure distribution (b) Surface heat transfer distribution (Jackson, Hillier and Soltani[61]). 99

3.14 Comparison of experimental and computational results for surface heat transfer distributions using Menter turbulence model on a cylindrical forebody at Mach 9 (Williams[105]). 100

3.15 CFD Pressure contours from an inviscid simulation of the shock train in the intake duct (thin-plate cowl) at Mach 4 (Medium resolution mesh 855 x 201). 104

3.16 CFD Pressure contours from an inviscid simulation of the shock train in the intake duct (thin-plate cowl) at Mach 4 (High resolution mesh 1709 x 401). 104

3.17 Comparison of forebody surface pressure distribution for the medium and high resolution mesh at Mach 4 (inviscid simulation) to show mesh convergence. 105

3.18 Comparison of the centrebody surface and cowl inner surface pressure distributions in the intake duct for the medium and high resolution mesh at Mach 4 (inviscid simulation) showing mesh convergence. . . 105

3.19 CFD Pressure contours from a turbulent simulation of the shock train in the intake duct (blunt cowl) at Mach 4 (Medium resolution mesh 855 x 201). 106

3.20 CFD Pressure contours from a turbulent simulation of the shock train in the intake duct (blunt cowl) at Mach 4 (High resolution mesh 1709 x 401). 106

3.21 Comparison of centrebody surface pressure distribution for the low, medium and high resolution mesh at Mach 6 (turbulent) to show mesh convergence. 107

3.22 Comparison of cowl internal surface pressure distribution for the low, medium and high resolution mesh at Mach 6 (turbulent) to show mesh convergence. 107

3.23 Comparison of cowl external surface pressure distribution for the low, medium and high resolution mesh at Mach 6 (turbulent) to show mesh convergence. 108

3.24 Comparison of the cowl external skin friction distribution for the low, medium and high resolution mesh at Mach 6 (turbulent) to show mesh convergence. 108

4.1 CFD Pressure contours from an inviscid simulation of the intake (no cowl) at Mach 5.5 showing the apex shock and isentropic compression focus point. 110

4.2 Schematic of the inlet wave system at the centrebody shoulder (no cowl) after the isentropic compression process on the forebody. . . . 110

4.3 CFD Contours from an inviscid simulation of the intake (no cowl) at on-design Mach 5.5; (a) pressure contours and (b) density contours. . 111

4.4 Cowl lip definition (a) thin-plate and (b) with a blunted lip; where θ_1 is the spike termination angle, θ_2 is the centrebody angle and δ_c is the cowl angle. 112

4.5 Schematics of inlet-associated wave interactions at off-design conditions. The intake is shown with a thin-plate cowl to initially simplify the problem. 113

4.6 Schematic of the wave system of an intake with shock-on-lip at Mach 4.8, showing the apex shock and compression fan focusing at the cowl lip. 115

4.7 CFD Density contours from an inviscid simulation of the intake (shock-on-lip Mach 4.8) intake with a 12 degree cowl and centrebody angle at Mach 4.8. 117

4.8 CFD Density contours from an inviscid simulation of the intake (shock-on-lip Mach 4.8) intake with a 6 degree cowl and centrebody angle at Mach 4.8. 117

4.9 Comparison of inlet flow profile for the intake with a 12 degree and a 6 degree centrebody and cowl angle at Mach 4.8 (taken at x = 0.194m).119

4.10 CFD Density contours from an inviscid simulation of the intake with a 12 degree cowl/centrebody angle at Mach 4.8 with the cowl lowered 0.5 mm. 120

4.11 CFD Density contours from an inviscid simulation of the intake with a 12 degree cowl angle at Mach 4.8 with a lowered cowl and modified centrebody. 120

4.12 CFD Density contours from an inviscid simulation of the intake (shock-on-lip Mach 4.8) intake with a 12 degree cowl and centrebody angle at Mach 4. 121

4.13 CFD Density contours from an inviscid simulation of the intake (shock-on-lip Mach 4.8) intake with a 12 degree cowl and centrebody angle at Mach 6. 121

4.14 CFD Density contours from an inviscid simulation of the intake (shock-on-lip Mach 4.8) intake with a 6 degree cowl and centrebody angle at Mach 6. 122

4.15 CFD Density contours from an inviscid simulation of the intake (shock-on-lip Mach 4.8) intake with an 18 degree cowl and centrebody angle at Mach 6. 122

4.16 Schematic of the wave system of an intake designed for shock-on-lip at Mach 5.5. 130

4.17 CFD Density contours from an inviscid simulation of the intake (shock-on-lip Mach 5.5) intake with a 12 degrees cowl and centrebody angle at Mach 4. 132

4.18 CFD Density contours from an inviscid simulation of the intake (shock-on-lip Mach 5.5) intake with a 12 degrees cowl and centrebody angle at Mach 5. 132

4.19 CFD Density contours from an inviscid simulation of the intake (shock-on-lip Mach 5.5) intake with a 12 degrees cowl and centrebody angle at Mach 5.5. 133

4.20 CFD Density contours from an inviscid simulation of the intake (shock-on-lip Mach 5.5) intake with a 12 degrees cowl and centrebody angle at Mach 6. 133

4.21 CFD Density contours from an inviscid simulation of the intake (shock-on-lip Mach 5.5) intake with a 12 degrees lowered cowl at off-design Mach 6. 135

4.22 CFD Density contours from an inviscid simulation of the intake (shock-on-lip Mach 5.5) intake with a 12 degrees forward cowl at off-design Mach 6. 135

4.23 Average pressure in the duct versus x-distance calculated from CFD simulations of the intake ($M_{sol} = 5.5$) at the freestream conditions (inviscid values). 139

4.24 Average Mach number versus x-distance calculated from CFD simulations of the intake ($M_{sol} = 5.5$) at the four freestream conditions (inviscid values). 139

4.25 Total pressure efficiency versus x-distance calculated from CFD simulations of the intake ($M_{sol} = 5.5$) at the four freestream conditions (inviscid values). 140

4.26 Kinetic energy efficiency versus x-distance calculated from CFD simulations of the intake ($M_{sol} = 5.5$) at the four freestream conditions (inviscid values). 140

4.27 CFD Density contours from an inviscid simulation of the intake with a 33 degree spike termination angle and a 12 degrees cowl angle at Mach 4. 142

4.28 CFD Density contours from an inviscid simulation of the intake with a 33 degree spike termination angle and a 12 degrees cowl angle (blunt) at Mach 4. 142

4.29 CFD Density contours from an inviscid simulation of the intake with a 33 degree spike termination angle and a 12 degrees cowl angle at Mach 5. 143

4.30 CFD Density contours from an inviscid simulation of the intake with a 33 degree spike termination angle and a 12 degrees cowl angle (blunt) at Mach 5. 143

4.31 CFD Density contours from an inviscid simulation of the intake with a 33 degree spike termination angle and a 12 degrees cowl angle at Mach 6. 144

4.32 CFD Density contours from an inviscid simulation of the intake with a 33 degree spike termination angle and a 12 degrees cowl angle (blunt) at Mach 6. 144

4.33 Centrebody and cowl inner surface pressures versus x-distance for the intake ($M_{sol} = 5.5$) with the thin-plate and blunt cowl at Mach 4. . . 145

4.34 Centrebody and cowl inner surface pressures versus x-distance for the intake ($M_{sol} = 5.5$) with the thin-plate and blunt cowl at Mach 5. . . 145

4.35 Centrebody and cowl inner surface pressures versus x-distance for the intake ($M_{sol} = 5.5$) with the thin-plate and blunt cowl at Mach 6. . . 146

4.36 Schematic of the ideal inlet flow where the apex shock and isentropic fan focus at the cowl lip, and the cowl shock focuses exactly on the shoulder. 147

4.37 Polar plot illustration with definition labels for the design lines on a centrebody angle versus cowl angle axis for a pre-specified spike termination angle. 149

4.38 No divergence. 151

4.39 Constraint 1. 151

4.40 Constraint 2. 152

4.41 Constraint 3. 152

4.42 Constraint 4. 153

4.43 Constraint 5. 153

4.44 Polar plot for the intake (shock-on-lip Mach 5.5) with a 33 degree spike termination angle at off-design condition Mach 4. 155

4.45 Polar plot for the intake (shock-on-lip Mach 5.5) with a 33 degree spike termination angle at off-design condition Mach 6. 155

4.46 CFD Pressure contours from an inviscid simulation of the intake (shock-on-lip Mach 5.5) intake with a 12 degrees cowl and centre-body angle at Mach 4. 156

4.47 CFD Pressure contours from an inviscid simulation of the intake (shock-on-lip Mach 5.5) intake with a 7 degrees cowl and centrebody angle at Mach 4. 156

4.48 CFD Pressure contours from an inviscid simulation of the intake with a 7 degrees cowl and centrebody angle at Mach 4; time-dependent results from (a) to (f) showing the formation of Mach reflection on the centrebody. 157

4.49 Comparison of surface pressure distribution for the intake (M_{sol} = 5.5) with a centrebody and cowl angle of 12 and 7 degrees at Mach 4 (inviscid CFD). 158

4.50 Polar plot for the intake (shock-on-lip Mach 5.5) with a 29 degree spike termination angle at off-design condition Mach 4. 160

4.51 Polar plot for the intake (shock-on-lip Mach 5.5) with a 29 degree spike termination angle at off-design condition Mach 5. 160

4.52 Polar plot for the intake (shock-on-lip Mach 5.5) with a 28 degree spike termination angle at off-design condition Mach 4. 161

4.53 Polar plot for the intake (shock-on-lip Mach 5.5) with a 28 degree spike termination angle at off-design condition Mach 6. 161

4.54 Polar plot for the intake (shock-on-lip Mach 5.5) with a 27 degree spike termination angle at off-design condition Mach 4. 162

4.55 Polar plot for the intake (shock-on-lip Mach 5.5) with a 27 degree spike termination angle at off-design condition Mach 6. 162

4.56 CFD Density contours from an inviscid simulation of the intake with a 29 degree spike term. angle and a 4 degrees cowl/centrebody angle at Mach 4. 163

4.57 CFD Density contours from an inviscid simulation of the intake with a 29 degree spike term. angle and a 7 degrees cowl/centrebody angle at Mach 5. 163

4.58 CFD Density contours from an inviscid simulation of the intake with a 27 degree spike term. angle and a 7 degrees cowl/centrebody angle at Mach 4. 164

4.59 CFD Density contours from an inviscid simulation of the intake with a 27 degree spike term. angle and a 12 degrees cowl/centrebody angle at Mach 6. 164

4.60 Comparison of surface pressure distribution for the spike termination angle $\theta_1 = 33$ and 29 degrees at Mach 4 to show the effect of reducing θ_1. 166

4.61 Comparison of surface pressure distribution for the spike termination angle $\theta_1 = 33$ and 27 degrees at Mach 6 to show the effect of reducing θ_1. 166

5.1 CFD Density contours from a laminar simulation of the intake (no cowl) at Mach 5.5; time-dependent contours from (a) to (c) to show laminar separation. 170

5.2 CFD Contours from a turbulent simulation of the intake (no cowl) at on-design Mach 5.5; (a) pressure contours and (b) density contours. . 171

5.3 Schematic of the inlet wave system and turbulent boundary-layer (no cowl) after the isentropic compression process on the forebody at Mach 5.5. 172

5.4 CFD Density contours from turbulent simulations of the intake (no cowl) at off-design Mach numbers (a) Mach 4 (b) Mach 5 and (c) Mach 6. 173

5.5 Surface pressure distribution of the intake (no cowl) at off-design Mach numbers (a) Mach 4 (b) Mach 5 and (c) Mach 6. 174

5.6 CFD Density contours from a turbulent simulation of the intake with a 12 degree cowl and centrebody angle at Mach 4; time-dependent contours from (a) to (h) to show boundary-layer separation on the centrebody. 176

5.7 Schematic to illustrate the flow phenomena in the vicinity of the reattachment region. The compression waves focus to form a reattachment shock. 177

5.8 Schematic to show the separation mechanism at inlet whereby the separation-induced shock wave reflects from the cowl inner surface to impinge onto the separated flow to drive the separation forwards. . . 179

5.9 CFD Contours from a turbulent simulation of the intake with a 33 degree spike termination angle and a 12 degree cowl and centrebody angle at Mach 4 with a modified cowl; (a) density contours; (b) Mach number contours. 180

5.10 Schematics to show the influence of the ratio of the boundary-layer thickness to the annulus height on the flow separation. (a) high ratio (b) low ratio. 181

5.11 CFD Density contours from a turbulent simulation of the intake with a 29 degrees spike termination angle a 12 degrees cowl and centrebody angle at Mach 4; time-dependent contours from (a) to (f). 183

5.12 CFD Contours from a turbulent simulation of the intake with a 27 degree spike termination angle and a 12 degree cowl/centrebody angle at Mach 4; (a) density contours; (b) Mach contours. 184

5.13 CFD Density contours from a turbulent simulation of the intake with a 27 degrees spike termination angle a 10 degrees cowl and centrebody angle at Mach 4; time-dependent contours from (a) to (f). 185

5.14 CFD Density contours from a turbulent simulation of the intake with a 27 degrees spike termination angle a 2 degrees cowl and centrebody angle at Mach 4; time-dependent contours from (a) to (f). 186

5.15 CFD Density contours from a turbulent simulation of the intake with a 12 degree cowl/centrebody angle at Mach 5; time-dependent contours from (a) to (h) to show boundary-layer separation on the centrebody. 189

5.16 CFD Density contours from a turbulent simulation of the intake with a 12 degree cowl and centrebody angle at Mach 5.5; time-dependent contours from (a) to (h) to show boundary-layer separation on the centrebody. 190

5.17 CFD Density contours from a turbulent simulation of the intake with a 12 degree cowl and centrebody angle at Mach 6; time-dependent contours from (a) to (h) to show boundary-layer separation on the centrebody. 191

5.18 CFD Density contours from turbulent simulations of the intake with a 12 degrees blunted cowl at off-design Mach 4. 193

5.19 CFD Density contours from turbulent simulations of the intake with a 12 degrees blunted cowl at off-design Mach 5. 193

5.20 Schematic of the intake geometry designed for shock-on-lip at Mach 5.5 with a backward-facing step on the centrebody and a thin-plate cowl. 194

5.21 CFD Density contours from a turbulent simulation of the intake with a backward-facing step (no cowl) at (a) Mach 4 (b) Mach 5 and (c) Mach 6. 196

5.22 Schematic of the flow phenomena in the intake with a backward-facing step and a thin-plate cowl, showing the cowl/step/boundary-layer flow system. 197

5.23 CFD Contours from a turbulent simulation of the intake with a 33 degree spike termination angle and a 12 degree cowl and centrebody angle with a backward-facing step at Mach 5.5; (a) density contours; (b) Mach number contours. 198

5.24 CFD Density contours from a turbulent simulation of the intake with a 12 degree cowl and backward-facing step on the centrebody at off-design Mach 4. 199

5.25 CFD Density contours from a turbulent simulation of the intake with a 12 degree cowl and backward-facing step on the centrebody at off-design Mach 5. 201

5.26 CFD Density contours from a turbulent simulation of the intake with a 12 degree cowl and backward-facing step on the centrebody at off-design Mach 6. 201

5.27 CFD Density contours from a turbulent simulation of the i1533 intake with a backward-facing step and blunted cowl at Mach 4. 204

5.28 CFD Density contours from turbulent simulations of the i1533 intake with a backward-facing step and blunted cowl at Mach 5. 205

5.29 CFD Density contours from turbulent simulations of the i1533 intake with a backward-facing step and blunted cowl at Mach 6. 206

5.30 Surface pressure distribution on the forebody versus x-distance for the i1533 intake with a backward-facing step at the three freestream conditions. 211

5.31 Centrebody and cowl inner surface pressure distribution; and 1D average pressure of the i1533 intake with a backward facing-step and at Mach 4. 211

5.32 Centrebody and cowl inner surface pressure distribution; and 1D average pressure of the i1533 intake with a backward facing-step and at Mach 5. 212

5.33 Centrebody and cowl inner surface pressure distribution; and 1D average pressure of the i1533 intake with a backward facing-step and at Mach 6. 212

5.34 Average pressure in the intake duct versus x-distance for the i1533 intake with a backward-facing step at the three freestream conditions. 213

5.35 Average Mach number in the intake duct versus x-distance for the i1533 intake with a backward-facing step at the three freestream conditions. 213

5.36 Total pressure efficiency in the intake duct versus x-distance for the i1533 intake with a backward-facing step at the three freestream conditions. 214

5.37 Kinetic energy efficiency in the intake duct versus x-distance for the i1533 intake with a backward-facing step at the three freestream conditions. 214

5.38 Pressure behind a normal shock in the duct versus x-distance for the i1533 intake with a backward-facing step at the three freestream conditions. 215

5.39 Mach number behind a normal shock in the duct versus x-distance for the i1533 intake with a backward-facing step at the three freestream conditions. 215

5.40 Exit pressure with a normal shock in the duct versus x-distance for the i1533 intake with a backward-facing step at freestream conditions. 216

5.41 Exit Mach number with a normal shock in the duct versus x-distance for the i1533 intake with a backward-facing step at freestream conditions. 216

5.42 Centrebody geometry definition for the i1533 and i1530 intakes. . . . 217

5.43 CFD Density contours from a turbulent simulation of the i1530 intake with a backward-facing step and blunted cowl at Mach 4. 218

5.44 CFD Density contours from turbulent simulations of the i1530 intake with a backward-facing step and blunted cowl at Mach 5. 219

5.45 CFD Density contours from turbulent simulations of the i1530 intake with a backward-facing step and blunted cowl at Mach 6. 220

5.46 Surface pressure distribution on the forebody versus intake x-distance for the i1530 intake with a backward-facing step at the three freestream conditions. 222

5.47 Centrebody and cowl inner surface pressure distribution; and 1D average pressure of the i1530 intake with a backward facing-step and at Mach 4. 222

5.48 Centrebody and cowl inner surface pressure distribution; and 1D average pressure of the i1530 intake with a backward facing-step and at Mach 5. 223

5.49 Centrebody and cowl inner surface pressure distribution; and 1D average pressure of the i1530 intake with a backward facing-step and at Mach 6.. 223

5.50 Average pressure in the intake duct versus x-distance for the i1530 intake with a backward-facing step at the three freestream conditions. 224

5.51 Average Mach number in the intake duct versus x-distance for the i1530 intake with a backward-facing step at the three freestream conditions. 224

5.52 Total pressure efficiency in the intake duct versus x-distance for the i1530 intake with a backward-facing step at the three freestream conditions. 225

5.53 Kinetic energy efficiency in the intake duct versus x-distance for the i1530 intake with a backward-facing step at the three freestream conditions. 225

5.54 Pressure behind a normal shock in the duct versus x-distance for the i1530 intake with a backward-facing step at freestream conditions. . . 226

5.55 Mach number behind a normal shock in the duct versus x-distance for the i1530 intake with a backward-facing step at freestream conditions. 226

5.56 Exit pressure with a normal shock in the duct versus x-distance for the i1530 intake with a backward-facing step at freestream conditions. 227

5.57 Exit Mach number with a normal shock in the duct versus x-distance for the i1530 intake with a backward-facing step at freestream conditions. 227

5.58 Performance map showing the compression ratio versus the total pressure efficiency for the i1533 and i1530 intakes at the three flight conditions (values taken at the start of the diffuser section). 228

5.59 Performance map showing the compression ratio versus the total pressure efficiency for the i1533 and i1530 intakes at the three flight conditions (values taken at the end of the diffuser section). 228

5.60 Performance map showing the compression ratio versus the kinetic energy efficiency for the i1533 and i1530 intakes at the three flight conditions (values taken at the start of the diffuser section). 229

5.61 Performance map showing the compression ratio versus the kinetic energy efficiency for the i1533 and i1530 intakes at the three flight conditions (values taken at the end of the diffuser section). 229

6.1 3D View of the Shyfe intake. 232

6.2 Schematic of hypersonic inlet flow after external compression showing the various flow-field characteristics present in the isolator section of the engine. 233

6.3 CFD Pressure contours to show the application of the back-pressure boundary condition on the intake to simulate combustion pressure rise; time-dependent contours from (top) to (bottom). 235

6.4 CFD Pressure contours from inviscid simulations of the intake (M_{sol} = 5.5) with a (a) 12 degrees and (b) 7 degrees cowl at off-design condition Mach 4. 236

6.5 CFD Density contours from inviscid simulations of the intake (M_{sol} = 5.5) with a centrebody and cowl angle of (a) 12 degrees and (b) 7 degrees; at off-design condition Mach 4 with an applied back pressure p_{comb}/p_{∞} of approximately 24. 238

6.6 CFD Mach number contours from an inviscid simulation of the intake (M_{sol} = 5.5) with a centrebody and cowl angle of 12 degrees at off-design condition Mach 4 with an applied back pressure p_{comb}/p_{∞} of approximately 41; time=4ms. 239

6.7 CFD Mach number contours from an inviscid simulation of the intake (M_{sol} = 5.5) with a centrebody and cowl angle of 7 degrees at off-design condition Mach 4 with an applied back pressure p_{comb}/p_{∞} of approximately 41; time=3.2 to 5.5ms. 240

6.8 CFD Mach number contours from an inviscid simulation of the intake (M_{sol} = 5.5) with a centrebody and cowl angle of 12 degrees at off-design condition Mach 6 with an applied back pressure p_{comb}/p_{∞} of approximately 47.2; time=3.2 to 5.5ms. 242

6.9 CFD Pressure contours from an inviscid simulation of the intake (M_{sol} = 5.5) with a centrebody and cowl angle of 12 degrees at Mach 6 (averaged inlet flow properties) with an applied back pressure p_{comb}/p_{∞} of approximately 47.2; time=5.5ms. 243

6.10 Comparison of the flow properties at the isolator exit for the intake (M_{sol} = 5.5) with a centrebody and cowl angle of 12 degrees at off-design condition Mach 6 with an applied back pressure p_{comb}/p_{∞} of approximately 47.2 for the 2D and averaged inlet flow properties case; (a) exit Mach number and (b) exit total pressure ratio. 244

6.11 Surface pressure distribution for the intake ($M_{sol} = 5.5$) with a centrebody and cowl angle of 7 degrees at off-design Mach 4 with an applied back pressure p_{comb}/p_∞ of approximately 41 at time intervals from time=2.9 to 5.5 ms. 245

6.12 Surface pressure distribution for the intake ($M_{sol} = 5.5$) with a centrebody and cowl angle of 12 degrees at off-design Mach 6 with an applied back pressure p_{comb}/p_∞ of approximately 47.2 at time intervals from time=0.16 to 1,0 ms. 245

6.13 CFD Density contours from an (a) inviscid simulation and (b) turbulent simulation of the intake ($M_{sol} = 5.5$) with a centrebody and cowl angle of 7 degrees at Mach 4 with an applied back pressure p_{comb}/p_∞ of approximately 41; time=0.30 ms. 246

A.1 Interaction of a shock wave with an expansion wave. 254

A.2 2D Drawing of the i1533 variant of the Shyfe intake from the apex to the combustor entry; and a close-up view of the blunted cowl geometry. 256

A.3 2D Drawing of the i1530 variant of the Shyfe intake from the apex to the combustor entry; and a close-up view of the blunted cowl geometry. 257

List of Tables

1.1 Aerodynamic design areas for the Shyfe vehicle program with specific analysis requirements for each area. This thesis work focuses on the intake system. 31

3.1 Transition parameters 95

3.2 Freestream conditions. 96

3.3 Comparison of shock angle, surface Mach number and surface pressure values from inviscid CFD simulations of a cone with a 10 degree semi-angle at Mach 5 for three mesh resolutions; compared with the Taylor-Maccoll analytical solution. 97

4.1 Test conditions for the Mach 4.8 intake. 116

4.2 Intake performance (M_{sol}=4.8): Values of cowl position, cowl/centrebody angles, total pressure efficiency, kinetic energy efficiency and mass capture ratio for the several configurations at the 3 flight conditions (inviscid values). 126

4.3 Test conditions for the Mach 5.5 intake. 130

4.4 Intake performance (M_{sol}=5.5): Values of cowl position, cowl/centrebody angle, total pressure efficiency, kinetic energy efficiency and mass capture ratio for the several configurations at 4 flight conditions (inviscid values). 137

4.5 Intake performance (M_{sol}=5.5): Values of cowl position, cowl angle, total pressure efficiency, kinetic energy efficiency and mass capture ratio for the intake with 12 and 7 degrees cowl angles at Mach 4 (inviscid values). 158

4.6 Values of spike termination angle, cowl/centrebody angle, mass capture ratio, kinetic energy efficiency and total pressure efficiency for intake configurations with reduced spike termination angles at 3 flight conditions (inviscid values). 167

5.1 Test conditions for the i1533 and i1530 intake. 203

5.2 Intake performance (M_{sol}=5.5): Values of freestream Mach number, cowl position, spike termination angle, cowl angle, total pressure efficiency, kinetic energy efficiency, mass capture ratio and compression ratio for the i1533 and i1530 intakes. (values taken at the start of the diffuser section). 230

5.3 Intake performance (M_{sol}=5.5): Values of freestream Mach number, cowl position, spike termination angle, cowl angle, total pressure efficiency, kinetic energy efficiency and compression ratio for the i1533 and i1530 intakes. (values taken at the end of the diffuser section). . . 230

6.1 Freestream conditions for the intake (shock-on-lip at Mach 5.5) at the three flight conditions showing the level of back pressure required in each case. 234

Chapter 1

Introduction

1.1 Hypersonic flight

The development of aircraft capable of flying at hypersonic speeds has generated much research interest within the aeronautical field. Research into hypersonics contributes to the understanding of flow phenomena in the aerospace environment, the design of hypersonic systems and eventually the realisation of next-generation aerospace technologies. The engineering challenges in designing a hypersonic vehicle require in-depth research in areas such as high-speed aerodynamics. As the Mach number increases, several new flow phenomena appear like strong shocks and real gas effects - a deeper understanding of which will aid the development of hypersonic technology. Supersonic combustion and high-temperature material science are other areas of interest. Some potential applications of hypersonic technology include future transportation systems, re-usable launch vehicles and high-speed missiles.

Engineering a practical propulsion system for flight at hypersonic speeds is one of the key technical challenges. Rocket propulsion is the conventional choice due to its technical simplicity in that all combustion reactants are carried on-board the vehicle and are unaffected by atmospheric conditions. In contrast to rockets, air-breathing propulsion systems sustain combustion using oxygen from the atmosphere and hence require a high-speed intake system. Although this is a complex technology to develop, it offers the prospect of improved efficiency and a lower vehicle

takeoff weight. Evaluation studies of advanced vehicle concepts have shown that air-breathing systems also improve mission flexibility, design robustness, reliability and safety.[38] Nonetheless, considerable advancement of air-breathing propulsion technology is required before it can find a use in hypersonic flight.

Several classes of hypersonic air-breathing propulsion systems have been proposed. Ramjets and scramjets are the simplest types in this category of propulsion system. Both types of engines dispense with the use of mechanical compression, taking advantage of the ram effect at high-speeds. The incoming air flow is compressed through a wave system in an engine/airframe integration process. For low flight Mach numbers, typically in the range Mach 3-5, the ramjet cycle is preferable in which the incoming flow is decelerated by the intake to subsonic conditions for combustion. Ramjet technology is well developed for flight speeds around Mach 3 with its main use in missile propulsion. For flight Mach numbers above 5, it becomes increasingly inefficient to decelerate the flow to subsonic conditions due to the high-temperatures and associated internal losses, and the flow speeds throughout the engine are kept supersonic in a scramjet - supersonic combustion ramjet. The high temperatures and pressures make the structural design of the engine exceedingly difficult. Moreover, both ramjet and scramjet engines produce no static thrust and therefore need an auxiliary propulsion system to propel them to the required speed for self-sustaining flight. In a scramjet engine, the main design problems include the efficient mixing of the fuel-air mixture and a stable supersonic combustion process. In the dual-mode concept the engine is capable of making the transition from ramjet to scramjet mode for flight over a range of Mach numbers. Even more complex systems have been proposed including combinations of the various engines such as the rocket-based combined cycle (RBCC) and the turbine-based combined cycle (TBCC) concepts which use an auxiliary propulsion system in the form of a turbojet engine or rocket to propel the vehicle to the ramjet takeover speed[79] around Mach 3. Such advanced vehicle concepts propose a conventional airfield take-off with a high-altitude cruise at hypersonic speeds, and even propose flight into orbit in a single-stage (SSTO). To reach orbital speed (Mach 25) the vehicle would require an additional rocket system for propulsion in the space environment. To date, few

hypersonic programmes have demonstrated flight with the use of an air-breathing system. Recently, the Hyper-X Program at NASA successfully launched the X-43 experimental vehicle for two 10-second flights at Mach 7 and 10 powered by scramjet technology.

Sustained Hypersonic Flight Experiment

The Sustained Hypersonic Flight Experiment (Shyfe) is a research and development program in the United Kingdom. The objective is to design and test a prototype vehicle capable of a sustained hypersonic flight. A brief technical overview of the programme has been published by Cain and Walton.[108]

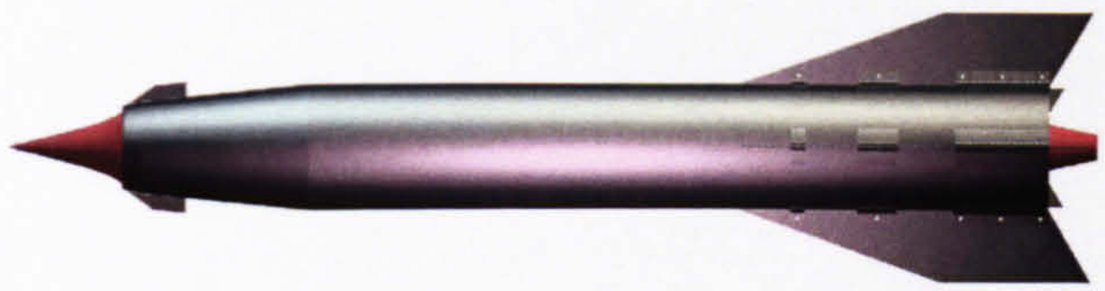


Figure 1.1: Conceptual picture of The Sustained Hypersonic Flight Experiment vehicle (side view). Copyright QinetiQ Ltd. Published with permission.

Intake	**Combustion**	**Nozzle**	**Externals**
Shock systems	Fuel injection	Exhaust flow	Shock interactions
Viscous effects	Fuel/air mixing	Plume analysis	Surface pressure
Isolator design	Combustion analysis		Heat transfer
Performance/drag	Thermal management		Incidence effects
Incidence effects			

Table 1.1: Aerodynamic design areas for the Shyfe vehicle program with specific analysis requirements for each area. This thesis work focuses on the intake system.

Cain makes an analysis of the various design configurations for a hypersonic vehicle, assessing that the optimum aerodynamic form for a hypersonic cruise vehicle with mass less than about 1 tonne is that of the conventional missile. Figure 1.1 presents a conceptual design of the Shyfe vehicle. The 1.5m long, 30kg test vehicle will be

boosted by a rocket to Mach 4 and 15km and will accelerate and climb under its own power to Mach 6 and 32km. The vehicle will cruise for 100 seconds at Mach 6 covering a range of 300km. The focus of the Shyfe experiment will be in achieving a steady-state hypersonic cruise at Mach 6 with vehicle forces and temperatures in equilibrium. New materials have allowed for the choice of a conventional ramjet cycle with subsonic combustion (combustor Mach number 0.1). The prototype will be constructed from C/SiC a ceramic matrix composite (CMC) material. The use of carbon-fibre-reinforced silicon carbide is desirable due to its ability to withstand the high-temperature hypersonic environment with the additional advantages of saving weight and improving performance. The material combines carbon fibres within a ceramic matrix and can withstand surface temperatures of up to 2200 K. The calculated stagnation temperatures reach 1600 K at Mach 6 and so heat transfer is not a major concern. Above 800 K, the vibrational energy of the molecules becomes important, however this is not a chemically reacting process but rather an alteration of some of the gas properties occurs. Above 2500 K the chemically reacting effects of high temperatures become significant. For the Shyfe vehicle operating conditions it is sufficient to treat the flow as an ideal gas.

The main aerodynamic design areas in the Shyfe programme are: intake, combustion, nozzle and external aerodynamics, presented in Table 1.1. A study of the intake system requires both experimental and numerical investigations on the shock-wave interactions and viscous effects that control the intake flow. These complex flows have a significant influence on the performance of the vehicle and a detailed analysis is required to understand these flow-field characteristics which are as yet not fully understood for flight in the hypersonic Mach number range. Another important consideration is the design of the isolator, which is a component of a ramjet or scramjet that is placed between the inlet and combustor with the purpose of isolating disturbances caused in combustion from propagating to the intake. The isolator also contains the shock system to decelerate the flow from supersonic to subsonic speeds in the ramjet. Detailed performance and drag assessment is required for the range of flight conditions from Mach 4 to 6. Angle-of-attack flows are also important as the vehicle will cruise at Mach 6 with a small incidence to maximise the lift/drag

ratio. Research is also required into the combustion system, particularly for the design of the fuel injection system and flow analysis for the fuel/air mixing processes. An important design aspect of the combustion system is the management of the high-temperatures that are generated during its operation. The final component that requires analysis is the propulsion nozzle. Data is also required for the external aerodynamics of the vehicle with a main concern being the interaction of shocks and boundary-layers on the vehicle surface. Incidence effects will also be investigated in this category, along with surface pressure and heat transfer. Several university and industry partners are collaborating on various aspects of vehicle design and development. This thesis work focuses on the intake aerodynamics of the Shyfe vehicle and carries out an in-depth numerical analysis of the flow-field characteristics.

1.2 Thesis objectives

The intake of a hypersonic propulsion system has an essential role in the engine cycle and its efficiency is directly related to the overall engine efficiency. Specifically, the intake flow field can influence the compression efficiency, combustion stability and external drag of the hypersonic vehicle, hence thrust and sustained flight. In investigating hypersonic flows for air-breathing propulsion, wind tunnel testing is highly expensive due to the numerous variables that intake flow is dependent on, e.g: intake geometry and flight conditions, and it may not always be able to duplicate required test conditions easily (e.g. M_∞, $Re_{x\infty}$, T_∞). CFD can be effectively used to investigate and form an understanding of complex flow phenomena, with perhaps its greatest advantage in its use to analyse internal flow fields. CFD can be used to predict and solve many of the flow problem areas and knowledge obtained can be used as guidelines for experimental research. Numerical simulations also have the added advantage of solving for the entire flow field, whereas in experimental flow visualisation, the flow field captured is restricted by the model design, hence making it difficult to analyse the internal flow. This thesis focuses on the investigation of the intake flow using numerical methods and knowledge gained from this work has contributed to the design of the Shyfe intake. The overall aim is to present an

analysis of the intake flow characteristics with a focus on efficient shock compression methods. The specific aims of this research are to present numerical simulations of the Shyfe intake at the range of Mach numbers which will be supported by theoretical analysis. The Shyfe geometry is a fixed-geometry intake where off-design performance is critical, and a particular focus of this work is on the intake flow characteristics at off-design conditions. Detailed analysis of the complex shock wave systems and interactions at the inlet are presented which allows the assessment of the intake performance for various configurations. This leads to the study of the effects of small changes in intake geometry and angles on the flow-field characteristics and performance. This research also extends to study the intake with a simulated combustion pressure rise to study inlet-isolator interaction.

Thesis layout

The layout of the thesis is as follows: The literature and supporting theory is presented in Chapter 2 with a review of research carried out in the field. Chapter 3 presents the numerical methods used in this research. Chapter 3 also presents the Shyfe intake geometry definition and a mesh convergence study to support the CFD simulations. Chapter 4 presents an inviscid analysis of the intake flow with a focus on the wave systems and their influence on intake performance. It is important to present inviscid cases first, so as to start with an explanation of the core inviscid flow-field without the added complexity of viscous effects. Chapter 5 presents a viscous flow analysis with an investigation of the flow separation and separation control, and a performance analysis for the final intake variants from the Shyfe Phase 1 programme[1]. The CFD cases presented in the preceding chapters model the intake flow with a supersonic outflow. Chapter 6 will present test cases of the intake flow with a simulated combustion pressure rise to investigate inlet-isolator interaction. Finally, Chapter 7 presents the conclusions from this research.

[1]The Shyfe Phase 1 programme from 2002-2004 was the initial research programme for the Shyfe vehicle. The Shyfe Phase 2 programme was started in 2005 and is currently in progress.

Chapter 2

Literature review

2.1 Ramjet/scramjet propulsion

The three main processes in the air-breathing engine cycle are compression, combustion and expansion. In a simple turbojet engine, the compression of the incoming air to suitable conditions for combustion is achieved through intake plus mechanical compressors. Fuel is then added for combustion to take place and the resultant hot gases are expanded through a turbine to produce thrust. Due to the limitations in turbine inlet temperatures, the turbojet engine cannot exceed speeds greater than about Mach 3. At these speeds, the compression process no longer requires mechanical compression and a ram compression of the intake air is feasible. The intake of a ramjet/scramjet engine then functions as the compressor by taking in air at a high Mach number and converting it to a lower Mach number and higher pressure by processing it through a series of compression (isentropic or shock) waves.

The intake of an air-breathing engine has a critical role in providing optimum pressure recovery and ensuring stable combustion in the engine. Figure 2.1 presents a schematic of a conventional ramjet engine with component station points (from a design by Oswatitsch, 1944). In the ramjet cycle, the incoming flow is compressed from point 1 (freestream) to point 2 by either an external or internal process in the intake. The flow is then decelerated to subsonic conditions in the isolator through a normal shock system and then diffused to maximise pressure recovery. Fuel is

injected and combustion takes place at subsonic speeds. The flow is then expanded and accelerated in a propulsion nozzle to exit at point 5. The scramjet undergoes a similar process, but after the flow is compressed in the intake, the flow speeds are kept supersonic throughout the engine. The combustion process in a scramjet takes place at supersonic speeds and the flow is further expanded to generate thrust.

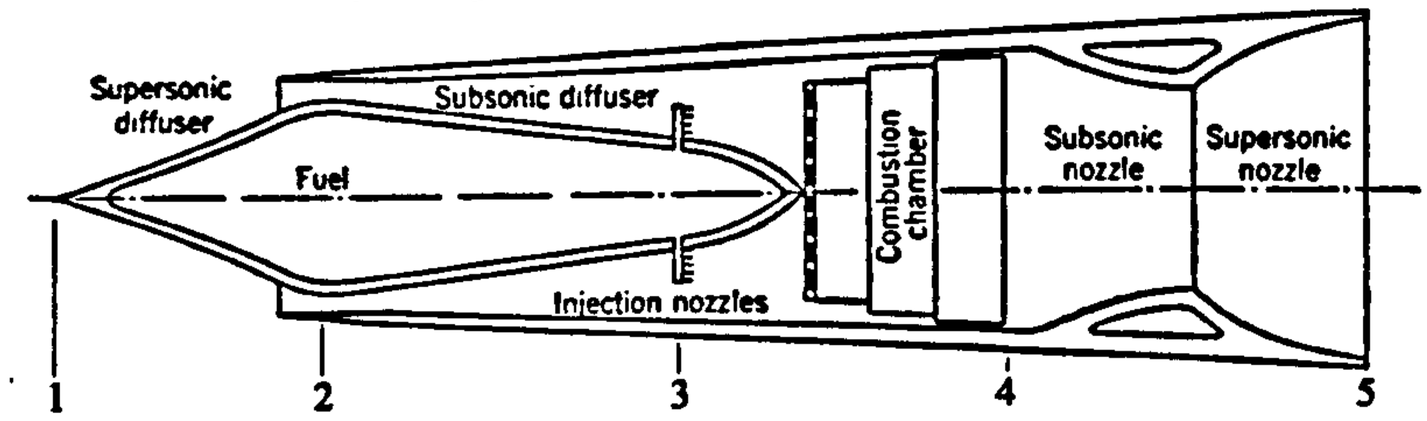


Figure 2.1: Conventional ramjet engine components (Oswatitsch 1944[22]).

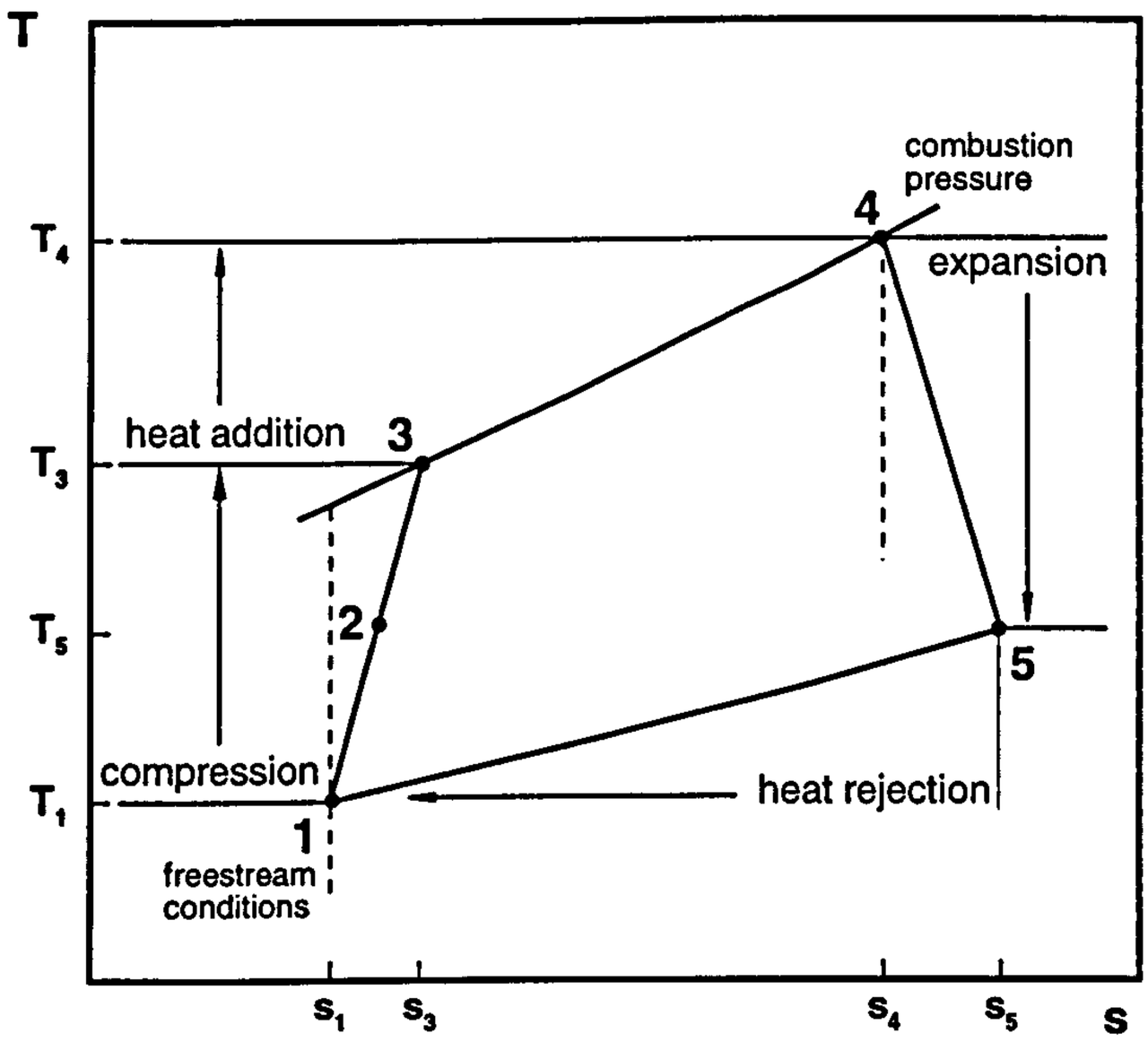


Figure 2.2: Temperature-entropy diagram of an air-breathing engine cycle, or Brayton cycle with corresponding component station points to Figure 2.1.[115]

Weber and MacKay[95] compared the scramjet engine to the conventional ramjet and concluded that a scramjet engine with a wedge inlet proved more efficient than a

conventional ramjet above Mach 5. With an isentropic compression inlet a scramjet was found to be more efficient than the ramjet above Mach 7.

The air-breathing engine cycle, or *Brayton cycle*, defines the processes through which an air-breathing engine produces thrust. The engine cycle consists of four main stages which are illustrated on a 'T-s' temperature-entropy diagram in Figure 2.2. Point 1 to Point 3 indicates the compression process from the freestream static temperature T_1 to the combustor entry static temperature T_3. In a conventional ramjet, this process decelerates the flow to subsonic conditions. Point 3 to Point 4 indicates the constant static pressure combustion process from the entry static temperature T_3 to the exit static temperature T_4. Point 4 to Point 5 indicates the expansion process from the combustor to the nozzle exit conditions at Point 5. The change in entropy from s_4 to s_5 indicates losses from shock waves and skin friction. Point 5 to Point 1 is the imaginary rejection of heat from the exhaust air back to freestream conditions.

2.1.1 Intake configuration

The simplest design for a high-speed intake is a basic duct which when placed in a supersonic stream forms a normal shock upstream of the cowl to transition the incoming flow from supersonic to subsonic conditions. Calculating the conditions downstream of a normal shock for a range of Mach numbers reveals the rapid deterioration of pressure recovery from transonic to low supersonic speeds. To put this in perspective, if a flow at Mach 5 is decelerated purely by a single normal shock, the total pressure recovery is only 6.17 percent. Since the exit flow in a ramjet intake must be subsonic, a normal shock will be required at some position in the duct.

Oswatitsch (1944) first came up with a theory of a supersonic external compression in stages. The principle theory is based on dividing the shock compression process into stages to reduce the eventual Mach number at the normal shock, hence minimising pressure loss. The two-shock intake is the simplest type of staged compression process, where a simple wedge or cone is placed in front of the duct to generate an oblique shock and then a normal shock at the inlet. Figure 2.3 (a). For a given

apex angle, the wedge shock is stronger than a conical shock, but the conical shock is followed by an isentropic compression, and is therefore more efficient. The stages can be further broken down into two oblique shocks and a normal shock in a three-shock intake, Figure 2.3 (b). Even two- and three-shock intakes are only reasonably efficient at low supersonic Mach numbers. This principle can be extended to any number of oblique shock waves generated on an external surface and leads to the concept of continuous isentropic compression. This is a process where a contoured forebody generates an isentropic compression fan. Theoretically, no loss in total pressure should be incurred through this type of compression process.

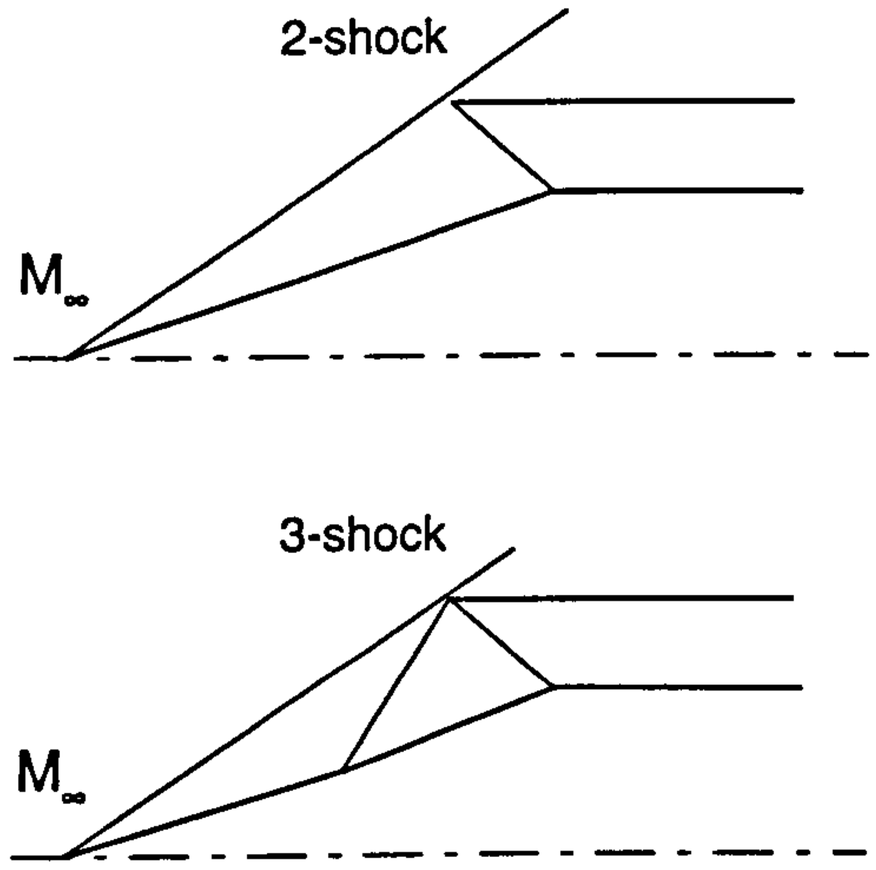


Figure 2.3: (a) 2-shock and (b) 3-shock external compression intakes.

Figure 2.4 shows a schematic of an external isentropic compression process where P is the point of intersection of the shock wave and the compression fan. For optimum pressure recovery, the cowl lip is placed at point P, a configuration known as the *shock-on-lip* condition. For all other conditions, the intake is said to be *off-design.* The angle δ_c defines the cowl leading edge angle. Previous studies on hypersonic intakes have shown that the angle δ_c is one of the most important design parameters. High external drag can be incurred by a large value for the angle δ_c. This type of supersonic compression of the flow by the forebody, does result in the flow being turned away from the engine axis, and therefore needs to be turned back to the axial

direction in the intake duct. These turning angles can be very large when designing an efficient compression surface. Figure 2.4 also illustrates a close-up view of the wave system with no cowl, showing the compression wave focusing to a point and meeting the apex shock wave to form a reflected shock. At this point, a vortex sheet arises and a reflected wave forms. The vortex sheet is positioned such that the pressure and flow direction are the same on either side of it. The cowl lip is usually placed just below point P, to ensure that the vortex sheet does not enter the intake. These flow features then become very important at off-design conditions where the point P moves position depending on the freestream Mach number.

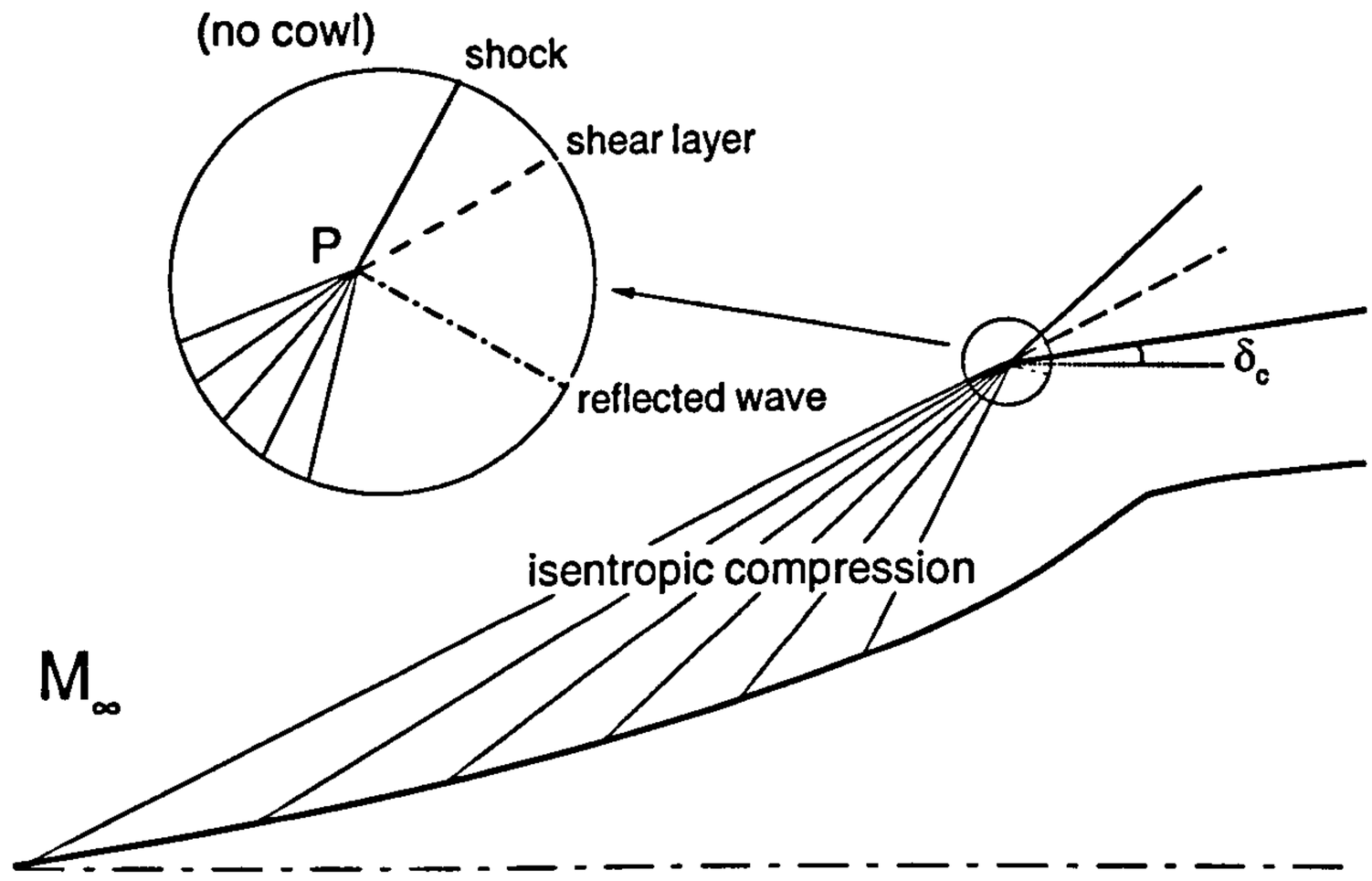


Figure 2.4: Ideal inlet-cowl configuration for an external compression intake and a close-up view of the wave system after isentropic compression on the forebody.

The isentropic compression process is similar to a reversed Prandtl-Meyer expansion flow. However, in reality, the leading edge of an intake forebody will have a finite thickness or angle, and therefore a shock of some strength will be generated from it. Connors and Meyer[58] calculated profiles on this basis and tabulated the results up to Mach 4.0. Connors' calculations[58] assume a one per cent loss in total pressure from this initial shock wave.

As mentioned earlier, this type of external compression results in the flow turning away from the engine axis, and then requiring to turn back into the axial direction. Isentropic compression methods can use fairly large angles, and Seddon[58] shows

the total turning angles for optimum multi-shock systems, and for the isentropic compression case, Figure 2.5. The final compression ratio relies on the final total turning angle of the flow, but in practice using large flow turning angles can lead to a strong shock-expansion interaction at the turning corner, and can also result in flow separation. Some intake designs keep the total turning angle lower and continue the isentropic compression process once the system has reflected from the cowl inner surface, such as the Hypersonic Research Engine (HRE) intake, shown in Figure 2.6. This avoids the focus of the wave system from entering the cowl to trigger flow instabilities, and keeps the final turning angle low to deter strong shock interactions and flow separation at the inlet annulus.

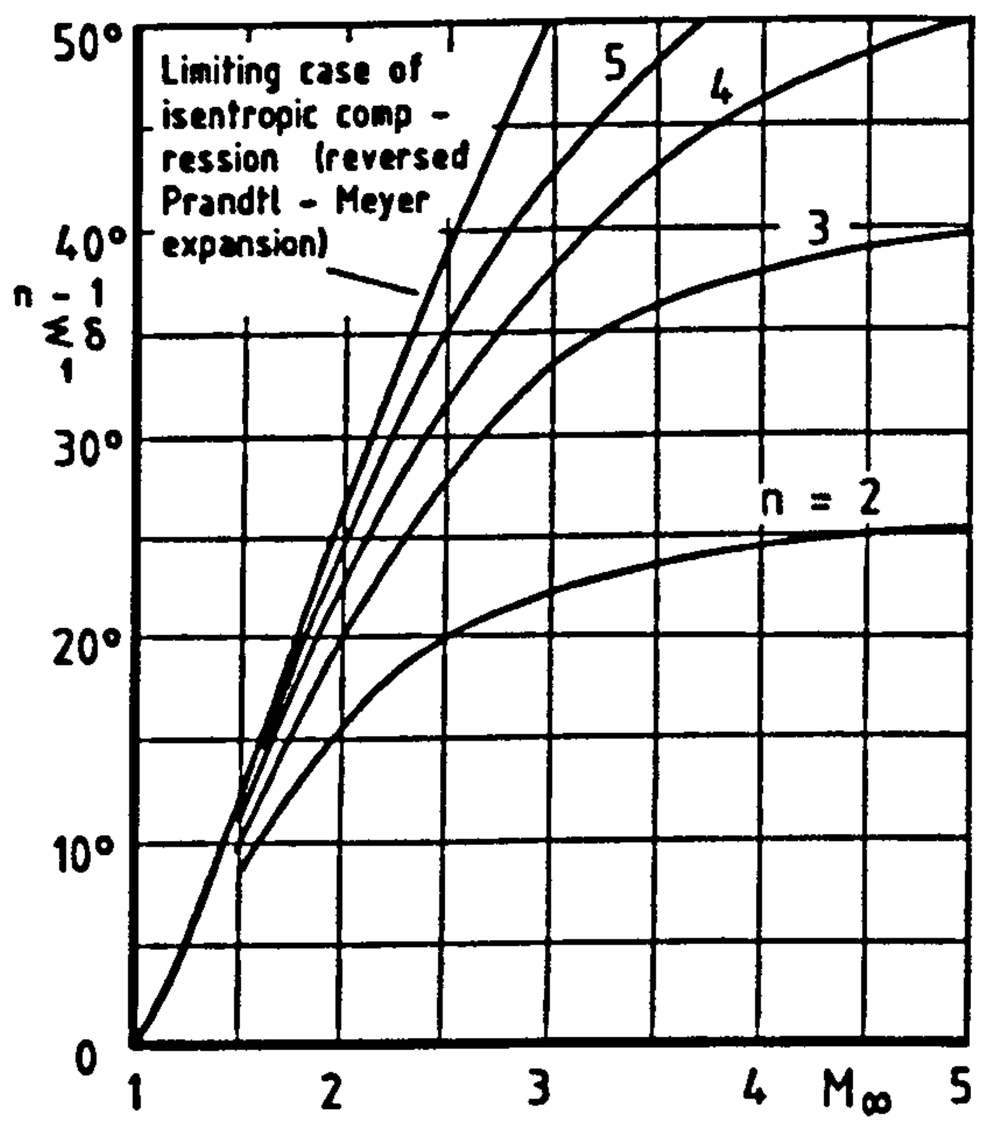


Figure 2.5: Total flow turning angle for optimum two-dimensional shocks (Seddon[58]).

Engine/Airframe integration

The previous discussion on staging a supersonic compression was specific to external compression type, or Oswatitsch intakes. Intakes can also achieve a staged compression process using an internal compression. The Busemann intake is an example of an internal compression design. Modular Busemann intakes, or waverider intakes, also stage compression using a complex design, as shown in Figure 2.6. The intake

of a hypersonic vehicle can generally either be of the axisymmetric type or can be designed as a two-dimensional sidewall compression intake, as shown in Figure 2.6. The sidewall compression intake can be installed on the underside of a hypersonic vehicle, as shown in Figure 2.7 such that the underside surface of the vehicle forebody then acts as part of the intake component by generating the shock waves required for compression. The aft section of the undersurface aids the expansion process.

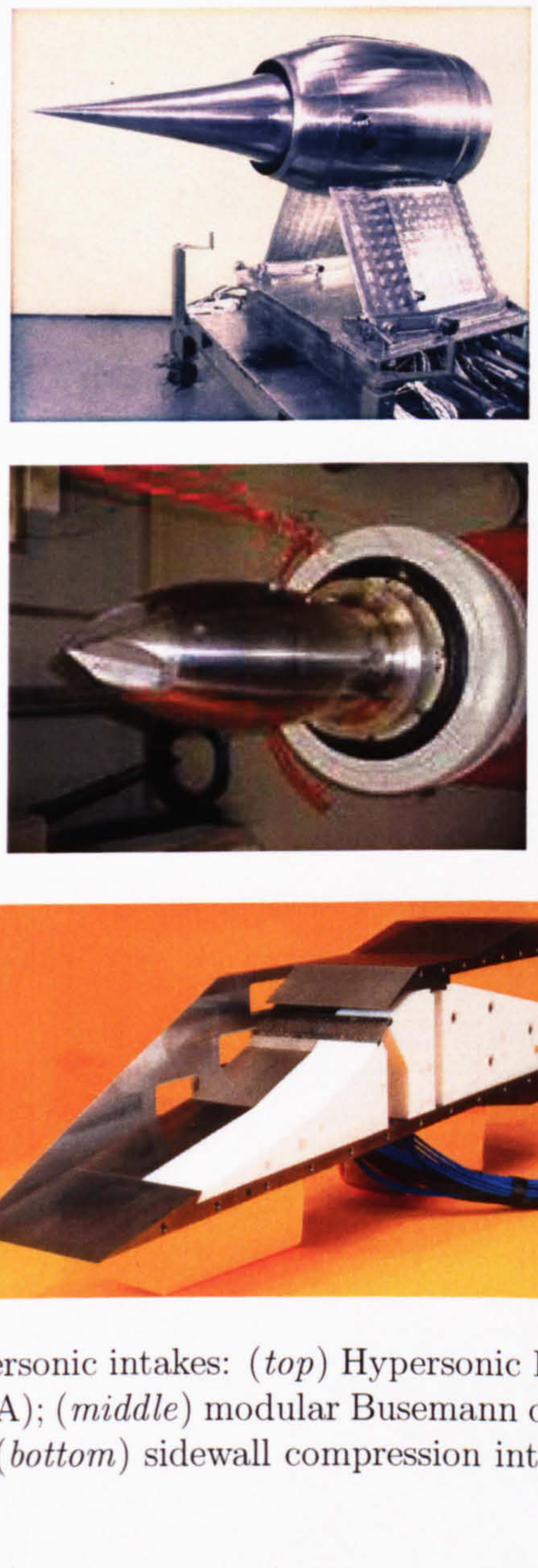


Figure 2.6: Types of hypersonic intakes: (*top*) Hypersonic Research Engine external compression intake (NASA); (*middle*) modular Busemann or waverider intake model (QinetiQ scramjet); and (*bottom*) sidewall compression intake model (DLR).

Multiple engines using sidewall compression type intakes can be installed on the vehicle alongside each other, such as on NASA's X-43 hypersonic vehicle. For a small-scale flight demonstrator or missile, an axisymmetric type intake is generally

preferred. Shock/boundary-layer interactions in a sidewall compression intake can lead to complex corner flows and side effects which are highly three-dimensional and can lead to non-uniform exit flow. Molder et al[85] compared the planar-type Prandtl-Meyer intake with the axisymmetric isentropic type intake and concluded a better overall performance for the axisymmetric designs.

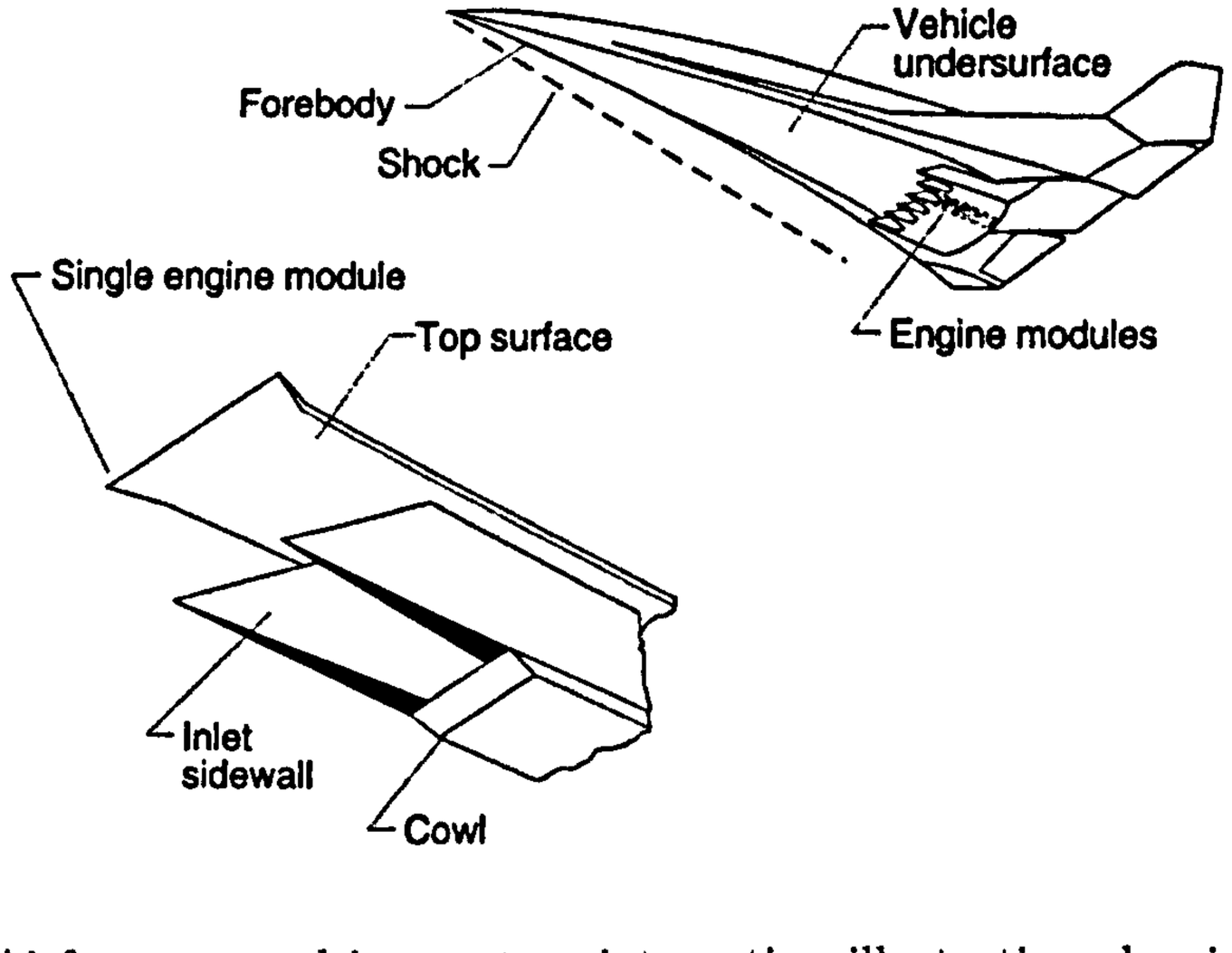


Figure 2.7: Airframe-propulsion system integration illustration showing an engine module that can be installed on the vehicle undersurface (Anderson et al.[9]).

Fixed/Variable geometry

The shock-on-lip condition, or on-design condition, is the optimum configuration for an intake where the apex shock and compression waves focus to the cowl lip. A fixed geometry intake is designed to function at on-design conditions at a specific design Mach number. As the Mach number falls below or above these conditions, the intake is said to operate at off-design conditions.

Efficient off-design operation of a fixed geometry intake is critical to the performance of a vehicle designed to function over a range of flight conditions. A variable geometry design can also be used by translating the centrebody spike to give the required throat area for intake starting and then varying the spike position to give optimum mass capture and contraction ratio over a range of flight conditions.

Variable geometry intakes require complex mechanical arrangement which makes the use of a fixed-geometry intake preferable for the design of small-scale demonstrators and missiles. NASA's Hypersonic Research Engine intake is an example of a variable geometry intake where the spike translates to provide near on-design operation from Mach 4 to 7.

2.1.2 Intake performance

As guided from the literature available, when assessing intakes one measures both the intake capability and the intake efficiency. When assessing intake capability, the compression ratio p_2/p_1 or the contraction ratio A_1/A_2 are generally used. In terms of the intake efficiency, a few of the key performance parameters that are pertinent to the present study are discussed in the following section.

Seddon[58] states that the loss of total pressure in the intake is translatable directly to a loss in engine thrust and can be related by Equation 2.1. X is thrust and K is a factor dependent on engine type that is greater than unity and closer to 1.5.

$$\frac{\Delta X}{X} = K.\frac{\Delta P}{P_\infty} \tag{2.1}$$

Wyatt[25] stated that the thrust of an air-breathing engine can be shown to be doubly dependent on the pressure recovery delivered by the air intake system. The mass flow ingested by the engine is directly proportional to the total pressure at the frontal area of the engine. The jet nozzle pressure, and hence jet thrust per unit of mass flow, is also proportional to the frontal engine pressure.

Thus, for each 1 percent loss in total pressure in the air intake system, there will be somewhat more than a 1 percent loss in the engine thrust, as stated by Wyatt.[25] This makes it evident that the total pressure losses in the engine must be kept to a minimum or else a large part of the thrust will be dissipated.

Total pressure efficiency

The total pressure efficiency is defined as the total pressure at the intake exit to the total pressure of the freestream, as shown in Equation 2.2.

$$\eta_{pr} = \frac{p_{03}}{p_{0\infty}} = \frac{(1+\frac{\gamma-1}{2}M_3^2)^{\frac{\gamma}{\gamma-1}}}{(1+\frac{\gamma-1}{2}M_\infty^2)^{\frac{\gamma}{\gamma-1}}}.\frac{p_3}{p_\infty} \tag{2.2}$$

The main contribution to the loss in total pressure is from shock waves in the intake flow-field. Total pressure losses can also occur from the friction on the walls of the intake duct both on the centrebody and on the cowl inner surface wall. Viscous or turbulent mixing, especially if it is associated with flow separation can also lead to total pressure losses in an intake. In hypersonic intakes, flow separation would take a severe form with the interaction of a boundary-layer and a shock wave.

Kinetic energy efficiency

Kinetic energy efficiency is defined as the ratio of the kinetic energy recovered by the intake at the end of the compression process, to the total kinetic energy available in the freestream, as shown in Equation 2.3 (conservation of mass requires that $m_\infty = m_3 = m_{3'}$). To calculate kinetic energy efficiency, the flow at the diffuser exit is expanded isentropically to freestream static pressure (condition 3').

$$\eta_{ke} = \frac{\frac{1}{2}m_{3'}U_{3'}^2}{\frac{1}{2}m_\infty U_\infty^2} = \frac{U_{3'}^2}{U_\infty^2} \tag{2.3}$$

Mahoney[66] derives the relationship between kinetic energy efficiency and total pressure recovery in an intake, which is given in Equation 2.4.

$$\eta_{ke} = 1 - \frac{5}{M_\infty^2}\left[\left(\frac{p_{0\infty}}{p_{03}}\right)^{\frac{1}{3.5}} - 1\right] \tag{2.4}$$

Mass capture ratio (MCR)

Mass capture ratio is a measure of the mass captured by the intake. At the shock-on-lip condition, the mass capture ratio is 1. If a fixed-geometry intake operates below the shock-on-lip Mach number, spillage of mass will occur. Figure 2.8 illustrates the mass capture spillage and intake area definitions. Mass is captured for all streamlines in A_2 and mass spillage will occur above this point. A_1 defines the area from the cowl lip to the axis of rotation. An intake operating at the shock-on-lip condition will capture all the mass within A_1. A_3 is the area from the cowl lip to the centrebody at that point and A_4 is the area at the intake throat. A_3/A_4 is defined as the contraction ratio. The contraction ratio is an essential design parameter in the intake as it can determine the self-starting characteristics (discussed in Section 2.1.3).

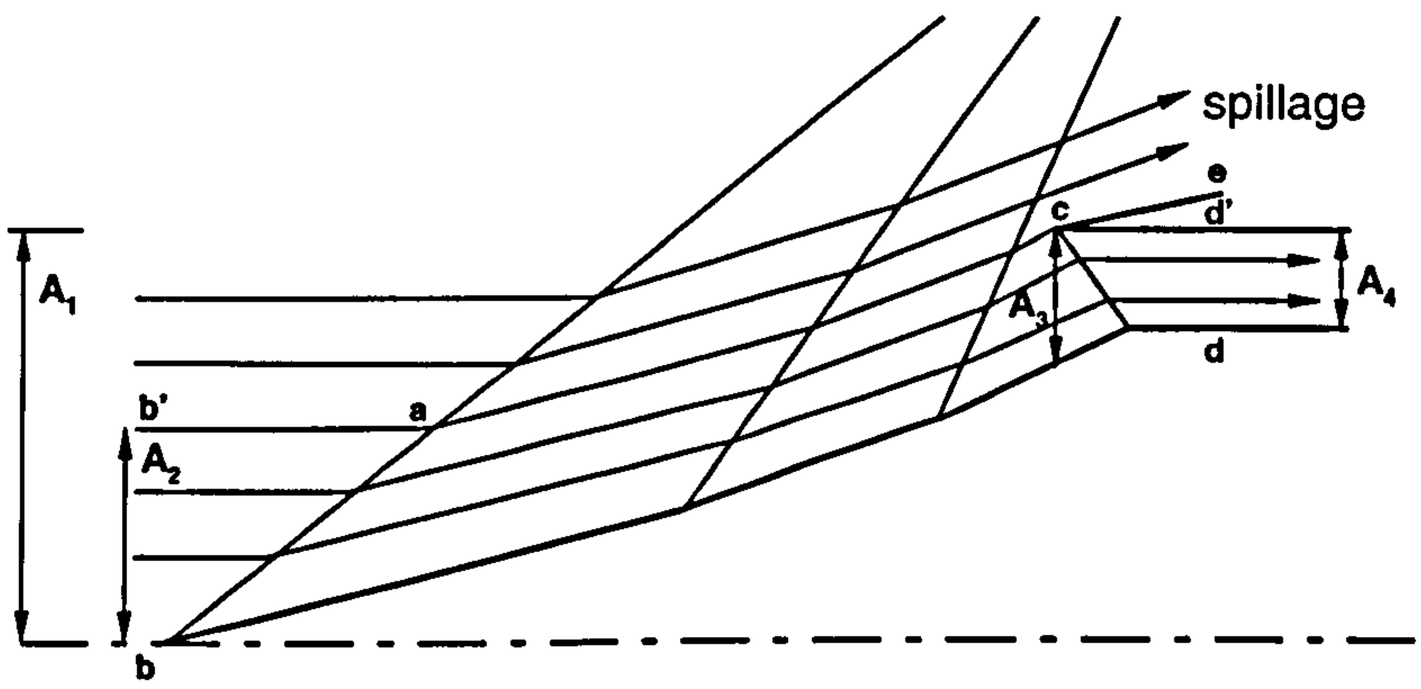


Figure 2.8: Area definitions and mass capture spillage.

The mass capture ratio is given by:

$$MCR = \frac{\dot{m}_2}{\dot{m}_1} \tag{2.5}$$

thus, defined as the ratio of the mass captured in A_2 divided by that captured in A_1, Equation 2.5. Mass spillage (i.e. MCR < 1.0) is undesirable for high-altitude low-density operation and during vehicle acceleration when high mass capture of the flow is required. For certain flight conditions however, mass spillage is required for intake starting and this can lead to an additional drag on the intake (also called additive drag or pre-entry drag) which will be defined in the next section.

Intake drag

An assessment must be made of the drag forces on an intake which act in the axial direction and directly reduce the engine thrust The drag coefficient C_d is given in Equation 2.6 where D is the drag force; q_∞ is the freestream dynamic pressure; and A_1 is the reference area as defined in Figure 2.8.

$$C_d = \frac{D}{q_\infty A_1} = \frac{D}{\frac{\gamma}{2} P_\infty M_\infty^2 A_1} \tag{2.6}$$

The drag coefficient can be spilt into the drag coefficient for the forces on the intake surfaces $C_{d_{intake}}$ and the drag coefficient for the additive drag $C_{d_{add}}$ (Van Wie[112]).

$$C_{d_{add}} = \int_a^c (P - P_\infty) dA_y \tag{2.7}$$

$$C_{d_{intake}} = \int_b^d P dA_y + \int_b^d \tau dA_x + \int_c^{d'} P dA_y + \int_c^{d'} \tau dA_x \tag{2.8}$$

where dA_x and dA_y are the axial and vertical surface area projections. A cowl drag coefficient can also be defined as (Van Wie[112]):

$$C_{d_{cowl}} = \frac{\int_c^e P dA_y + \int_c^e \tau dA_x}{q_\infty A_1} \tag{2.9}$$

The area definitions and reference stations are given in Figure 2.8.

2.1.3 Self-starting

As an engine is accelerated from subsonic to supersonic speeds, a shock wave forms at the inlet, and a *self-starting* intake is one that is able to swallow this shock system and operate in supersonic conditions without unstarting. An *intake unstart* is a result of the shock system in the intake duct propagating upstream from the throat and spilling out of the inlet. The flow experiences a sudden increase in static pressure upstream of the cowl leading edge surface.

Once an intake is started it can be unstarted by (1) the separation of the flow at inlet; or (2) a high level of back pressuring from the combustion chamber which can cause the terminal shock system to propagate forwards into the duct and out of the intake. Flow separation can occur either if the intake contraction is too great or from shock/boundary-layer interactions in the intake flow. Research has found that intake starting is dependent on the local Mach number, contraction ratio and diffuser pressure recovery.[112] An initial estimation of the required contraction ratio for a self-starting intake can be made using the one-dimensional Kantrowitz-Donaldson limit (1945) which assumes a normal shock at the start of the intake contraction and calculates the area ratio required to produce sonic conditions at the throat, as shown in Equation 2.10 (after Van Wie[112]). The area ratios are shown in Figure 2.8. For more complicated geometries, data obtained from experiments are generally used as guidelines for the required intake contraction ratios.

$$\left[\frac{A_3}{A_4}\right] = \frac{1}{M_3}\left[\frac{(\gamma+1)M_3^2}{(\gamma-1)M_3^2+2}\right]^{\frac{\gamma}{\gamma-1}}\left[\frac{\gamma+1}{2\gamma M_3^2-(\gamma-1)}\right]^{\frac{1}{\gamma-1}}\left[\frac{1+\gamma-\frac{1}{2}M_3^2}{\gamma+\frac{1}{2}}\right]^{\frac{\gamma+1}{2(\gamma-1)}} \tag{2.10}$$

2.2 Intake flow characteristics

2.2.1 Shock wave systems

The most dominant flow characteristic in a high-speed intake is the interaction between the various shock waves and these can result in complex wave systems at inlet. These wave systems can either result from the interaction between two or more shock waves, or from the interaction of a shock wave with an expansion wave. The resulting wave systems can also interact with the viscous boundary-layer to form complex flow fields which can affect overall performance of the engine. Much of hypersonic intake research focuses on studying such wave interactions which are not well understood and contribute to the highest losses in the air-breathing engine.

Shock/shock interaction

Shock/shock interactions, also known as 'interfering' flows can significantly affect the performance of an intake by causing anomalous pressure and heat transfer on the leading edge of the cowl. Edney carried out the first comprehensive study on shock/shock interactions by investigating the impingement of an oblique shock on the stand-off shock formed at a blunt leading edge. The different types of interactions depend on the oblique shock angle and the impingement position, and the interactions are categorised into six distinct patterns; Type I to Type VI.

Figure 2.9 (after reference[112]) illustrates the six Edney interactions according to the interaction point relative to the stand-off shock at the blunt leading edge. On the figures, BS is the bow shock at the blunt leading edge; IS the impinging shock; SL the shear layer and TS the transmitted shock wave. The TS shock in the Type I and II cases can impinge the boundary-layer to cause separation. In the Type III case the shear layer generated from the interaction of the BS shock with the IS shock lies close to the surface and can generate high heat transfer rates. Of all six types of shock/shock interactions, Type IV which occurs when the shock intersection is located near the cowl lip centreline, leads to the most severe surface heat transfer. Type IV pattern is where the leading edge shock impinges on the bow shock in a

region where the flow behind is subsonic. A small supersonic jet forms within the subsonic region in front of the body which separates two subsonic regions there. Shear layers separate the subsonic regions with supersonic regions inside the jet. The jet terminates in a jet bow shock just in front of the surface causing high local loads in pressure and heat transfer which increase with Mach number.

As the impingement point becomes higher, the shock/shock interaction pattern changes from Type IV to V. The Type V interaction is analogous to the Type II interaction with the only difference in that a jet is formed at the interaction point instead of a shear layer. The Type VI interaction differs from the other types due to the expansion fan generated at the shock interaction point. The expansion reflects onto the surface and does not generate significant heat transfer. These types of shock/shock interactions radically change the shock that is generated by the cowl.

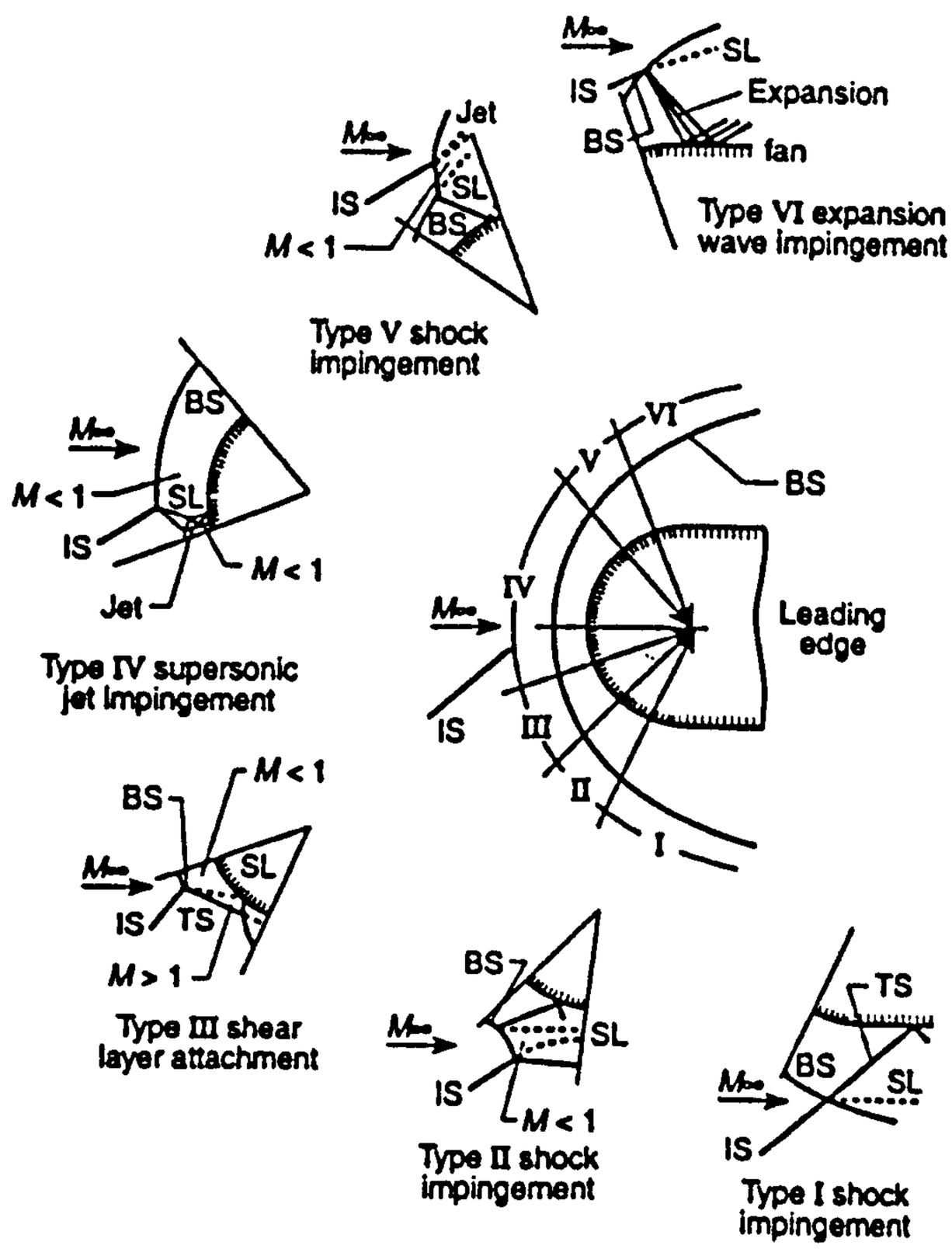


Figure 2.9: Impingement of an oblique shock (IS) on the stand-off shock (BS) formed at a blunt leading edge categorised into six distinct patterns I to VI by Edney.[13]

RAL LOUGHBOROUGH UNIV

Figure 2.10 presents a graph of the surface pressure distribution and heat transfer rate distribution for a Type IV shock/shock interaction. These tests were conducted at Mach 8.03 and a unit Reynolds number of 1.55 x 10^6. The data, presented by Wieting and Holden[65] shows the peak heat transfer rates occurring where the supersonic jet impinges on the body surface. Edney reported that these pressure distributions would be sensitive to viscous effects - either laminar or turbulent, and found a high level of turbulence in the jet from experimental studies. He stated that the peak heating is not only dependent on the peak pressure generated by the jet, but also on the width of the jet, the angle with which the jet impinges on the surface of the body and whether the jet is laminar or turbulent.[13,65] Experimental data has shown that the Type IV interaction increases heat transfer above the undisturbed, maximum stagnation point value by a factor of 5-10 at Mach 4.6, with even larger multiples possible at higher freestream Mach numbers.[115] Studies have quoted peak heating rate augmentations of up to 17 times and stagnation pressure augmentations of up to 8 times the unimpinged conditions for axisymmetric bodies.

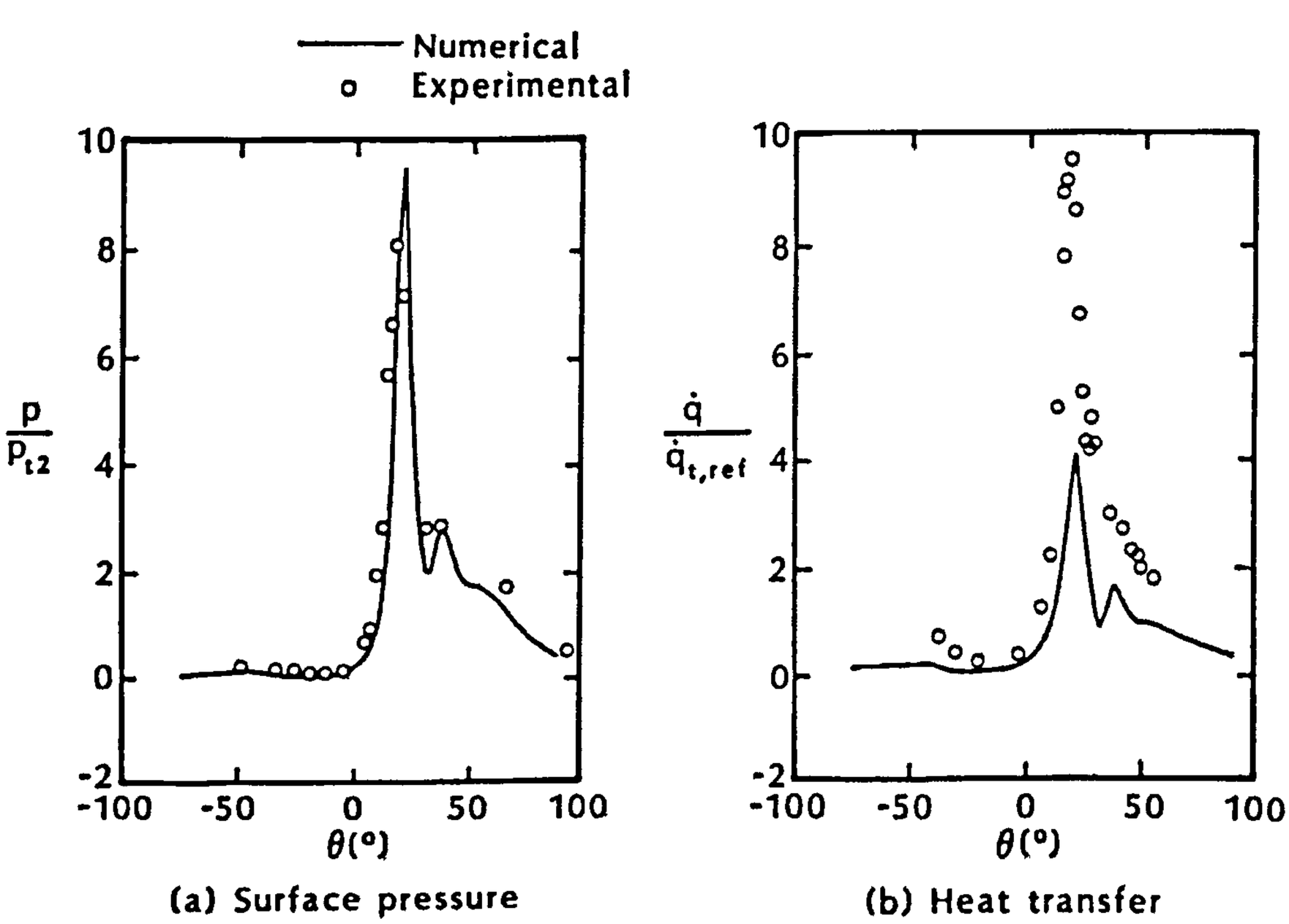


Figure 2.10: Type IV Edney interaction surface pressure and heat transfer distributions; comparison between numerical and experimental results (Bertin[65]).

White and Rhie[60] numerically analysed the peak heat transfer rates over a cowl leading edge at hypersonic speeds comparing unimpinged and impinged conditions. Figure 2.11 illustrates the effect of shock impingement obtained by CFD and shows the characteristic Type IV interaction. The predicted stagnation pressure augmentation was on the order of 5.4 times the unimpinged condition.[60]

Experimental data by Weiting et al.[10] showed significantly greater pressure and heat transfer augmentation values of 12 and 28 respectively at higher hypersonic conditions of Mach 16. Sobel[23] obtained numerical predictions of the cowl leading edge heat transfer in the presence of shock impingement, stating that heat transfer associated with the shock/shock interaction is correspondingly higher than the stagnation point heat transfer in the absence of shock interaction. The severity of the heat transfer amplification in the presence of incident-shock/bow-shock interaction depends on the strength of the incident shock and the location of the interactions.

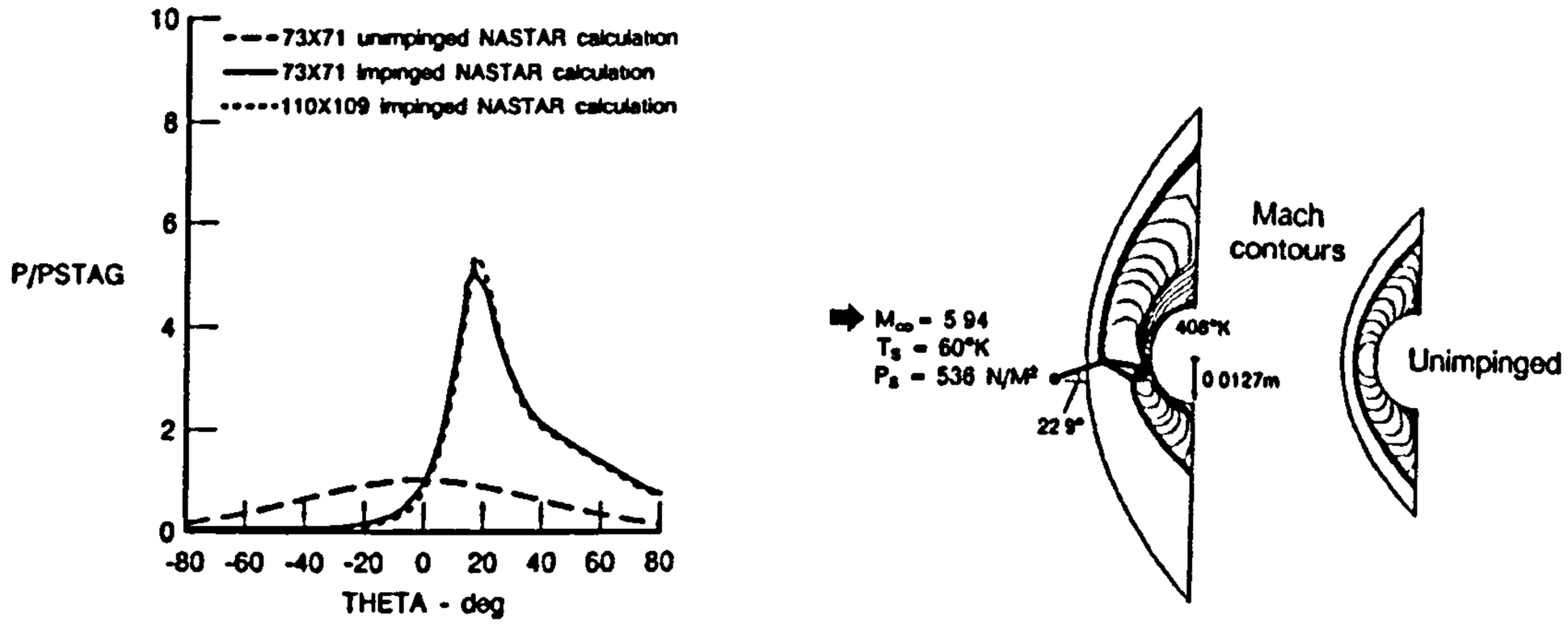


Figure 2.11: (a) Comparison of shock structure with and without shock impingement from numerical prediction at Mach 5.94 (b) Comparison of surface static pressure with and without shock impingement (White et al.[60]).

Yamamoto et al.[118] investigated shock/shock interactions both by experiment and computations for low and high angle-of-attack configurations. The results stating that as the angle of attack is increased to high values, local peak heating in the shock interaction region in general increases with a higher increase in surface heating on the windward side. Shock/shock interactions have a very relevant relation to the intake flow problem due to the interaction between the several shock waves in the

system. The interaction of the apex shock with the bow shock at the cowl can lead to high leading edge surface pressure and heat transfer rates at the cowl leading edge. Stollery[65] predicted that three shock waves interact at the cowl lip: (1) the bow shock wave produced by the cowl lip, (2) the bow shock wave originating at the vehicle leading edge, and (3) an oblique shock produced by the compressive turning of the flow at the intake ramp. The interaction of these shock waves produces a perturbation in the flow field which affects the flow at the cowl-lip surface.

Regular/Mach reflection

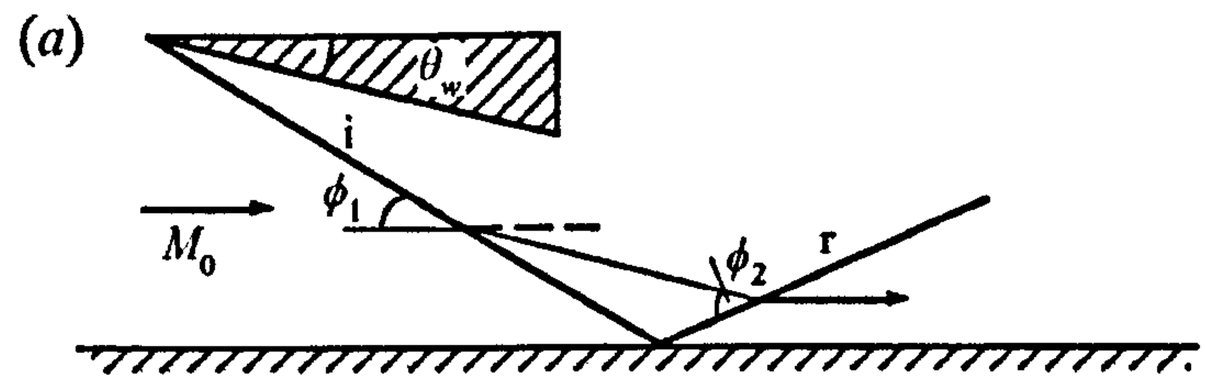


Figure 2.12: Illustration of the reflection of a shock wave as either (a) regular reflection or (b) Mach reflection (Li and Ben-Dor[73]).

The reflection of a shock wave can take two forms (a) regular reflection and (b) Mach reflection, as illustrated in Figure 2.12. When the Mach number is very small or the value of the shock angle (ϕ_1 on the schematic) is large, regular reflection of the shock becomes impossible. This results in a process known as *Mach reflection.* The incident shock forms a Mach stem (nearly normal shock) at the wall with a reflected shock wave emanating from the intersection of the triple point T, Figure 2.12 (b). The flow behind the Mach stem is subsonic and the flow behind the reflected shock is

supersonic, generating a slipstream s from the Mach reflection triple point. Classical shock theory proposes the detachment and von Neumann criteria for transition from regular to Mach reflection.

Figure 2.13 shows the domains for the different types of reflection and transition criteria. When ϕ_1 is above the detachment criterion only Mach reflection can occur and when ϕ_1 is below the von Neumann criterion only regular reflection can occur. The domain where both regular and Mach reflection are possible is known as the dual-solution domain. Generally there appears to be a hysteresis phenomenon, whereby if the wedge angle is increased from small values (ditto for the shock angle) regular-to-Mach transition occurs at the detachment boundary, whereas if Mach reflection exists, the transition from Mach-to-regular reflection occurs at the lower von Neumann boundary.

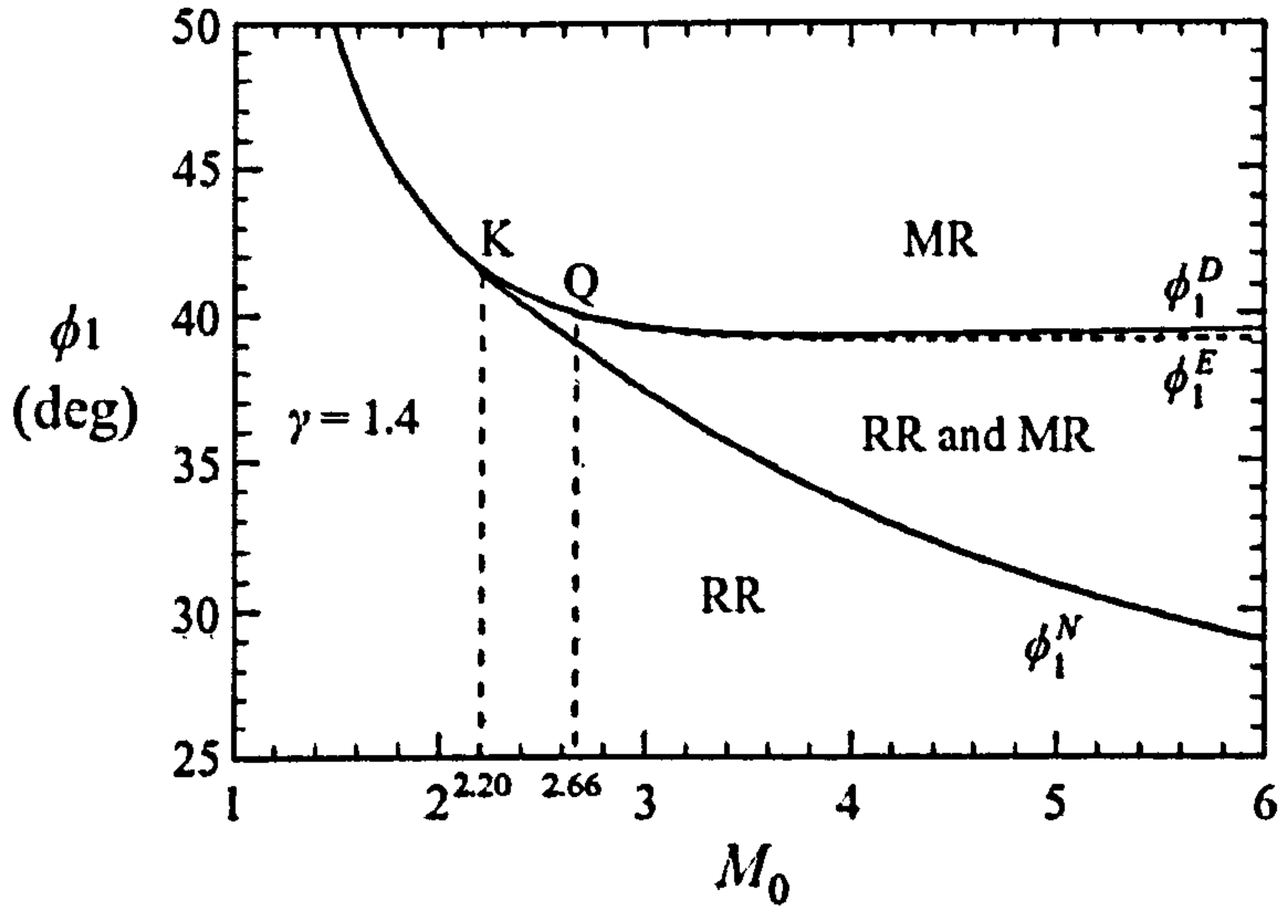


Figure 2.13: Transition from regular to Mach reflection according to the detachment and von Neumann criteria showing the dual-solution domain (Li and Ben-Dor[73]).

Shock/expansion interaction

Mach reflection can also occur when a shock wave reflecting onto a surface is acted on by an expansion fan from that surface, see Figure 2.14. In an intake flow this would occur for example when the cowl shock impinges onto the centrebody and is acted on by the corner expansion fan as the intake flow is turned into the duct.

Ideally the cowl shock would reflect onto the centrebody, at the expansion corner, effectively cancelling out the expansion fan at the corner.

In reality, off-design conditions cause the shock to impinge upstream or (usually) well downstream of the expansion corner. For the upstream case the shock reflection process is straightforward. For the downstream case the impinging cowl shock is now affected by the expansion fan and in some cases will lead to Mach reflection. Figure 2.14 illustrates this flow problem, where the cowl shock reflection is influenced by the corner expansion at the intake shoulder. The expansion fan accelerates the flow and turns it towards the wall increasing the flow deflection angle. At interactions of sufficient strength Mach reflection will be formed on the centrebody. The strength of the shock wave increases as the wave passes through the expansion fan. Thus, greater total pressure losses will be incurred across the shock wave after the interaction. Mach reflection in the intake flow will also increase flow non-uniformity.

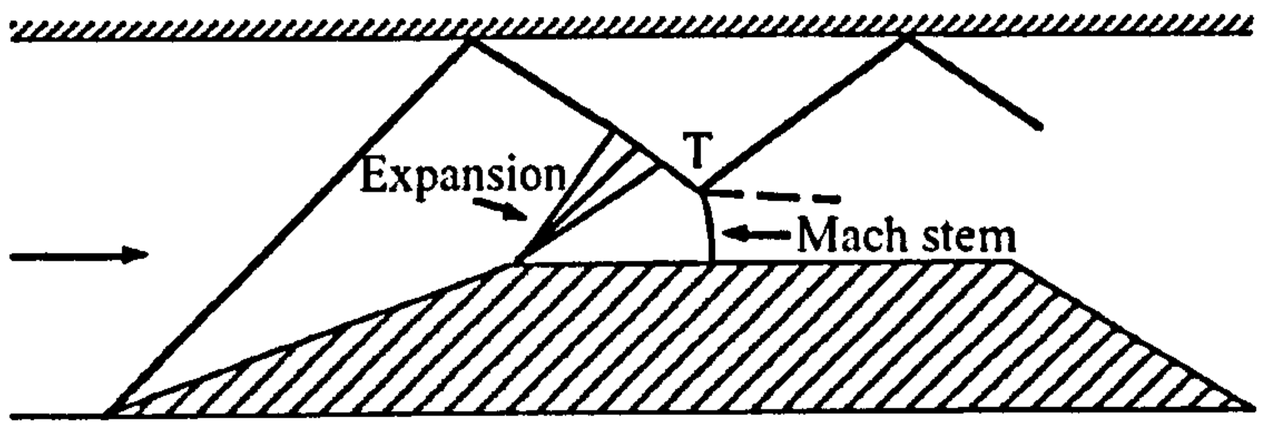


Figure 2.14: Illustration of a cowl shock reflecting from the centrebody and being acted on by the corner expansion fan to form a Mach reflection (Ben-Dor[73]).

Hillier[86] studied the shock-wave/expansion-wave interaction and the details of the transition from regular to Mach reflection in a simplified model of the intake problem. In the study, a shock wave impingement occurs under the influence of an expansion fan formed at a shoulder. Firstly, the basic distortion of the incident shock by the expansion fan is modelled by the rotational method of characteristics to provide an exact result. A parameter study was then carried out for M_1 versus δ (flow turning at the expansion corner) to provide the conditions, post shock wave, at incidence upon the afterbody and to then determine the possible reflection conditions at the body surface. Figure 2.15 presents the resultant predicted transition boundaries according to the detachment and von Neumann conditions. The figure also shows

the detachment boundary for the cowl shock. A CFD simulation was carried out at Mach 2 at 0.5 degrees below the detachment criterion boundary, point (c) on Figure 2.17, which shows the detail in the Mach number and flow deflection plane of the test cases corresponding to CFD simulations that were carried out in the study.

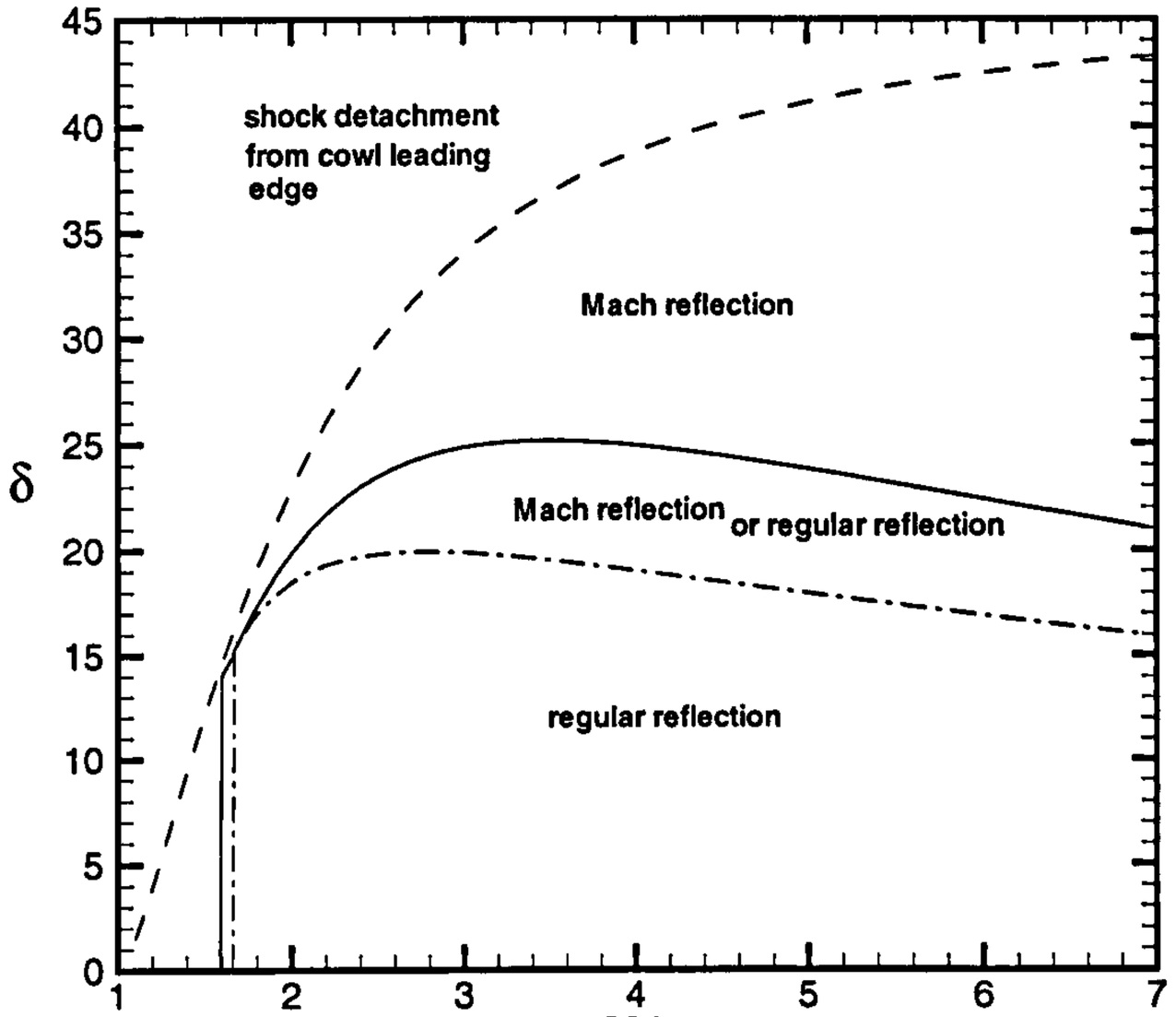


Figure 2.15: Variation of predicted angle, from method of characteristics, for detachment from the cowl leading edge and transition between regular and Mach reflection, on the downstream surface, according to the von Neumann and detachment criteria. (Bachchan and Hillier[86]).

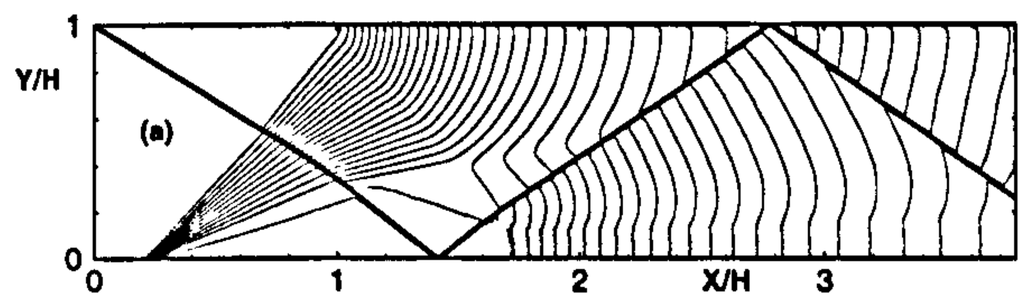


Figure 2.16: Regular reflection simulation for incident flow at 0.5 degrees below the incident angle for regular-to-Mach transition according to the detachment criterion: Mach 2.0 at 5% intervals in ρ/ρ_∞; point (c) on Figure 2.17 (Bachchan and Hillier[86]).

The shock wave reflects onto the centrebody as regular reflection, seen in Figure 2.16. The next set of results focuses on the Mach reflection case. The cases tested

are seen on Figure 2.17 with corresponding simulations in Figure 2.18. The flow deflection angle is now increased by 1 degree, and so 0.5 degree above the detachment boundary, Figure 2.18 (a) producing Mach reflection.

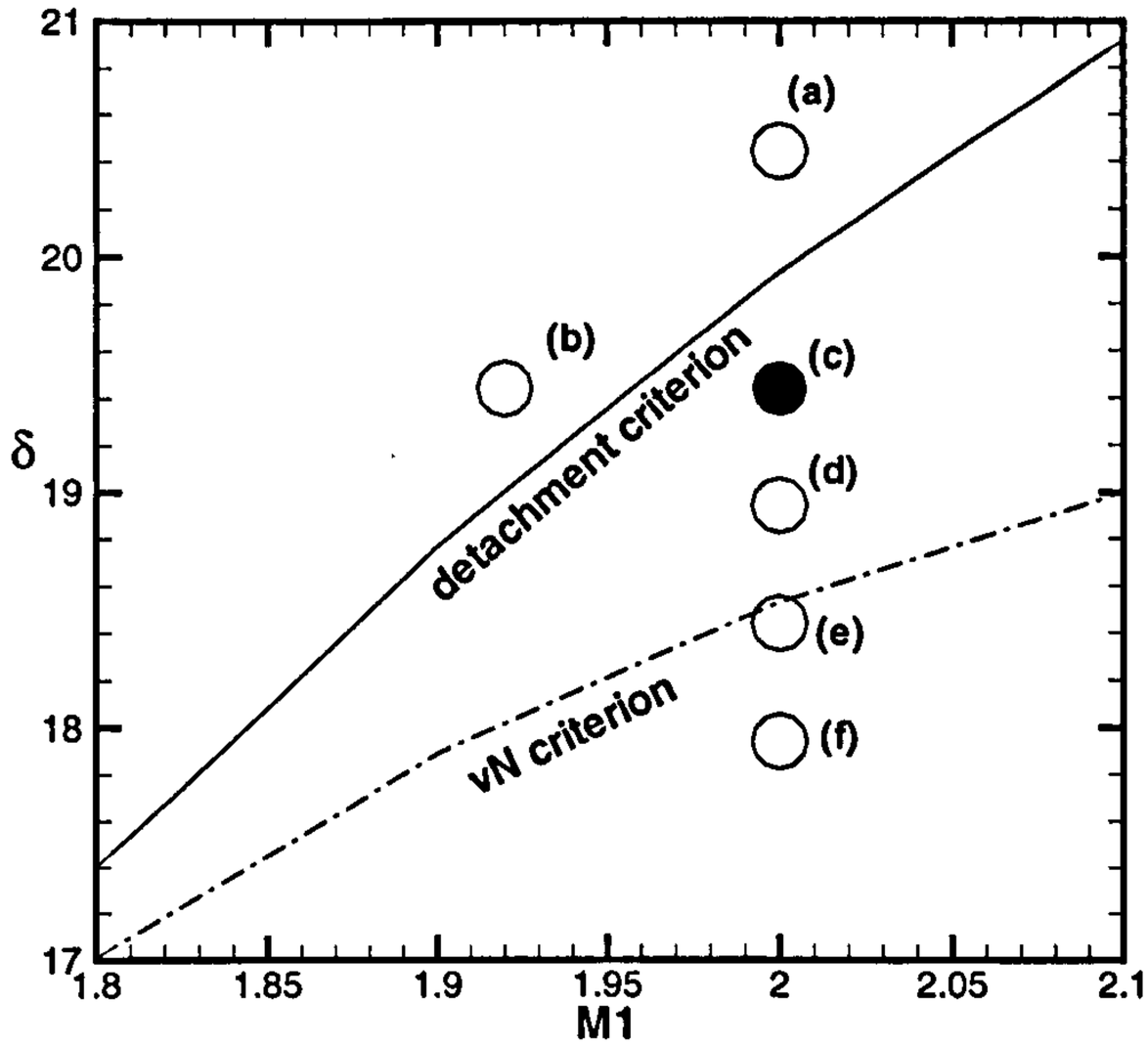


Figure 2.17: Detail in the Mach number and flow deflection plane showing the test cases corresponding to CFD simulations in the Figure 2.18 (Bachchan and Hillier[86]).

Starting again from the original point (c) the Mach number is then reduced to 1.92 at point (b), and so the solution crosses the detachment boundary. Figure 2.18 (b) shows Mach reflection on the surface. Starting with the solution from point (b), the Mach number is increased back to 2, point (c).

The solution in Figure 2.18 (c) shows Mach reflection is formed. The solution for both Figure 2.16 and Figure 2.18 (c) are for the same case showing the dual-solution possibility of regular and Mach reflection. The Mach number is held constant and the flow deflection angle is lowered further by 0.5 degrees so that the solution remains in the dual-solution domain. Again, Mach reflection is formed on the surface, seen in Figure 2.18 (d). The flow deflection is then reduced in increments until the solution crosses the von Neumann boundary until regular reflection is achieved as seen from the contours in Figure 2.18 (e) and Figure 2.18 (f).

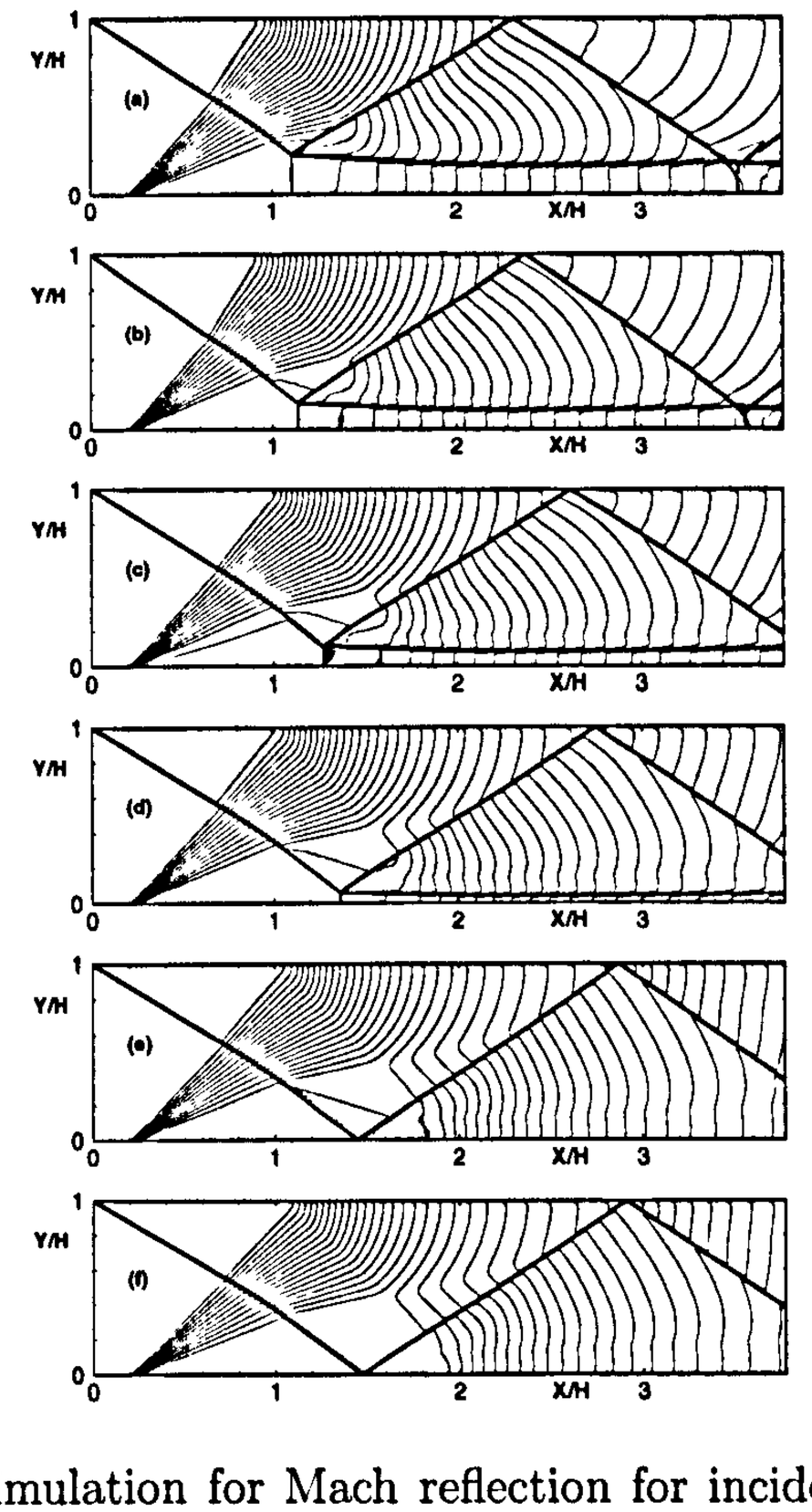


Figure 2.18: CFD simulation for Mach reflection for incident perturbed from the Mach 2.0 regular reflection case of Figure 2.16. (a) incidence increased by 1.0 degrees; (b) incidence maintained at original value and Mach number reduced to 1.92; (c) Mach number returned to original value; (d) Mach number held fixed and incidence reduced by 0.5 degrees; (e) further reduction by 0.5 degrees; (f) a further reduction by 0.5 degrees (Bachchan and Hillier[86]).

Tani et al.[110] conducted Mach 4 scramjet inlet studies by modifying the inlet inner surfaces by serration, to weaken the cowl shock wave, and to compensate the pressure decrease caused by the expansion wave generated at the throat corner. The serration of the inlet inner surface at the throat was expected to work as a series of cavities, over which a free boundary would form, in an effort to weaken the expansion wave. It was concluded that a convex type inlet relaxed the cowl shock strength, and small serrations could be utilised for cancelling the throat-corner expansion wave. The interaction between shock and expansion waves can also occur at the cowl lip region when the apex shock focuses towards the inner cowl surface and is acted on by the cowl expansion fan. This can lead to Mach reflection on the cowl inner

surface wall. Mach reflection in an intake can lead to increased total pressure losses and non-uniformities in the intake and should be avoided in the intake flow.

Shock/boundary-layer interaction

The impingement of a shock wave of sufficient strength onto a boundary-layer can cause the flow to separate. Research on this phenomenon has been documented to some extent in the literature[30, 44, 121] with less understanding of the flow mechanisms at hypersonic speeds. Figure 2.19 (a) presents a schematic of the flow-field characteristics of a shock/laminar boundary-layer interaction. At the point of separation, a separation shock wave is induced. The flow then expands past the separation bubble and re-compresses, generating a series of weak Mach waves that coalesce to form the reattachment shock wave (similar to the isentropic compression process).

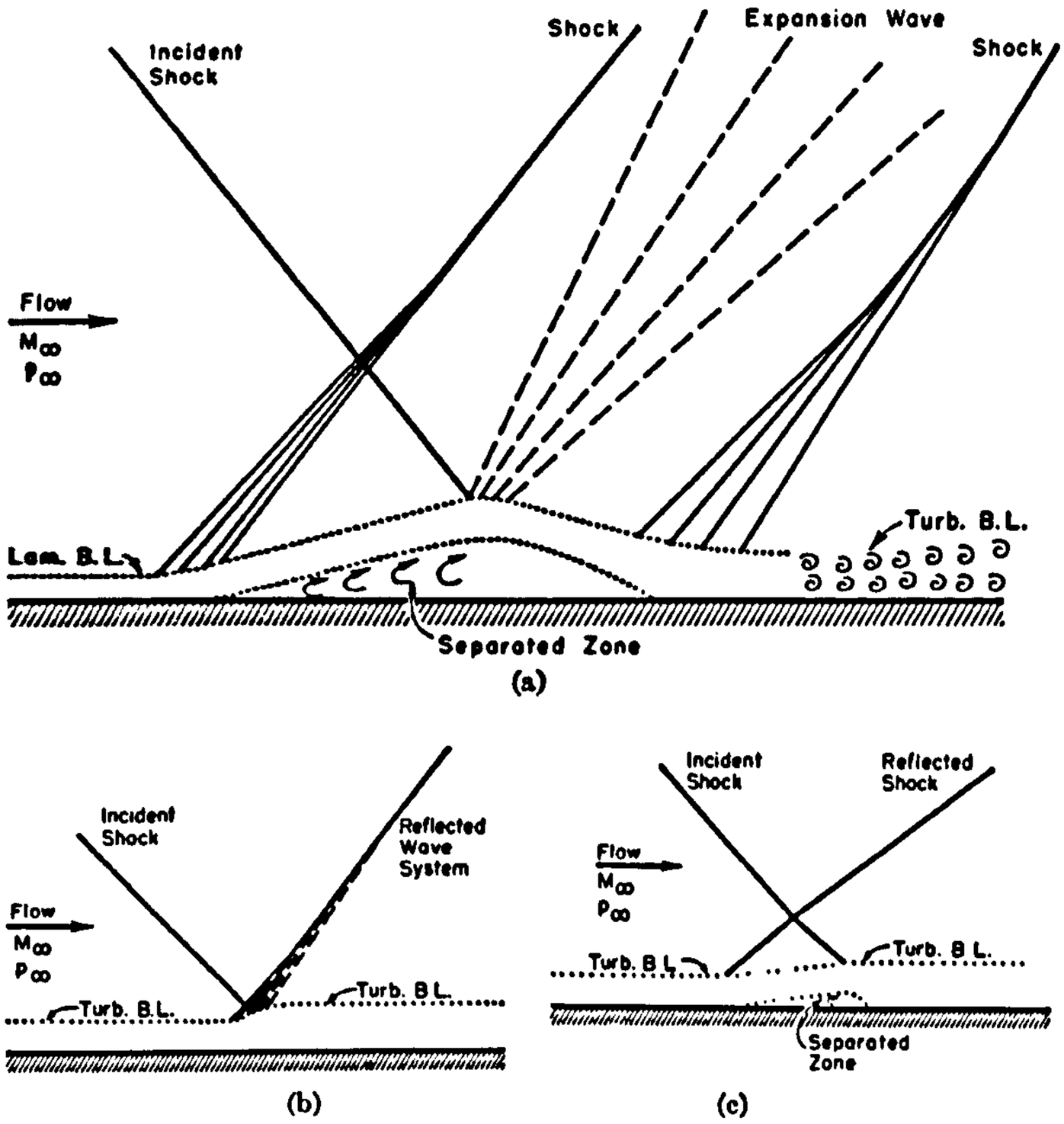


Figure 2.19: Shock/boundary-layer interaction flow physics (Shapiro[7]).

From the point of separation, the shear stress becomes negative and the flow reverses with a region of recirculating flow in the separated region. The flow reversal in the separated region is a result of the low velocity fluid inside the boundary-layer, reaching a point where the kinetic energy of the fluid is not enough to pass the fluid through the adverse pressure gradient. Laminar boundary-layers are more susceptible to flow separation than turbulent boundary-layers where momentum rates are higher. For this reason, there is a need to trigger transition early enough on the vehicle forebody to ensure an attached boundary-layer.

Figure 2.19 (b) and (c) illustrate the shock/turbulent boundary-layer interaction showing the interaction in (b) and with a separation zone in (c) where the reflected shock forms before the impingement of the incident shock resulting in crossing shocks. Figure 2.20 illustrates the basic differences between shock/turbulent-boundary-layer interaction in supersonic and hypersonic flows as summarised by Knight et al.[105] The separation shock forms within the separating turbulent boundary in both cases, and lies closer to the surface for the hypersonic case.

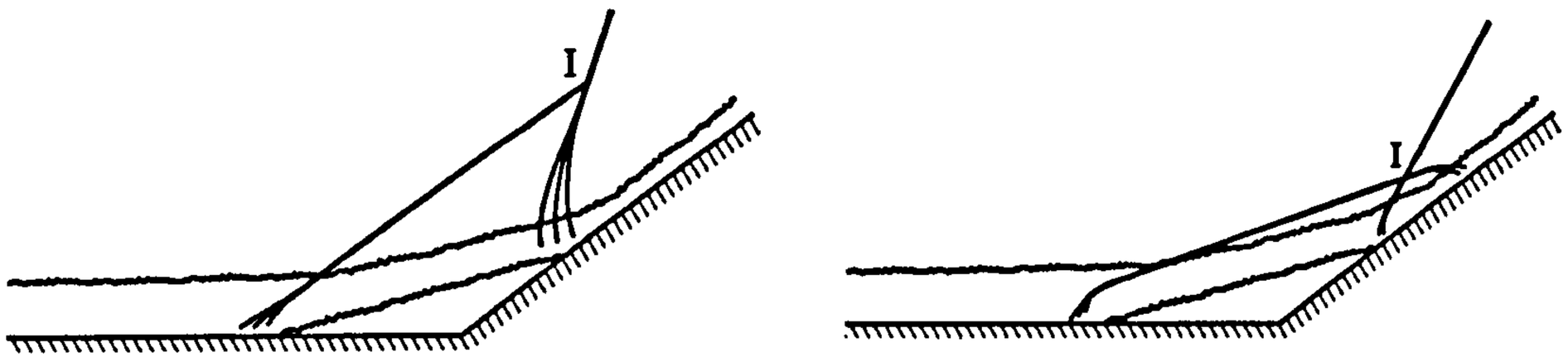


Figure 2.20: Shock/turbulent-boundary-layer interaction flow characteristics in (left) supersonic and (right) hypersonic flow (Knight et al.[105]).

The interaction of the separation shock with the reattachment shock also lies closer to the surface near reattachment. The most likely occurrence of separation due to a shock/boundary-layer interaction in an intake flow is from the impingement of a cowl shock onto the centrebody boundary-layer. Shock/boundary layer interaction can also occur on the forebody surface as the incoming air flow is compressed through a series of shock waves. The multiple shock reflections in the isolator can also cause separation from shock/boundary-layer interactions, as well as separation through the adverse pressure gradient through a terminal shock system in a ramjet.

This type of interaction in the intake flow field can lead to undesirable flow qualities such as non-uniformities in the flow profile, losses in total pressure, increased heat transfer rates and the added complexity of even more shock waves in the flow. Separated flow in the intake can also cause an effective contraction of the duct which can provoke an intake unstart. In the intake duct, multiple shock reflections and interactions can increase the likelihood of flow separation and can lead to performance losses in the intake. Intake designers have incorporated ways of controlling separation in the intake by bleeding the boundary-layer as it turns into the intake duct. This can include the use of suction slots or diverters in the intake geometry.

Several interesting studies[27,43,69,80,81,120] have also been conducted on the influence of the expansion corner on a shock/boundary-layer interaction. Chew and Squire[34] concluded from their investigation that the expansion corner had an effect on the upstream interaction region when the interaction occurred less than 3-4δ_1 (displacement thickness) from the corner.

Chung and Lu[69] stated that the shock impingement past an expansion corner affects the shock/boundary-layer interaction due to the expansion fan affecting the incoming characteristics of the boundary-layer. The expansion produces a thickening of the incoming boundary-layer[69] and an increase in the Re_w. White[80] reported that the separation actually becomes more prevalent when the shock/boundary-layer interaction is moved closer to the expansion corner, and also concluded that there appeared to be no effect of the corner on the size of the separation so long as the separation is fully contained either upstream or downstream of the expansion fan.

2.2.2 Spike and cowl blunting

To regulate heat transfer to the hypersonic vehicle the surfaces are usually designed with leading edges bluntness. For vehicles constructed with composite materials, machining constraints can also result in a blunted geometry. Figure 2.21 presents a schematic of an external compression intake with spike and cowl lip blunting.

The blunted spike tip generates an entropy layer which can contribute to losses and non-uniformities in the intake flow and with a significant blunting can displace the

apex shock, and hence affect the intake mass capture. Furthermore, the detached shock wave generated by the blunted leading edge can be intersected by the leading edge shock wave to form a shock/shock interaction system, with increased pressure and heat transfer loads to the vehicle.

Cubbison and Samanich[97] studied the effect of spike-tip and cowl-lip blunting on an external compression intake at Mach 3.0. They found that pressure recovery was only slightly reduced by spike blunting due to the stagnation point moving inside the cowl lip when blunting is added to it. The blunted spike also incurred a slight increase in the overall drag coefficient due to a small amount of spillage caused by bluntness, and this drag penalty was found to increase linearly with increasing lip bluntness. The shock structure was found to be essentially independent of tip contour and was found to be a function only of the basic spike design.

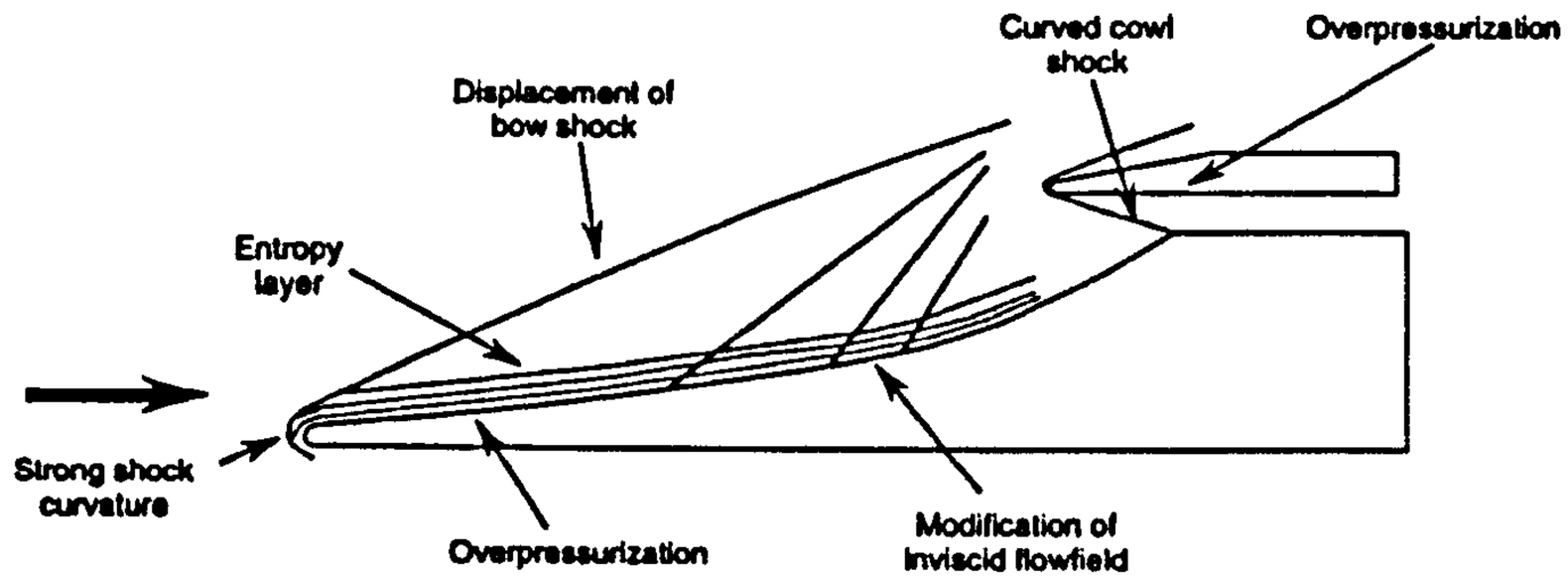


Figure 2.21: Effects of leading-edge bluntness (Van Wie[112]).

Van Wie et al.[28] carried out a combined experimental and analytical investigation on a scramjet inlet with a small nose bluntness at Mach 10. The test data showed a decrease in intake performance by approximately 4 to 5 percent, caused by the thick entropy layer generated by the blunt nose which is swallowed by the intake. The presence of the entropy layer also resulted in a reduced inlet mass capture.

Hsia[119] studied the flow-field of an axisymmetric scramjet inlet at Mach 5 using Navier-Stokes computations to study the internal flow structure. The geometry included blunting at the spike tip and at the cowl lip. Hsia concluded that bluntness had insignificant effects on the internal intake shock structure. However, the local heating and stress became important at hypersonic speeds.

2.2.3 Cowl positioning

Another feature of the inlet geometry that can effect performance is the positioning of the cowl relative to the centrebody. Holland[100] studied the effects of cowl position of a scramjet inlet at Mach 10 using experiments and CFD simulations, and found a slight increase in centreline pressure distribution as a result of the forward placement of the cowl. It was also found that the pressure distribution on the cowl is driven primarily by the internal shock locations. The forward placement of the cowl was also found to have a large influence on the mass capture of the inlet, as more of the turned flow is prevented from spilling.

Holland[100] also studied the effect of Reynolds number on the internal shock structure of a sidewall compression scramjet inlet at Mach 10. The study found that a decrease in the Reynolds number led to the increased displacement of the sidewall boundary layer and resulted in the forward movement of the shock impingement position. The internal shock structure was found to be highly sensitive to changes in Reynolds number, which indicates the challenges in designing an intake for operation at a range of flight conditions.

Work conducted by Van Wie et al.[28] on a scramjet inlet also studied the sensitivity of the inlet operation to cowl position. The main issue investigated here was the position of the cowl shock relative to the centrebody shoulder. The report states that for any given Mach number and angle of attack, a cowl position can be found that will produce the cowl shock-on-shoulder condition. This condition, where the cowl shock is cancelled out on the centrebody shoulder is desirable because the inefficiencies caused by the non-uniformity of flow at the inlet throat are minimised. The studies showed that the position of the cowl shock at the centrebody shoulder, which is controlled by the cowl position, has a significant influence on the intake efficiency and uniformity of the flow supplied to the combustion chamber.

2.2.4 Angle-of-attack

The increase in the angle-of-attack can significantly affect the flow characteristics in the intake, and generally high-speed intakes will operate at fairly low angles.

An increase in the angle-of attack will lead to the apex shock moving outwards on the windward side, and moving inwards on the leeward side, as illustrated in Figure 2.22. The boundary-layer characteristics will also change and will affect the pressure recovery due to the thickening of the leeward boundary-layer.[58]

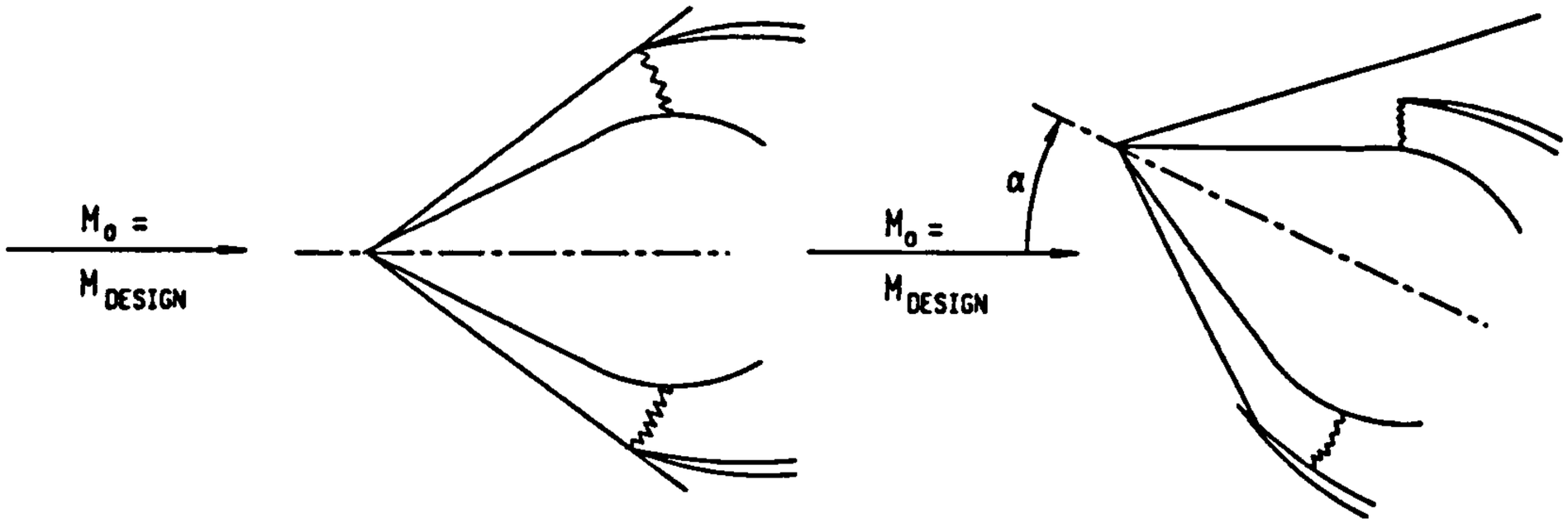


Figure 2.22: Two operating conditions of an axisymmetric intake with a single-surface conical centrebody (a) 0 deg α (b) high value of α (Mahoney[66]).

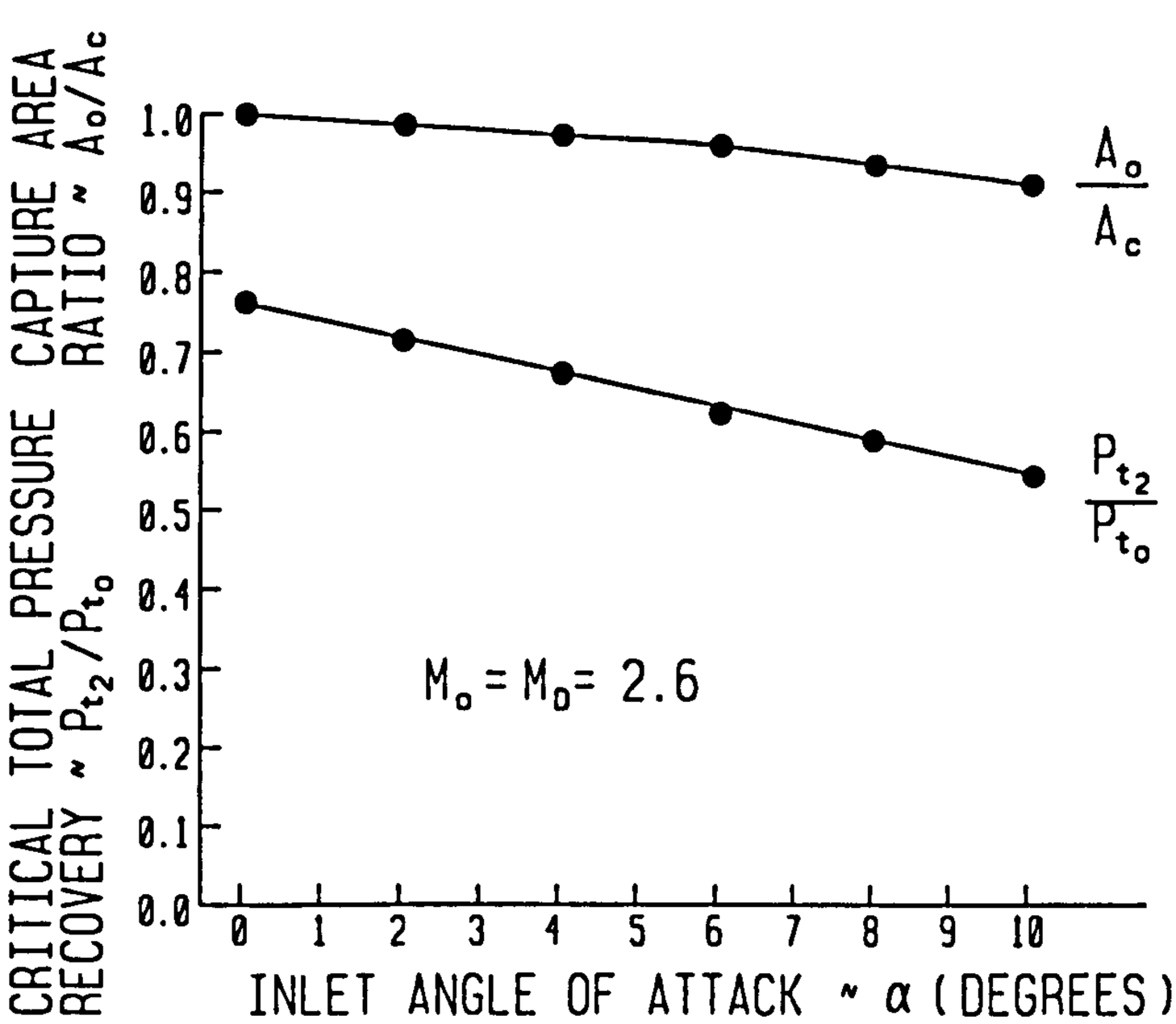


Figure 2.23: Effect of angle of attack on the measured performance of an axisymmetric semi-isentropic inlet (Mahoney[66]).

This can lead to various unfavourable off-design characteristics and interactions in the intake which can provoke an intake unstart. Some form of boundary-layer control may be required for the intake to function at angle-of-attack. Mahoney[66] states that as the conical body is yawed or pitched, it would be expected that crossflow increases the surface Mach number on the leeward side compared with the zero incidence case, and decreases the surface Mach number on the windward side. At the same time, the leeward surface static pressure decreases and the windward surface static pressure increases with the zero incidence case. Figure 2.23 plots capture area ratio and critical total pressure recovery against inlet angle of attack for an inlet operating at the design Mach number (Mach 2.6) showing decreasing performance with increasing angle of attack.[66]

2.2.5 Oscillations (buzz)

The oscillations of shock waves in an inlet, referred to as *buzz* was first identified by Oswatitsch (1944) in a study conducted on axisymmetric inlets.[96] This phenomenon, whereby the internal ramjet shock oscillates inside the intake can cause the intake to fluctuate between unstarted and started conditions. Buzzing in a supersonic diffuser can cause severe pressure fluctuations and can disrupt the combustion process of the engine and also lead to structural failure. Figure 2.24 shows a typical sequence of shock positions during one cycle of a buzzing intake showing the forward and rearward movement of the shock waves at inlet.[58]

Ferri and Nucci[58] determined from experimental investigations that the shock oscillation initiated when the vortex sheet from the triple point moved below the cowl lip to enter the intake duct, a phenomenon which is known as the *Ferri criterion.* In this aspect, designing the inlet such that the vortex sheet always lies above the cowl lip is a way of preventing buzz. Shock/shock and shock/boundary-layer interactions which lead to Mach reflection or separated flows in the duct can also generate vortex sheets which propagate from the interaction regions to initiate buzz.

Buzz can also be initiated if Mach reflection occurs at inlet and generates a slip stream which convects downstream. Pressure fluctuations between the inlet wave

system and the isolator can cause the internal shock system to oscillate. In an ideal intake flow, buzzing should be avoided or suppressed to low oscillation amplitudes.

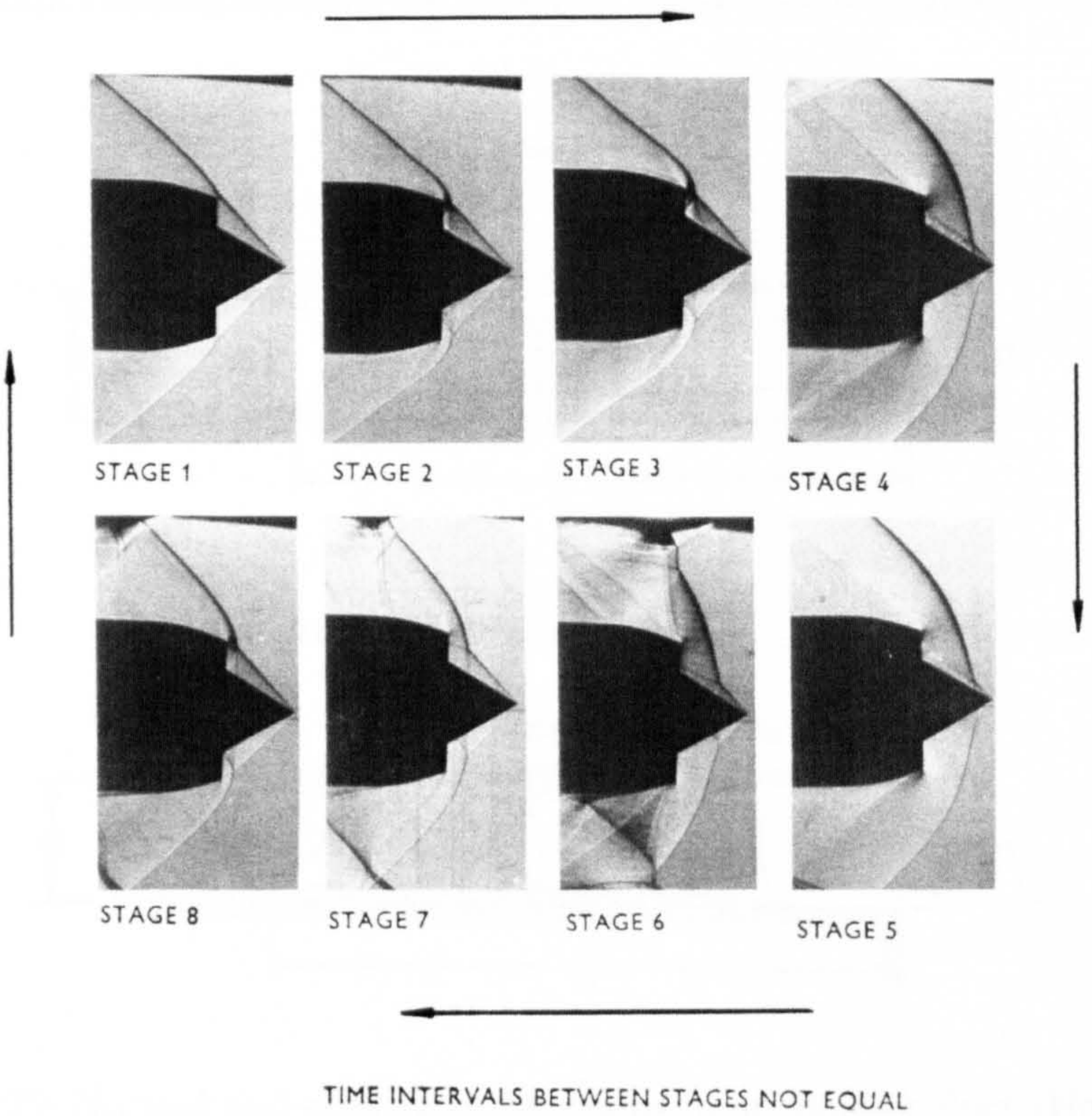


Figure 2.24: Typical shock positions during one cycle of intake shock oscillation showing the forward and rearward movement of the shock position (Seddon[58]).

2.3 Isolator flow characteristics

2.3.1 Shock train phenomenon

The section of the intake which extends from the inlet annulus to the combustor entrance is known as the *isolator*. The primary purpose of the isolator is to prevent any disturbances which may occur in mixing and combustion from propagating upstream to the intake. The second function of the isolator is to diffuse the supersonic flow to suitable conditions for combustion. In a ramjet engine, the isolator must diffuse the incoming supersonic flow to subsonic conditions and maximise total pressure recovery to the combustor. In scramjets, the flow is diffused from high su-

personic flow speeds to lower supersonic speeds to deliver the flow to the supersonic combustion chamber. The configuration of the isolator with the inlet and combustor is an important consideration in the design of a hypersonic engine.

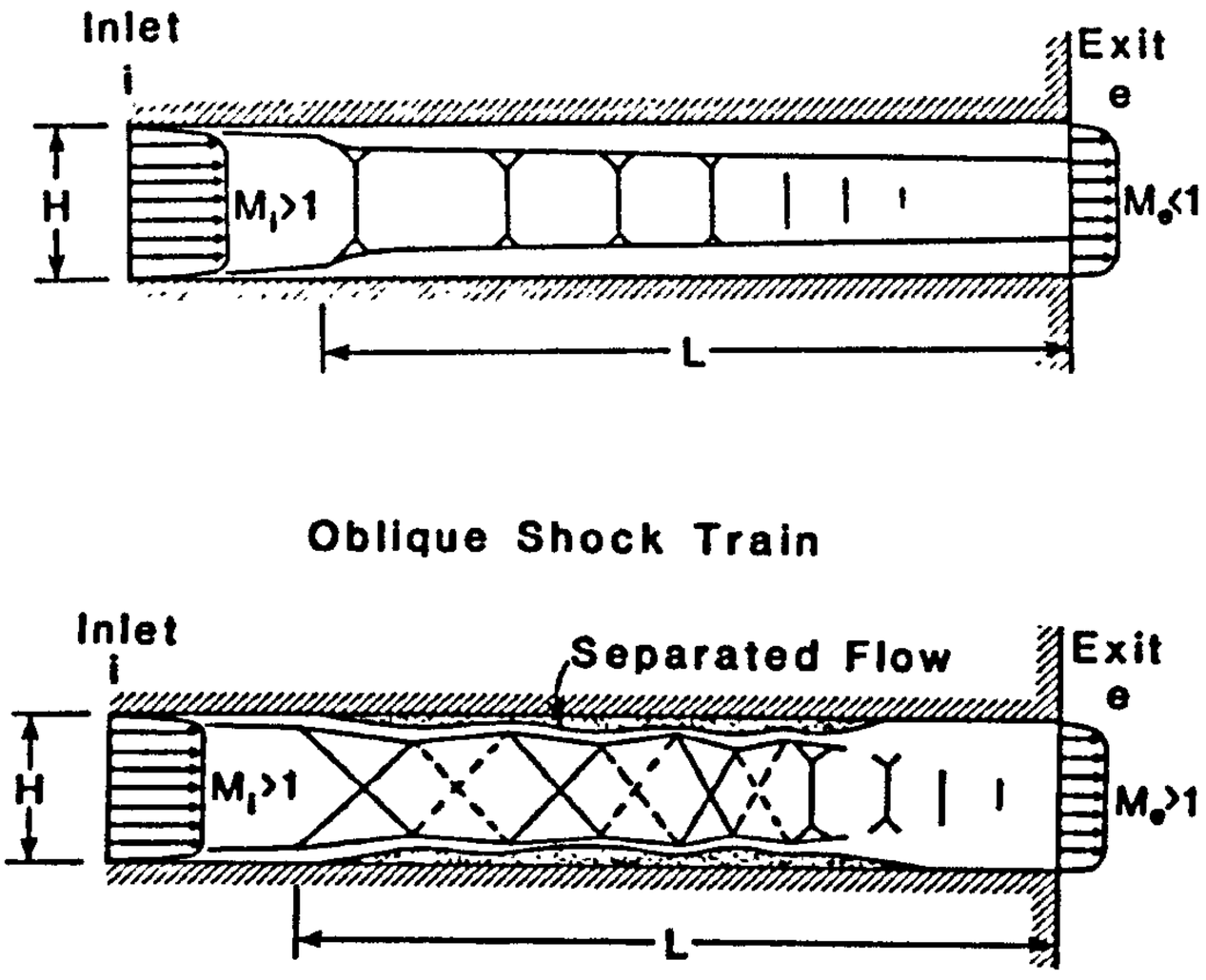


Figure 2.25: Normal and oblique shock trains in an isolator duct (Heiser[115]).

The flow through the isolator contains a series of complex multiple shock waves which interact with the incoming turbulent boundary-layer. The isolator receives the supersonic flow from the intake and contains a *shock train.* Depending on the incoming flow speed this can either be a normal shock train or an oblique shock train. Figure 2.25 illustrates both the normal and oblique shock trains in the isolator. At lower intake Mach numbers and thicker boundary-layers the pattern forms a normal shock train, and at higher intake Mach numbers and thinner boundary-layers, the pattern forms an oblique shock train.[115] The normal shock train can interact with the duct boundary-layer to form lambda-type shocks at the wall. The flow at the end of the normal shock train is subsonic speed, whereas the flow after an oblique shock train remains supersonic. In a ramjet intake, the deceleration of the flow from supersonic to subsonic speeds usually occurs across a terminal shock that forms at the throat. The throat is defined as the section of the duct with the minimum

height. The presence of a shock train in a diverging duct can contribute to the adverse pressure gradient already present in the diffuser flow field. This can lead to separation of the boundary-layer in the diffuser with loses in total pressure recovery and increased flow non-uniformities.

McLafferty et al.[39] found that by increasing the throat length to contain the entire shock train, thus introducing a parallel duct just after the centrebody shoulder, the shock/boundary-layer interactions are confined in this section before the duct diverges as the diffuser section. Research on the supersonic flow in diffusers is well documented in the literature.[42,75,76,89] The shock train mechanism allows the supersonic duct flow to adjust to a back pressure higher than the inlet pressure by shifting up or down the duct. If the isolator pressure recovery is insufficient for the high pressure levels required in the combustor, the high back pressure will cause the flow to unstart. The presence of subsonic regions in the intake boundary-layer allow for this upstream influence in the duct. The interaction of the shock train with the incoming boundary-layer can also lead to separated flow regions in the isolator. The quality of flow entering the isolator, in terms of uniformity can also affect the stability of this terminal shock system. In designing the isolator section it is crucial to keep the losses from the shock-train and its interactions to a minimum. One of the important aspects in isolator design is the adequate length of the isolator to contain the entire length of the shock train.

Isolators can be designed as either constant-area or variable-area. Studies carried out by Lustwerk (after Waltrup[89]) on shock trains in constant area ducts first revealed that thin boundary-layers led to the normal shock forming in the duct. As the boundary-layer thickness increases, a normal shock train with lambda-type shocks form in the duct, and further thickening leads to oblique shocks forming. The second element to affect the transition from a single normal shock in the duct to the normal shock train and then to the oblique shock train is the Mach number.

McLafferty et al.[39] found that the shock train length increased with Mach number and decreased with initial boundary-layer displacement thickness. McLafferty et al. concluded (after reference[35]): (1) the pressure recovery will be maximised if the length of the isolator duct is approximately equal to the length of the shock train,

(2) the length of the shock train required to obtain the complete static pressure rise increases with an increase in the boundary-layer thickness relative to the duct diameter, and (3) the profile at the exit of the diffuser becomes less uniform if the length of the isolator is less than the length of the shock train.

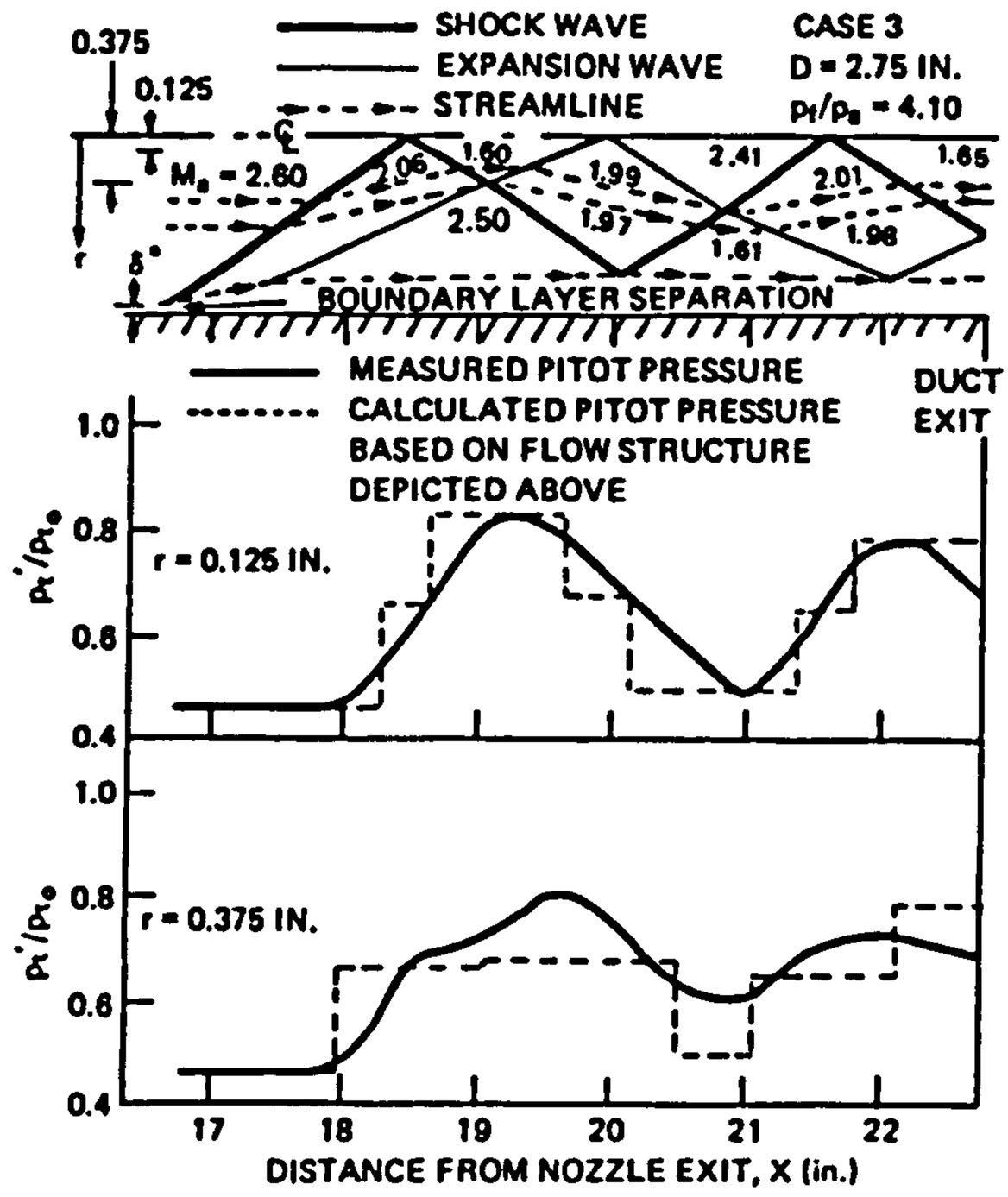


Figure 2.26: Simplified representation of shock structure and comparison with pitot pressure surveys in a cylindrical duct (Waltrup and Billig[89]).

Waltrup and Billig[89] conducted several studies on the structure of shock trains in cylindrical shaped ducts, obtaining experimental data in the duct for a range of freestream supersonic Mach numbers. Figure 2.26 shows an example of the wave structure obtained from this study, showing the representative flow with pitot measurements obtained from different radial positions. The comparisons show the general structure of the shock train with both the compression and expansion process consisting of multiple waves which produce continuous changes in the total pressure.

2.3.2 Isolator geometry

Mahoney[66] presents a design study of the configuration of the inlet, throat and diffuser section for a low, intermediate and high design Mach number intake from Mach 2 to 4. The three designs are shown in Figure 2.27 (a) for low Mach 2 design; (b) Mach 3 design and (c) for a high Mach 4 intake design.

The three intakes compress the flow from the design Mach number to a combustor entry Mach number of 0.3. The designs shows that the length of the supersonic diffusers increase in length with increasing operating Mach number, with a corresponding decrease in annulus height. For the low Mach number case, the length of the shock train is zero, hence the length of the inlet throat is zero. The Mach 3 design requires a throat of 4 times the annulus height to contain a shock train of that length, and a throat of 8 times the annulus height for the Mach 4 design.

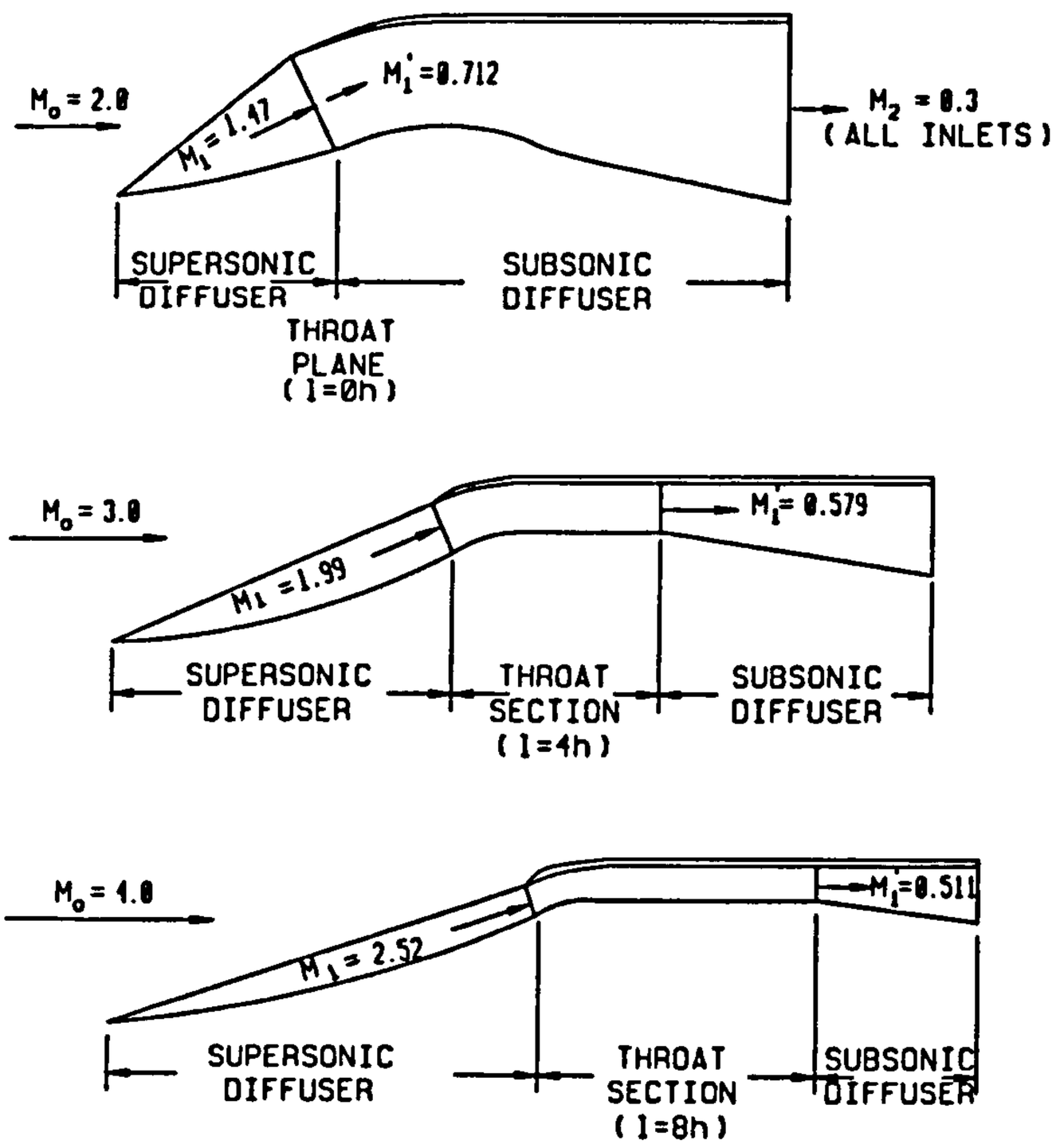


Figure 2.27: Comparative sketches of a family of inlets designed in accordance with conservative practices as described in the work of Mahoney.[66]

Work carried out by Waltrup and Billig[89] on shock trains showed that the length of the isolator is an important parameter to ensure that the shock train is fully contained in the duct. Their study (after reference[115]) derived a widely used correlation to predict the length of the shock train in a cylindrical duct, shown in Equation 2.11.

$$\frac{L}{H} = \frac{\sqrt{\frac{\theta}{H}}}{\sqrt[4]{Re_\theta}} \cdot \frac{(50(\frac{p_e}{p_i} - 1) + 170(\frac{p_e}{p_i} - 1)^2)}{(M_i^2 - 1)} \tag{2.11}$$

$$\frac{p_e}{p_i} = \frac{2\gamma_c}{\gamma_c + 1} M_i^2 - \frac{\gamma_c - 1}{\gamma_c + 1} \tag{2.12}$$

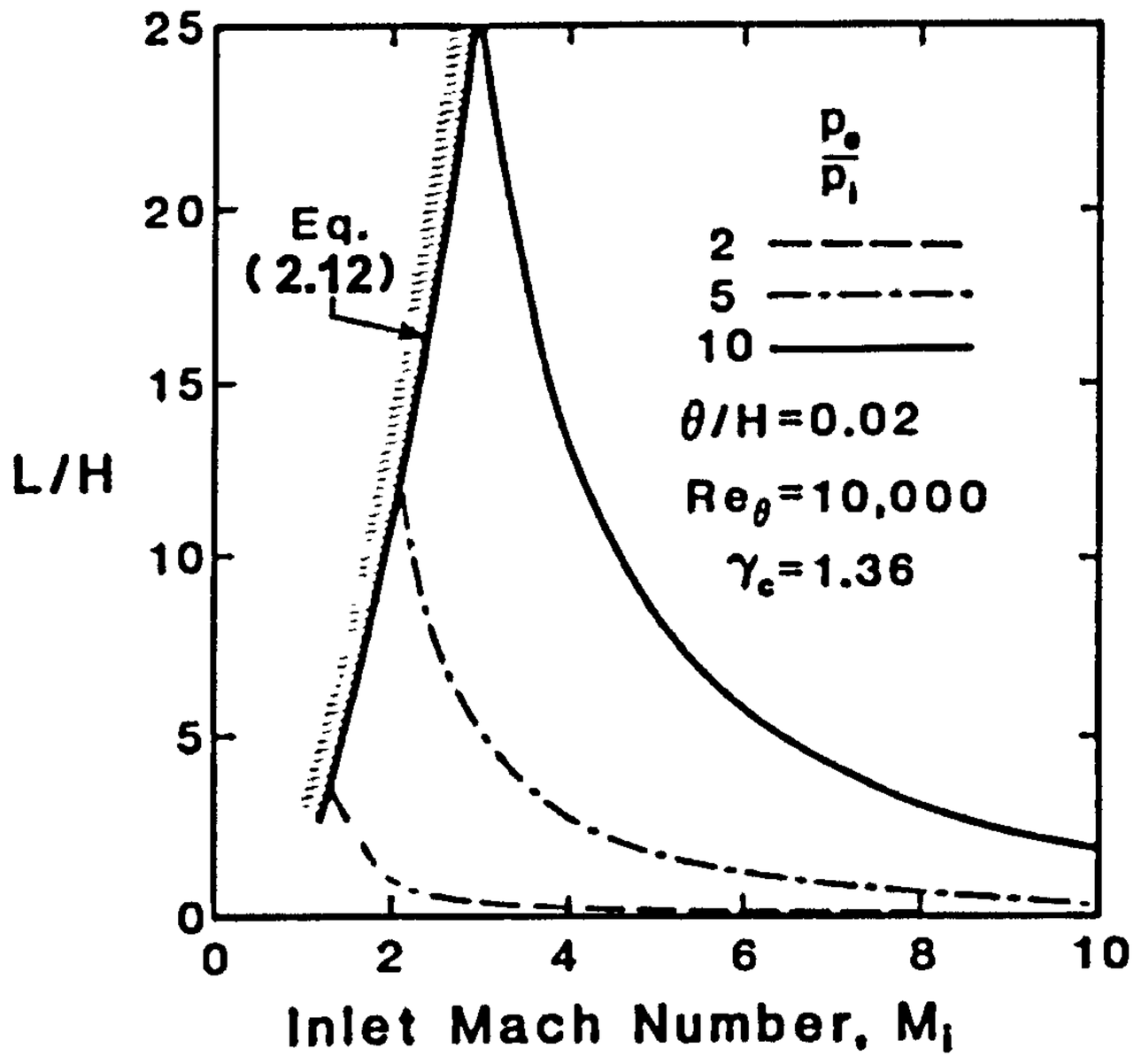


Figure 2.28: Ratio of shock train axial length to duct height as a function of inlet Mach number and back pressure ratio for an isolator or constant area diffuser with typical inlet condition (Heiser and Pratt[115]).

The correlation relates the inlet Mach number M_i, the back pressure ratio $\frac{p_e}{p_i}$, the inlet boundary-layer momentum thickness θ and the inlet Reynolds number Re_θ to predict the required L/H of the parallel section. Figure 2.28 shows a graph of results from Equation 2.11 for typical values of inlet conditions and back pressure ratios

up to Mach 10. The boundary on the left-hand side of the graph is calculated from Equation 2.12 which shows the maximum static pressure ratio that can be obtained for a specific inlet Mach number. The graph shows that the ratio of L/H can vary significantly depending on the value of back pressure required for the intakes operating at lower Mach numbers. For the higher Mach number range, the value of L/H is less wide-ranging.

Lin et al.[75,76] performed several numerical studies on shock trains in constant area isolators. The number of secondary shocks and the spacing between consecutive shocks was found to increase with Mach number and the computed shock length at the different tested conditions and back pressures compared well with the Waltrup-Billig correlation. It was also reported that for both normal and oblique shock trains, the shock length increases with back pressure, and a higher pressure recovery or better shock isolation can be achieved by a longer duct. There is of course the penalty of a heavier weight. So whereas the shock length increases at a rate that also goes up with the back pressure, it becomes less cost effective to trade engine weight with pressure recovery at higher back pressures.

Pratt and Heiser[31] carried out detailed comparisons of constant-area and variable-area isolators, concluding that in ramjet mode, a constant-area isolator is only marginally able to contain the normal shock required for subsonic combustor entry, and that any perturbation from this state with either disgorge the thermal throat or unstart the inlet. Therefore, a variable-area isolator will be required to stabilise the terminal normal shock for use over a range of flight conditions.

Several experimental tests have been carried out at NASA Langley by Emami et al.[35] to investigate the inlet-isolator performance in an airframe-integrated ramjet/scramjet engine at Mach 4. Figure 2.29 presents a schematic of the model used in this study which consists of a compressional ramp, sidewall, isolator and an expanding section downstream of the isolator. Three different cowl lengths were tested, each with various isolator lengths. The foreplate is varied in length to study the effect of varying the incoming boundary-layer characteristics on the inlet performance.

Extensive parameter studies were conducted by Emami et al. providing a database of information for various aspects of inlet-isolator flows from the inlet unstart char-

acteristics to the isolator back pressure characteristics, isolator effectiveness and the effect of flow-distortion on the inlet-isolator maximum pressure.

Emami et al. studied both the intake unstart characteristics due to flow separation in the inlet and from excessive back pressuring when simulating combustion pressure rise. In studying the effect of flow separation to intake unstart, the data showed that the interaction of the cowl shock with the inlet boundary-layer is critical, as this interaction leads to flow separation that can unstart the intake. The investigation of the intake with a back pressure showed that the degree of maximum sustainable combustor pressure rise before an intake unstart was found to depend on the inlet geometry, contraction ratio and on the isolator length.

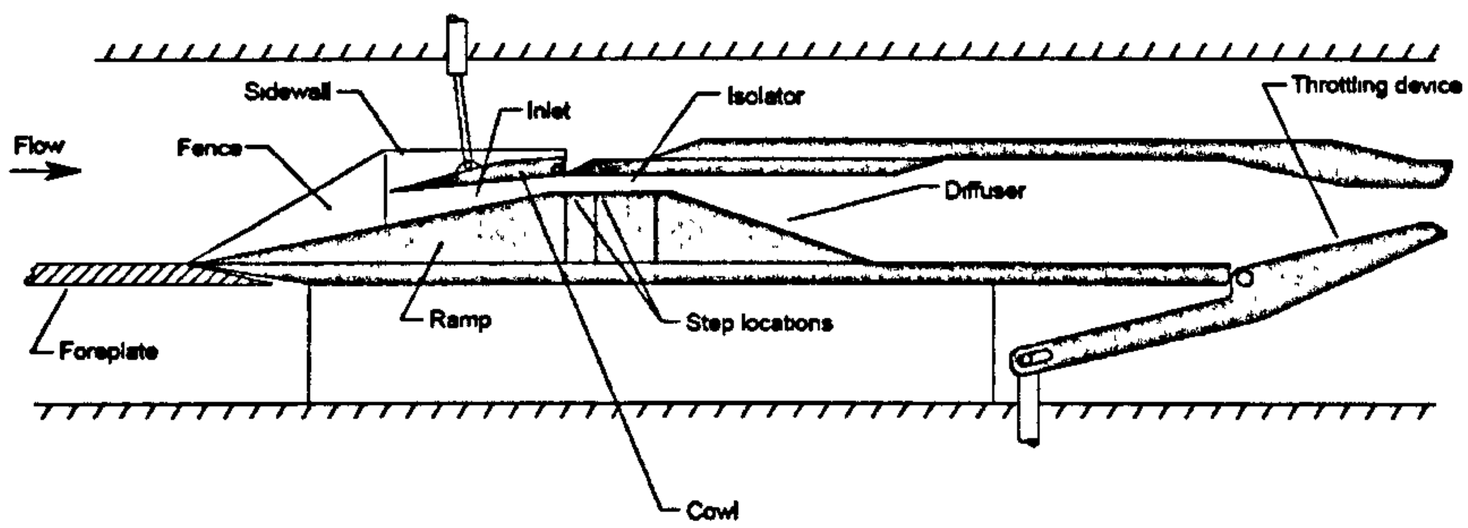


Figure 2.29: Schematic diagram of the model used for parametric inlet-isolator tests at Mach 4 at NASA Langley Research Centre (Emami et al.[35]).

From the data obtained on the isolator back pressure characteristics, Emami et al. showed that the performance of the isolator is dependent on the inlet geometry, forebody boundary-layer thickness and on the isolator length. The combined inlet-isolator maximum back pressure capability was again increased with increasing isolator length, but that once the shock train was considered to be fully contained within the isolator, further addition of isolator length did not continue to increase the isolator pressure level. Figure 2.30 shows the maximum inlet-isolator back pressure level for various isolator lengths with a specific cowl length (2.5 in) obtained by Emami et al. The general trend shows that the maximum sustainable back pressure is increased as contraction ratio (dependent on the inlet cowl length and angle) is increased. As isolator length is increased, the maximum sustainable back pressure that is necessary for combustion operation is also increased.

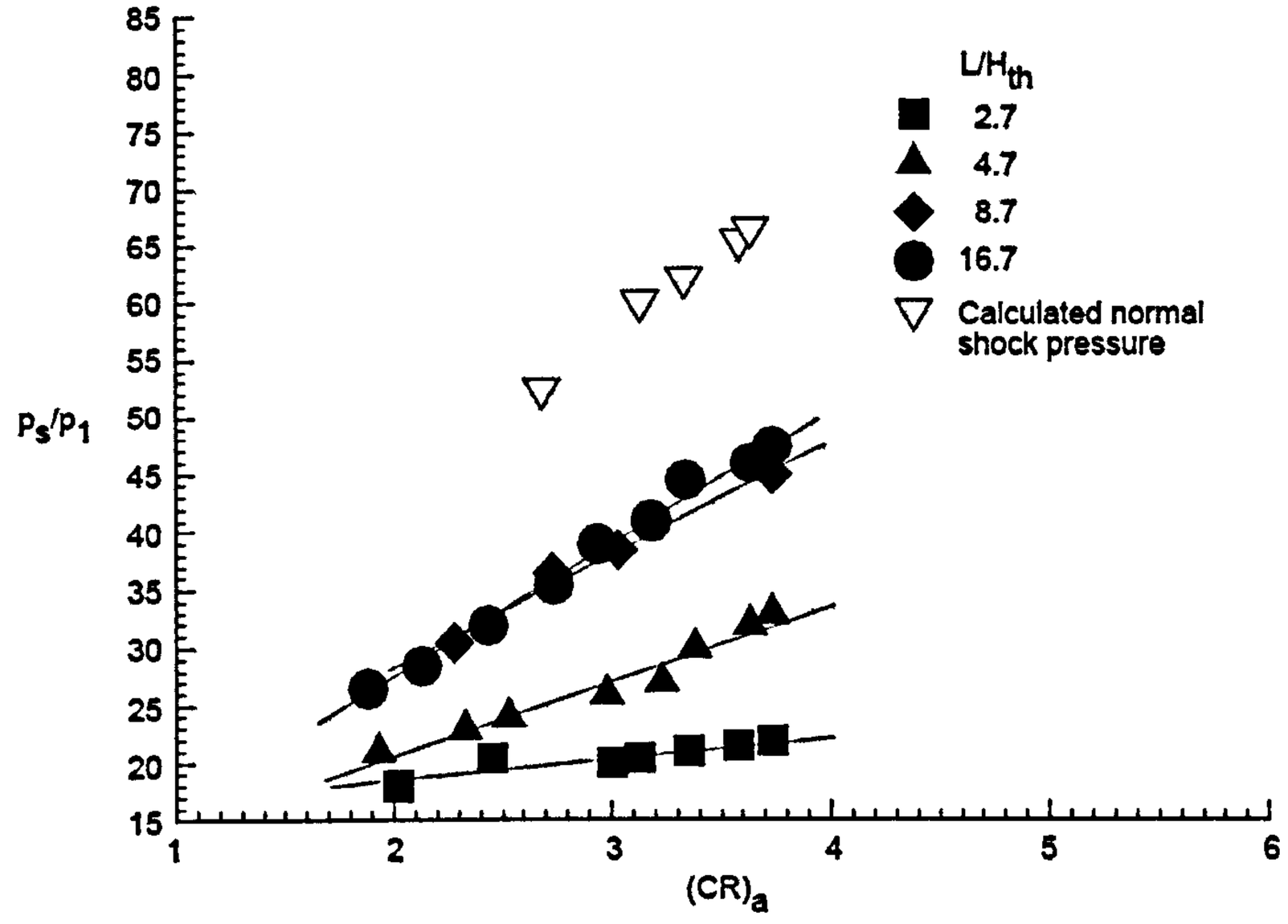


Figure 2.30: Inlet-isolator maximum back pressure with constant-area isolator length (L/H) of 2.7, 4.7, 8.7 and 16.7 for 2.5-in cowl; thin boundary-layer (Emami et al.[35]).

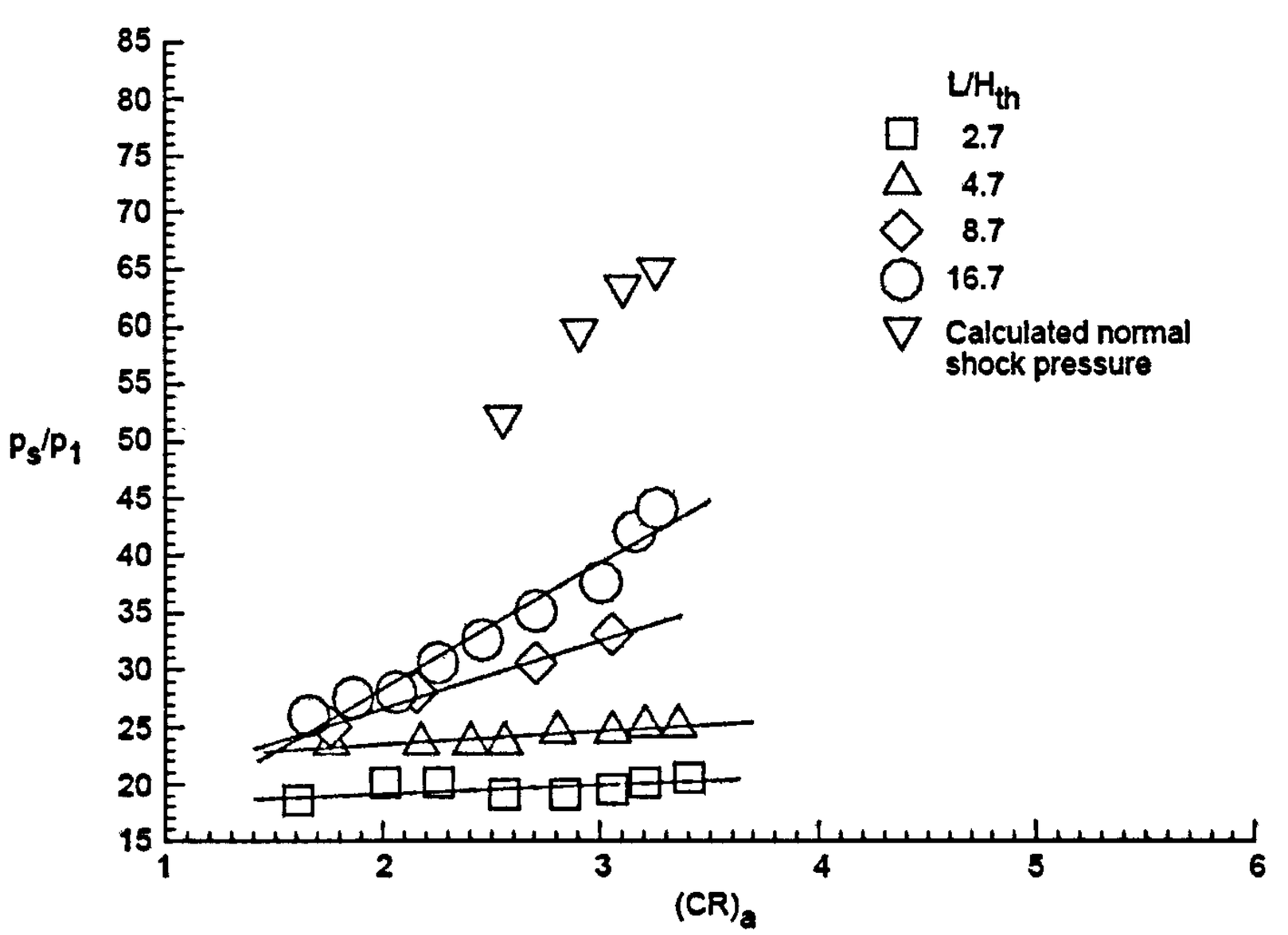


Figure 2.31: Inlet-isolator maximum back pressure with constant-area isolator length (L/H) of 2.7, 4.7, 8.7 and 16.7 for 2.5-in cowl; thick boundary-layer (Emami et al.[35]).

When this value reaches its maximum, the maximum back pressure levels are negligible with further increasing isolator length. Figure 2.31 presents the same test cases as in Figure 2.30 but now with an additional forebody plate added to increase the incoming boundary-layer thickness.

The results show a decrease in the maximum sustainable back pressure for the thicker incoming boundary-layer case. It was found that the thicker boundary-layer added to the flow distortion in the duct which led to higher losses and decreased isolator performance. Similar test cases were carried out for a cowl with an increased length of 4.4-in, for thin and thick boundary-layer cases. The results from the thicker boundary-layer test cases are shown in Figure 2.32. The same general trends are seen, however the maximum sustainable back pressure levels are now increased for the higher contraction ratios achieved with the longer cowl case.

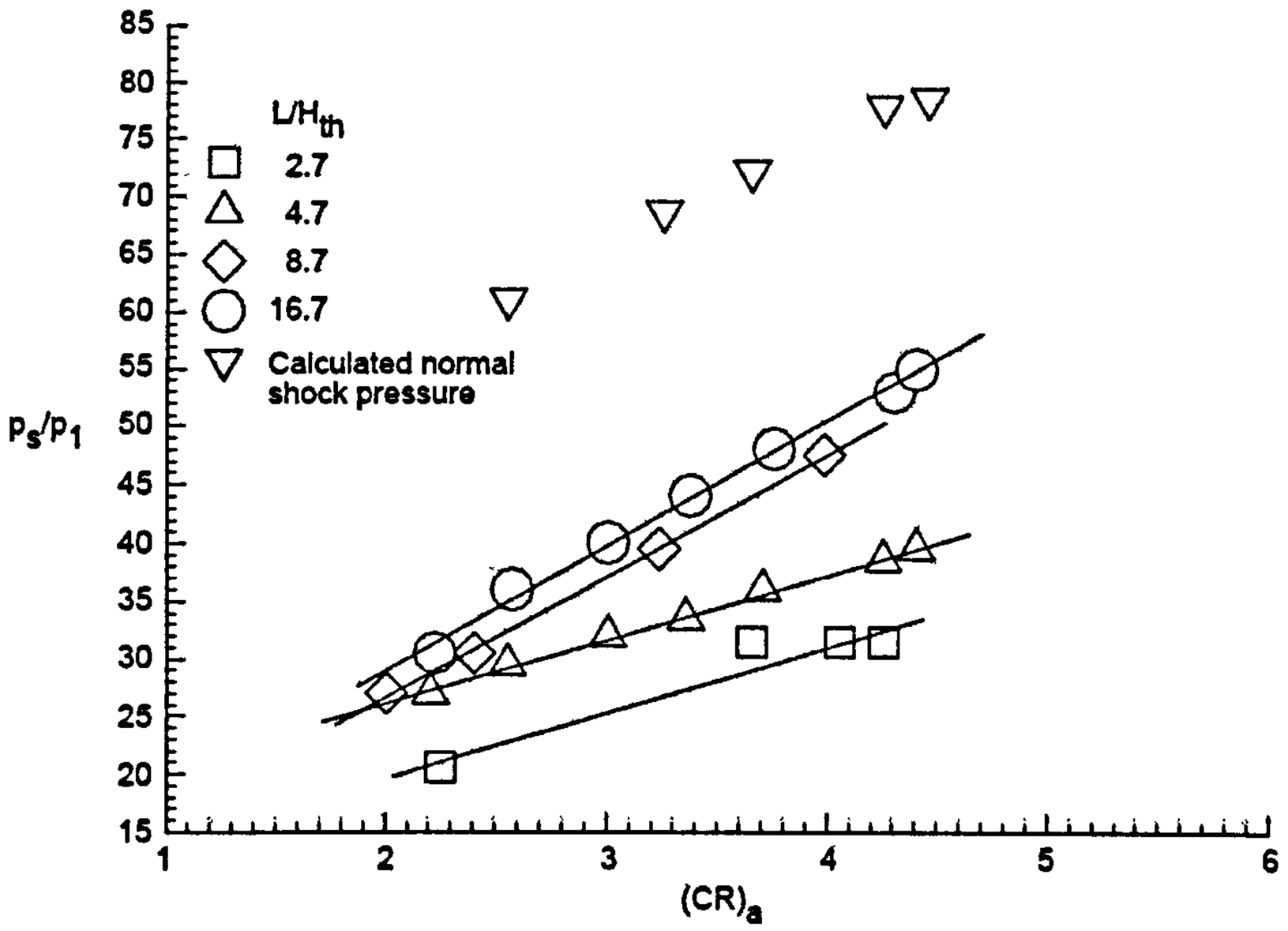


Figure 2.32: Inlet-isolator maximum back pressure with constant-area isolator length (L/H) of 2.7, 4.7, 8.7 and 16.7 for 4.4-in cowl; thick boundary-layer (Emami et al.[35]).

Reinartz et al.[91,92] produced numerical and experimental comparisons of flow in a hypersonic intake with a varying isolator geometry at Mach 4 and 5 flight conditions. Figure 2.33 shows the two-dimensional mixed compression intake model where l defines the isolator length and h the isolator height. The model design allows the

isolator length to be varied within the range of 29.3 - 99.3mm by the insertion of additional pieces. The results from this study concluded that the sustainable intake back pressure is strongly influenced by the length of the isolator.

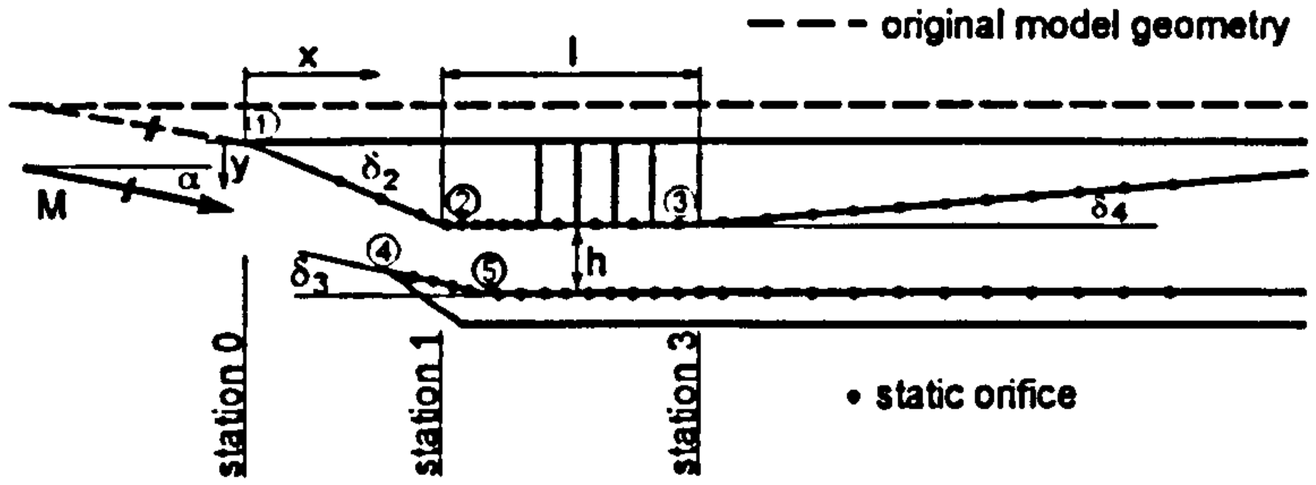
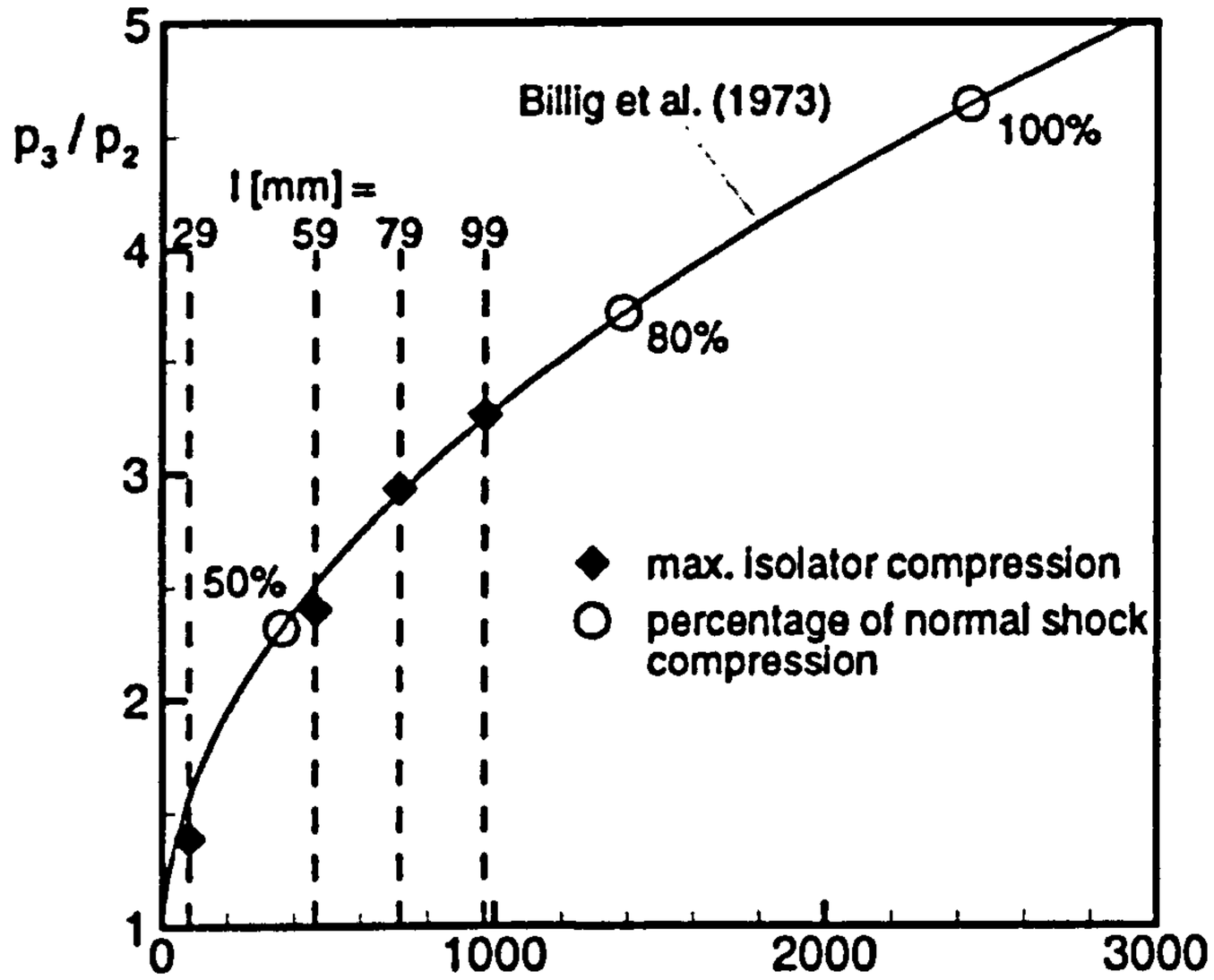


Figure 2.33: Two-dimensional mixed compression inlet-isolator model tested at Mach 4 and 5 conditions (M_{sol}=3.0) by Reinartz et al.[91] (Aachen University/DLR)



$$\frac{(M^2-1)\, l/h\, Re_\theta^{0.2}}{(\theta/h)^{0.5}}$$

Figure 2.34: Waltrup-Billig empirical correlation for isolator length and computed maximum compression ratios for different isolator lengths (Reinartz et al.[91]).

An extremely short isolator was shown to give the most unfavourable performance in terms of compression efficiency. Increasing the isolator length was found to reduce

the pressure sensitivity of the inlet. The results again showed that above a certain isolator length, no further increase in the sustainable back pressure was possible. Figure 2.34 from the work of Reinartz present a graph of the Waltrup-Billig correlation for isolator length and computed maximum compression ratios. Experimental values obtained compared well with the correlation curve. The graph shows that the maximum compression ratio is obtained when the complete isolator (99mm) contributes to the pressure buildup. The slope of the correlation curve shows that for a small increase in length of the short isolator (29mm) a much larger pressure gain can be made when comparing to a similar increase in length of the longest isolator used in this study (99mm).

Figure 2.35 compares flow patterns obtained from experiment and CFD for the intake with an applied back pressure ratio $p_{back}/p_{\infty} = 7$ showing complex shock and expansion interactions in the duct. The high back pressure results in both the upper and lower boundary-layers separating and generating additional shock waves in the flow. Separation of the boundary-layer can be seen in the schlieren picture, however, the structure of the shock waves in the vicinity of the separated region can only be determined from the numerical solution.

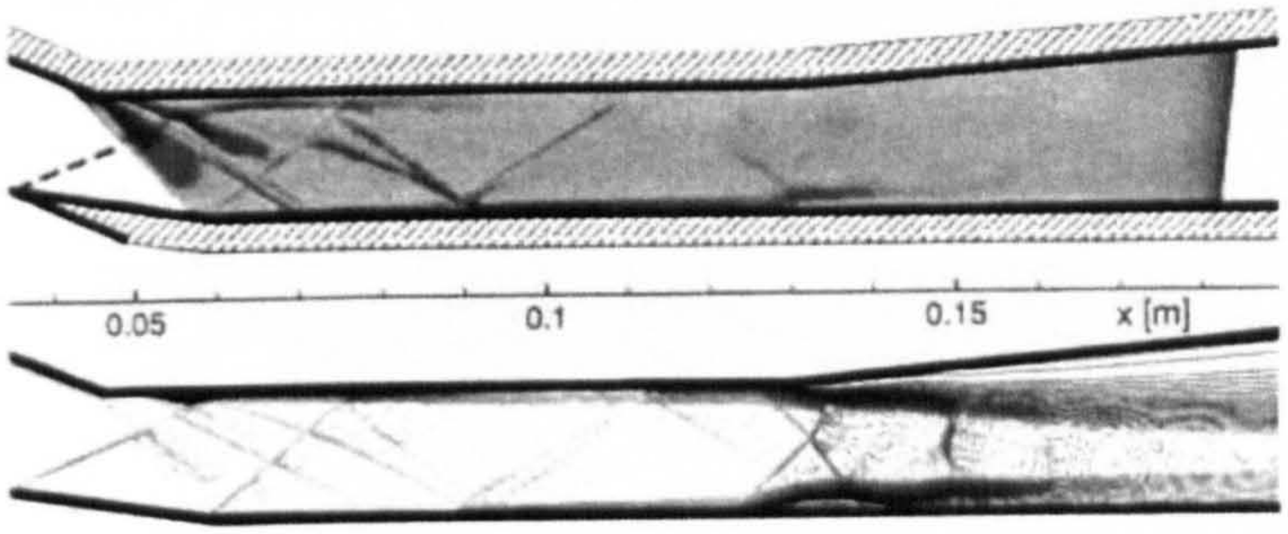


Figure 2.35: Comparison of a schlieren picture (top) and corresponding CFD Mach contours (bottom) with a specified back pressure ratio of 7. (Reinartz et al.[91]).

Duncan and Thomas[12] carried out numerical studies on a ramjet inlet at Mach 3.5 focusing on the effect of high back pressure levels on flow separation in the duct. It was found that as the back pressure is increased, the increased pressure levels within the subsonic portion of the boundary-layer increases the displacement thickness which forces the flow further away from the wall. This reduces the effective

cross sectional area of the throat and increases the likelihood of flow separation.

Ding et al.[26] conducted a series of numerical tests on the isolator flow by determining the effect of inlet flow distortion on isolator performance. The distortion arises as a result of the interaction of uncancelled cowl shocks and expansion waves in the isolator. In two cases studied, the cowl shock was first designed to partially cancel out at the corner expansion to produce a regular flow as seen in Figure 2.36, with a second test carried out with a cowl shock designed to impinge after the corner expansion to cause a distortion in the flow field, as seen in Figure 2.37. The results suggested that intake back pressure capability is increased with decreasing inlet flow distortion. The flow structure produced in Figure 2.36 resulted in higher sustainable back pressures when compared to the distorted flow structure in Figure 2.37.

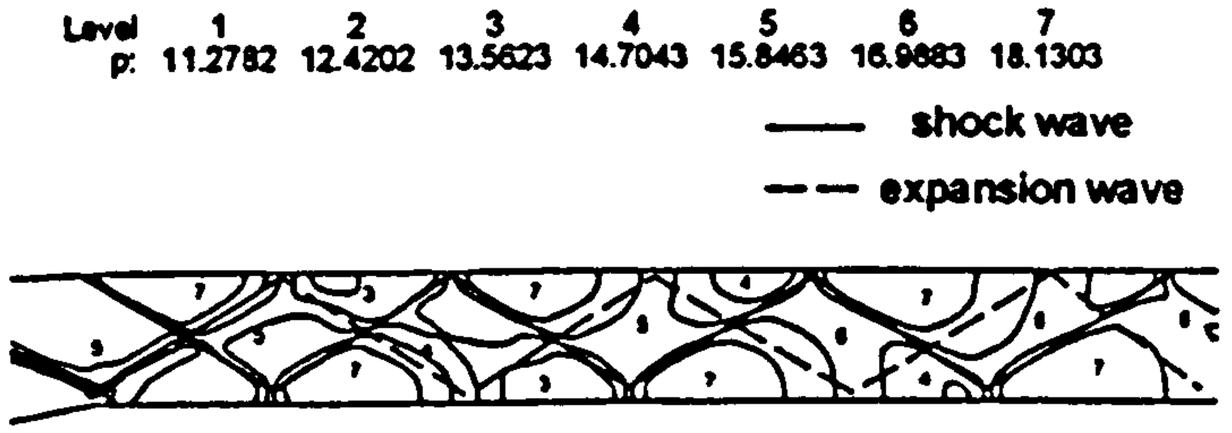


Figure 2.36: Static pressure contours in an isolator ($M_\infty = 4$) to shows regular intersection and reflection between shocks and expansion waves (Ding et al.[26]).



Figure 2.37: Static pressure contours in an isolator ($M_\infty = 4$) to show irregular intersection and reflection between shocks and expansion waves (Ding et al.[26]).

This chapter has presented a review of the existing knowledge and research carried out in the field. A review of the various configurations for ramjet and scramjet intakes has been presented. Several of the important performance parameters used in high-speed intake analysis have been defined. Various studies on the flow characteristics of high-speed intakes have also been presented with a focus on the shock/shock, shock/expansion and shock/boundary-layer interactions which are so dominant in

the intake flow-field. Complex wave interactions at the inlet have shown to lead to high heating and flow non-uniformities which deteriorate intake performance. These can also lead to shock oscillations or buzz in the intake. Studies have also been presented on the specific geometry of the spike and cowl which have been shown to have a significant effect on the intake flow quality and performance. Discussion of the isolator component has also been presented in this chapter. The main concern with the isolator is that it should be designed such that it contains the entire length of the shock train to provide optimum performance. Complex wave interactions and separated flows in the isolator duct have shown to reduce the pressure recovery and back pressure capability which can lead to a reduced overall engine performance.

Chapter 3

Numerical methods

3.1 CFD methodology

This chapter presents an overview of the CFD methods used in this research. In the field of hypersonics, Computational Fluid Dynamics (CFD) has significant advantages. Hypersonic experiments are expensive to carry out and require state-of-the-art precision data acquisition technology. CFD can be used as an effective tool to design a good wind-tunnel model before committing to manufacture. The other great advantage of using CFD is its use in modelling internal flows which can be difficult to capture in an experiment. CFD can also be used to isolate certain flow field parameters to understand the contribution of a single parameter on a flow system. The output data from a CFD simulation also produces extensive information on a flow-field. The CFD code used to carry out this work has been developed within the Department of Aeronautics at Imperial College by Hillier,[36] Kirk et al.[49] and has been extensively used to solve a range of compressible flow problems. Fundamental studies comparing CFD with experimental data obtained from the Imperial College Hypersonic facility have been documented in publications.[36] Recent code validation studies have also been published by the Hypersonics Group at Imperial College and can be found in the work of Jackson,[61] Williams,[105] Creighton[98] et al.

3.1.1 Mesh generation

The first important step in producing a good CFD solution is the generation of a good mesh. The mesh methodology uses a *structured* system of quadrilateral cells in a finite-volume procedure that stores flow variables at the centre of a cell and calculates the fluxes at the cell interfaces. Figure 3.1 illustrates a typical cell structure in the mesh, indicating the numbering for cells and interfaces. The resolution of the mesh is an important aspect of the procedure, but since a high resolution mesh can result in a long run time, the likely accuracy of solution and efficiency of run time is assessed before committing to a mesh. Fine mesh resolution is also important in areas where the solution is rapidly changing, e.g. shock-shock interactions and boundary-layers, and a grid stretching technique is used to increase the resolution of the mesh in such regions. Specific examples of meshes generated for this research are presented in Section 3.2 with mesh convergence assessment results.

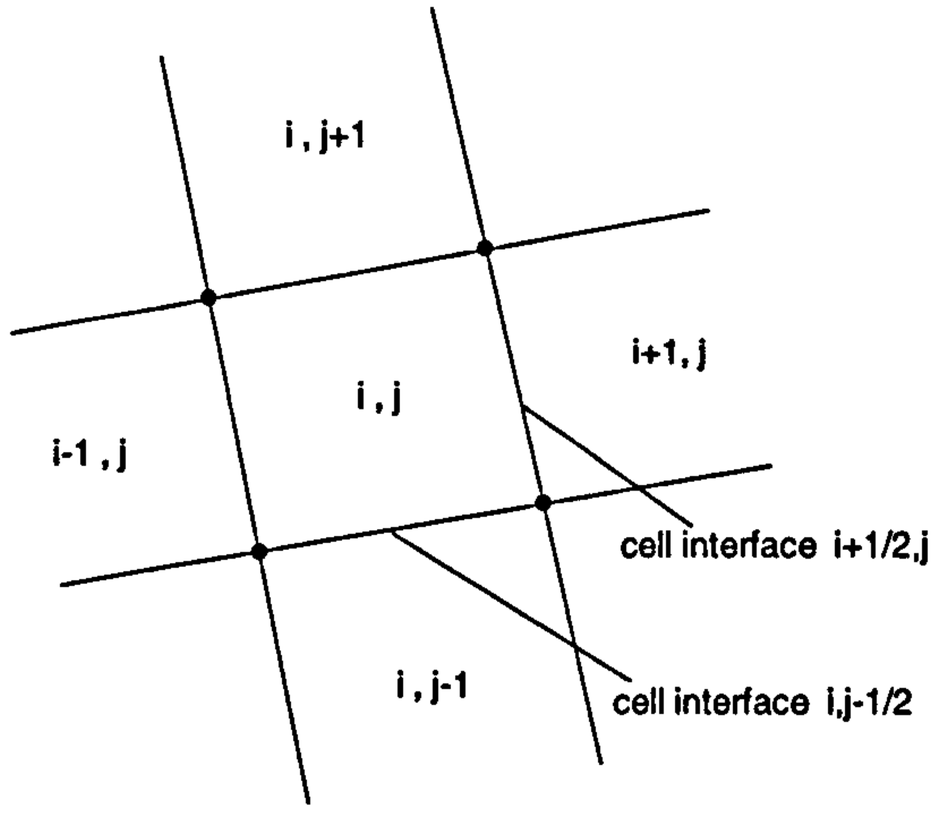


Figure 3.1: Typical cell structure in a mesh.

3.1.2 Euler solver

The basic flow solver can be run either as an Euler (inviscid) solver or as a Navier-Stokes solver, either laminar or with one of several turbulence models. The code is second-order accurate in space and time and for this study the code is implemented as two-dimensional and axisymmetric. In cylindrical coordinates (x,r) the Euler

equations can be written in vector form, Equation 3.1.

$$\frac{\partial \mathbf{Q}}{\partial t} + \frac{\partial \mathbf{F}}{\partial x} + \frac{\partial \mathbf{G}}{\partial r} = \mathbf{S} \tag{3.1}$$

Here, the conservative variables $\mathbf{Q}$, flux vectors $\mathbf{F}$, $\mathbf{G}$ and the 'source' term $\mathbf{S}$ are:

$$\mathbf{Q} = \begin{bmatrix} \rho \\ \rho u \\ \rho v \\ E \end{bmatrix} \qquad \mathbf{F} = \begin{bmatrix} \rho u \\ \rho u^2 + p \\ \rho uv \\ u(E+p) \end{bmatrix} \qquad \mathbf{G} = \begin{bmatrix} \rho v \\ \rho uv \\ \rho v^2 + p \\ v(E+p) \end{bmatrix} \qquad \mathbf{S} = -\frac{1}{r} \begin{bmatrix} \rho v \\ \rho uv \\ \rho v^2 \\ v(E+p) \end{bmatrix} \tag{3.2}$$

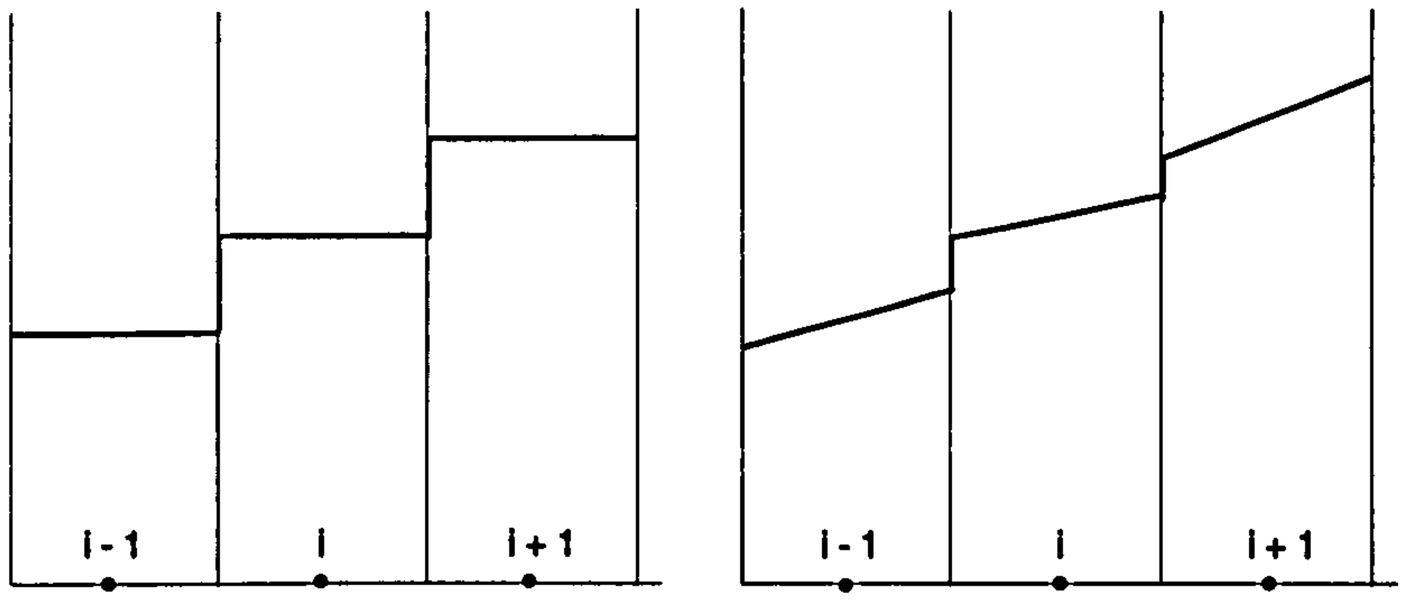


Figure 3.2: Piecewise constant (left) and piecewise linear (right) gradient calculation.

The variables p, ρ, u, v, E are pressure, density, x-component of velocity, r-component of velocity and total energy per unit volume respectively. The Euler equations are solved using an explicit second-order Godunov method based on the 'Generalised Riemann Problem' of Ben-Artzi.[14] Flow-field variables are stored at the cell centres and for a second-order calculation, piecewise linear spatial gradients are calculated, see Figure 3.2. First-order methods i.e. piecewise constant calculations are diffusive and can smear out the flow variables. However, second-order calculations require a

constraint to limit the amplitude of the gradients, and a monotone limited centred difference is used. The fluxes at the cell interfaces are then determined using the Generalised Riemann problem (GRP).

The solver splits the inviscid calculation in two directional sweeps. The mesh is discretised into two quasi-normal directions ξ and η and Equation 3.17 is then solved in one dimensional sweeps in both directions. The sequence of operator sweeps that is used to update the solution vector $\mathbf{Q}$ in both directions is given by Equation 3.3. Here L_η and L_ξ are the operators which update the solution in both mesh directions and L_s is the operator for the source term.

$$\mathbf{Q}^{n+1} = \mathbf{Q}^n \left[L_\eta \left(\frac{\Delta t}{2}\right) L_\xi \left(\frac{\Delta t}{2}\right) L_s(\Delta t) L_\xi \left(\frac{\Delta t}{2}\right) L_\eta \left(\frac{\Delta t}{2}\right) \right] \tag{3.3}$$

3.1.3 Navier-Stokes solver

The Navier-Stokes solver is based on the two-dimensional axisymmetric Navier-Stokes equations which are the governing equations for viscous flow. In cylindrical coordinates (x,r) the laminar equations can be written as Equation 3.4 where the subscript $\mathbf{i}$ denotes the convective (i.e. 'Euler' terms or inviscid) terms and the subscript $\mathbf{v}$ denotes the diffusive terms.

$$\frac{\partial \mathbf{Q}}{\partial t} + \frac{\partial \mathbf{F_i}}{\partial x} + \frac{\partial \mathbf{G_i}}{\partial r} + \mathbf{S_i} = \frac{\partial \mathbf{F_v}}{\partial x} + \frac{\partial \mathbf{G_v}}{\partial r} + \mathbf{S_v} \tag{3.4}$$

The conservative variables $\mathbf{Q}$, and the inviscid flux vectors $\mathbf{F_i}$ and $\mathbf{G_i}$ in Equation 3.4 (the same as Equation 3.2) are:

$$\mathbf{Q} = \begin{bmatrix} \rho \\ \rho u \\ \rho v \\ E \end{bmatrix} \qquad \mathbf{F_i} = \begin{bmatrix} \rho u \\ \rho u^2 + p \\ \rho uv \\ u(E+p) \end{bmatrix} \qquad \mathbf{G_i} = \begin{bmatrix} \rho v \\ \rho uv \\ \rho v^2 + p \\ v(E+p) \end{bmatrix} \tag{3.5}$$

The viscous flux vectors $\mathbf{F_v}$ and $\mathbf{G_v}$ are given by:

$$\mathbf{F_v} = \begin{bmatrix} 0 \\ \tau_{xx} \\ \tau_{xr} \\ u\tau_{xx} - v\tau_{xr} - q_{xx} \end{bmatrix} \qquad \mathbf{G_v} = \begin{bmatrix} 0 \\ \tau_{rx} \\ \tau_{rr} \\ u\tau_{rx} - v\tau_{rr} - q_{rr} \end{bmatrix} \tag{3.6}$$

The source terms $\mathbf{S_i}$ and $\mathbf{S_v}$ are given by:

$$\mathbf{S_i} = \frac{1}{r}\begin{bmatrix} \rho v \\ \rho uv \\ \rho v^2 \\ v(E+p) \end{bmatrix} \qquad \mathbf{S_v} = -\frac{1}{r}\begin{bmatrix} 0 \\ \tau_{rx} \\ \tau_{rr} - \tau_{\theta\theta} \\ u\tau_{rx} - v\tau_{rr} - q_{rr} \end{bmatrix} \tag{3.7}$$

The heat fluxes due to thermal conduction in the axial and radial directions are given by the Equations 3.8 and 3.9. The thermal conductivity k can be obtained from the Prandtl number given by Equation 3.10, where Cp is constant.

$$q_{xx} = -k\frac{\partial T}{\partial x} \tag{3.8}$$

$$q_{rr} = -k\frac{\partial T}{\partial r} \tag{3.9}$$

$$Pr = \frac{C_p\mu}{k} = 0.72 \tag{3.10}$$

The dynamic viscosity μ which is dependent on temperature can be calculated from Keyes law in Equation 3.11 where μ_{ref}=1.418 x 10^{-6}, a=116.4 and b=5.

$$\frac{\mu}{\mu_{ref}} = \frac{T^{0.5}}{1 + aT^{-1}10^{-b/T}} \tag{3.11}$$

For Newtonian fluids, the viscous stresses are given in Equations 3.12 to 3.15.

$$\tau_{xx} = 2\mu\frac{\partial u}{\partial x} + \lambda\left(\frac{\partial u}{\partial x} + \frac{\partial v}{\partial r} + \frac{v}{r}\right) \tag{3.12}$$

$$\tau_{rr} = 2\mu\frac{\partial v}{\partial r} + \lambda\left(\frac{\partial u}{\partial x} + \frac{\partial v}{\partial r} + \frac{v}{r}\right) \tag{3.13}$$

$$\tau_{\theta\theta} = 2\mu\frac{v}{r} + \lambda\left(\frac{\partial u}{\partial x} + \frac{\partial v}{\partial r} + \frac{v}{r}\right) \tag{3.14}$$

$$\tau_{xr} = \tau_{rx} = \mu\left(\frac{\partial u}{\partial r} + \frac{\partial v}{\partial x}\right) \tag{3.15}$$

The second coefficient of viscosity λ, or 'bulk' viscosity is related to the dynamic viscosity μ by Equation 3.16.

$$\lambda = -\frac{2}{3}\mu \tag{3.16}$$

The inviscid and viscous fluxes are separately solved using an operator splitting method to improve the solution accuracy and run-time efficiency. The Navier-Stokes equations are separated into the convective and diffusive parts shown in Equations 3.17 and 3.18 with **S** denoting the source terms. The equations are solved in separate operator sweeps to achieve convection-diffusion splitting.

$$\frac{\partial \mathbf{Q}}{\partial t} = -\frac{\partial \mathbf{F_i}}{\partial x} - \frac{\partial \mathbf{G_i}}{\partial r} - \mathbf{S_i} \tag{3.17}$$

$$\frac{\partial \mathbf{Q}}{\partial t} = \frac{\partial \mathbf{F_v}}{\partial x} + \frac{\partial \mathbf{G_v}}{\partial r} + \mathbf{S_v} \tag{3.18}$$

Equation 3.19 outlines the procedure for solving the equations from time level n to $n+1$. $L_i(\Delta t)$ is the operator that advances the convective terms, and $L_v(\Delta t)$ the

operator that advances the diffusive terms. The solution is first advanced by half a time step with operator L_v. This is followed by a full time step with operator L_i and then a final half step with the operator L_v. The symmetry of the method ensures that a second-order accurate solution is achieved.

$$\mathbf{Q}^{n+1} = \mathbf{Q}^n \left[L_v \left(\frac{\Delta t}{2} \right) L_i(\Delta t) L_v \left(\frac{\Delta t}{2} \right) \right] \tag{3.19}$$

3.1.4 Turbulence modelling

For turbulence modelling, the one-equation variant of the k-ϵ model formulated by Menter (1997) is implemented. The two-equation model solves two coupled partial differential equations, Equation 3.20 for the turbulence kinetic energy k, and Equation 3.21 for the dissipation rate ϵ. The kinematic eddy viscosity ν_t, which requires k and ϵ is given in Equation 3.22. The closure coefficients for the standard k-ϵ model and further discussions are given in Wilcox.[24]

$$\frac{\partial k}{\partial t} + U_j \frac{\partial k}{\partial x_j} = \tau_{ij} \frac{\partial \bar{U}_i}{\partial x_j} - \epsilon + \frac{\partial}{\partial x_j} \left[(\nu + \nu_t/\sigma_k) \frac{\partial k}{\partial x_j} \right] \tag{3.20}$$

$$\frac{\partial \epsilon}{\partial t} + U_j \frac{\partial \epsilon}{\partial x_j} = c_{\epsilon 1} \frac{\epsilon}{k} \tau_{ij} \frac{\partial U_i}{\partial x_j} - c_{\epsilon 2} \frac{\epsilon^2}{k} + \frac{\partial}{\partial x_j} \left[(\nu + \nu_t/\sigma_\epsilon) \frac{\partial \epsilon}{\partial x_j} \right] \tag{3.21}$$

$$\nu_t = c_\mu \frac{k^2}{\epsilon} \tag{3.22}$$

The Menter one-equation variant, called the (k-ϵ)$_{1E}$ model is assessed against the Baldwin-Barth one-equation and standard k-ϵ model in Menter.[82] The comparisons show very close similarity to the standard two-equation k-ϵ model near the boundary-layer edge where good agreement with experiment was made. The Baldwin-Barth model showed poor predictions near the boundary-layer edge. The (k-ϵ)$_{1E}$ model also gives almost identical results to the standard k-ϵ model for zero pressure gradient boundary-layers. For stronger adverse pressure gradient flows improved predictions

were made by the (k-ϵ)$_{1E}$ model compared to the standard k-ϵ model predictions. The simplicity of the (k-ϵ)$_{1E}$ equations also makes it easier to implement in a solver.

The transformation of the one-equation Menter variant is based on Bradshaw's assumption that (in many circumstances) the turbulent shear stress is proportional to the turbulence kinetic energy. The eddy viscosity $\tilde{\nu}_t$ is defined in Menter[82] by Equation 3.23. To form a single transport equation, the time derivative is expressed by Equation 3.24. The equation relates the eddy viscosity to k and ϵ.

$$\tilde{\nu}_t = c_\mu \frac{k^2}{\epsilon} \tag{3.23}$$

$$\frac{D\tilde{\nu}_t}{Dt} = c_\mu \left[2\frac{k}{\epsilon}\frac{Dk}{Dt} - \frac{k^2}{\epsilon^2}\frac{D\epsilon}{Dt} \right] \tag{3.24}$$

Closure requires two additional equations. The definition of the eddy viscosity is input into the single transport equation to replace ϵ. The second equation is based on Bradshaw's assumption so that:

$$Production_k = Dissipation_k$$

Another assumption is that the diffusion coefficients in the turbulence kinetic energy and dissipation rate equations 3.20 and 3.21, σ_k and σ_ϵ are identical:

$$\sigma_k = \sigma_\epsilon = \sigma \tag{3.25}$$

These assumptions are suitable for high Reynolds number flows and for low Reynolds number terms damping functions must be applied. In the Menter variant, the high Reynolds number eddy viscosity $\tilde{\nu}_t$ is multiplied by a damping function to arrive at the correct eddy viscosity value ν_t, Equation 3.26.

$$\nu_t = D_2 \tilde{\nu}_t \tag{3.26}$$

$$D_2 = 1 - e^{-(\tilde{\nu}_t / A^+ \kappa \nu)^2} \tag{3.27}$$

$$\kappa = 0.41 \tag{3.28}$$

$$A^+ = 13 \tag{3.29}$$

Menter's variant of the one-equation k-ϵ model, derived from the above system of equations where $\sigma = \sigma_k = 1.0$, in its final form is shown in Equation 3.30. The Menter turbulence equation is solved simultaneously with the Navier-Stokes equations (Equation 3.5). In the latter μ is replaced by $\mu + \mu_t$ (or ν by $\nu + \nu_t$) and k by $k + k_t$. That is, add together molecular values plus turbulence values.

$$\frac{D\tilde{\nu_T}}{Dt} = c_1 D_1 \tilde{\nu_T} S - c_2 E_{le} + \frac{\partial}{\partial x_j}\left[\left(\nu + \frac{\tilde{\nu}_t}{\sigma}\right)\frac{\partial}{\partial x_j}(\tilde{\nu}_t)\right] \tag{3.30}$$

The coefficients of the one-equation variant are as follows:

$$c_1 = (c_{\epsilon 2} - c_{\epsilon 1})\sqrt{c_\mu} = 0.144 \tag{3.31}$$

$$c_2 = \frac{c_1}{\kappa^2} + \frac{1}{\sigma} = 1.86 \tag{3.32}$$

$$D_1 = \frac{\nu_t + \nu}{\tilde{\nu}_t + \nu} \tag{3.33}$$

The strain rate S is expressed as:

$$S = \sqrt{U_{ij}(U_{ij} + U_{ji})} \tag{3.34}$$

The destruction term E_{1e} is calculated from Equation 3.35:

$$E_{1e} = c_3 E_{BB} \tanh\left(\frac{E_{k-\epsilon}}{c_3 E_{BB}}\right) \tag{3.35}$$

where the terms are given by:

$$E_{BB} = \frac{\partial \tilde{\nu}_t}{\partial x_j} \cdot \frac{\partial \tilde{\nu}_t}{\partial x_j} \tag{3.36}$$

$$E_{k-\epsilon} = \tilde{\nu}_t^2 \left(\frac{\frac{\partial S}{\partial x_j}\frac{\partial S}{\partial x_j}}{S^2} \right) \tag{3.37}$$

$$c_3 = 7.0 \tag{3.38}$$

3.1.5 Block-marching

Block-marching is a method used to improve the run time efficiency of a CFD simulation. Instead of solving for the entire domain, a starting block of a set number of cells can be specified and the code then calculates the solution within this block until the solution has converged. The entire block then moves in cell increments in the i-direction when the upstream column of cells has converged, and marches until the entire domain is solved. The convergence is dependent on a specified density residual which is defined in Equation 3.39.

The density history of a CFD simulation reveals whether the simulation has converged to a steady, or a stationary state. Block-marching can only be used in flows where upstream influence is negligible. For cases where the intake is tested with a back pressure to simulate combustion pressure rise[1] - for the purpose of investigating the inlet-isolator interactions - the block-marching method cannot be used.

$$Residual = \sum_{j=1}^{jmax} \frac{\rho_j^n - \rho_j^{n-1}}{\rho_j^{n-1}} \tag{3.39}$$

[1]This method is described in detail in chapter 6

3.2 Numerical set-up

3.2.1 Geometry definition

The Shyfe intake is a fixed-geometry axisymmetric intake. Figure 3.3 presents a full view of the Shyfe vehicle. The focus of this present study is to model the flow in the intake system, from the spike tip to the combustor entry and including the modelling of flow in the isolator. The original spike geometry was designed by QinetiQ's Hypersonics Group[107] using a Method of Characteristics calculation.



Figure 3.3: The Sustained Hypersonic Flight Experiment conceptual picture, copyright QinetiQ, Farnborough (Published with permission).

Figure 3.4 presents a 2D drawing of the intake with geometry definitions. The intake is primarily defined by the Mach number at which the shock-on-lip condition is achieved, M_{sol}. At this condition, the waves generated from the apex and from the isentropic compression surface focus at the cowl lip. The isentropic compression surface terminates on the spike at the angle θ_1 called the spike termination angle. The flow is then turned into the intake duct by the centrebody/cowl configuration. The centrebody angle after the shoulder is θ_2 which is designed to be parallel to the cowl inner surface which is defined by angle δ_c in a short duct placed after the intake annulus. The duct then diverges further downstream where the diffuser section is no longer parallel. The cowl is designed with a blunt leading edge, shown in the close-up view in Figure 3.4. Initial studies of the intake flow have been carried out with the cowl modelled as a thin-plate, coincident with the inner surface of the actual cowl. The angles θ_1, θ_2 and δ_c, and the value of M_{sol} are varied in a parameter study.

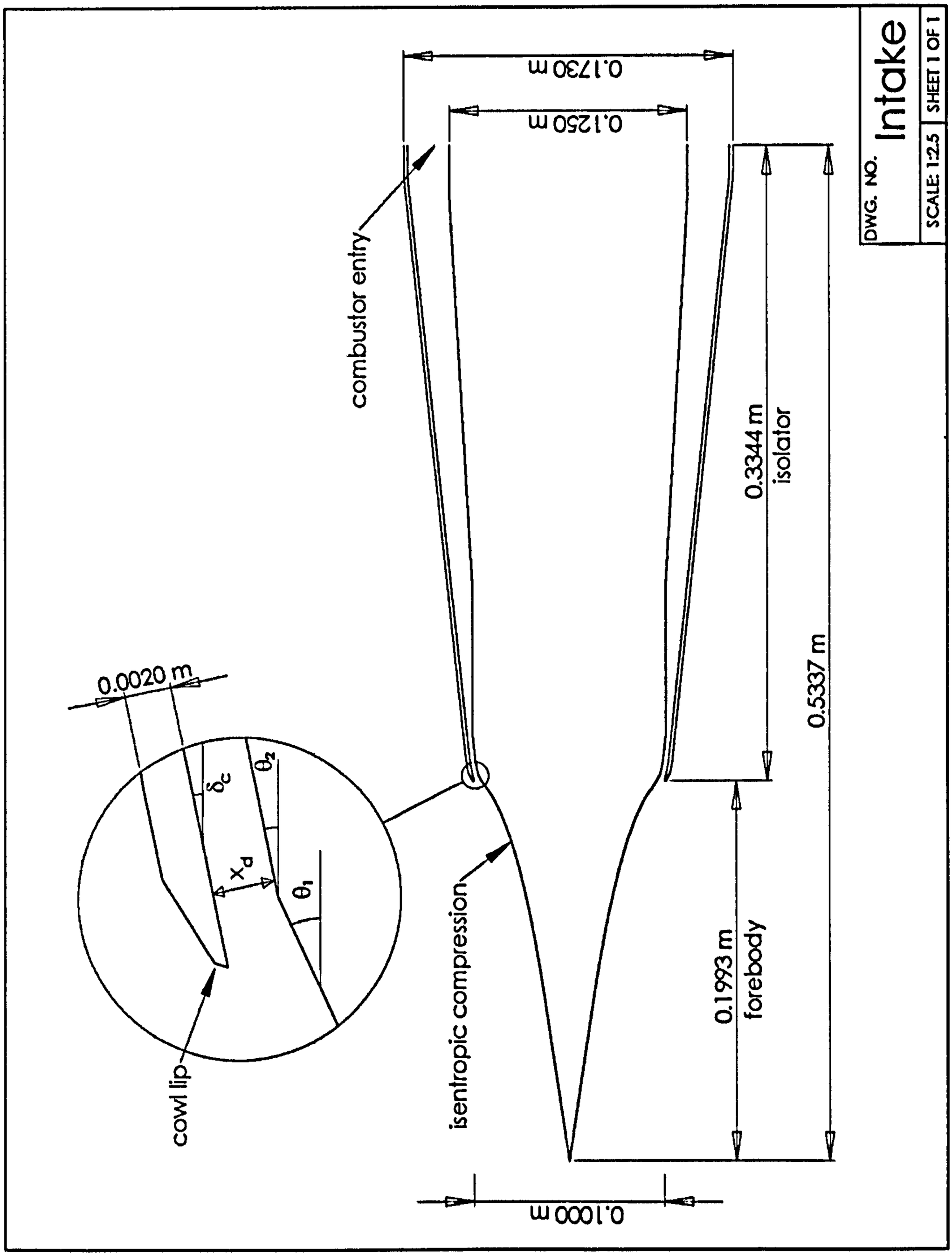


Figure 3.4: 2D Drawing of an initial variant of the Shyfe intake from the apex to the combustor entry; and a close-up view of the blunted cowl geometry. Further geometries will be explained in the thesis and also in the appendix section.

3.2.2 Mesh configuration

All meshes constructed are structured and made up of quadrilateral cells. The main mesh structure consists of a set of blocks, each of which contains a set of cells, which are constructed around the solid geometry of the intake model.

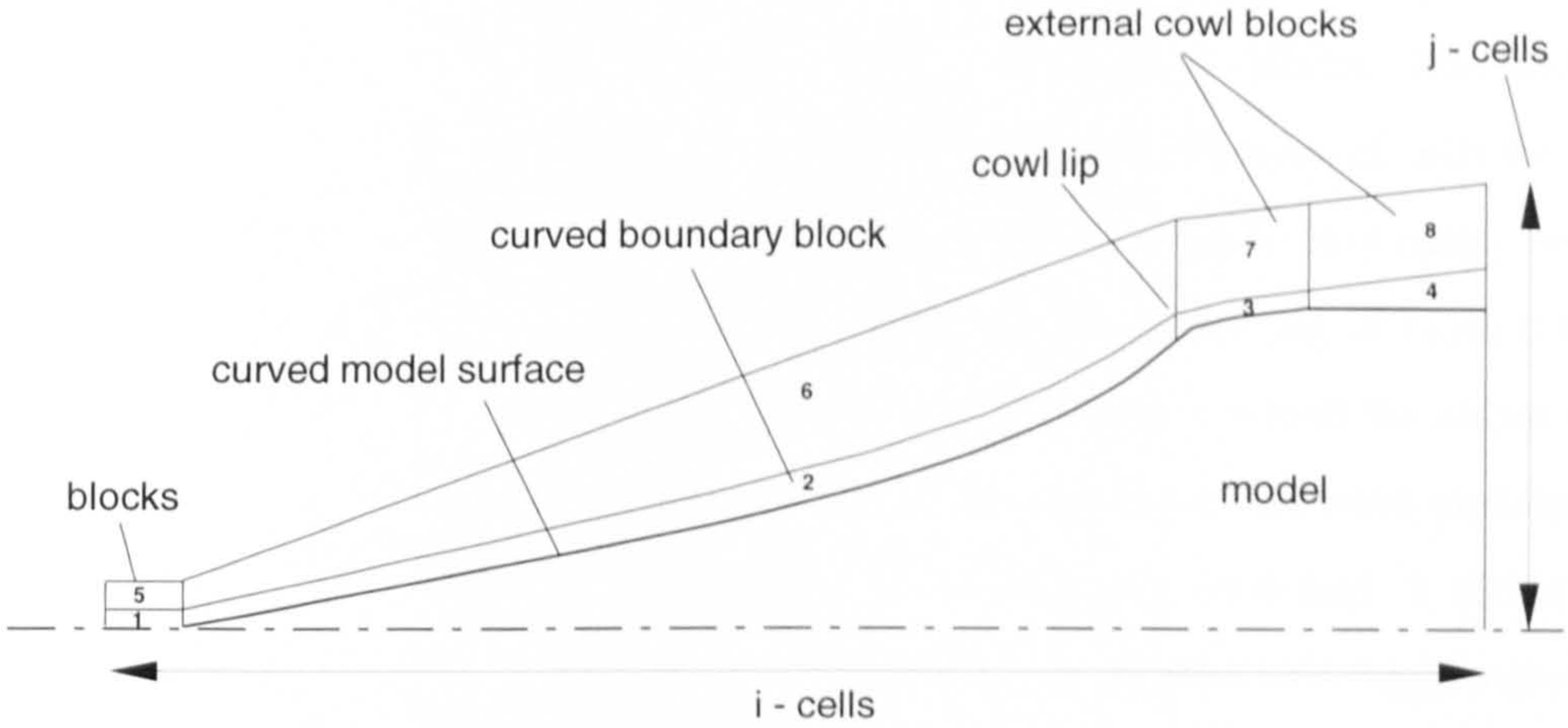


Figure 3.5: Methodology of the mesh block structure (close-up of the inlet).

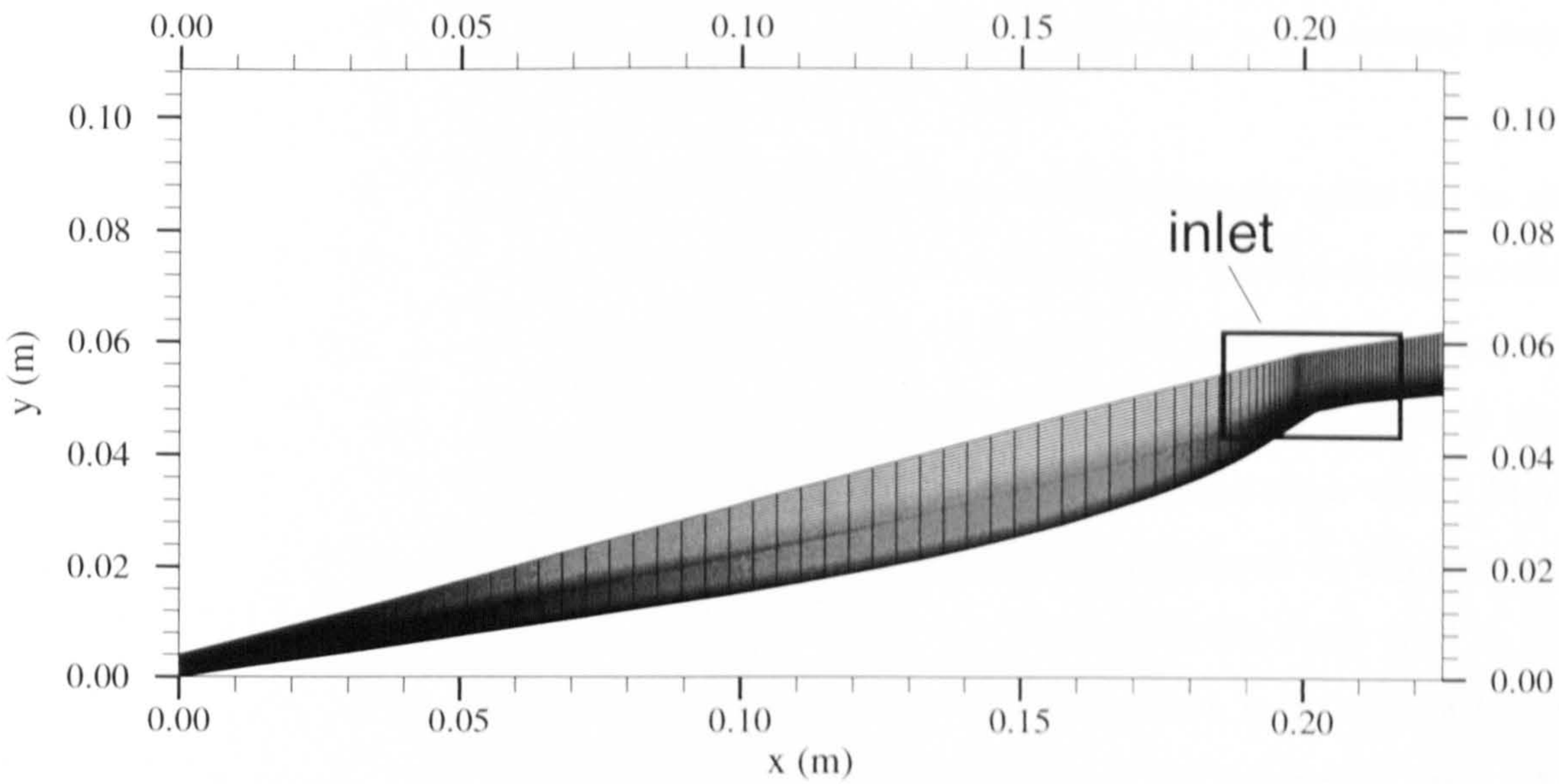


Figure 3.6: Intake mesh with a thin-plate cowl in the geometry from the spike leading edge up to the end of the parallel section; for illustration purposes only every second point is plotted (the full isolator and diffuser section is not shown).

Figure 3.5 illustrates the methodology for the mesh from the spike tip to the isolator section for the thin-plate cowl case. The figure shows 8 blocks in total, 4 blocks on the intake surface from left to right in the i-direction, and two levels of blocks in the j-direction. Each block consists of a designated number of cells. Block 1 and 5 lie ahead of the apex of the forebody. The curved boundary block 2 lies on the curved surface of the forebody and is constructed with curved surfaces on its top and bottom surfaces. Block 3 starts at the cowl leading edge and continues to the end of the parallel section. Block 4 contains the isolator section. The first 'j-level' which contains blocks 1, 2 ,3 and 4 contain the highest number of cells for accurate boundary-layer resolution on the forebody/centrebody and to accurately resolve the flow in the intake duct. The apex shock wave lies below the top of block 6 to ensure capture of the entire flow-field. The two blocks 7 and 8 which lie above the cowl exterior are kept coarse due to the focus of the study on the wave system at inlet and the internal flow-field. The cells in each block are stretched in either the i or j direction to put the maximum number of cells in regions with high concentration of flow features. For example, blocks 2 and 6 are compressed in the positive i-direction by decreasing the number of i-cells near the apex and compressing and hence, increasing the number of cells near the inlet annulus. The flow-field at the annulus will require the maximum concentration of cells due to the several shock reflections and interactions that appear in this region.

Figure 3.6 presents a plot of the intake mesh extending from the spike tip to the end of the parallel section. The diffuser section extends from the end of the parallel section up to the combustor entry. Figure 3.6 indicates the inlet section which is a major focus of this study. Figure 3.7 (a) shows a detailed view of a mesh in that region with a thin-plate cowl in the geometry. To construct the mesh with a blunt cowl geometry, an extra j-level of 4 blocks is inserted into the mesh on top of blocks 1-4. Figure 3.7 (b) shows a close-up view of this mesh with the blunt cowl in the geometry. The cells inside the cowl are irrelevant since there is no calculation in this region. Typical mesh sizes are around 1000 cells in the i-direction, and 200-400 cells in the j-direction, depending on the individual test case. For example, at the lower Mach numbers the apex shock focuses well above the cowl lip and so a

larger radius mesh with increased number of cells is required. For cases where the apex shock focuses into the annulus the mesh outer radius and cell number can be reduced. The cell numbers are the highest number that could be used in terms of the computational power available. In several simulations, the mesh is terminated after the parallel section to reduce run time when focusing on the flow-field at inlet.

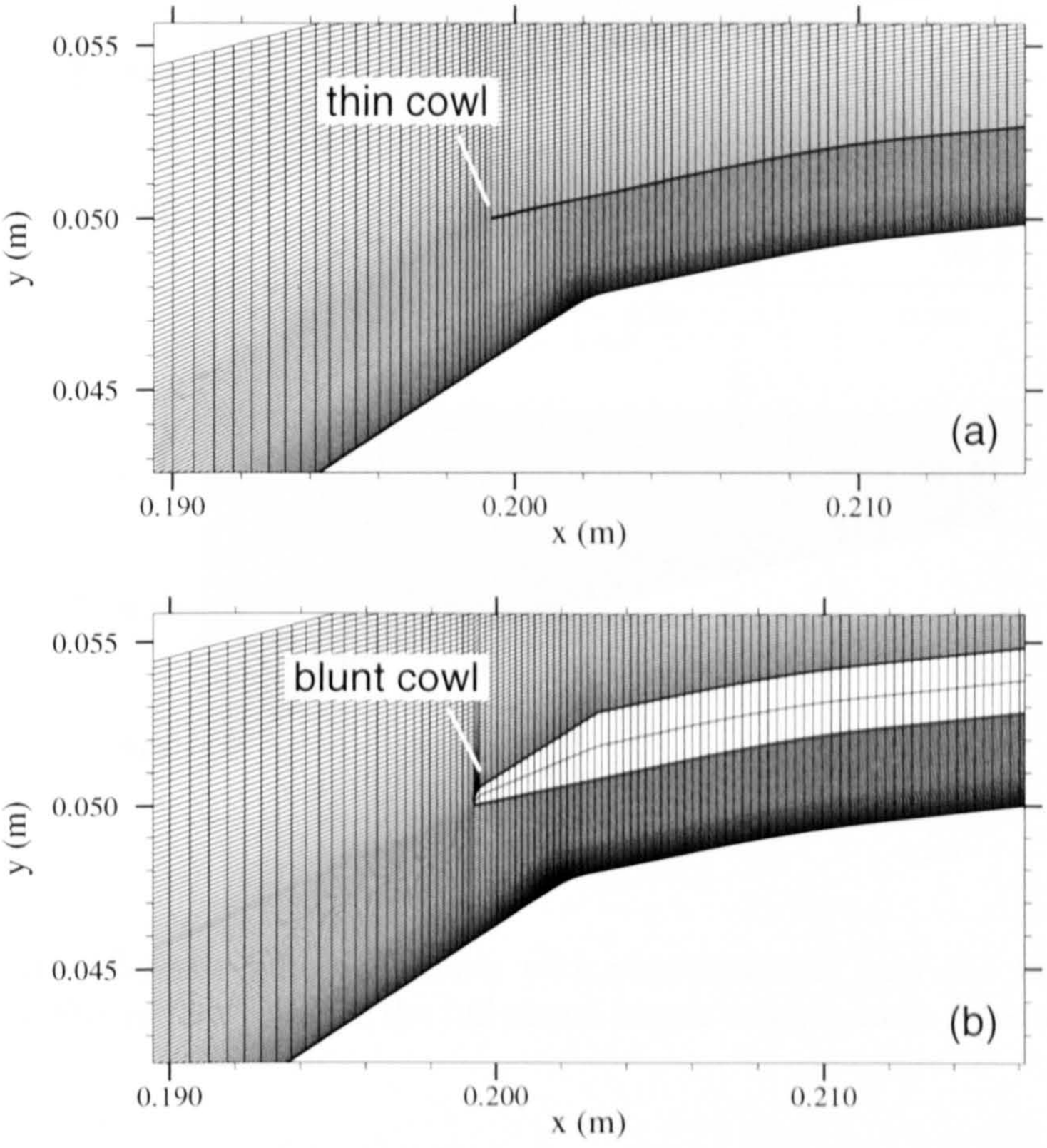


Figure 3.7: Intake mesh with a (a) thin-plate and (b) blunt cowl in the geometry.

3.2.3 Boundary-layer refinement

Mesh refining is used to improve the boundary-layer resolution in viscous simulations. An initial simulation calculates the flow properties in the boundary-layer, and a new mesh is then generated based on these flow properties. The mesh is adjusted to set a y^+ value of 1 (say) in the surface cells for the full chord length. This results

in the compression of the cells adjacent to the body surface to give high-resolution in the boundary-layer. Figure 3.8 shows a typical mesh close to the surface before (a) and after (b) mesh refinement.

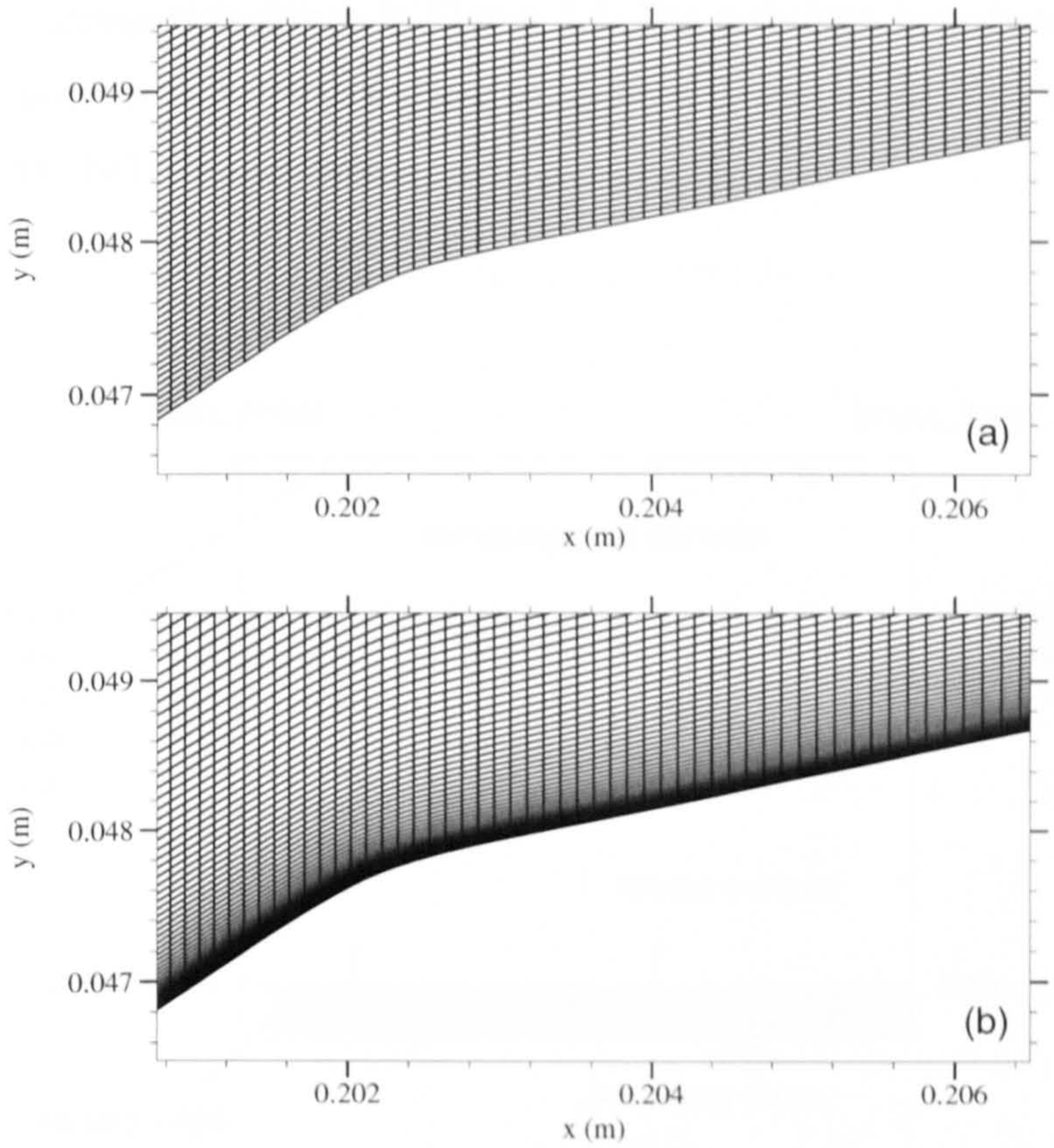


Figure 3.8: Boundary-layer meshing with stretched cells near the wall by fitting $y+$=1 in the surface cells for the full chord length using a mesh reforming method.

3.2.4 Initial and boundary conditions

All cells in the computational domain are initialised with the freestream flow variables U_∞, V_∞, p_∞ and ρ_∞ and the solver starts the simulation from this state. The computation is then time-marched from the initial state, until the steady state is achieved or until it reaches a stationary state. The left and top boundary use an inflow boundary condition. The outflow conditions are calculated at the right boundary of the domain for cases with a supersonic outflow condition. For cases where the intake is tested with a simulated combustion pressure rise, a downstream

back pressure condition is applied, and this is described in detail in chapter 6. The boundary cells on the solid surfaces are imposed with the no-slip velocity condition (i.e. u_w=0, v_w=0). The wall thermal condition is set to adiabatic (i.e. $\dot{q} = 0$) corresponding to equilibrium flight conditions. An illustration of the application of these boundary conditions is shown in Figure 3.9. For turbulent boundary-layer cases, a transition point is imposed in the boundary-layer to switch the Navier-Stokes model from laminar to turbulent flow.

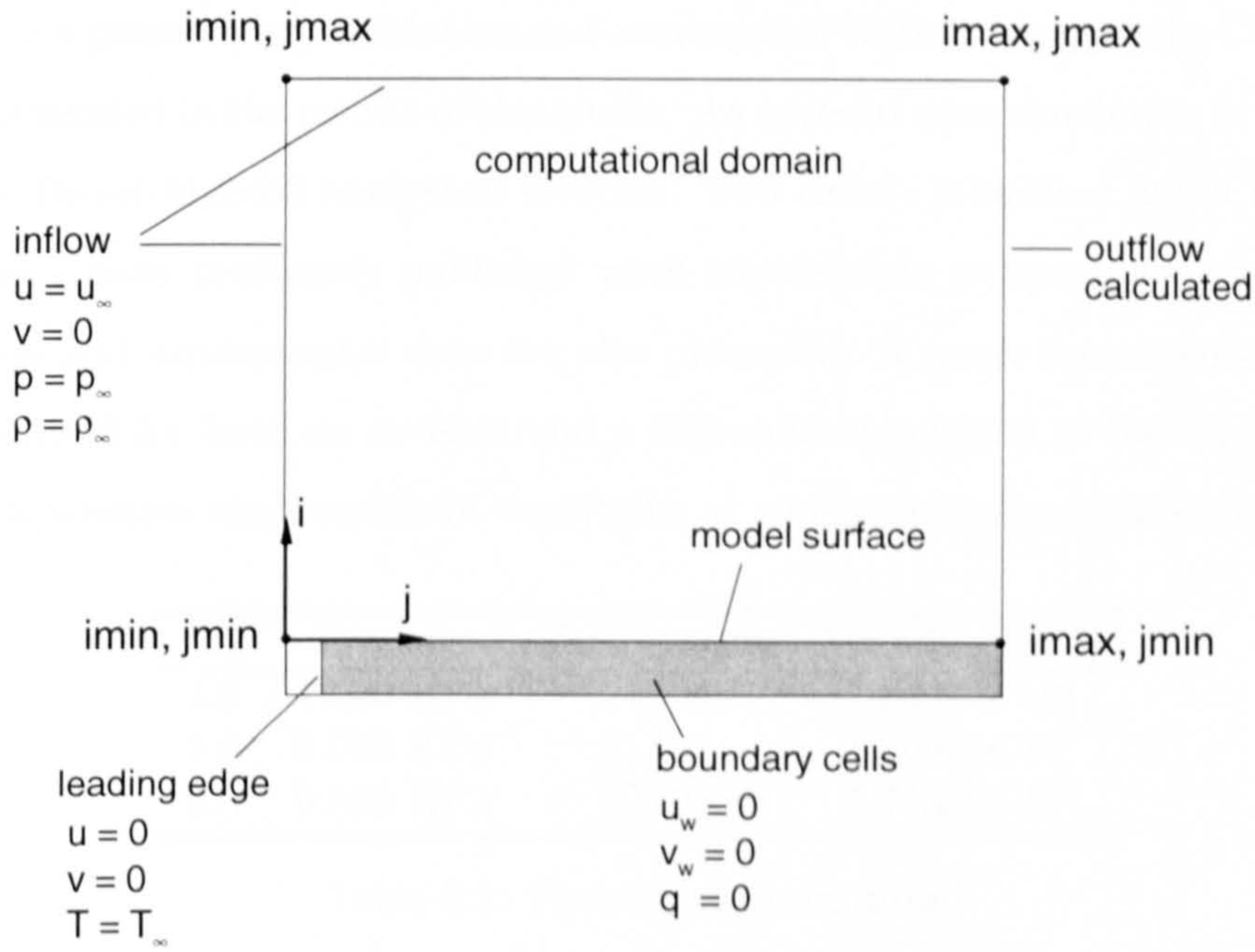


Figure 3.9: Application of CFD boundary conditions.

M_∞	Unit Re (m^{-1})	x_{tr} (m)	x_l (m)
4.0	1.6437 x 10^7	0.100	0.0125
5.0	1.3698 x 10^7	0.050	0.0125
5.5	7.3366 x 10^6	0.050	0.0125
6.0	1.7135 x 10^6	0.050	0.0125

Table 3.1: Transition parameters

Table 3.1 documents the Mach numbers and unit Reynolds numbers for the four

flight conditions tested. Natural transition data for the centrebody is not known. It is clear from the later results (see chapter 4) that the severe compression on the forebody will cause separation of a laminar boundary-layer. For safety, in the final Shyfe design, early transitions will therefore be required. Table 3.1 specifies the position of onset of transition, x_{tr}, and the distance over which transition is completed x_l in the simulations.

3.3 Validation and convergence

This section presents key validation and convergence tests to support the CFD simulations presented in the results of this thesis. An inviscid cone simulation is validated with the Taylor-Maccoll analytical solution. Two cases - a laminar and a turbulent CFD case - from previously published work which made comparisons between the CFD code and experimental data are also presented. A mesh convergence study is also presented for both an inviscid and a turbulent simulation of the Shyfe intake. Table 3.2 presents the freestream conditions at which the cases are tested.

M_∞	Pressure	Temperature	Unit Re (m^{-1})
4.0	12.00 KPa	217 K	1.6437 x 10^7
5.0	8.000 KPa	217 K	1.3698 x 10^7
6.0	0.890 KPa	228 K	1.7135 x 10^6

Table 3.2: Freestream conditions.

3.3.1 Taylor-Maccoll case

The supersonic flow over a cone at zero-incidence is known as the Taylor-Maccoll flow. In this flow, a conical shock wave attaches to the cone apex and the flow properties are constant along any ray from the apex of the cone. The flow behind the conical shock wave is also irrotational. Figure 3.10 illustrates the Taylor-Maccoll flow model where δ_c is the cone semi-angle, β is the shock wave angle and the subscript c denotes surface conditions. The solution to the Taylor-Maccoll flow can be obtained by a Runge-Kutta integration where given either the cone semi-angle

or shock wave angle, an iteration can be performed to obtain flow properties along incremental rays from the vertex and at the cone surface. For an inviscid adiabatic flow over a cone with a 10 degree semi-angle at Mach 5, data obtained from CFD is compared to the Taylor-Maccoll solution. Table 3.3 presents values of shock angle, surface Mach number M_c and surface pressure p_c/p_∞ values obtained from CFD solutions for three resolutions of meshes showing excellent convergence of the solution. Figure 3.11 and 3.12 present pressure contours from inviscid simulations of the cone at Mach 5 from both the low resolution and the high resolution CFD simulations, showing the rays of constant pressure from the cone vertex.

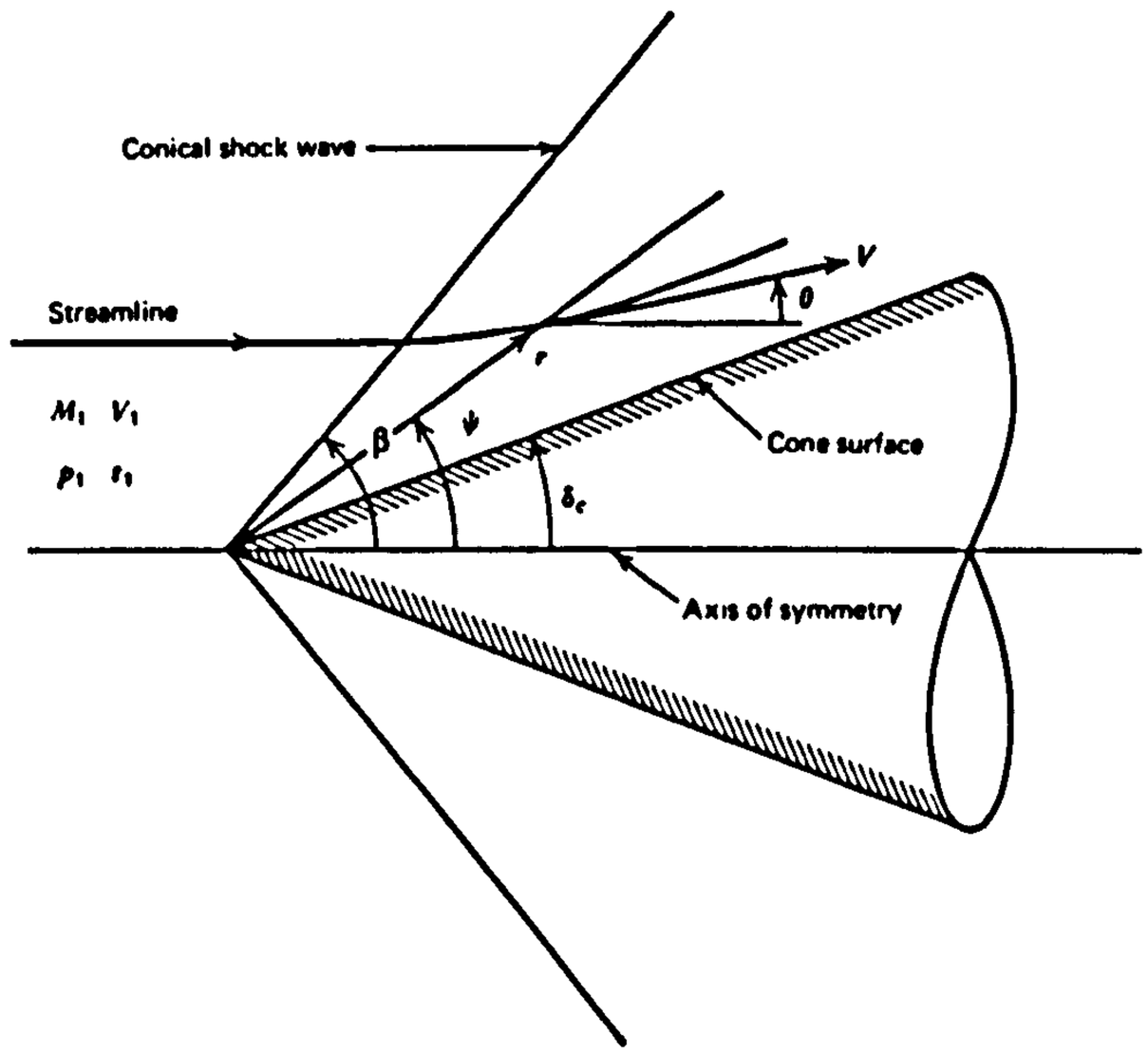


Figure 3.10: Flow model for Taylor-Maccoll flow over a cone (Zucrow[67]).

Case	i x j	β (deg)	M_c	p_c/p_∞
Low resolution CFD	211 x 26	15.633	4.2906	2.3055
Med resolution CFD	411 x 51	15.636	4.2916	2.3063
High resolution CFD	811 x 101	15.589	4.2920	2.3076
Taylor-Maccoll (analytical)	-	15.555	4.29	2.317

Table 3.3: Comparison of shock angle, surface Mach number and surface pressure values from inviscid CFD simulations of a cone with a 10 degree semi-angle at Mach 5 for three mesh resolutions; compared with the Taylor-Maccoll analytical solution.

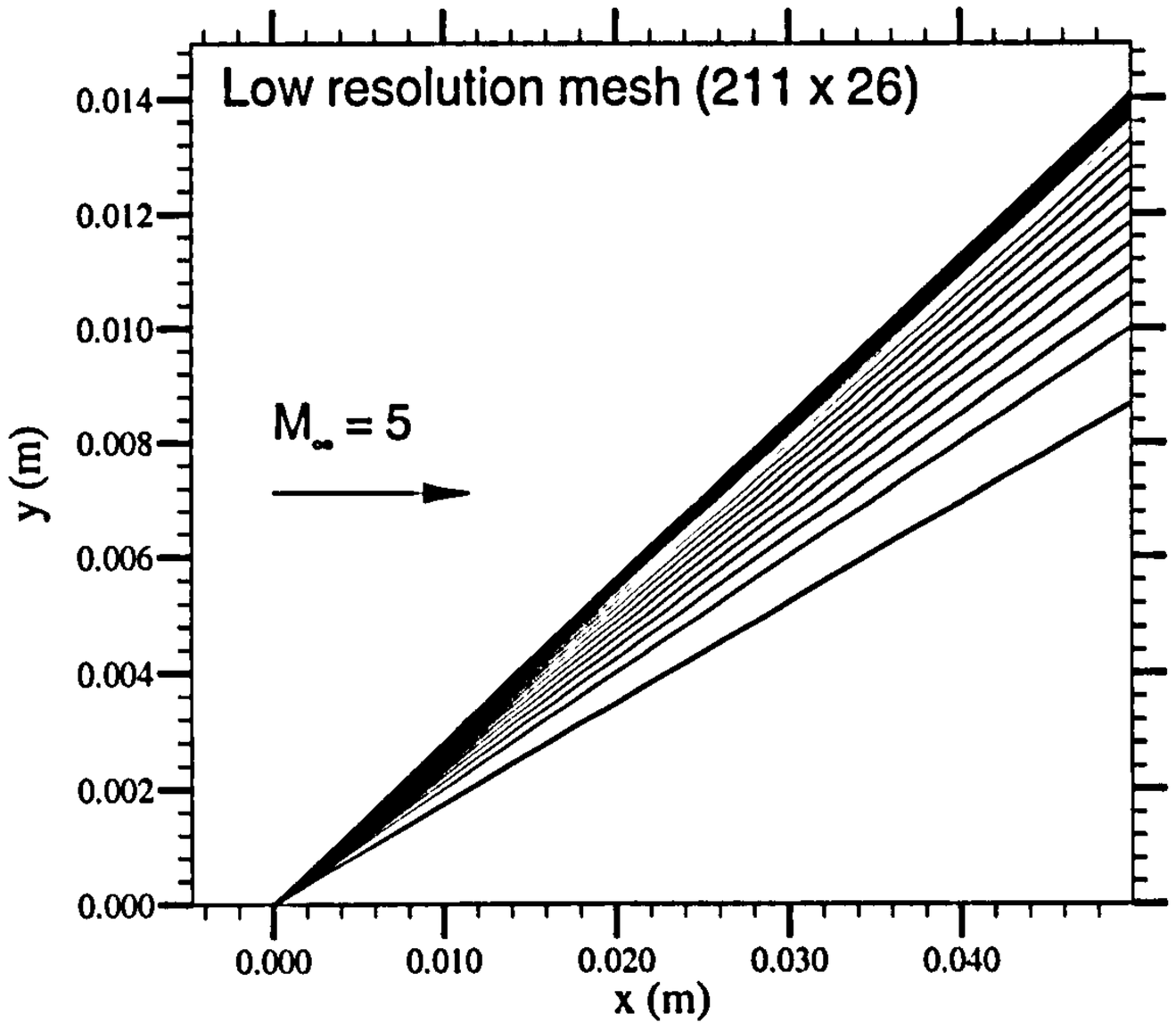


Figure 3.11: CFD Pressure contours from an inviscid simulation of flow over a cone with a 10 degree semi-angle at freestream Mach 5 (low resolution mesh).

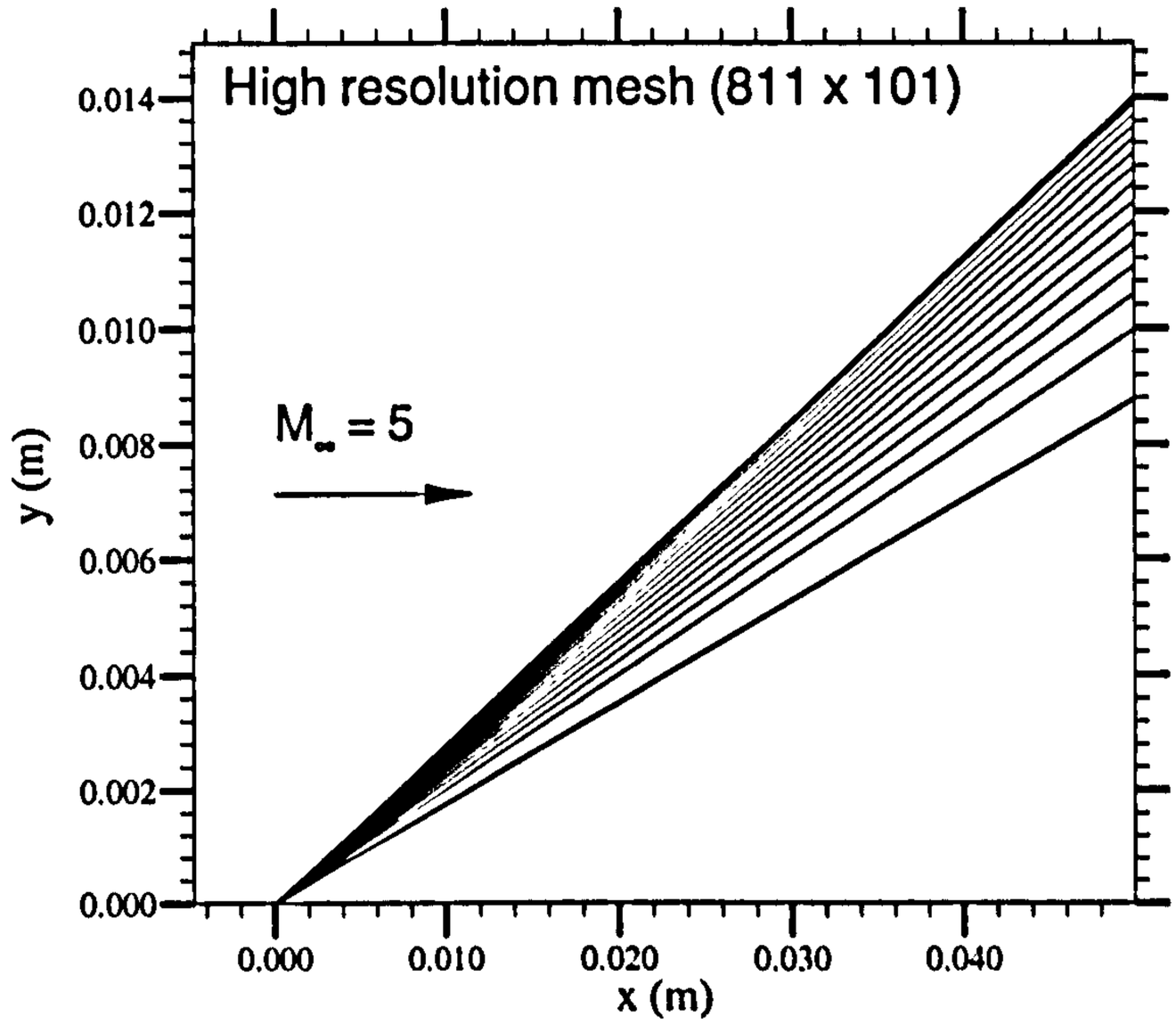


Figure 3.12: CFD Pressure contours from an inviscid simulation of flow over a cone with a 10 degree semi-angle at freestream Mach 5 (high resolution mesh).

3.3.2 CFD and experiment

Several benchmark cases to validate the laminar CFD computations have been carried out within the Hypersonics Group at Imperial College. Jackson, Hillier and Soltani[61] conducted a combined experimental and computational study of a surface cavity in a low Reynolds number flow at Mach 9.

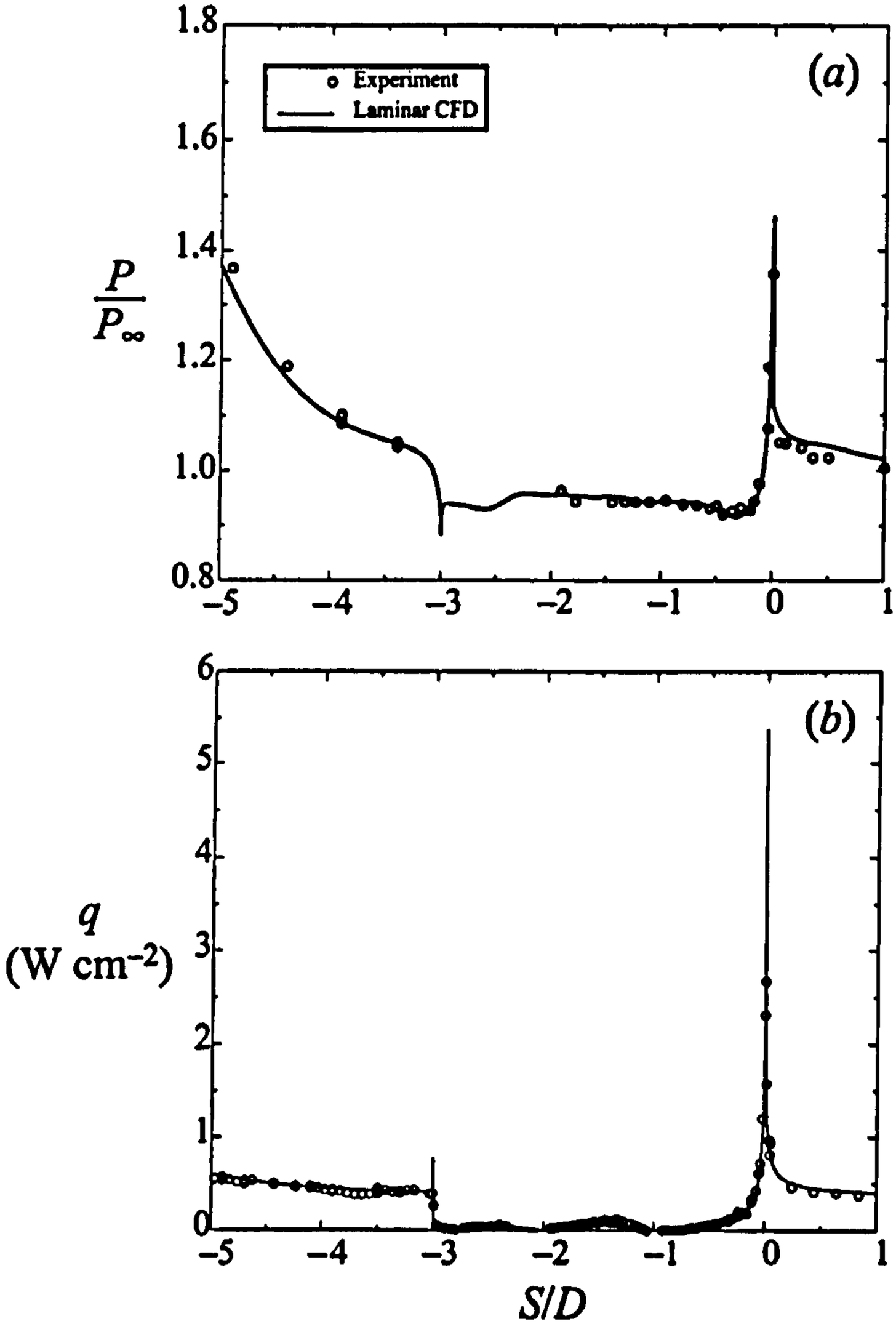


Figure 3.13: Comparison of experimental and laminar computational results for a low Reynolds number cavity flow (L/D=1) at Mach 9; (a) Surface pressure distribution (b) Surface heat transfer distribution (Jackson, Hillier and Soltani[61]).

Jackson studied a range of cavity length-to-depth (L/D) ratios up to a maximum of 8, corresponding to flows where the free shear layer bridges the entire cavity. Figure 3.13 (a) presents both experimental and laminar CFD surface pressure distribution along the body surface with a cavity with L/D = 1. The distance S represents a wetted distance along the body surface, normalised by the cavity depth D. The separation lip is at -3 and the reattachment lip is at 0. The experimental and CFD pressure data show excellent agreement, particularly at the reattachment lip.

Figure 3.13 (b) compares heat transfer measurements with laminar CFD data for the same cavity case, showing excellent agreement at the separation and reattachment points. Some discrepancies in the data were found on the cavity floor, and this difference was found to be connected with the unsteadiness in heat transfer in the flow. Jackson suggested that this was due to the flow on the cavity floor being turbulent, or three-dimensionally unsteady. Further details of this study can be found in the work of Jackson.[61]

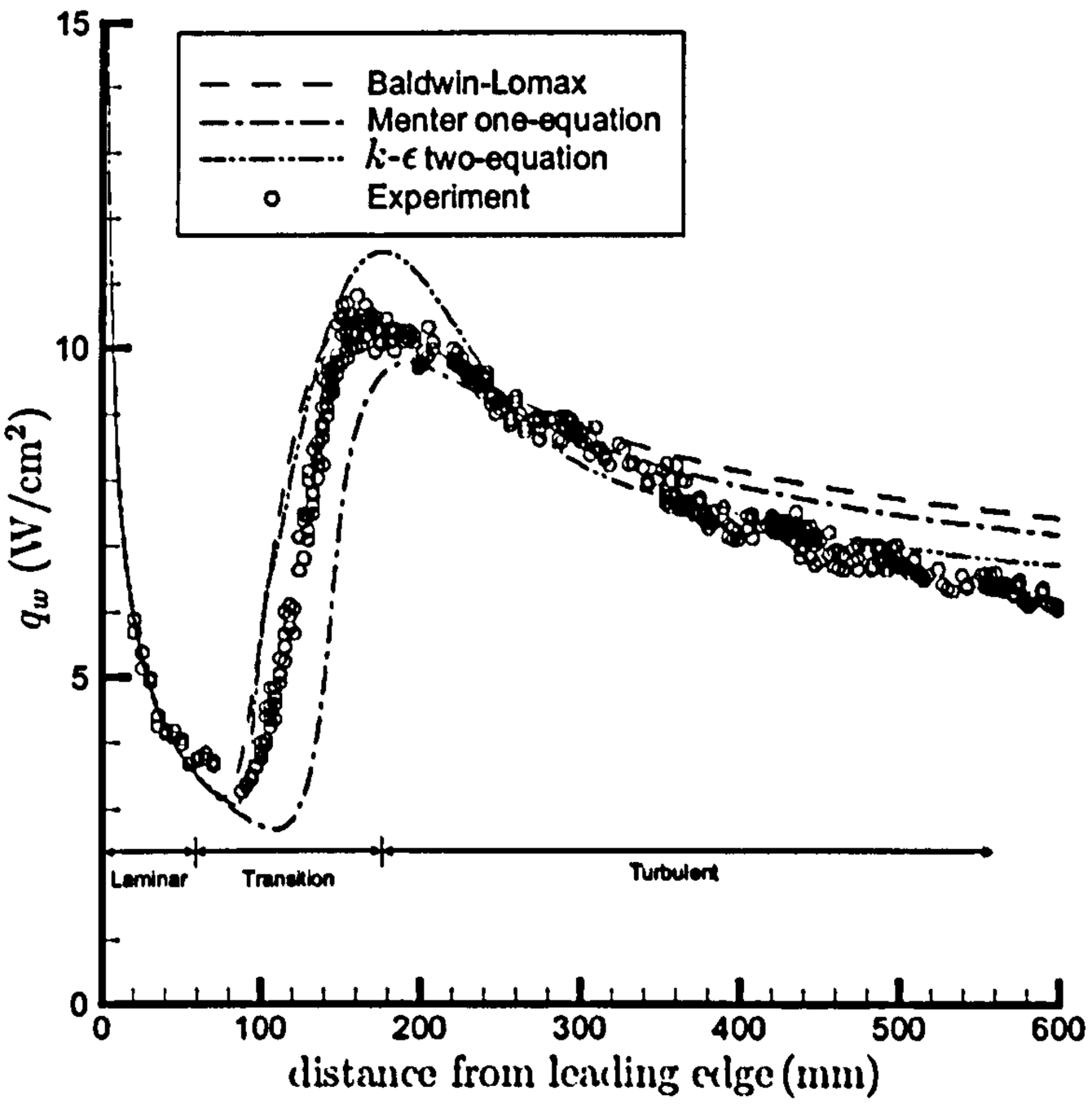


Figure 3.14: Comparison of experimental and computational results for surface heat transfer distributions using Menter turbulence model on a cylindrical forebody at Mach 9 (Williams[105]).

Williams[105] provides a comparison of experimental and CFD prediction of heat transfer on a cylindrical forebody at Mach 9, shown in Figure 3.14. Three turbulence models were compared to experimental data; the Baldwin-Lomax, the k-ϵ two-equation, and the Menter one-equation model. All turbulence models were computed with the same transition parameters.

Figure 3.14 shows the laminar boundary-layer from 0mm to 70mm from the leading edge, with transition to fully turbulent flow around 108mm. In the laminar region, the models show excellent agreement with experiment, and close agreement is also made in the transitional and turbulent regions for the all three models. The Menter model is used in all the turbulent computations presented in this thesis as this was found to be a good way of reducing computational expense (1-equation model) whilst still retaining a good approximation of the flow physics. Further comparisons of CFD prediction and experimental data can be found in the work of Williams.[105]

3.3.3 Mesh convergence (inviscid)

An important aspect of producing a well-resolved accurate CFD solution is the convergence of the mesh. Two mesh convergence tests have been carried out for key CFD cases presented in the results of this thesis - an inviscid case and a turbulent case. The discussion of the flow physics for both cases will be presented in the results section. By mesh refinement and mesh coarsening, an assessment can be made on the accuracy of the result and on run-time efficiency of a mesh. Surface pressure and skin friction values are compared to assess the mesh at which the solution converges, so that any further refinement of the mesh would produce little or no change in the solution. For inviscid cases, it was possible to increase the resolution to a highly dense mesh due to the short run-time of the inviscid computations. Due to numerous geometry modifications, it was not feasible to carry out mesh convergence tests for every geometry, only that all other cases with a similar set-up (in terms of geometry, flow conditions etc.) are satisfied by the use of a mesh of similar resolution.

The first mesh convergence test case carried out is for an intake with a thin-plate cowl at Mach 4, modelled as an inviscid flow. Figure 3.15 presents pressure contours

from a computed solution of this case, with a mesh size of 855 x 201 cells. The contours show the shock system in the intake duct after external compression on the forebody. The flow in the duct is a series of oblique shocks and expansions in the parallel section before the duct diverges as the diffuser section. The mesh is then refined by doubling the cells in the i and j directions to produce a high resolution mesh of 1709 x 401 cells. Figure 3.16 shows the computed solution for this case where it can be seen that the shock waves and expansion waves are noticeably sharper due to the increased mesh resolution.

Figure 3.17 presents a graph of the forebody surface pressure distributions from converged solutions of both the medium resolution and the high resolution meshes, showing that the mesh is excellently converged and giving an accurate representation of the flow-field. In this case, the run-time efficiency is not a major issue so that it was not necessary to carry out a case with a reduced resolution. Figure 3.18 shows the intake duct flow surface pressures on the centrebody and on the cowl internal surface for both mesh resolutions. The pressure pattern is due to the reflecting shock waves and expansion waves in the parallel section of the intake. The predictions show excellent agreement with each other, in a region where the solution is changing rapidly. It can be concluded from this test case that the original mesh size of 855 x 201 is a suitable mesh for the inviscid flow cases which provided accurate representation of the flow-field with an acceptable run-time efficiency.

3.3.4 Mesh convergence (turbulent)

A mesh convergence test is also presented for the most complicated geometry computed in this thesis. Figure 3.19 presents pressure contours from a turbulent simulation of an intake with a blunted cowl at Mach 6. The intake geometry includes a backward-facing step which was incorporated to control separation. The details of the flow physics of this geometry will be discussed in the results section. The purpose of presenting this case in this section is to make an assessment of the mesh convergence for the most elaborate case. For this case three mesh resolutions were tested. Figure 3.19 presents contours from the converged solution with a mesh size

of 955 x 323. The mesh is then doubled in the i and j directions to produce a mesh size of 1909 x 645. Figure 3.20 presents the pressure contours from the converged solution for this case. The internal flow structure is the same for both cases, with sharper contours appearing in the high resolution case. The 955 x 323 mesh was also coarsened by halving the number of cells in the i and j directions to produce a low resolution mesh of 478 x 162 cells (contours not presented).

Figure 3.21 presents the forebody surface pressure distribution from the spike apex to the inlet throat for all three meshes showing an excellent comparison of the pressures computed from the medium and high resolution test cases. The low resolution mesh slightly underpredicts pressure values on the forebody and at the centrebody shoulder. Figure 3.22 presents centrebody surface pressure distributions from the centrebody shoulder to the end of the intake duct again showing good comparison of the pressures computed from the medium and high resolution cases.

Figure 3.23 plots the surface pressure distribution on the cowl exterior surface for the three meshes showing excellent convergence. The flow in this region is not as complex as the internal flow and hence a well-resolved solution is obtained for all meshes. Figure 3.24 presents values for the skin friction on the cowl external surface showing excellent mesh convergence for the medium and high resolution mesh.

The results show that an excellent level of convergence can be achieved on the external flow-field of the intake, i.e. forebody and cowl exterior surface, with a medium resolution mesh. For the internal intake flow-field - which consists of multiple wave reflections, interactions and separated flows - the medium resolution mesh provides a good level of convergence whilst maintaining the CFD run-time efficiency. Realistically, the medium resolution (955 x 323) is the maximum number of cells that could have been used given the extensive time taken to compute high resolution cases. For all turbulent simulations presented in this thesis, this size of mesh is used. The tests presented in this section have presented a mesh convergence analysis of key CFD cases and the solutions presented in the results chapters satisfy these guidelines.

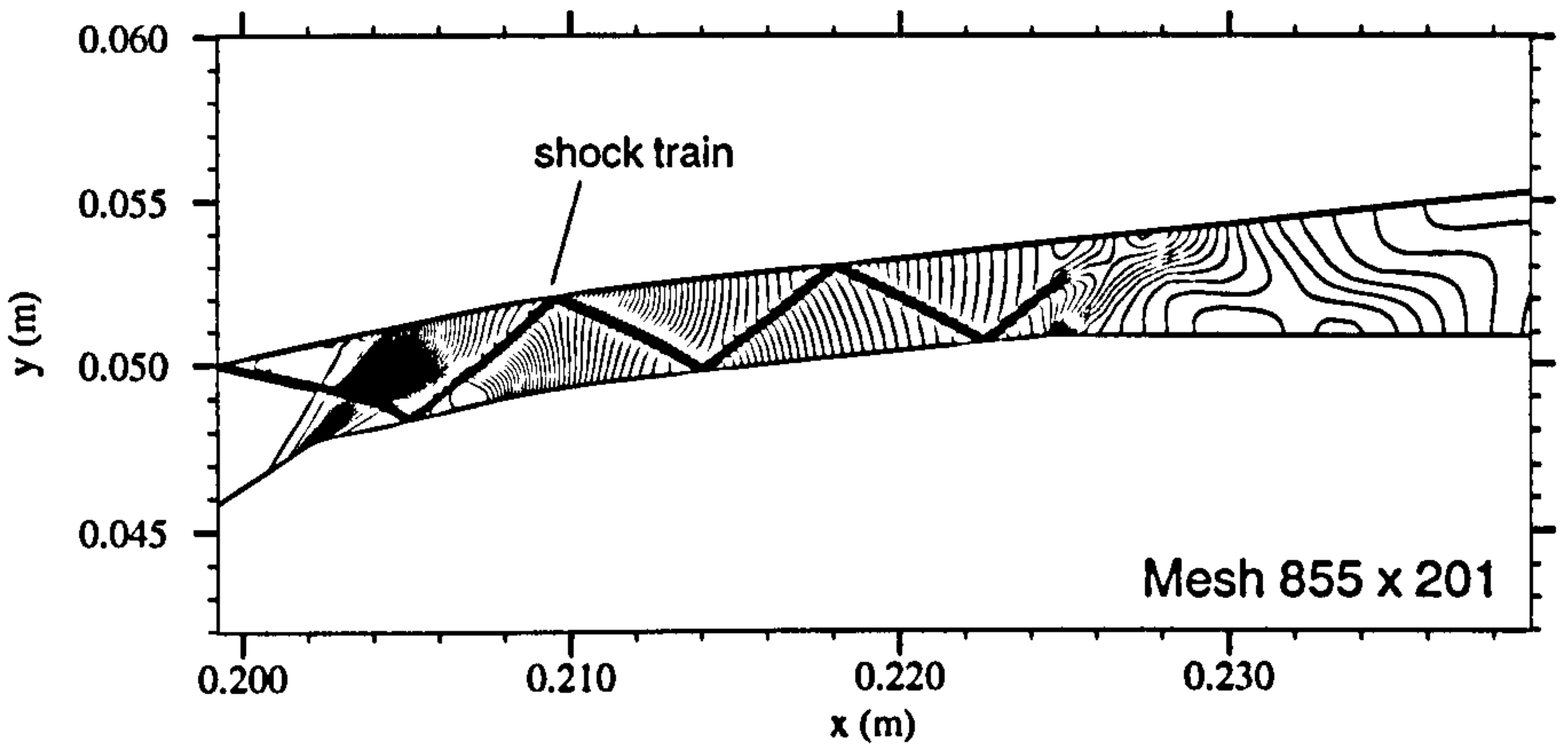


Figure 3.15: CFD Pressure contours from an inviscid simulation of the shock train in the intake duct (thin-plate cowl) at Mach 4 (Medium resolution mesh 855 x 201).

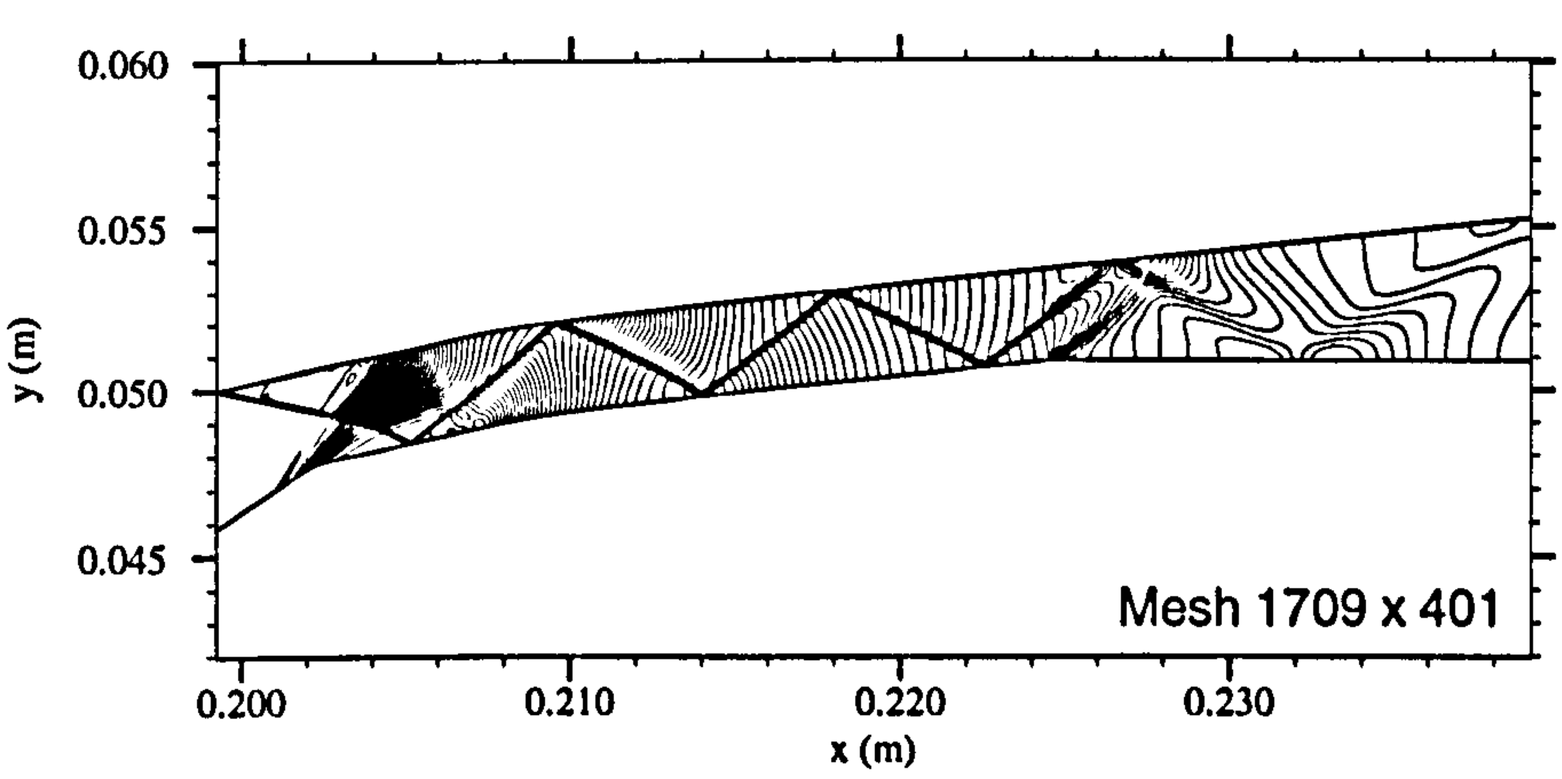


Figure 3.16: CFD Pressure contours from an inviscid simulation of the shock train in the intake duct (thin-plate cowl) at Mach 4 (High resolution mesh 1709 x 401).

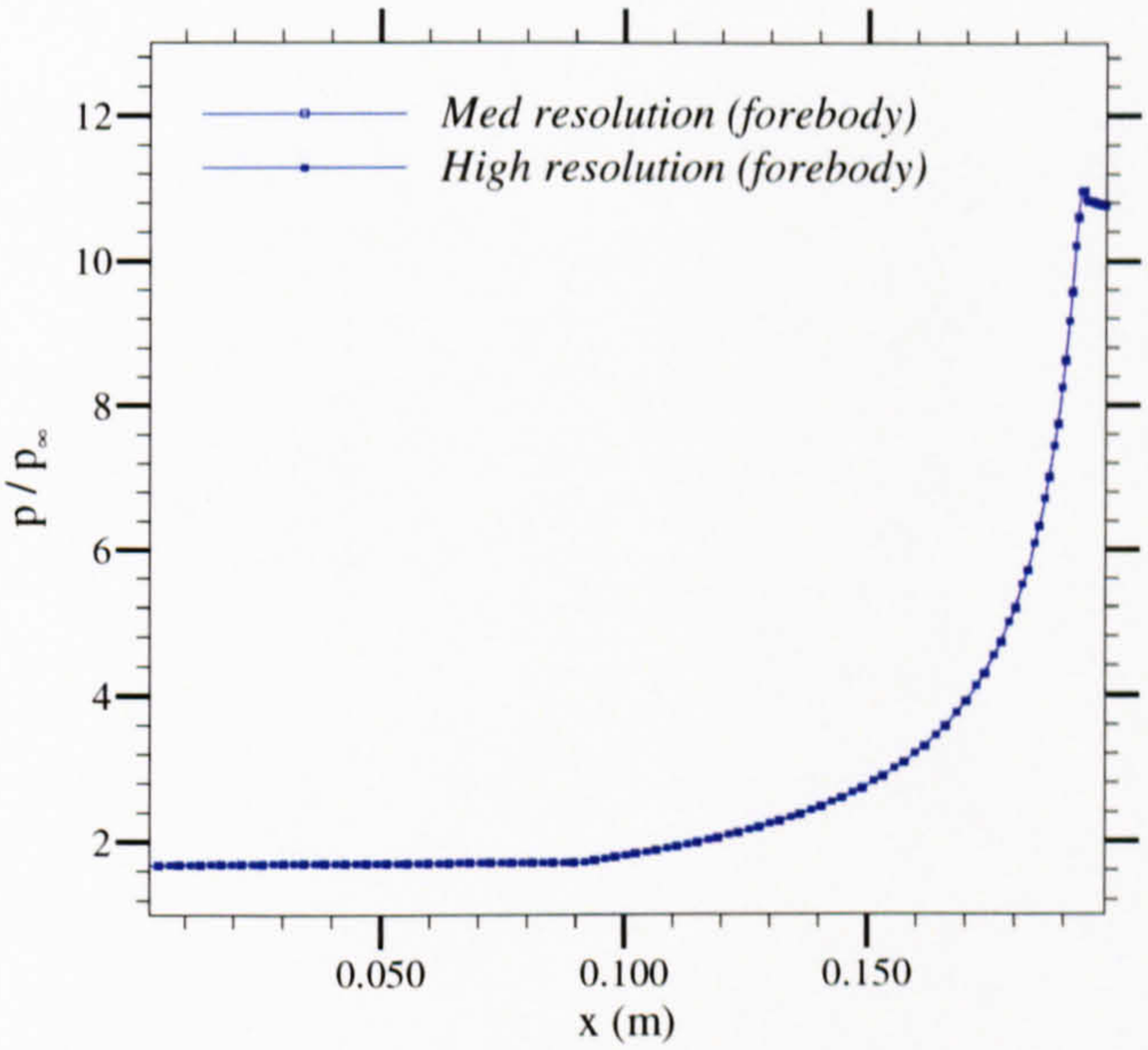


Figure 3.17: Comparison of forebody surface pressure distribution for the medium and high resolution mesh at Mach 4 (inviscid simulation) to show mesh convergence.

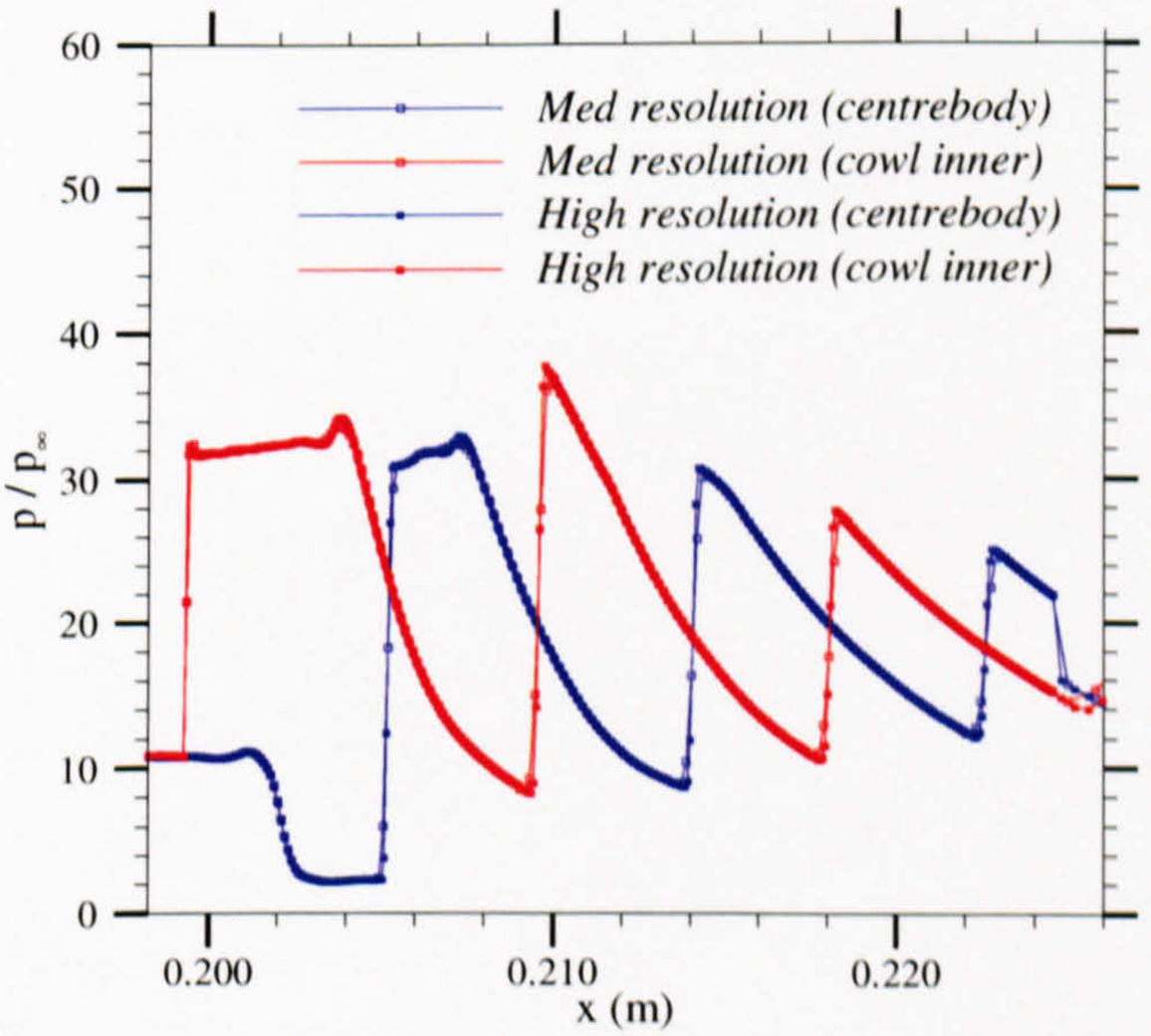


Figure 3.18: Comparison of the centrebody surface and cowl inner surface pressure distributions in the intake duct for the medium and high resolution mesh at Mach 4 (inviscid simulation) showing mesh convergence.

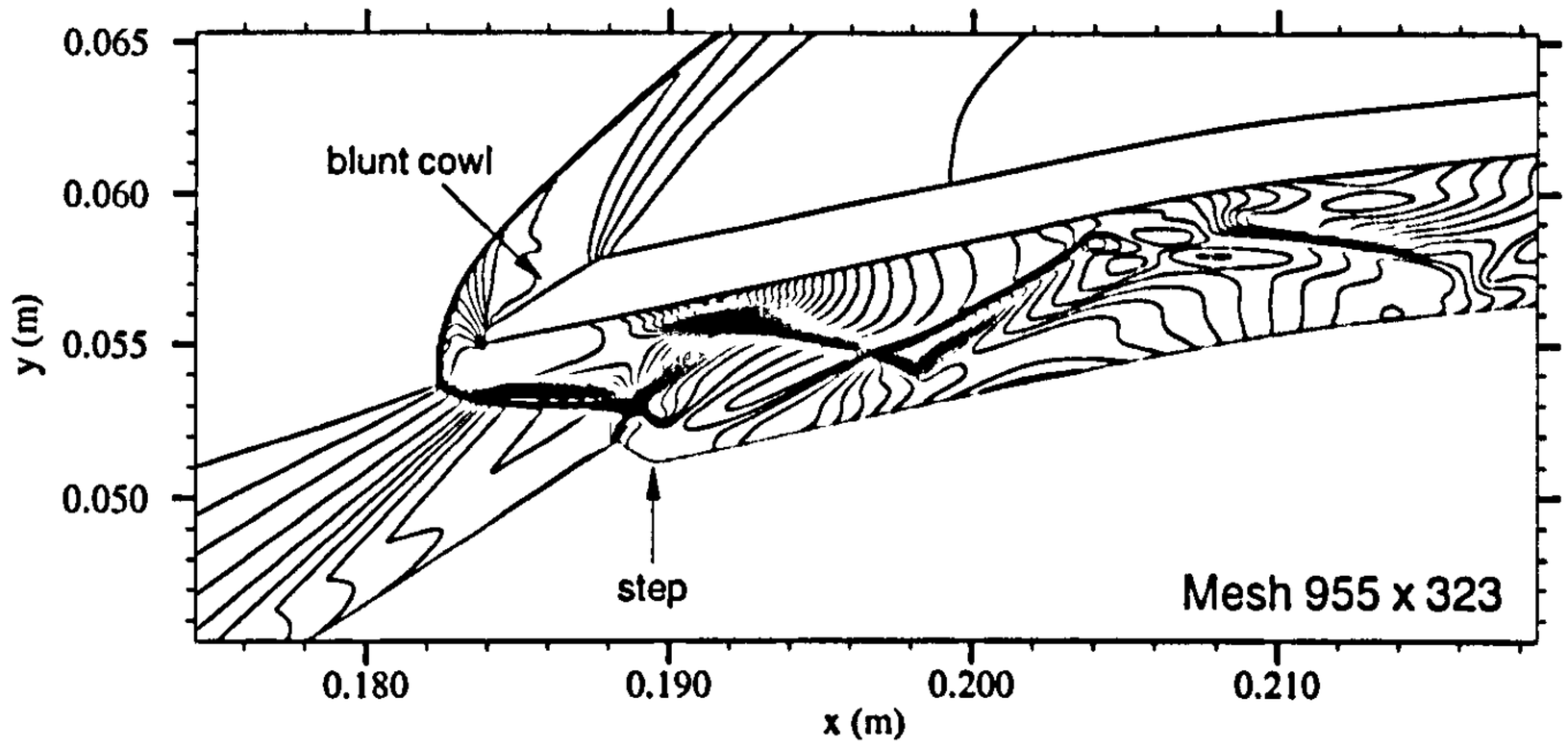


Figure 3.19: CFD Pressure contours from a turbulent simulation of the shock train in the intake duct (blunt cowl) at Mach 4 (Medium resolution mesh 855 x 201).

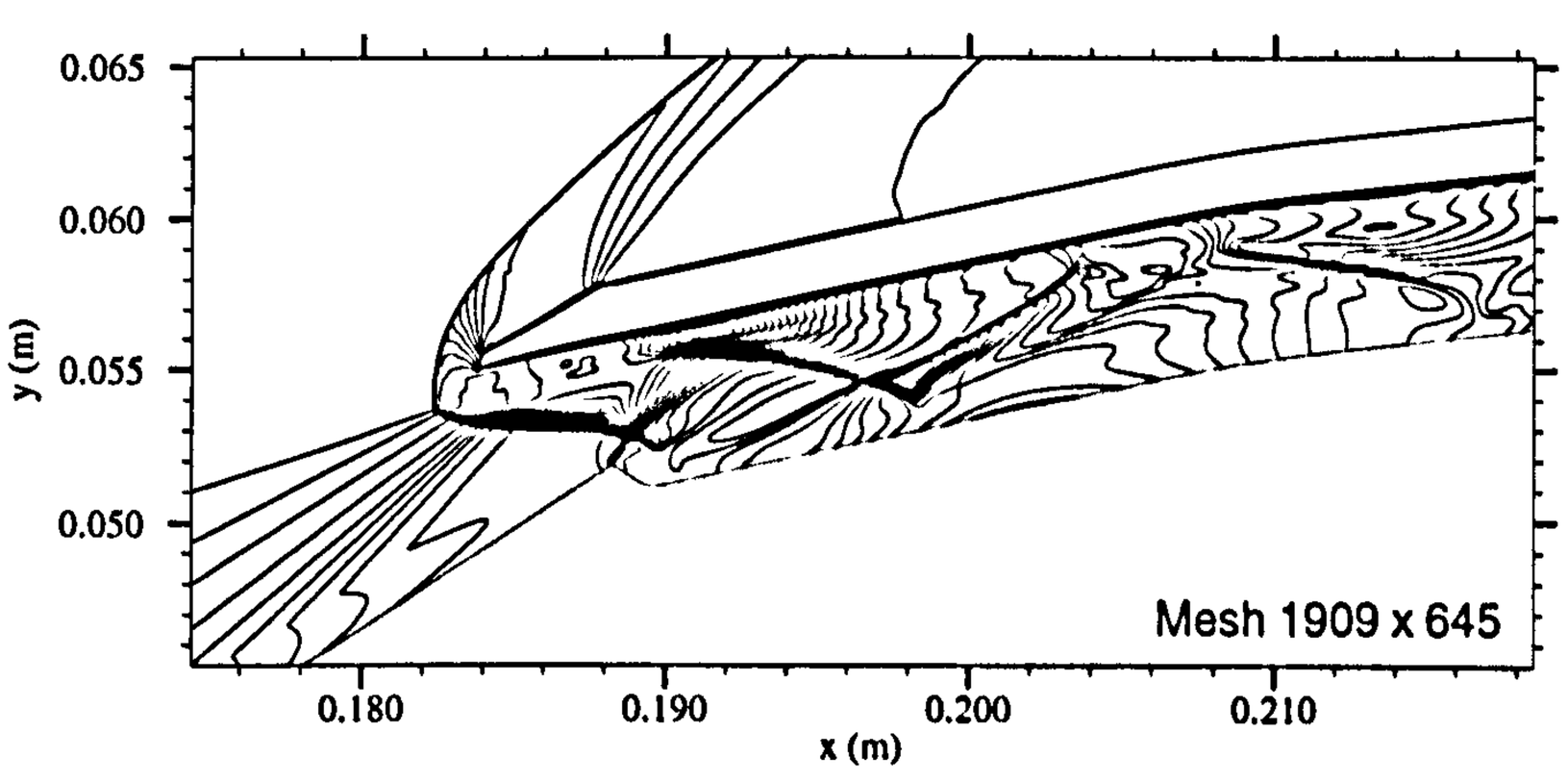


Figure 3.20: CFD Pressure contours from a turbulent simulation of the shock train in the intake duct (blunt cowl) at Mach 4 (High resolution mesh 1709 x 401).

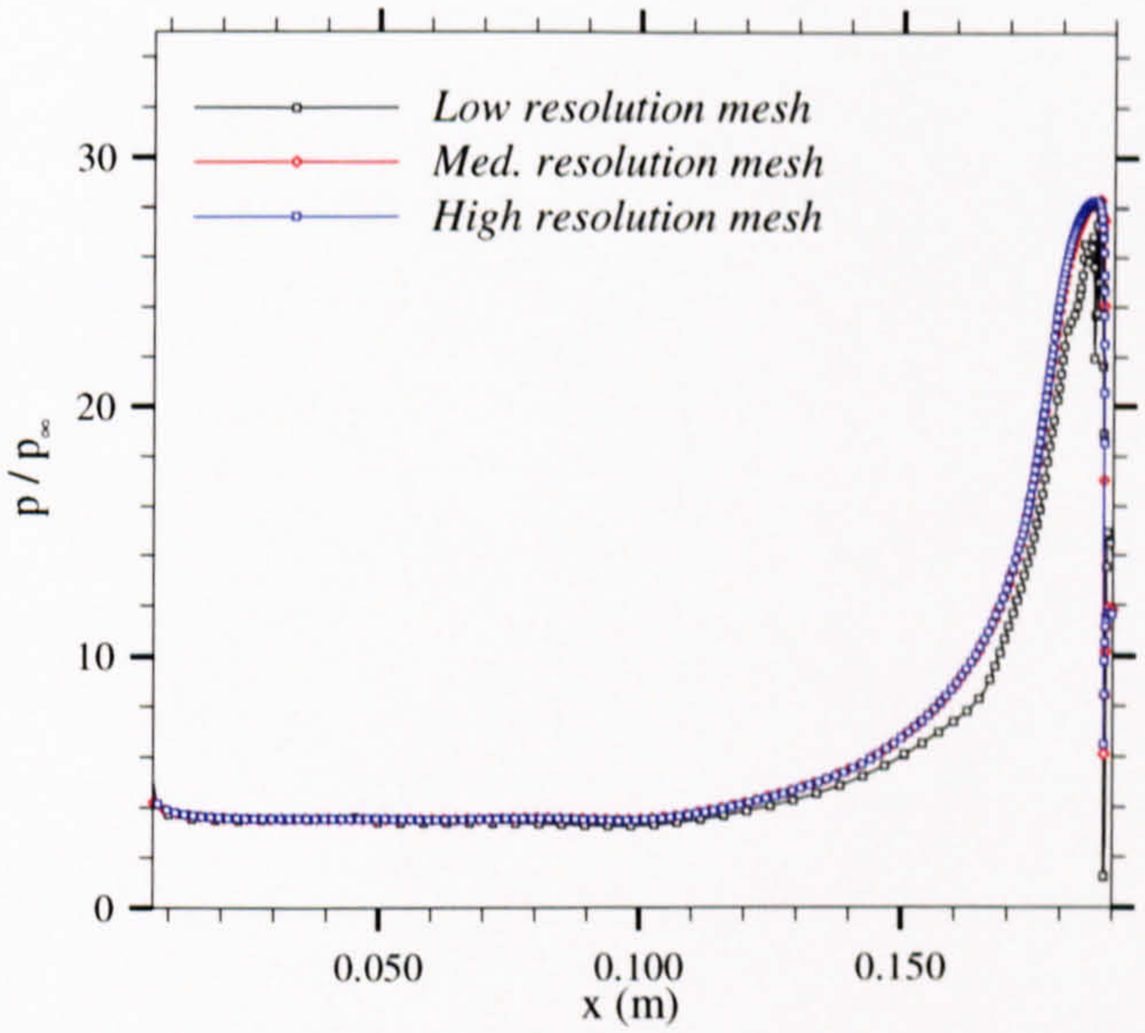


Figure 3.21: Comparison of centrebody surface pressure distribution for the low, medium and high resolution mesh at Mach 6 (turbulent) to show mesh convergence.

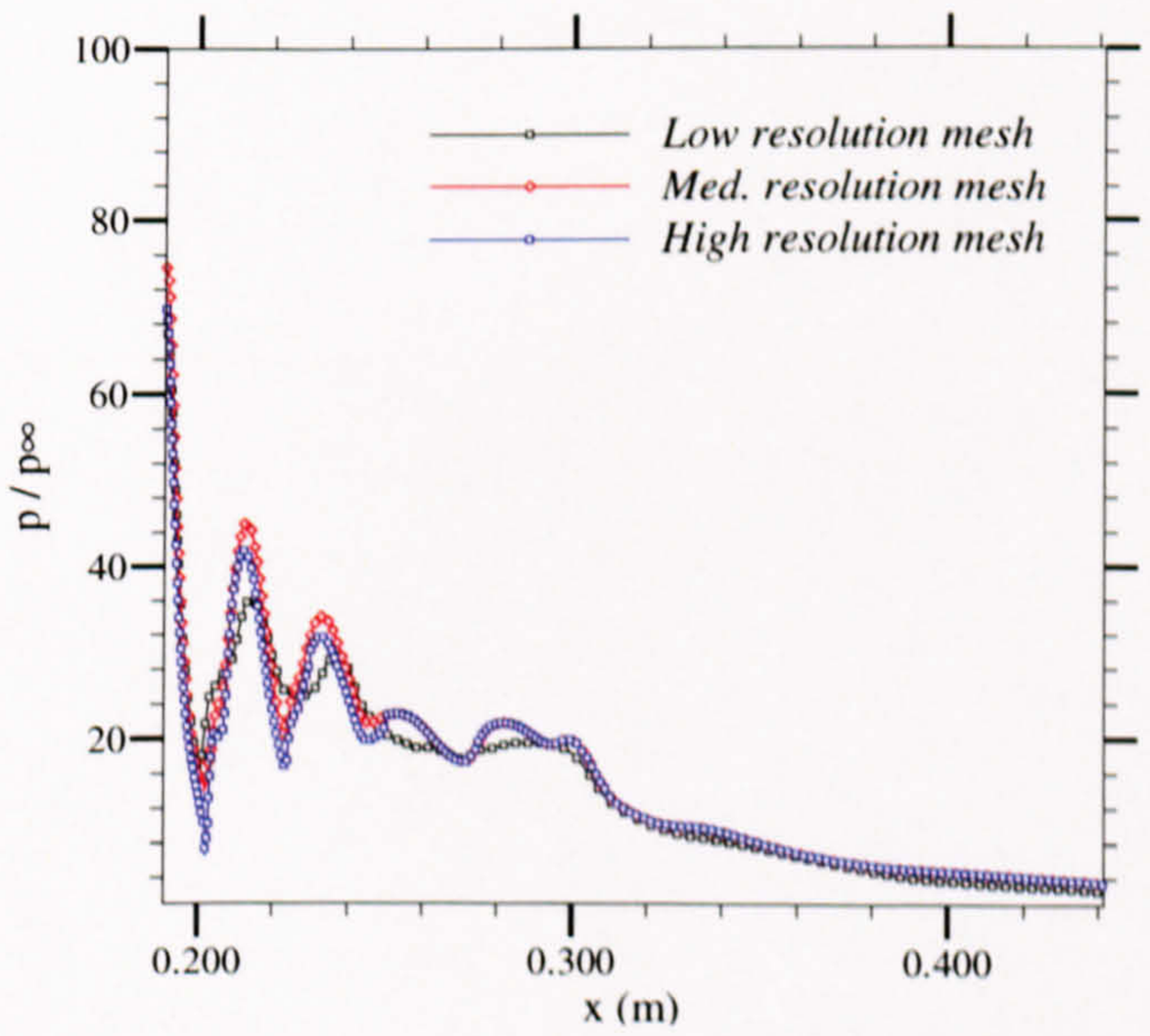


Figure 3.22: Comparison of cowl internal surface pressure distribution for the low, medium and high resolution mesh at Mach 6 (turbulent) to show mesh convergence.

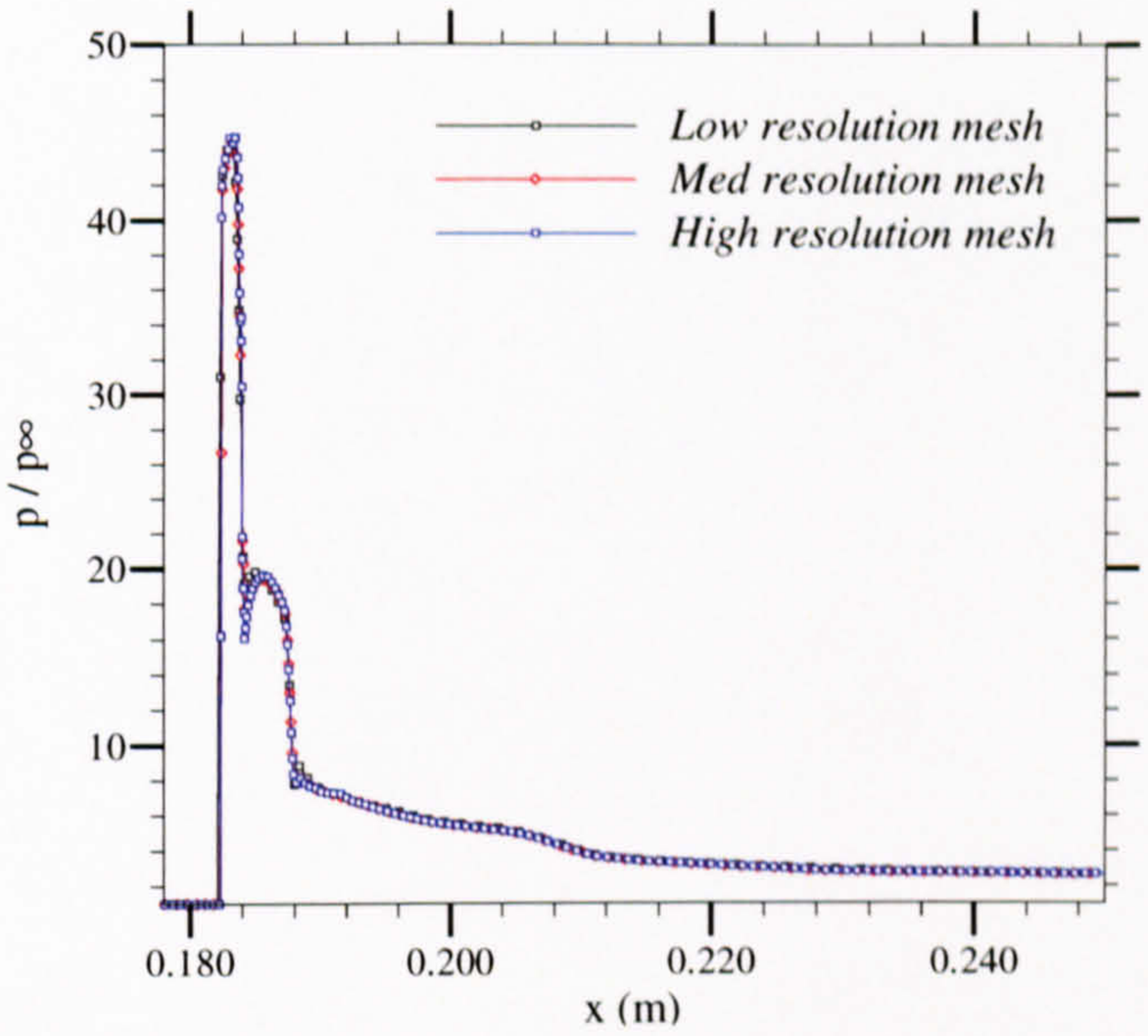


Figure 3.23: Comparison of cowl external surface pressure distribution for the low, medium and high resolution mesh at Mach 6 (turbulent) to show mesh convergence.

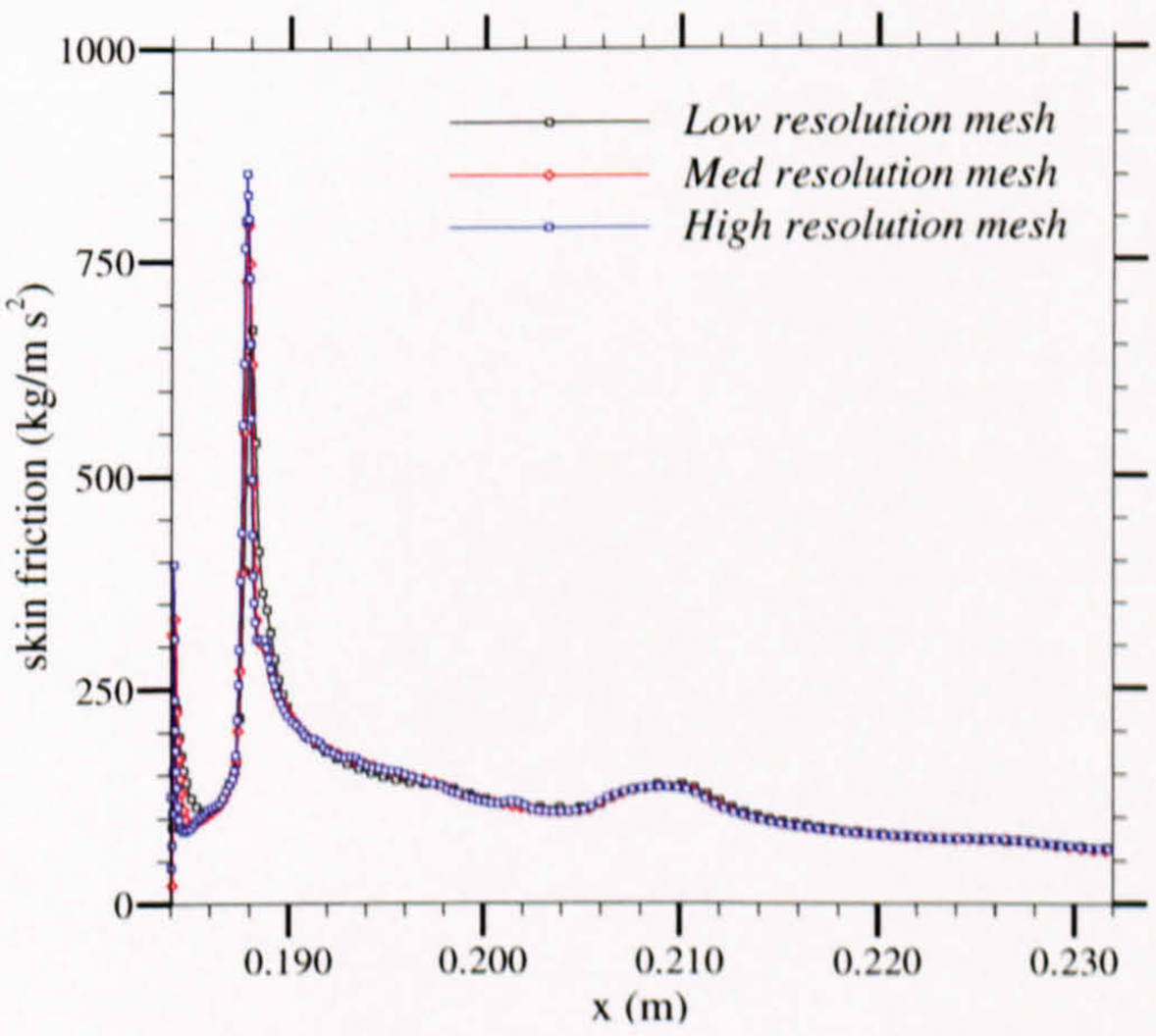


Figure 3.24: Comparison of the cowl external skin friction distribution for the low, medium and high resolution mesh at Mach 6 (turbulent) to show mesh convergence.

Chapter 4

Intakes with supersonic outflow I

4.1 Wave system at the forebody (no cowl)

4.1.1 Design condition

High-speed inlets can be designed with both an internal and external shock compression process by engine/airframe integration. The Shyfe intake consists of an axisymmetric forebody which provides an external isentropic compression of the incoming air flow. The aerodynamics and performance of the intake at zero angle of attack and with a fully supersonic flow throughout the engine is presented in this chapter. The results presented in this chapter focus on the core inviscid flow-field without the added complexity of viscous effects. Detailed viscous analysis will be presented in chapter 5. Figure 4.1 presents pressure contours from an inviscid simulation of the intake at Mach 5.5 with no cowl. The contours show the apex shock and the isentropic compression fan generated on the forebody.

Figure 4.2 presents a schematic of the wave system at the focus point, showing the intersection of the various waves. The compression waves focus to a point and then form a focused shock wave, with an expansion wave propagating into the post-compression flow field. The point of intersection of these waves is called the *triple-point*. The static pressure rise across the focused shock must equal the pressure rise through the isentropic compression fan and reflected wave, and so is balanced across

a free shear layer depicted by the dotted line on Figure 4.2. This is the most efficient forebody compression method for high-speed inlets. Specifically, this process takes the high Mach number flow M_∞, and compresses it isentropically to a lower Mach number M_1 in region 1 on Figure 4.2. Figure 4.3 (a) and (b) present pressure and density contours from a converged inviscid simulation of this process (no cowl) at the design Mach number 5.5. The purpose of showing both pressure and density contours are the flow features that are revealed in the constant density plots, such as the shear layer between the shock and expansion waves in Figure 4.3 (b).

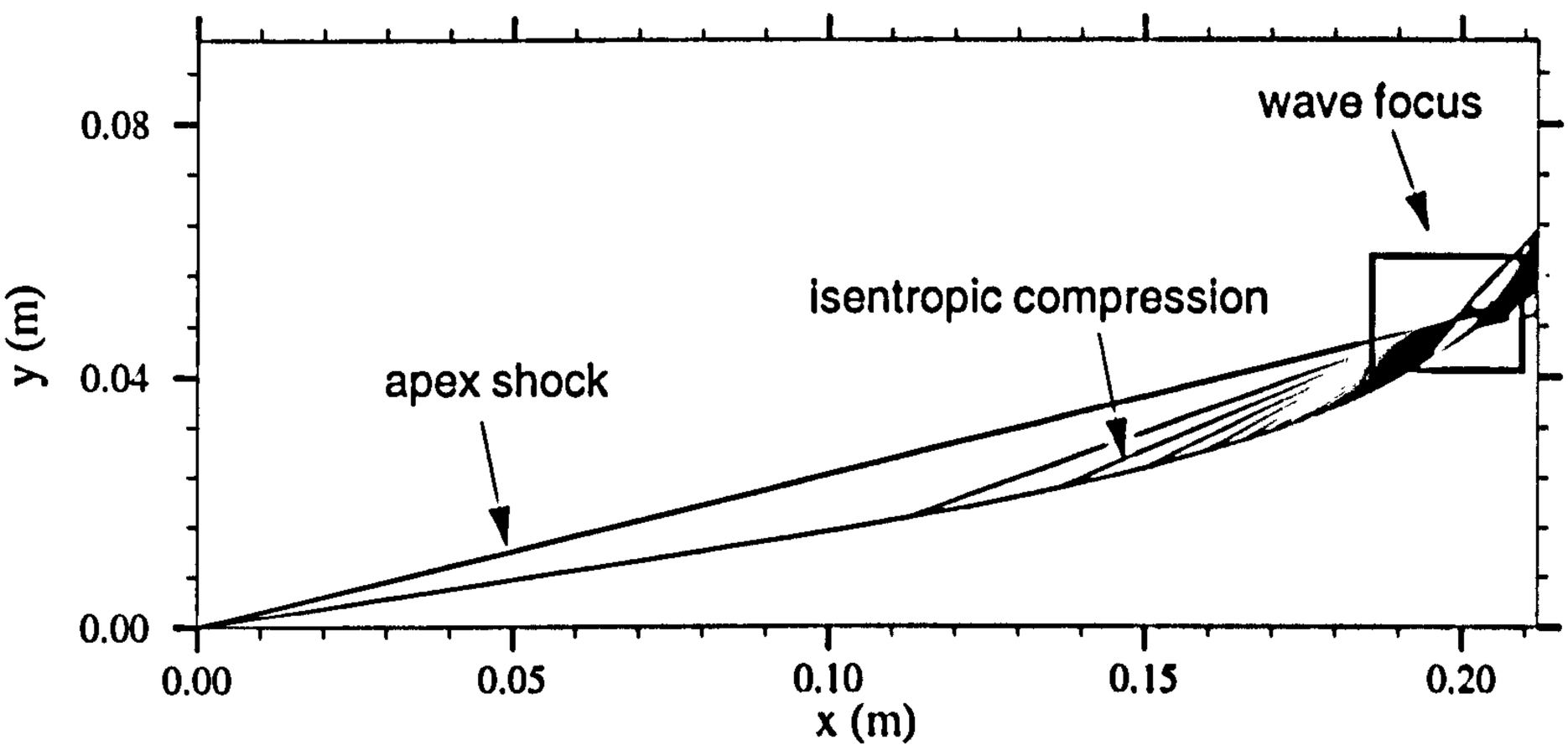


Figure 4.1: CFD Pressure contours from an inviscid simulation of the intake (no cowl) at Mach 5.5 showing the apex shock and isentropic compression focus point.

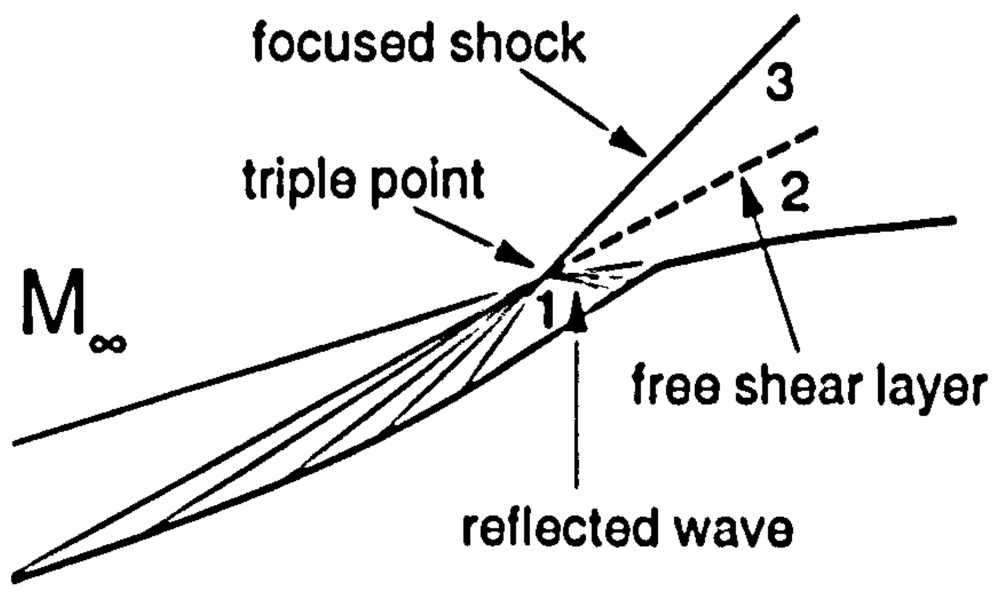


Figure 4.2: Schematic of the inlet wave system at the centrebody shoulder (no cowl) after the isentropic compression process on the forebody.

The compression process decelerates the Mach 5.5 freestream to approximately Mach 3 in region 1, with a static pressure rise to approximately 25 times the freestream static pressure. There is an approximate 2.5 percent loss in total pressure which is incurred across the initial apex shock wave. The Mach number behind the focused shock wave in region 3, is approximately 1.9.

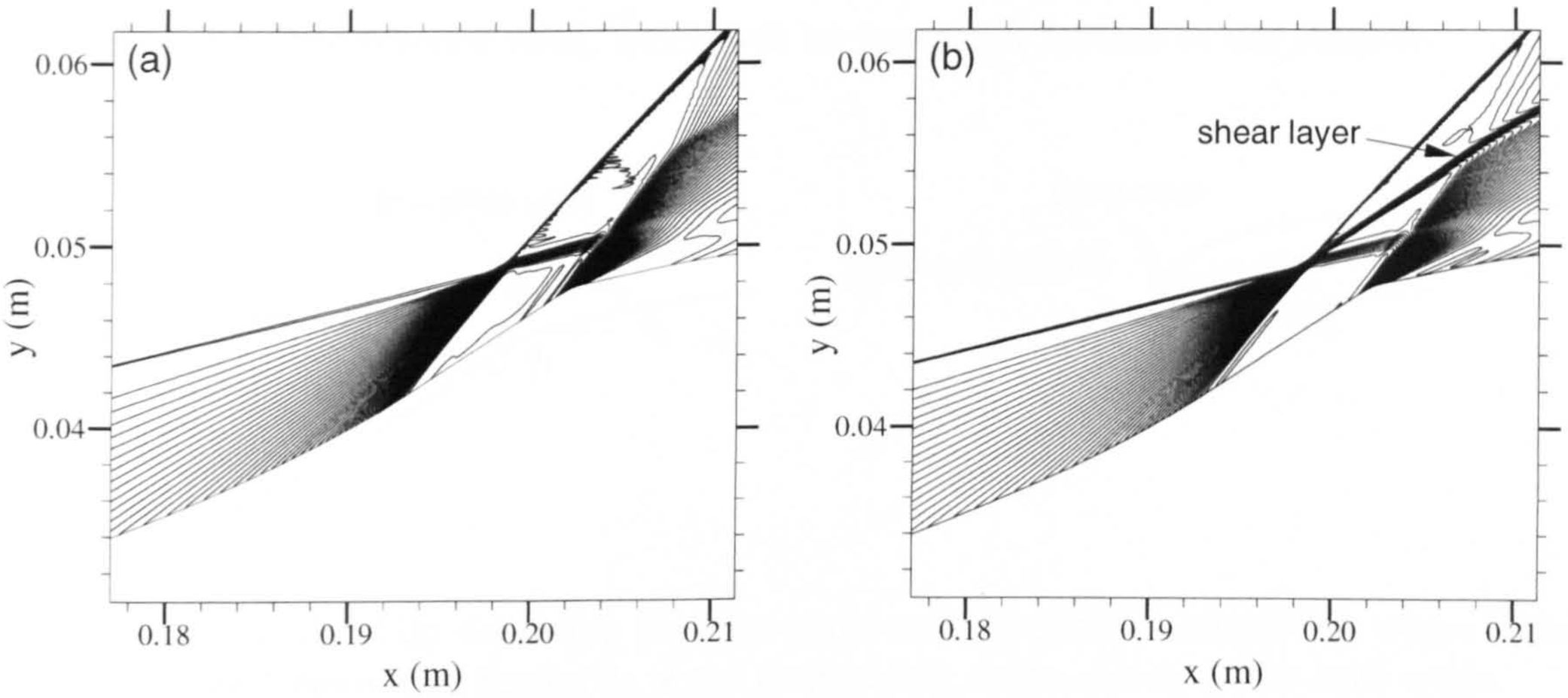


Figure 4.3: CFD Contours from an inviscid simulation of the intake (no cowl) at on-design Mach 5.5; (a) pressure contours and (b) density contours.

4.2 Intake off-design wave interactions

At zero angle of attack, an intake is off-design when the Mach number goes below or above that of the shock-on-lip condition. At these conditions, the leading edge shock wave from the spike tip focuses away from the cowl leading edge, and can result in complex wave interactions at the inlet annulus. The first step taken in analysing the intake off-design flow is to study the inviscid flow field without the added complexity of viscous effects and flow separation.

Figure 4.4 defines both (a) the thin-plate cowl, and (b) the cowl with a blunted lip (b). The angle θ_1 defines the angle at which the spike terminates, and the angles θ_2 and δ_c are the centrebody and cowl angles respectively. The isolator is parallel for a short distance before diverging further into the duct as the diffuser. For

simplicity, the intake is initially modelled using a thin-plate cowl in the geometry. In reality, the cowl leading edge would probably have to be blunted, either deliberately - to manage leading edge heat transfer rates - or as a consequence of maintaining structural integrity. Initially, however, in order to separate the inlet wave system from the shock system created by a blunt cowl, the analysis is carried out using a thin-plate cowl. This allows for a more focused study of the flow characteristics created by the blunted cowl, which will be presented further in the chapter.

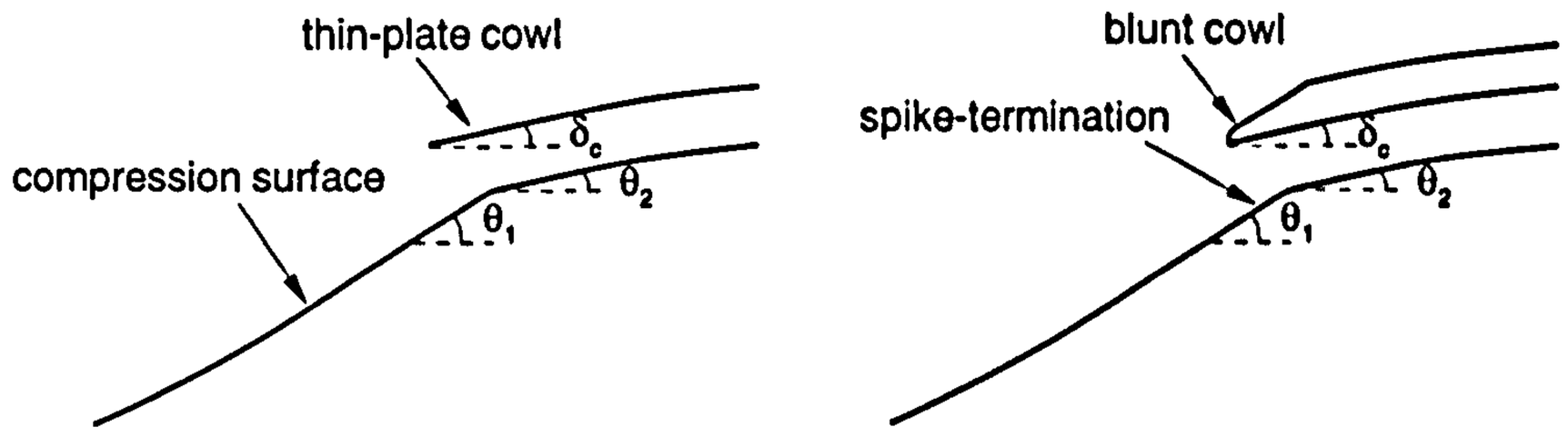
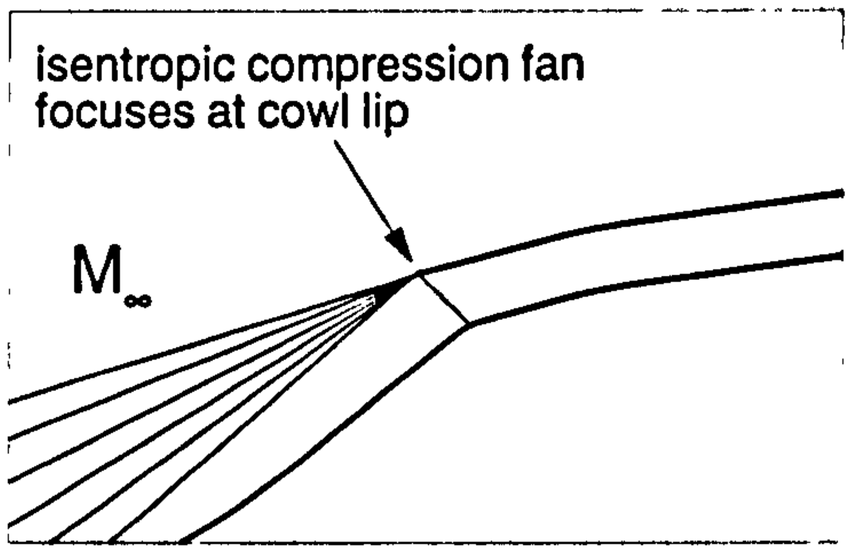


Figure 4.4: Cowl lip definition (a) thin-plate and (b) with a blunted lip; where θ_1 is the spike termination angle, θ_2 is the centrebody angle and δ_c is the cowl angle.

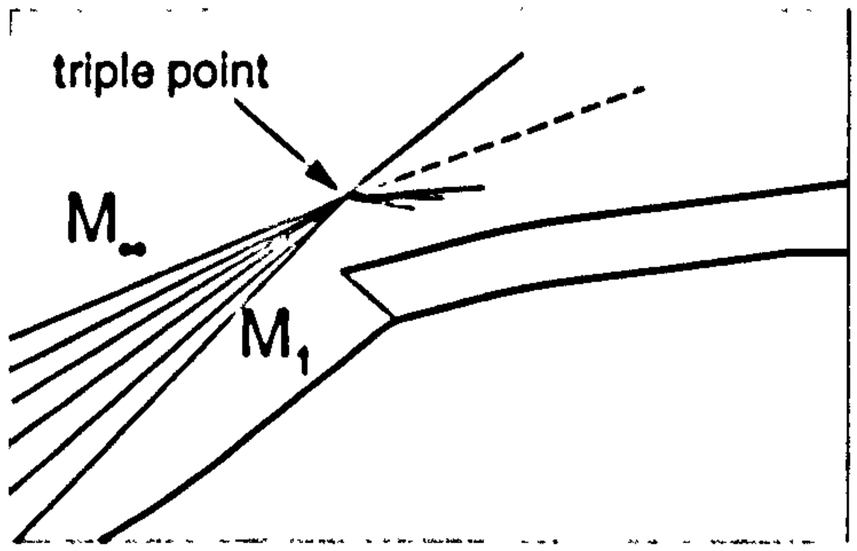
4.2.1 Interaction types

Various off-design wave interactions can be considered. Figure 4.5 (a) shows a schematic for the on-design case where the isentropic compression fan exactly focuses at the cowl leading edge. This is the optimum configuration for the inlet where it is assumed that an attached shock wave forms at the cowl leading edge and that this shock exactly cancels out on the centrebody shoulder in what is known as the shock-on-shoulder condition. The centrebody is referred to as being *downstream* of this shoulder and the forebody as being *upstream*.

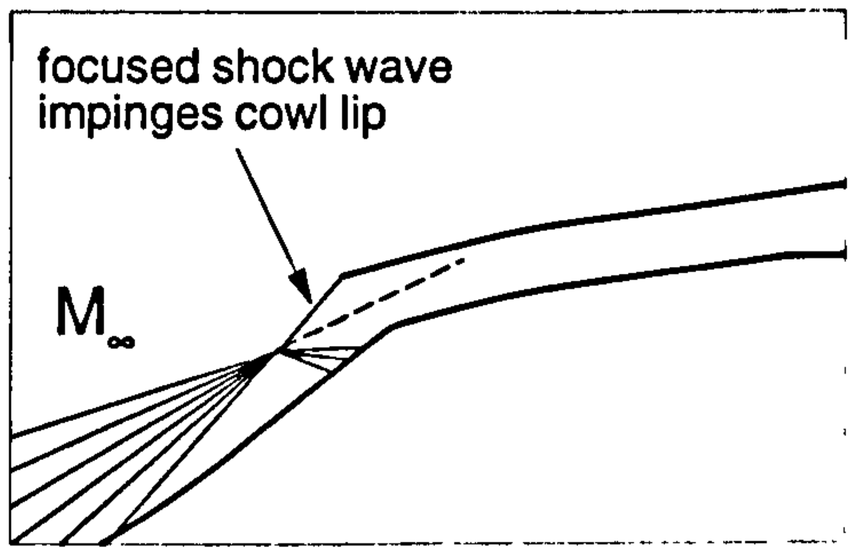
The fundamental physical process that then determines the flow at inlet is the reflection of a shock wave - either an incoming shock onto the cowl surface and/or a cowl-generated shock reflecting onto the centrebody surface - and the presence and effect of an expansion fan from the cowl and/or centrebody on this shock wave. At off-design conditions, the cowl-generated shock will impinge either upstream or downstream of the expansion shoulder to cause imperfections in the flow-field.



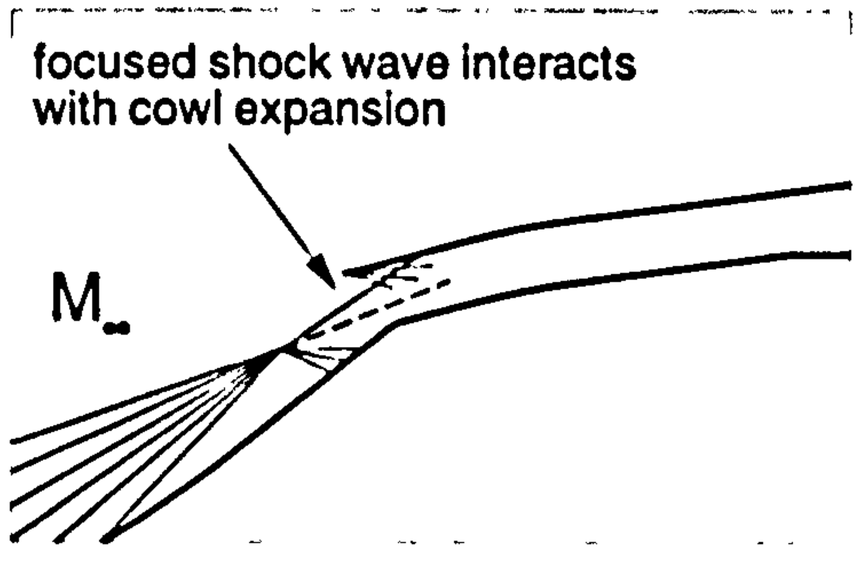
(a) On-Design



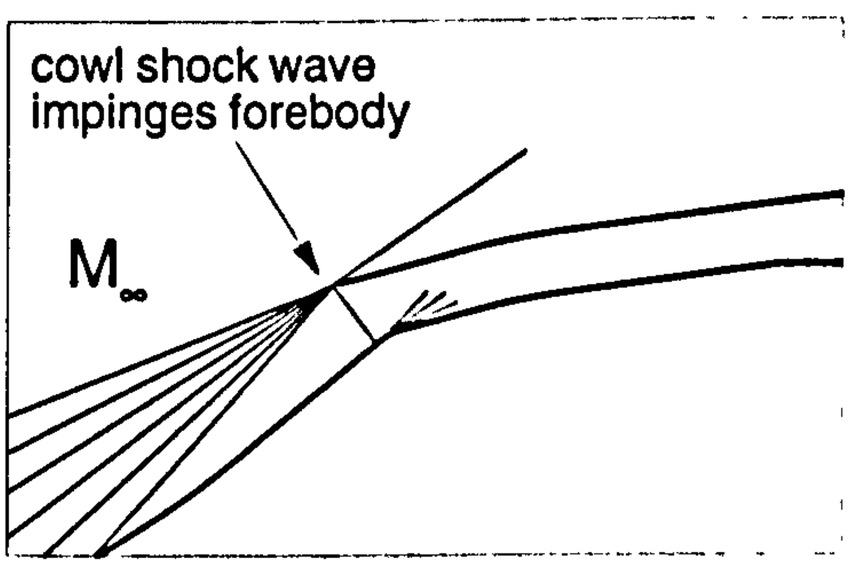
(b) Type 1 Interaction



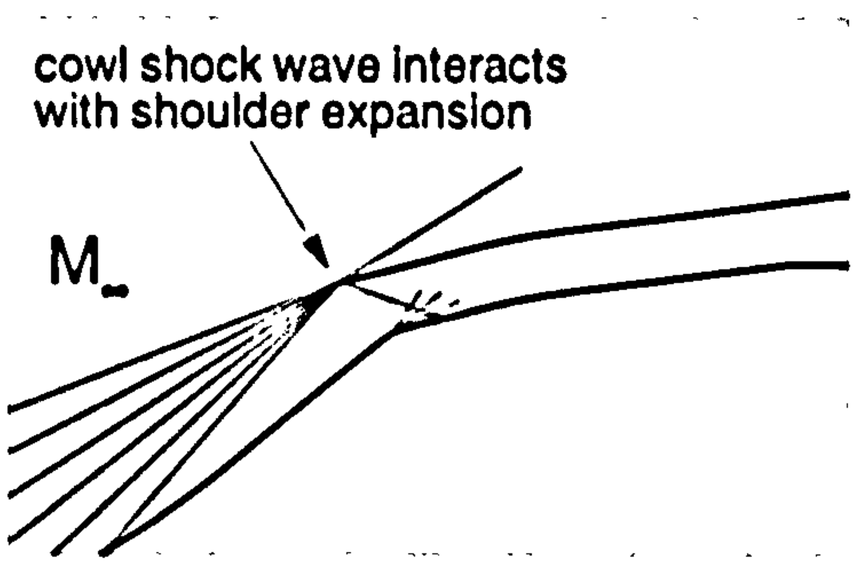
(c) Type 2 Interaction



(d) Type 3 Interaction



(e) Type 4 Interaction



(f) Type 5 Interaction

Figure 4.5: Schematics of inlet-associated wave interactions at off-design conditions. The intake is shown with a thin-plate cowl to initially simplify the problem.

For impingement upstream, the assessment of the shock reflection process is straightforward, although the downstream flow may be complex. The impingement of the cowl shock downstream of the shoulder expansion leads to interaction between the two wave systems and can result in complex flows.

The shock will either reflect as *regular* reflection or as *Mach* reflection. This phenomenon is described in detail in chapter 2, section 2.2.1. In the Type 1 off-design interaction, seen in Figure 4.5 (b), the cowl leading edge lies in region 1, a condition that occurs when the freestream Mach number is lower than the intake design Mach number. Rather than off-design, however, this case is regarded as potentially the ideal. The on-design case and Type 1 interactions are similar in that the shock wave has the same properties due to the approach conditions being the same, with the only difference being the spillage of flow incurred in a Type 1 interaction.

The Type 2 interaction in Figure 4.5 (c) sees the focused shock wave that radiates from the focus of the apex shock and isentropic compression fan impinging exactly on the cowl leading edge, with the free shear layer entering the inlet duct. Figure 4.5 (d) shows a Type 3 interaction where the focused shock system impinges on the interior surface of the cowl. In this case, the shock wave is then affected by the expansion wave originating from the cowl leading edge, in a shock-expansion interaction. This type of wave interaction can lead to a Mach reflection at the cowl inner surface which can propagate forwards to cause a shock detachment at the cowl lip. In both the Type 2 and Type 3 interactions, the free shear layer flows into the inlet which can cause flow instabilities downstream.

The Type 4 interaction, in Figure 4.5 (e) corresponds to the cowl shock wave impinging the forebody, where it undergoes either regular reflection or Mach reflection. The inlet model in this case, is designed for external compression with the cowl lip positioned far aft for the impingement of the cowl shock on the forebody. This type of interaction would be more likely in an internal compression inlet. Figure 4.5 (f), shows the Type 5 interaction where the shock wave impinges on the centrebody and from which it will reflect either as regular reflection or Mach reflection. This has a similarity to the Type 3 interaction, in that the impinging shock is acted on by the expansion fan from the upstream shoulder, increasing the probability of

Mach reflection on the centrebody. The Type 4 and Type 5 interactions have an important influence on inlet performance due to the loss in total pressure through a Mach reflection. A Mach reflection can also result in the shock propagating forwards to cause a shock detachment and in the worst case an inlet unstart. Both the Type 4 and Type 5 cases can arise with a Type 1, 2 or 3 interaction. Another important consequence of a Mach reflection at the centrebody, is the resulting flow non-uniformities downstream, which can deteriorate isolator performance. The details of the effects of these unfavourable shock systems on the isolator performance will be discussed in chapter 6.

4.3 Intake with shock-on-lip at Mach 4.8

Initial studies were carried out on an intake with a shock-on-lip Mach number of 4.8 before the intake was re-designed for shock-on-lip condition at Mach 5.5. Some interesting results produced from this study are presented in the following section. Figure 4.6 shows a schematic of the intake design with a thin-plate cowl. The cowl lip position lies at an x-position of 184.4 mm and a y-position of 50 mm. The cowl leading edge angle and centrebody angle after the shoulder are parallel at 12 degrees. The spike terminates at an angle of 33 degrees.

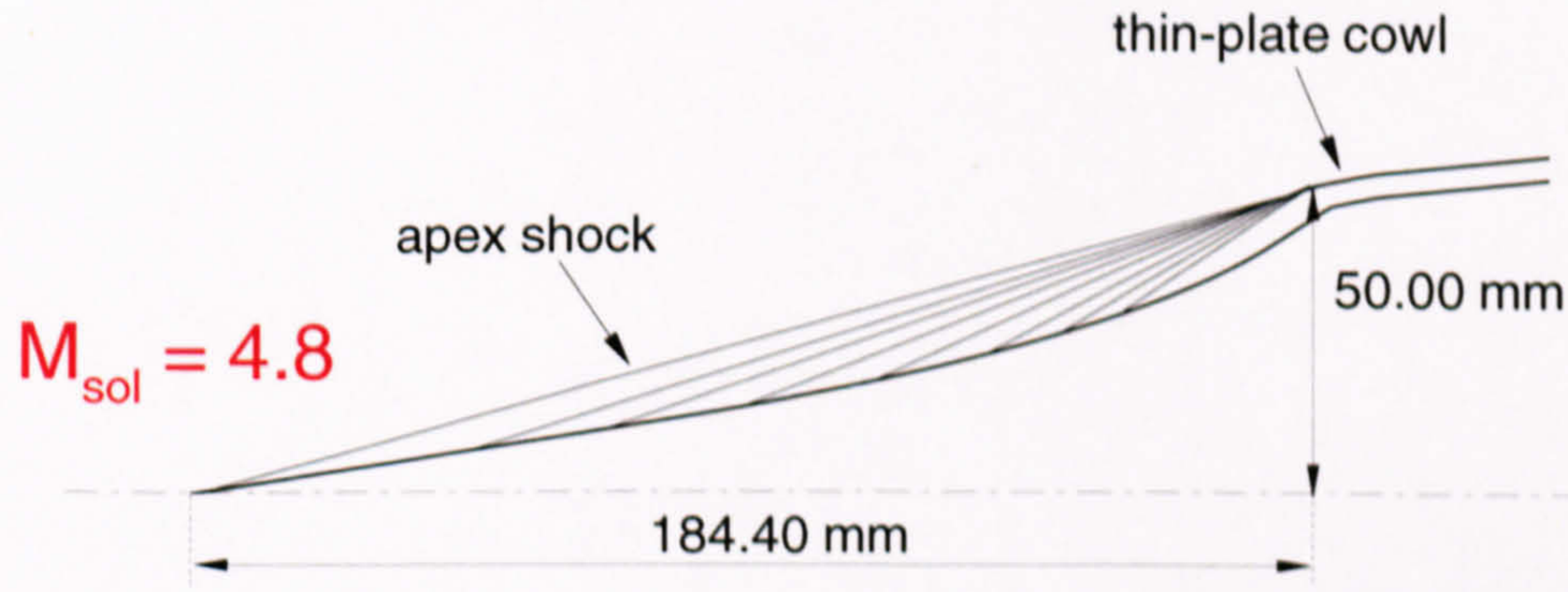


Figure 4.6: Schematic of the wave system of an intake with shock-on-lip at Mach 4.8, showing the apex shock and compression fan focusing at the cowl lip.

Table 4.1 presents the freestream Mach number M_∞, static pressure p_∞, static

temperature T_∞ and unit Reynolds number for the three conditions at which the inlet is tested. Mach 4.8 is the on-design case where the shock-on-lip condition is achieved. The off-design cases are at Mach 4 and Mach 6. The conditions correspond to an altitude of 15km at Mach 4 up to an altitude of 32km at Mach 6 for the ramjet intake[1]. The shock-shock and shock-expansion type interactions discussed previously are essentially inviscid interactions, and hence the intake flow-field is initially analysed as an inviscid flow. This enables the focus on the wave systems without the added complexity of viscous effects and boundary-layer separation.

M_∞	Pressure	Temperature	Unit Re (m^{-1})
4.0	12.00 KPa	217 K	1.64×10^7
4.8	8.00 KPa	217 K	1.31×10^7
6.0	0.89 KPa	228 K	1.71×10^6

Table 4.1: Test conditions for the Mach 4.8 intake.

4.3.1 Design/Off-design conditions

Inviscid CFD simulations carried out to investigate the flow phenomena in the intake for the on- and off-design conditions from Mach 4 to 6 are presented in this section. A mesh size of 985 x 201 is used, with a grid stretching applied in the region of the cowl lip to adequately resolve the flow, and yet be computationally efficient enough to carry out a range of test cases. The mesh convergence for these CFD results satisfy the guidelines presented in chapter 3, section 3.3.3. The flow domain is initialised with freestream conditions and the solution is time-marched to a steady-state.

Figure 4.7 shows density contours from an inviscid simulation of the intake at on-design condition Mach 4.8. In this flow-field, the triple point falls below the cowl lip (Type 2) so that the post-focused shock conditions are the approach conditions. The focused shock wave intends to reflect from the cowl inner surface and at these conditions (Mach number and flow turning) results in shock detachment at the cowl.

[1]The original Mach 4.8 design was later modified by increasing M_{sol} to Mach 5.5. The majority of the results presented in this thesis model the Mach 5.5 shock-on-lip intake flow-field.

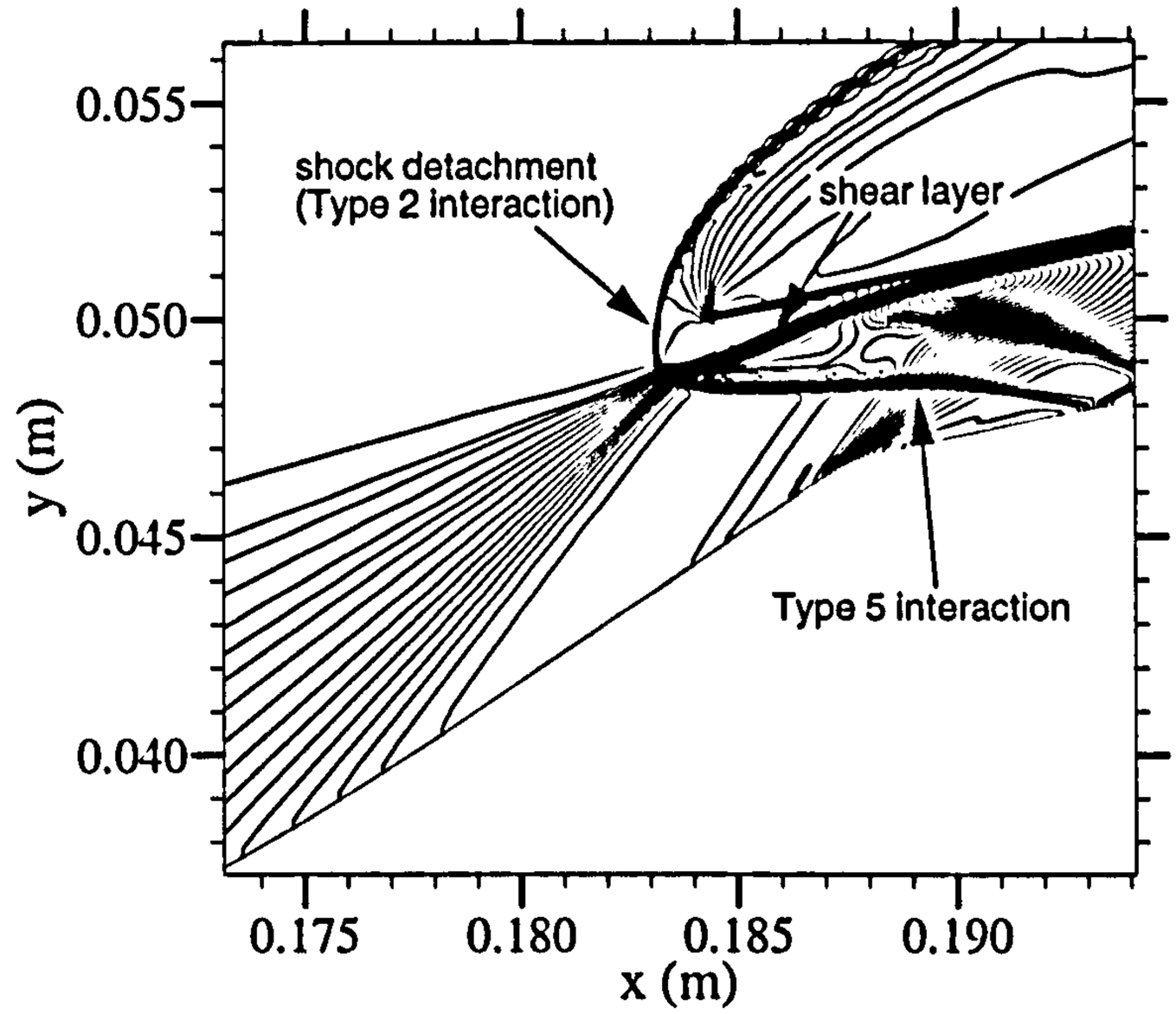


Figure 4.7: CFD Density contours from an inviscid simulation of the intake (shock-on-lip Mach 4.8) intake with a 12 degree cowl and centrebody angle at Mach 4.8.

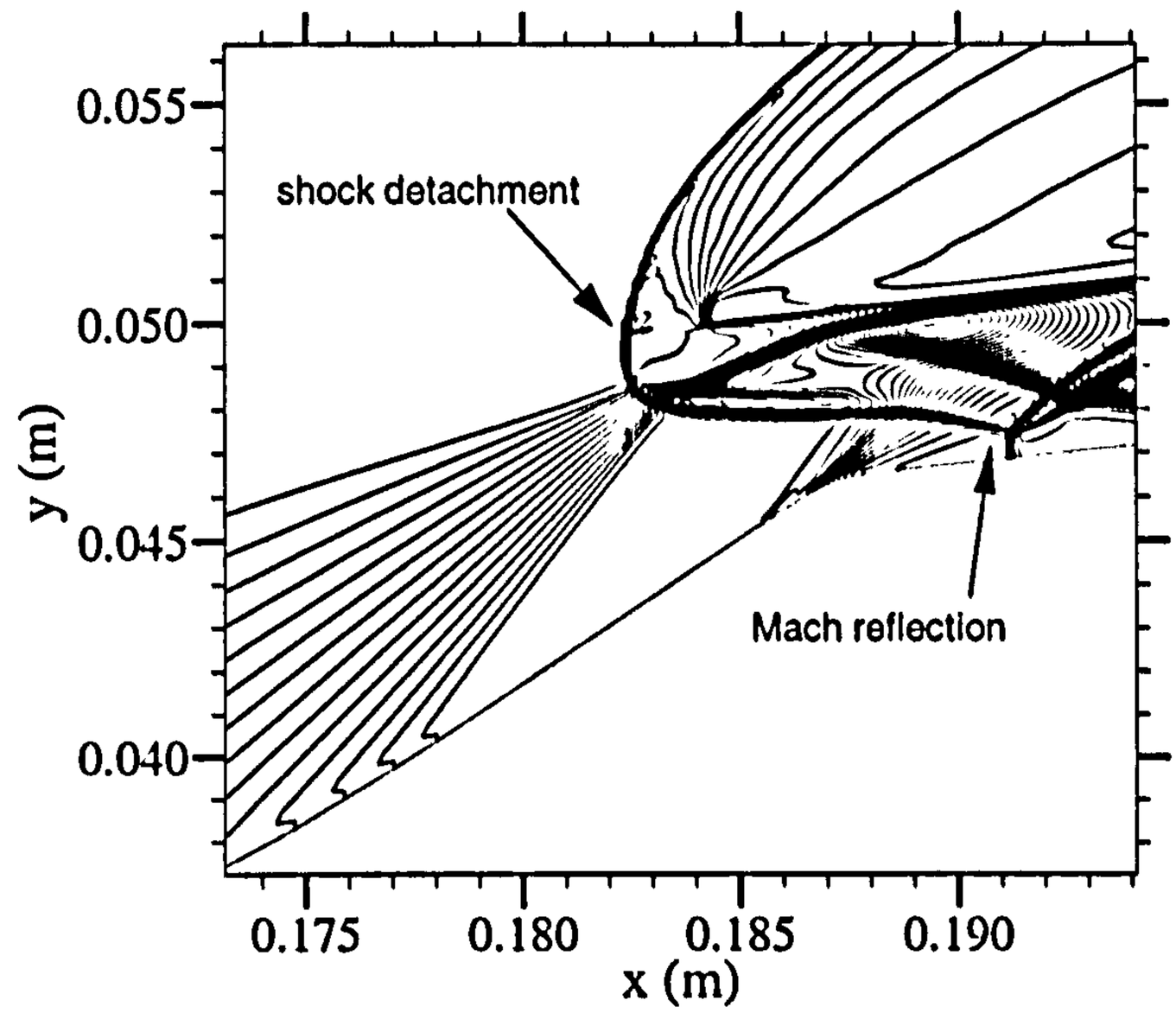


Figure 4.8: CFD Density contours from an inviscid simulation of the intake (shock-on-lip Mach 4.8) intake with a 6 degree cowl and centrebody angle at Mach 4.8.

In reality, the boundary-layer on the forebody would cause the shock system to shift upward such that the triple point would focus above the cowl lip to form an attached shock wave (Type 1). In Figure 4.7, the compression process decelerates the Mach 4.8 freestream flow to $M_1 \simeq 2.72$ after the isentropic compression on the forebody. The flow condition behind the shock detachment is subsonic.

The density contours show the shear layer that forms from the interaction point of the forebody wave system (apex shock and compression fan) with the detached shock at the cowl. Shock detachment leads to a reversed flow region just behind the detached shock which causes mass spillage. The duct flow profile is also non-uniform because part of the incoming flow is processed through the detached (normal) shock, and a mixed subsonic/supersonic flow enters the intake. The Type 5 interaction also arises in this flow as the cowl shock impinges downstream of the shoulder expansion. The cowl-generated shock is acted on by the expansion wave resulting in a *curved* cowl shock. This is a critical interaction in this flow-field due to the possibility of the formation of Mach reflection on the centrebody. In this case, the shock reflects from the centrebody as regular reflection, seen in Figure 4.7.

The cowl/centrebody angles are then reduced to 6 degrees, and hence the flow turning angle at inlet is increased i.e. For the case in Figure 4.7, θ_1 - δ_c = 33 - 12 = 21 degrees. In this case, θ_1 - δ_c = 33 - 6 = 27 degrees. Figure 4.8 shows density contours from an inviscid simulation of the intake with a 6 degrees cowl/centrebody angle at Mach 4.8 which results in a larger shock detachment at the cowl lip with increased mass spillage. The shock/expansion interaction (Type 5) is also a stronger interaction which leads to the cowl shock reflecting from the centrebody as Mach reflection, seen in Figure 4.8. Mach reflection produces a subsonic streamtube behind the Mach stem and a shear layer is generated between the post-reflected shock flow and the subsonic stream. The presence of Mach reflection in the flow, introduces an added non-uniformity in the flow profile, and with the flow non-uniformity caused by shock detachment leads to a severely non-uniform duct flow. This can be seen in the velocity profiles for both cases in Figure 4.9 (taken at x = 0.194m), where U is plotted against height from the duct surface. Mach reflection will no doubt provoke shock oscillations due to the upstream influence effect in the subsonic flow regions,

and the non-uniformity of the flow will affect downstream performance.

In investigating various inlet geometric configurations, it was found that the shock detachment at Mach 4.8, Figure 4.7 was indeed eliminated by lowering the duct, i.e. reducing the frontal inlet radius, so that the wave system shifts from a Type 2 to a Type 1 interaction. The cowl is lowered by 0.5 mm and the triple point focuses above the cowl lip in a Type 1 interaction, and the post-compression fan conditions are now the approach conditions. Figure 4.10 presents density contours from this case at Mach 4.8, showing an attached shock at the cowl lip, and thus eliminating the cowl shock detachment seen in the previous cases. The cowl shock then impinges the centrebody just near the shoulder expansion fan, so only slightly off-design, and leads to a Mach reflection on the centrebody.

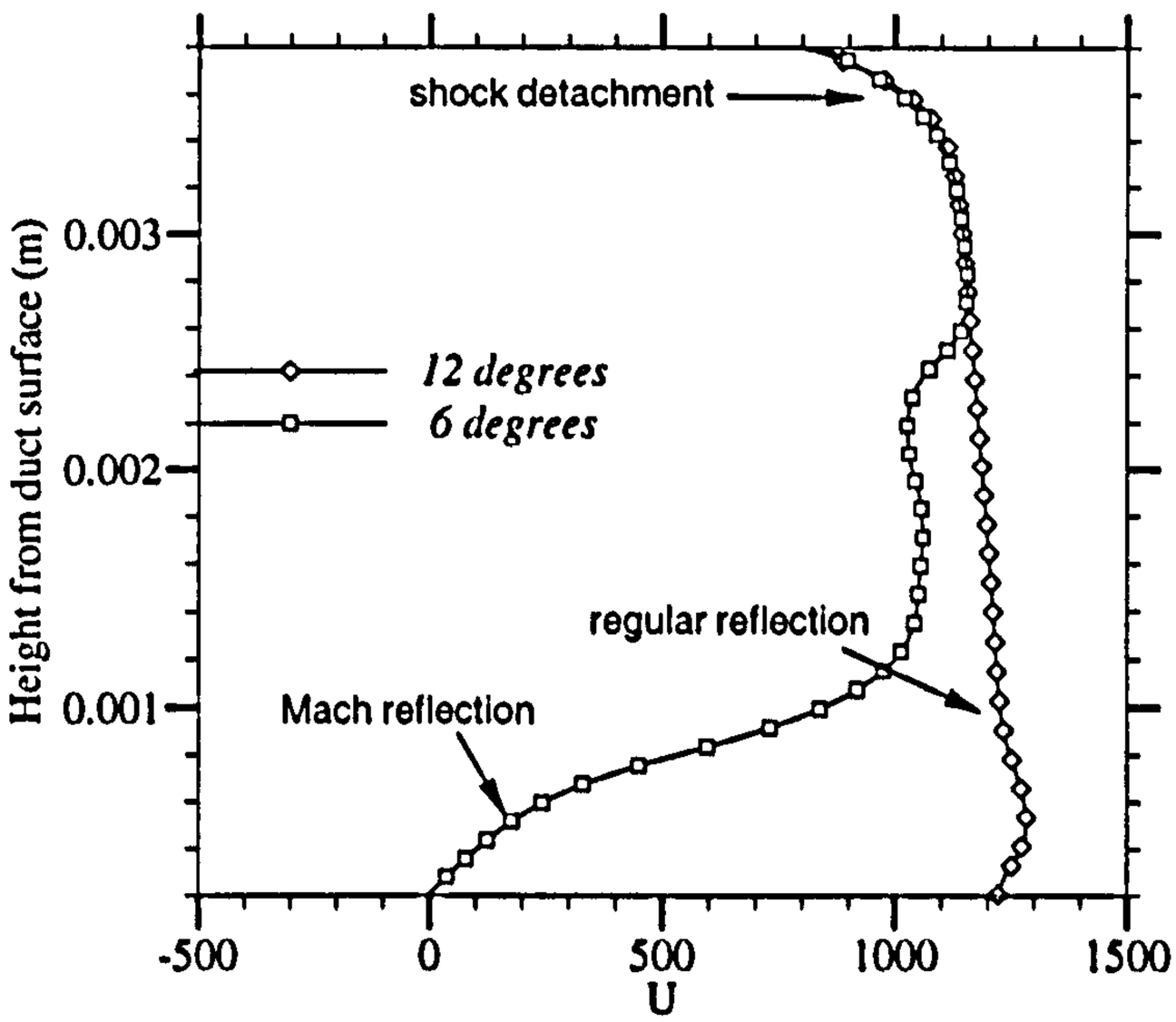


Figure 4.9: Comparison of inlet flow profile for the intake with a 12 degree and a 6 degree centrebody and cowl angle at Mach 4.8 (taken at x = 0.194m).

The Mach reflection then propagates forwards and stabilises at inlet in a lambda-type shock formation, seen in Figure 4.10. The flow just behind the Mach stem forms a vortex-like structure, seen in the density contours. Due to the large Mach stem, a major portion of the duct flow just behind the lambda shock is subsonic.

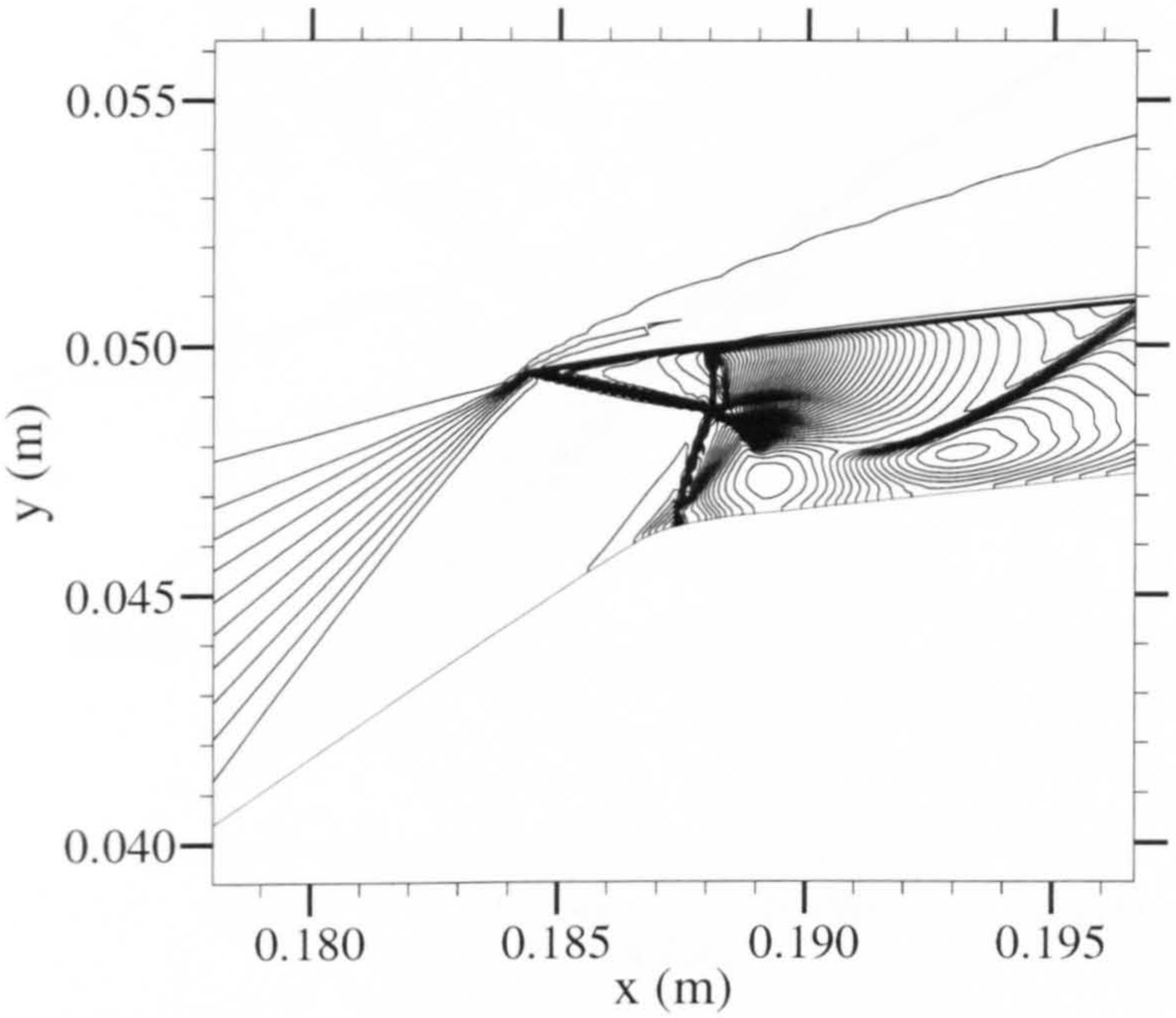


Figure 4.10: CFD Density contours from an inviscid simulation of the intake with a 12 degree cowl/centrebody angle at Mach 4.8 with the cowl lowered 0.5 mm.

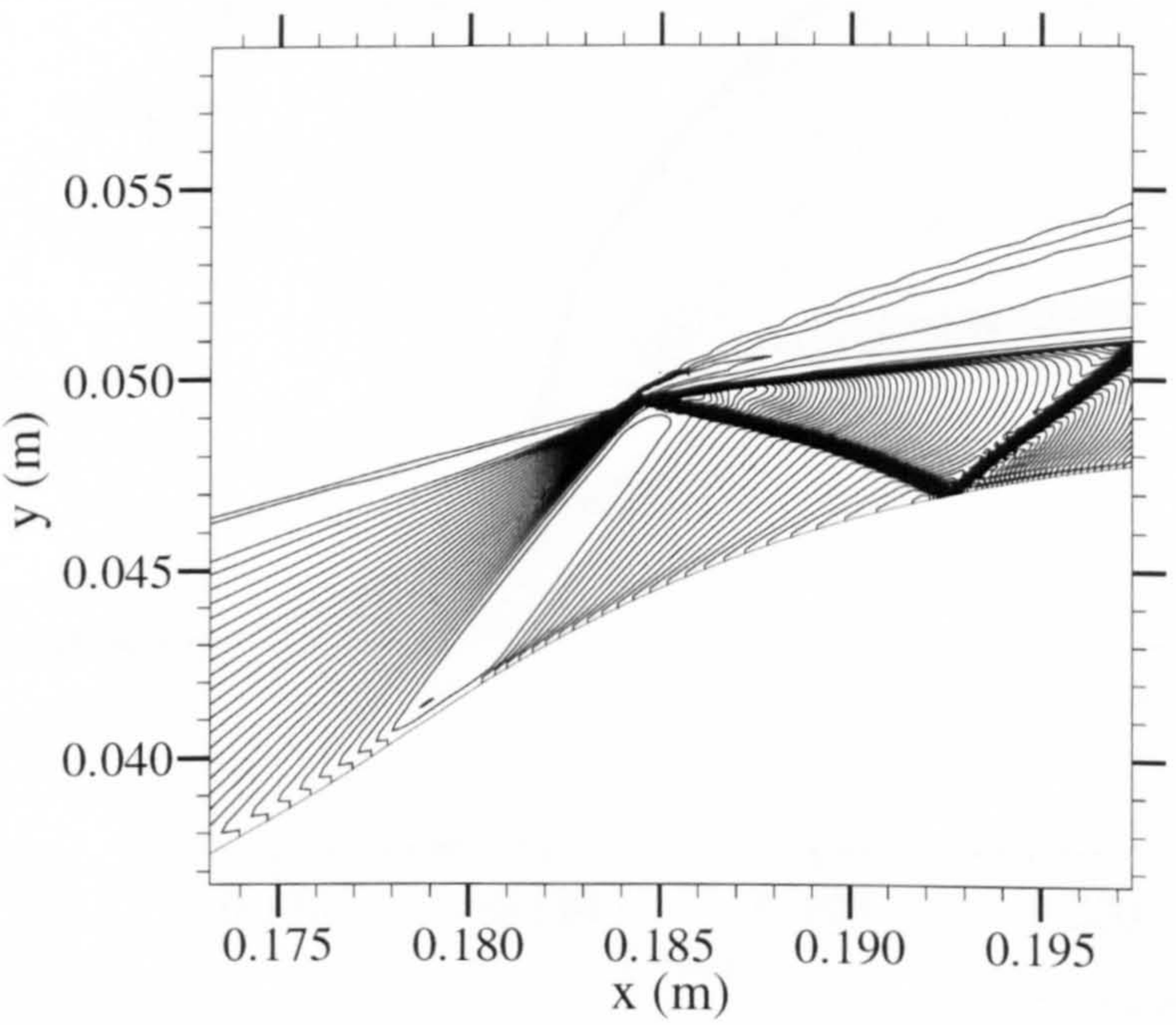


Figure 4.11: CFD Density contours from an inviscid simulation of the intake with a 12 degree cowl angle at Mach 4.8 with a lowered cowl and modified centrebody.

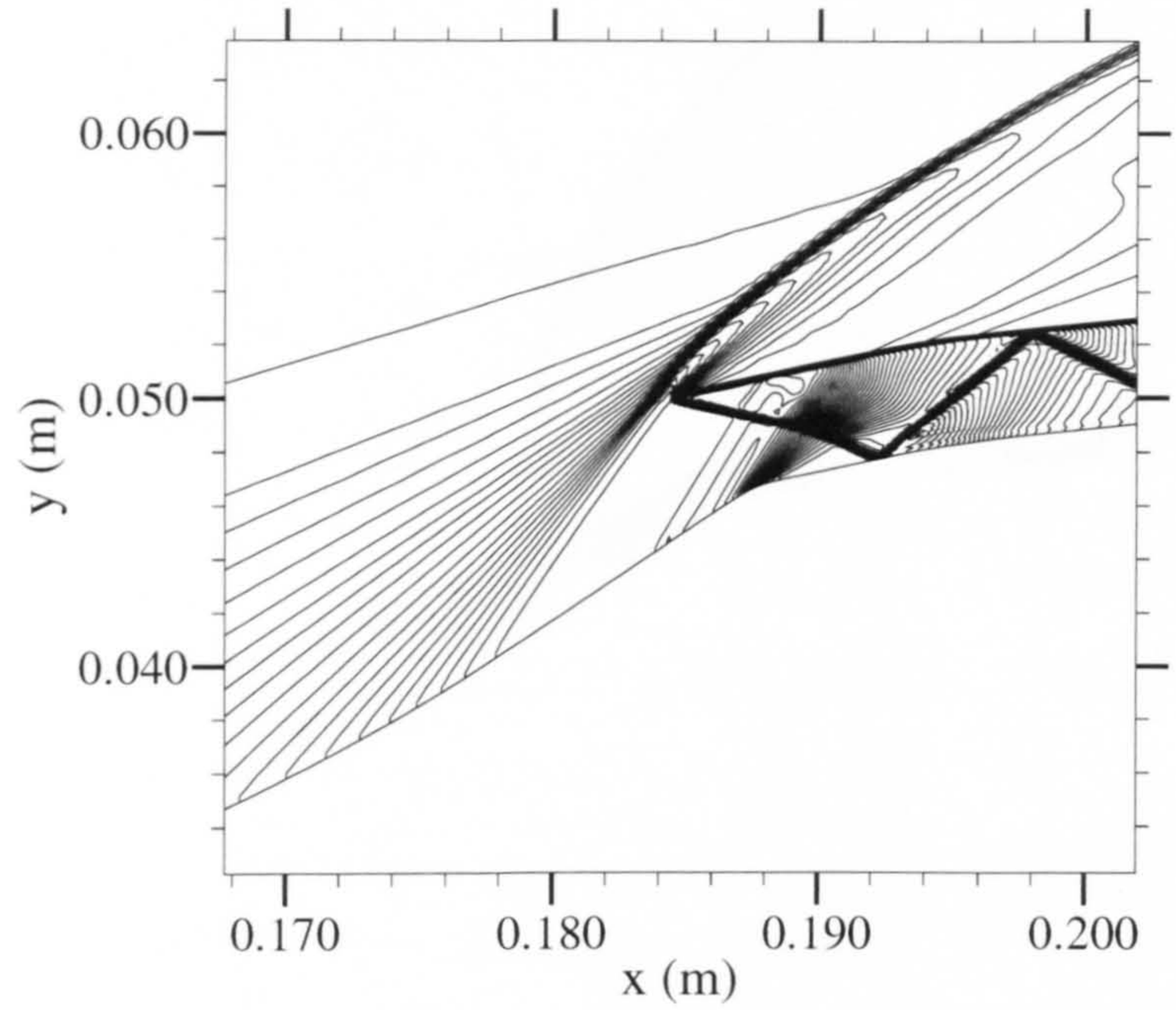


Figure 4.12: CFD Density contours from an inviscid simulation of the intake (shock-on-lip Mach 4.8) intake with a 12 degree cowl and centrebody angle at Mach 4.

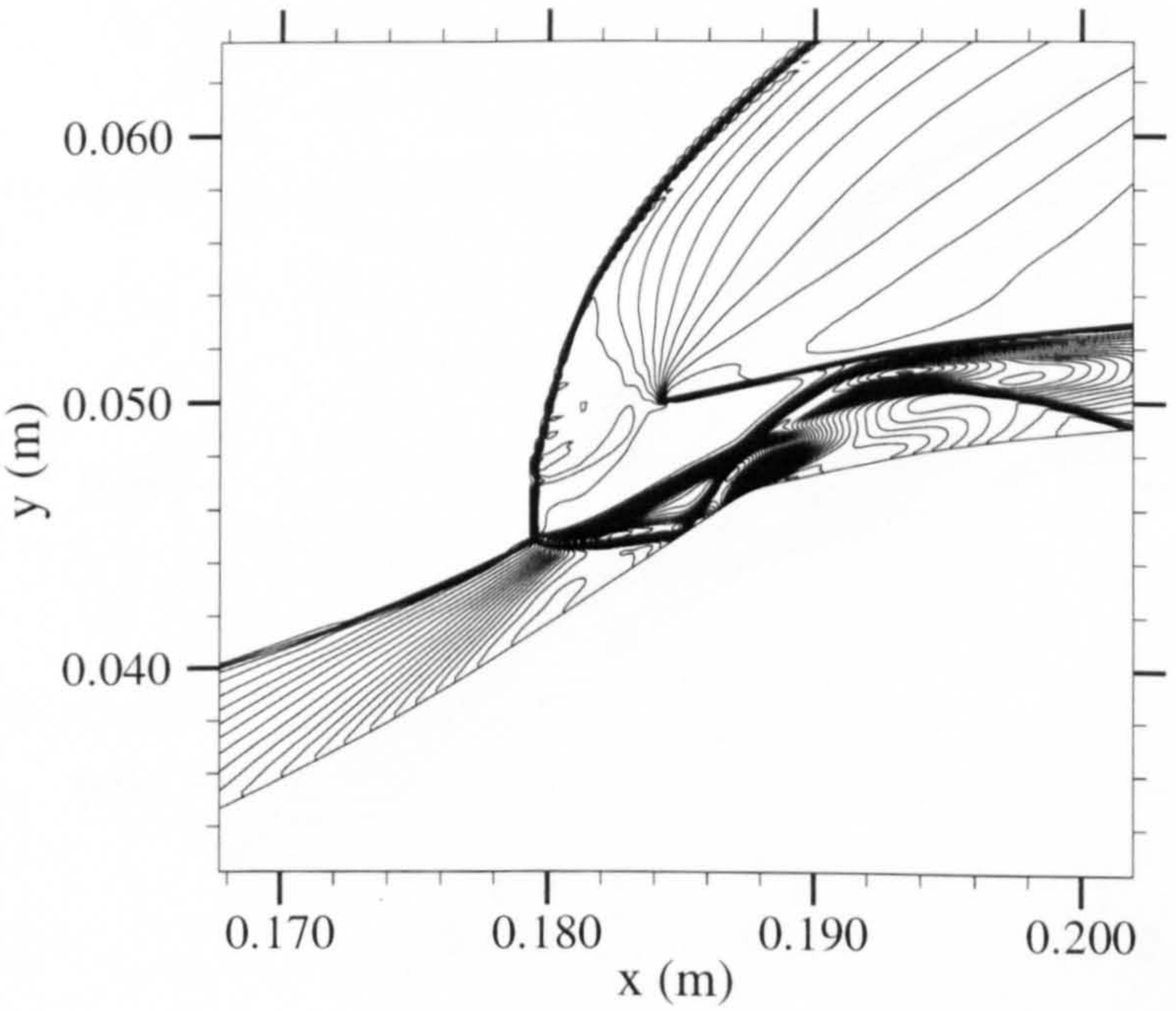


Figure 4.13: CFD Density contours from an inviscid simulation of the intake (shock-on-lip Mach 4.8) intake with a 12 degree cowl and centrebody angle at Mach 6.

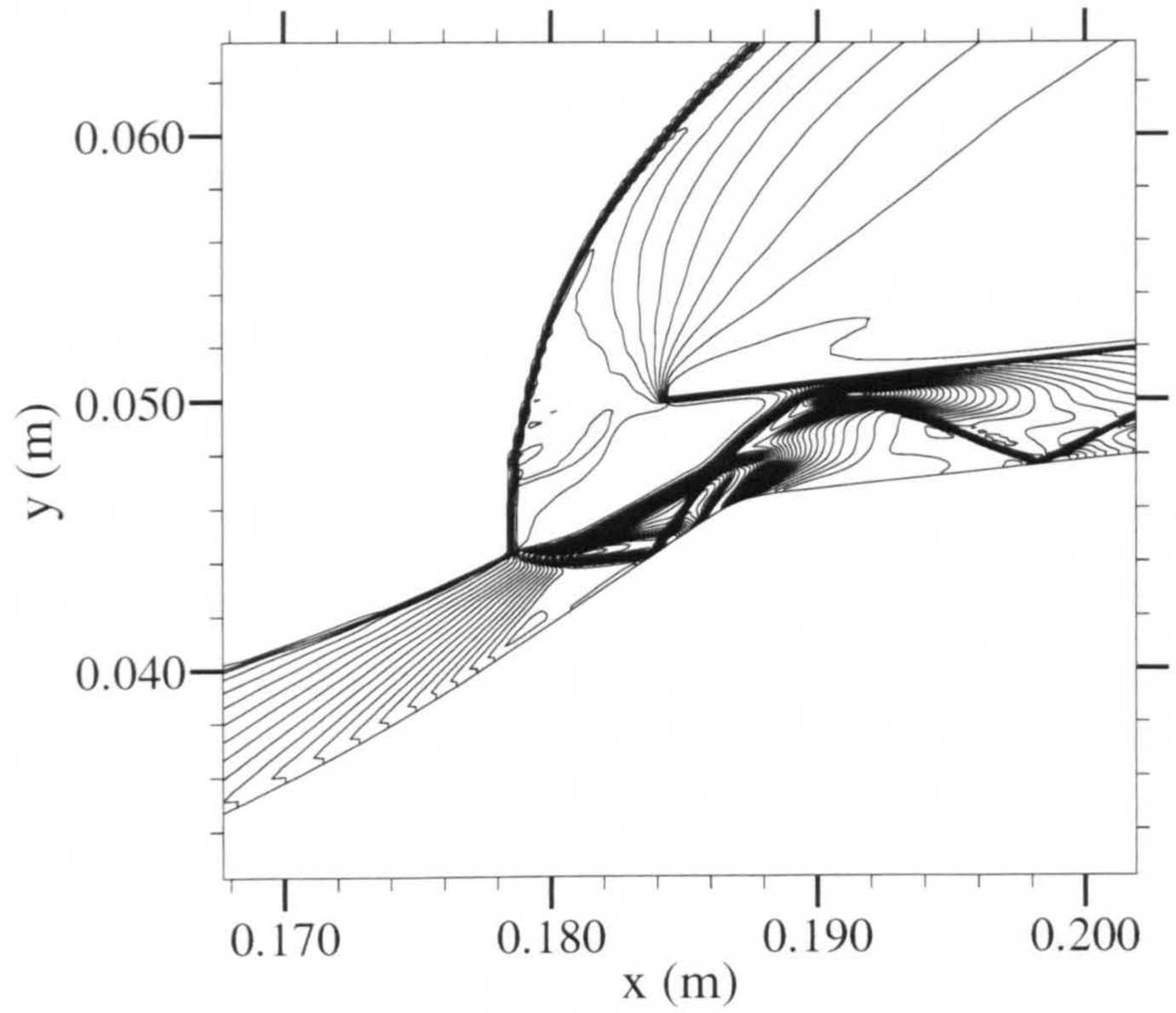


Figure 4.14: CFD Density contours from an inviscid simulation of the intake (shock-on-lip Mach 4.8) intake with a 6 degree cowl and centrebody angle at Mach 6.

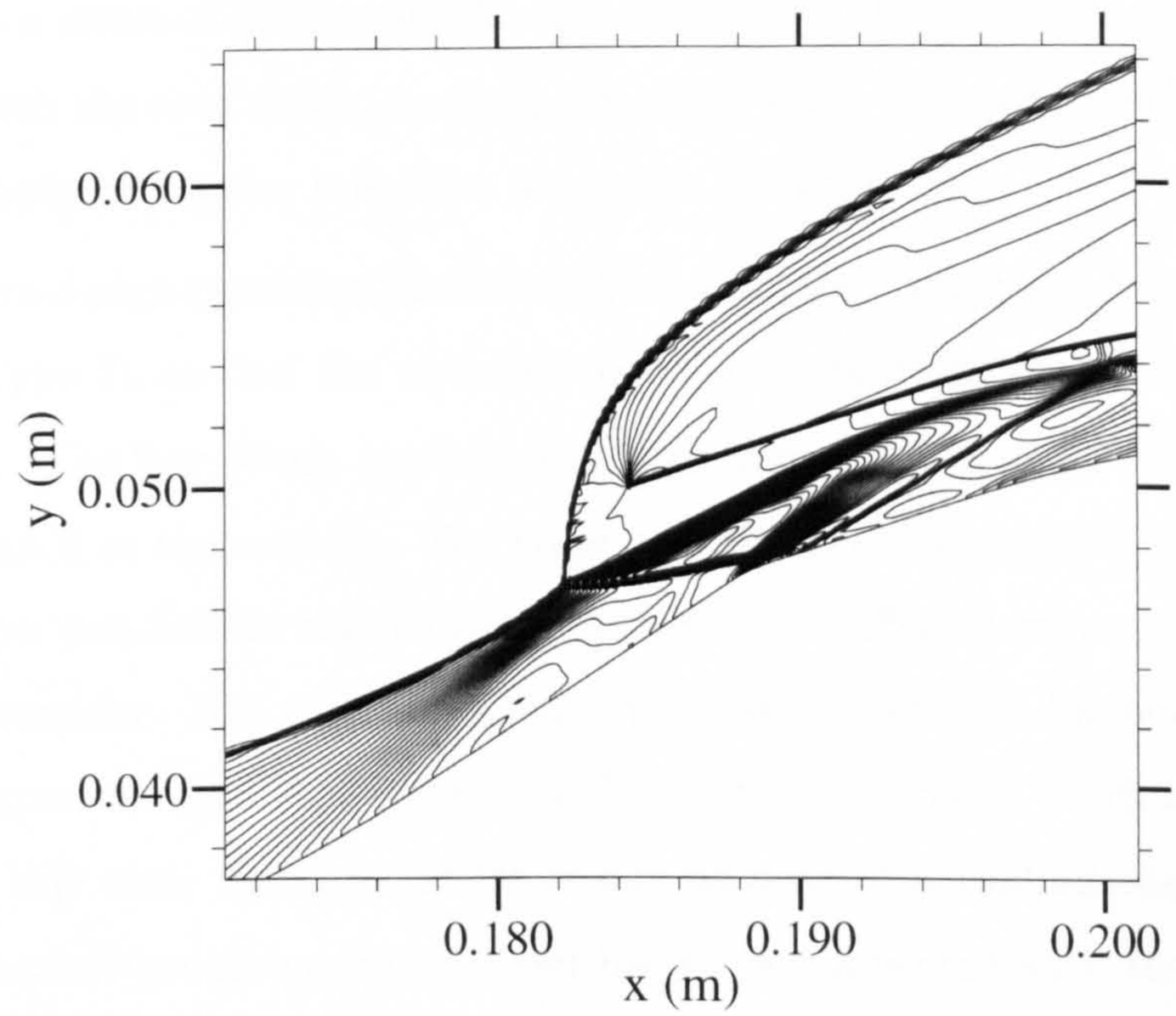


Figure 4.15: CFD Density contours from an inviscid simulation of the intake (shock-on-lip Mach 4.8) intake with an 18 degree cowl and centrebody angle at Mach 6.

To weaken the shoulder expansion, the centrebody shape was modified with a gradual contour, as opposed to a sharp expansion corner, seen in the density contours in Figure 4.11 where a weakened expansion region interacts with the reflected cowl shock. The expansion weakens the cowl shock, and is now less likely to result in a Mach reflection at the centrebody and, as seen in the contours, regular reflection occurs. This results in a near-uniform flow at inlet, but the gradual curvature at the shoulder made it a poor design choice because when considering viscous effects and flow separation, any boundary-layer separation at the centrebody could easily propagate forwards onto the forebody, and instigate an intake unstart. It was decided that the intake design with a centrebody shoulder would be a better design and so the modified centrebody design in Figure 4.11 was not explored further.

Figure 4.12 shows inviscid density contours of the intake with a 12 degree cowl angle at off-design condition Mach 4. The Mach number in this case is only just below the design Mach number of 4.8, and there is a slight spillage of compressed flow as the leading edge shock lies above the cowl lip (Type 1). The cowl shock reflects onto the centrebody aft of the shoulder expansion fan, and the shock system reflects in the duct as a series of oblique shocks and expansions. The shoulder expansion wave interacts with the cowl shock, to *curve* the shock wave. The cowl shock reflects from the centrebody as regular reflection as seen in the contours.

At the above-design condition Mach 6, Figure 4.13, the triple point focuses below the cowl lip (Type 2), so that the post-focused shock conditions are the inlet approach conditions. The low Mach number and high flow turning angle cause the shock wave to detach at the cowl lip. The large cowl shock detachment causes a region of reversed flow just behind the detachment, which can affect flow quality and leading edge heat transfer. The cowl shock system impinges onto the forebody, before the shoulder expansion and then reflects in the duct as a series of shock and expansion waves. In this case, the detachment is not because of a leading edge radius, due to the thin-plate geometry, and instead has to be connected with the detail of the annulus flow, as will be shown later. There is a penalty for having such a strong shock at the cowl lip and since the mass capture is small it will certainly appear as cowl drag. Also, flow non-uniformities caused by a shock detachment can lead to

unfavourable downstream performance in the isolator section.

In trying to reduce the shock detachment at Mach 6, CFD simulations were carried out by varying the cowl and centrebody angle and effectively changing the flow turning angle at inlet. Figure 4.14 shows a density contour plot of the intake at Mach 6 with reduced cowl and centrebody angles of 6 degrees. The shock detachment is now larger, due to the higher turning angle of the flow. This identifies the flow turning angle as the cause of the detachment problem at inlet. Figure 4.15 shows a density contour plot of the intake at Mach 6 with increased cowl and centrebody angles of 18 degrees to reduce the effective turning angle at the inlet annulus. The shock detachment at the cowl lip is attenuated, but the cowl pressure drag will now certainly increase due to the higher cowl angle.

For the case with a 6 degree cowl/centrebody angle, Figure 4.14, the cowl shock system reflects onto the forebody. As the cowl angle is increased, from Figure 4.14 to 4.13, the shock detachment is reduced and the impingement of the shock system from the cowl moves aft towards the centrebody shoulder and impinges closer to the shoulder expansion fan.

Increasing the shock-on-lip Mach number to 5.5 was seen as the solution to the severe shock detachment at the Mach 6 condition, such that at Mach 6, the intake would be operating only slightly above the design condition. As a result, the intake had to be made larger in size.

4.3.2 Intake performance

A 1D intake flow analysis is carried out to provide the average one-dimensional flow properties in the intake duct from the two-dimensional CFD solution and is used to calculate intake performance measures. To obtain the one-dimensional data from the CFD solution a *conservation averaging* method is used (also called stream-thrust averaging in the literature). The averaged values allow the calculation of the performance and efficiency parameters for the intake. The non-uniform flow-field is effectively mixed out conserving the mass, momentum and energy of the flow.

Equations 4.1 to 4.3 for mass, momentum and energy are given as:

$$Mass: \quad \frac{\gamma P M^2}{U} = constant \tag{4.1}$$

$$Momentum: \quad P(1+\gamma M^2) = constant \tag{4.2}$$

$$Energy: \quad U^2\left(\frac{1}{2}+\frac{1}{(\gamma-1)M^2}\right) = constant \tag{4.3}$$

Eliminating p and u between the above gives:

$$[(\gamma-1)M^4+2M^2]/(1+\gamma M^2) = constant \tag{4.4}$$

$$or \quad [2\gamma M_1^2-(\gamma-1)]M_2^4-[2\gamma M_1^4+2]M_2^2+[(\gamma-1)M_1^4+2M_1^2] = 0 \tag{4.5}$$

Equation 4.5 has two roots for M_2^2.

$$M_2^2 = M_1^2 \tag{4.6}$$

$$or \quad M_2^2 = \frac{(\gamma-1)M_1^2+2}{2\gamma M_1^2-(\gamma-1)} \tag{4.7}$$

If $M_1 \geq 1$ then $M_2 \leq 1$, and if $M_1 \leq 1$ then $M_2 \geq 1$

From Equation 4.7, with Equations 4.1 and 4.2 gives:

$$\frac{p_2}{p_1} = \frac{2\gamma M_1^2-(\gamma-1)}{(\gamma+1)} \tag{4.8}$$

$$\frac{\rho_2}{\rho_1} = \frac{u_2}{u_1} = \frac{(\gamma+1)M_1^2}{2+(\gamma-1)M_1^2} \tag{4.9}$$

An iterative procedure is used to obtain the Mach number, and then the remaining flow properties of pressure, temperature, density and total temperature can be solved for. From the one-dimensional flow properties obtained from conservation averaging the values of total pressure efficiency, kinetic energy efficiency and other performance measures can be calculated. Clearly conservation averaging captures some of the desirable quantities (e.g. it provides the correct mass flow rate) but

use of the averaged properties still requires care however. Entropy, for example, evaluated from the averaged properties will be in error (Van Wie[112]), nor will total pressure. Nonetheless, average values for the properties, obtained from this correct conservation-averaging is almost certainly better than other approaches such as simple mass-averaging or area-averaging methods.

Table 4.2 presents the calculated total pressure efficiencies, kinetic energy efficiencies and mass capture ratios for the various configurations tested. The efficiency values are calculated from the converged inviscid CFD simulations and so do not account for pressure losses due to friction and boundary-layer separation. Hence, the values indicate the pressure losses incurred purely from the inlet shock systems. These values will be shown to be much lower when accounting for viscous losses, discussed in chapter 5. The first three rows present the values for the original intake design with a 12 degrees cowl/centrebody angle at the three freestream conditions.

M_∞	Intake design	x_c (m), y_c (m)	δ_c / θ_2	η_{pr}	η_{ke}	MCR
4.0	Original design	0.1844, 0.0500	12 degrees	0.723	0.970	0.787
4.8	Original design	0.1844, 0.0500	12 degrees	0.747	0.981	0.961
6.0	Original design	0.1844, 0.0500	12 degrees	0.471	0.966	0.825
4.8	Reduced δ_c	0.1844, 0.0500	6 degrees	0.616	0.967	0.946
6.0	Reduced δ_c	0.1844, 0.0500	6 degrees	0.328	0.945	0.799
6.0	Increased δ_c	0.1844, 0.0500	18 degrees	0.472	0.969	0.922
4.8	Lowered cowl	0.1844, 0.0495	6 degrees	0.509	0.954	0.993
4.8	Contoured design	0.1844, 0.0495	6 degrees	0.586	0.964	0.992

Table 4.2: Intake performance (M_{sol}=4.8): Values of cowl position, cowl/centrebody angles, total pressure efficiency, kinetic energy efficiency and mass capture ratio for the several configurations at the 3 flight conditions (inviscid values).

For below-design Mach 4, the calculated total pressure efficiency is 72.3 percent and the kinetic energy efficiency is 97 percent. The intake mass capture is calculated to be 78.7 percent. The spillage loss in this case occurs due to the intake operating at below design conditions and so the triple point is focused well above the cowl lip. A small 2 percent total pressure loss is incurred across the apex shock with the remaining 19 percent total pressure loss incurred across the cowl shock system at inlet. For the same geometry at on-design condition Mach 4.8, the calculated total

pressure efficiency is 74.7 percent and the kinetic energy efficiency is 98.1 percent. The mass capture is now increased to 96.1 percent as the intake is operating at its design Mach number. Theoretically this value should be 100% however, as seen in Figure 4.7, the triple point is focused slightly below the cowl lip (Type 2) to cause shock detachment. This results in a reversal of flow just behind the detached shock and hence a spillage of mass. The presence of the boundary-layer in this case would cause the triple-point to be displaced upwards to focus at the cowl lip and provide a 100% mass capture of the compressed flow. The total pressure losses in this case are associated with the loss in total pressure through the detached cowl shock.

For the original geometry at the above-design condition Mach 6, the total pressure efficiency is calculated to be 47.1 percent and kinetic energy efficiency is 96.6 percent. The intake mass capture is calculated to be 82.5 percent. The spillage of mass is again due to the shock detachment at Mach 6, seen in Figure 4.13. The shock detachment is significantly larger compared to that at Mach 4.8, and hence a greater spillage of mass is incurred. Due to the larger shock detachment at Mach 6, higher total pressure losses are also incurred and hence a reduced value for the total pressure efficiency to 47.1 percent, compared to 74.7 percent at Mach 4.8. The kinetic energy efficiency increases from Mach 4 to 4.8, and is then reduced to its lowest value at Mach 6, which is again due to the kinetic energy loss associated with shock detachment as the flow is reduced to subsonic speeds behind detachment.

The next performance values are calculated for the intake with reduced cowl and centrebody angles after the shoulder from 12 degrees to 6 degrees. CFD simulations were carried out for this geometry at Mach 4.8 and Mach 6. For the Mach 4.8 case, a total pressure efficiency of 61.6 percent is calculated and a kinetic energy efficiency of 96.7 percent. Mass capture is calculated to be 94.6 percent. Comparing this case to the original geometry with a 12 degrees cowl/centrebody angle at Mach 4.8, shows a decrease in the mass capture ratio from 96.1% to 94.6%. The contours for the 6 degree cowl/centrebody angle case in Figure 4.8 show the larger shock detachment at inlet which results in an increased flow reversal region, and hence a reduction in the mass capture. The total pressure efficiency also reduces as the cowl angle is reduced to 6 degrees, again due to the higher total pressure losses through the larger

detached shock. Reduced kinetic energy efficiency is also incurred for this case. The flow-field in this case produced Mach reflection on the centrebody, as seen in Figure 4.8 and this would only contribute to the decrease in total pressure efficiency and kinetic energy efficiency as the flow behind the Mach stem is of subsonic conditions. The reduced cowl angle would however reduce the cowl pressure drag and so a trade-off situation between pressure loss and drag does exist.

For the intake with a reduced 6 degree cowl/centrebody angle at Mach 6, the total pressure efficiency is 32.8 percent, and kinetic energy efficiency is 79.9 percent. Mass capture is calculated to be 79.9 percent. Comparing these values to those calculated for the intake with a 12 degree cowl/centrebody angle at Mach 6 shows a reduced mass capture ratio from 82.5% to 79.9%. Again a larger shock detachment is seen for the case with a reduced cowl angle, seen in Figure 4.14. Total pressure efficiency and kinetic energy efficiency are also reduced as cowl angle is reduced at Mach 6.

The intake is also tested with an increased cowl angle to 18 degrees to reduce the effective flow turning angle in an effort to reduce the shock detachment at the cowl lip, however this will result in higher cowl pressure drag. For this geometry at Mach 6, the total pressure efficiency is 47.2 percent and the kinetic energy efficiency is 96.9 percent. The mass capture ratio is calculated to be 92.2 percent. Comparing these values to the original geometry at Mach 6 (12 degrees cowl/centrebody angle), it is found that mass capture is indeed increased, a direct consequence of the fact that the size of the shock detachment is reduced, seen in Figure 4.15. The total pressure efficiency and the kinetic energy efficiency are almost identical for both these cases.

The cowl was lowered by 0.5mm to focus the triple point at the cowl lip and avoid a shock detachment at Mach 4.8, however this resulted in a Mach reflection at inlet as seen in the density contours in Figure 4.10. For this case the total pressure efficiency is 50.9 percent and the kinetic energy efficiency is 95.4 percent. Shock detachment at the cowl lip is avoided which increases the mass capture ratio from 96.1 percent to 99.3 percent. However, the lower position of the cowl had resulted in Mach reflection at inlet and so greater total pressure losses are now incurred - total pressure efficiency is reduced from 74.4 percent to 50.9 percent.

The modification of the centrebody geometry to produce a weakened expansion, as in Figure 4.11, results in an improved total pressure efficiency of 58.6 percent and a kinetic energy efficiency of 96.4 percent. The increase in the total pressure efficiency is because Mach reflection is avoided. However the total pressure efficiency is still lower than for the original geometry at Mach 4.8 (74.7 percent) because the lower cowl position produces a stronger cowl shock wave and therefore higher total pressure losses. The mass capture ratio is increased as the cowl is lowered from 96.1 percent to 99.2 percent, and this is because shock detachment (and flow reversal behind detachment) is avoided in the case where the cowl has been lowered.

In assessing these performance measures it is evident that they are interrelated, and that the rise in one performance measure results in the fall of another. Hence, from a design perspective, the difficulty of achieving an optimum configuration for the fixed-geometry configuration over a range of flight conditions becomes apparent.

4.4 Intake with shock-on-lip at Mach 5.5

As mentioned before, the increase of the intake shock-on-lip Mach number was seen as a solution to the large area of shock detachment at the cowl lip at Mach 6. Figure 4.16 presents a schematic of the Mach 5.5 intake design, showing the new cowl lip position at 199.3mm, 50mm. The spike termination angle is maintained at 33 degrees, with a 12 degree cowl/centrebody angle, blended to 6 degrees further in the parallel section. The three freestream conditions at which the intake is tested are given in Table 4.3. The design case is at Mach number 5.5 where the shock-on-lip condition is achieved. The off-design conditions tested are at Mach 4, 5 and 6.

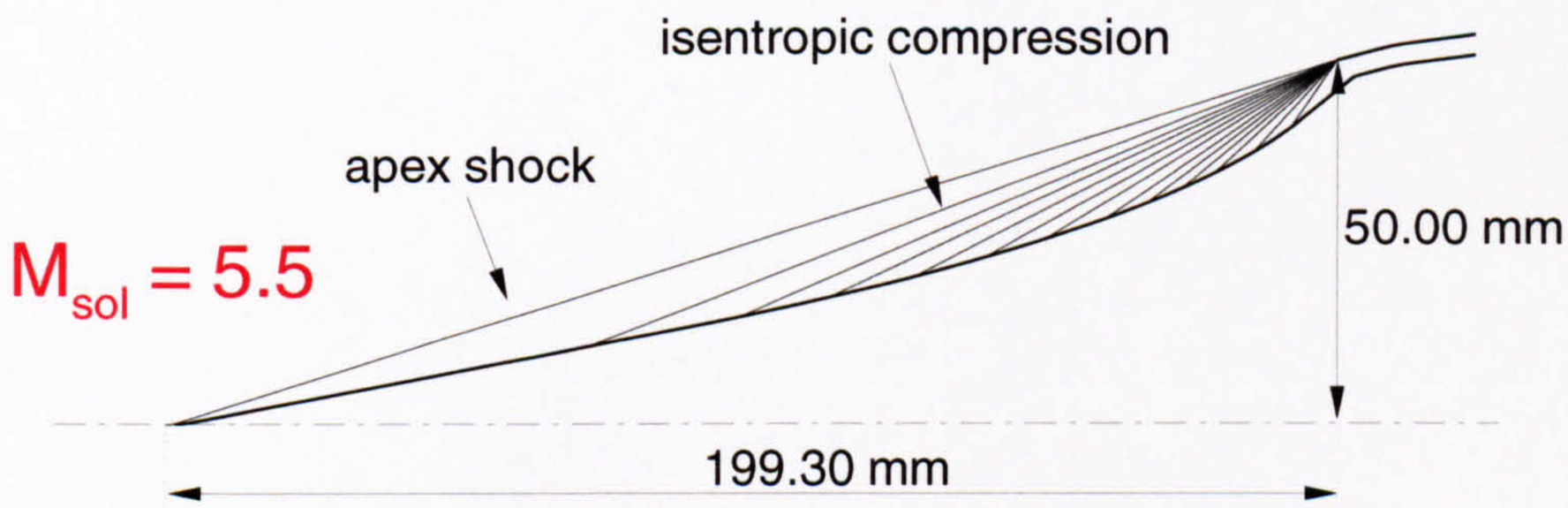


Figure 4.16: Schematic of the wave system of an intake designed for shock-on-lip at Mach 5.5.

M_∞	Pressure	Temperature	Unit Re (m^{-1})
4.0	12.00 KPa	217 K	1.6437 x 10^7
5.0	8.000 KPa	217 K	1.3698 x 10^7
5.5	4.014 KPa	222 K	7.3366 x 10^6
6.0	0.890 KPa	228 K	1.7135 x 10^6

Table 4.3: Test conditions for the Mach 5.5 intake.

4.4.1 Design/Off-design conditions

Previously in the chapter, in Figure 4.5, both the on-design and various off-design cases for the intake were discussed. The first case in Figure 4.5 showed the on-design case which, in reality, is a difficult condition to achieve.

Figure 4.17 presents density contours from an inviscid simulation of the intake at below-design Mach 4. The contours shows a Type 1 inlet interaction where the leading edge shock focuses above the cowl lip. This leads to a significant spillage of mass. With the triple point focused above the cowl lip, the free shear-layer now lies above the cowl, thus avoiding entering the annulus and generating disturbances or flow difficulties downstream in the intake duct. The M_1 conditions are the post-compression fan conditions with $M_1 \simeq 2.37$. An attached shock transmitted from the cowl lip is acted on by the shoulder expansion (Type 5) and reflects from the centrebody as a regular reflection. The shock system then reflects from the centre-body and cowl inner surfaces as a wave train of oblique shocks and expansions in the intake duct.

The density contours at the Mach 5 condition are presented in Figure 4.18. The intake is just below the design condition, and so the triple-point shifts downwards to focus slightly above the cowl lip. There is still a small amount of mass spillage above the cowl. The intake approach conditions are again the post-compression fan conditions, where $M_1 \simeq 2.82$. The cowl shock interacts with the shoulder expansion (Type 5) and reflects from the centrebody as regular reflection.

At on-design condition Mach 5.5, the focus of the isentropic fan falls below the cowl lip in a Type 2 interaction, so that the focused shock from the triple point approaches the cowl lip to cause shock detachment, shown in the density contours in Figure 4.19. The presence of the boundary-layer would shift the triple point upward to focus at the cowl lip to the on-design condition. The inviscid flow field in Figure 4.19 shows the interaction has shifted from an on-design shock system to a Type 2 interaction. The shock detachment at the cowl lip leads to flow reversal and spillage of mass. Detachment will also result in increased pressure losses at inlet, though the high loss streamtube is only a small part of the total flow.

At the Mach 6 condition, the density contours of which are shown in Figure 4.20, the focused shock wave would try to impinge on the cowl surface and forms a Mach reflection with subsonic flow regions at inlet. The system then propagates forwards to eventually lead to a large shock detachment at the cowl lip.

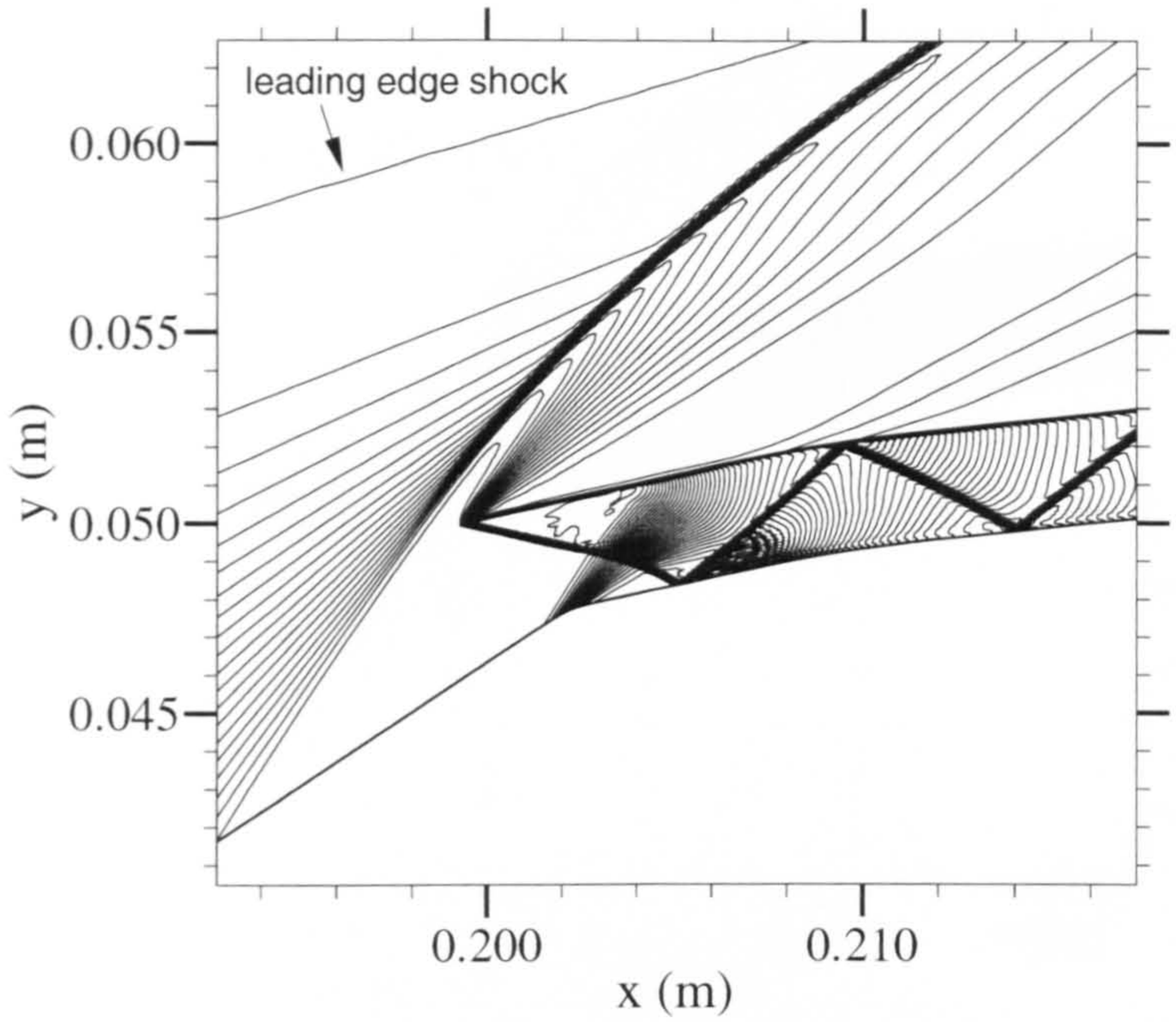


Figure 4.17: CFD Density contours from an inviscid simulation of the intake (shock-on-lip Mach 5.5) intake with a 12 degrees cowl and centrebody angle at Mach 4.

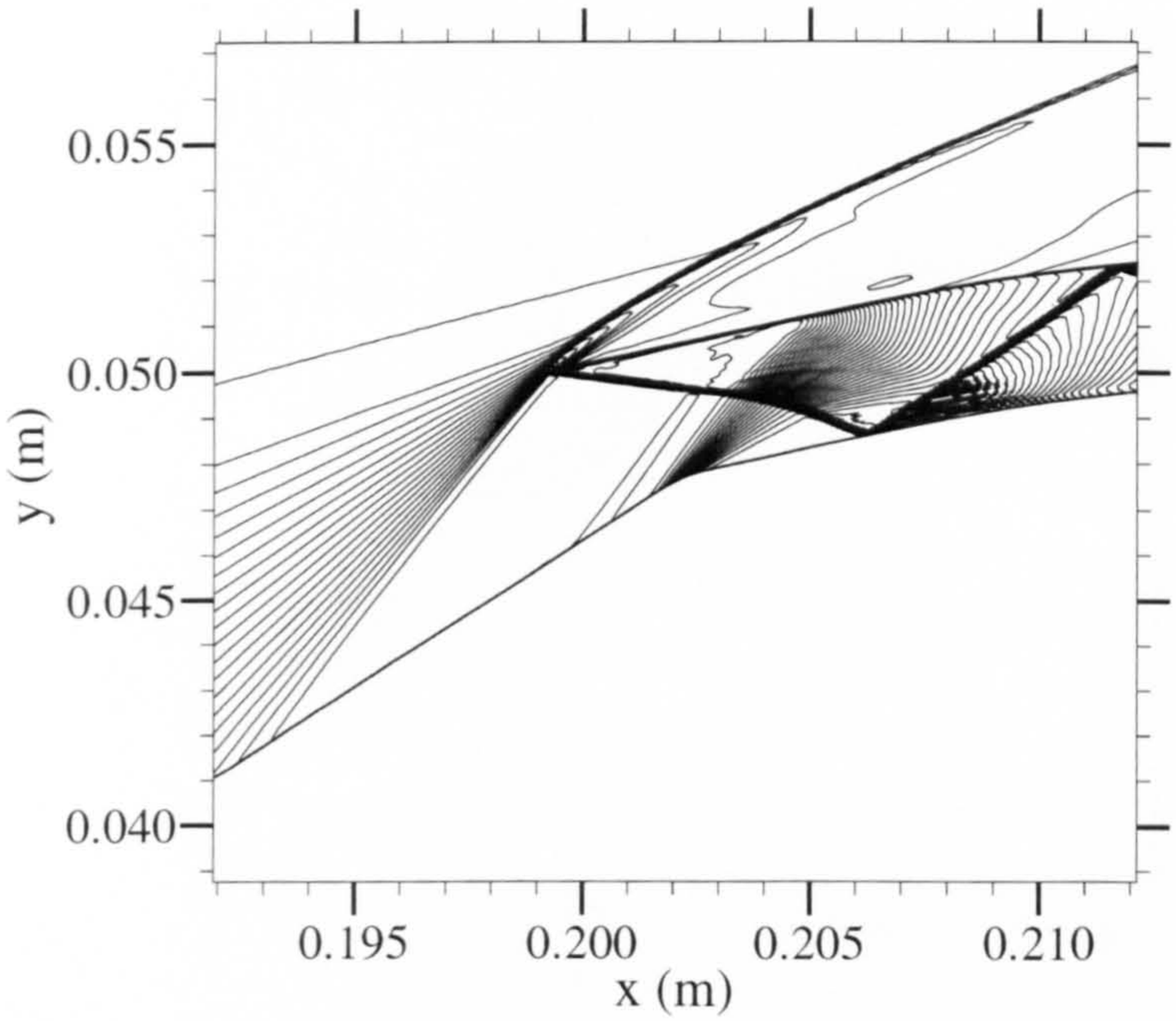


Figure 4.18: CFD Density contours from an inviscid simulation of the intake (shock-on-lip Mach 5.5) intake with a 12 degrees cowl and centrebody angle at Mach 5.

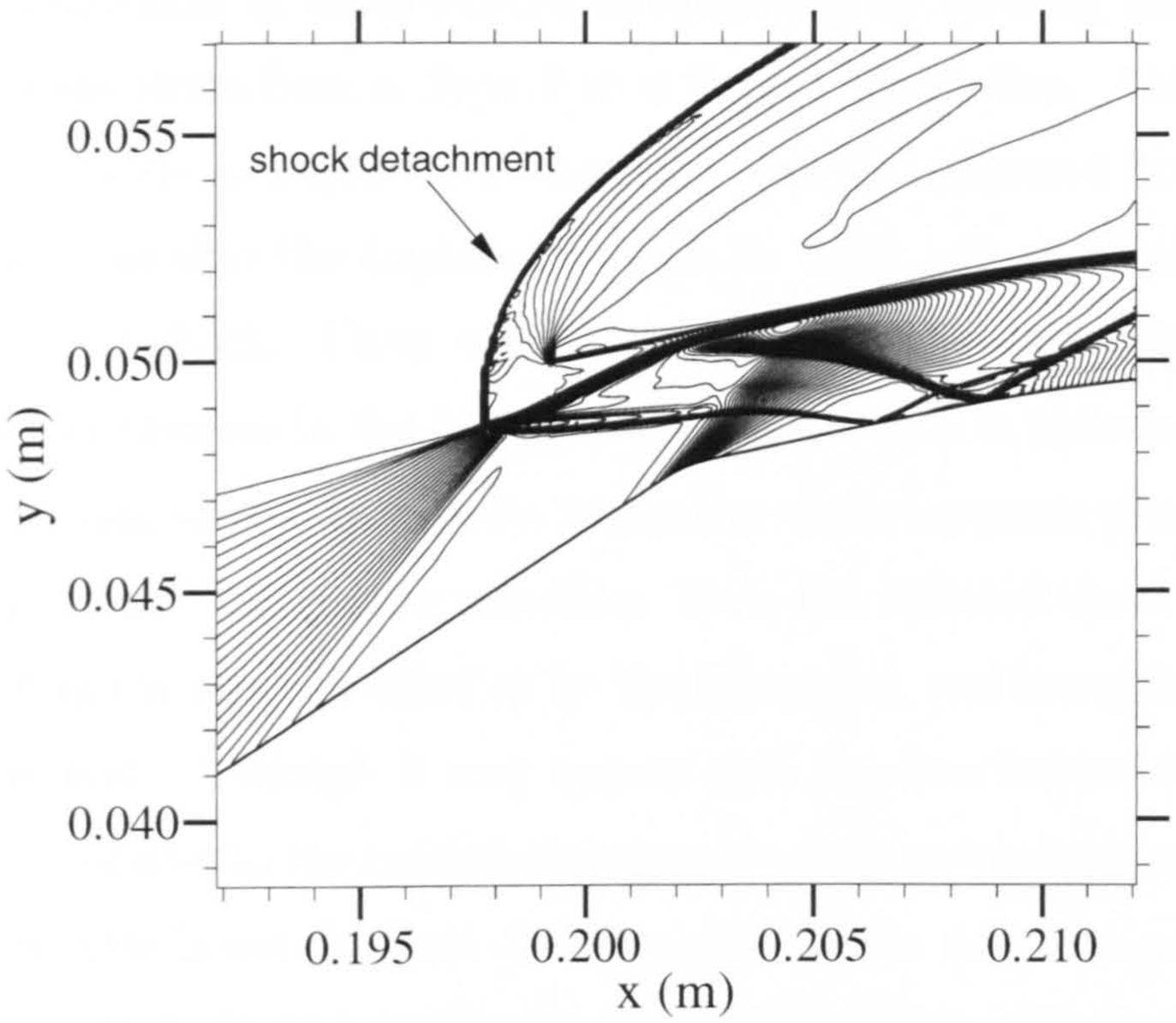


Figure 4.19: CFD Density contours from an inviscid simulation of the intake (shock-on-lip Mach 5.5) intake with a 12 degrees cowl and centrebody angle at Mach 5.5.

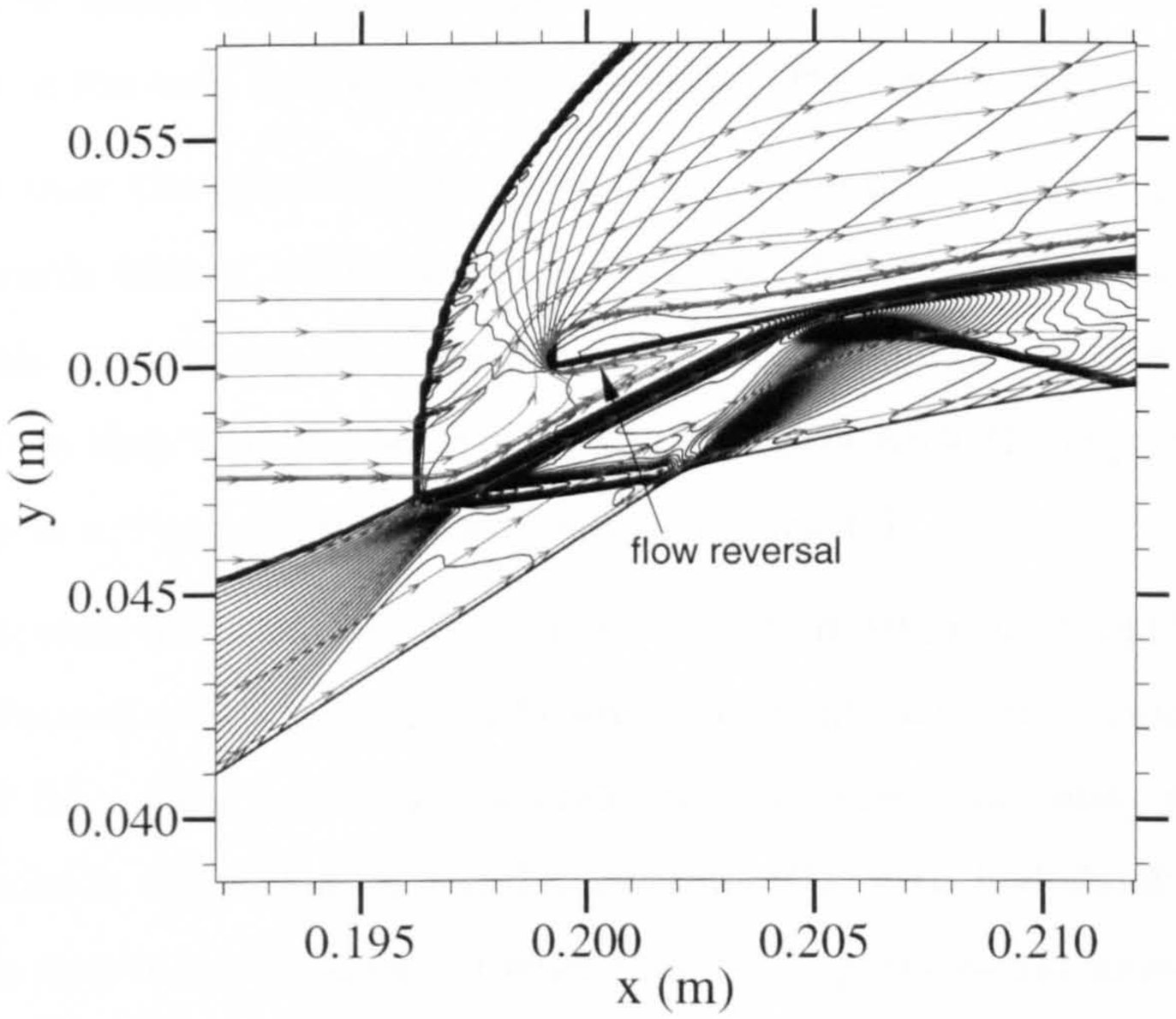


Figure 4.20: CFD Density contours from an inviscid simulation of the intake (shock-on-lip Mach 5.5) intake with a 12 degrees cowl and centrebody angle at Mach 6.

The shock detachment at Mach 6 could be eliminated by lowering the duct, so that the wave system shifts from a Type 2 to a Type 1 interaction. This is shown in the density contours in Figure 4.21 where the cowl lip is lowered from y_c=0.050m to y_c=0.0492m, so that the triple-point tends to focus just above the cowl lip to form an attached shock. These cases clearly indicate the sensitivity of the wave system to small changes in the inlet geometry. This case is also an example of a Type 5 interaction at the centrebody, where the shock interacts with the shoulder expansion and reflects as regular reflection. Here, the reflected shock wave forms a *curved shock* as the shock is acted on by the expansion, and strengthens the shock closer to the wall. Although it may appear that the flow behind this impinging shock wave is parallel to the centrebody, since the cowl and centrebody are parallel to each other, this is not the case. The expansion wave turns the post-shock flow towards the centrebody and accelerates the pre-shock flow. The angle of the cowl and centrebody are critical here, due to the possibility of the shock forming a Mach reflection, which could lead to flow non-uniformities and total pressure losses, and in the worst case could lead to the shock system propagating forwards to unstart the inlet. The intake duct flow in this case is near-uniform conditions due to shock attachment at the cowl lip and regular reflection of the cowl shock on the centrebody.

In the next case, the lowered cowl lip position of the previous configuration is now moved forwards from x_c=0.1993m to x_c=0.197m. Figures 4.22 shows density contours for this case (Mach 6). This now places the cowl leading edge ahead of the triple point so that the focused shock wave interacts with the expansion fan from the cowl lip in a Type 3 interaction (refer to Figure 4.5).

The shock system forms Mach reflection at the cowl inner surface (in the early stages of the simulation) which propagates forwards to eventually cause shock detachment at the cowl lip. As a result, a non-uniform flow enters the inlet, with increased pressure losses in the region behind detachment. The detached shock has moved so far forwards that it is now ahead of where the triple point would have formed. This condition causes the slip stream from the triple point to flow into the duct which can trigger flow disturbances and poor flow quality downstream.

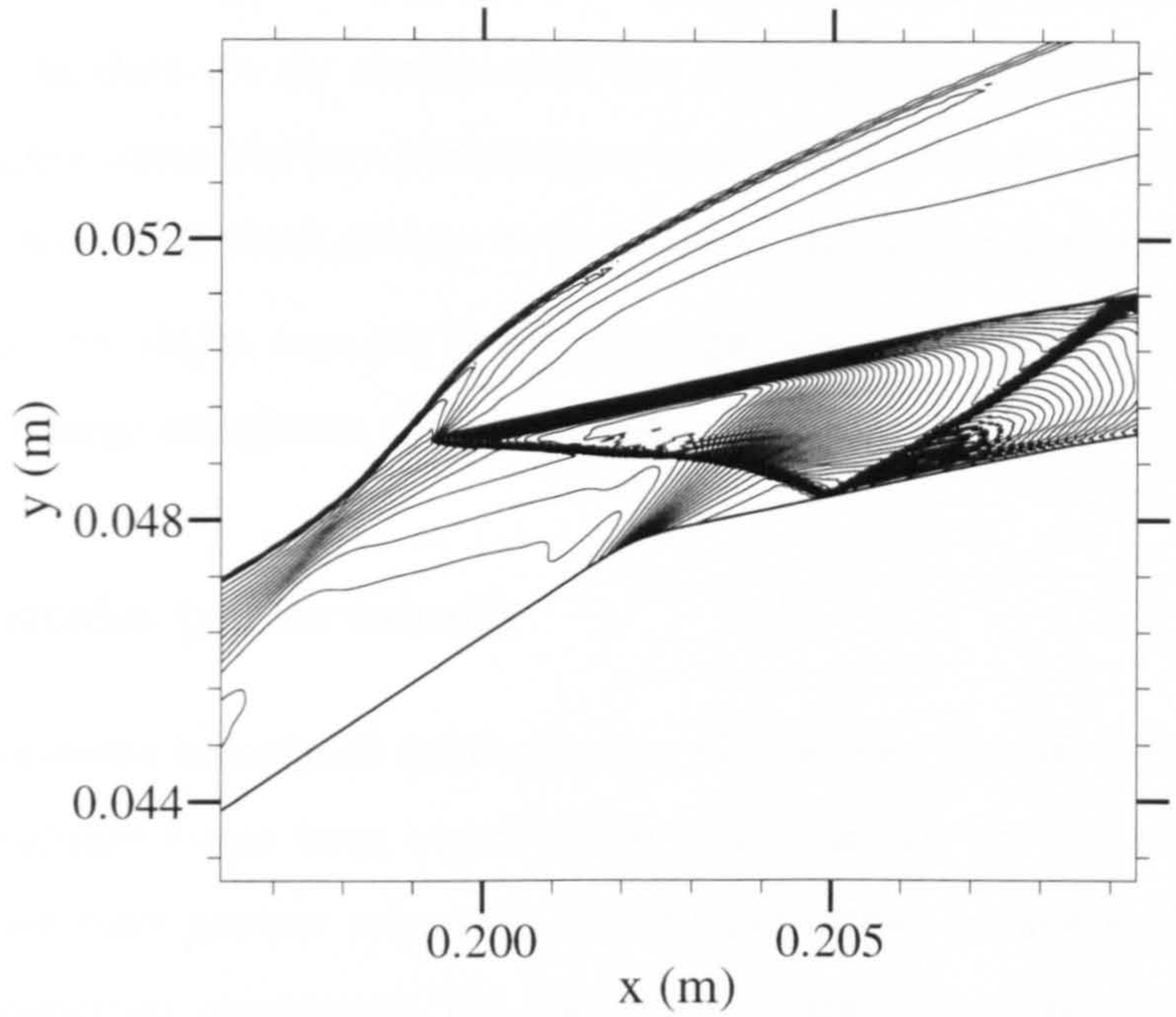


Figure 4.21: CFD Density contours from an inviscid simulation of the intake (shock-on-lip Mach 5.5) intake with a 12 degrees lowered cowl at off-design Mach 6.

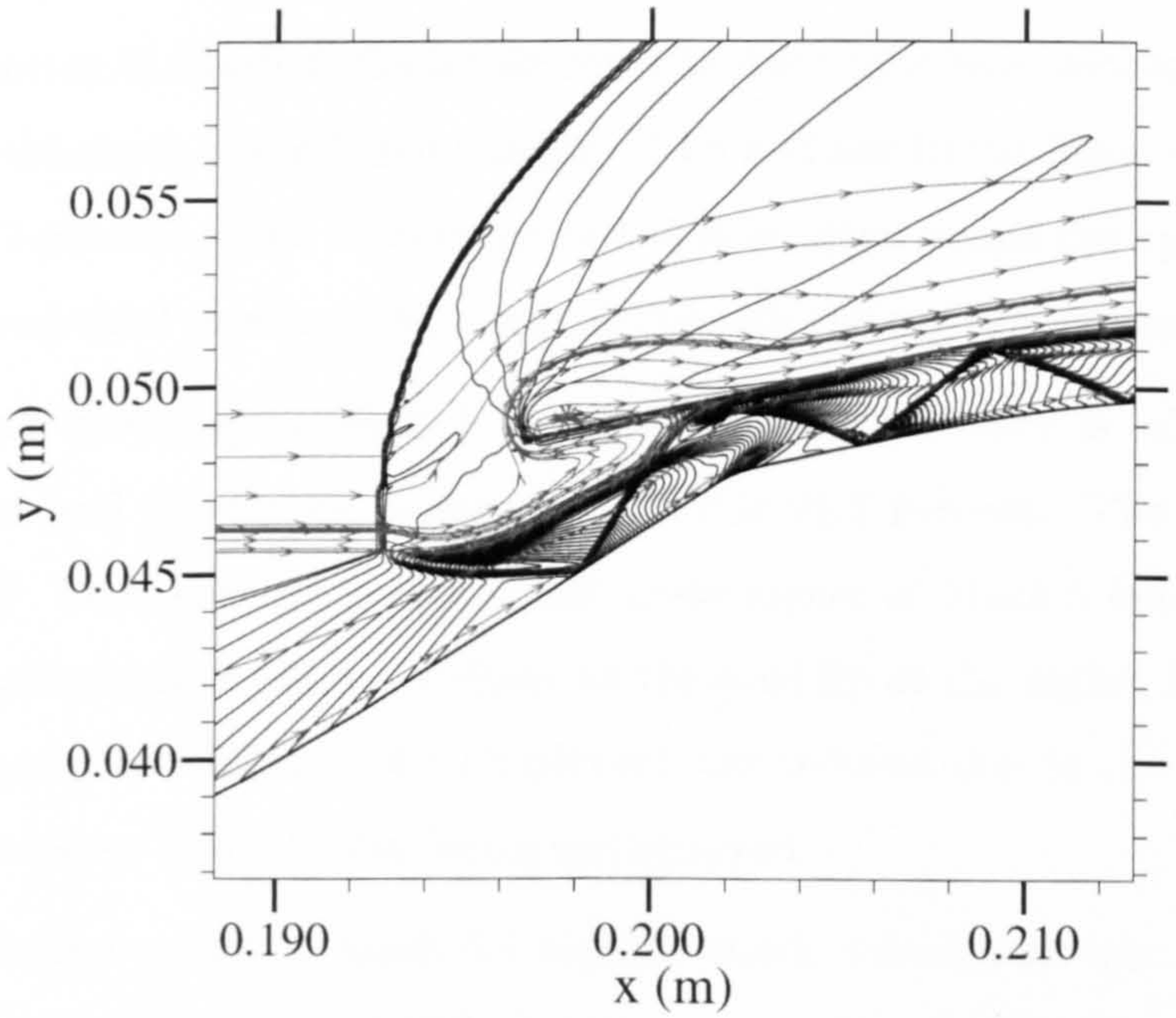


Figure 4.22: CFD Density contours from an inviscid simulation of the intake (shock-on-lip Mach 5.5) intake with a 12 degrees forward cowl at off-design Mach 6.

The subsonic flow behind the detached shock flows parallel with the supersonic flow that enters the duct via the compression fan. A mixed subsonic-supersonic flow can produce highly unsatisfactory performance in a ramjet inlet due to the requirement to stabilise a normal shock system in the isolator (discussed in chapter 6).

Thus, even very slight changes in the inlet geometry can lead to large flow-field changes and large changes in the performance of the intake.

4.4.2 Intake performance

Table 4.4 presents calculated total pressure efficiencies, kinetic energy efficiencies and mass capture ratios from conservation averaging, for the several cases tested. The first four rows present values for the original intake geometry ($M_{sol} = 5.5$) at the four freestream conditions. For the Mach 4 case, the total pressure efficiency is 70.5 percent and the kinetic energy efficiency is 96.7 percent. The mass capture ratio is calculated to be 60.9 percent. The focus of the triple point well above the cowl lip for this case explains the high mass spillage. The shock-on-lip condition for this geometry is at Mach 5.5, and so Mach 4 is well below this condition. For the intake geometry at Mach 4, the intake mass capture ratio was calculated to be 78.7 but the intake shock-on-lip Mach number of 4.8 is closer to the Mach 4 condition. A very small 2 percent of the total pressure loss is incurred across the apex shock with the remaining total pressure loss incurred through the cowl shock wave at inlet.

For the same geometry at Mach 5 the total pressure efficiency is calculated to be 62.2 percent and the kinetic energy efficiency is 91.7 percent. The mass capture ratio is 92.7. Mass capture is now significantly higher at Mach 5 because the apex shock and compression fan focus closer to the cowl lip at the higher Mach number. The total pressure efficiency of 62.2 percent has reduced due to the stronger cowl shock wave across which higher losses are incurred.

At the on-design condition Mach 5.5 a slight shock detachment was formed at the cowl lip due to the downward shift of the shock system from a Type 1 to Type 2 interaction, shown in Figure 4.19. The total pressure efficiency is 70.3 percent and the kinetic energy efficiency is 98.2 percent. The mass capture is calculated to be

95.2 percent. Mass capture is higher still due to the intake operating at its design condition, however, detachment at the cowl lip causes a slight mass spillage. The total pressure losses are also due to the losses incurred in the detachment region.

M_∞	Intake design	x_c (m), y_c (m)	δ_c / θ_2	η_{pr}	η_{ke}	MCR
4.0	Original design	0.1993, 0.0500	12	0.705	0.967	0.609
5.0	Original design	0.1993, 0.0500	12	0.622	0.971	0.927
5.5	Original design	0.1993, 0.0500	12	0.703	0.982	0.952
6.0	Original design	0.1993, 0.0500	12	0.690	0.985	0.894
6.0	Lowered cowl	0.1993, 0.0492	12	0.432	0.962	0.958
6.0	Forward cowl	0.1970, 0.0486	12	0.358	0.954	0.869

Table 4.4: Intake performance (M_{sol}=5.5): Values of cowl position, cowl/centrebody angle, total pressure efficiency, kinetic energy efficiency and mass capture ratio for the several configurations at 4 flight conditions (inviscid values).

For the intake geometry at Mach 6, the calculated total pressure efficiency is 69 percent and the kinetic energy efficiency is 98.5 percent. The mass capture ratio is 89.4. The reduction in mass capture is due to the large shock detachment at the cowl lip which causes flow reversal and mass spillage, seen in Figure 4.20. Total pressure losses are also incurred across the detached shock. The general trend seems to show a loss in total pressure through a detached shock, or a loss in total pressure of similar quantity across a strong attached cowl shock wave. Although the total pressure efficiency for attached/detached shocks seems to be in a similar range, it must be considered that detachment causes flow non-uniformity which will only lead to further deterioration of downstream performance in the ramjet. Detachment also leads to reduced mass capture ratios. The kinetic energy efficiency which is near 1 for the higher Mach number range, increases as Mach number increases with its highest value of 98.5 percent at Mach 6. Compared to the intake geometry ($M_{sol} = 4.8$) at Mach 6 for which total pressure efficiency was calculated to be 47.1 percent, the intake geometry ($M_{sol} = 5.5$) has an improved total pressure efficiency of 69.0 percent at Mach 6. Kinetic energy efficiency is also improved from 96.6 percent for the intake ($M_{sol} = 4.8$) to 98.5 percent for the intake ($M_{sol} = 5.5$), as is mass capture ratio which was calculated to be 82.5 percent for the intake ($M_{sol} = 4.8$), and is 89.4 percent for the intake ($M_{sol} = 5.5$) at Mach 6. The shock detachment

at Mach 6 was eliminated by lowering the cowl, as seen in Figure 4.21, and the total pressure efficiency for this case is calculated to be 43.2 percent. The kinetic energy efficiency is 96.2 percent and the mass capture ratio is 95.8 percent. Although detachment is eliminated, a high loss in total pressure is incurred across the stronger cowl shock at the inlet with a total pressure efficiency of 43.2% compared to 69% for the original cowl position case. However, shock attachment now means that the flow reversal caused by shock detachment is avoided which results in a higher mass capture ratio of 95.8% compared to 89.4% for the detached case at Mach 6. Kinetic energy efficiency has also reduced for the lowered cowl case from 98.5% to 96.2%.

The Type 3 interaction where the focused shock interacts with the cowl expansion was shown in the case in Figure 4.22 where the cowl position was moved forward. The total pressure efficiency for this case is 35.8 percent which is due to the large shock detachment at inlet. The kinetic energy efficiency is calculated to be 95.4 percent which is the lowest value of all configurations. The mass capture ratio for this case was calculated to be 86.9 percent which is the lowest mass capture value of all cases tested at Mach 6. The severe shock detachment will also lead to increased flow non-uniformity in the intake duct and affect isolator performance.

Figure 4.23 and 4.24 show the average pressure and Mach number distribution in the intake duct for the four freestream conditions. Figure 4.25 shows a graph of the total pressure efficiency distribution for the intake geometry ($M_{sol} = 5.5$) at the four freestream conditions. It should be reminded that these values are calculated from the inviscid flow field data and hence do not account for total pressure losses associated with boundary-layer growth. In general the most serious contribution of total pressure losses in inlets occurs from shock waves. This graph indeed shows that most of the total pressure losses are incurred by the initial inlet shock system.

Figure 4.26 plots the kinetic energy efficiency through the intake duct for the four free stream conditions showing the initial losses incurred from the inlet shock system.

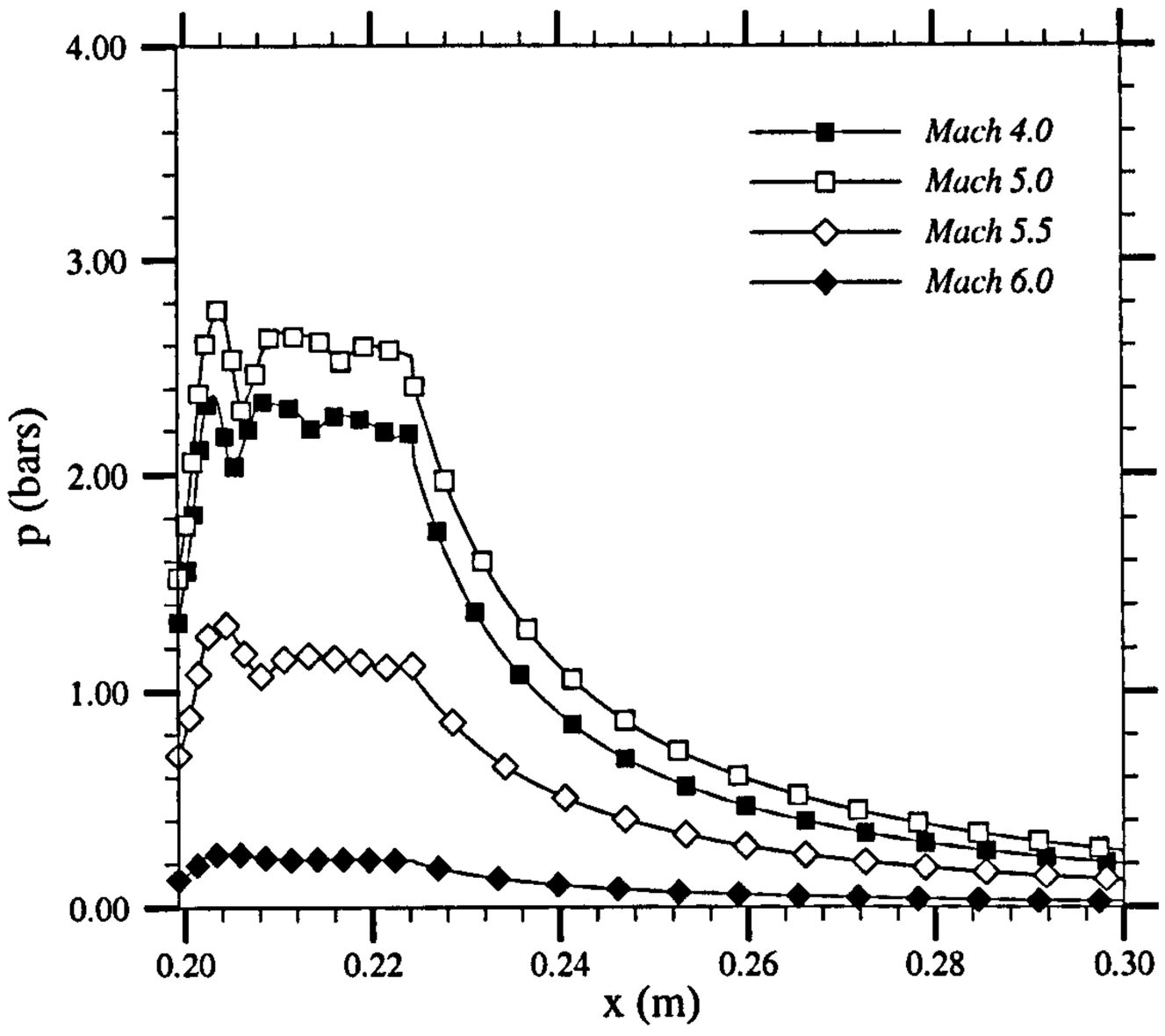


Figure 4.23: Average pressure in the duct versus x-distance calculated from CFD simulations of the intake ($M_{sol} = 5.5$) at the freestream conditions (inviscid values).

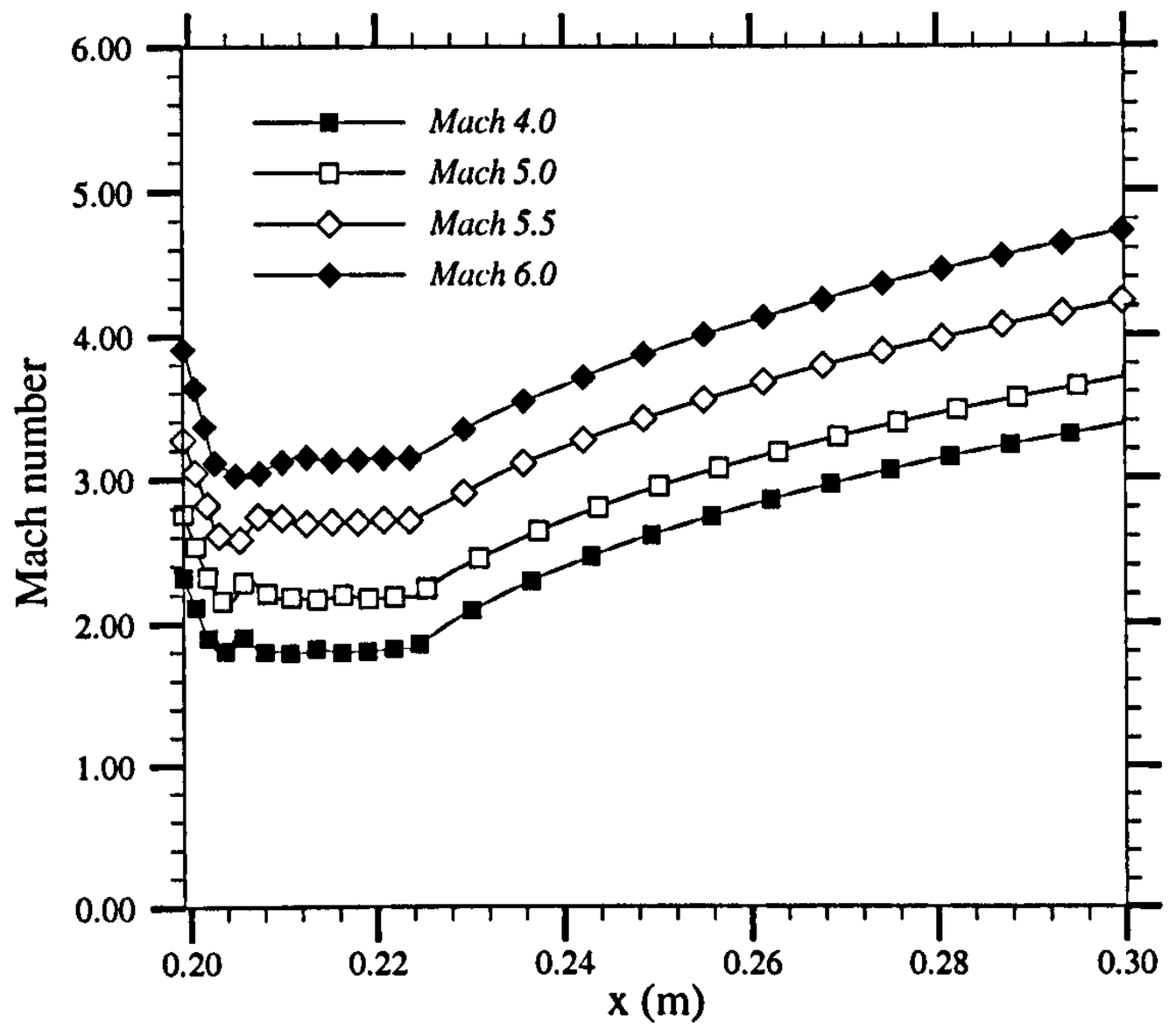


Figure 4.24: Average Mach number versus x-distance calculated from CFD simulations of the intake ($M_{sol} = 5.5$) at the four freestream conditions (inviscid values).

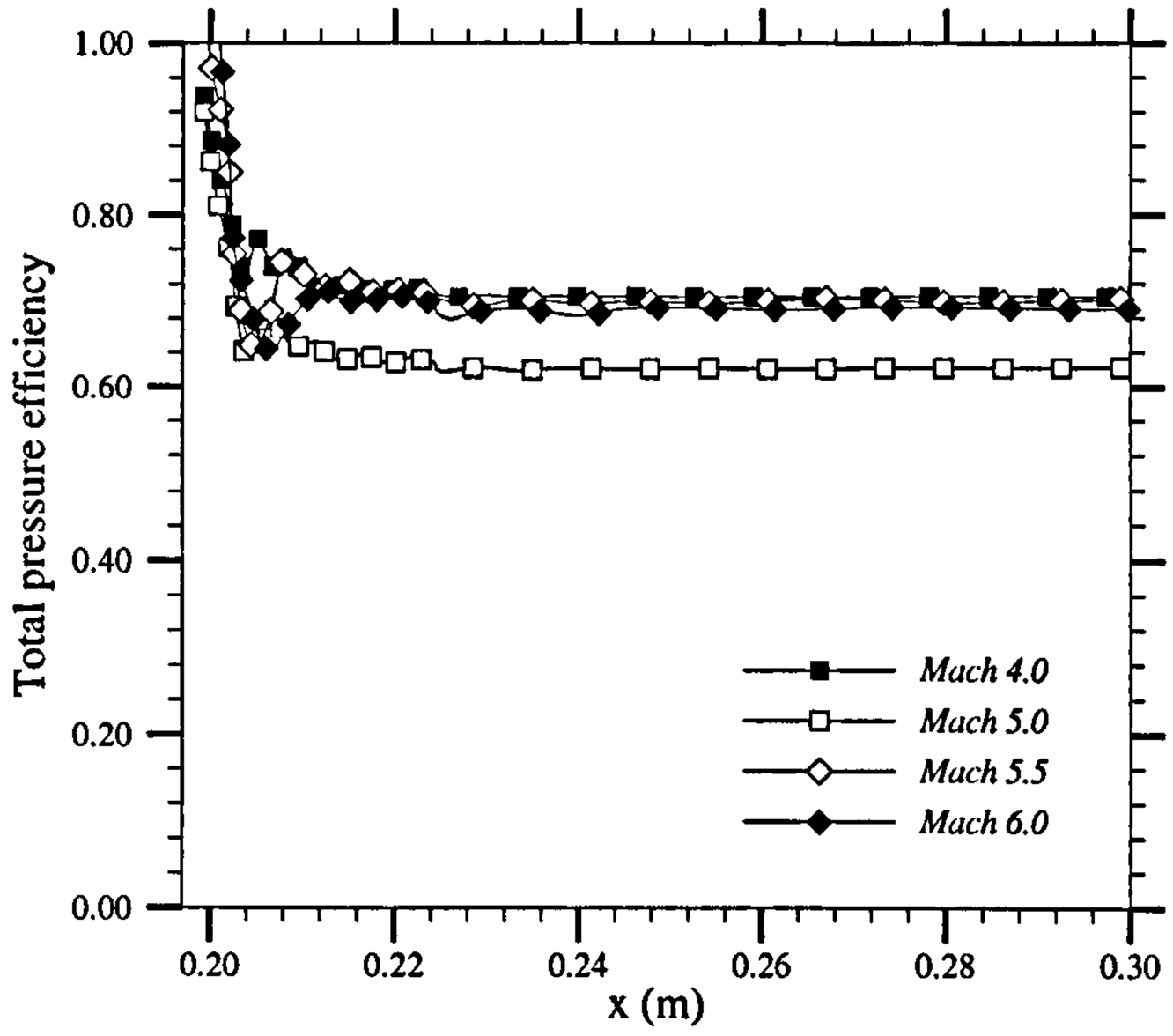


Figure 4.25: Total pressure efficiency versus x-distance calculated from CFD simulations of the intake ($M_{sol} = 5.5$) at the four freestream conditions (inviscid values).

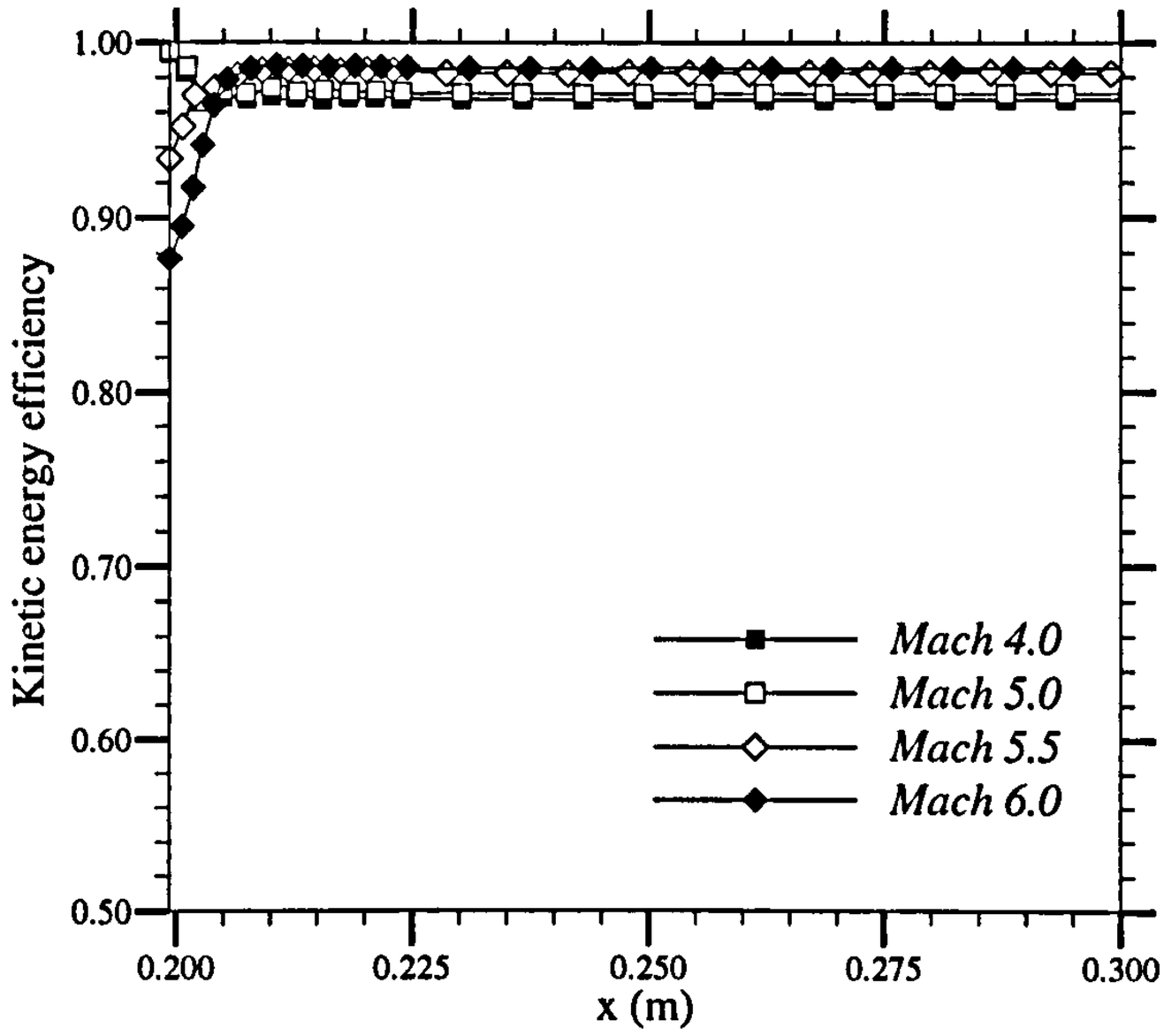


Figure 4.26: Kinetic energy efficiency versus x-distance calculated from CFD simulations of the intake ($M_{sol} = 5.5$) at the four freestream conditions (inviscid values).

4.4.3 Effects of cowl blunting

In studying the flow at the cowl lip region, it is important to note that the actual intake has a blunted leading edge to the cowl. Inviscid simulations were carried out to compare the flow with a thin-plate cowl to that with a blunt cowl to study the effects of bluntness on the flow-field. The initial cowl angle is 12 degrees with the blunt cowl having a thickness of 2mm. Figure 4.28 shows density contours from an inviscid simulation of the intake with a 12 degrees blunted cowl at Mach 4, compared to the flow with the intake with a thin-plate cowl shown in Figure 4.27. In both cases, the apex shock focuses above the cowl lip, with a cowl shock reflecting onto the centrebody as regular reflection. For the case with a thin-plate cowl, an attached shock wave forms the cowl lip. For the blunt cowl case, the cowl shock is slightly detached due to leading edge bluntness, but the internal shock systems are identical. The entropy layer generated by the blunt cowl is visible in the contours.

For the Mach 5 case, the density contours are shown in Figure 4.30 and the cowl shock is slightly more detached, as the apex shock moves closer to the cowl lip. Comparing this to the thin-plate case in Figure 4.29 the internal shock systems are again the same, with a slight shift forward in the cowl shock for the blunted case.

At Mach 6, shown in Figure 4.32, the apex shock moves below the cowl lip, and leads to large-scale shock detachment. This shock system is also seen in the case with the thin-plate cowl in Figure 4.31, and it hence confirms that the inlet shock systems are hardly affected by cowl bluntness. This case shows that shock detachment is not a consequence of cowl bluntness, but rather due to the high flow turning angle and the precise location of the focus of the forebody compression process.

Figures 4.33 to 4.35 present the centrebody and cowl inner surface pressure distributions for the thin-cowl and the blunted cowl cases at the three Mach numbers showing similar internal flow structures for both thin-plate and blunted cowl cases.

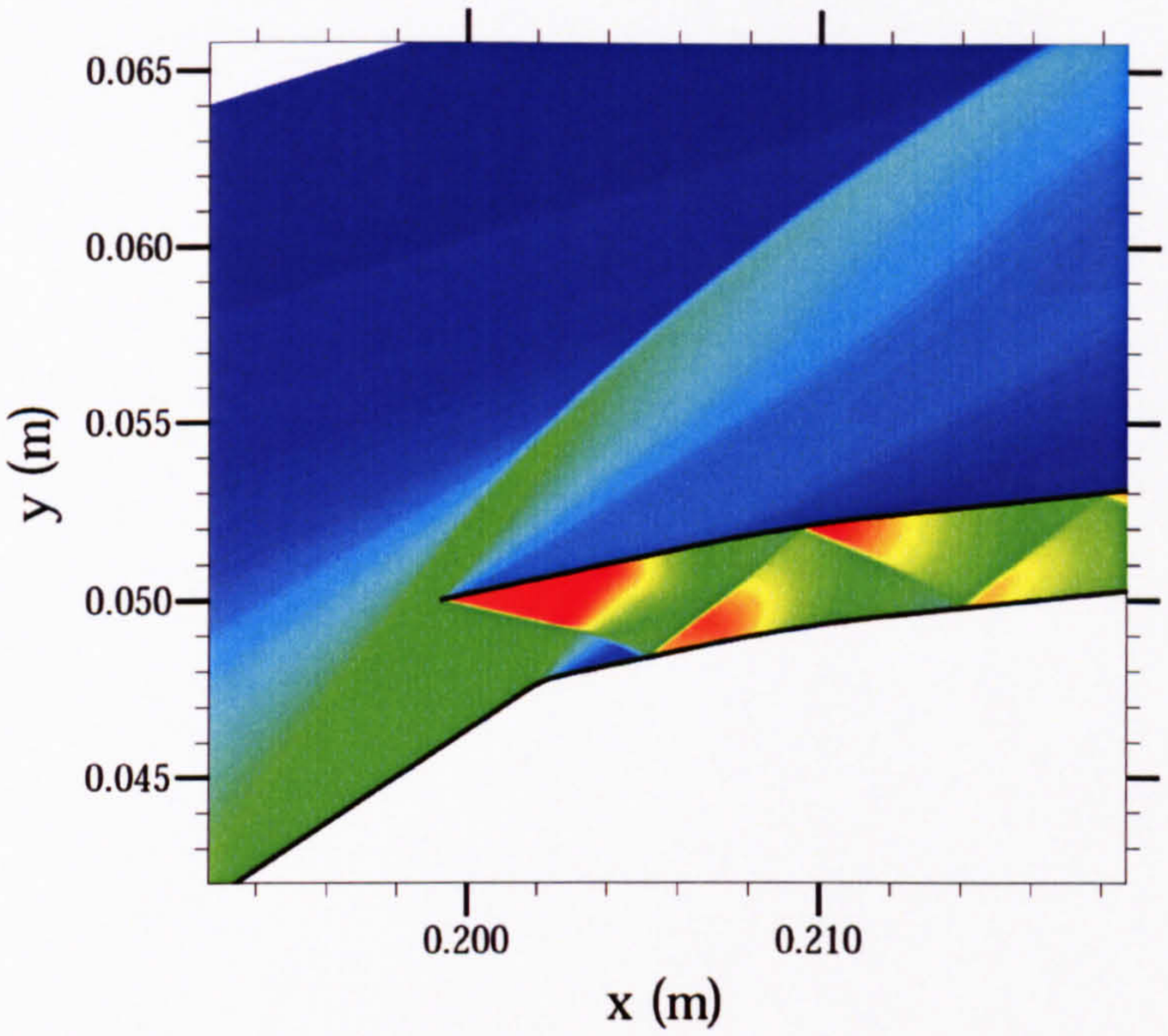


Figure 4.27: CFD Density contours from an inviscid simulation of the intake with a 33 degree spike termination angle and a 12 degrees cowl angle at Mach 4.

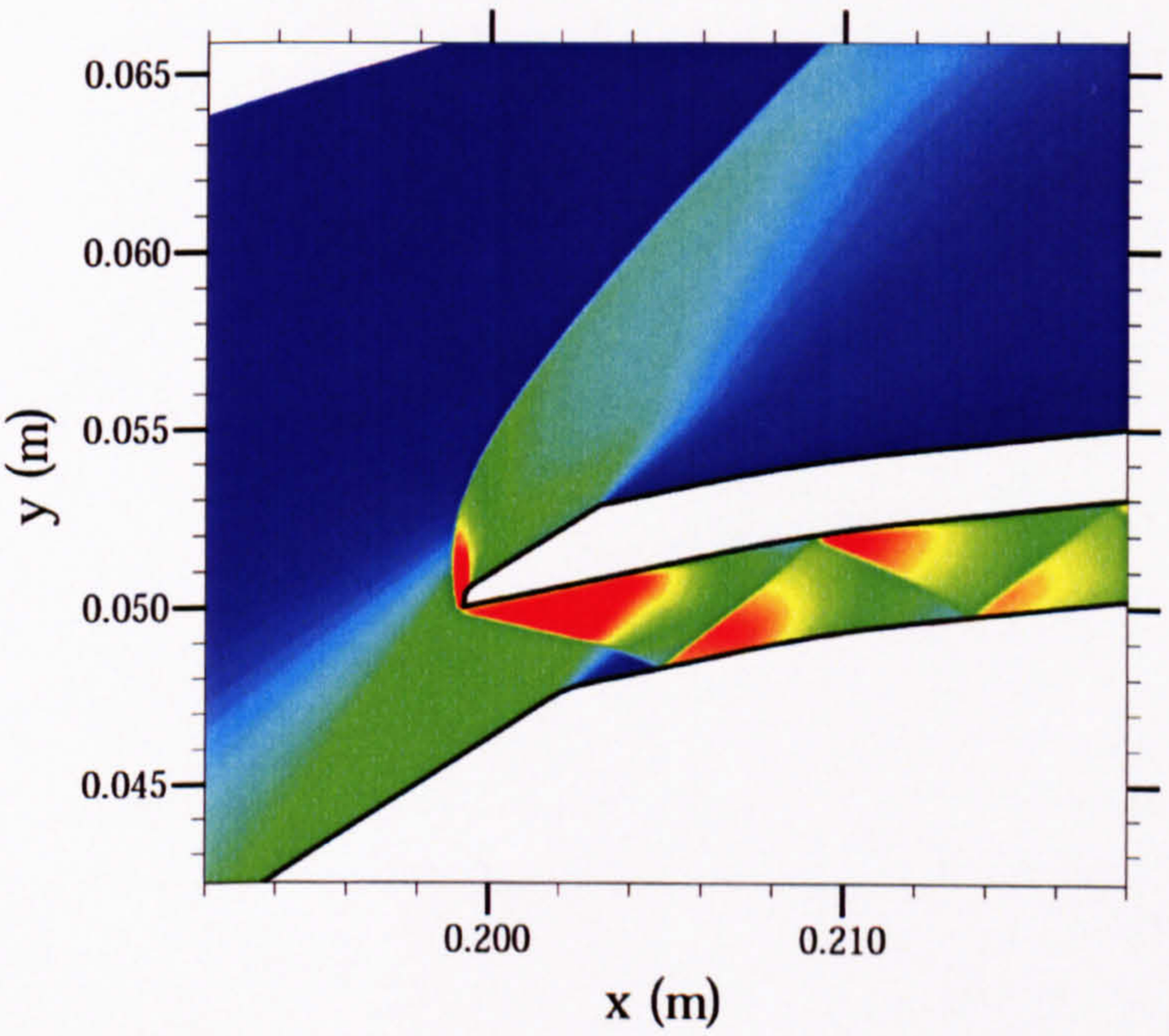


Figure 4.28: CFD Density contours from an inviscid simulation of the intake with a 33 degree spike termination angle and a 12 degrees cowl angle (blunt) at Mach 4.

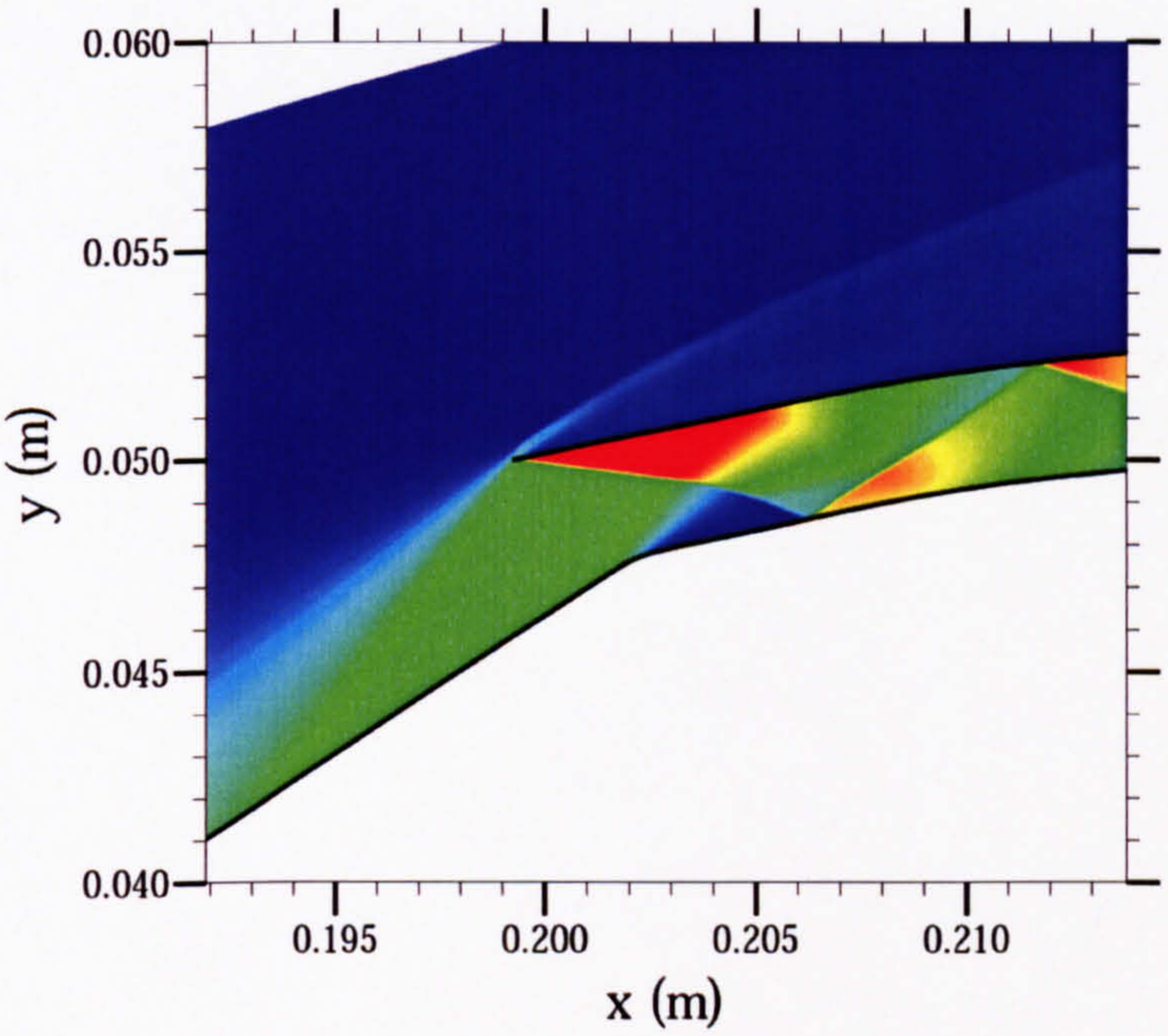


Figure 4.29: CFD Density contours from an inviscid simulation of the intake with a 33 degree spike termination angle and a 12 degrees cowl angle at Mach 5.

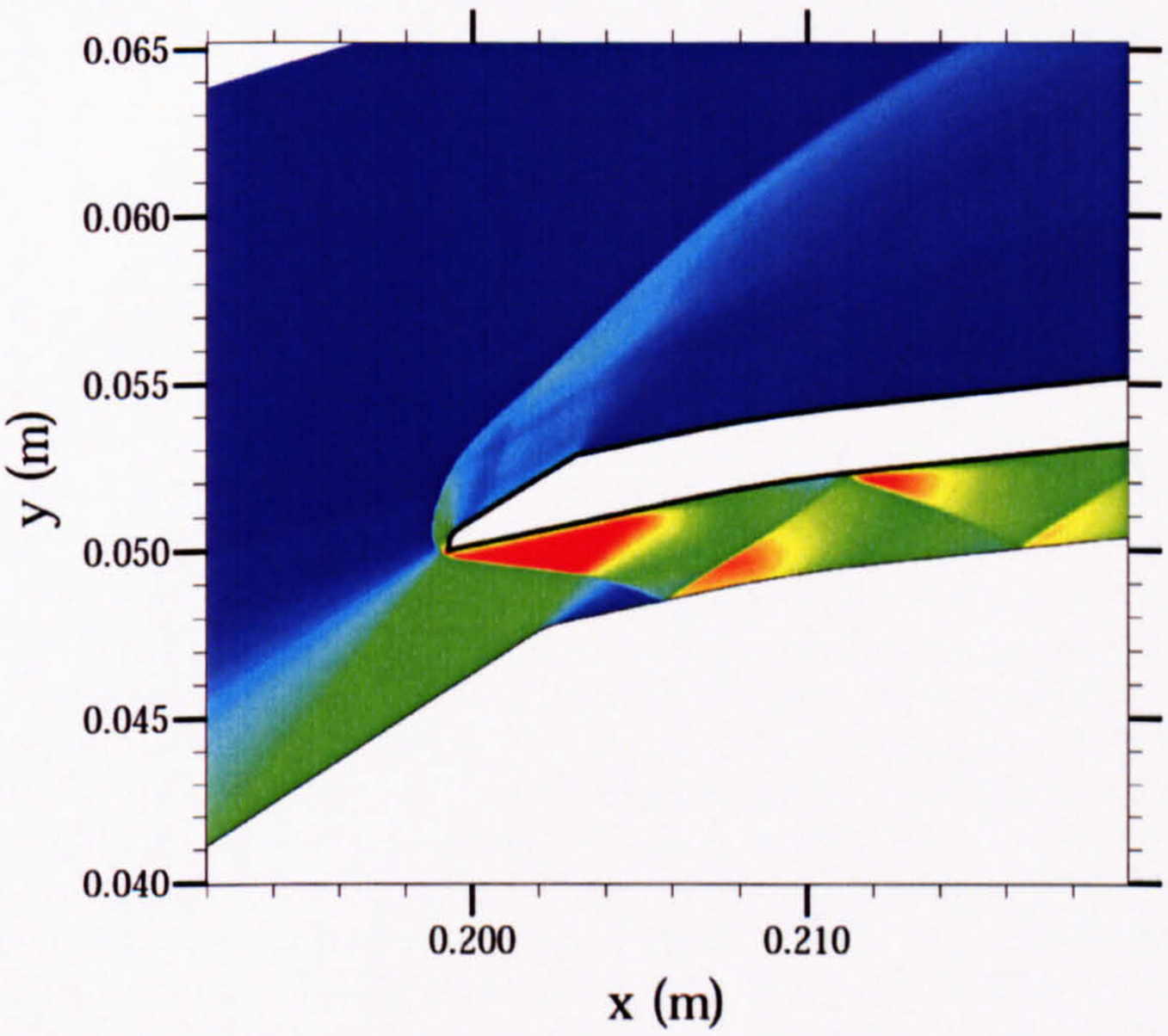


Figure 4.30: CFD Density contours from an inviscid simulation of the intake with a 33 degree spike termination angle and a 12 degrees cowl angle (blunt) at Mach 5.

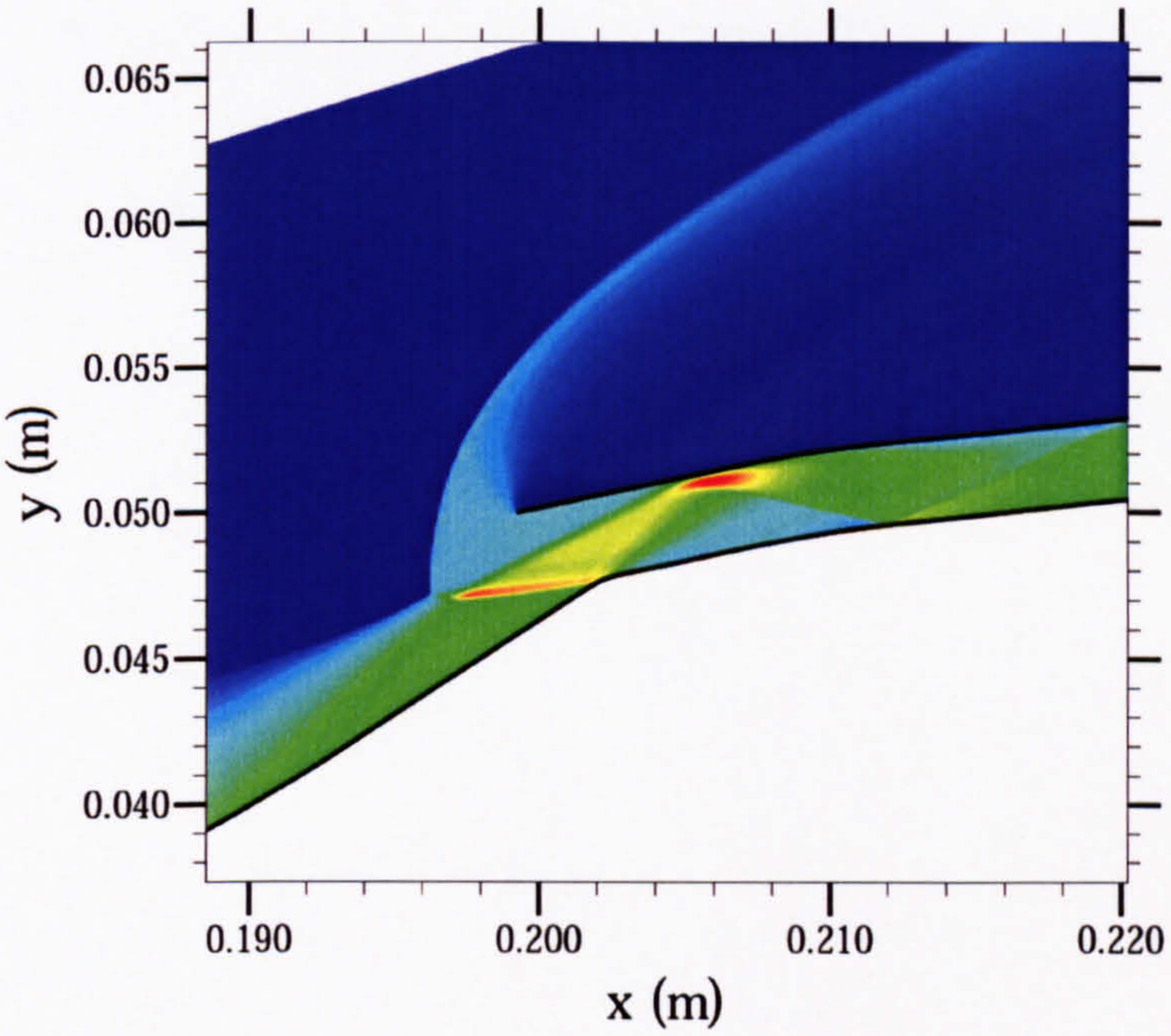


Figure 4.31: CFD Density contours from an inviscid simulation of the intake with a 33 degree spike termination angle and a 12 degrees cowl angle at Mach 6.

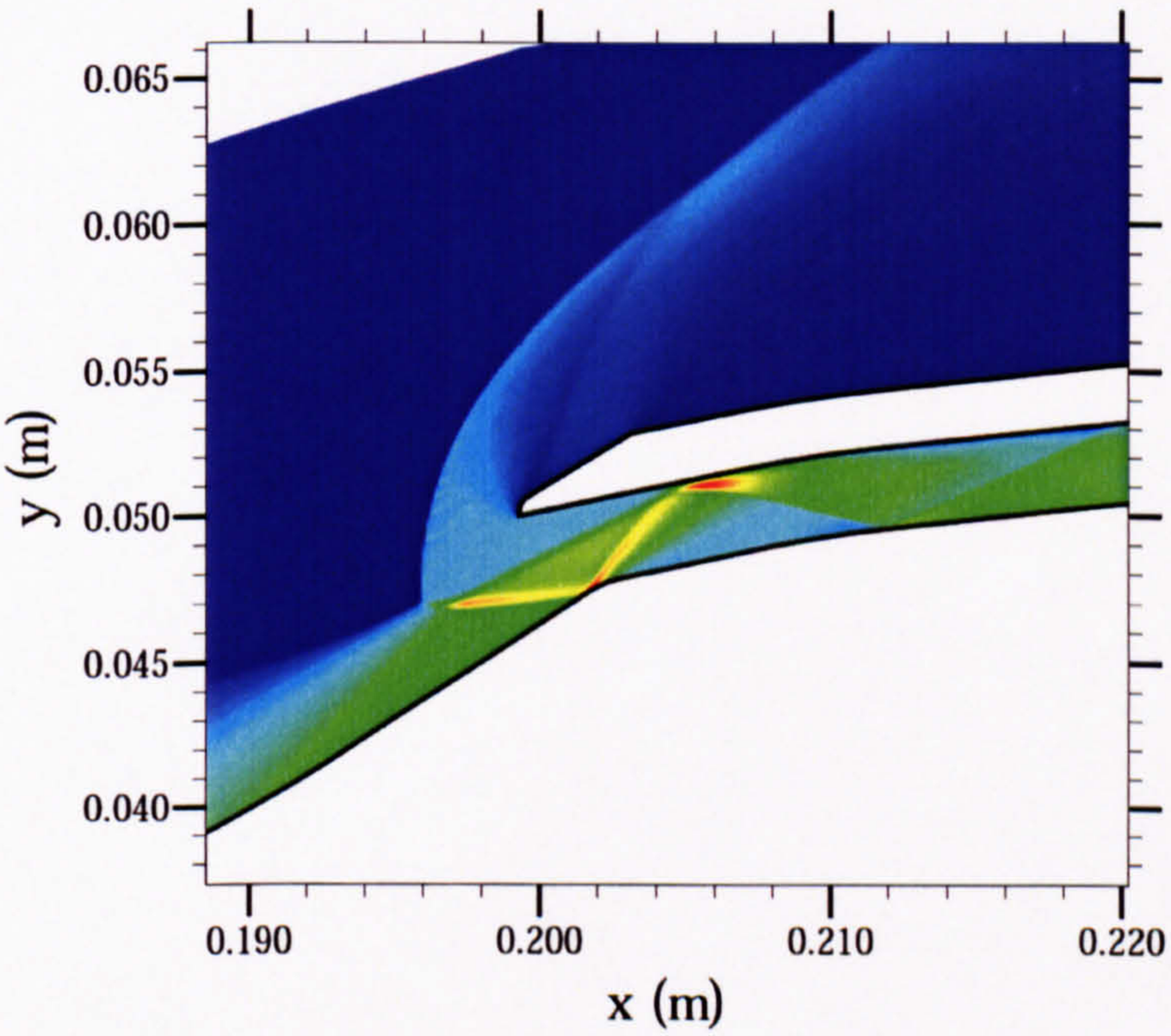


Figure 4.32: CFD Density contours from an inviscid simulation of the intake with a 33 degree spike termination angle and a 12 degrees cowl angle (blunt) at Mach 6.

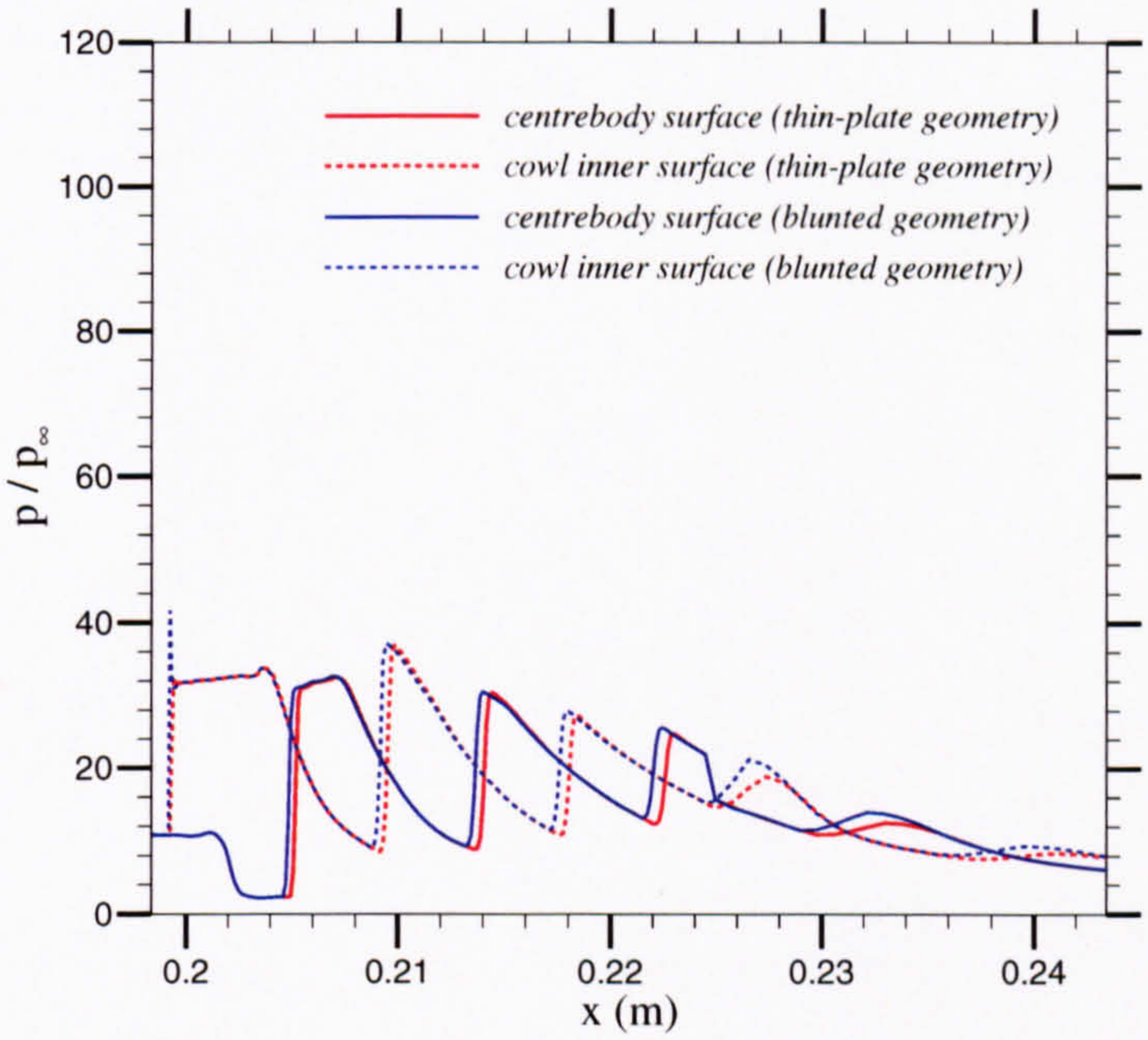


Figure 4.33: Centrebody and cowl inner surface pressures versus x-distance for the intake ($M_{sol} = 5.5$) with the thin-plate and blunt cowl at Mach 4.

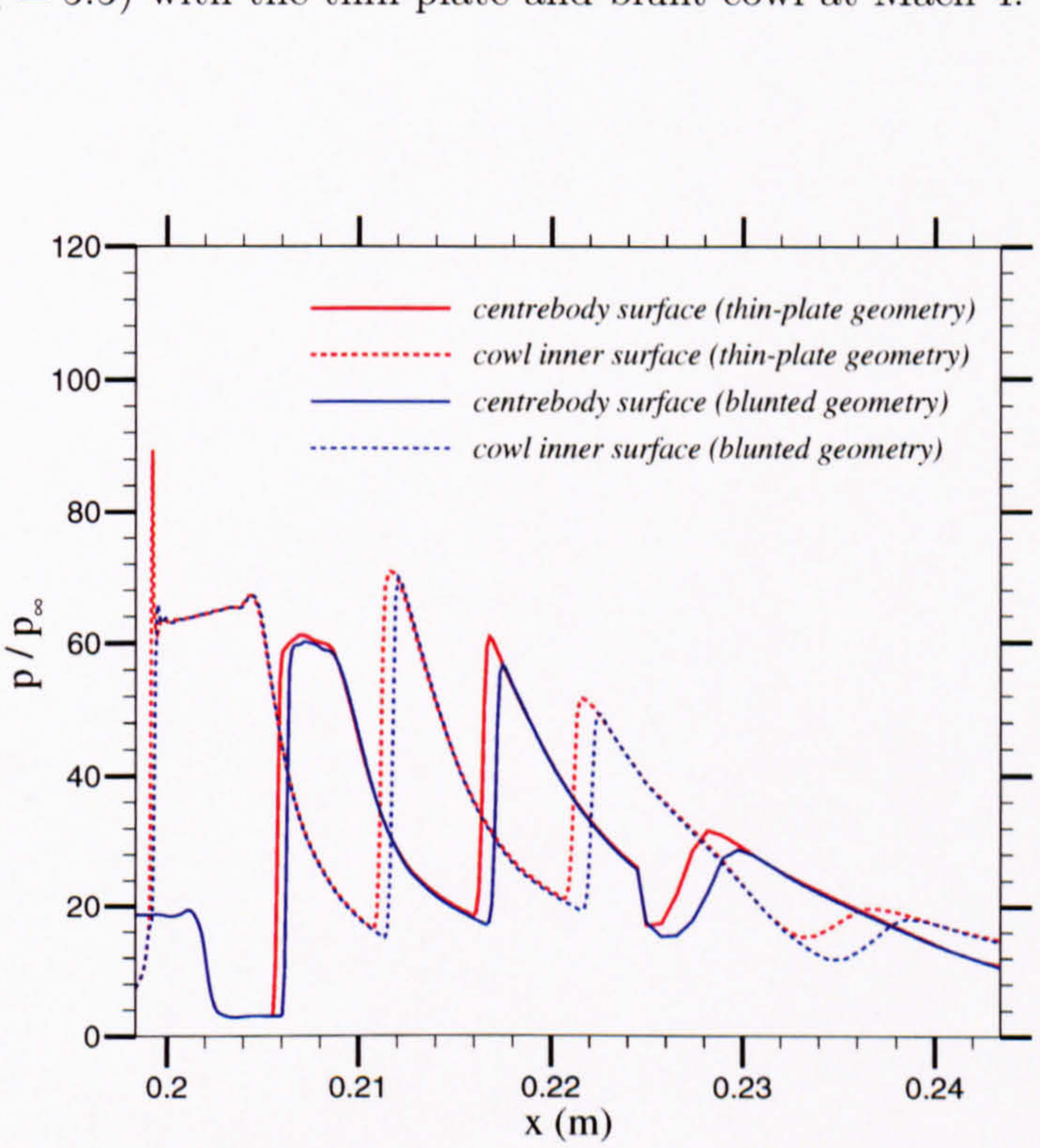


Figure 4.34: Centrebody and cowl inner surface pressures versus x-distance for the intake ($M_{sol} = 5.5$) with the thin-plate and blunt cowl at Mach 5.

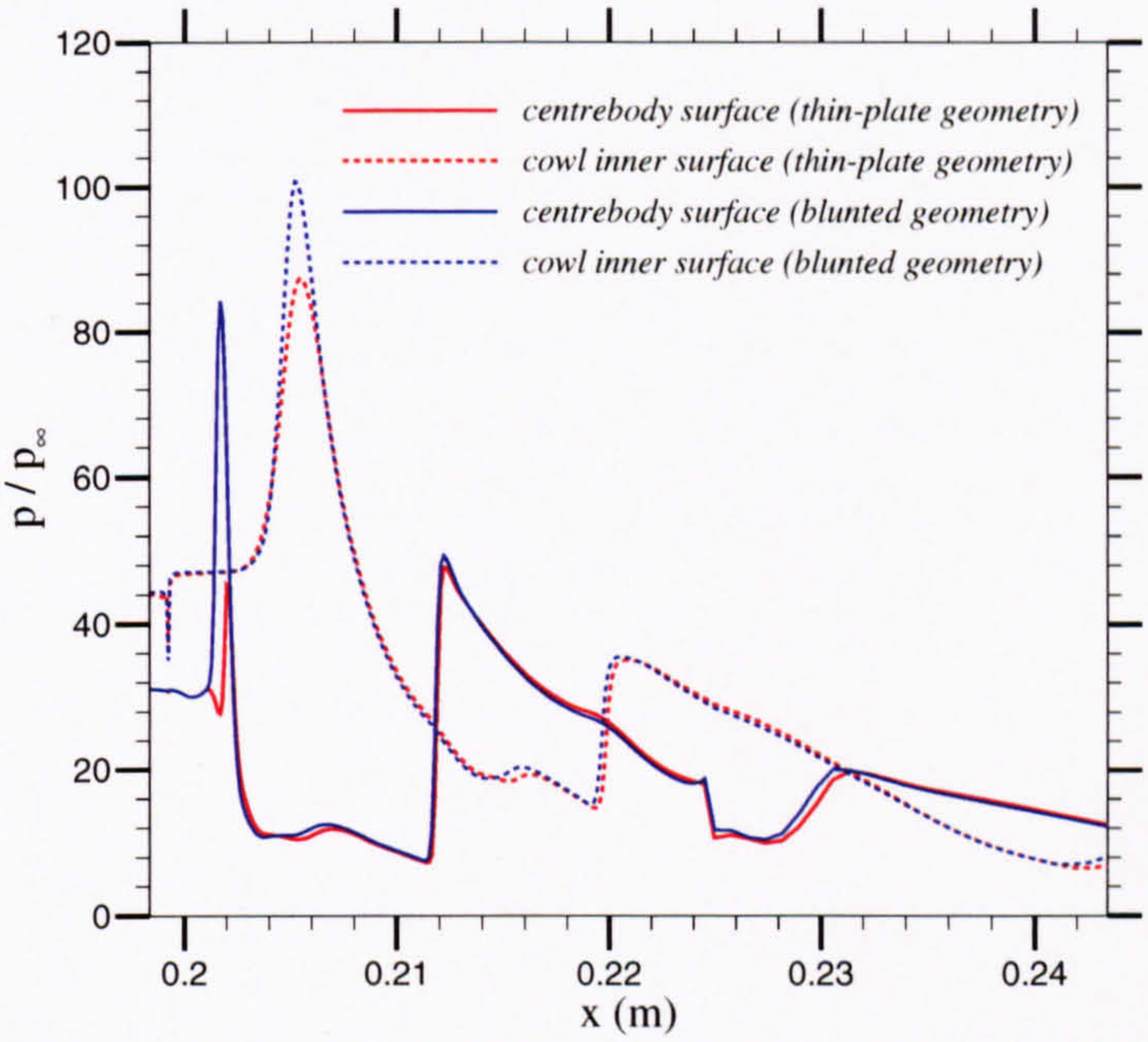


Figure 4.35: Centrebody and cowl inner surface pressures versus x-distance for the intake ($M_{sol} = 5.5$) with the thin-plate and blunt cowl at Mach 6.

4.5 Theoretical analysis

4.5.1 Shock-expansion interaction analysis

To run extensive well-resolved CFD simulations for various configurations requires a substantial CPU effort. Many of the critical features associated with the off-design inlet flow-field relate directly to the interaction between a shock wave and an expansion wave of the opposite family. This has led to the development of an approximate analysis for the one-on-one shock-expansion interaction, which is in good agreement with the numerical results. Figure 4.36 illustrates the ideal flow case where the apex shock wave and the forebody isentropic compression fan focus exactly at the cowl leading edge at the shock-on-lip condition. The shock system from the cowl leading edge then focuses exactly on the centrebody shoulder S.

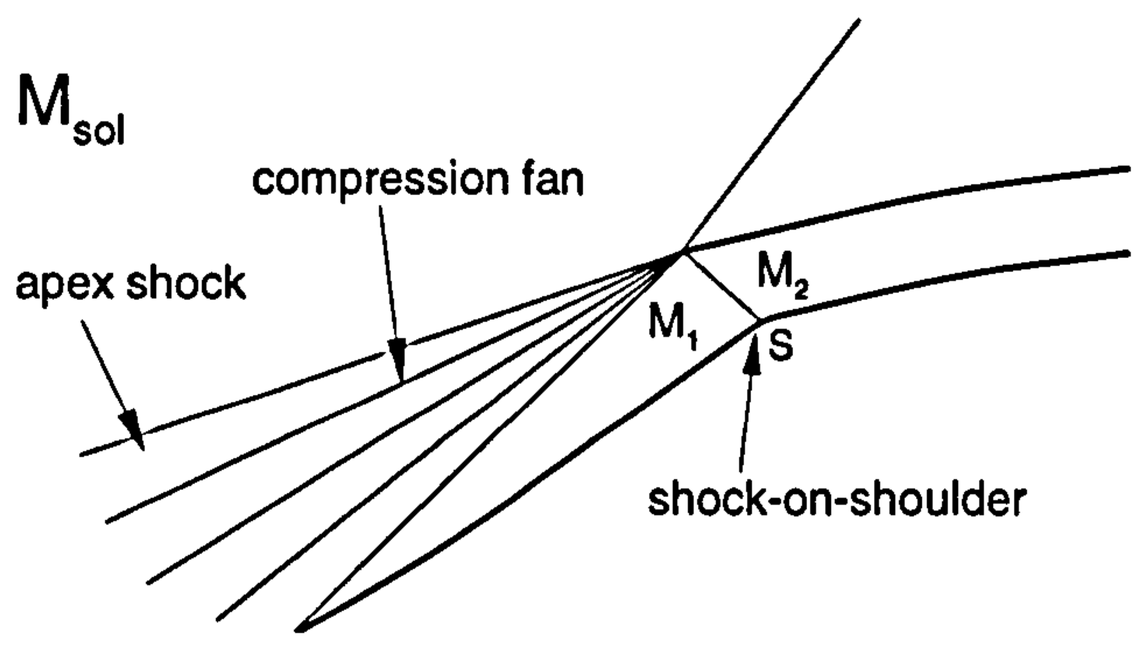


Figure 4.36: Schematic of the ideal inlet flow where the apex shock and isentropic fan focus at the cowl lip, and the cowl shock focuses exactly on the shoulder.

For convenience it is assumed that there is a uniform flow in region 1 - this is not too far from reality, since although the flow is axisymmetric, the intake annulus height is very small compared with the radial distance from the body axis. The problem with the flow in Figure 4.36 is that it is unlikely to be realised in practice, indeed it may even be undesirable from the viewpoint of self-starting flows. A range of off-design conditions have been presented in Figure 4.5, and have been shown in the CFD simulations of the previous sections. Of these off-design type interactions, two interactions - Type 3 and Type 5 result from the interaction of a shock wave with

an expansion wave. For example, Figure 4.5 (d) described a particularly serious off-design case where the focused shock wave tends to propagate inside the inlet. This shock wave, in an ideal situation, would reflect from the interior surface of the cowl. Before reaching the surface, however, the shock wave is acted-on by an expansion wave system formed at the cowl leading edge - assuming, as is the usual case, that the inner surface of the cowl still has an upward inclination δ_c.

In Figure 4.5 (f) the shock wave from the cowl leading edge radiates onto the centrebody, but its trajectory takes it downstream of the shoulder S so that the shock wave is again acted upon by an expansion. In the resulting shock wave reflection from the centrebody surface there is a high probability of Mach reflection occurring. At the very least this would then generate flow non-uniformities downstream of the inlet, leading to diffuser inefficiencies. At the worst it could lead to boundary-layer separation and/or the shock system propagating forwards out of the intake to cause an intake unstart. All these interactions can be modelled by CFD and to assess the full impact of off-design effects, full CFD and/or experimental modelling is required.

A preliminary assessment of the basic safe operating domain (a design that does not produce shock detachment or Mach reflection) can be made using a simple Method of Characteristics calculation however. The program essentially predicts the distortion of a known shock (say from the cowl leading edge) by a known expansion fan (say from the forebody/centrebody shoulder) and calculates the permitted reflection condition on the surface. More detail of this method can be found in Appendix A.1.

Polar plots are constructed which assume the detachment criterion for this calculation to determine the regular-to-Mach reflection boundary. The plots present a polar presentation where the two axes are the cowl interior inclination angle and the centrebody angle. For a self-starting design these two angles must be close to each other. This allows the consideration of an operating domain of cowl angle versus centrebody angle for a pre-specified spike termination angle. The lines that define the operating regime are the lines that determine Mach reflection, for the two cases considered above (Type 3 and Type 5 interactions) - shock detachment from the cowl lip and the case (rare, and usually leading to Mach reflection) where the cowl shock impinges upon the centrebody upstream of the shoulder. A final important point is

to recognise that the above operating constraints are not specifically connected with the details of the cowl leading edge and general geometry as shown in section 4.4.3 where full CFD simulations show very similar off-design flows for simulations using thin-plate cowls and those with finite thickness and blunted leading edge cowls.

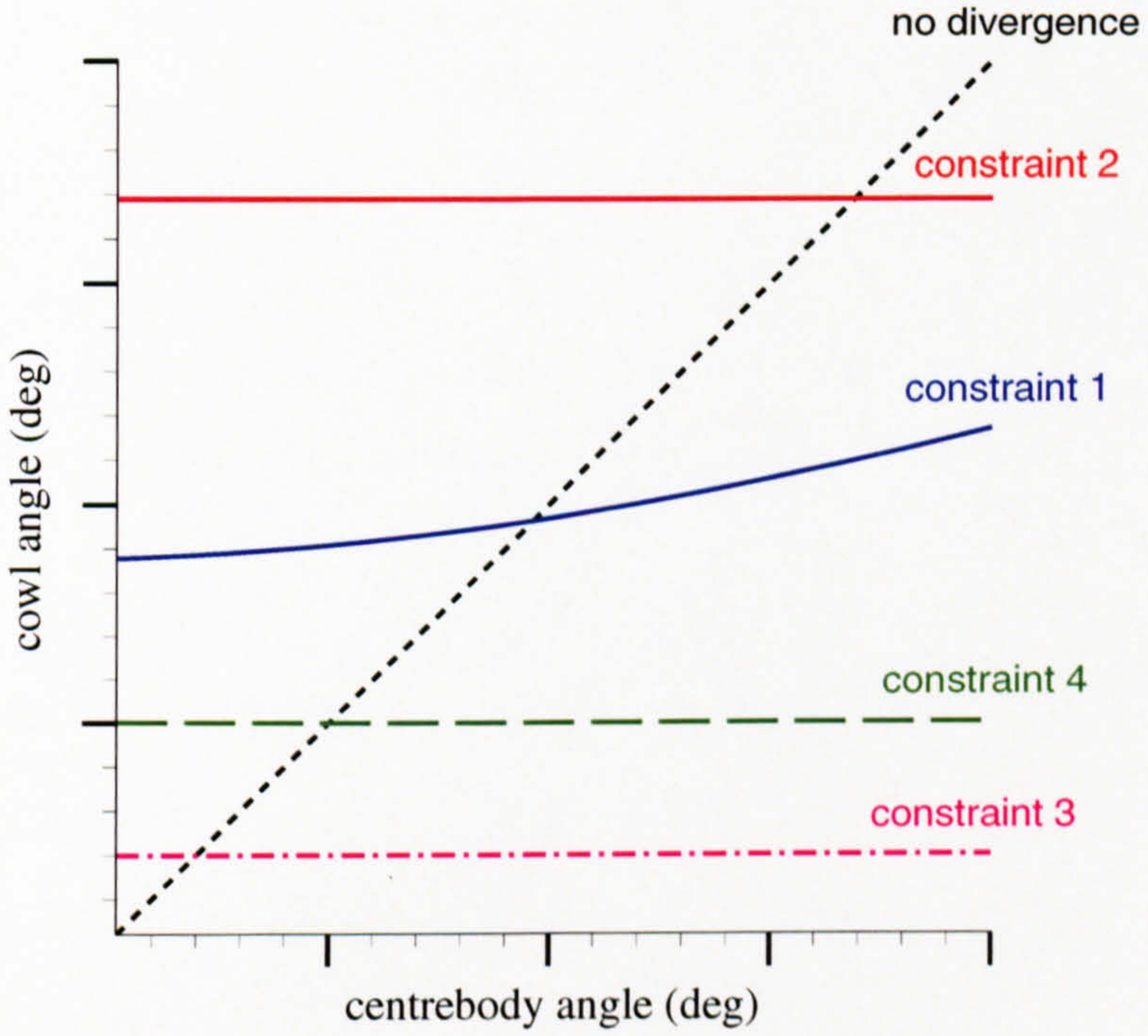


Figure 4.37: Polar plot illustration with definition labels for the design lines on a centrebody angle versus cowl angle axis for a pre-specified spike termination angle.

Figure 4.37 illustrates the main features of the polar plot generated from the theoretical analysis for a specific spike termination angle and Mach number, plotted on a cowl angle versus centrebody angle axis. Five constraints are defined, in order of their importance in controlling the intake flow (in this design).

- **No-divergence**: This line is where the cowl and centrebody are parallel to each other, as illustrated in Figure 4.38. Assuming that only convergence is likely, but only very small amounts of convergence to permit inlet self-starting, the inlet would be designed to operate on the no-divergence line or slightly to the right hand side of it.

- **Constraint 1:** This design line defines the boundary between *regular* and *Mach* reflection on the centrebody such that to maintain regular reflection the inlet, as illustrated in Figure 4.39. should operate above this line. If the angles fall below the design values, Mach reflection will occur. The isentropic compression fan will always in this case produce attachment at the cowl leading edge if configured as a Type 1 interaction. This is the most critical interaction in this intake flow.

- **Constraint 2:** If the focused shock wave in the Type 2 interaction (refer to Figure 4.5) impinges the cowl lip, then attachment at the cowl leading edge occurs if the inlet operates above the constraint 2 design line, illustrated in Figure 4.40. If the values of the angles fall below this design line, shock detachment will occur at the cowl lip.

- **Constraint 3:** This design line defines the boundary between shock attachment and shock detachment for the conditions behind the compression fan, as shown in Figure 4.41.

- **Constraint 4:** This design line defines the boundary between *regular* and *Mach* reflection on the forebody such that to maintain regular reflection the inlet should operate above this lines, as illustrated in Figure 4.42.

- **Constraint 5:** This design line defines the boundary between *regular* and *Mach* reflection of the focused shock as it reflects from the cowl inner surface, shown in Figure 4.43. In this complex interaction, lowering the cowl angle will lead to a higher flow turning angle and increase the likelihood of Mach reflection. Increasing the cowl angle however, leads to the expansion fan from the cowl affecting the focused shock wave as it intends to reflect from the cowl interior surface. For all cases presented in this section, regular reflection cannot be maintained inside the cowl when the focused shock enters the annulus and so there are no angles in the domain where regular reflection can occur. Hence the constraint 5 lines do not appear in any of the polar plots.

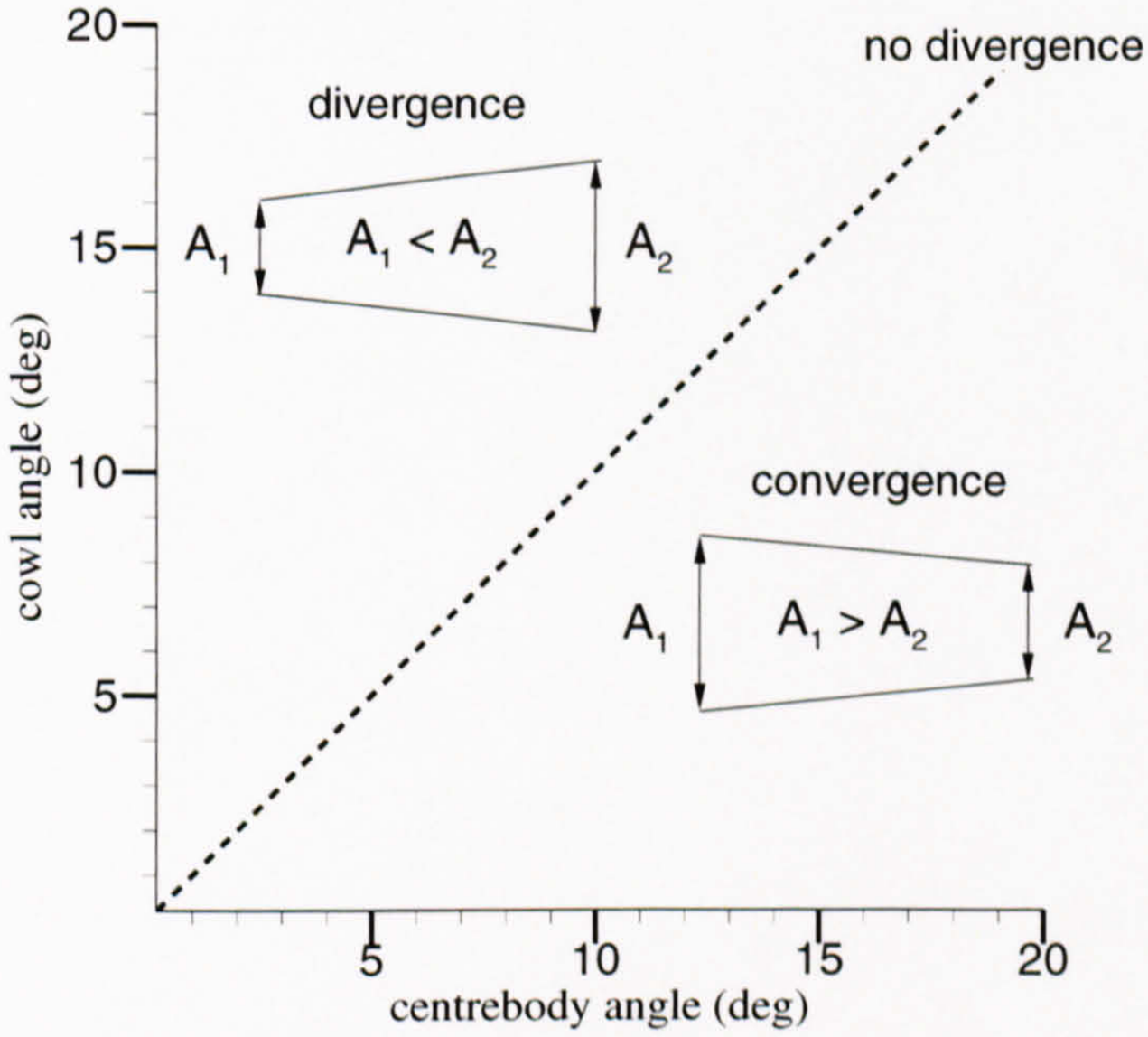


Figure 4.38: No divergence.

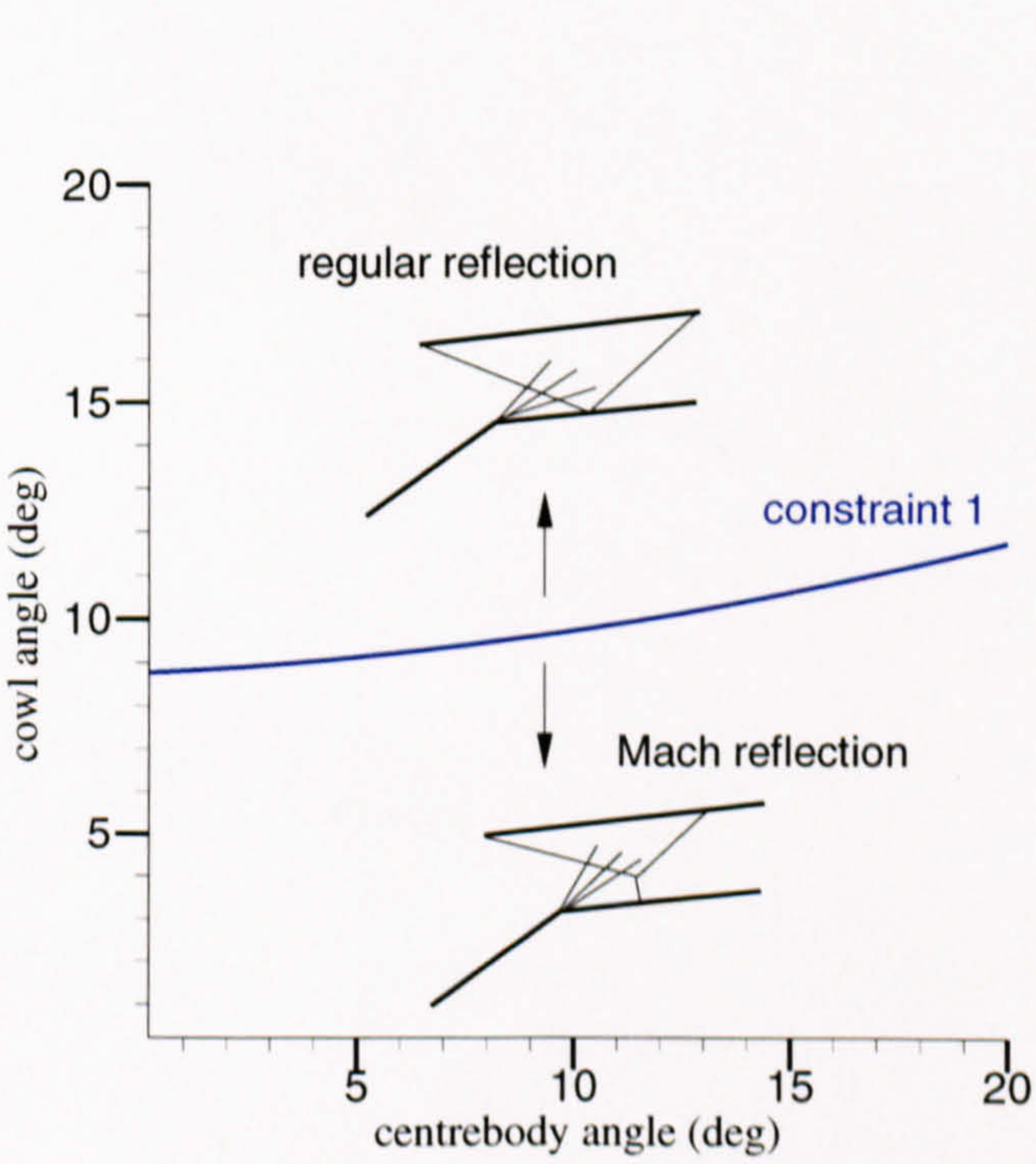


Figure 4.39: Constraint 1.

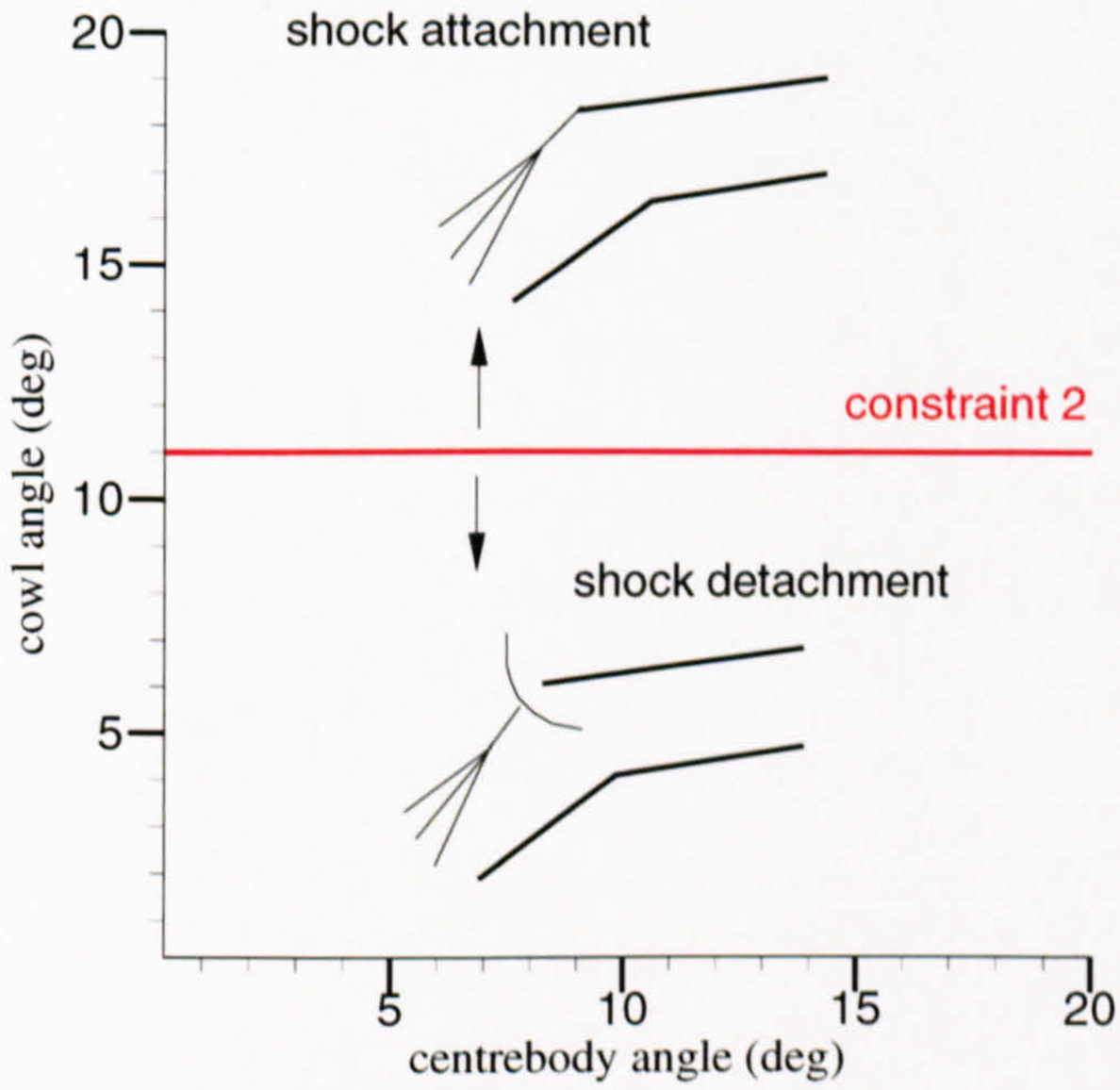


Figure 4.40: Constraint 2.

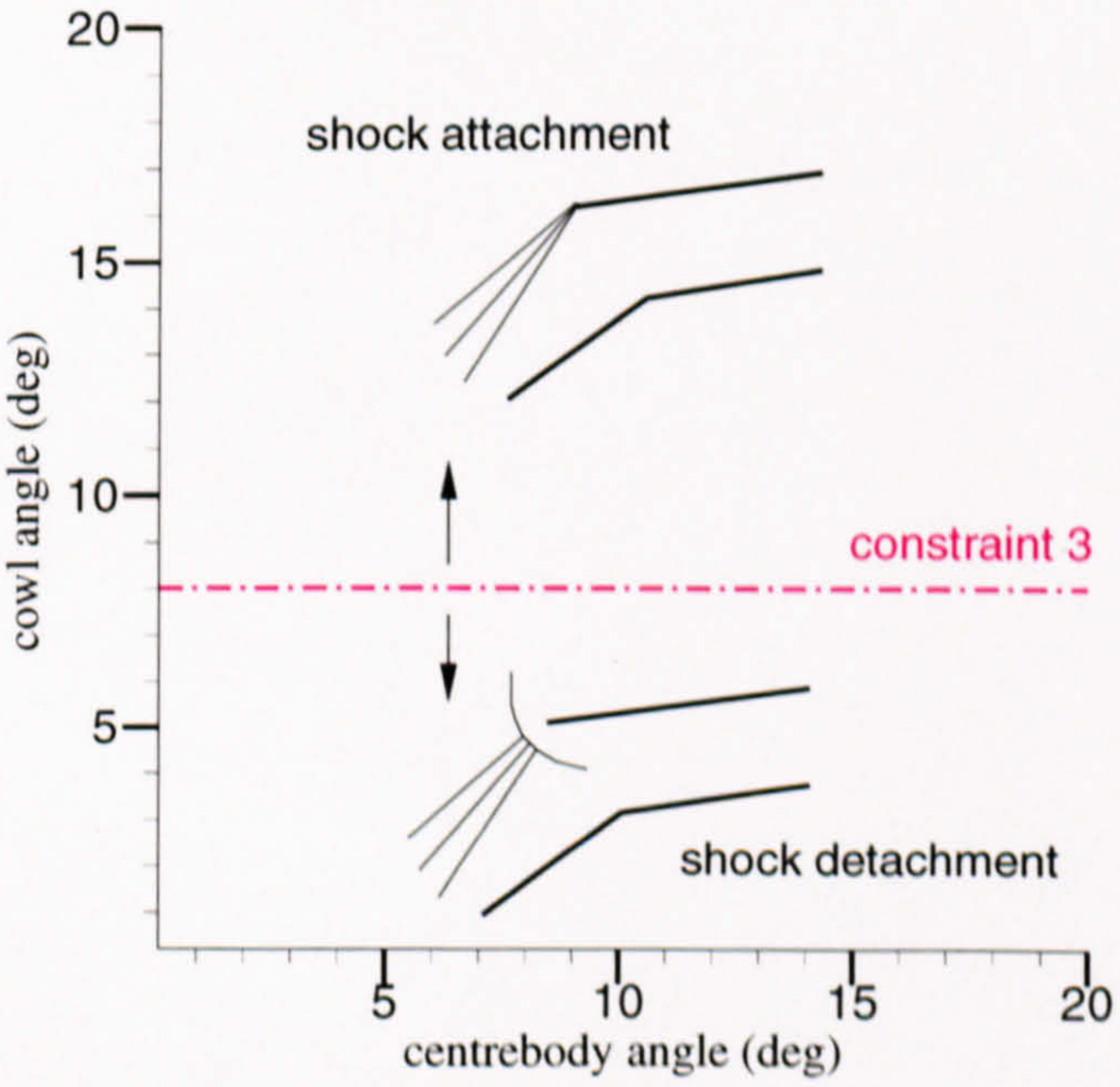


Figure 4.41: Constraint 3.

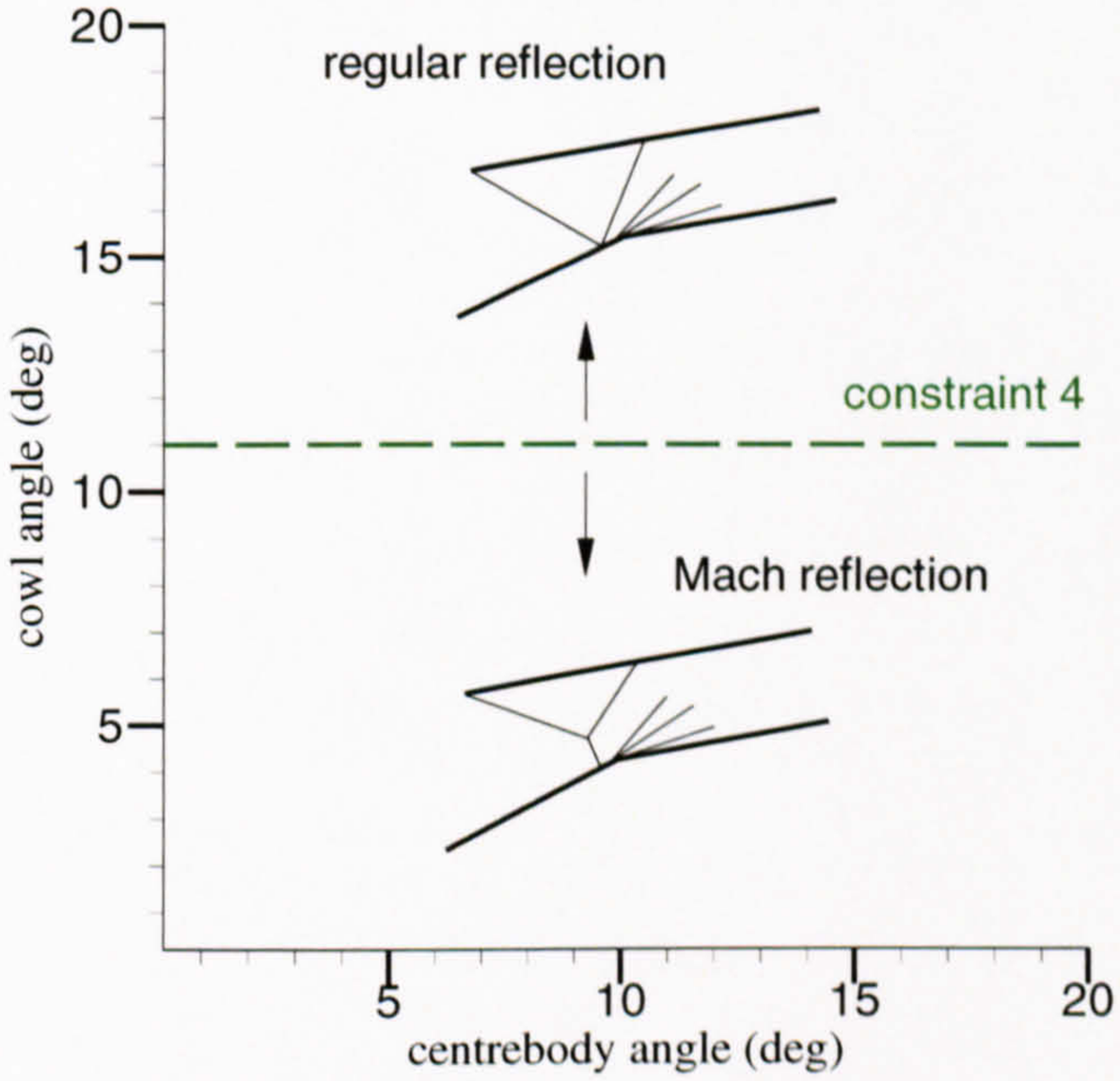


Figure 4.42: Constraint 4.

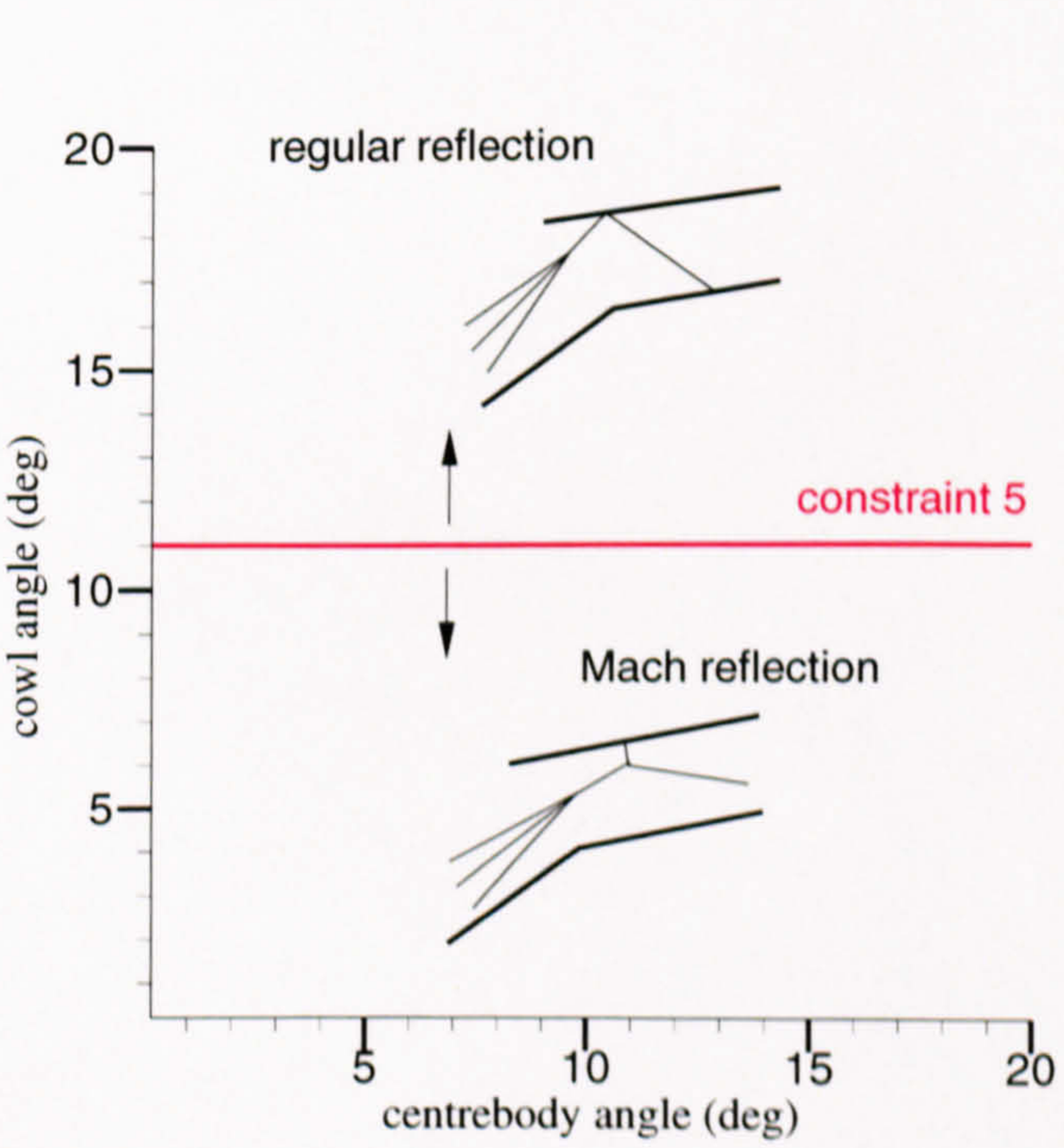


Figure 4.43: Constraint 5.

4.5.2 Results from parameter study

Figure 4.44 and 4.45 are polar plots generated from the theoretical analysis for the intake ($M_{sol} = 5.5$) with a 33 degree spike termination angle at Mach 4 and Mach 6 respectively. Figures 4.44 suggests that for this design, a 12 degree cowl/centrebody angle would be sufficient to avoid Mach reflection on the centrebody, but that Mach reflection would occur if the cowl shock wave impinges on the forebody, though it is highly unlikely that the shock wave will impinge on the forebody in this design.

Figure 4.46 is a close-up view of the CFD modelling of the inlet with the 12 degrees cowl/centrebody angle at Mach 4, showing regular reflection of the cowl shock on the centrebody. From the polar plot in Figure 4.44, it is found that decreasing the inlet cowl-centrebody angles to 7 degrees would suggest that Mach reflection should occur at the centrebody as the design moves below the constraint 1 line. Figure 4.47 shows the CFD simulation of the inlet with a reduced cowl and centrebody angle of 7 degrees, showing Mach reflection on the centrebody. Here, the reflected cowl shock impinges the centrebody closer to the shoulder expansion, and the interaction results in a complex shock system forming at inlet. There is a separated region behind the Mach stem, with resultant non-uniformities in the duct flow. Figure 4.48 shows time-dependent pressure contours to show the Type 5 interaction at inlet where the cowl shock is first seen reflecting onto the centrebody where it is acted on by the shoulder expansion fan. The impingement point then moves forward towards the expansion fan and form a Mach stem, seen in Figure 4.48 (b). The reflected shock from the Mach reflection triple point then moves upwards to impinge the cowl inner surface, and propagates forwards towards the cowl lip. The shock system stabilises in this position in a lambda-type shock, Figure 4.48 (f).

Figure 4.49 plots centrebody surface pressure distribution for the two cases, showing a shift forward in the shock system when Mach reflection occurs, seen as the sharp pressure rise in the plot. In this case, re-profiling of the shoulder by both changing the centrebody angle at impingement and altering the influence of the shoulder expansion on the incident shock can enable regular reflection on the centrebody.

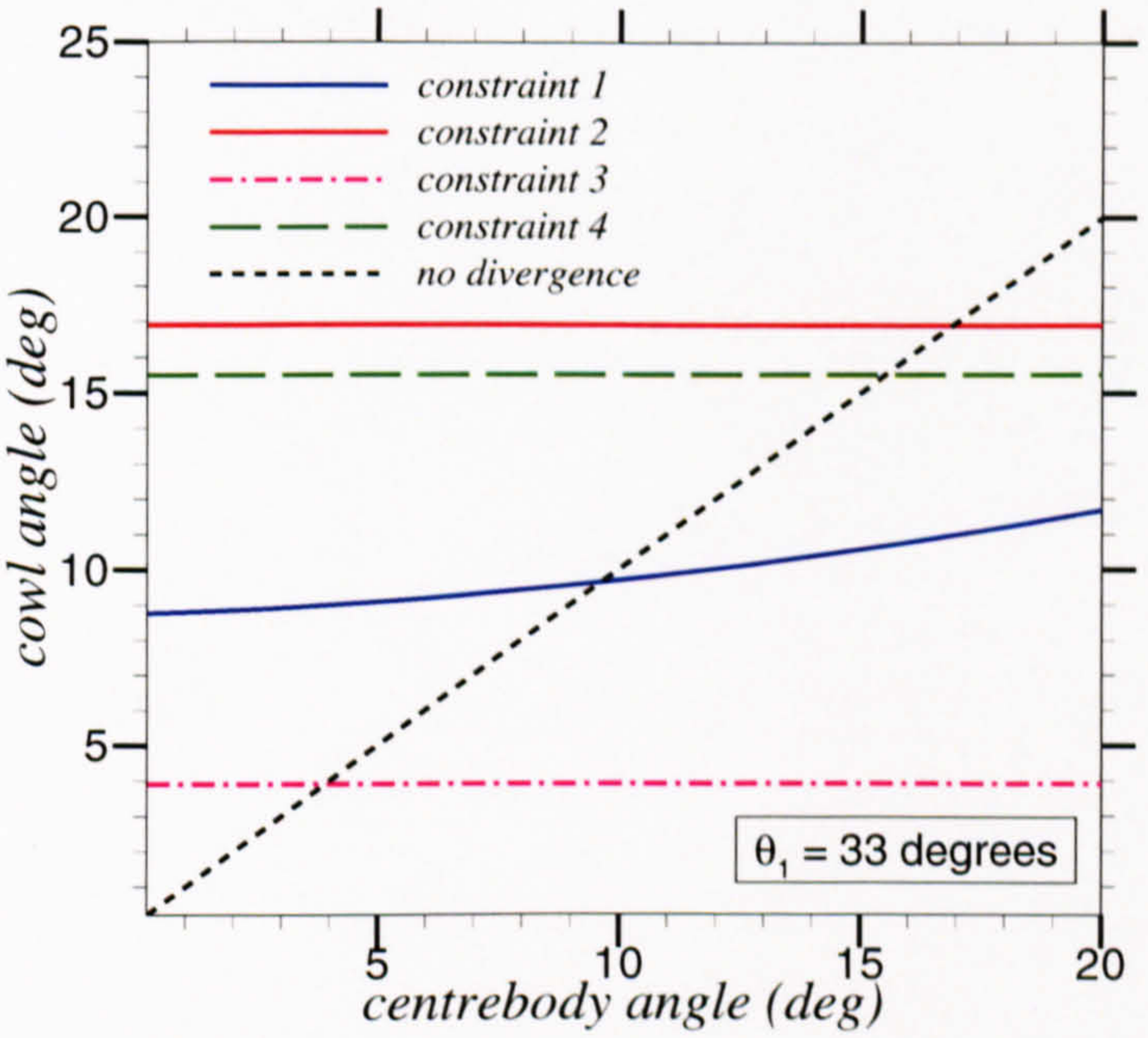


Figure 4.44: Polar plot for the intake (shock-on-lip Mach 5.5) with a 33 degree spike termination angle at off-design condition Mach 4.

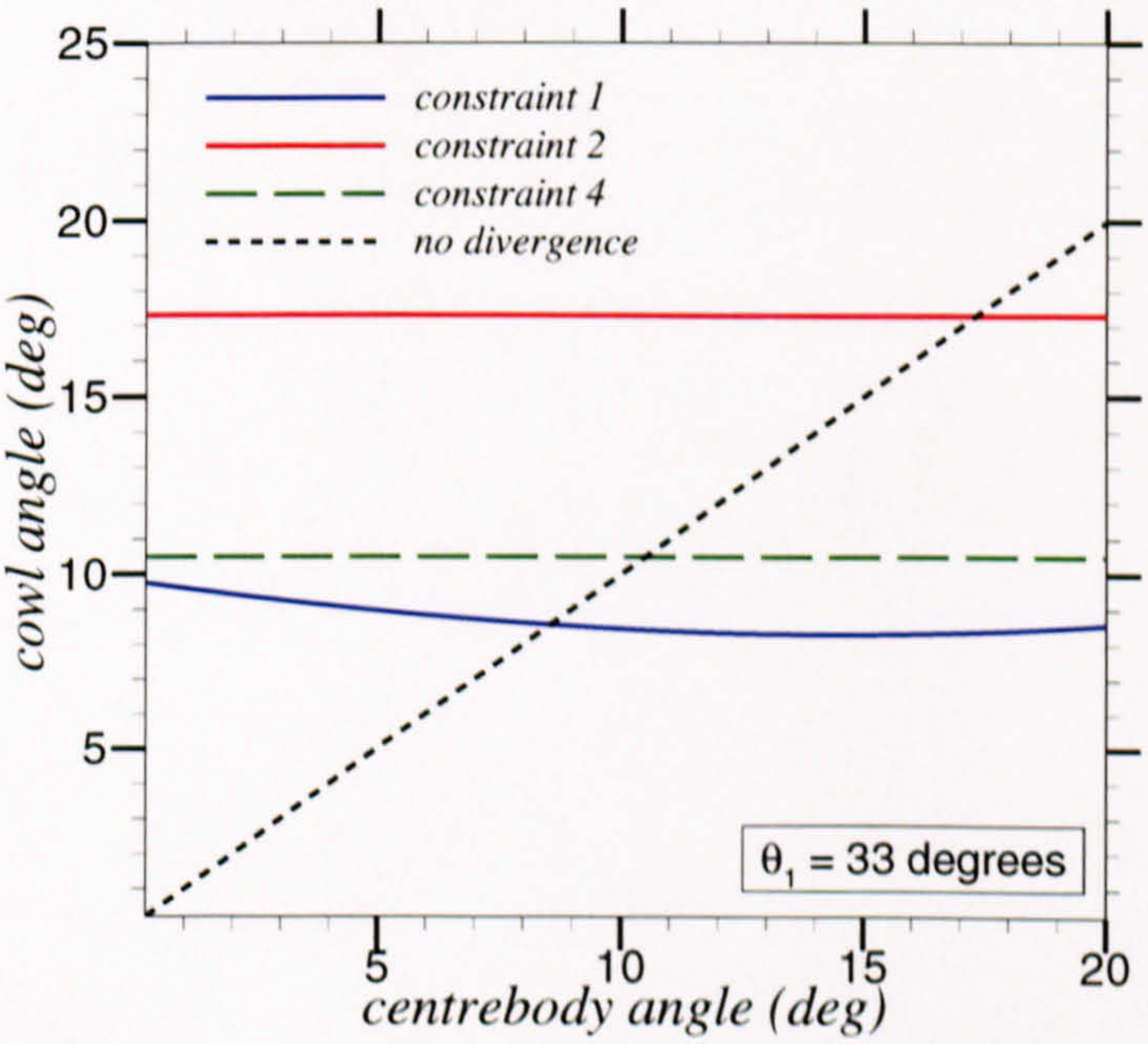


Figure 4.45: Polar plot for the intake (shock-on-lip Mach 5.5) with a 33 degree spike termination angle at off-design condition Mach 6.

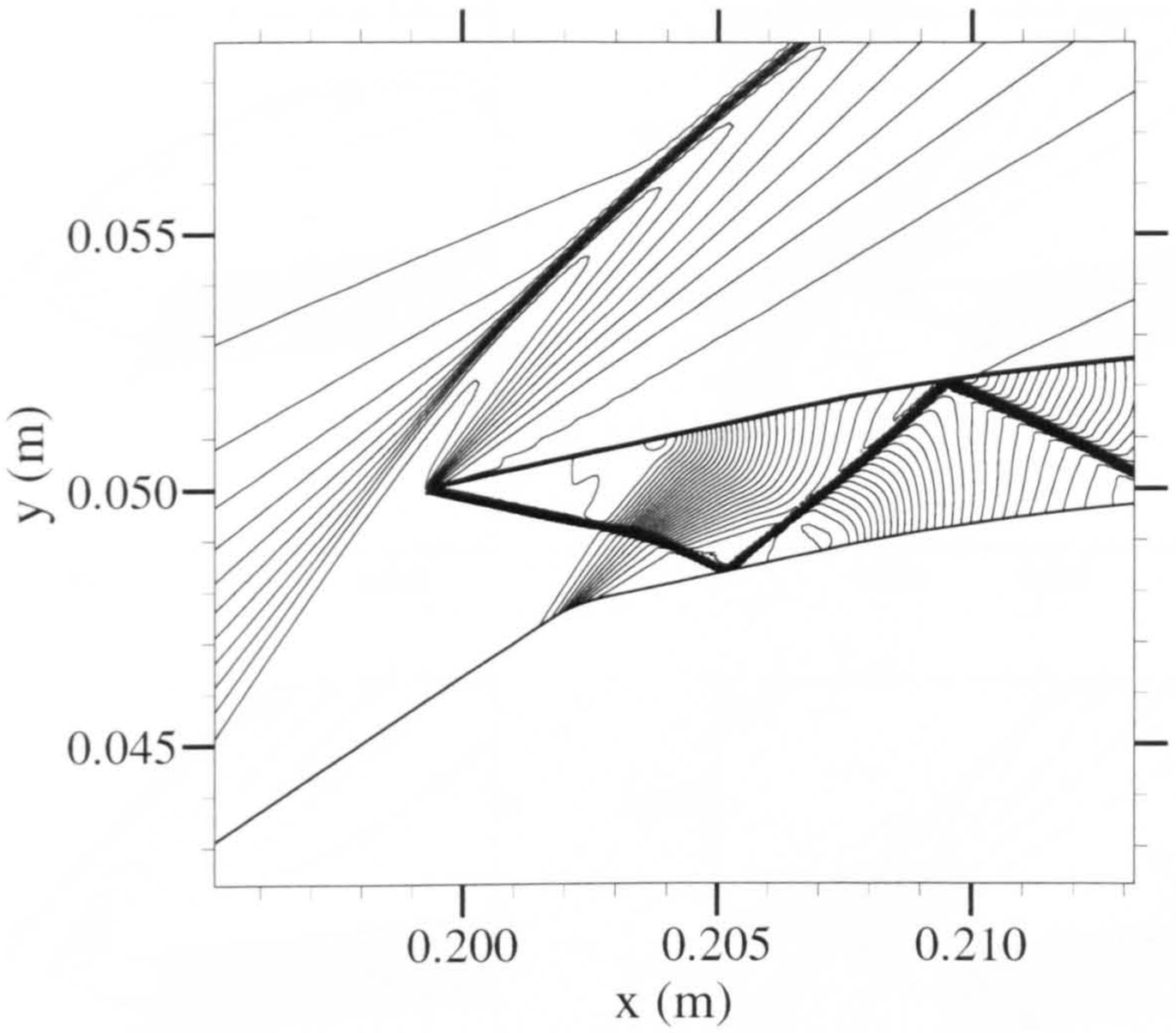


Figure 4.46: CFD Pressure contours from an inviscid simulation of the intake (shock-on-lip Mach 5.5) intake with a 12 degrees cowl and centrebody angle at Mach 4.

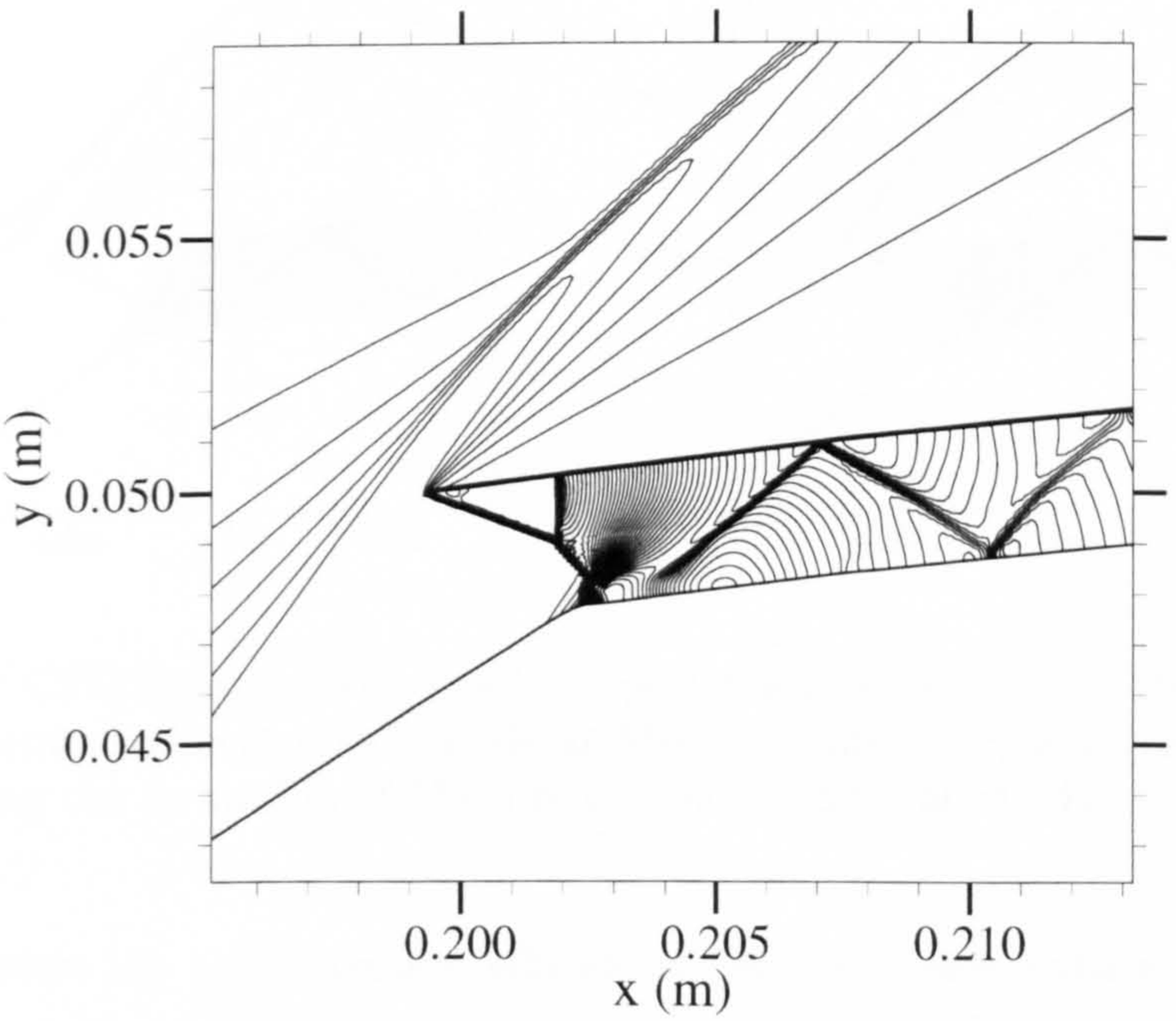


Figure 4.47: CFD Pressure contours from an inviscid simulation of the intake (shock-on-lip Mach 5.5) intake with a 7 degrees cowl and centrebody angle at Mach 4.

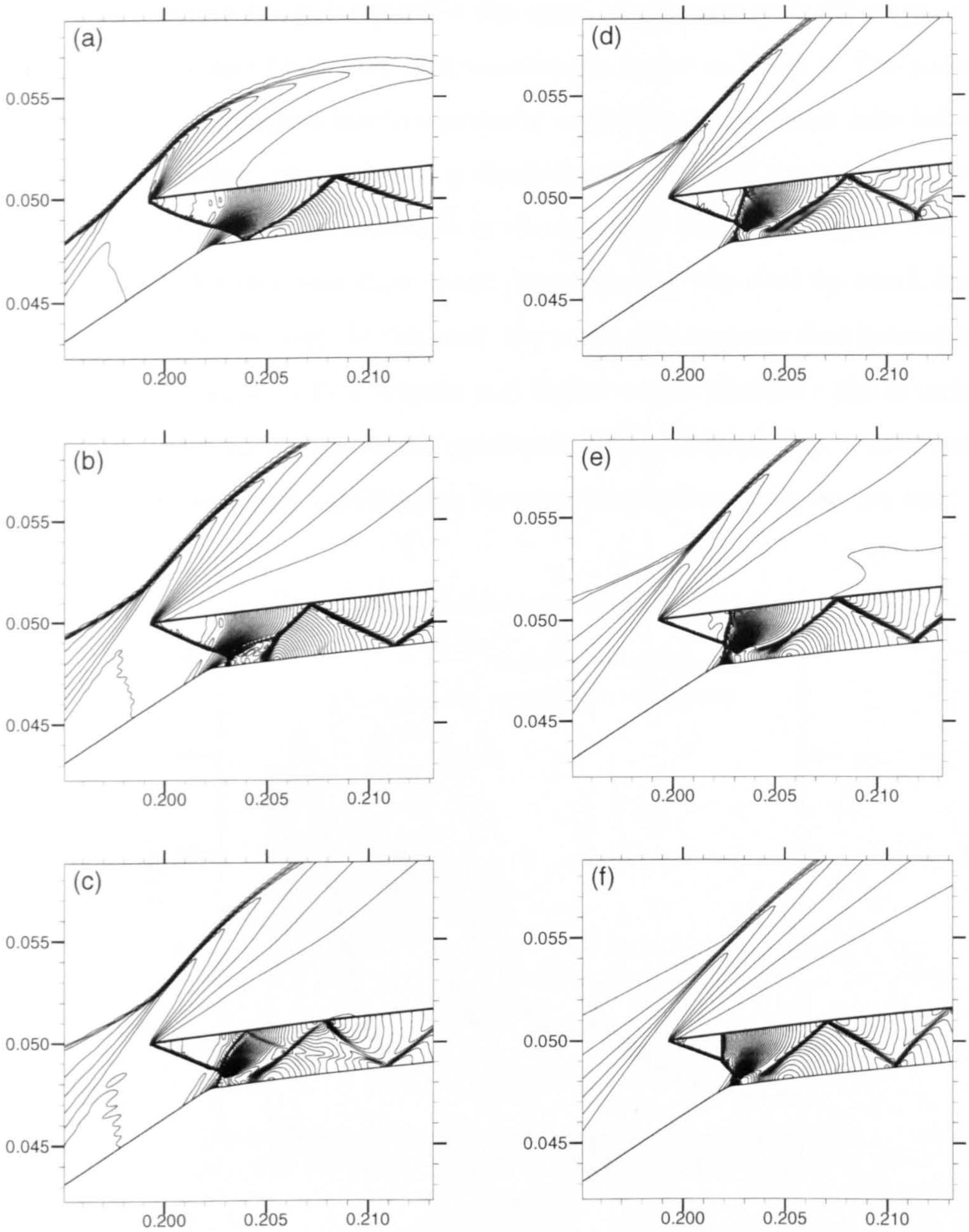


Figure 4.48: CFD Pressure contours from an inviscid simulation of the intake with a 7 degrees cowl and centrebody angle at Mach 4; time-dependent results from (a) to (f) showing the formation of Mach reflection on the centrebody.

Table 4.5 shows the total pressure efficiencies for both cases with a value of 70.5 percent for the case with regular reflection (inviscid values) and a value of 64.7 percent for the case where Mach reflection occurs (7 degrees cowl). Kinetic energy efficiency also decreases when Mach reflection occurs from 96.7% to 95.9%.

Figure 4.45 presents the polar plot for the same intake geometry (33 degrees spike termination angle and 12 degrees cowl/centrebody angle) at Mach 6. The polar plot shows that for a 12 degrees cowl/centrebody angle the design point falls below the constraint 2 line which suggests that a shock detachment will occur at the cowl lip. This case has already been presented in the previous section in Figure 4.20. The density contours for this case show shock detachment at the cowl lip which leads to flow reversal above the cowl. In this case, the polar plot suggests that increasing the cowl/centrebody angle to 17.5 degrees and higher would eliminate the detachment as the design point moves above the constraint 2 line. Realistically, a cowl external angle of 18 degrees would significantly increase the pressure drag on the cowl.

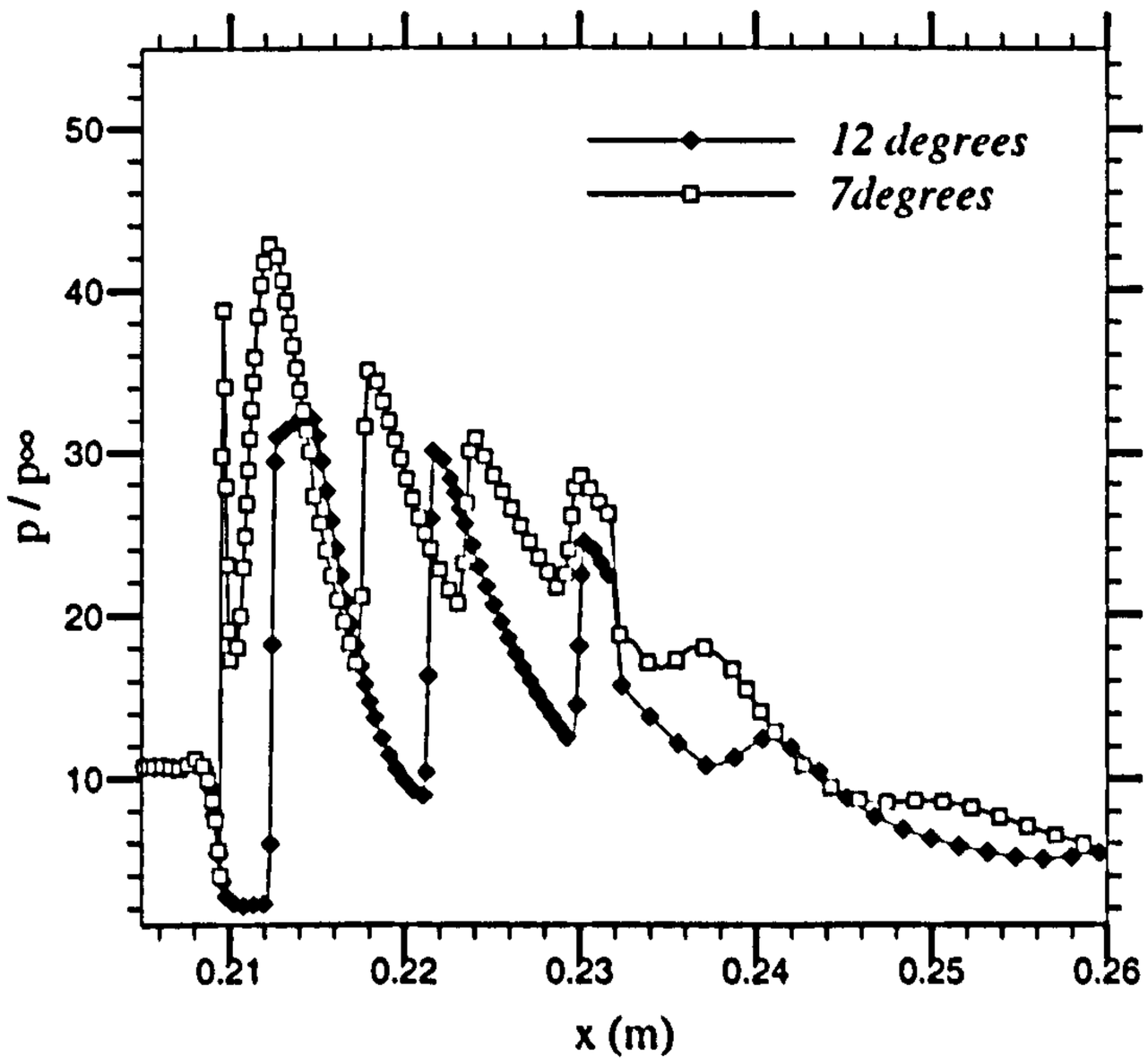


Figure 4.49: Comparison of surface pressure distribution for the intake ($M_{sol} = 5.5$) with a centrebody and cowl angle of 12 and 7 degrees at Mach 4 (inviscid CFD).

Shock system	x_c (m), y_c (m)	δ_c / θ_2	η_{pr}	η_{ke}	MCR
Regular reflection	0.1993, 0.0500	12	0.705	0.967	0.609
Mach reflection	0.1993, 0.0500	7	0.647	0.959	0.609

Table 4.5: Intake performance (M_{sol}=5.5): Values of cowl position, cowl angle, total pressure efficiency, kinetic energy efficiency and mass capture ratio for the intake with 12 and 7 degrees cowl angles at Mach 4 (inviscid values).

4.5.3 Reducing the spike-termination angle

In investigating the shock waves at inlet, it becomes apparent that the turning angle of the incoming flow is important. Reducing the angle at which the spike terminates, θ_1, and hence reducing the flow turning angle at inlet is one way of reducing the possibility of a shock detachment/Mach reflection at inlet. However, this reduces the inlet compression ratio, and can reduce overall engine performance, and the designer is faced with a trade-off between the compression ratio and flow quality.

Studies were carried out by reducing the spike termination angle θ_1 to 29, 28 and 27 degrees. Polar plots were generated for several cases at various Mach numbers, shown in Figures 4.50 to 4.55. Figures 4.50 and 4.51 show polar plots for a design with a reduced spike-termination angle of 29 degrees at Mach 4 and 5 respectively. The boundaries between shock detachment and shock attachment at the cowl lip (constraint 2 line), and regular and Mach reflection on the centrebody (constraint 1 line) are reduced, indicating the safer operating conditions when designing with smaller forebody angles. Moving the design well into the safety zone will however produce less intake compression and a higher inlet Mach number, so that the downstream performance may not be as satisfactory.

CFD simulations were carried out with a modified design of the intake with a reduced spike termination angle of 29 degrees. Figure 4.56 shows density contours of the intake with a 29 degree spike termination angle with a 4 degree cowl/centrebody angle at Mach 4. The polar plot (Figure 4.50) suggests Mach reflection will occur on the centrebody for this configuration. The contours indeed show Mach reflection of the cowl shock on the centrebody, with a recirculation region just behind the Mach stem. The flow downstream is now non-uniform with a subsonic streamtube behind the Mach stem. Figure 4.57 presents density contours for the intake with the reduced 29 degree spike termination angle at Mach 5, with a 7 degree cowl/centrebody angle. The polar plot (Figure 4.51) suggests that for this case, the cowl shock will reflect the centrebody as regular reflection. Reducing the spike termination angle in this case, regular reflection can be maintained with a reduced cowl angle, and this will be beneficial in reducing cowl pressure drag, although reducing compression ratio.

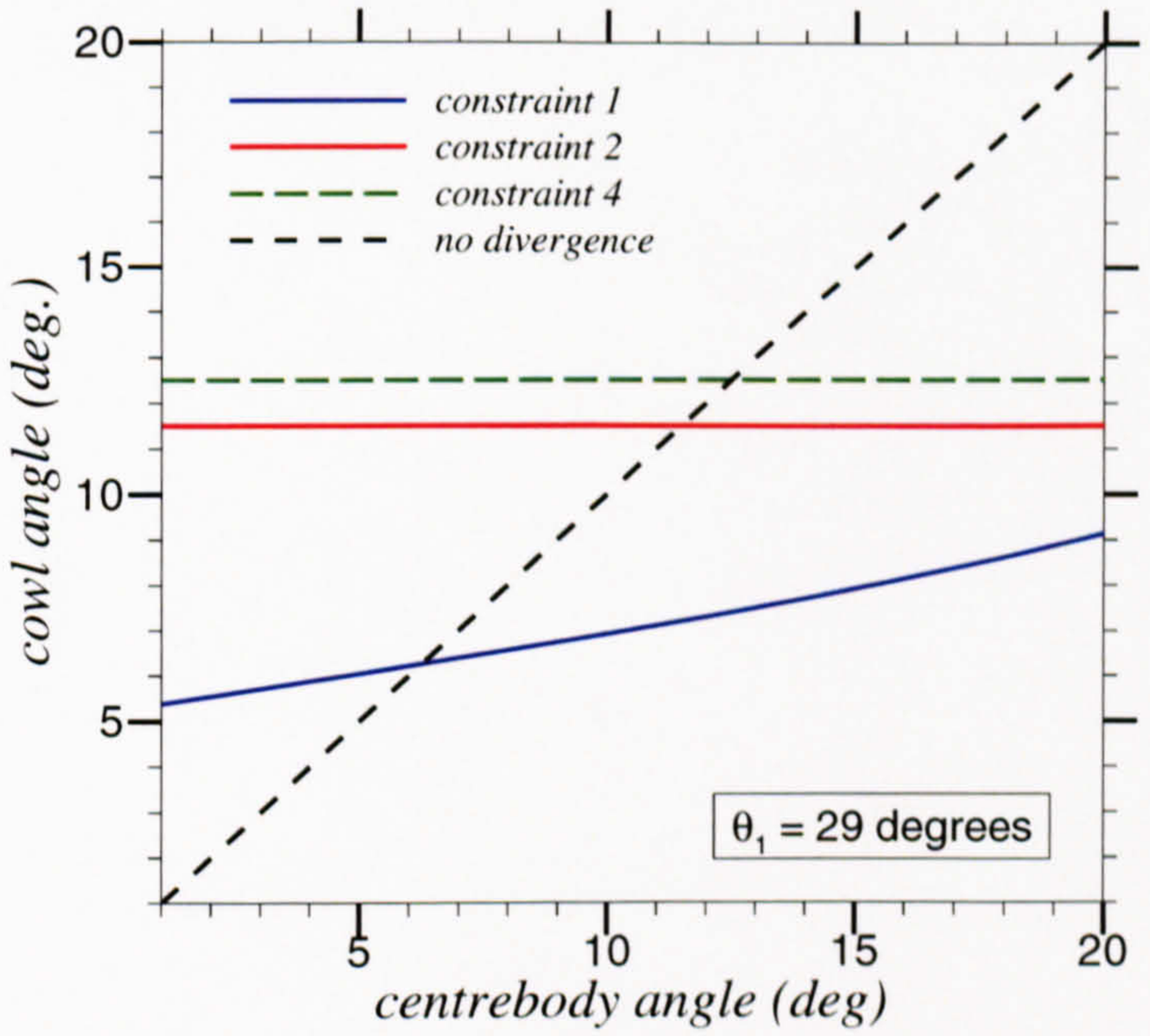


Figure 4.50: Polar plot for the intake (shock-on-lip Mach 5.5) with a 29 degree spike termination angle at off-design condition Mach 4.

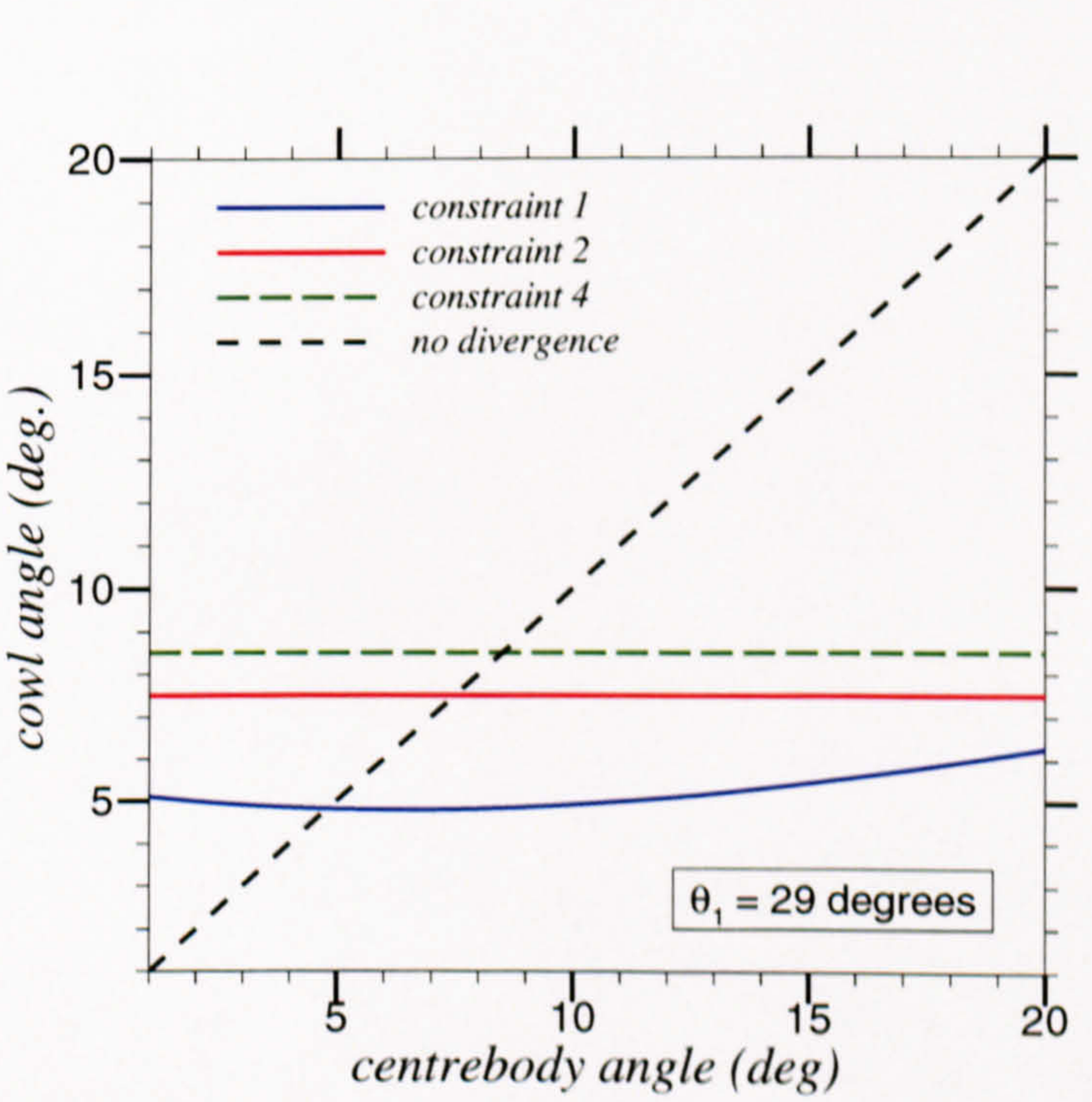


Figure 4.51: Polar plot for the intake (shock-on-lip Mach 5.5) with a 29 degree spike termination angle at off-design condition Mach 5.

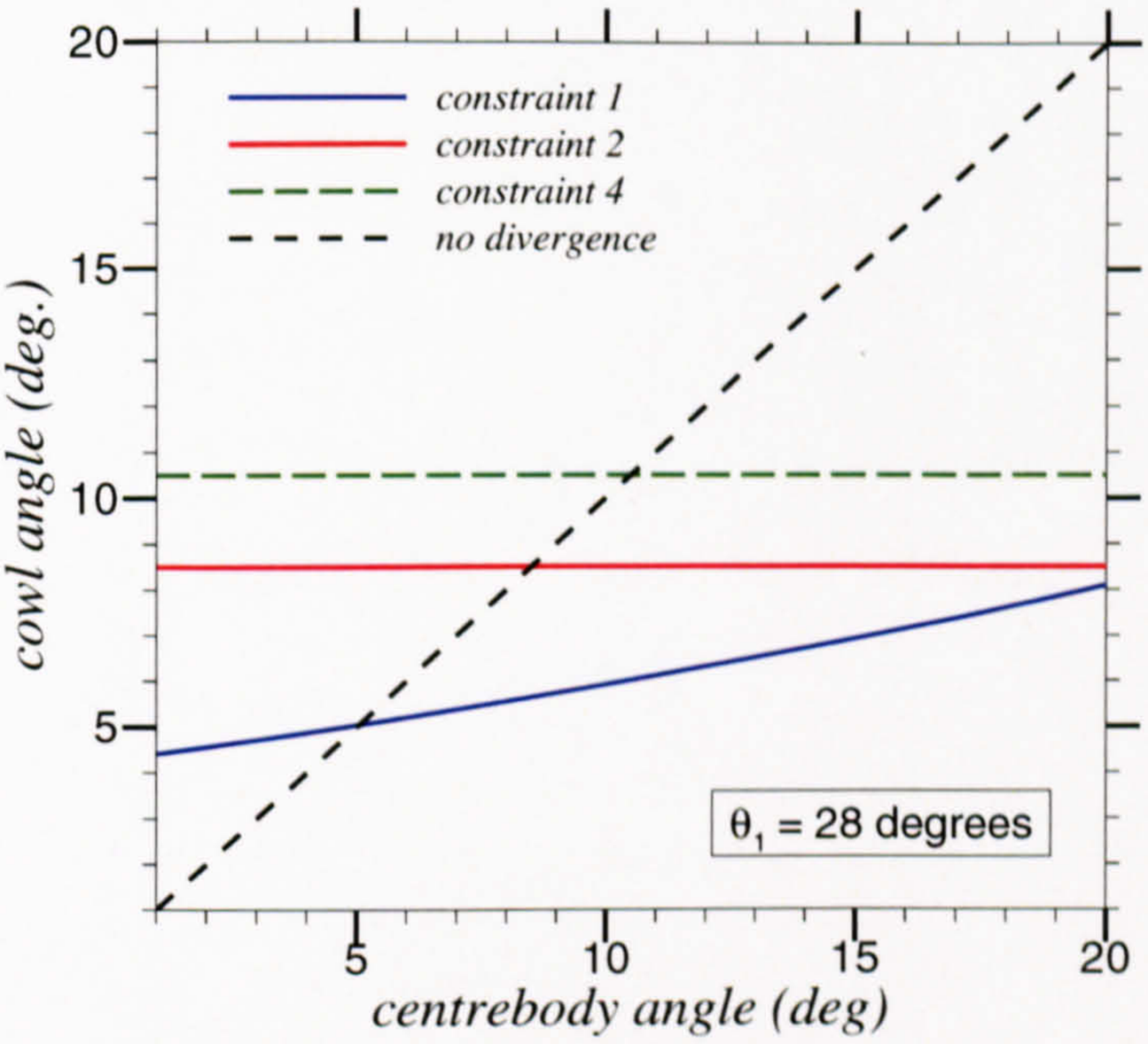


Figure 4.52: Polar plot for the intake (shock-on-lip Mach 5.5) with a 28 degree spike termination angle at off-design condition Mach 4.

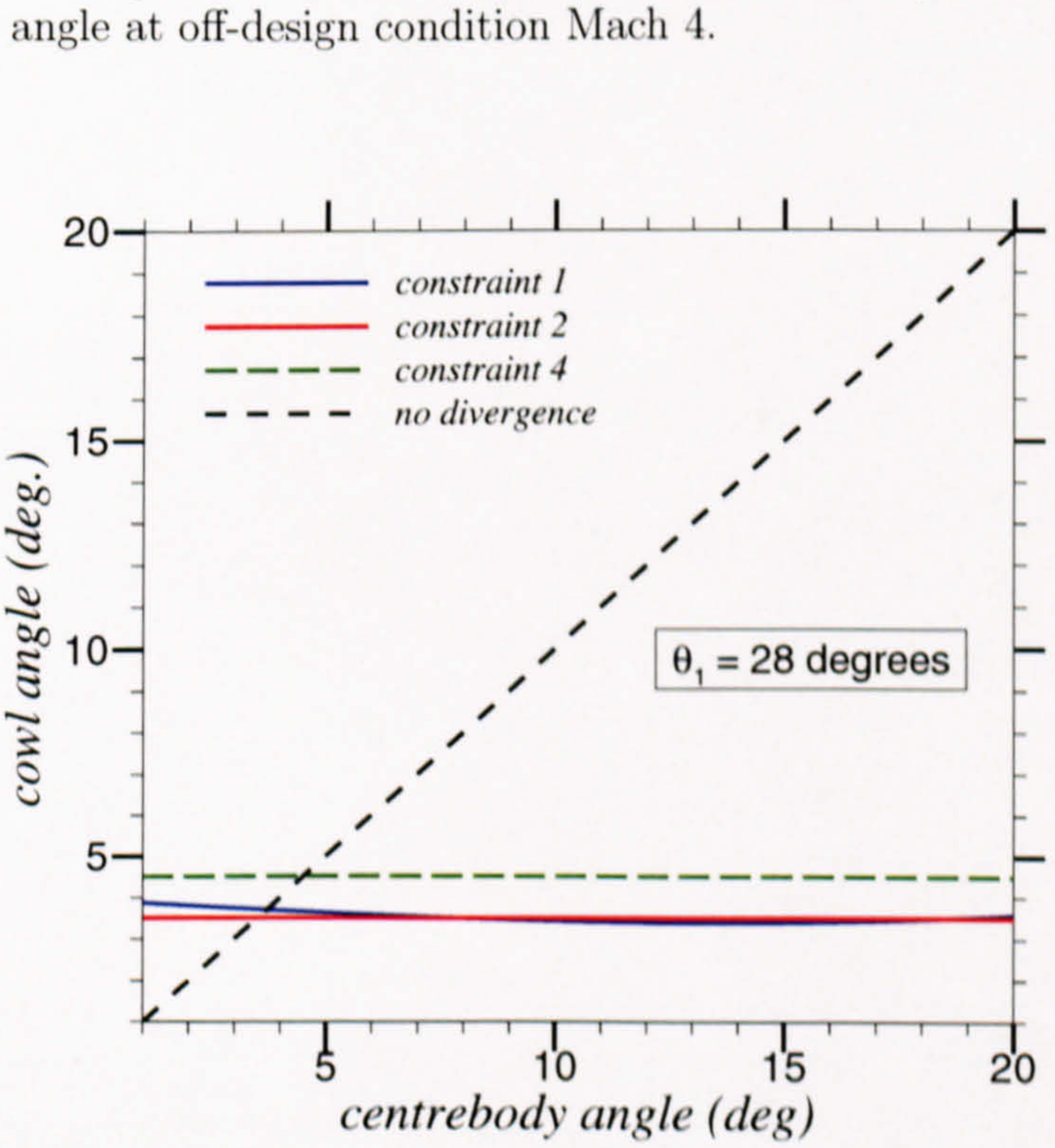


Figure 4.53: Polar plot for the intake (shock-on-lip Mach 5.5) with a 28 degree spike termination angle at off-design condition Mach 6.

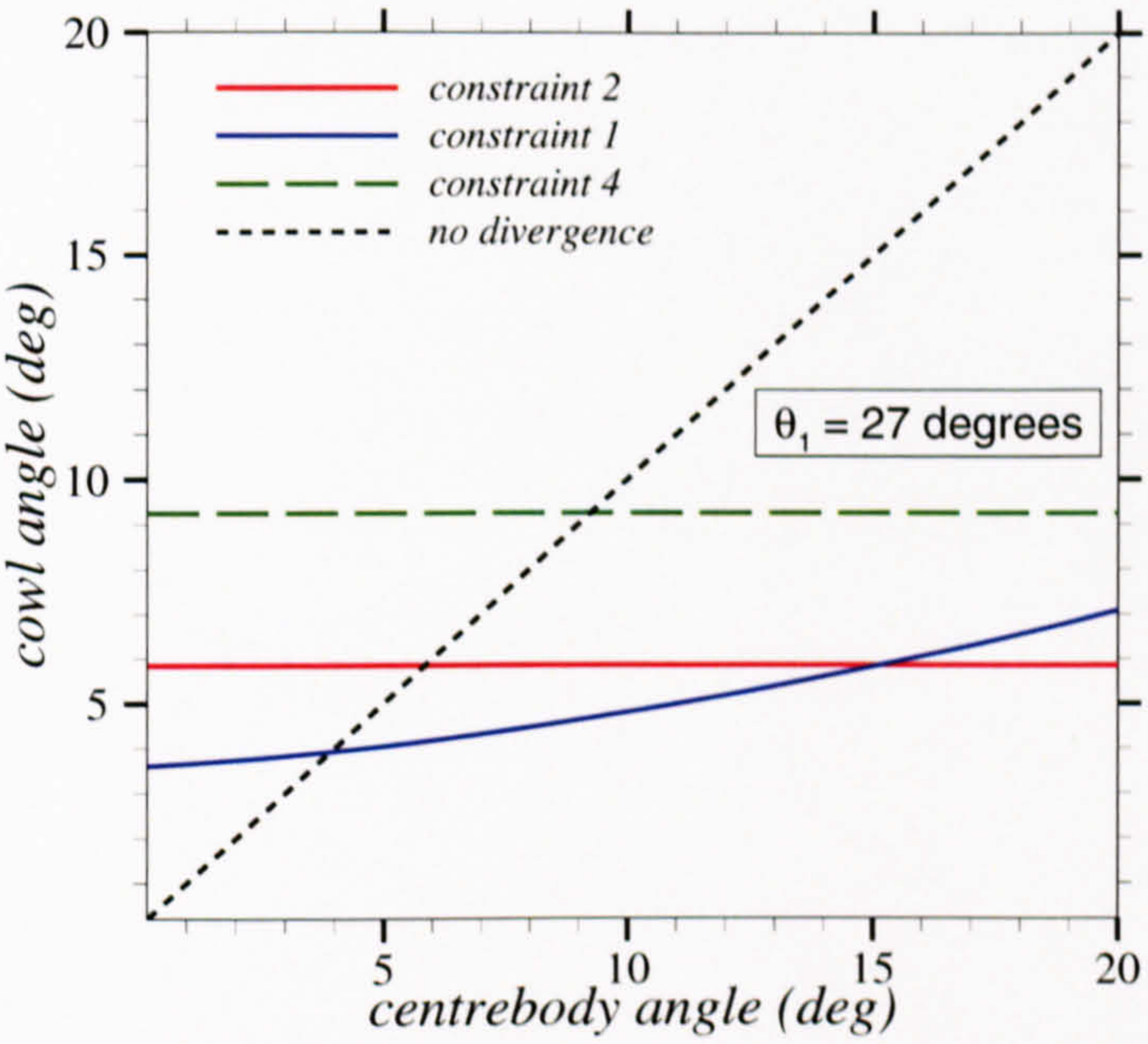


Figure 4.54: Polar plot for the intake (shock-on-lip Mach 5.5) with a 27 degree spike termination angle at off-design condition Mach 4.

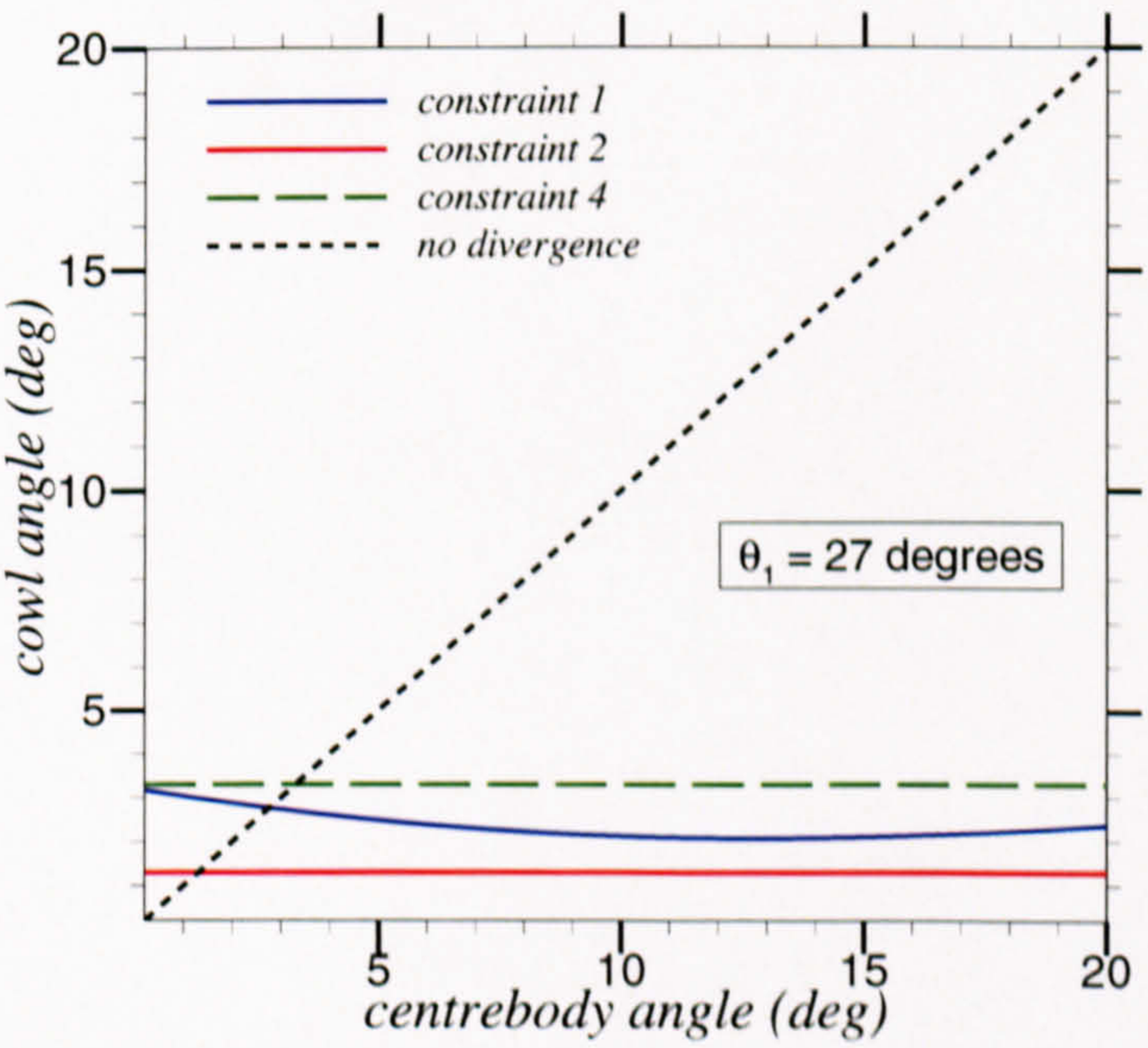


Figure 4.55: Polar plot for the intake (shock-on-lip Mach 5.5) with a 27 degree spike termination angle at off-design condition Mach 6.

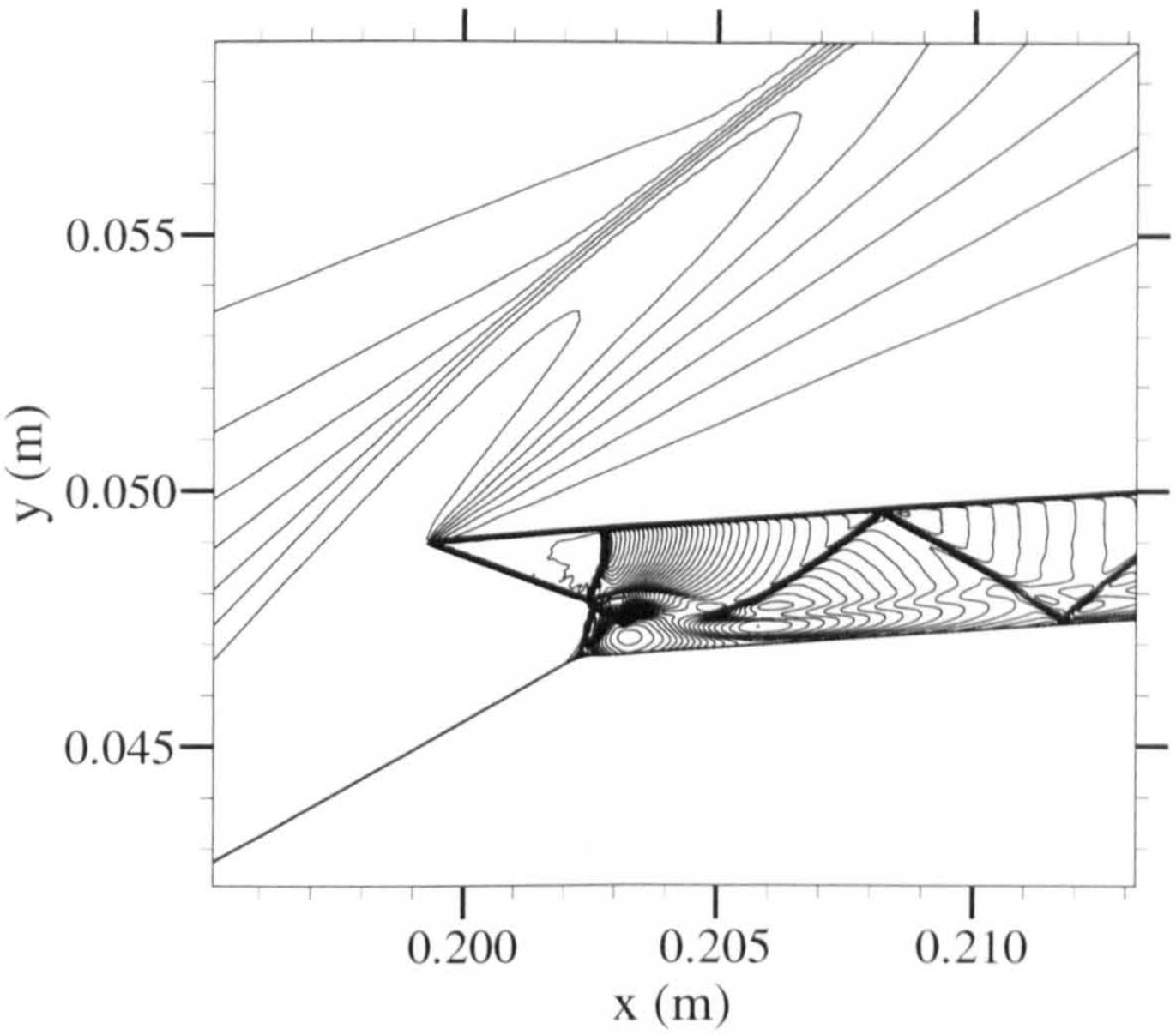


Figure 4.56: CFD Density contours from an inviscid simulation of the intake with a 29 degree spike term. angle and a 4 degrees cowl/centrebody angle at Mach 4.

Figure 4.57: CFD Density contours from an inviscid simulation of the intake with a 29 degree spike term. angle and a 7 degrees cowl/centrebody angle at Mach 5.

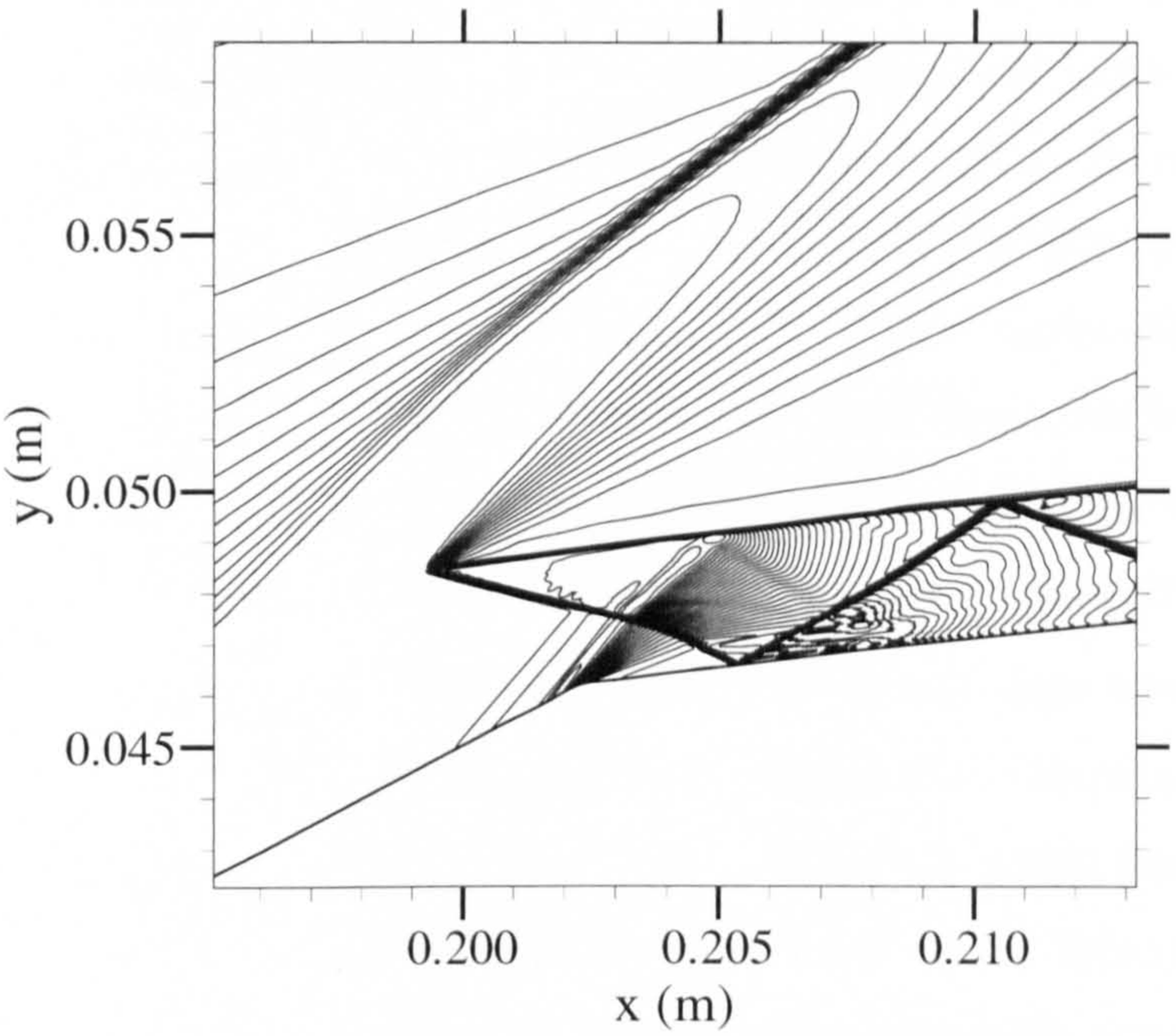


Figure 4.58: CFD Density contours from an inviscid simulation of the intake with a 27 degree spike term. angle and a 7 degrees cowl/centrebody angle at Mach 4.

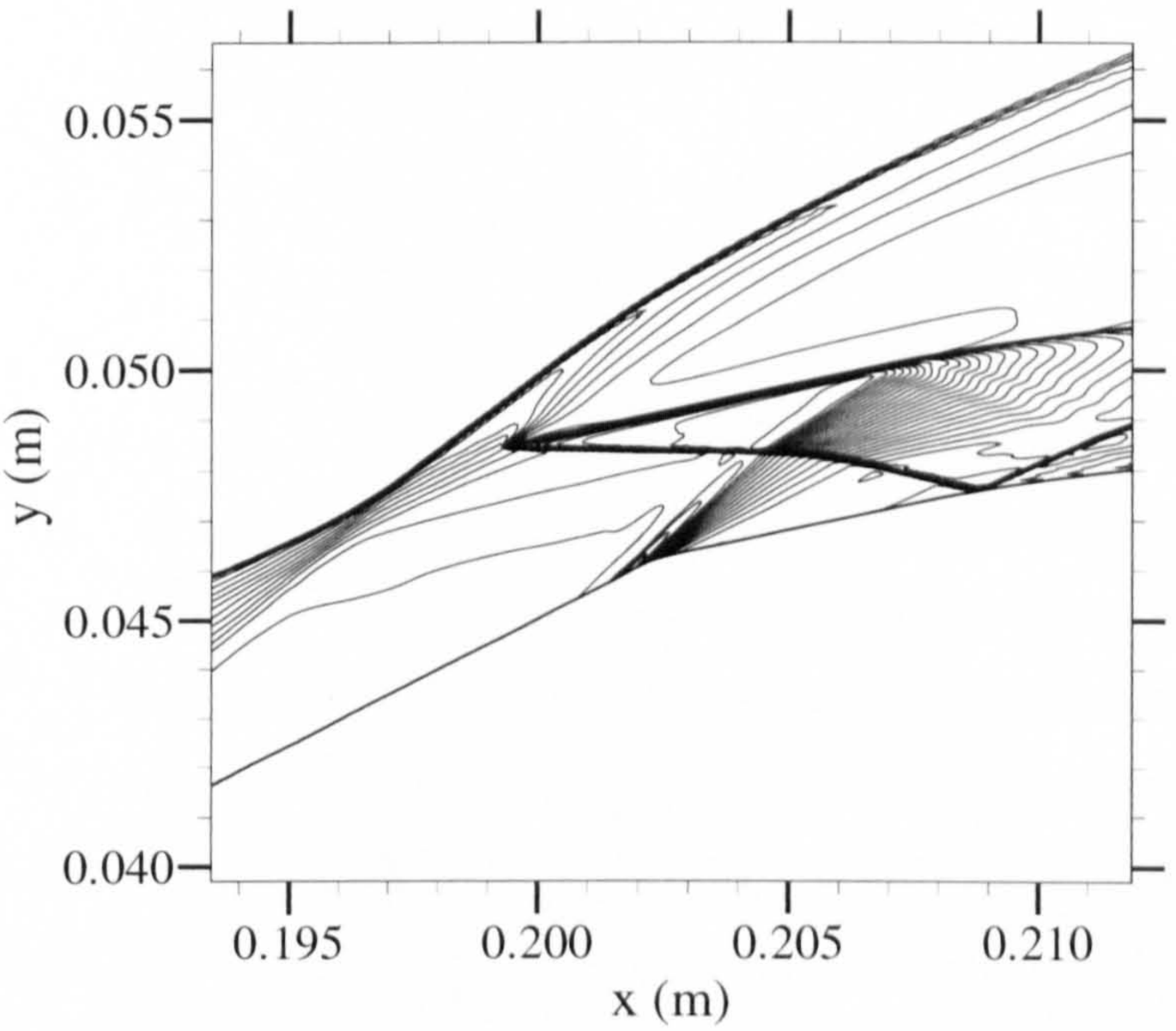


Figure 4.59: CFD Density contours from an inviscid simulation of the intake with a 27 degree spike term. angle and a 12 degrees cowl/centrebody angle at Mach 6.

Reducing the spike termination angle even further to 27 degrees, the Mach 4 polar plot in Figure 4.54 shows that with a 7 degree cowl/centrebody angle at the reduced 27 degrees forebody geometry, regular reflection should occur at the centrebody, and this is indeed seen in a full CFD simulation in Figure 4.58. The density contours show the cowl shock impinging the centrebody and reflecting as regular reflection. Hence by reducing the forebody angle to 27 degrees, the cowl angle can be reduced to 7 degrees to maintain regular reflection at the centrebody. Again, this reduction from 12 degrees to 7 degrees in cowl angle can be beneficial in external drag reduction.

From the Mach 6 polar plot for the intake with a reduced spike termination angle of 27 degrees, shown in Figure 4.55, with the original cowl/centrebody angle of 12 degrees, the inlet is now operating above the constraint 2 design line and so shock attachment should occur at the cowl lip. Figure 4.58 shows this case at Mach 6 with the reduced forebody angle of 27 degrees where the shock is now attached at the cowl lip. This case can be compared to Figure 4.20 which was presented in the previous section, where the original inlet with a 33 degrees forebody angle at Mach 6 produced a shock detachment at the cowl lip. So, reducing the forebody angle lowers the likelihood of shock detachment and associated pressure losses, hence resulting in a good quality uniform inlet flow, but with the penalty of lower compression ratio.

Figure 4.60 presents the centrebody surface pressure distribution for two geometries with varied spike termination angle; 33 and 29 degrees at Mach 4. The geometry with θ_1 of 33 degrees is configured with a 12 degree cowl/centrebody angle. The geometry with θ_1 of 29 degrees is configured with a 4 degree cowl/centrebody angle. This causes the discrepancy in the shock pattern after forebody compression. However, the important feature of this plot is the reduction in the forebody compression when reducing θ_1 from 33 degrees to 29 degrees. For the 33 degrees case, the forebody compresses the flow to approximately 10.7 times the freestream pressure, and this is reduced to 9 times the freestream pressure when θ_1 is reduced to 29 degrees.

Figure 4.61 presents the centrebody surface pressure distribution for the two forebody angles at Mach 6, showing a marked decrease in forebody compression from the 33 degrees to 27 degrees forebody angles.

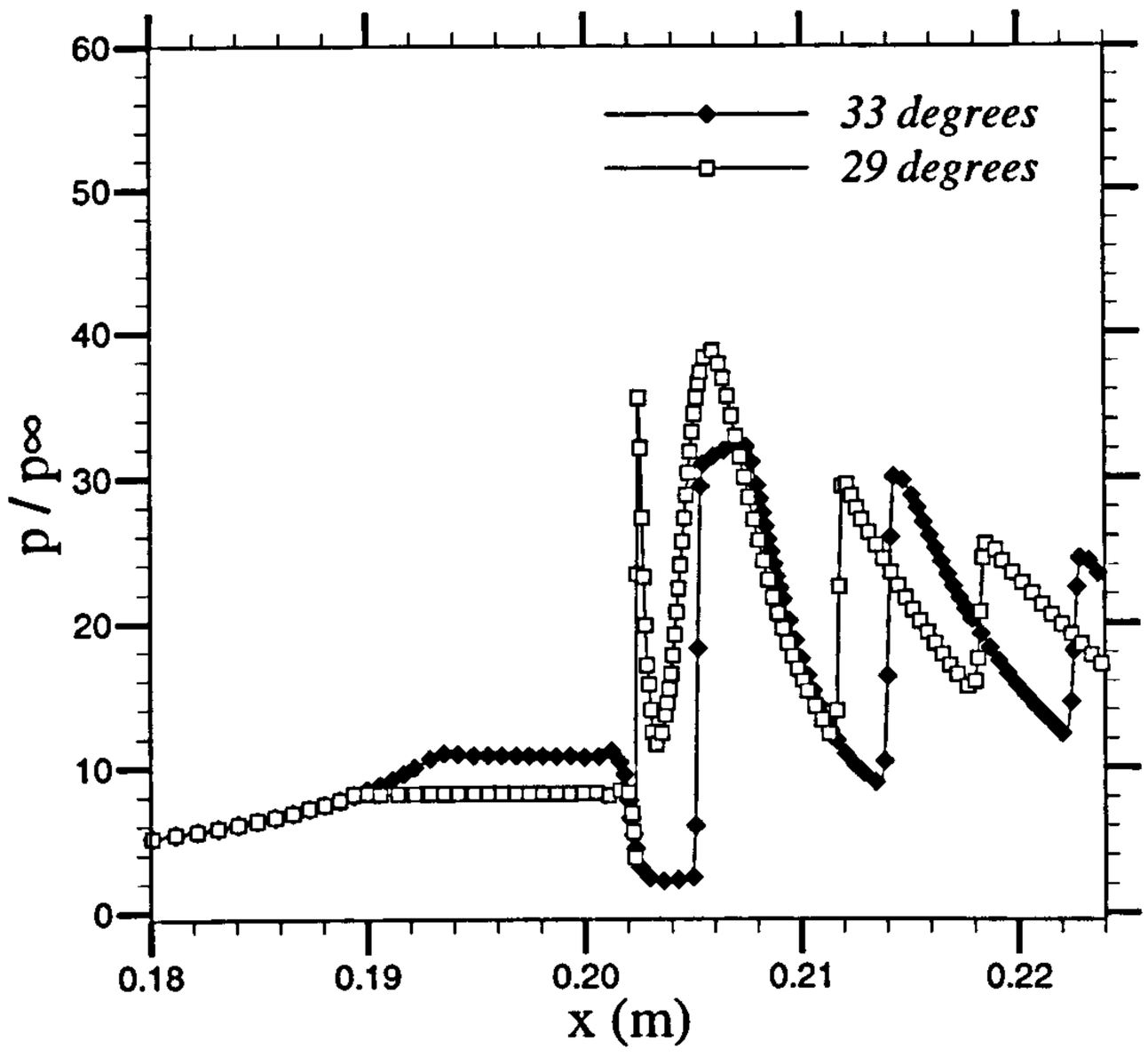


Figure 4.60: Comparison of surface pressure distribution for the spike termination angle $\theta_1 = 33$ and 29 degrees at Mach 4 to show the effect of reducing θ_1.

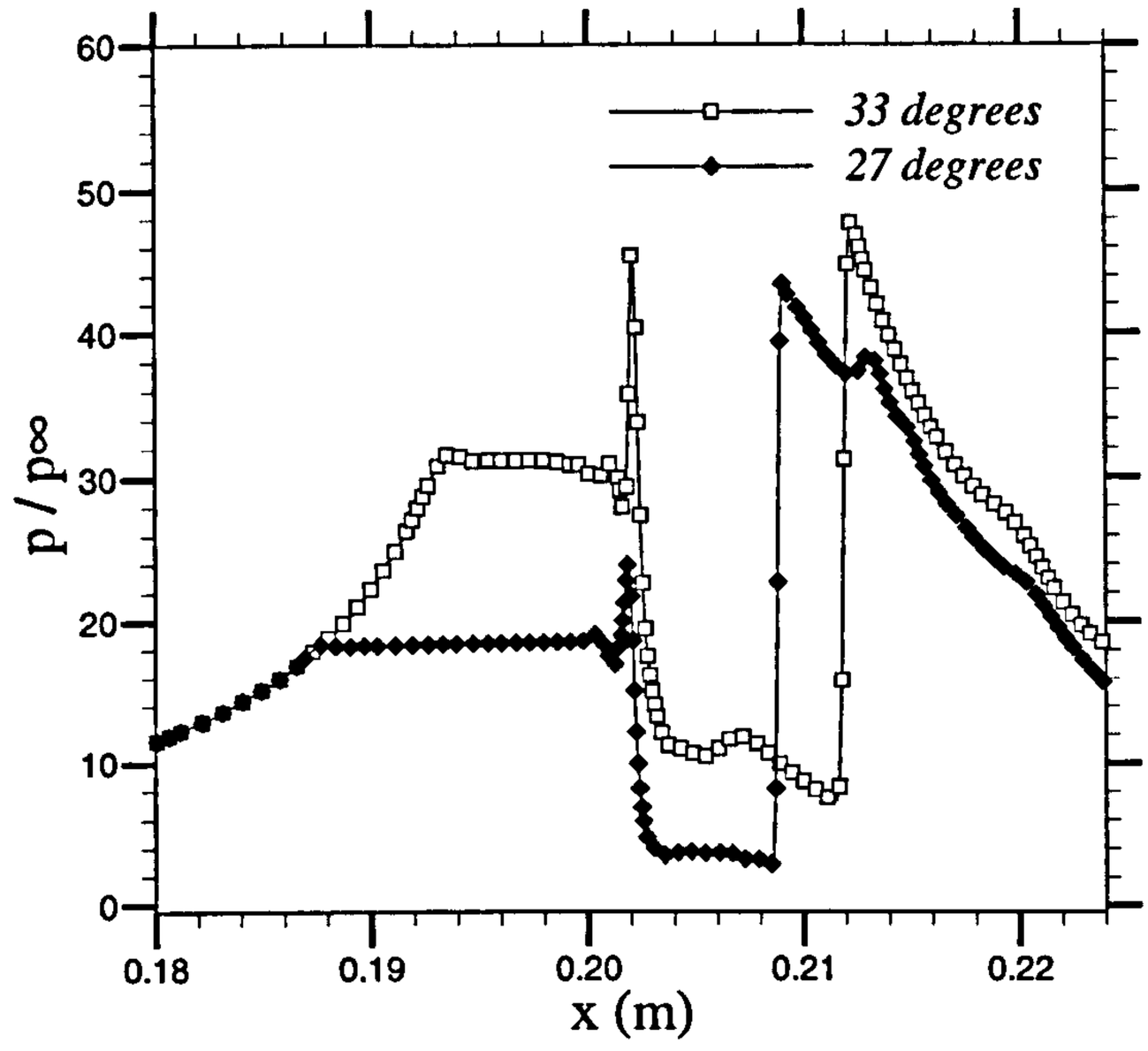


Figure 4.61: Comparison of surface pressure distribution for the spike termination angle $\theta_1 = 33$ and 27 degrees at Mach 6 to show the effect of reducing θ_1.

The intake with a 33 degrees spike termination angle compresses the flow to approximately 31 times freestream pressure. For the intake with a reduced spike termination angle of 27 degrees the forebody compresses the flow to approximately 18 times the freestream pressure.

Table 4.6 presents values for total pressure efficiencies, kinetic energy efficiencies and mass capture ratios for the various cases tested with reduced spike termination angles. For the intake with a reduced θ_1 to 29 degrees and with a 4 degrees cowl/centrebody angle at Mach 4 the total pressure efficiency is 63.7 percent and the kinetic energy efficiency is 95.7 percent. The mass capture ratio is 51.7 percent. The mass capture is markedly low due to the intake operating at below design conditions.

The total pressure losses are associated with the Mach reflection on the centrebody for this case, seen in Figure 4.56. For the intake with the 29 degree spike termination angle and a 7 degree cowl/centrebody angle at Mach 5, the total pressure efficiency is calculated to be 57.4 percent and kinetic energy efficiency is 96.5 percent. Mass capture ratio is increased to 75.8 percent as the intake is operating just below its design condition. The high total pressure loss is due to the strong cowl shock.

M_∞	x_c (m), y_c (m)	θ_1	δ_c / θ_2	η_{pr}	η_{ke}	MCR
4.0	0.1993, 0.0489	29 degrees	4 degrees	0.637	0.957	0.517
5.0	0.1993, 0.0489	29 degrees	7 degrees	0.574	0.965	0.758
4.0	0.1993, 0.0484	27 degrees	7 degrees	0.702	0.967	0.479
6.0	0.1993, 0.0484	27 degrees	12 degrees	0.669	0.983	0.908

Table 4.6: Values of spike termination angle, cowl/centrebody angle, mass capture ratio, kinetic energy efficiency and total pressure efficiency for intake configurations with reduced spike termination angles at 3 flight conditions (inviscid values).

For the intake with θ_1 reduced to 27 degrees and with a 7 degrees cowl/centrebody angle at Mach 4, the total pressure efficiency is 70.2 percent and kinetic energy efficiency is 96.7 percent. Mass capture ratio is 47.9 percent which is low - again due to the low Mach number. Comparing these values to those calculated for the intake with the original θ_1 value of 33 degrees and with a 7 degrees cowl/centrebody angle (values shown in Table 4.6) shows an increase in the total pressure efficiency

from 64.7% to 70.2 % as the spike termination angle is reduced to 27 degrees. This is because for the original design (θ_1 =33 deg.) Mach reflection forms on the centrebody with a 7 degrees cowl/centrebody angle. Kinetic energy efficiency also increase from 95.9% to 96.7%. However, mass capture ratio is markedly reduced when θ_1 is reduced from 33 to 27 degrees - from 60.9% t0 47.9%.

For the final case tested for an intake with θ_1 reduced to 27 degrees, and with a 12 degrees cowl/centrebody angle at Mach 6, the contours of which can be seen in Figure 4.59, the total pressure efficiency is 66.9 percent and the kinetic energy efficiency is 98.3 percent. The mass capture ratio is calculated to be 90.8 percent. This case can be compared to the original design (θ_1 =33 deg.) with a cowl/centrebody angle of 12 degrees at Mach 6 where shock detachment occurs. Total pressure efficiency is reduced as spike termination angle is reduced (from 33 to 27 degrees) from a value of 69.0% to 66.9% and this is due to the stronger cowl shock for the reduced θ_1 case. Kinetic energy efficiency stays almost the same as θ_1 is reduced, from a value of 98.5% to 98.3%. Mass capture ratio also stays almost the same, from a value of 89.4% to 90.8% when θ_1 is reduced from 33 to 27 degrees.

From these performance values, it is evident that various mechanisms contribute to the losses in total pressure, kinetic energy and mass capture in the intake. The results presented in this chapter give an indication of the complexity in designing a fixed geometry inlet delivering good performance at a wide range of operating conditions. Although the assumptions behind the shock-expansion analysis are restrictive it is evident that cowl lip bluntness and viscous effects would tend to increase the effect, in that any design should operate as far *into the comfort zone* as possible. Wave reflection on the centrebody means that the 'hard won' compression on the forebody has been expanded back to low pressures before experiencing significant compression again. This is undesirable and can lead to large compression ratios across the reflected wave system and possible associated boundary-layer interactions.

Chapter 5

Intakes with supersonic outflow II

5.1 Flow separation at inlet

The previous chapter was primarily concerned with studying the influence of wave interactions in controlling the intake flow. It was found that the wave interactions could significantly affect the quality of flow entering the intake and contribute to aerodynamic losses and inlet flow non-uniformities. This chapter will present an analysis of the intake flow including viscous effects and will discuss the problem of flow separation. The control of flow separation will also be addressed in this chapter.

Flow separation can be instigated by many factors, and identifying the cause of separation and finding methods to control separation in the intake system is a challenging flow physics problem. Flow separation at the inlet of a hypersonic vehicle can result in aerodynamic losses and flow non-uniformities which can affect compression efficiency and combustion stability and can influence the overall engine performance. Flow separation can also lead to the displacement of the inlet shock system and the generation of additional shock waves in the flow which can lead to complex flows. Another concern with a separated boundary-layer in the intake duct is the effective alteration of the area regions which can have an affect on intake starting. Small separations are expected in the intake duct, and as long as sufficient mass capture and efficiency is achieved, small separations can to some extent be acceptable. However, large separated regions at the inlet annulus are unacceptable.

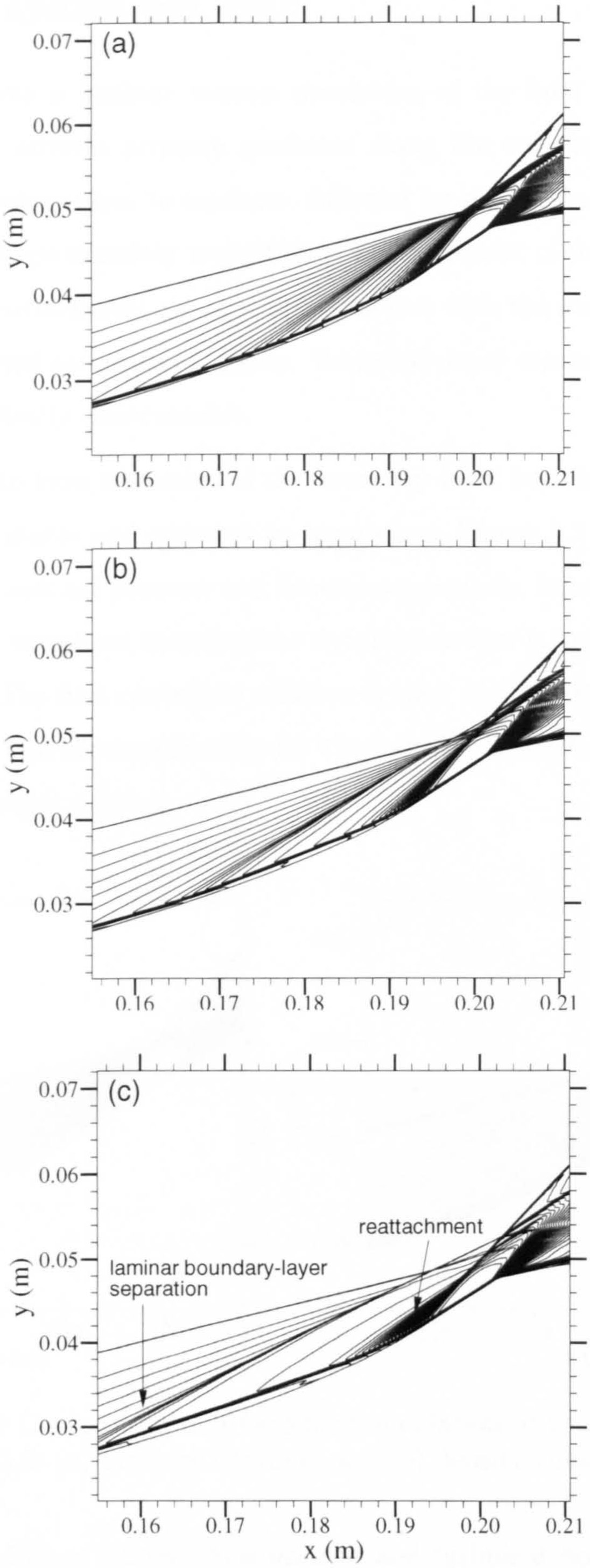


Figure 5.1: CFD Density contours from a laminar simulation of the intake (no cowl) at Mach 5.5; time-dependent contours from (a) to (c) to show laminar separation.

5.1.1 Flow system (no cowl)

Figure 5.1 presents a laminar viscous simulation of the inlet (no cowl) at Mach 5.5. The strong adverse pressure gradients along the compression surface cause the laminar boundary-layer to separate, followed by reattachment which is seen in Figure 5.1 (c) at approximately x=0.0192m. Reattachment of the laminar-boundary layer induces a reattachment shock which combines with the isentropic compression fan to form a mixed compression region. Boundary-layer separation of this kind on the forebody is clearly unacceptable.

The next step is to force transition of the boundary-layer from laminar to turbulent, to make it more stable and resistant to separation. Figure 5.2 (a) and (b) present contour plots of constant pressure and density respectively, from a turbulent viscous simulation where transition from laminar to turbulent flow is imposed at 50mm from the spike apex. The first converged solution is then used to refine the mesh, to fit a value of $y^+ = 1$ in the surface cells for the full chord length, and the solution is re-run to a converged solution.

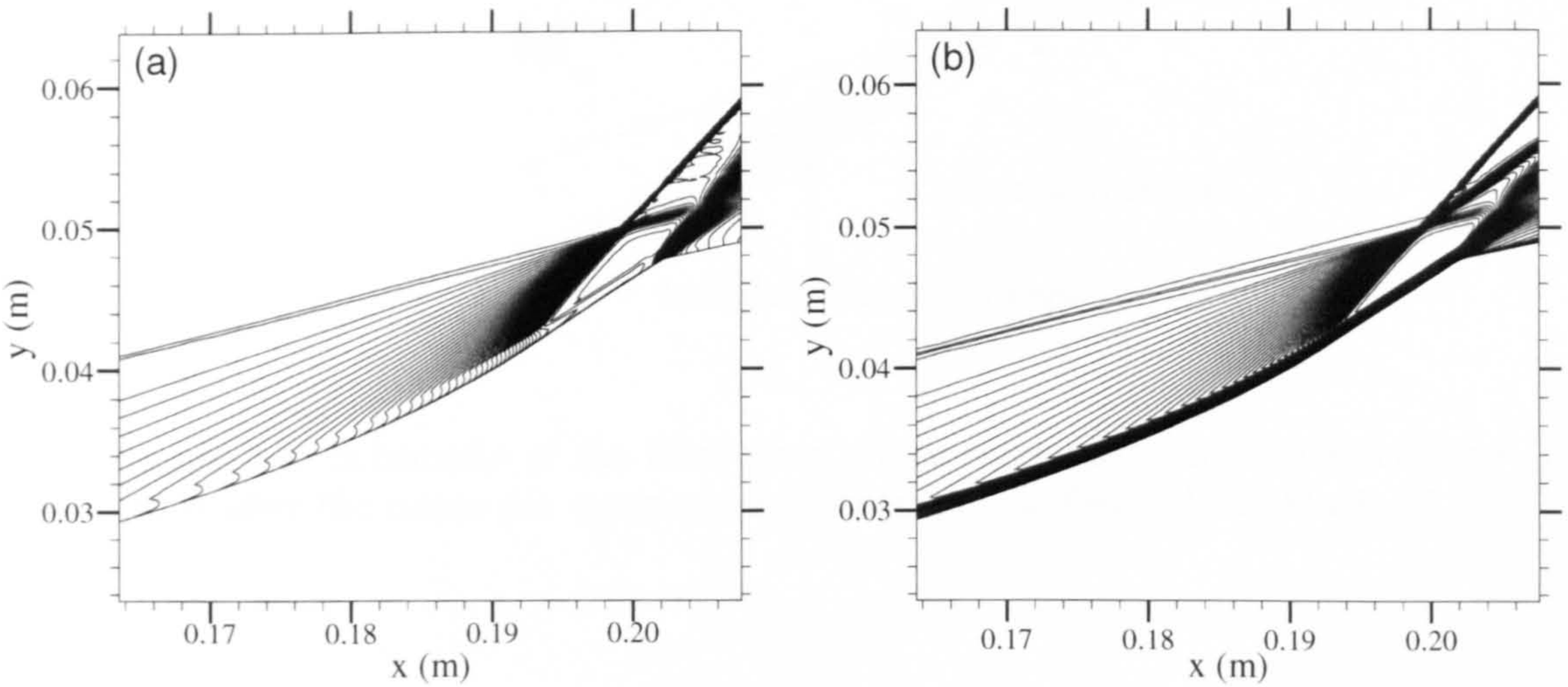


Figure 5.2: CFD Contours from a turbulent simulation of the intake (no cowl) at on-design Mach 5.5; (a) pressure contours and (b) density contours.

The contours in Figure 5.2 (b) show an attached turbulent boundary-layer on the forebody. A turbulent boundary-layer contains more momentum than the fluid in a laminar boundary-layer, and therefore, the turbulent boundary-layer is more able to

pass through the adverse pressure gradient region without separating. This result indicates the need to operate at a high enough Reynolds number, or to trigger transition early enough on the forebody to ensure a turbulent boundary-layer and avoid laminar boundary-layer separation on the forebody. Computing the boundary-layer on the body displaces the shock system slightly, as expected, and the focus of the triple point (Figure 5.2) is the cowl lip design point.

Figure 5.3 shows a schematic of the wave system at inlet with the boundary-layer. The only difference between the turbulent case and the inviscid case (shown in Figure 4.3 in section 4.1.1) is the displacement of the inlet wave system due to the presence of the boundary-layer. The flow then accelerates past the expansion corner and the boundary-layer stays attached on the centrebody. Flow separation is unlikely to occur past the expansion corner due to the favourable pressure gradients through the expansion fan which promote boundary-layer attachment at the wall.

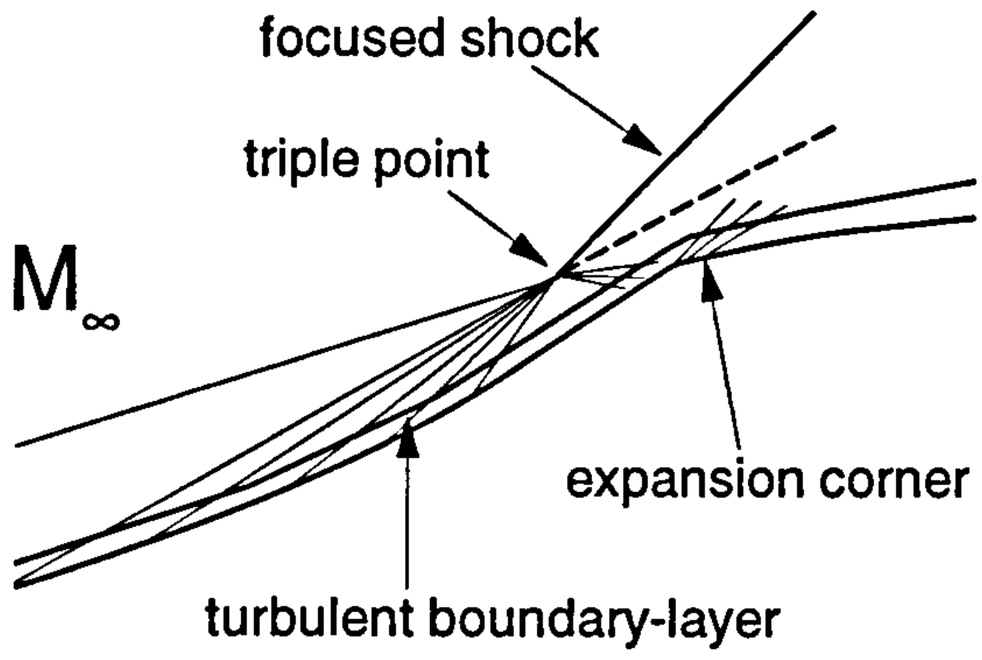


Figure 5.3: Schematic of the inlet wave system and turbulent boundary-layer (no cowl) after the isentropic compression process on the forebody at Mach 5.5.

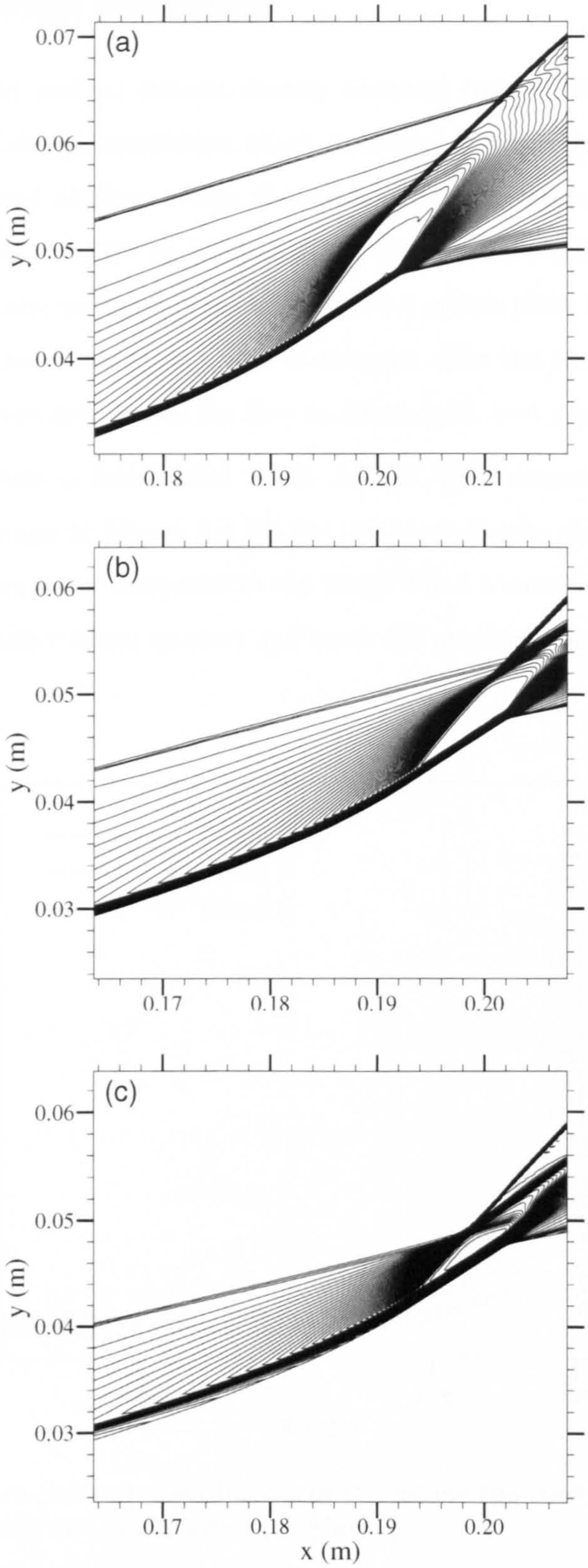


Figure 5.4: CFD Density contours from turbulent simulations of the intake (no cowl) at off-design Mach numbers (a) Mach 4 (b) Mach 5 and (c) Mach 6.

5.1.2 Off-design conditions

Figure 5.4 (a), (b) and (c) present density contours from turbulent simulations of the intake at off-design conditions Mach 4, 5 and 6 respectively. Transition for all cases is imposed at 50mm from the spike apex. At Mach 4, the compression process decelerates the flow to $M_1 \simeq 2.37$ with a static pressure rise to 10.7 times the freestream static pressure, seen in Figure 5.5 which plots the surface pressure distribution for the three cases versus x-distance. For the Mach 5 condition, the compression process decelerates the flow to $M_1 \simeq 2.82$, and p/p_∞ of 18.4.

At Mach 6, the flow is decelerated to $M_1 \simeq 3.19$, and compressed to p/p_∞ of 31. The density contours in Figure 5.4 (c) for the Mach 6 case show a visibly thicker forebody boundary-layer compared to the Mach 4 and 5 cases in Figure 5.4 (a) and (b), due to the higher Mach number and lower Re number conditions at Mach 6.

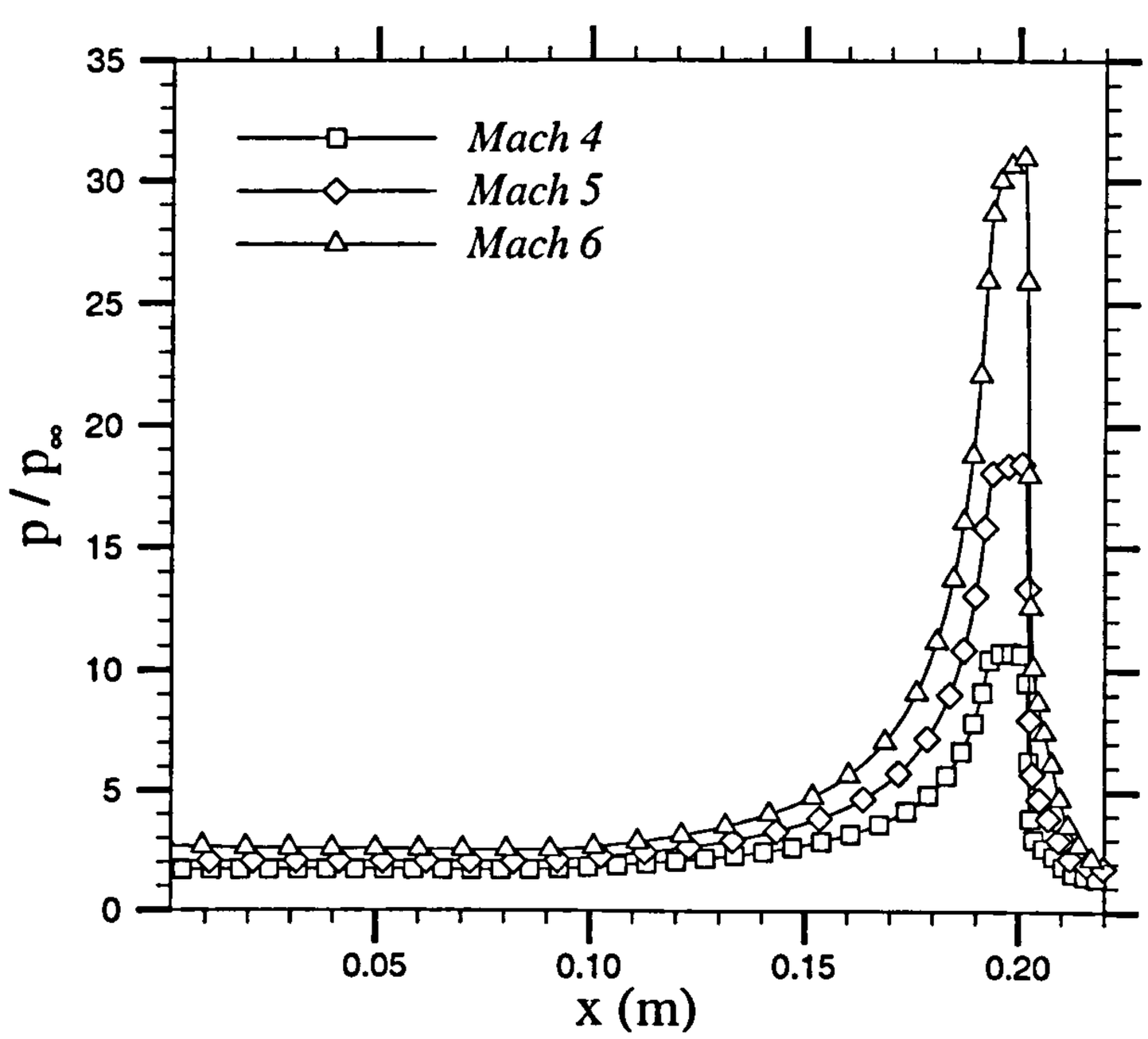


Figure 5.5: Surface pressure distribution of the intake (no cowl) at off-design Mach numbers (a) Mach 4 (b) Mach 5 and (c) Mach 6.

5.1.3 Flow separation process

Turbulent simulations were carried out on various intake configurations and flight conditions to study the behaviour of the intake boundary-layers. Figure 5.6 presents time-dependent density contours from a simulation of the intake with a 33 degree spike termination angle, and a 12 degree cowl/centrebody angle at Mach 4. In the first contour plot (a) the cowl shock is seen impinging on the centrebody boundary-layer. The interaction of the cowl shock with the centrebody boundary-layer is the principal mechanism leading to flow separation in the intake due to the high level of adverse pressure gradients imposed on the boundary-layer. If the cowl shock impinges the boundary-layer with sufficient strength, then flow separation will most likely occur. The contours in Figure 5.6 show that the centrebody boundary-layer is separated slightly by the impingement of the cowl shock on the centrebody.

The starting flow is still developing in contours (a) to (d). At this stage, the separated region is fairly small, as the flow is still in the process of evolving. The nature of the starting flow of the CFD simulation is such that the cowl shock gets progressively stronger as the conditions evolve from the initialised freestream conditions to the final state of the flow field. The cowl shock wave radiates on to the centrebody surface aft of the shoulder expansion, and reflects back to the cowl inner surface.

In plot (b) the contours show that the separated region has expanded in scale. The separation position, and the associated separation shock wave are positioned just downstream of the expansion corner. The reflected cowl shock from the centrebody surface coalesces with the reattachment shock, which is formed by the compression waves generated at the reattachment point. This mechanism is illustrated in Figure 5.7 where a close view of the reattachment region shows the formation of a compression fan generated by the reattaching shear layer. The compression fan then focuses to form a focused reattachment shock, a system similar to the wave system generated by the forebody isentropic flow (Figure 5.3).

In Figure 5.6 (b) a weak separation shock is also beginning to form at the front of the separated region and this shock then reflects from the cowl inner surface wall.

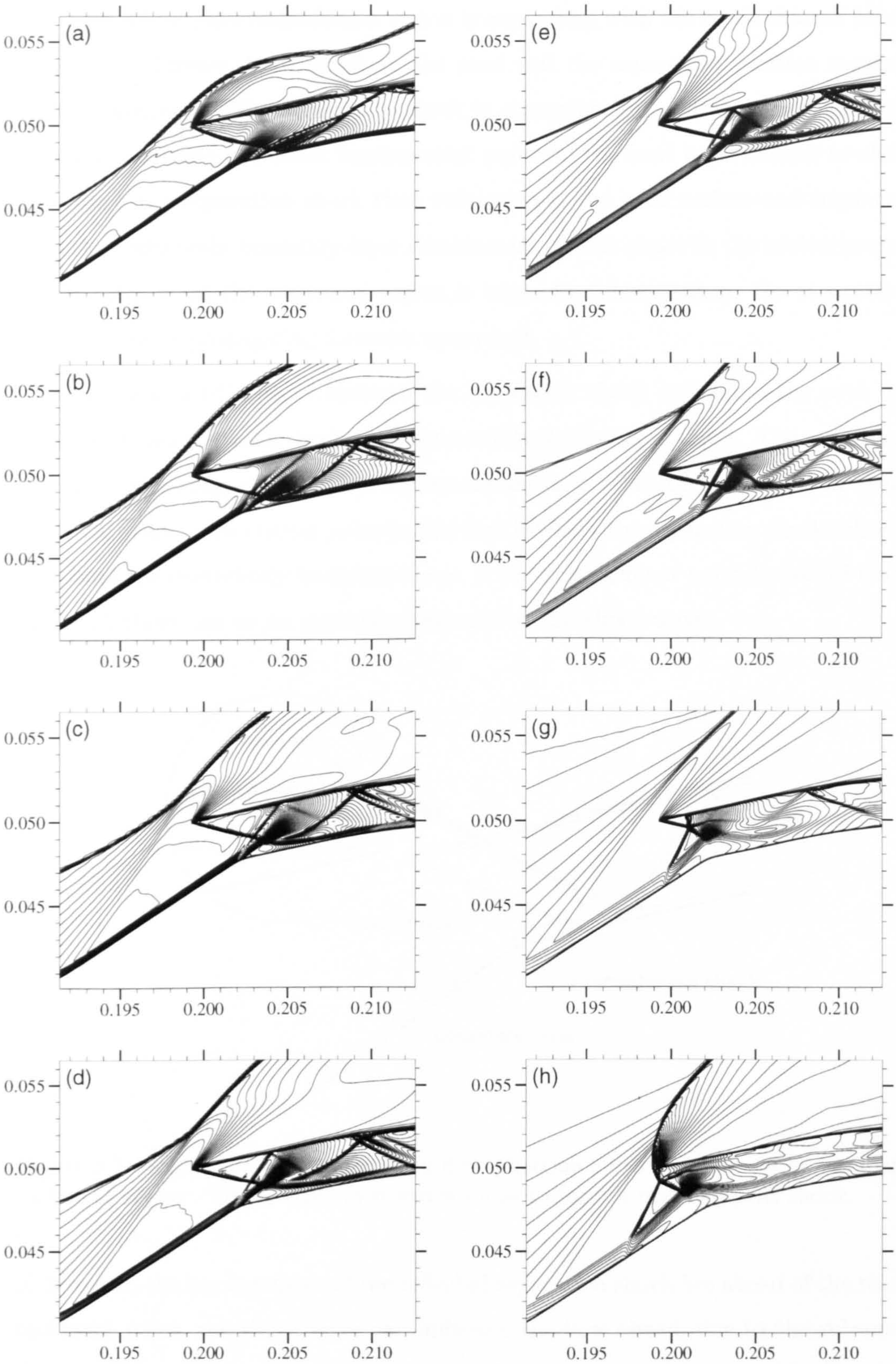


Figure 5.6: CFD Density contours from a turbulent simulation of the intake with a 12 degree cowl and centrebody angle at Mach 4; time-dependent contours from (a) to (h) to show boundary-layer separation on the centrebody.

In Figure 5.6 (c), the recirculation region is expanding with the reattachment point propagating further downstream in the duct and the separation position moving slightly upstream. The separation shock is strengthening and the shock angle is increasing, causing the shock impingement point on the cowl inner surface to shift forwards. The separation shock then reflects from the cowl surface and impinges onto the centrebody boundary-layer downstream of, but closer to the reattachment region. Hence, as the separated region is expanding downstream, the separation shock system is propagating forwards towards it.

The contours in (d) clearly indicate the separation shock impinging the cowl inner surface and reflecting back onto the centrebody boundary-layer. The separated region is expanding still and the separation shock is reflecting closer to the reattachment point. The critical point in this flow is where the separation shock reflects back onto the centrebody boundary-layer. If the impingement point lies aft of reattachment there can be no upstream influence of this shock wave.

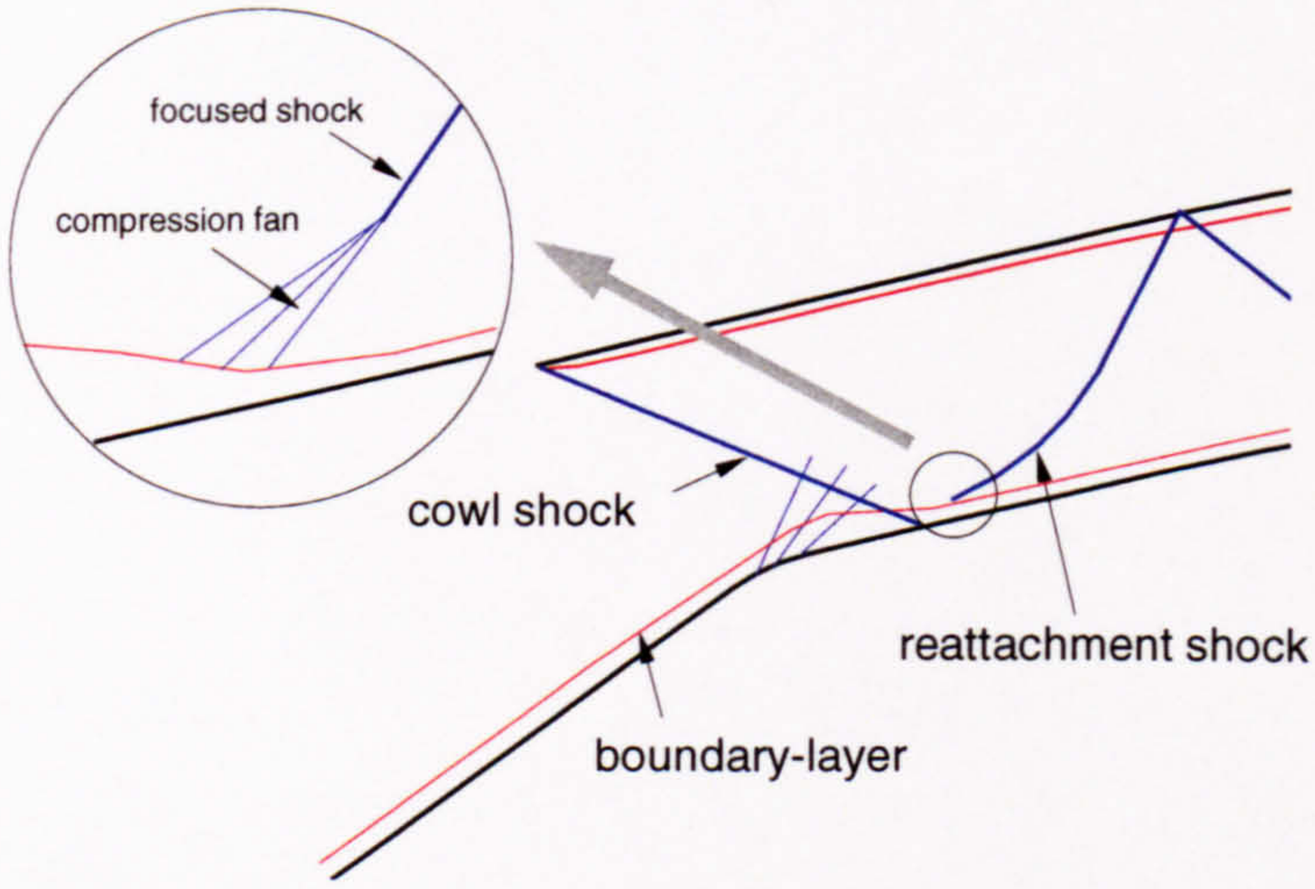


Figure 5.7: Schematic to illustrate the flow phenomena in the vicinity of the reattachment region. The compression waves focus to form a reattachment shock.

If, however, the impingement of the reflected separation shock lies ahead of the reattachment point, the shock wave can influence the flow ahead, due to the subsonic flow conditions in the separation region. The contours in (e) show this situation now occurring. Slight separation of the cowl inner surface boundary-layer can also

be seen, in the region where the reattachment shock wave impinges the cowl inner surface. The contour plot (f) shows the condition getting worse, as the separated region is expanding and the reflected separation shock is seen impinging the separated region. The reflected separation shock must in effect be an important factor in driving the separation. It seems that the separation shock is attenuated with a small separation, and that as the separation region expands the shock is increasing in strength.

At this stage, the separation position is also propagating forwards onto the forebody. Thus, in Figure 5.6 (g), the separation shock interacts with the cowl shock to form a complex shock system. The separation shock seems to have formed a Mach reflection on the cowl inner wall, and a slip surface emanates from this interaction point. In Figure 5.6 (h), this system is forced forwards to finally cause shock detachment at the cowl leading edge. The solution in plot (h) is the final converged steady-state solution for this flow field. This kind of flow separation in the intake leads to an unacceptable flow quality - in terms of non-uniformity and pressure losses - and will almost certainly have a detrimental effect on the overall engine performance.

Induced shocks

The previous solution makes it evident that a complex flow separation process occurs in the intake. The presence of several shock waves, expansion fans and wave interactions make it difficult to identify the influence of a particular shock system on the flow separation. The process described in the previous case seems to indicate a self-sustaining process, where separation is driven to a greater degree by the close interaction of the shock waves in the system. One of the assertions made is that the impingement of the reflected separation shock back onto the centrebody boundary-layer causes an upstream influence within the separated region which in effect drives the boundary-layer separation forwards and out of the intake.

Figure 5.8 shows a schematic of the process, where the separation shock impinges the cowl inner surface at point 1, and then propagates forwards through point 2 to point 3. The separation-induced shock wave reflects from the cowl surface to

impinge back onto the separated region and drives the separation forwards onto the forebody. If the reflected separation shock impinges the centrebody boundary-layer aft of the reattachment point, it cannot influence the upstream flow due to the supersonic flow conditions after reattachment. If the impingement occurs before reattachment, then the shock wave can influence the flow field due to the subsonic flow within the separated region. In this event, the impingement of the reflected separation shock will drive the subsonic flow forwards and propagate the separation to a greater degree. In the worst case, the propagation of the separation could lead to the flow reversing out of the intake and an intake unstart.

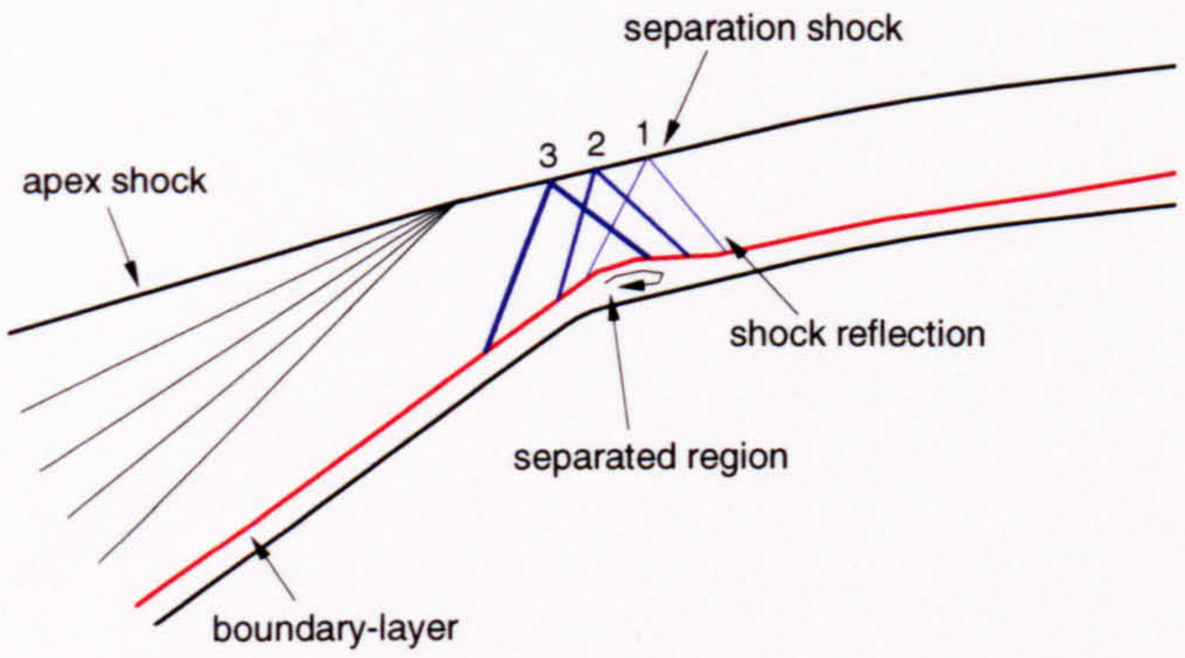


Figure 5.8: Schematic to show the separation mechanism at inlet whereby the separation-induced shock wave reflects from the cowl inner surface to impinge onto the separated flow to drive the separation forwards.

To investigate whether this is a true explanation for the process, a test case was carried out by cutting back the downstream length of the thin-plate cowl such that the separation shock would be unable to reflect from the cowl inner surface to impinge back onto the centrebody boundary-layer.

Figure 5.9 shows (a) density contours and (b) Mach number contours from a turbulent simulation of the intake at Mach 4 - steady-state, with a downstream section of the cowl removed, so as to stop the separation shock from reflecting from the cowl inner surface. The density contours in Figure 5.9 (a) show the boundary-layer separating slightly past the centrebody shoulder, and reattaching downstream in the duct. Separation does not in this case propagate forwards onto the forebody

and lead to a complex interaction. This flow-field should be compared with the full cowl simulation of Figure 5.6 (h). This solution identifies an important phenomenon, whereby the separation can become *self-sustaining*. This can only occur if the separation shock can reflect back, from the cowl, onto the separation bubble. One factor that determines the length of a separation region is the thickness of the approach boundary-layer; the thicker the boundary-layer the longer the separation region. Shyfe is a small scale, low Reynolds number design, so that the forebody boundary-layer is thick compared to the cowl-centrebody annulus, so that it would be prone to this phenomenon. Higher Reynolds number - large scale designs would have a reduced ratio of 'δ_1' to 'H' so that this phenomenon might be avoided.

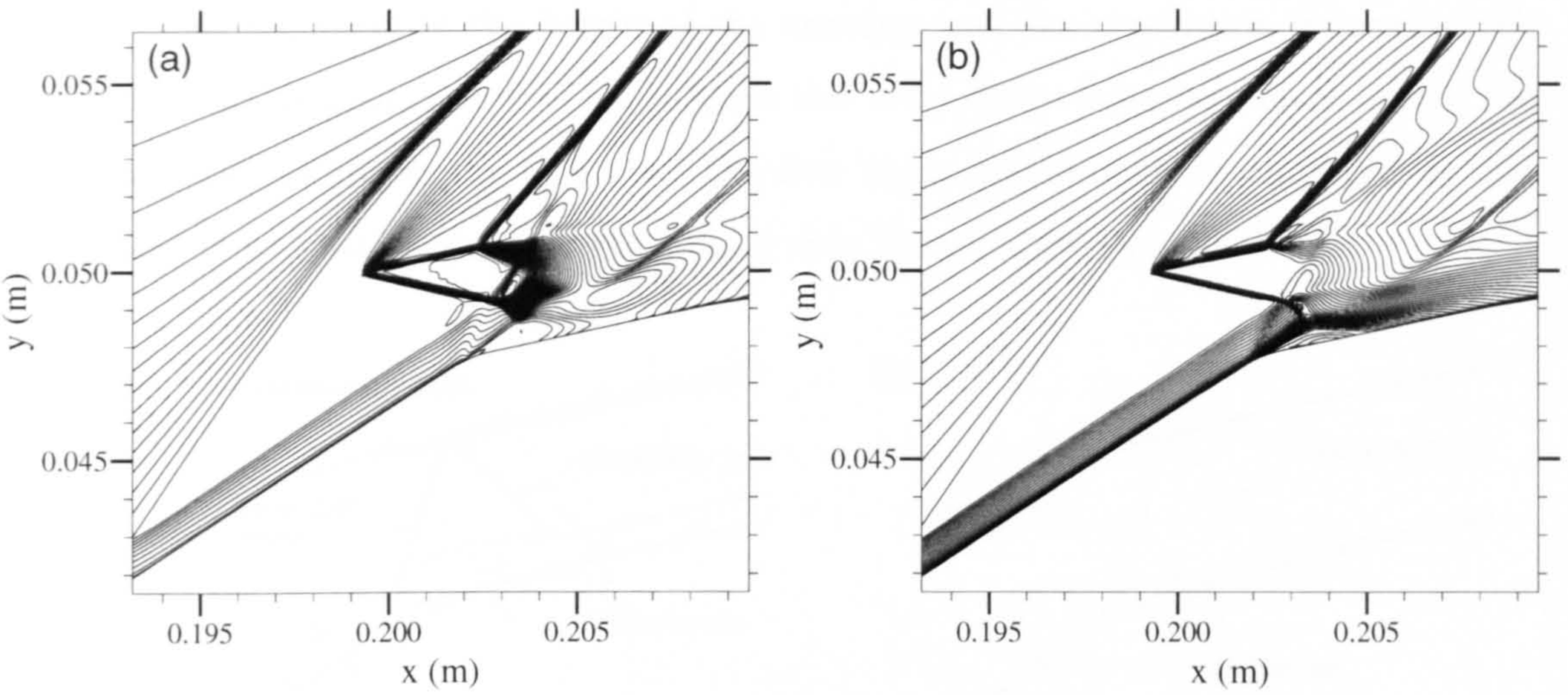


Figure 5.9: CFD Contours from a turbulent simulation of the intake with a 33 degree spike termination angle and a 12 degree cowl and centrebody angle at Mach 4 with a modified cowl; (a) density contours; (b) Mach number contours.

This result could suggest that an expansion fan generated from the cowl inner surface of sufficient strength to cancel out the separation shock, could also be used in a closed duct to deter the separation shock from reflecting and interacting - and hence sustaining the centrebody boundary-layer separation. The complication with implementing this type of control technique is that the position of the separation shock is likely to change as the Mach number increases. At the low Reynolds number Mach 6 condition, the boundary-layer thickness is greater, as shown in Figure 5.4, and this could affect the separation shock strength, which could lead to difficulties

in using an expansion at the cowl inner surface to cancel out the separation shock.

Ratio of δ_1/H

Thus, the critical parameter in this flow field is the ratio of the thickness of the inlet boundary-layer to the inlet annulus. The previous solutions showed that the boundary-layer dominates the flow at inlet, and that the separation shock is able to reflect from the cowl inner surface wall to impinge back onto the centrebody boundary-layer to affect the process. Figure 5.10 illustrates this phenomenon, showing the process for (a) a high ratio and (b) a low ratio of the boundary-layer displacement thickness to the annulus height. In Figure 5.10 (a) the boundary-layer is about a quarter of the height of the annulus, and the separation-induced shock wave reflects from the cowl to impinge the centrebody boundary-layer before the reattachment point. In this case, the flow separation would be amplified by the reflected separation shock impingement onto the separated region.

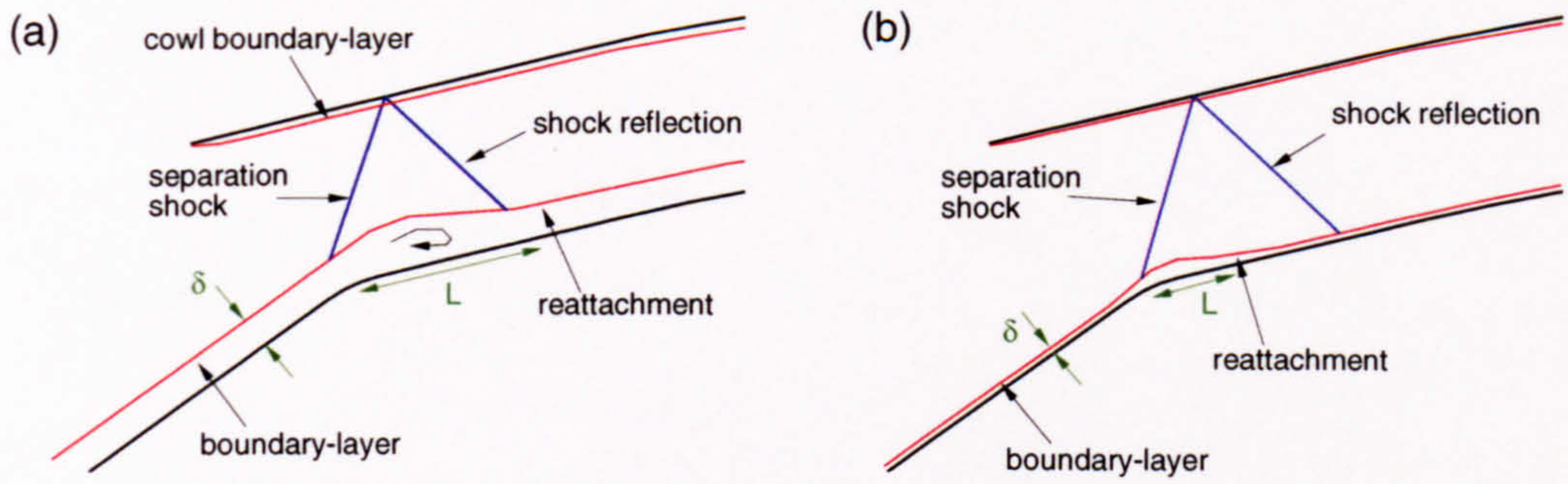


Figure 5.10: Schematics to show the influence of the ratio of the boundary-layer thickness to the annulus height on the flow separation. (a) high ratio (b) low ratio.

Figure 5.10 (b) shows the same system with a low ratio of displacement thickness to the annulus height. The separation shock, induced by the separation at the shoulder reflects from the cowl inner surface wall to impinge the centrebody boundary-layer well aft of the reattachment point. In this case, the reflected separation shock would be unable to affect the process. Hence there should exist a critical boundary-layer displacement thickness for an intake design which escapes this flow phenomenon.

The critical aspect in the Shyfe intake design is the narrow annulus where the boundary-layer is at least a fifth of the flow in the duct at the high Reynolds number condition, and even more so at low Reynolds number conditions. CFD results from work carried out on a hypersonic intake designed by CIAM, Russia[6] were presented at the Russian Hypersonics Workshop which the author attended in February 2003. The CFD results showed an intake with a boundary-layer thickness about a 1/10th of the height of the annulus. Slight separation followed by reattachment of the centrebody boundary-layer occurred after the shoulder. Small separation shocks were induced, but did not reach the cowl inner surface due to the large relative distance involved. With no impingement by the separation shock on the cowl inner surface, and no reflection of the separation shock, the intake displayed good flow quality.

There are a few methods that could be used to stop the separation shock reflecting onto the boundary-layer to promote separation. Firstly, a larger annulus would ensure that any separation-induced shocks would reflect from the cowl inner surface and impinge the centrebody boundary-layer well past the reattachment. As mentioned before, an expansion fan generated from the cowl inner surface could be used to cancel out the separation shock, or obstruct it from reflecting back onto the separated region. The intake could be operated at a higher Reynolds number, at which condition the boundary-layer thickness is thinner, leading to a flow-field type in Figure 5.10 (b).

5.1.4 Effects of small changes in geometry

The spike termination angle θ_1 is then reduced from 33 degrees to 29 degrees and the cowl is maintained at 12 degrees. Figure 5.11 shows density contours from a turbulent simulation of this intake configuration at Mach 4. Figure 5.11 (a) presents a plot from early in the computation where the flow is still converging to its steady-state; Figure 5.11 (f) presents the steady-state solution for this case. Similar to the previous case in Figure 5.6, the boundary-layer separates and induces a separation shock which then drives the separation forwards onto the forebody. This also results

in a slightly detached shock wave at the cowl leading edge. The separation shock impinges the detached shock above the cowl lip and so the slip stream from this interaction does not propagate into the duct.

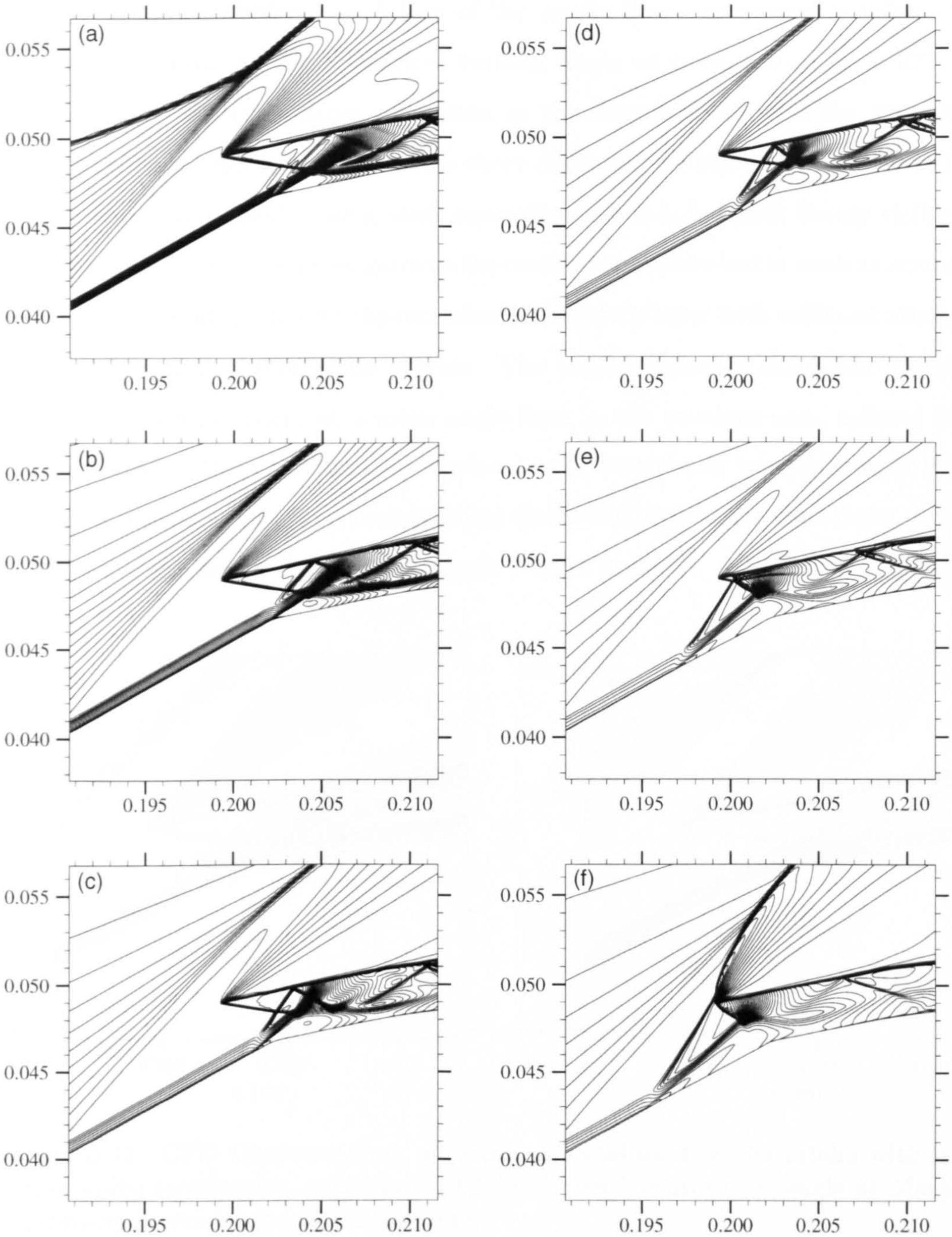


Figure 5.11: CFD Density contours from a turbulent simulation of the intake with a 29 degrees spike termination angle a 12 degrees cowl and centrebody angle at Mach 4; time-dependent contours from (a) to (f).

In this case the flow turning angle at inlet is θ_1 - δ_c = 29 - 12 = 17 degrees. The spike termination is now reduced to 27 degrees and the cowl/centrebody angle is maintained at 12 degrees. Figure 5.12 (a) shows density contours and (b) Mach contours from a turbulent simulation of the intake flow - converged solution - for this case at Mach 4. Here the flow turning angle at inlet is θ_1 - δ_c = 27 - 12 = 15 degrees. There is slight separation as the flow turns around the expansion corner and then reattachment occurs a short distance into the parallel section. The separated region is small, and a weak separation shock is induced, barely visible in the contours. This shock propagates to the cowl inner surface but is weak in strength and does not impinge back on the centrebody boundary-layer with sufficient strength to reinforce the flow separation process. The weak separation shock also radiates from the separation point at a lower angle than in the previous case, reflects from the cowl inner surface and impinges back onto the centrebody boundary-layer aft of the reattachment point. The reattachment shock radiates to the cowl inner surface to cause a slight separation of the boundary-layer there.

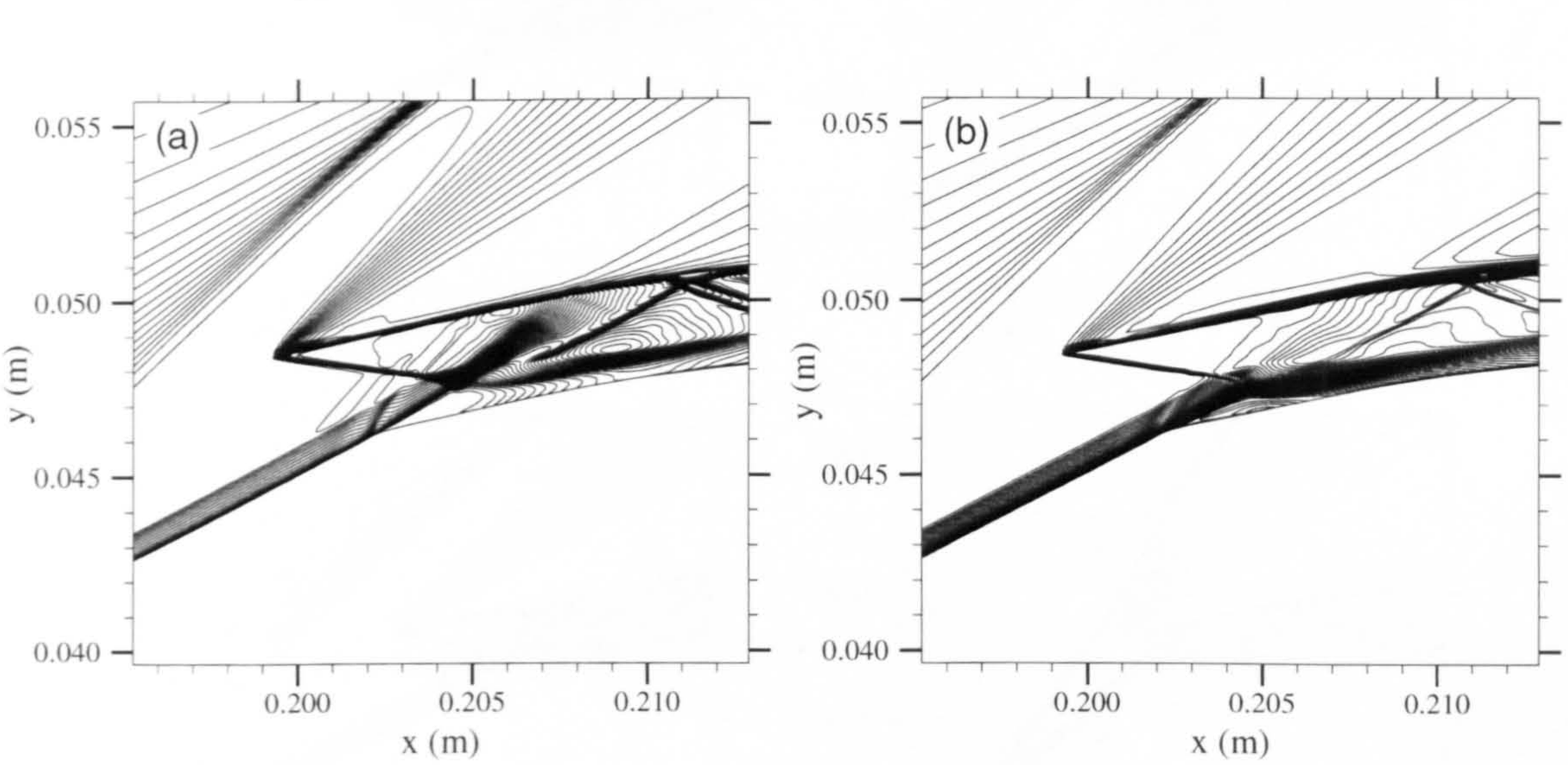


Figure 5.12: CFD Contours from a turbulent simulation of the intake with a 27 degree spike termination angle and a 12 degree cowl/centrebody angle at Mach 4; (a) density contours; (b) Mach contours.

The reduction of the compression angle in the intake has the consequence of reducing the compression ratio, and also the strength of the cowl shock which impinges onto the boundary-layer. This is the main cause for separation at inlet and so reducing the

strength of this shock wave will reduce the likelihood of separation. The penalty for achieving a controlled separation in this geometry results in a reduced compression ratio for the intake which will reduce the downstream performance.

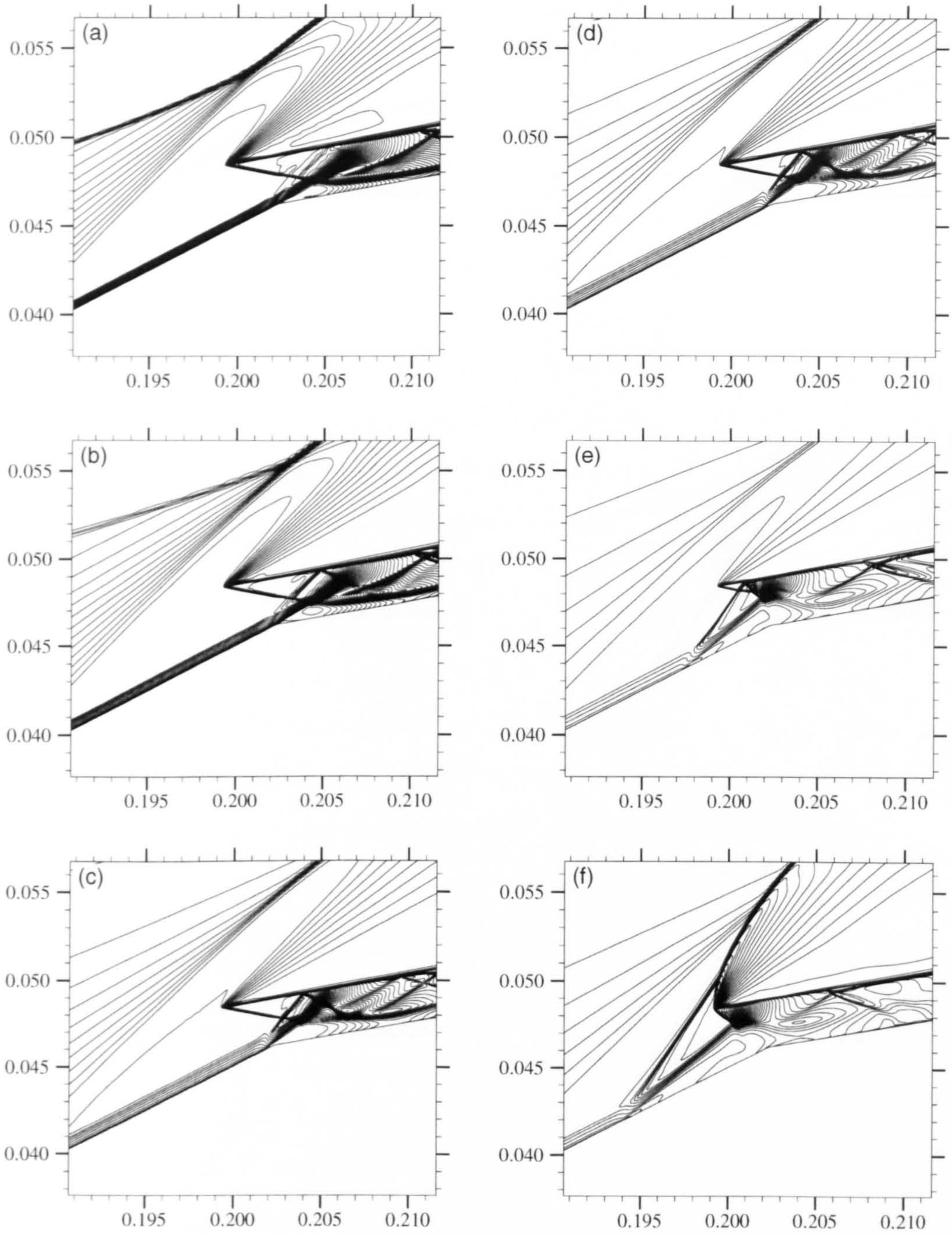


Figure 5.13: CFD Density contours from a turbulent simulation of the intake with a 27 degrees spike termination angle a 10 degrees cowl and centrebody angle at Mach 4; time-dependent contours from (a) to (f).

The spike termination angle is maintained at 27 degrees, and the cowl and centre-body angles are now reduced to 10 degrees, so that the flow turning angle. is now increased back to 17 degrees i.e. θ_1 - δ_c = 27 - 10 = 17 degrees.

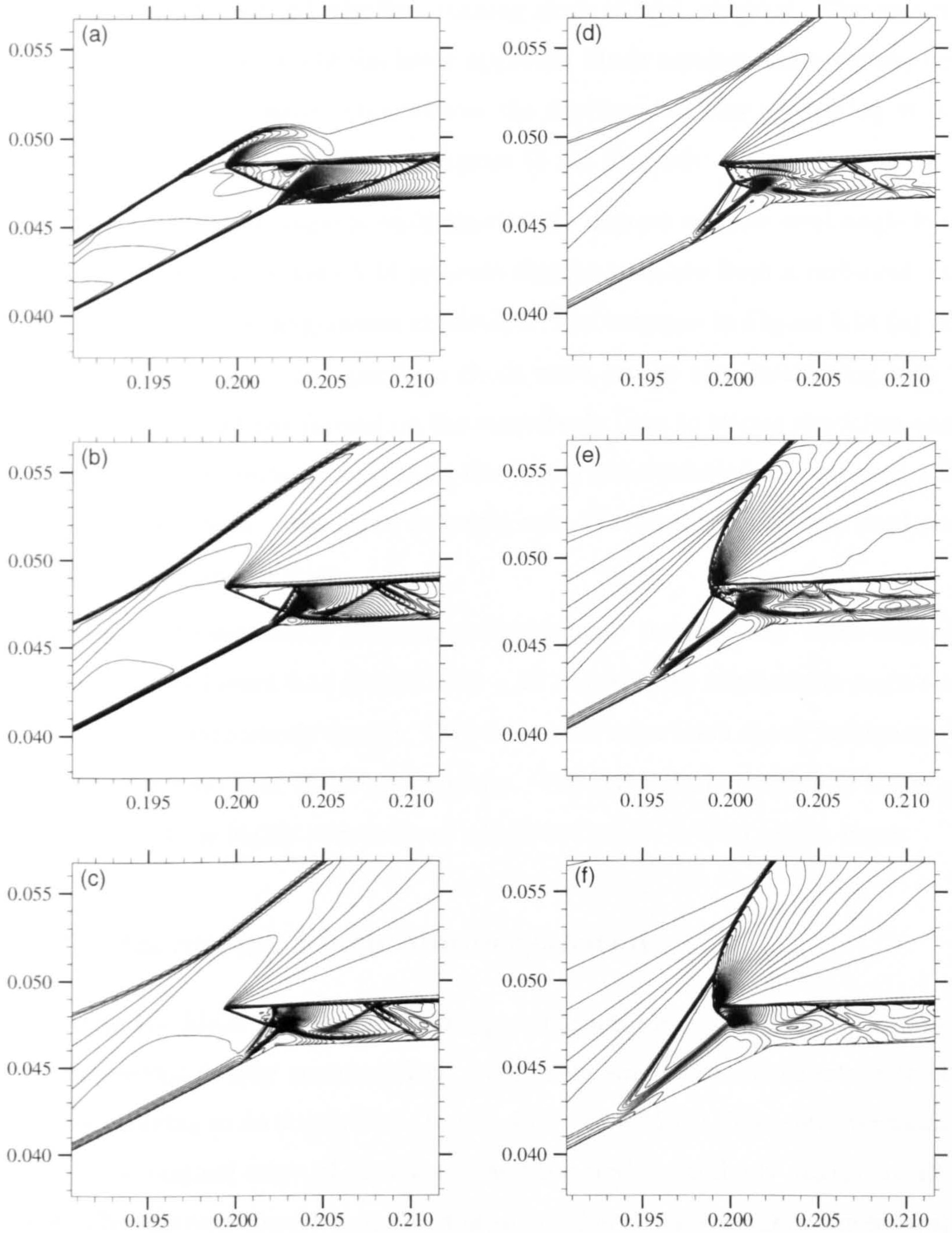


Figure 5.14: CFD Density contours from a turbulent simulation of the intake with a 27 degrees spike termination angle a 2 degrees cowl and centrebody angle at Mach 4; time-dependent contours from (a) to (f).

Figure 5.13 presents density contours for this case, showing boundary-layer separation at the inlet, which then propagates to the forebody. This case can be compared to 29 degrees with 12 degree centrebody/cowl angle because although the spike termination angle is reduced, the flow turning angle is kept constant. The reduction of the spike angle, results in the lower approach Mach number and pressure, hence a weaker cowl shock wave. This reduces the likelihood of flow separation at inlet. However in this case separation propagates to the forebody.

The spike termination angle is maintained at 27 degrees and the cowl angle is now lowered to 2 degrees. Figure 5.14 presents density contours from a turbulent simulation of this intake configuration at Mach 4. The contours in Figure 5.14 (a) show the flow evolving, and the separation shock wave can be seen interacting with the Mach reflection that has formed on the centrebody (due to strong shock/expansion interaction). The contours in (f) show the steady state solution for this case, where the separation shock propagates forwards onto the forebody and the cowl shock detaches at the leading edge.

In this case, the separation propagates further onto the forebody when compared with the case in Figure 5.11 (intake with a 29 degree spike termination angle and a 12 degree cowl/centrebody angle). This causes the separation shock to impinge the cowl shock system well above the cowl lip. The recirculation region is larger and the flow quality is highly non-uniform which will result in even higher losses.

5.1.5 Increasing Mach number/altitude

Increasing the Mach number to off-design condition Mach 5, Figure 5.15 presents time-dependent density contours from a turbulent simulation of the intake to show the flow evolving to its steady state from 5.15 (a) to 5.15 (h). The spike termination angle is the original angle of 33 degrees, and the cowl/centrebody angles are 12 degrees. The contours show the similar flow separation process whereby the separation is *self-sustained* by the impingement of the separation shock onto the recirculation region. The separation propagates onto the forebody, and results in a slight shock detachment at the cowl lip. There is a small region of subsonic flow just behind the

detachment, and a non-uniformity in the flow field in the duct.

Increasing the Mach number to Mach 5.5, Figure 5.16 presents time-dependent density contours for the intake at the on-design condition. The separation shock again drives the separation forwards onto the forebody, and this results in the a large shock detachment at the cowl lip. The separation shock reduces the post-shock Mach number and increases the angle of incidence of the flow. These combine, presumably, to reach detachment conditions at the cowl leading edge. The flow behind the shock detachment is subsonic and reverses out of the inlet and above the cowl. Part of the incoming intake flow is now processed through the detached shock which results in a flow non-uniformity in the duct. The large height of the boundary-layer in this case results in reattachment occurring further downstream in the duct. The duct flow profile is now made up of the boundary-layer, the supersonic compressed flow and the flow processed through the detached shock which results in a very mixed flow entering the isolator. The reversal of flow at the cowl means that the mass capture at inlet is reduced. The flow-field in Figure 5.16 (d) (before the forward propagation of separation) can be compared to a previously presented inviscid case of this flow, chapter 4, Figure 4.19 where the inviscid solution had shown a shock detachment at the cowl lip, but the presence of the boundary-layer in this case causes the shock system to shift up from a Type 2 to a Type 1 interaction to form an attached shock at the cowl lip. The detachment in this case is provoked by the flow separation and not because of the wave interaction at inlet. At Mach 6, the high Mach number-low Reynolds number condition results in a thicker boundary-layer on the forebody as seen in Figure 5.17, than for the Mach 4 case in Figure 5.6. The separation at the shoulder induces a shock wave which impinges the cowl inner surface to cause a slight separation. The separation propagates forwards onto the forebody, to eventually result in a large shock detachment at inlet. This results in flow non-uniformities at inlet, reversed flow and high losses. The small physical scale of the inlet when combined with the low Reynolds number conditions, particularly at Mach 6 can lead to a significant thickness of the boundary-layer compared to the inlet annulus height. All the turbulent viscous simulations presented for this inlet design indicate high aerodynamic losses due to shock-boundary-layer interaction and flow separation.

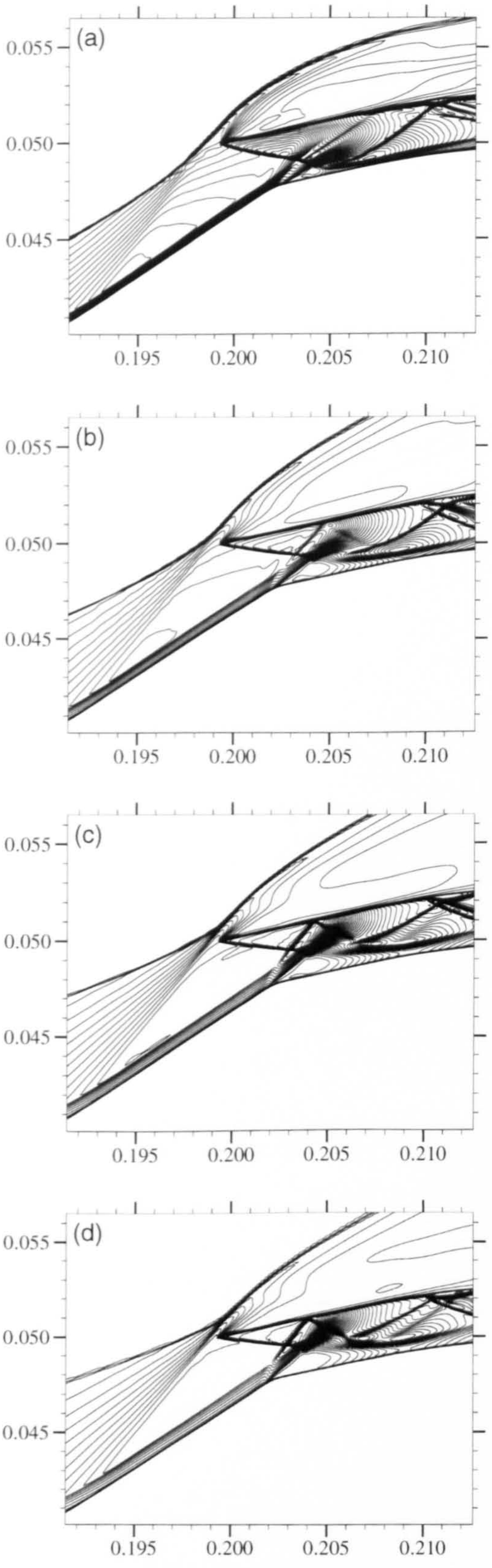


Figure 5.15: CFD Density contours from a turbulent simulation of the intake with a 12 degree cowl/centrebody angle at Mach 5; time-dependent contours from (a) to (h) to show boundary-layer separation on the centrebody.

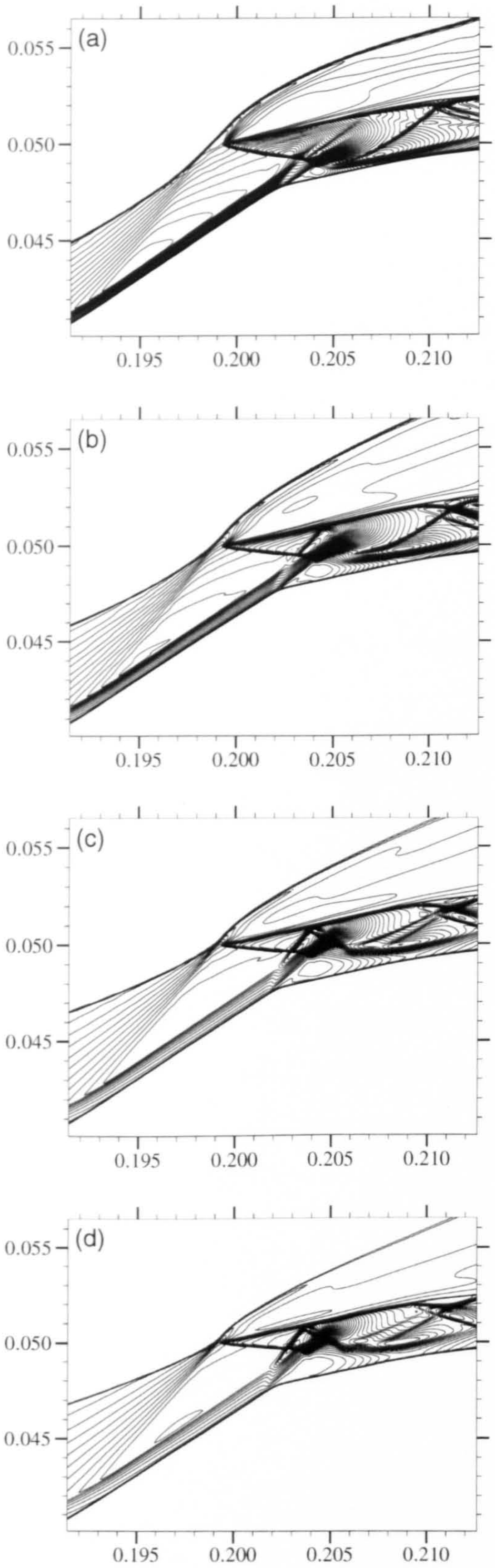


Figure 5.16: CFD Density contours from a turbulent simulation of the intake with a 12 degree cowl and centrebody angle at Mach 5.5; time-dependent contours from (a) to (h) to show boundary-layer separation on the centrebody.

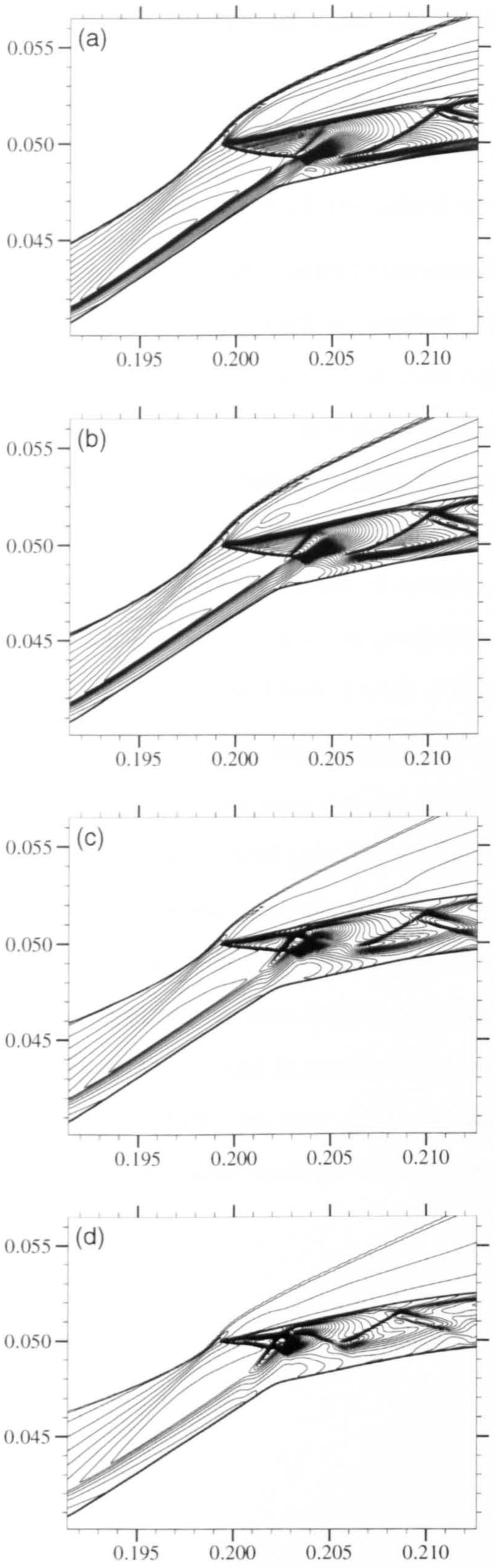


Figure 5.17: CFD Density contours from a turbulent simulation of the intake with a 12 degree cowl and centrebody angle at Mach 6; time-dependent contours from (a) to (h) to show boundary-layer separation on the centrebody.

5.1.6 Effects of cowl blunting

All the computations presented so far in this chapter have modelled the intake with a thin-plate cowl. The blunted cowl is now added to the geometry to investigate the flow characteristics with the added shock system from the blunted lip.

Figure 5.18 presents density contours from a turbulent simulation of the intake with a blunted cowl at Mach 4 (original 33 degrees spike termination angle; 12 degrees cowl/centrebody angle). This case can be compared to the contours in Figure 5.6 (h) which show the steady-state solution for the intake at Mach 4 with a thin-plate cowl. Both cases display similar flow characteristics, with a slight detachment of the cowl shock at the lip. Hence, the detachment is related to the flow turning angle at inlet and not a consequence of cowl bluntness. The flow separates at the centrebody shoulder and the separation propagates forwards onto the forebody as seen for this intake geometry at Mach 4 with a thin-plate cowl.

Figure 5.19 shows density contours from a turbulent simulation of the intake at Mach 5. This flow-field can be compared to the same case with a thin-plate cowl, shown in Figure 5.15 (h). Both cases display similar characteristics. Separation of the boundary-layer occurs after the shoulder and the separation propagates forwards onto the forebody. The separation shock impinges the cowl shock detachment and a shear layer can be seen behind this impingement point. The shock system at inlet is highly complex, and is producing a very non-uniform inlet flow. Clearly these flows are unacceptable as they result in high losses and non-uniformities in the intake duct and methods must be explored to control this type of flow separation at inlet.

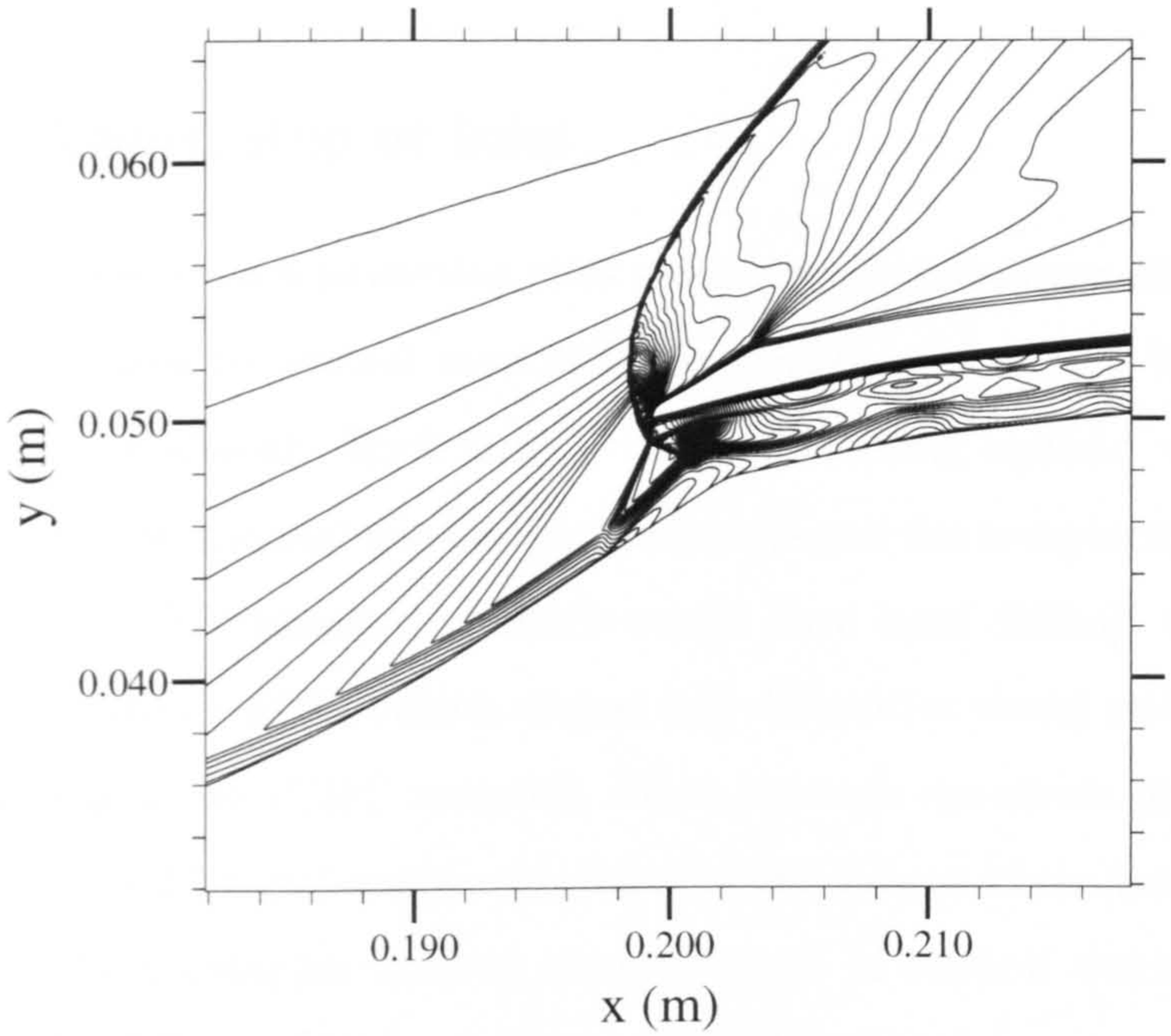


Figure 5.18: CFD Density contours from turbulent simulations of the intake with a 12 degrees blunted cowl at off-design Mach 4.

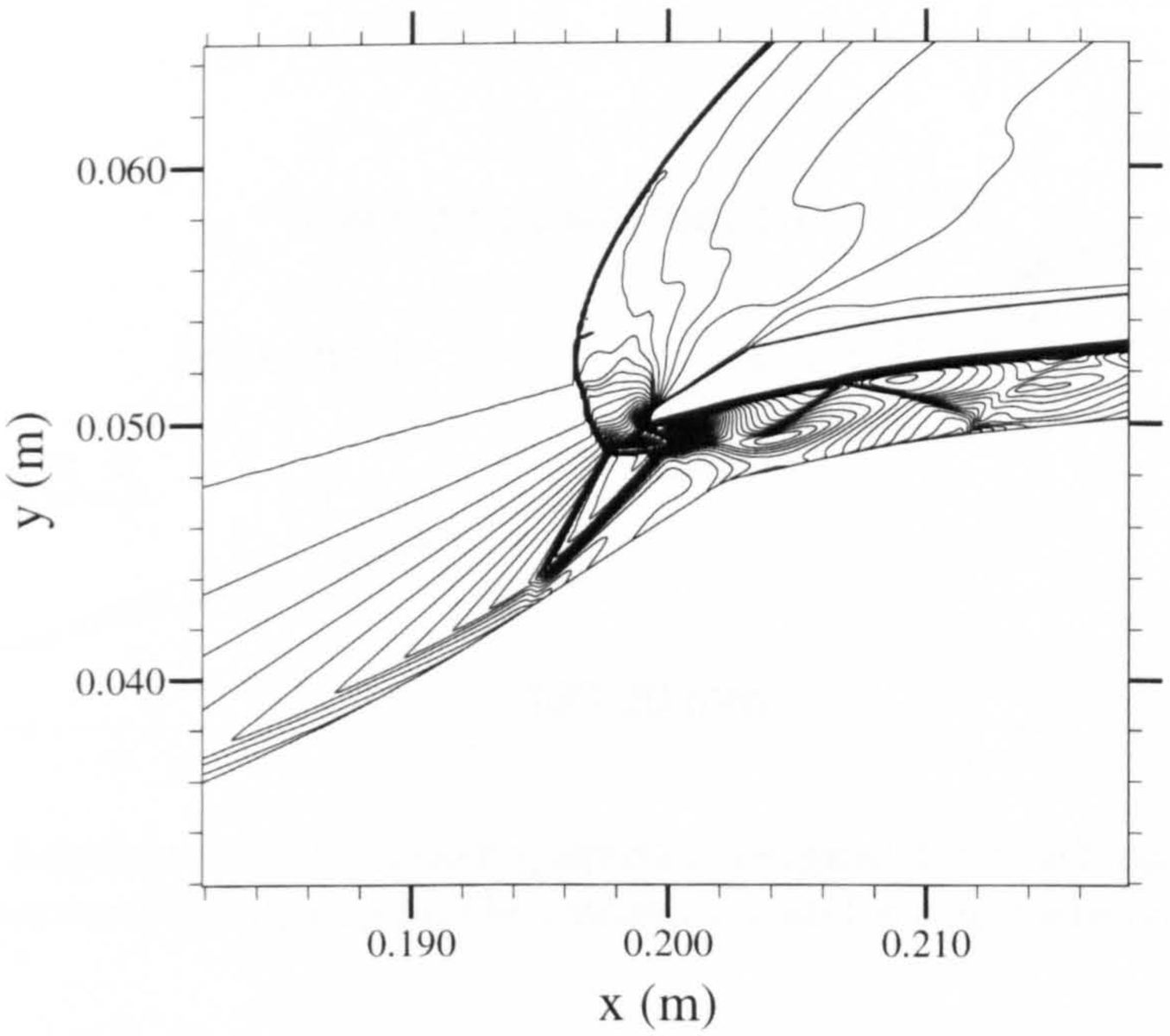


Figure 5.19: CFD Density contours from turbulent simulations of the intake with a 12 degrees blunted cowl at off-design Mach 5.

5.2 Separation control at inlet

5.2.1 Backward step at inlet

Boundary-layer bleeds such as suction slots and diverters have been effectively used in high-speed intakes to control separation as documented in the literature.[53,58] However for the small-scale Shyfe vehicle using a bleeding method would be unfavourable due to the material machining constraints and the complexity of integrating such a system. The bleeding methods would have been difficult to implement because of the small size of the vehicle and as well difficulties would arise in inserting a bleeding system in the C/SiC material, either through the struts or through the cowl. The cowl could be perforated with holes to bleed some of the boundary-layer, but this would be a complex method since the rate of suction would have to be controlled for the different Mach numbers and angles-of-attack.

Simplicity in design is an important feature of the Shyfe demonstrator. For this reason, simple passive techniques are desired to improve boundary-layer robustness, and control flow separation by making small modifications to the geometry.

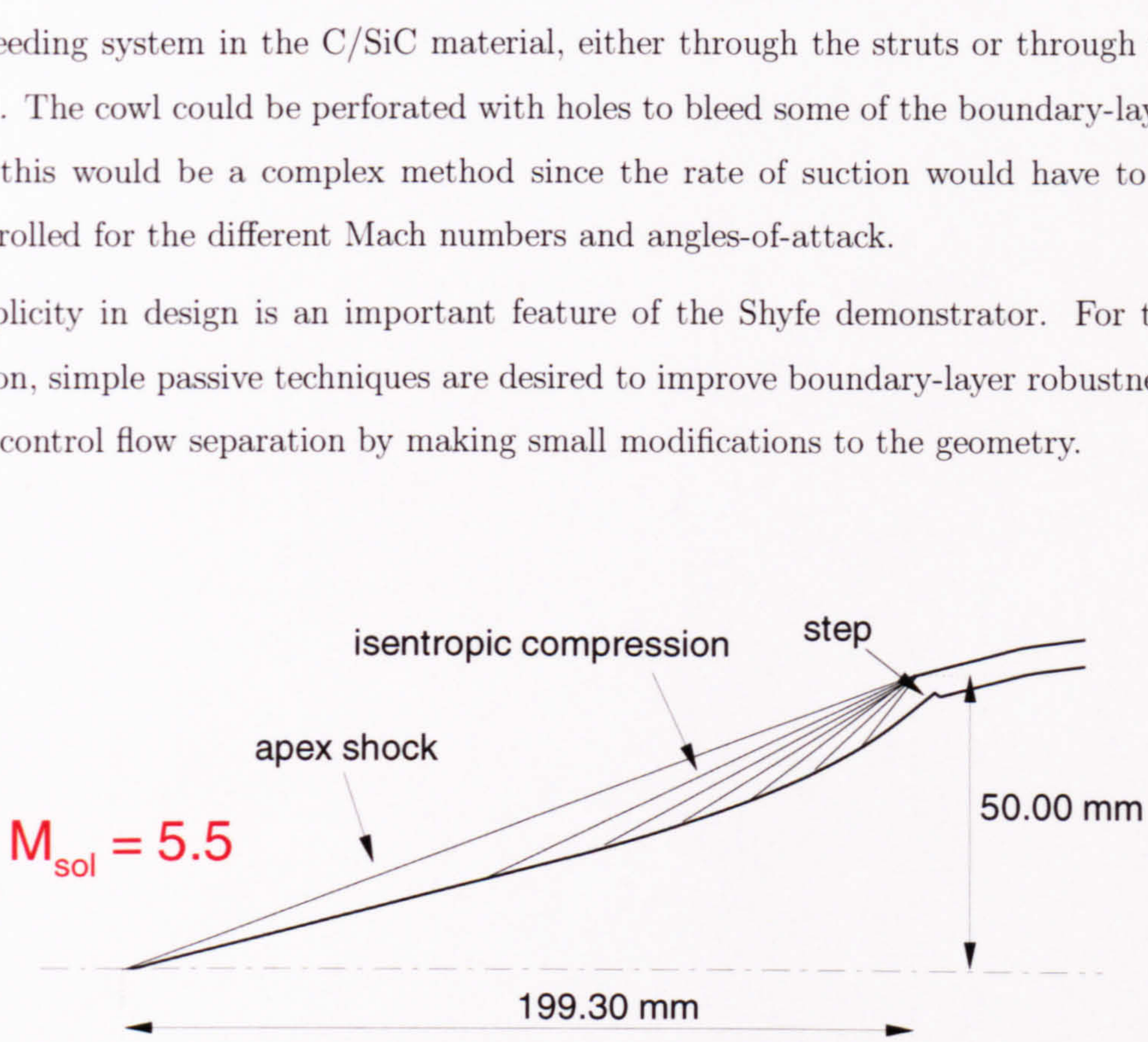


Figure 5.20: Schematic of the intake geometry designed for shock-on-lip at Mach 5.5 with a backward-facing step on the centrebody and a thin-plate cowl.

Vortex traps, or subsonic dumps have long been proved to be an effective method for improving flow in high-speed intakes.[53] This method can be implemented in the Shyfe vehicle by introducing a backward-facing step at the centrebody shoulder.

The step height was arbitrarily chosen as 1mm (approximately the thickness of the incoming boundary-layer), and provides a region in the duct where the boundary-layer is dumped as it turns the corner into the intake duct. Due to machining constraints, the backward-facing step was designed with a 45 degree angle.

Figure 5.20 presents a schematic of the intake, designed for shock-on-lip at Mach 5.5, with the backward-facing step at the centrebody shoulder. The step also provides a obstruction for the terminal shock, should it propagate forwards to the inlet annulus.

5.2.2 Flow system (no cowl)

Initially the intake geometry with a backward-facing step on the centrebody is analysed in the absence of the cowl to form an understanding of the basic incoming flow system. Figures 5.21 (a) presents density contours from turbulent simulations of the centrebody and step at off-design condition Mach 4. The contours show the apex shock and compression fan focusing above the given cowl lip position. The turbulent boundary-layer is attached at the forebody and separates after the step/expansion corner. The boundary-layer then reattaches after the step, with a small recirculation region just aft of the step. There are pockets of subsonic flow, and a pressure drop in the region behind the step with a reversal of flow. The Mach number in the constant pressure zone, just before the shoulder is approximately 2.37. The flow then accelerates around the step/expansion corner to approximately Mach 3.1.

Separation of the boundary-layer at the step corner does not induce a shock wave, as the boundary-layer is pulled downwards toward the base region of the step, and hence preventing a displacement from which a shock wave could potentially be generated. Reattachment of the boundary-layer past the recirculation region induces a reattachment shock and the post-shock flow then decelerates to approx. Mach 2.8.

Figure 5.21 (b) shows the same system at Mach 5, where the apex shock and compression fan now focus closer to the forebody. Similar features are seen in this case to the case at Mach 4, with the boundary-layer separating past the step/expansion corner, and then reattaching at the centrebody and inducing a shock wave at the reattachment point. The recirculation region is slightly larger for the Mach 5 case.

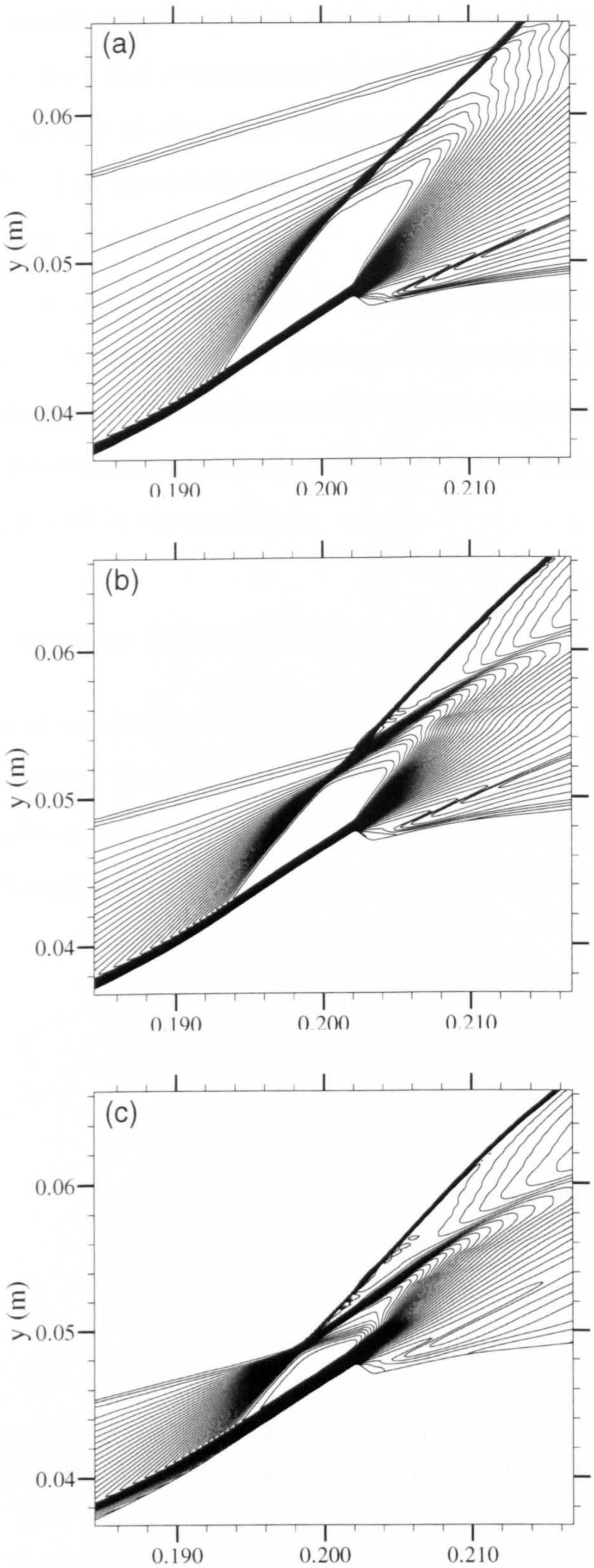


Figure 5.21: CFD Density contours from a turbulent simulation of the intake with a backward-facing step (no cowl) at (a) Mach 4 (b) Mach 5 and (c) Mach 6.

Figure 5.21 (c) presents density contours at Mach 6. The thicker forebody boundary-layer and the apex shock and compression fan focus even closer to the forebody. The boundary-layer separates at the step/expansion corner, and then reattaches again on the centrebody. The separated region is larger at Mach 6, and a reattachment shock wave is seen at that point.

As the Mach number increases from 4 to 6, the triple point system focuses closer to the centrebody and the expansion fan generated from the triple point increasingly affects the step/expansion. In all these cases, the flow separation is a consequence of the step with the contours giving an indication of the natural scale of separation in the absence of a cowl in the geometry.

5.2.3 Flow system (thin-plate cowl)

The thin-plate cowl is then introduced into the flow-field. Figure 5.22 shows a schematic of the various flow-field characteristics in the complex system generated by the cowl/step/boundary-layer system. The schematic shows the apex shock and compression fan focusing to a point and then radiating as a focused shock.

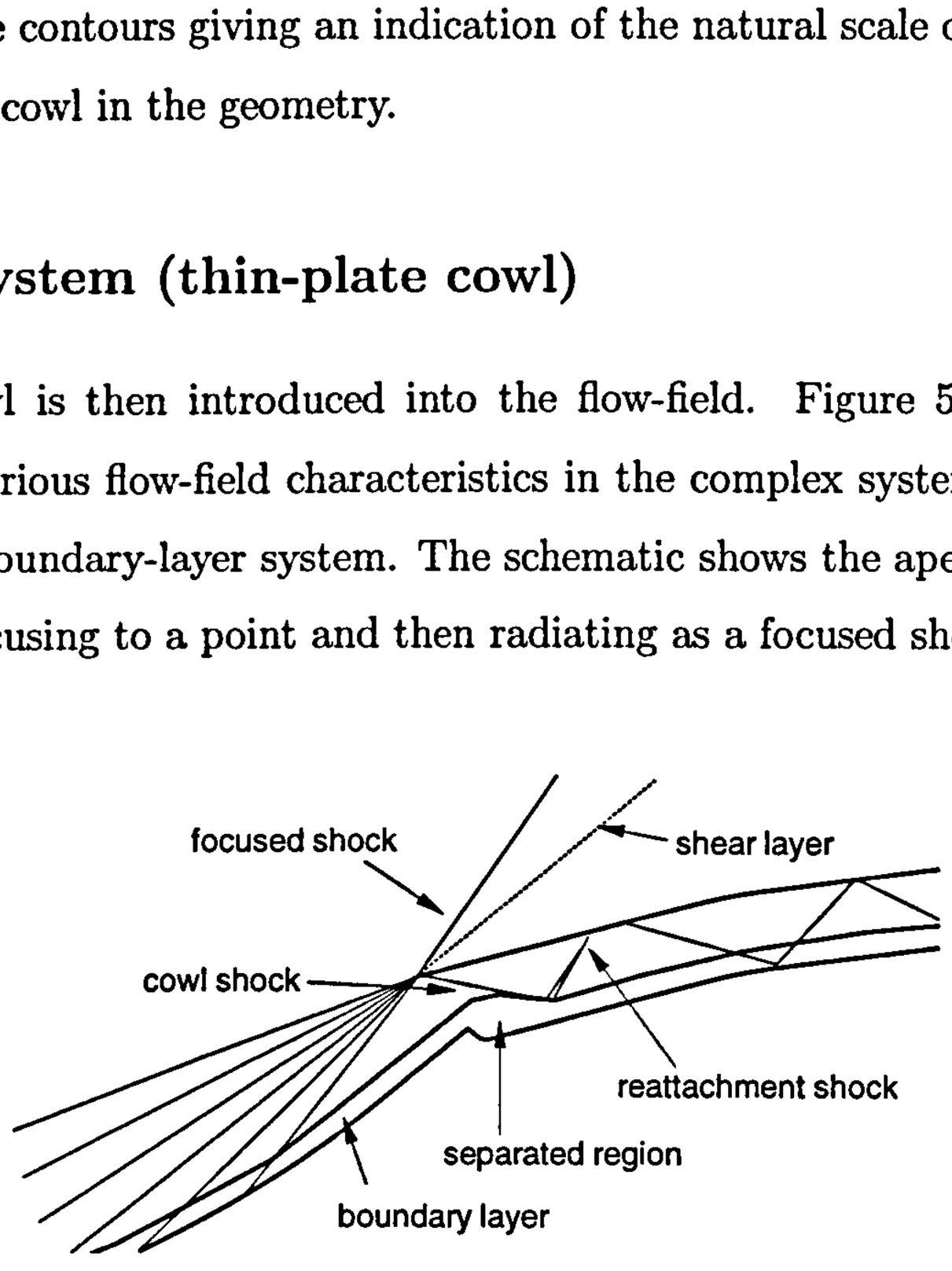


Figure 5.22: Schematic of the flow phenomena in the intake with a backward-facing step and a thin-plate cowl, showing the cowl/step/boundary-layer flow system.

The forebody boundary-layer can separate at the step corner with reattachment on the centrebody into the duct. Reattachment of the centrebody boundary-layer can induce a reattachment shock wave which can then reflect from the cowl inner surface

and propagate in this manner downstream. The impingement of the reattachment shock wave onto the cowl inner surface can lead to separation of the cowl boundary-layer and further complicate the system. The cowl shock wave can also influence this system as it can interact with the expansion fan at the step corner, and lead to boundary-layer separation and separation shock waves.

The triple point can focus above or below the cowl lip, and can determine whether the reflection of the shock at the cowl lip results in shock attachment or detachment. The shear layer can also lie below or above the cowl depending on the positioning of the triple point with the cowl lip. All these flow structures interact with each another and will determine the quality of the flow entering the inlet and will eventually affect the downstream performance of the intake.

This system at inlet will eventually determine the quality of flow entering the combustor in terms of pressure recovery and flow uniformity. With the numerous factors that can determine the eventual characteristics of this particular flow field, it becomes increasingly difficult to determine the cause and effect of such flows.

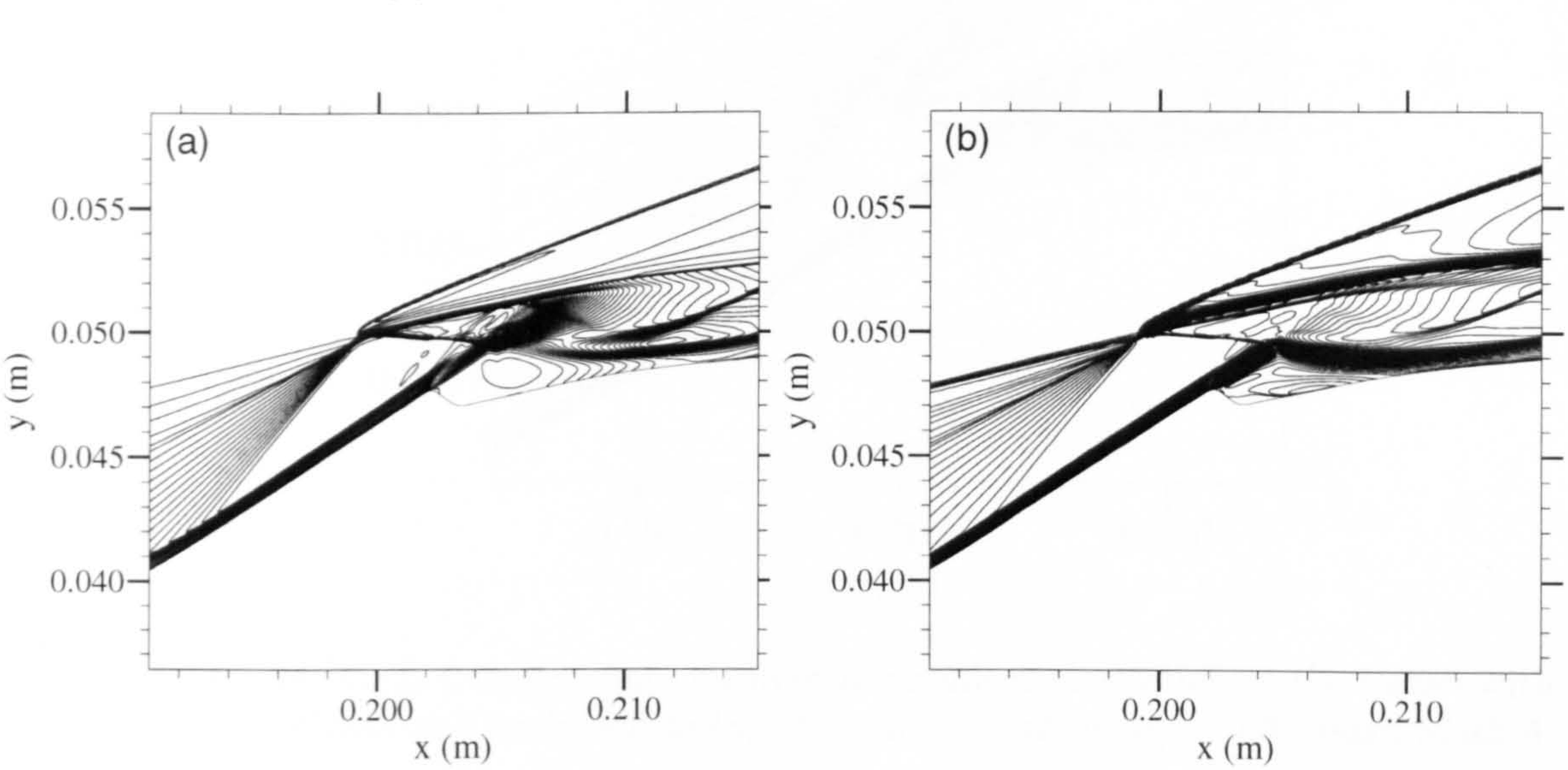


Figure 5.23: CFD Contours from a turbulent simulation of the intake with a 33 degree spike termination angle and a 12 degree cowl and centrebody angle with a backward-facing step at Mach 5.5; (a) density contours; (b) Mach number contours.

The thin-plate cowl of 12 degrees is introduced into the geometry, and turbulent simulations are carried out for the various flight conditions. The first interesting

case to study the cowl/step/boundary-layer system, is the intake flow at on-design conditions. The inviscid results for the same geometry with no step at the centrebody had shown a slight shock detachment at the cowl lip due to the triple point focusing below the cowl lip (Type 2 interaction).

Figure 5.23 presents (a) density contours and (b) Mach number contours from a turbulent simulation of the intake with a step and thin-plate cowl at on-design Mach number 5.5. The presence of the boundary-layer in the flow field causes the shock system to shift upwards to form an attached shock at the cowl lip (Type 2 to Type 1 interaction). This flow field should be compared to the turbulent simulation of the intake with no step on the centrebody at Mach 5 shown in section 5.1.5.

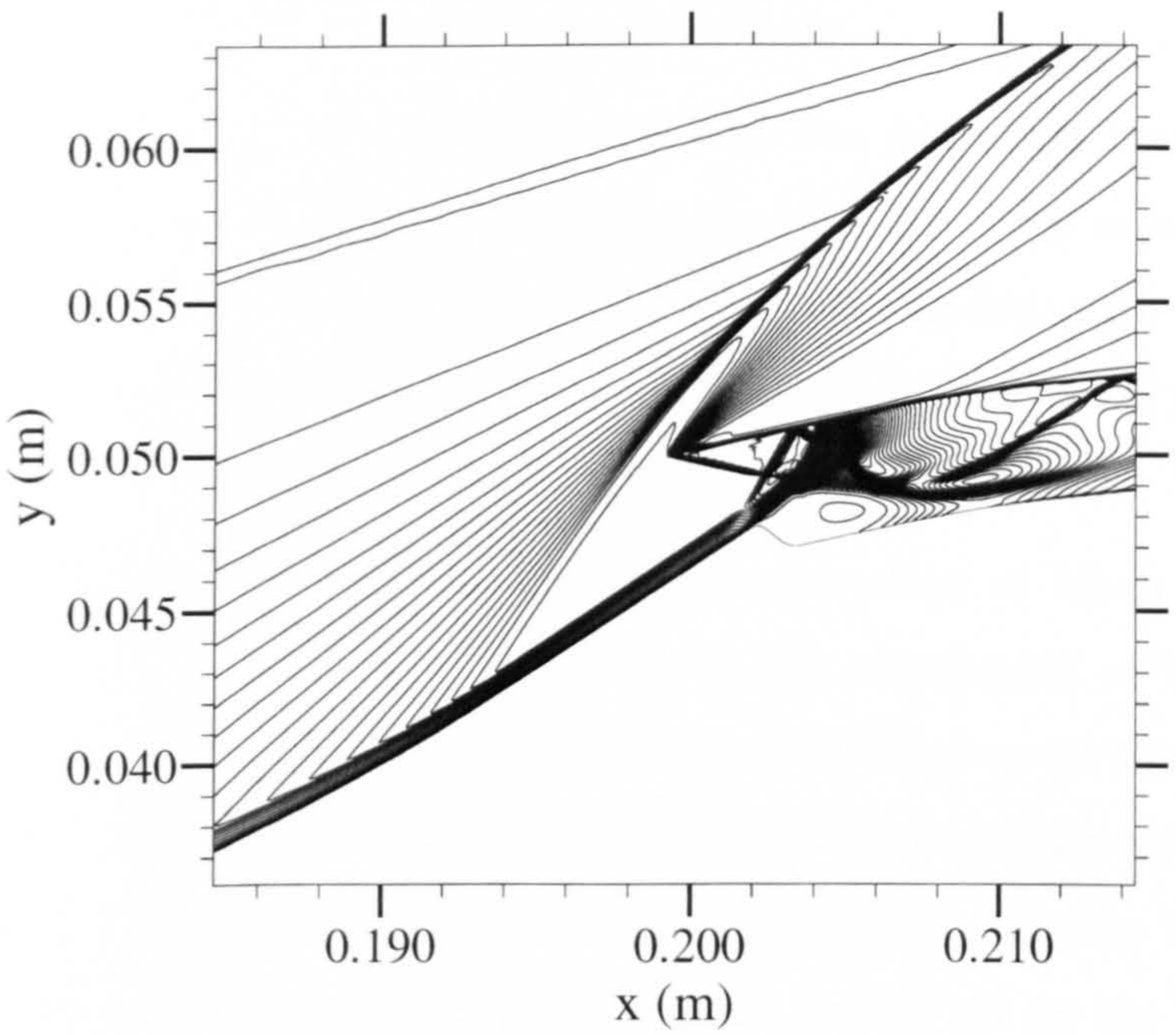


Figure 5.24: CFD Density contours from a turbulent simulation of the intake with a 12 degree cowl and backward-facing step on the centrebody at off-design Mach 4.

For that case, the boundary-layer separation led to a detached shock system at inlet and this resulted in a highly non-uniform inlet flow. The density contours in Figure 5.23 show the boundary-layer separating past the step/expansion corner, and inducing a weak separation shock. The cowl shock wave interacts with first the induced shock, and then with the corner expansion, resulting in a *curved* cowl

shock. There is a large region of recirculation just behind the step, and the flow then reattaches and induces a reattachment shock. The cowl inner surface boundary-layer is also seen in the contours. The flow field characteristics are then studied for the various off-design conditions from Mach 4 to 6.

Figure 5.24 plots density contours from a turbulent computation of the intake with the backward-facing step and a thin-plate cowl at below-design Mach 4. The contours again show the characteristic below-design flow where the main shock focuses high above the cowl lip, causing mass flow spillage. The boundary-layer is attached at the forebody and separates at the step, inducing a separation shock. The separation shock reflects from the cowl inner surface and with sufficient strength can cause separation of the boundary-layer there. The boundary-layer reattaches downstream of the step and this generates a reattachment shock.

Figure 5.25 shows a density contour plot of this flow system at Mach 5. The apex shock and compression fan focus closer to the cowl lip. The attached turbulent boundary-layer separates past the step, and then reattaches, with a recirculation region behind the step. The separation at inlet is controlled by the presence of the step, and a good quality flow enters the duct.

Figure 5.26 presents density contours of the intake flow at Mach 6. The triple point impinges the cowl lip and leads to a shock attachment at the cowl. The density contours show the thicker turbulent boundary-layer on the forebody separate at the step/expansion corner. At this condition, the boundary-layer thickness is significant in comparison to the duct height and is dominating the inlet flow. The cowl shock interacts with the corner expansion further aft as the Mach number increases and intersects the boundary-layer as it separates but this interaction does not induce a separation shock. The boundary-layer then reattaches downstream, with a recirculation region just behind the step.

The separated region is larger for the Mach 6 case than for the lower Mach number cases. Reattachment of the boundary-layer induces compression-like Mach waves which radiate as a reattachment shock wave. The reattachment shock then reflects in the duct as a series of oblique shocks. The presence of the step in this geometry leads to the separation of the boundary-layer from the centrebody surface.

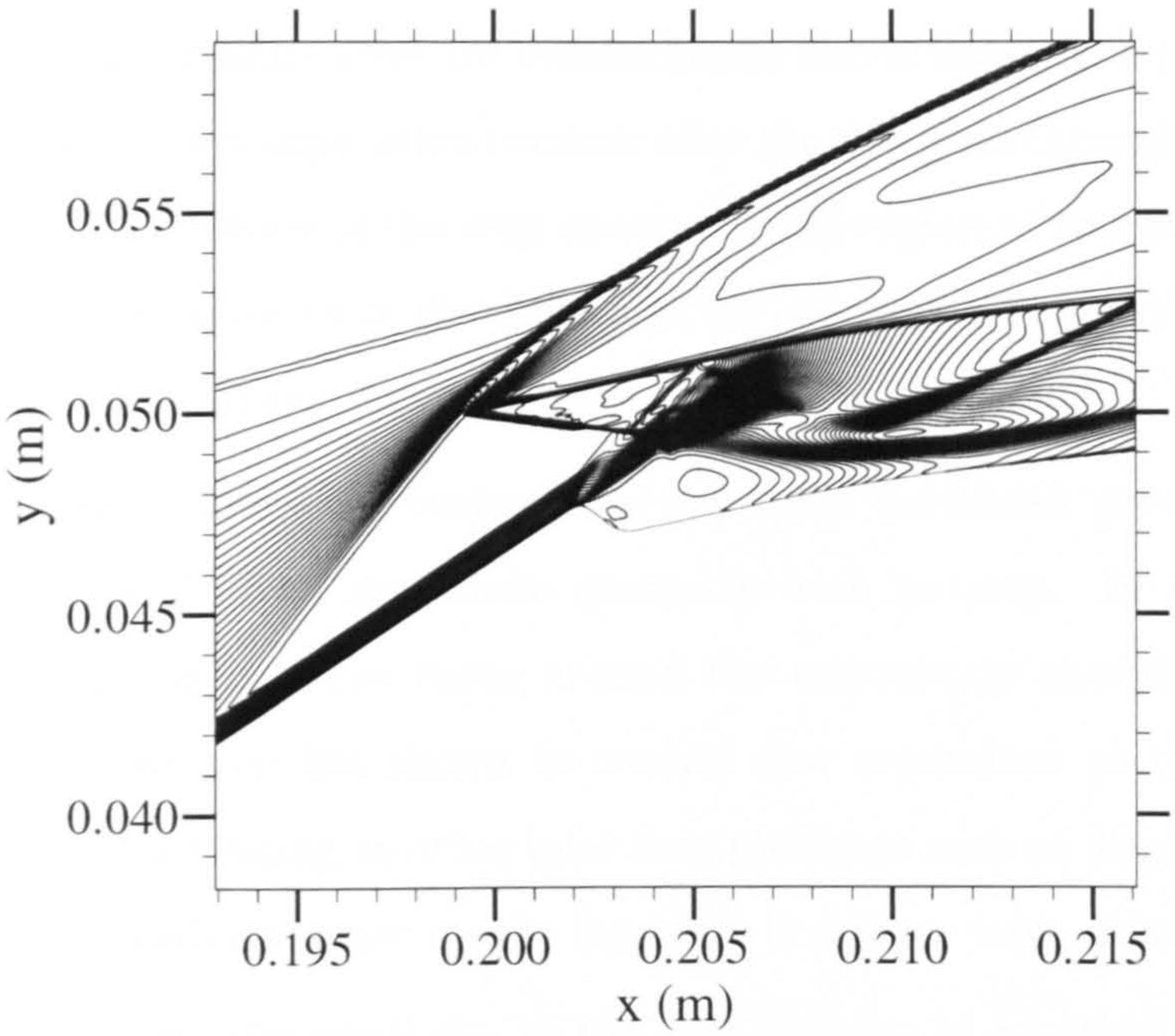


Figure 5.25: CFD Density contours from a turbulent simulation of the intake with a 12 degree cowl and backward-facing step on the centrebody at off-design Mach 5.

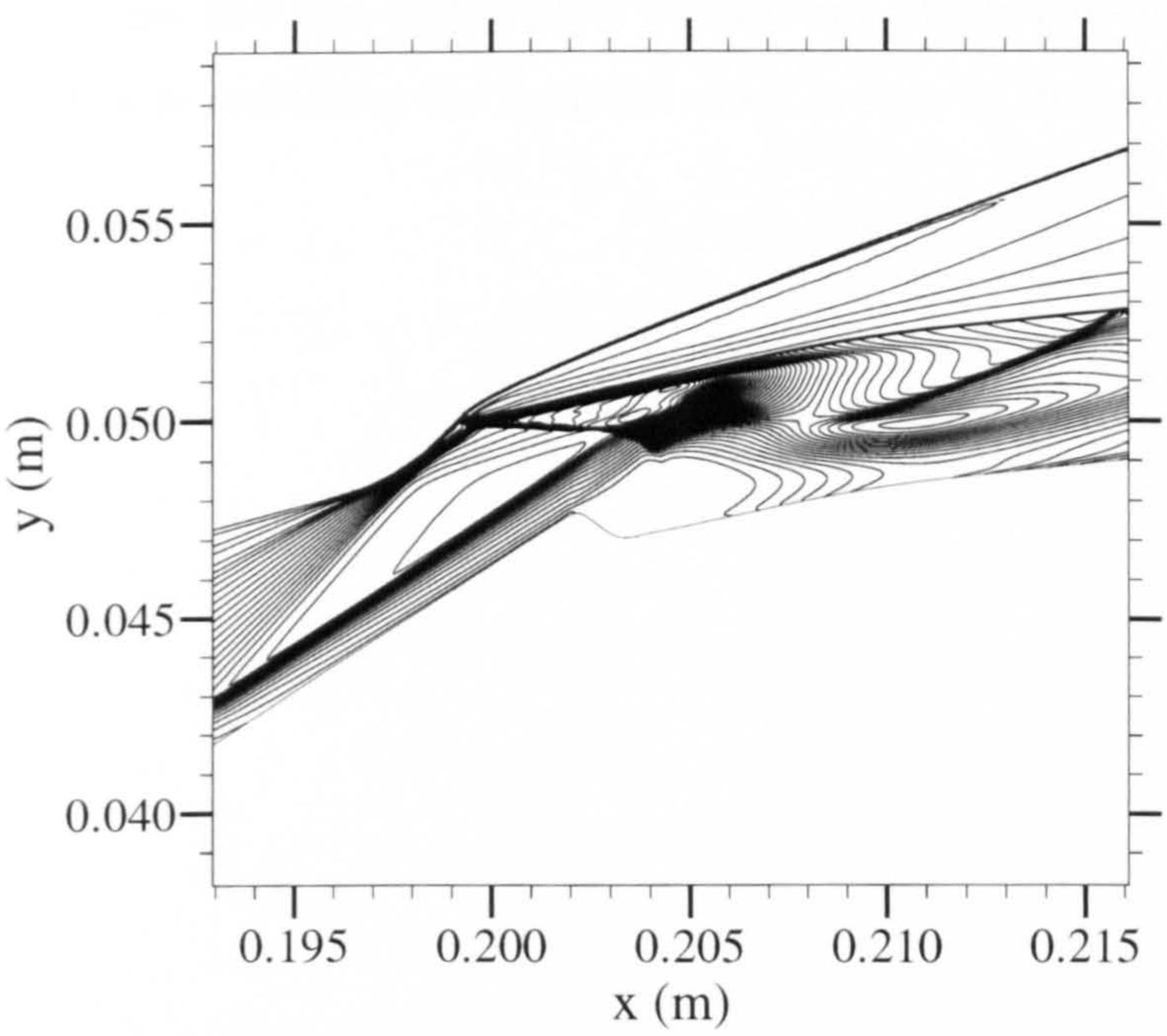


Figure 5.26: CFD Density contours from a turbulent simulation of the intake with a 12 degree cowl and backward-facing step on the centrebody at off-design Mach 6.

As the flow passes through the expansion fan at the step corner, it loses pressure and then rapidly gains pressure after the reattachment shock wave. The presence of the step attenuates any flow separation because after the flow goes through an expansion at the corner, the presence of the step causes a small region of recirculation behind it, with a lower pressure than the stream of air above it. This region of lowered pressure promotes boundary-layer reattachment at the centrebody.

These simulations should be compared to the cases presented previously in this chapter in section 5.1.5 of the intake geometry with no step. In all cases large separation occurs as the flow turns around the centrebody shoulder. Although the presence of the step has shown to control flow separation at the centrebody shoulder, it is not attending to other inlet flow problems such as Mach reflection on the centrebody, Mach reflection on the forebody and wave interactions.

As mentioned before, the small size of the inlet annulus is a critical aspect of this design, because the inlet boundary-layer and flow separations dominate the flow entering the duct, and will affect intake flow quality, intake efficiency and downstream performance. The boundary-layer dominates the intake duct flow, and any flow separation will increase flow non-uniformities downstream. Flow non-uniformities can lead to difficulties in stabilising the terminal shock system in the ramjet isolator.

5.3 i1533 intake analysis

The following section presents computations for two intake geometries designed during the final phase of the Shyfe 1 program. The intakes are modelled with a supersonic outflow condition at three freestream conditions, given in Table 5.1. Details of both intake geometries, the i1533 and i1530 can be found in Appendix A.2.

M_∞	Pressure	Temperature	Unit Re (m^{-1})	P_{comb} (bars)
4.0	12.00 KPa	217 K	1.6437 x 10^7	7.8
5.0	8.000 KPa	217 K	1.3698 x 10^7	8.6
6.0	0.890 KPa	228 K	1.7135 x 10^6	1.2

Table 5.1: Test conditions for the i1533 and i1530 intake.

The first results presented are for the i1533 intake which is designed for shock-on-lip condition at Mach 5.5. The initial cone angle of the earlier variants was increased from 12 to 15 degrees followed by the isentropic compression surface. This is done to increase the distribution of the compression on the forebody between the apex shock generated by the cone and the isentropic compression fan, and hence improve boundary-layer characteristics at inlet. The higher cone angle is also expected to improve the flow at incidence, as an increased angle will reduce the cross-flow on the intake lee-side and reduce the likelihood of flow separation by increasing boundary-layer robustness. The spike termination angle is 33 degrees and the flow is then turned into a 12 degree cowl/centrebody parallel duct of 105.5mm length. The backward-facing step is incorporated to control flow separation as shown previously, and the annulus height is increased to 6.9mm.

Figure 5.27 presents density contours from a turbulent simulation of the intake at off-design condition Mach 4. Transition is imposed at 50mm from the spike leading edge. The apex shock and compression fan focus above the cowl lip causing mass flow spillage. A bow shock is generated at the cowl leading edge, and this cowl shock interacts with the shoulder expansion as it impinges onto the centrebody.

The boundary-layer separates past the step/expansion corner creating a region of recirculation just behind the step. The flow then reattaches at approximately 0.167m,

generating a reattachment shock wave at this point. The reattachment shock reflects from the cowl inner surface in a series of oblique shocks in the parallel duct. Separation at the step corner generates a slight separation shock which reflects onto the cowl inner surface. This interaction causes a slight flow separation of the cowl inner surface boundary-layer.

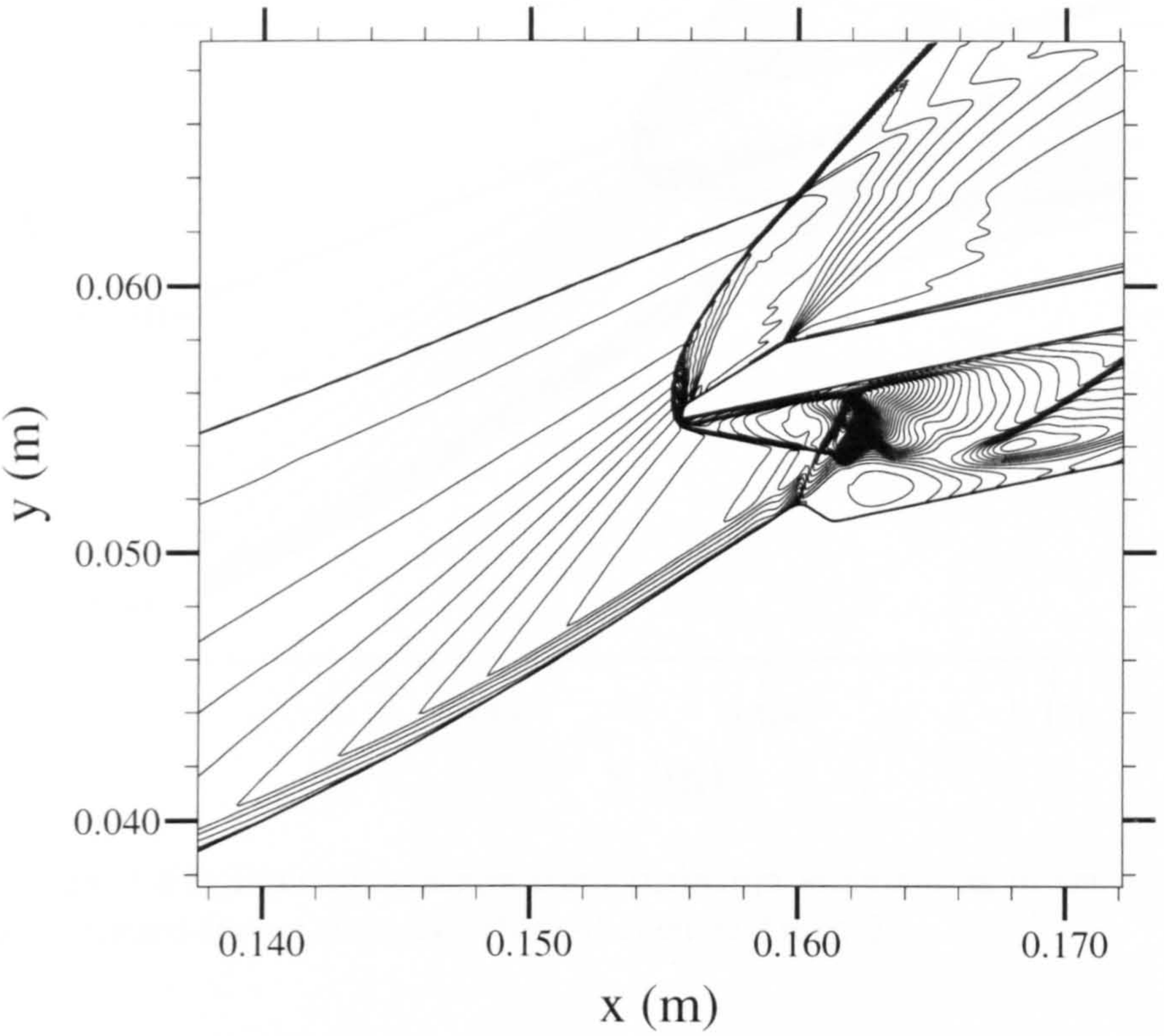


Figure 5.27: CFD Density contours from a turbulent simulation of the i1533 intake with a backward-facing step and blunted cowl at Mach 4.

Figures 5.28 present density contours of the intake at Mach 5. As the freestream Mach number is slightly below the design Mach number, the apex shock and compression fan focus closer above the cowl, reducing the mass flow spillage. The boundary-layer separates at the step/expansion corner and reattaches further downstream at approximately 0.198m. The cowl shock is slightly detached and interacts with the centrebody boundary-layer and expansion fan at the step corner. The separation does not induce a separation shock as seen at Mach 4. At Mach 5 the recirculation region is larger and the reattachment of the boundary-layer is gradual

compared to at Mach 4. The gradually reattaching flow generates a weak compression fan which radiates as a reattachment shock.

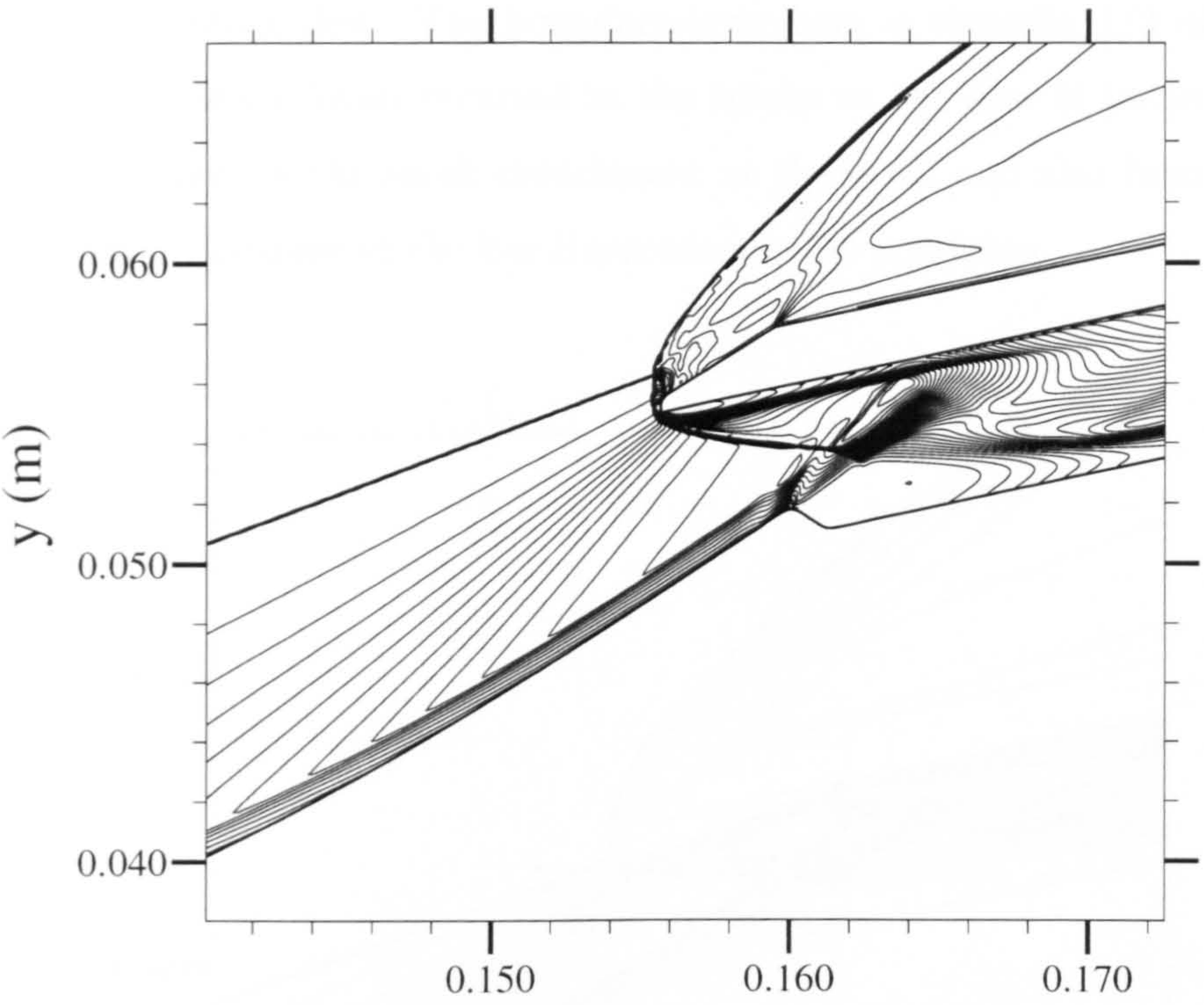


Figure 5.28: CFD Density contours from turbulent simulations of the i1533 intake with a backward-facing step and blunted cowl at Mach 5.

Figure 5.29 presents density contours from a turbulent simulation of the intake at Mach 6. The conditions at Mach 6 are above-design, and so the apex shock and compression fan focus below the cowl lip. The focused shock that radiates from the triple point aims towards the cowl lip. The Mach number behind the focused shock wave, which is in now the approach Mach number (M_1), is lower than the post-compression fan Mach number, and this leads to a detachment of the shock wave as it reflects from the cowl. The large flow turning angle at the corner also contributes to this result. The region of the flow behind the detached shock is subsonic which then results in a mixed subsonic/supersonic flow entering the duct.

The boundary-layer separates at the step/expansion corner and reattaches downstream inducing a reattachment shock. The thicker incoming boundary-layer results

in the larger separated region. The separation of the flow does not induce a separation shock, which is due to the weaker cowl shock as a result of detachment. This flow-field highlights the issue of the annulus being too narrow as the boundary-layer dominates the intake flow. The boundary-layer here is virtually 1/3 of the duct height. The pressure losses incurred in the intake as the flow is turned into the duct are increased by the shock detachment at the cowl, and also from the large boundary-layer thickness at the low Reynolds number condition.

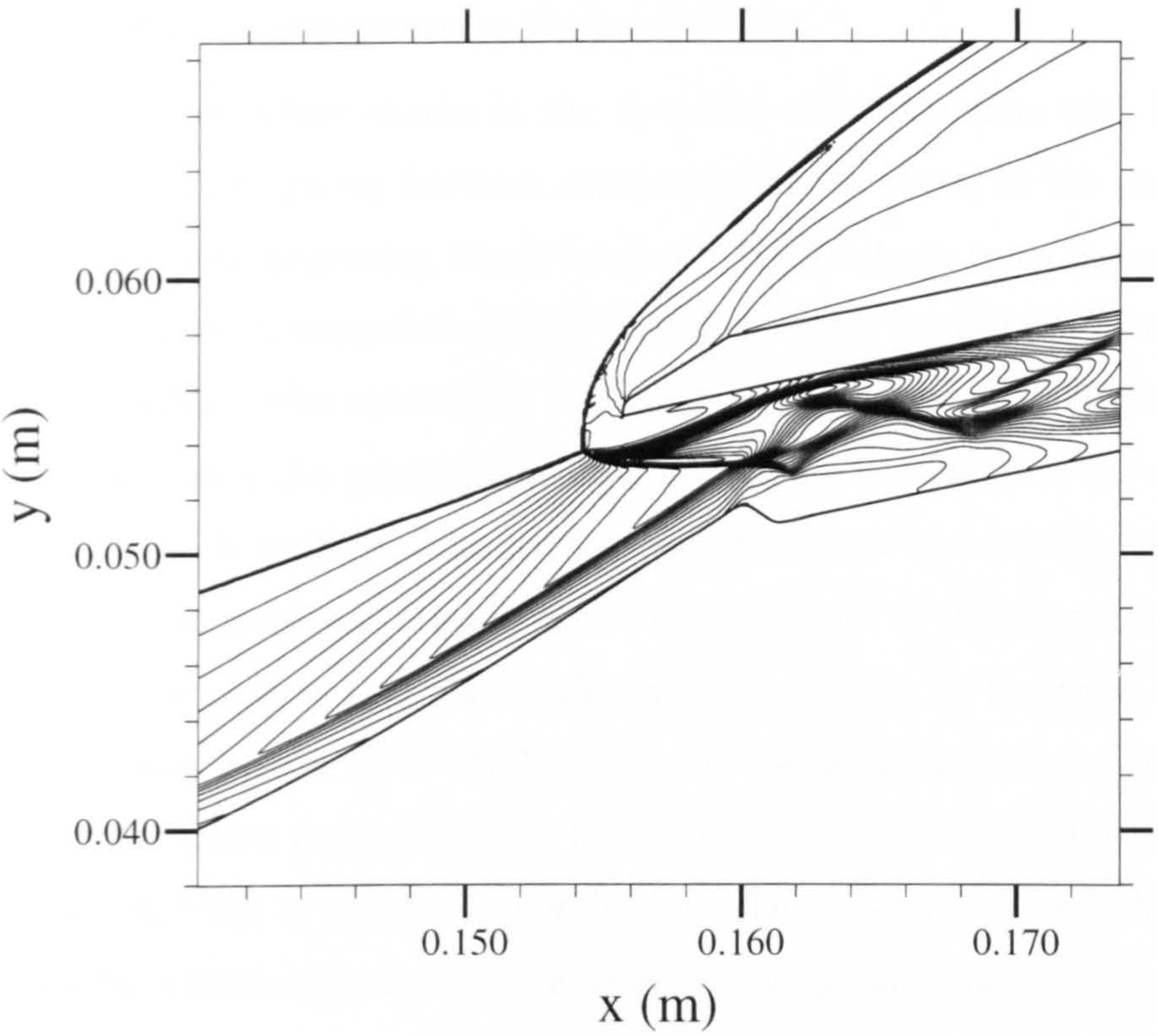


Figure 5.29: CFD Density contours from turbulent simulations of the i1533 intake with a backward-facing step and blunted cowl at Mach 6.

Figure 5.30 presents a plot of the surface pressure distribution on the forebody surface from the apex leading edge up to the centrebody shoulder at the three freestream conditions. The compression pressure ratio rises to 10, i.e. 10 times the freestream pressure at Mach 4. At Mach 5, the pressure ratio rises to 19 times the freestream pressure, and at Mach 6, to a pressure ratio of 28. The graph shows the initial gradual rise in pressure followed by a sharp increase in the pressure through

the isentropic compression which increases with increasing spike termination angle.

Figure 5.31 - 5.33 present plots of the surface pressure distributions for the centre-body and cowl inner surfaces in the intake duct at the three freestream conditions. The initial rise in pressure on the cowl inner surface is the rise in pressure through the cowl shock wave. As the Mach number increases from 4 to 6, Figure 5.31 (Mach 4) to 5.32 (Mach 6), the strength of the cowl shock increases as seen from this initial pressure rise. The diamond patterned plot describes the alternating fluctuations in pressures on the centrebody and cowl surfaces as the flow traverses through a series of oblique shocks and expansions in the parallel duct.

The number of secondary shocks in the flow-field stays the same with increasing Mach number. The spacing between consecutive shock waves in the pattern also stays the same with increasing Mach number. As the shock train passes through the parallel section, it dissipates and the flow then enters the diffuser section which begins at x=0.27m. The centrebody and cowl pressures are virtually the same in the diffuser section and a gradual reduction in pressure is seen up to the end of the diffuser. The shock train pressure pattern appears to get increasingly irregular as the Mach number increases. An important characteristic of this flow-field which is revealed in these plots is that the shock train is increasing in length as the Mach number increases from 4 to 6. At Mach 4, the shock train dissipates within the parallel section shown in Figure 5.31. However at Mach 5 and Mach 6, it appears that the shock train is not fully contained in the parallel section, which might necessitate for a further increase in the length of the parallel duct.

Several studies on isolator flows (Waltrup,[89] Emami,[35] Reinartz[91]) have stated the need to contain the entire length of the shock train within the parallel duct to achieve optimum pressure recovery. A further reason to contain the shock train within the parallel duct is that the presence of a shock train in the diffuser (during ramjet operation) will further contribute to the pressure gradient to increase the likelihood of flow separation in the diffuser. The consequences of flow separation in the diffuser are a reduced total pressure recovery and an increasingly non-uniform exit flow profile. Separation in the diffuser will also result in a decrease in the post-terminal shock diffusion which is essential for optimum ramjet pressure recovery.

One-dimensional average values were obtained from the two-dimensional flow-field by conservation averaging to carry out a performance analysis of the intake. Figures 5.31 - 5.33 also plot the average pressure in the intake duct for the three conditions. Figure 5.34 shows the average pressure (in bars) in the duct for the three conditions. The initial fluctuation in the graph occurs in the recirculation region behind the step where the flow is unsteady. A plot of these values at different time-intervals would reveal a fluctuation in the values in that region. The pressure drops rapidly through the initial part of the shock train and then levels off as the shock train dissipates up to the end of the parallel section. The flow then enters the diffuser and a steady drop in pressure occurs as the flow accelerates to the exit.

Figure 5.35 plots the average Mach number in the intake duct for the three flight conditions. For the Mach 4 case, the Mach number initially increases through the shock train and then stays constant to the end of the parallel section. The flow then enters the diffuser and accelerates to the exit to Mach 3.4. Similar pattern in Mach number distribution is seen at Mach 5 and after the flow enters the diffuser it accelerates to Mach 3.5 to the end of the section. The plot for the Mach 6 case shows a general decrease in Mach number through the shock train with the flow then accelerating to the end of the diffuser to Mach 3.2. The presence of a thicker boundary-layer at the low-Reynolds Mach 6 condition explains the lower Mach number values in the diffuser section, and the divergence from the Mach 4 and 5 distributions. The inlet Mach number increases with increasing Mach number.

Figure 5.36 shows the total pressure efficiency across the intake duct from the annulus to the end of the diffuser section. From this graph it is evident that most of the total pressure losses are incurred at the inlet shock system due to the various wave interactions and reflections. Pressure losses can occur from shock waves, friction on the walls and boundary-layer separation but the majority of this loss occurs from shock waves. The highest total pressure recovery at the inlet position is at Mach 4, approximately a factor of 0.70. This steadily decreases through the intake duct to 0.38 at the isolator exit. For the Mach 5 case, the total pressure recovery factor at inlet is approximately 0.5, decreasing to 0.24 at the end of the duct. The highest loss in total pressure at inlet occurs at Mach 6 due to the higher shock strength, a

factor of approx. 0.34 decreasing to 0.08 at the isolator exit. The gradual loss in total pressure through the duct is due to the growing viscous boundary-layer.

Table 5.2 and 5.3 present performance values for the i1533 and i1530 intakes at two positions in the intake duct. Table 5.2 shows the mass capture ratios at the three freestream conditions; 72 percent at Mach 4, 95 percent at Mach 5 and 97 percent at Mach 6. At Mach 4 and 5 mass flow spillage leads to a reduction in the mass capture. At Mach 6 shock detachment causes mass spillage at inlet.

Figure 5.37 shows the kinetic energy efficiency in the intake for the three cases. At the inlet entry, the highest kinetic energy efficiency is for the Mach 4 case and the lowest is for the Mach 6 case. The gradual decline in the kinetic energy efficiency across the intake duct is again due to viscous losses. The thicker boundary-layer at Mach 6 leads to higher losses compared to the Mach 4 and 5 cases.

With calculated average values of Mach number and pressure in the duct, it is possible to make a simple calculation to obtain the flow properties in the duct if a normal shock were to be stabilised at any position. For subsonic combustion ramjet operation, a terminal normal shock must be stabilised in the duct to decelerate the flow from supersonic to subsonic speeds. Figure 5.38 presents a graph of the pressure (in bars) behind a normal shock in the duct at the three flight conditions. Each point on the plot is obtained by using the known average flow properties at that position and calculating for the post normal shock properties. Figure 5.39 plots the Mach number behind the normal shock for every position along the duct.

Figure 5.40 shows a graph of the calculated pressure (in bars) at the diffuser exit if a normal shock is stabilised in the duct. For operation at Mach 4, a back pressure of approximately 7.8 bar is required to be sustained.[107] The graph indicates that at Mach 4, the terminal shock position would have to be near the inlet annulus to sustain this level of back pressure. For the Mach 5 case, a back pressure level of 8.6 bar is required, and the graph shows that this shock could be stabilised approximately midway into the parallel section. For the Mach 6 condition a back pressure level of 1.2 bar is required and the graph suggests that this back pressure level is sustainable if a normal shock were to stabilise in the diffuser section. Figure 5.41 present a graph of Mach number at the isolator exit if a normal shock were

stabilised in the duct. The graph shows that if a normal shock were stabilised further upstream, subsonic diffusion will allow for the flow to decelerate to suitable conditions for combustion (Mach 0.1). As the normal shock wave is stabilised further downstream in the duct, the exit Mach number increases.

The graphs show that calculations based on the averaged flow properties predict that the intake can sustain the back pressure levels required for subsonic ramjet operation. In reality however, difficulties will arise in sustaining back pressure due to the non-uniformity in the duct flow. The correlation between flow non-uniformity and sustainable back pressure will be discussed in more detail in chapter 6.

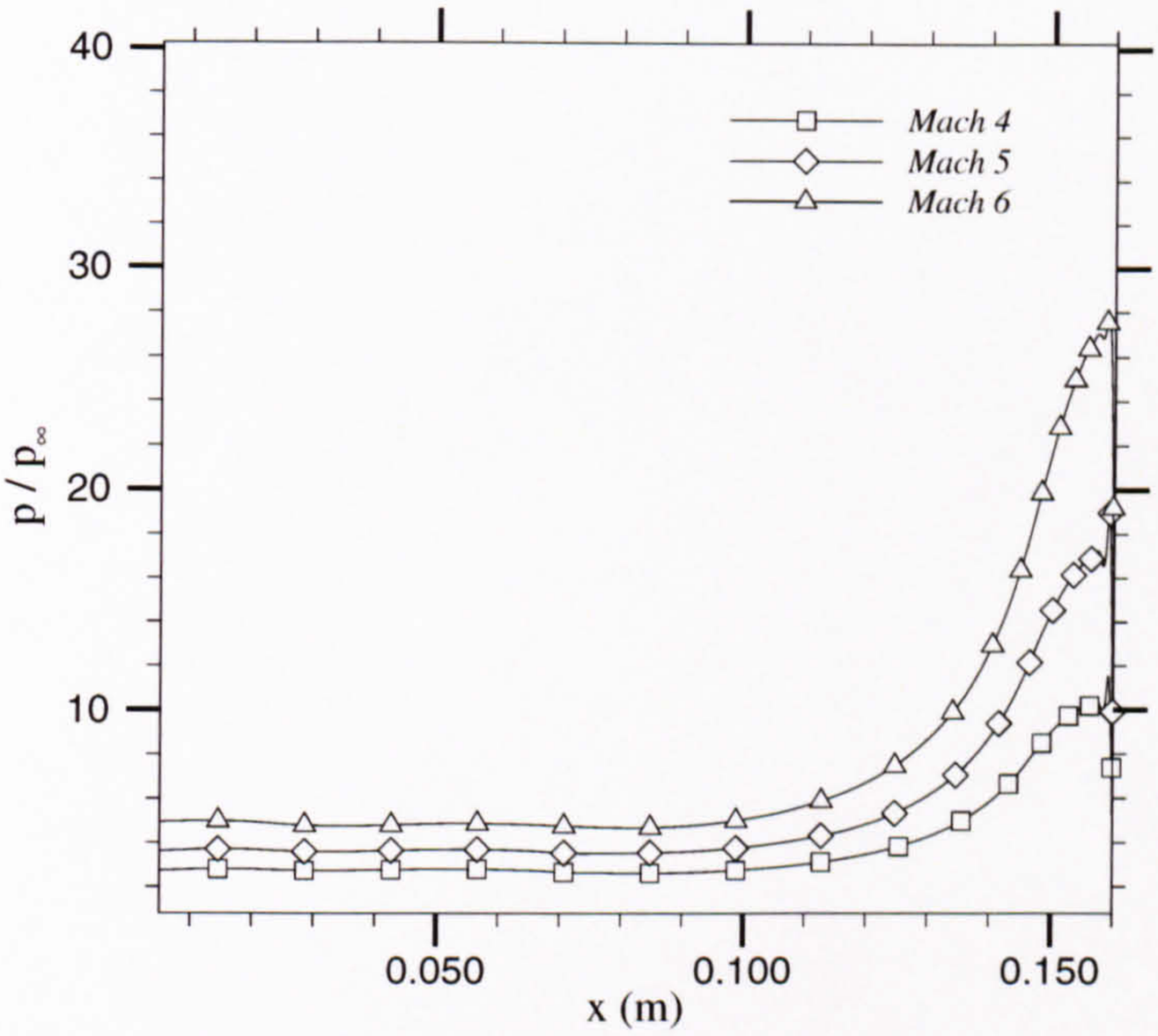


Figure 5.30: Surface pressure distribution on the forebody versus x-distance for the i1533 intake with a backward-facing step at the three freestream conditions.

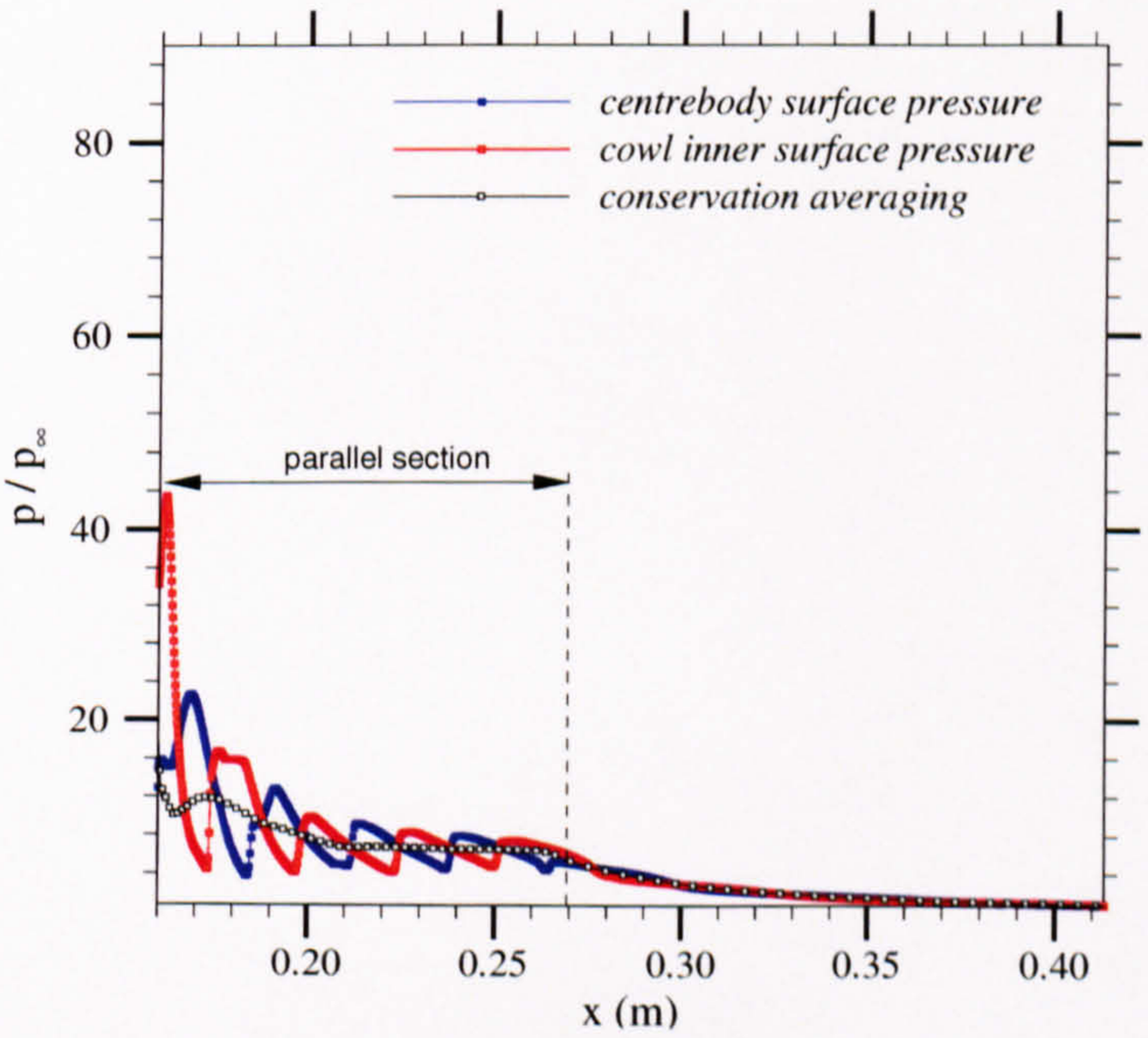


Figure 5.31: Centrebody and cowl inner surface pressure distribution; and 1D average pressure of the i1533 intake with a backward facing-step and at Mach 4.

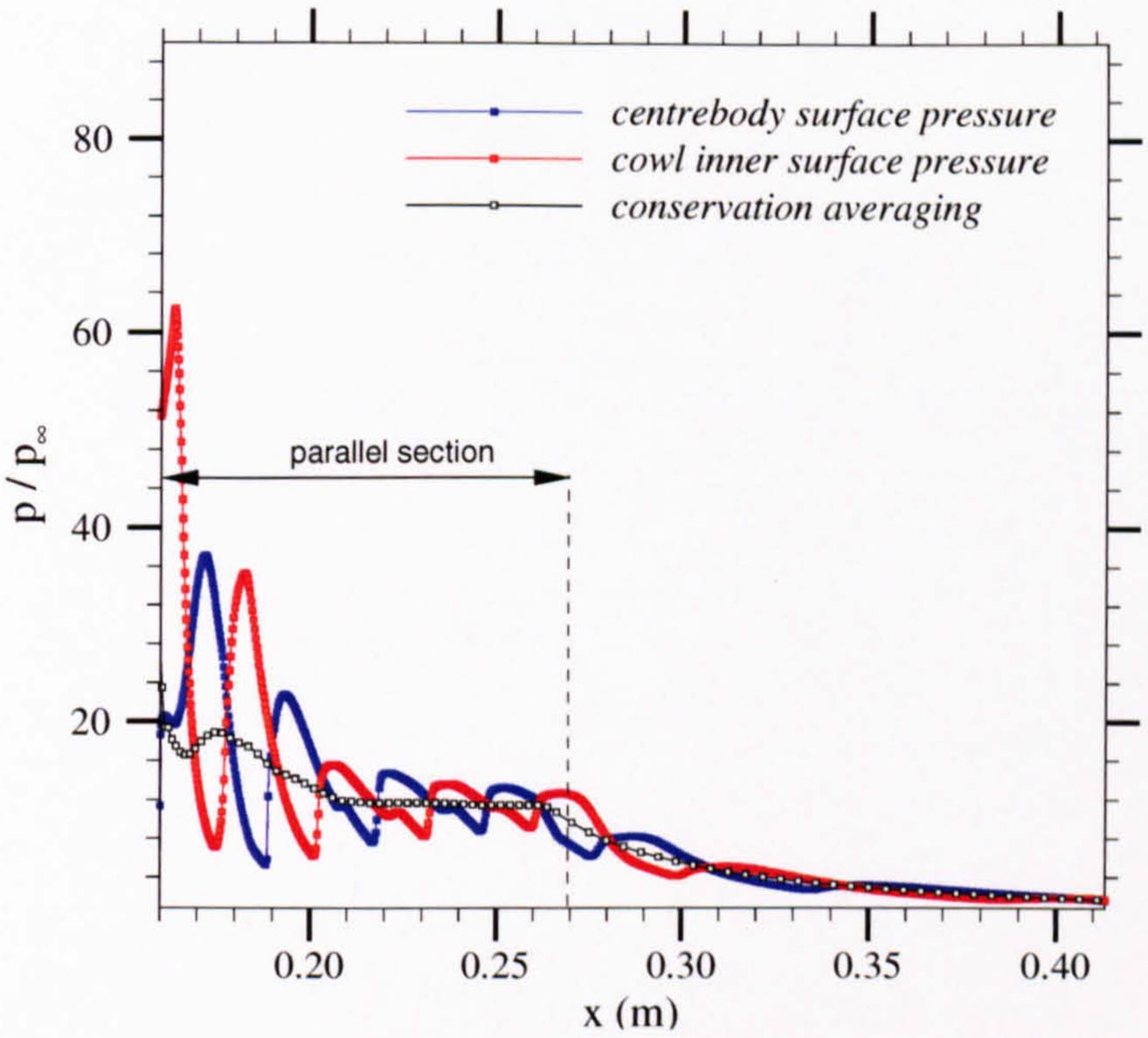


Figure 5.32: Centrebody and cowl inner surface pressure distribution; and 1D average pressure of the i1533 intake with a backward facing-step and at Mach 5.

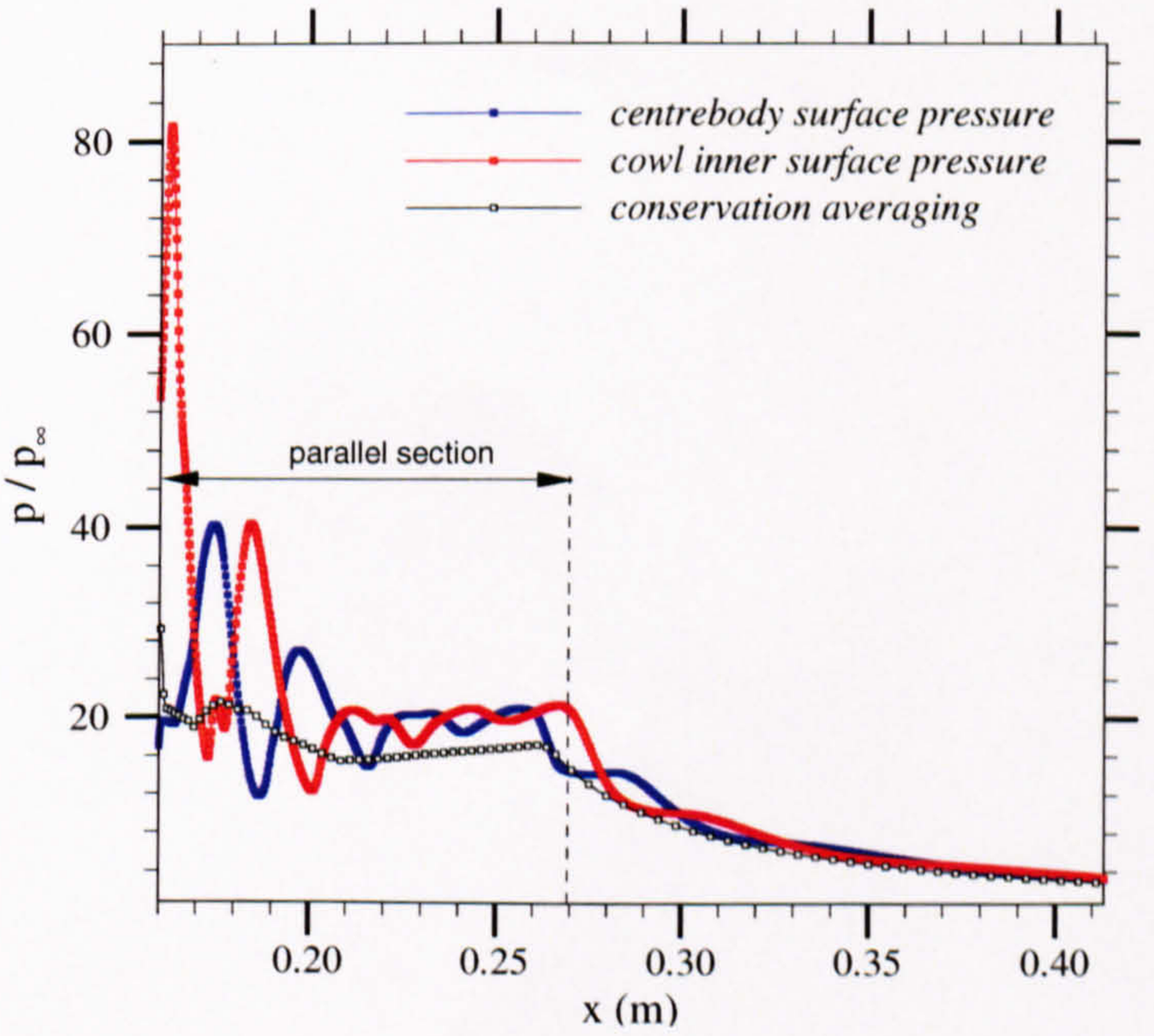


Figure 5.33: Centrebody and cowl inner surface pressure distribution; and 1D average pressure of the i1533 intake with a backward facing-step and at Mach 6.

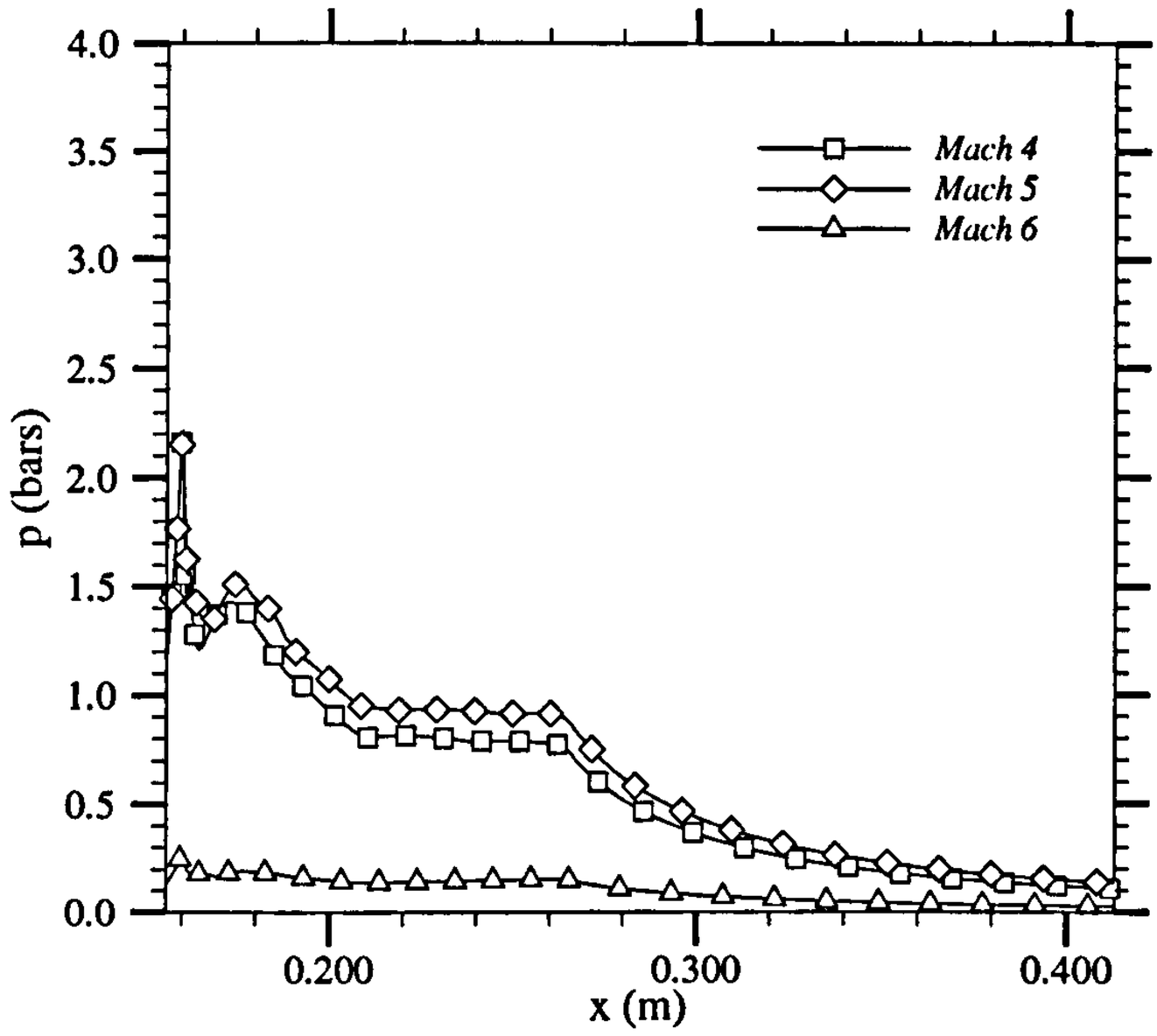


Figure 5.34: Average pressure in the intake duct versus x-distance for the i1533 intake with a backward-facing step at the three freestream conditions.

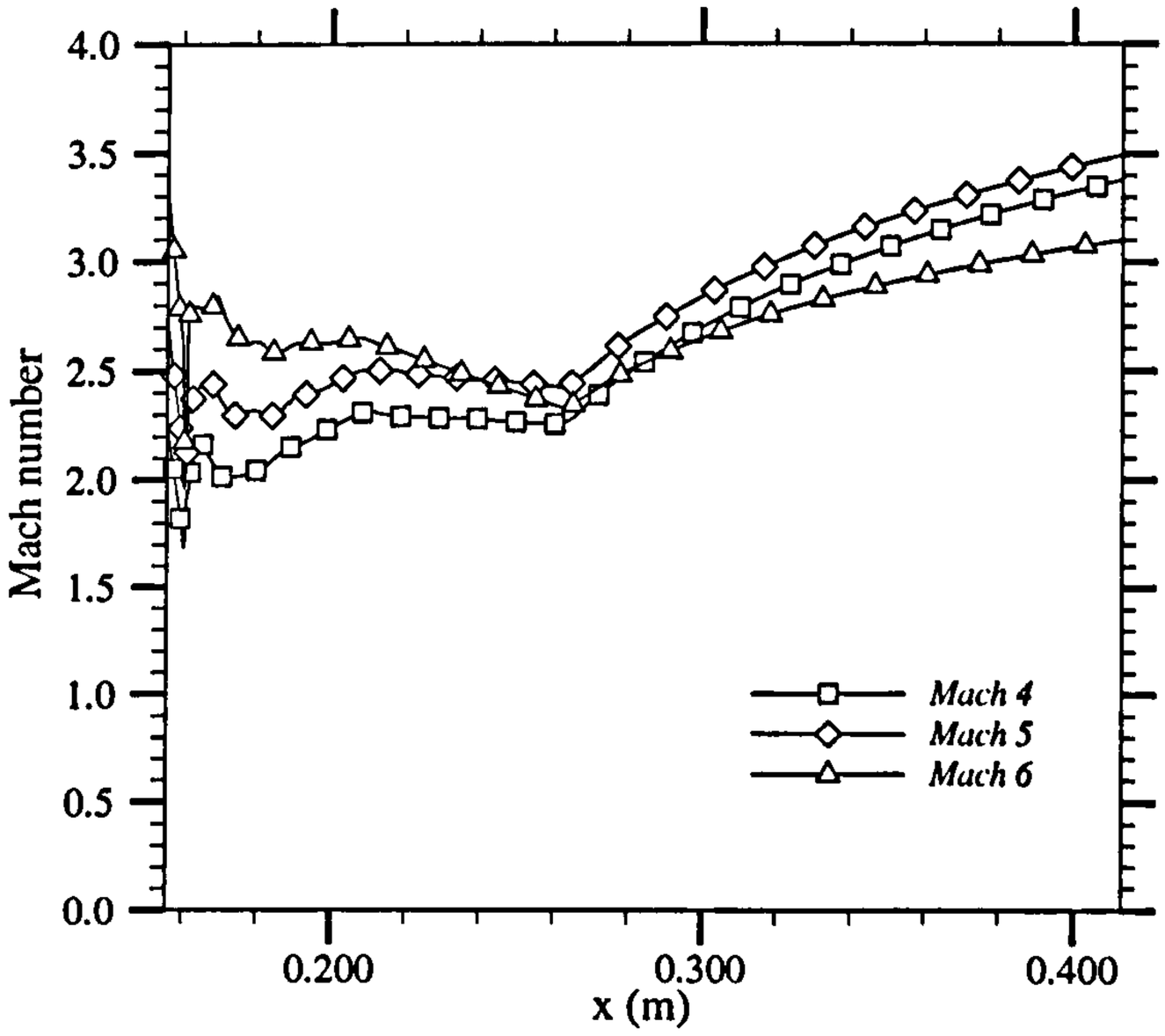


Figure 5.35: Average Mach number in the intake duct versus x-distance for the i1533 intake with a backward-facing step at the three freestream conditions.

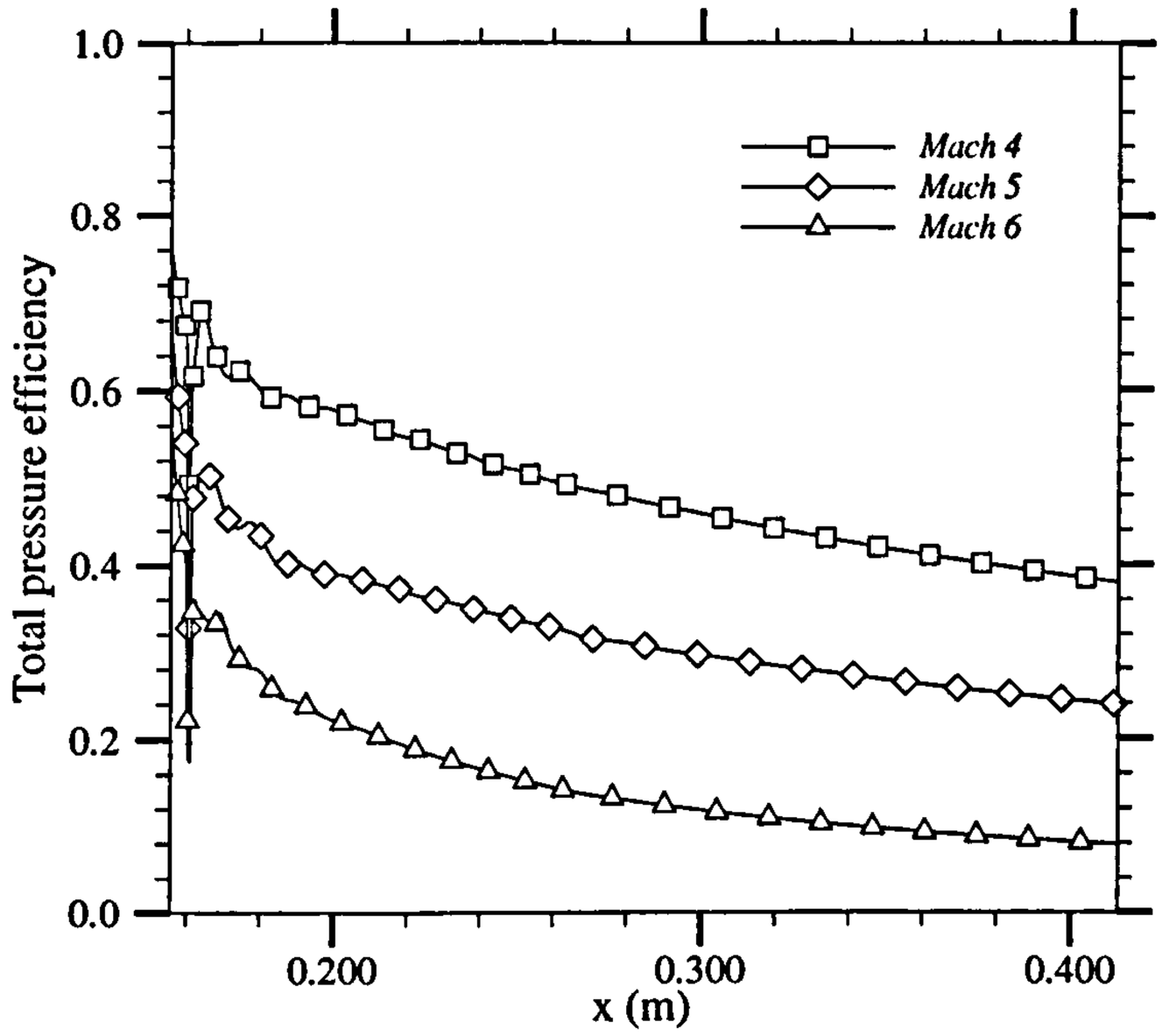


Figure 5.36: Total pressure efficiency in the intake duct versus x-distance for the i1533 intake with a backward-facing step at the three freestream conditions.

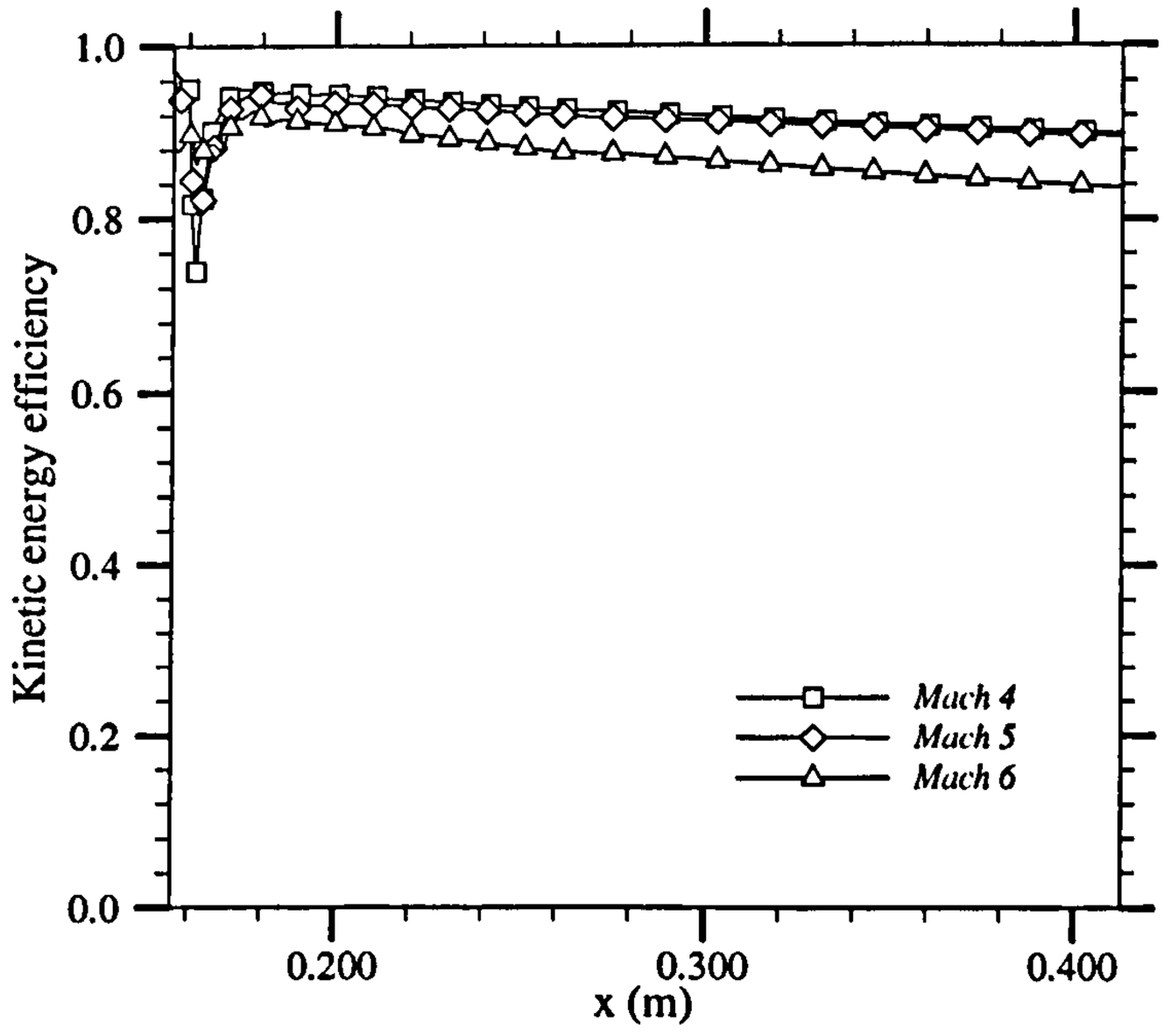


Figure 5.37: Kinetic energy efficiency in the intake duct versus x-distance for the i1533 intake with a backward-facing step at the three freestream conditions.

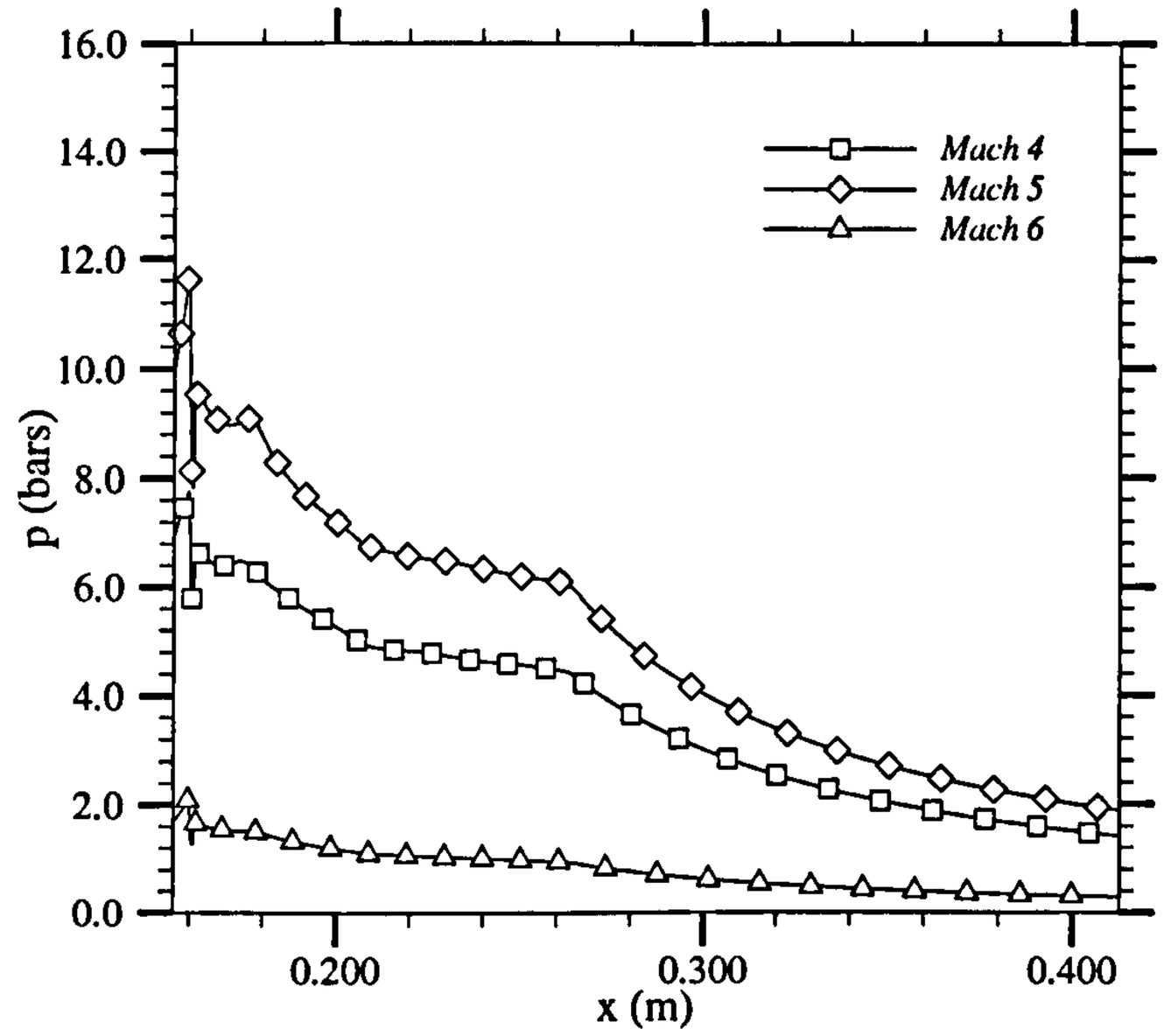


Figure 5.38: Pressure behind a normal shock in the duct versus x-distance for the i1533 intake with a backward-facing step at the three freestream conditions.

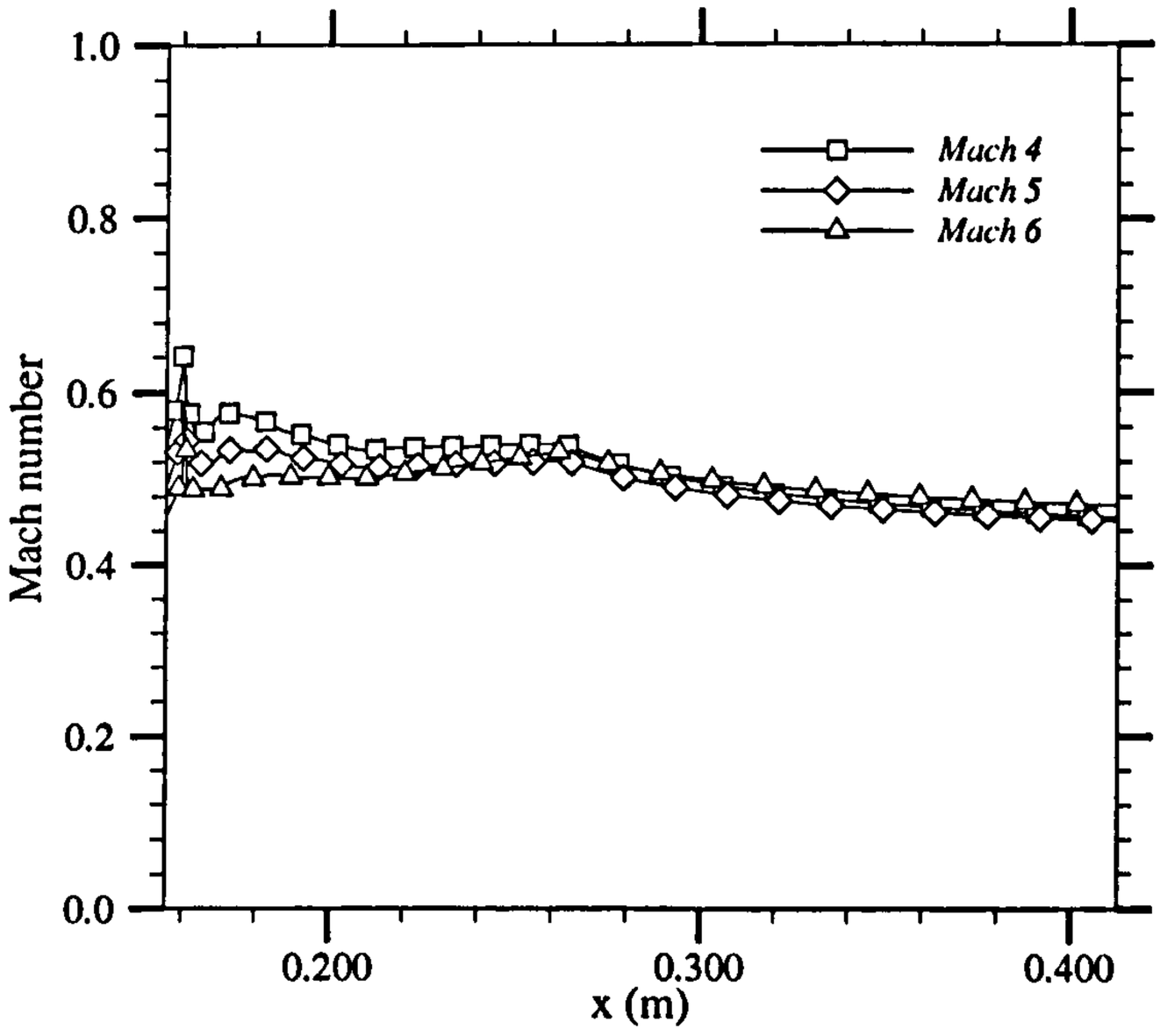


Figure 5.39: Mach number behind a normal shock in the duct versus x-distance for the i1533 intake with a backward-facing step at the three freestream conditions.

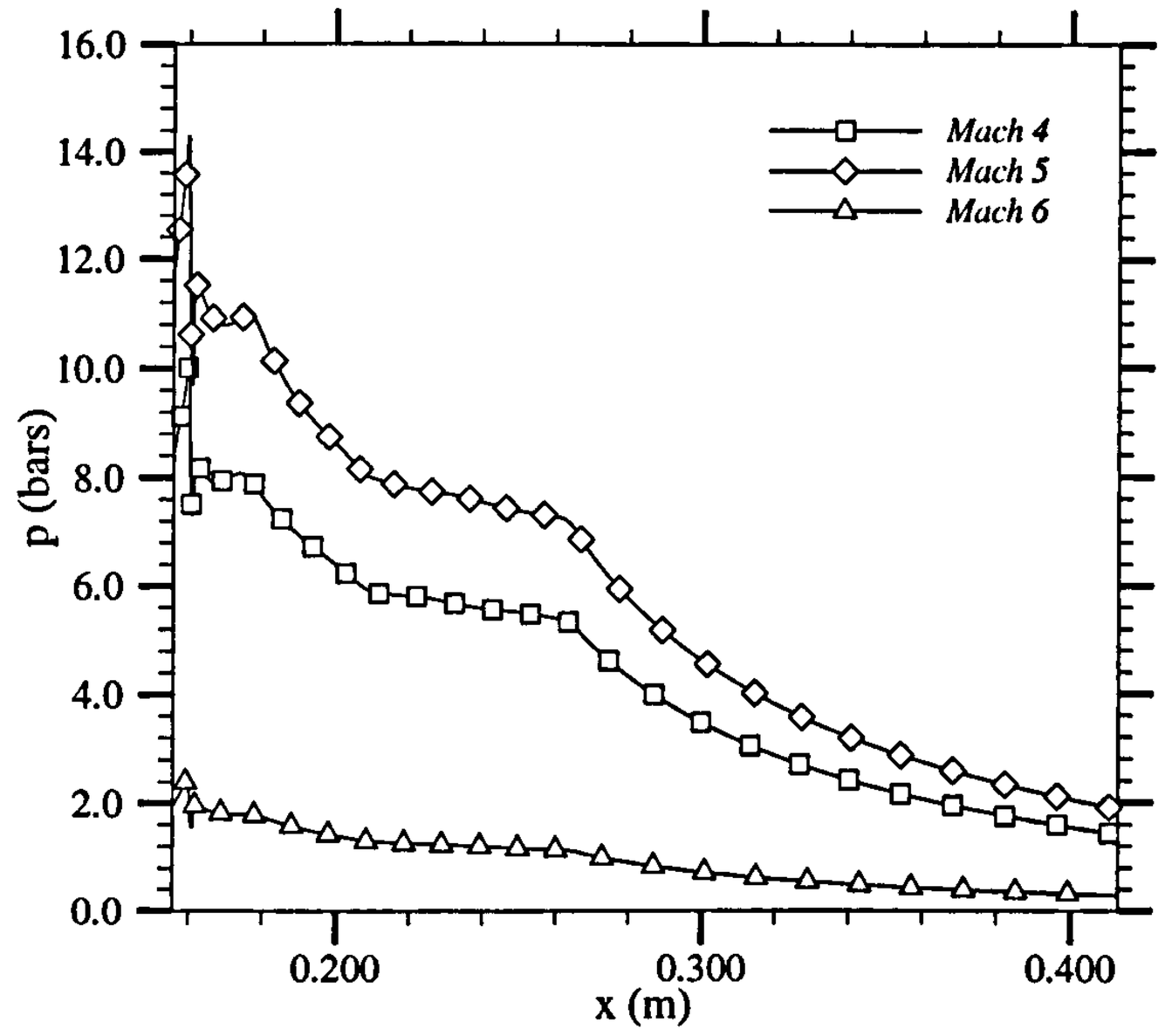


Figure 5.40: Exit pressure with a normal shock in the duct versus x-distance for the i1533 intake with a backward-facing step at freestream conditions.

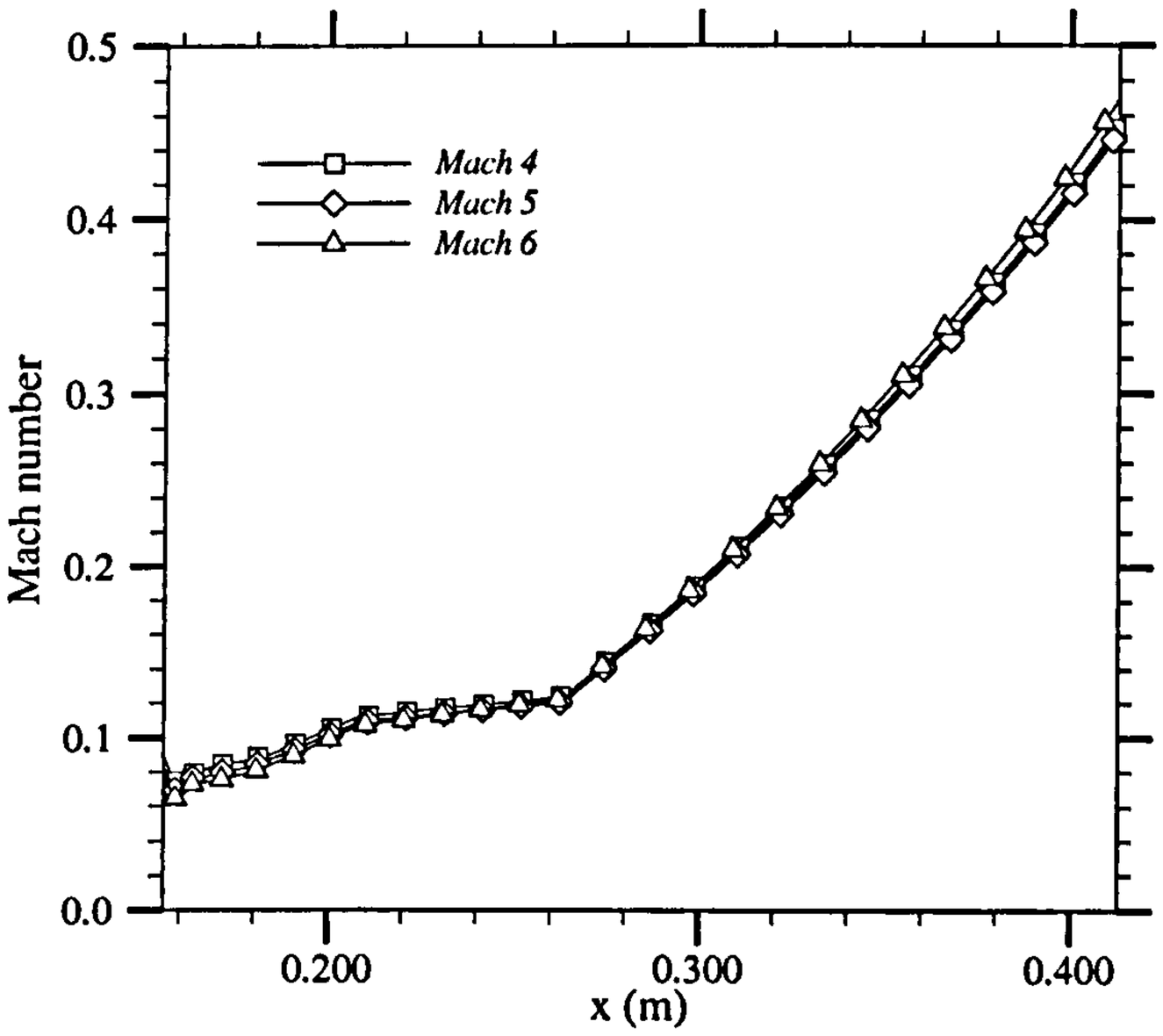


Figure 5.41: Exit Mach number with a normal shock in the duct versus x-distance for the i1533 intake with a backward-facing step at freestream conditions.

5.4 i1530 intake analysis

The i1530 intake is designed with an initial 15 degree cone angle followed by isentropic compression with a spike termination angle of 30 degrees. Figure 5.42 defines the centrebody geometry for the two designs i1533 and i1530. In the latter case, the cowl angle is lowered to 6 degrees, as is the centrebody angle (to maintain a parallel section) and the parallel section is extended to 130.1mm (see Appendix A.2).

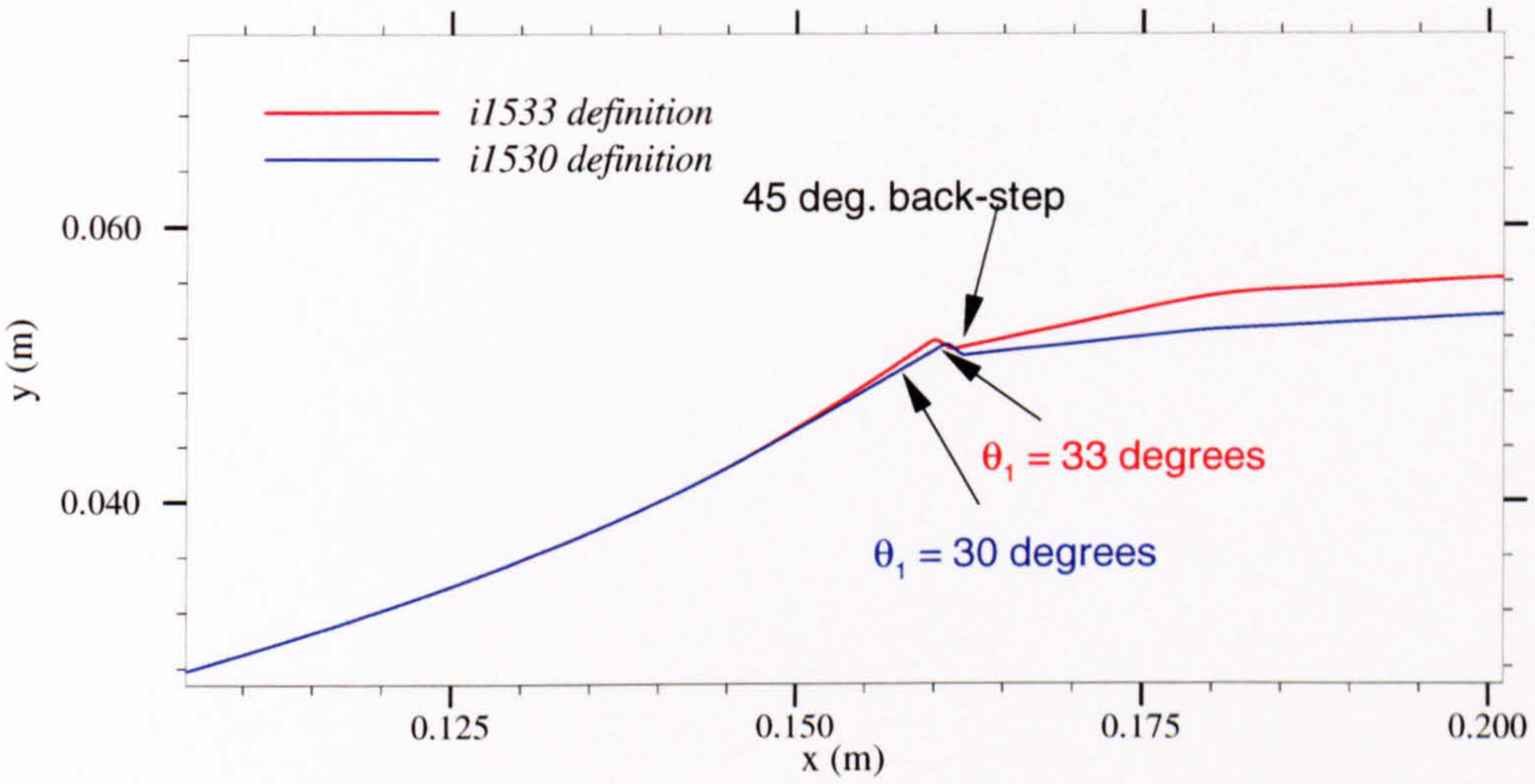


Figure 5.42: Centrebody geometry definition for the i1533 and i1530 intakes.

Figure 5.43 presents density contours from a turbulent simulation of the i1530 intake at off-design condition Mach 4. Transition is imposed at 50mm from the spike leading edge. Again, the apex shock and compression fan focus above the cowl lip causing mass spillage. The boundary-layer separates at the step/expansion corner and then reattaches downstream in the duct. Figure 5.44 presents density contours of the intake at Mach 5. The separation of the boundary-layer past the step/expansion corner induces a weak separation shock which impinges on the cowl inner surface boundary-layer to cause a slight separation there. The recirculation zone increases as Mach number is increased. Figure 5.45 shows density contours of the intake at Mach 6. Similar flow features are seen in this case as for the i1533 intake at Mach 6, with a thicker incoming boundary-layer and shock detachment at the cowl leading-edge. The recirculation zone behind the step is largest at Mach 6. Figure 5.46 plots the surface pressure distribution on the forebody for the three flight conditions.

At Mach 4, the forebody compresses the flow to 8 times the freestream pressure. At Mach 5, to 13.5 times freestream pressure and at Mach 6, 21 times freestream pressure. The values show a drop in compression ratio on the forebody when compared to the i1533 intake (spike termination angle of 33 degrees).

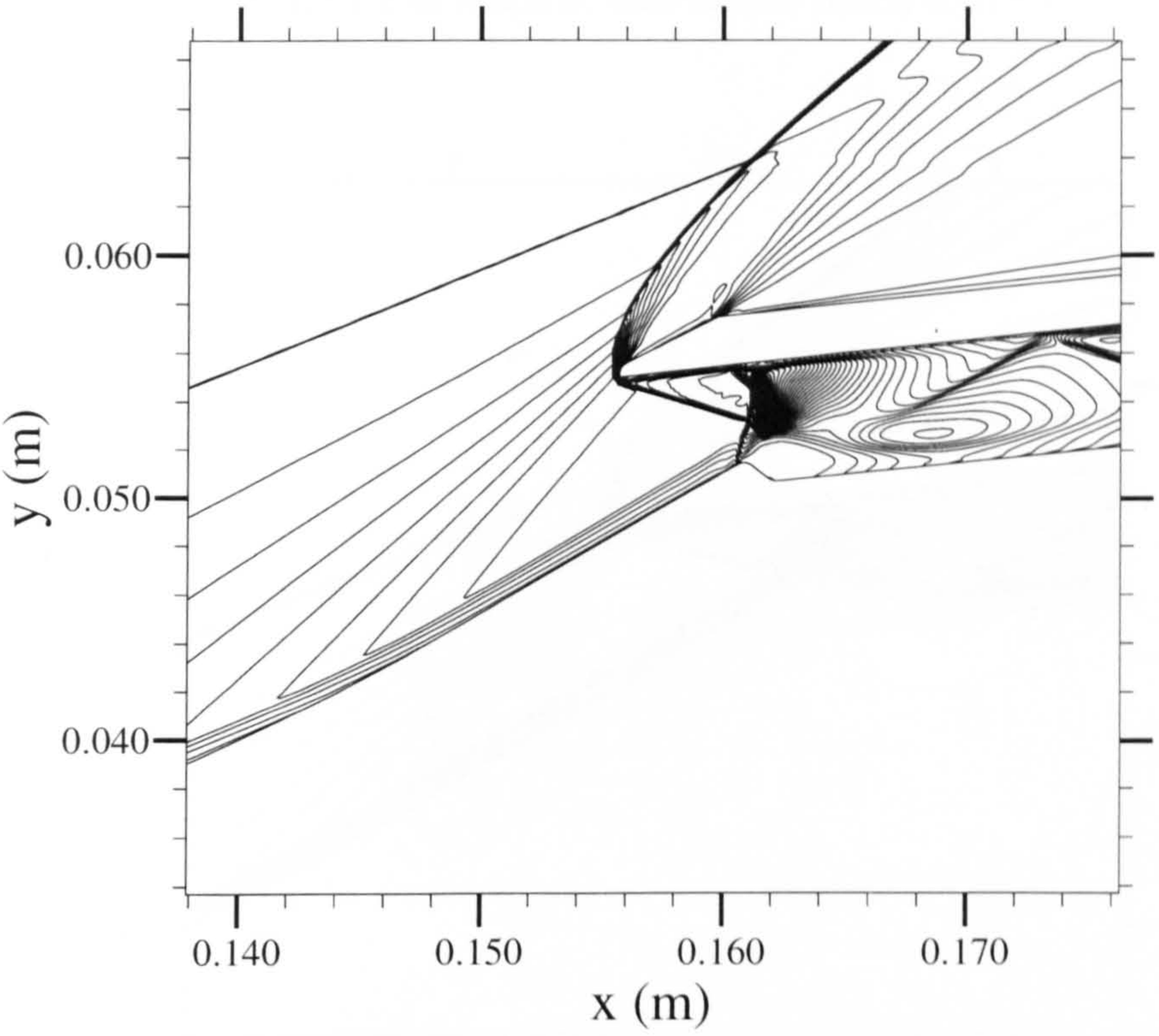


Figure 5.43: CFD Density contours from a turbulent simulation of the i1530 intake with a backward-facing step and blunted cowl at Mach 4.

Figures 5.47 - 5.49 present centrebody and cowl inner surface pressure distributions at the three Mach numbers. The initial pressure rise through the cowl shock is markedly higher for the i1530 intake. The flow turning angle at inlet is higher; θ_1 - δ_c = 30 - 6 = 24. (For the i1533 intake the flow turning angle is 33 - 12 = 21 degrees.) Figures 5.50 and 5.51 plot the average pressure and Mach number in the duct respectively. Figure 5.52 plots the total pressure efficiency through the intake duct for the three Mach numbers. The initial pressure loss is again incurred through the inlet shock system, which is highest at the Mach 6 condition where the cowl shock strength is greatest, and where shock detachment occurs at the cowl lip.

The total pressure recovery at the end of the isolator is 0.37 at Mach 4. At Mach 5 the total pressure recovery is 0.23 and at Mach 6 the lowest value of 0.08. The total pressure recovery is again seen to steadily decline through the isolator section due to viscous losses. Table 5.2 and 5.3 show the performance values for the i1530 intake taken at two positions in the duct. Mass capture ratio is calculated to be 71.9 percent at Mach 4; 94.2 at Mach 5; and 96.3 at Mach 6.

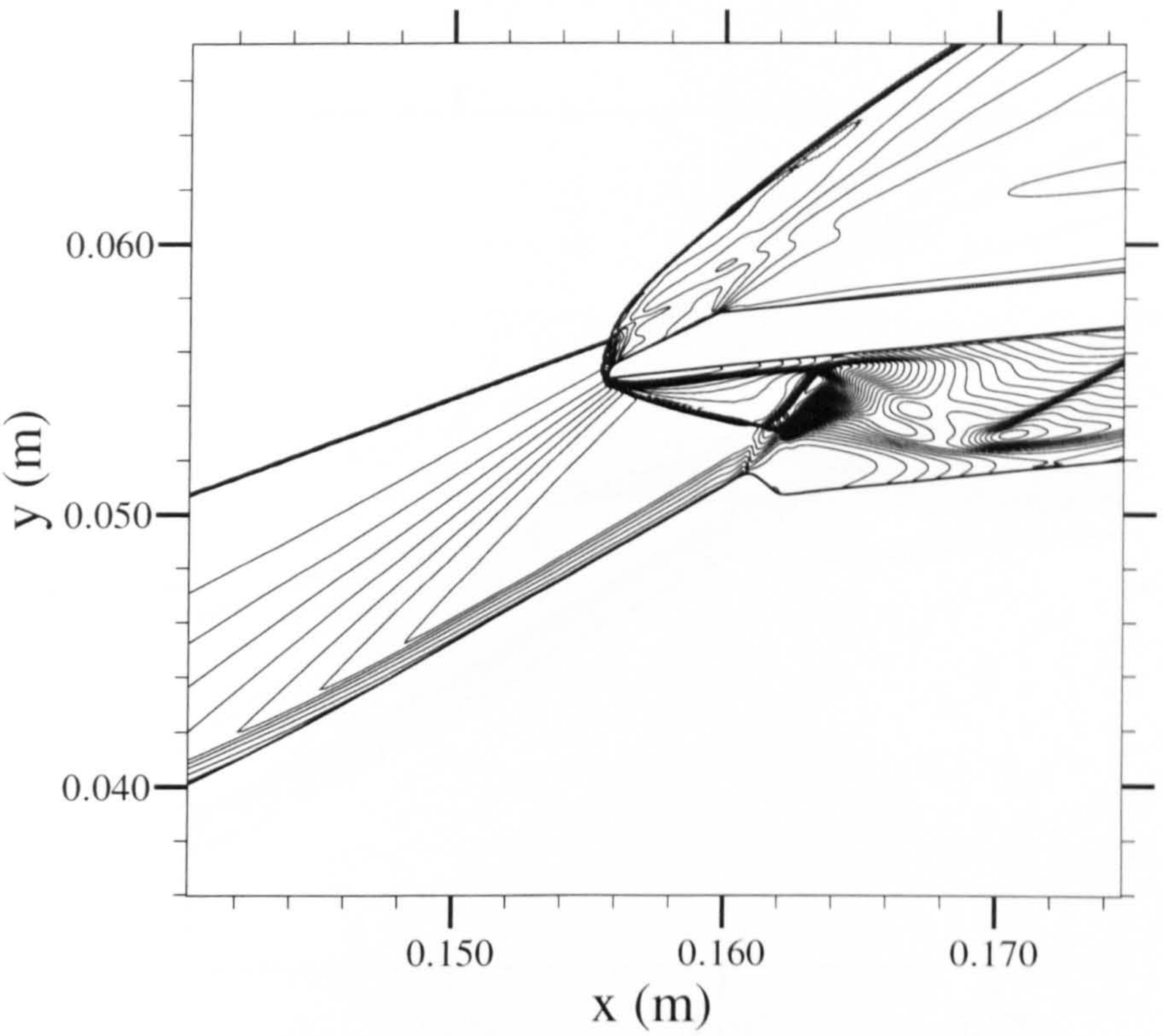


Figure 5.44: CFD Density contours from turbulent simulations of the i1530 intake with a backward-facing step and blunted cowl at Mach 5.

Figure 5.53 presents the kinetic energy efficiency through the intake duct at the three Mach numbers. The higher values for kinetic energy efficiency are seen for the Mach 4 and 5 flight conditions, approximately a factor of 0.90. At Mach 6, a lower value for kinetic energy efficiency is seen, approximately 0.84 at the end of the isolator. This is due to shock detachment at the cowl lip, and also the thicker inlet boundary-layer at Mach 6. Figure 5.54 and 5.55 present the pressure and Mach number behind a normal shock in the duct. Figure 5.56 presents calculated values

for the exit pressure (in bars) if a normal shock were to be stabilised in the isolator duct given the averaged flow properties from the computed CFD solution. This is the best case scenario, in that these values are calculated from averaged properties in the duct. The presence of flow non-uniformity is almost certainly likely to cause complexities in stabilising a shock in the isolator duct and hence will reduce this value. Comparing these values to those calculated for the i1533 intake, the level of sustainable back pressure is reduced for the i1530 intake.

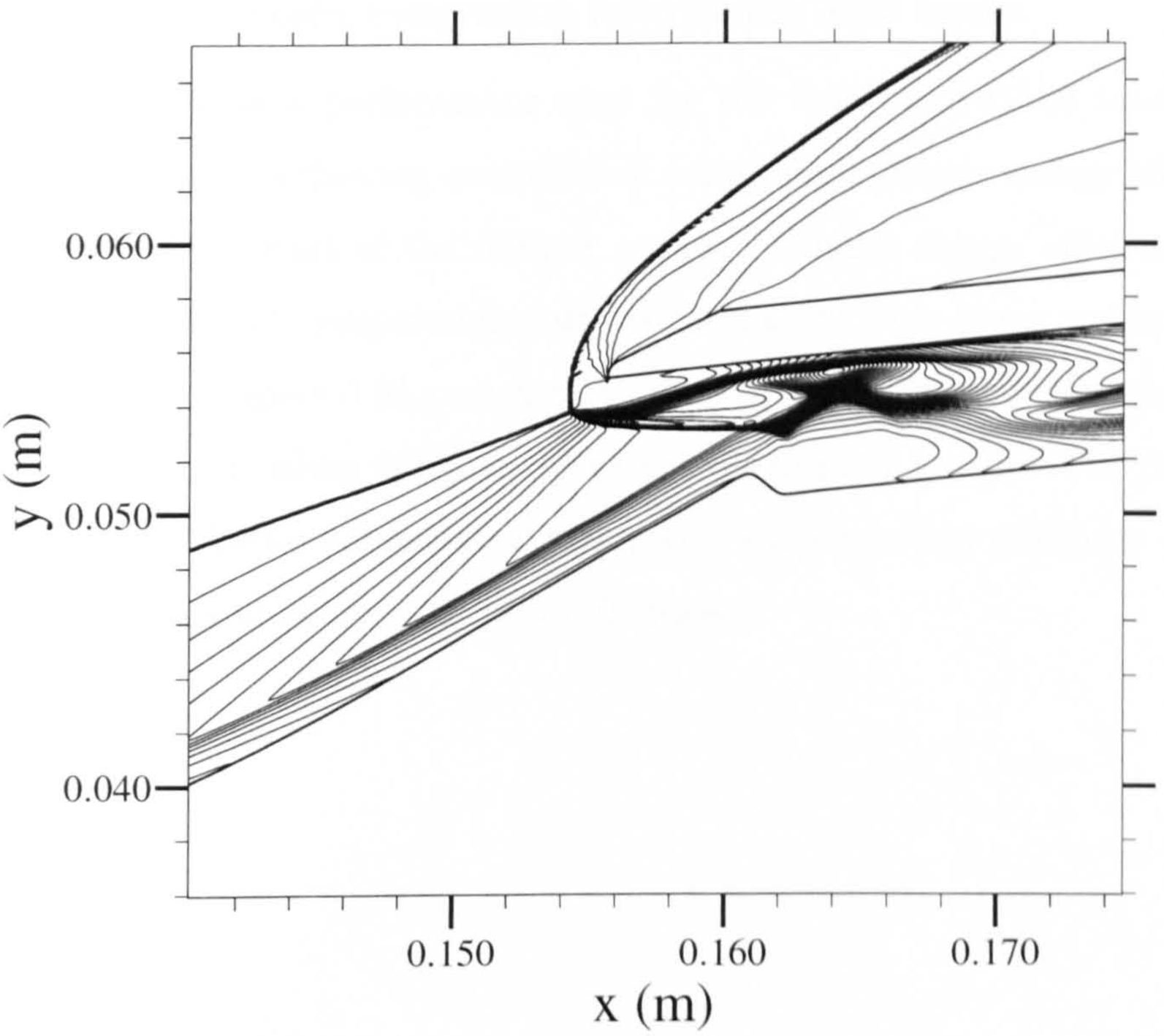


Figure 5.45: CFD Density contours from turbulent simulations of the i1530 intake with a backward-facing step and blunted cowl at Mach 6.

Figure 5.57 presents calculated values for the exit Mach number if a normal shock stabilised in the duct. The graph shows the need to stabilise the terminal shock in the beginning of the diffuser section so that subsonic diffusion can reduce the Mach number to the required Mach 0.1 in the combustor. The further downstream the shock is stabilised, the less subsonic diffusion will occur.

Figure 5.58 presents a performance map for the i1533 and i1530 intakes at the three

flight conditions showing compression ratio versus total pressure efficiency. The values are taken at the start of the diffuser section and so represent the values if a normal shock is stabilised at this position. The trend shows a reduction in total pressure efficiency as Mach number increases, and compression ratio increases and is consistent for both intakes, with a lower performance for the i1530 intake. Figure 5.59 presents the performance map of compression ratio versus total pressure efficiency, with values now taken at the end of the diffuser section. The same trend is seen as in Figure 5.58 with lower total pressure efficiencies calculated for the i1530 intake, but slightly higher compression ratio for the i1530 intake.

Figure 5.60 presents a performance map for the i1533 and i1530 intakes at the three flight conditions showing compression ratio versus kinetic energy efficiency for values taken at the start of the diffuser section. Kinetic energy efficiency reduces as Mach number and compression ratio is increased, with lower performance for the i1530 intake. Figure 5.61 presents the map of compression ratio versus kinetic energy efficiency for values taken at the end of the diffuser section. The i1530 intake produces slightly better compression ratio, with kinetic energy efficiency decreasing as Mach number and compression ratio increases.

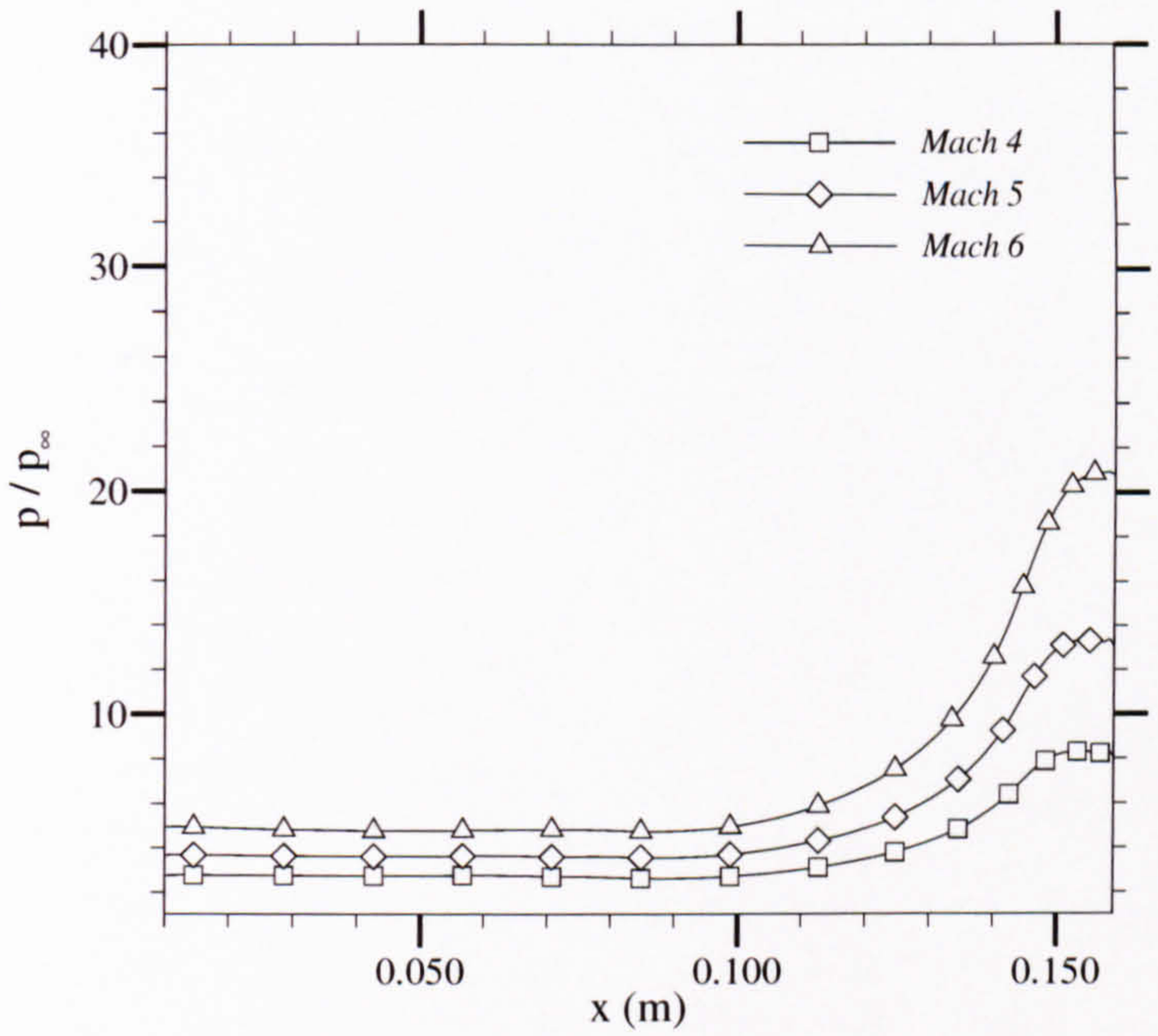


Figure 5.46: Surface pressure distribution on the forebody versus intake x-distance for the i1530 intake with a backward-facing step at the three freestream conditions.

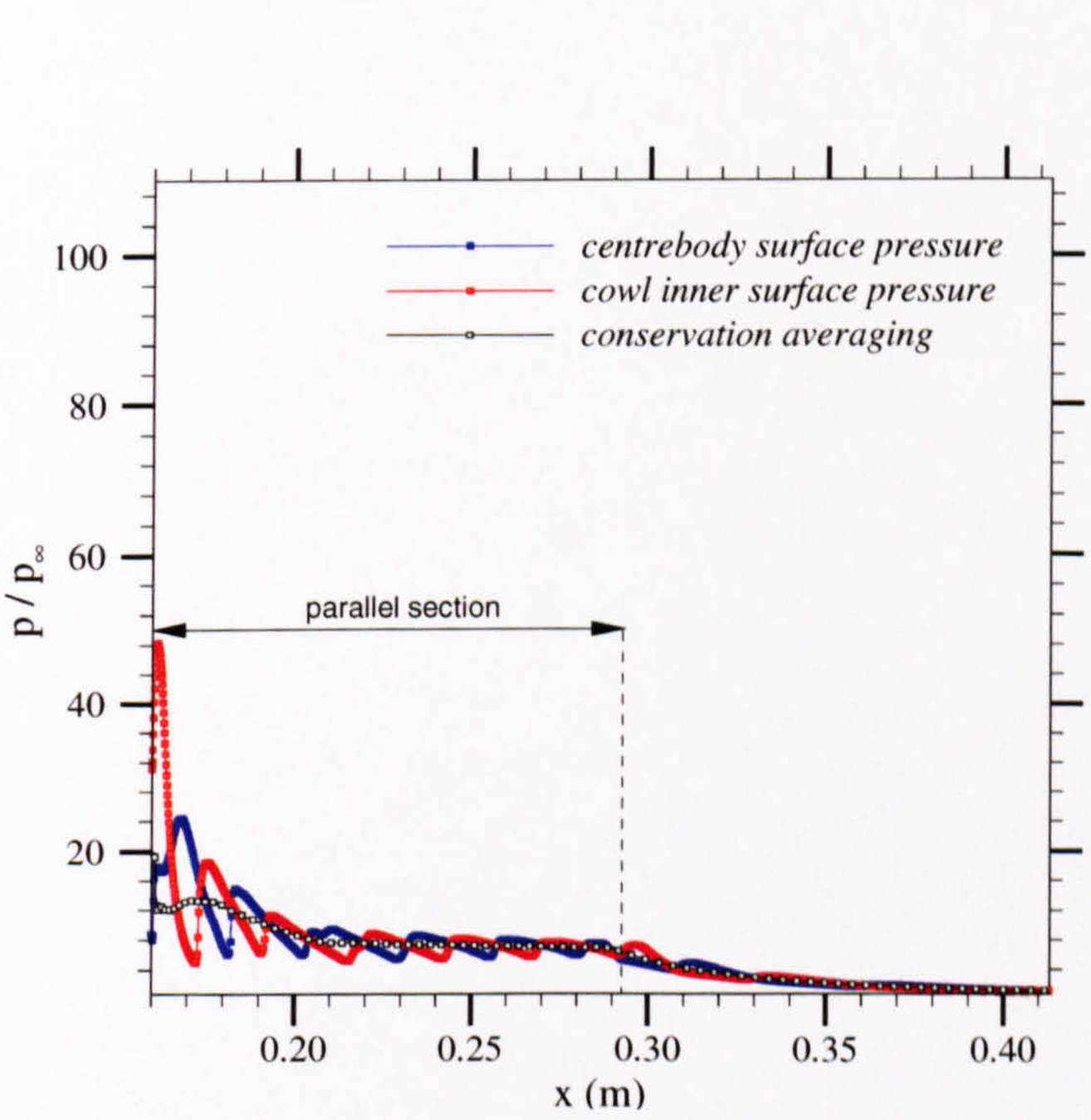


Figure 5.47: Centrebody and cowl inner surface pressure distribution; and 1D average pressure of the i1530 intake with a backward facing-step and at Mach 4.

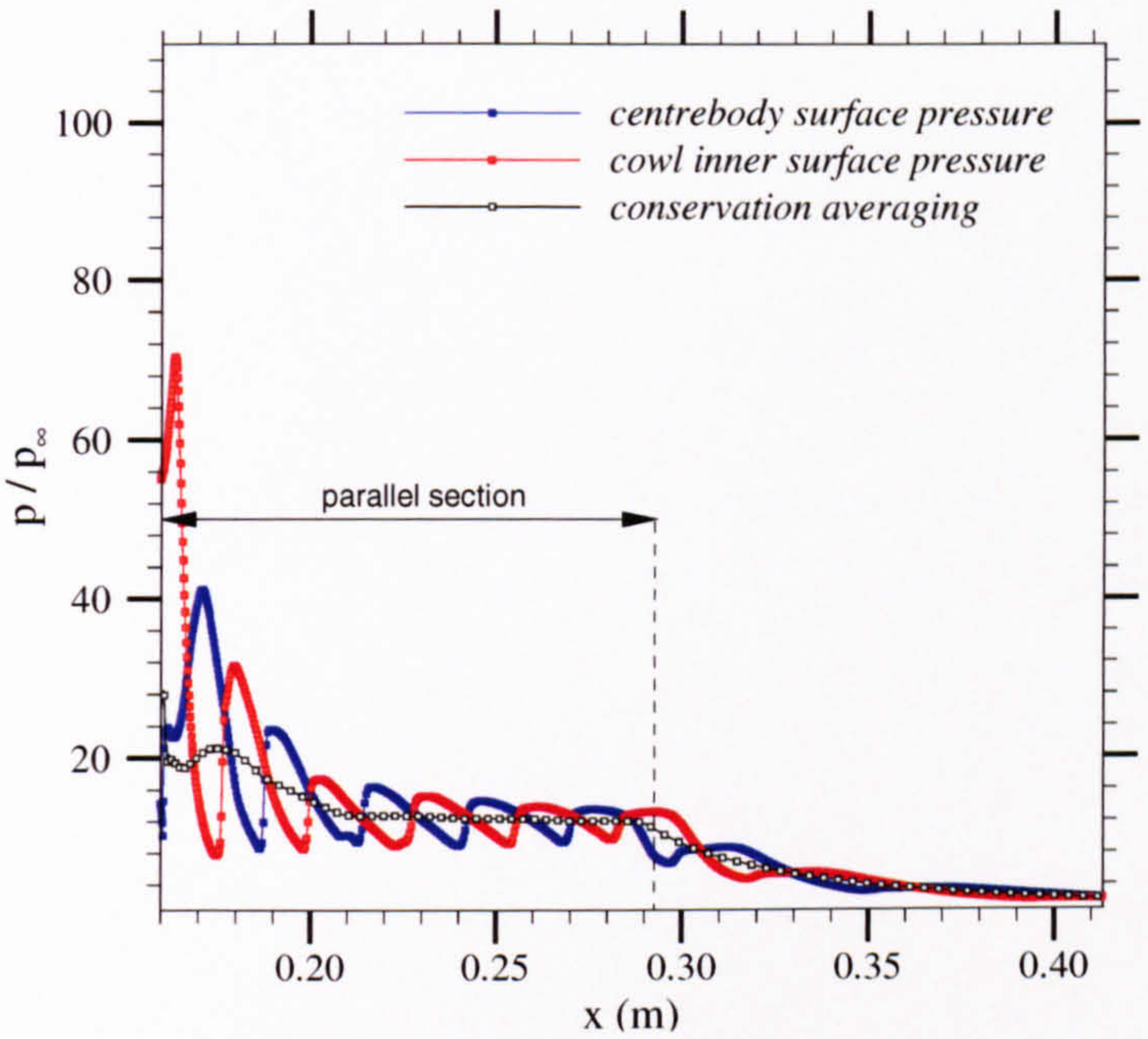


Figure 5.48: Centrebody and cowl inner surface pressure distribution; and 1D average pressure of the i1530 intake with a backward facing-step and at Mach 5.

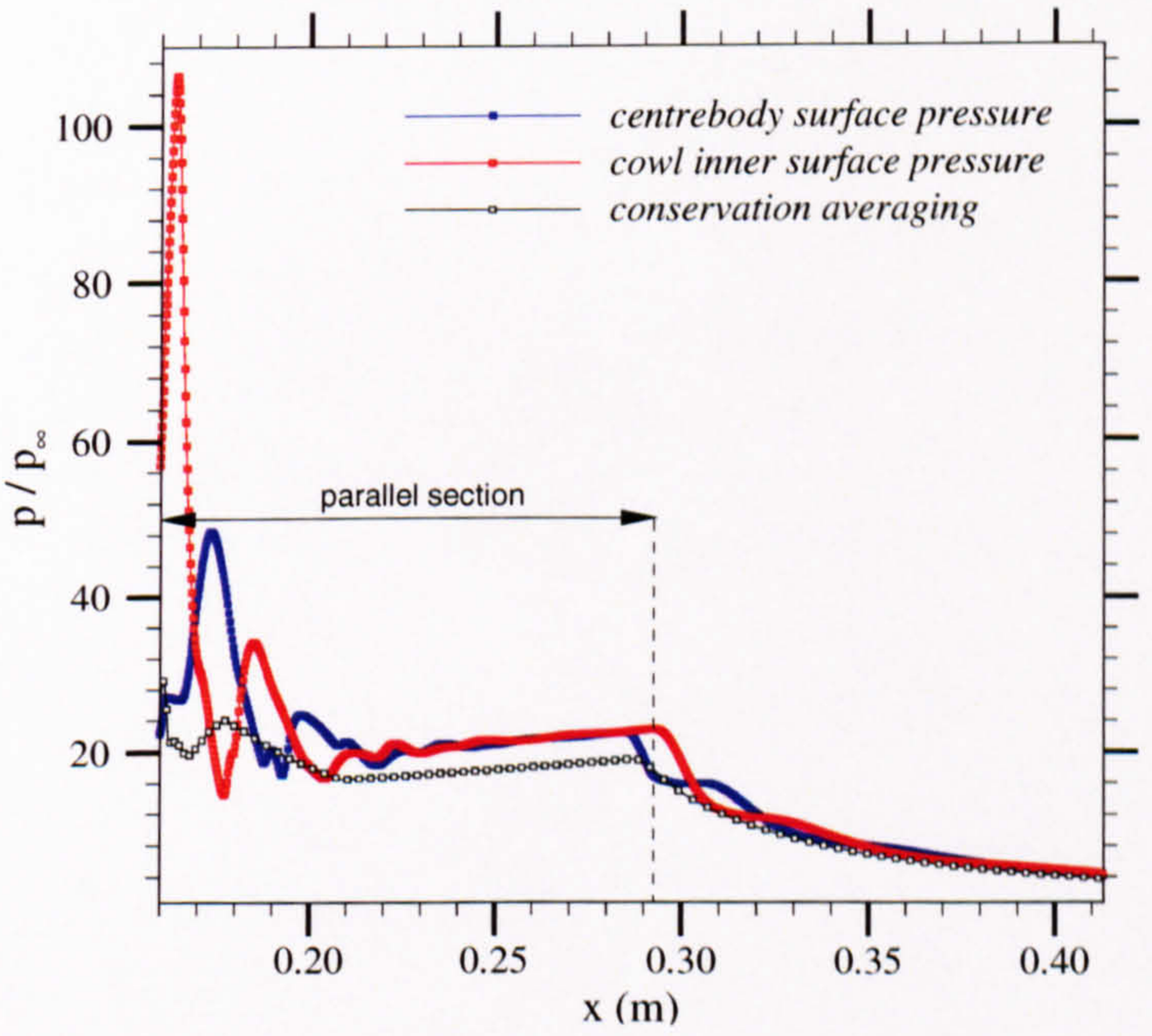


Figure 5.49: Centrebody and cowl inner surface pressure distribution; and 1D average pressure of the i1530 intake with a backward facing-step and at Mach 6..

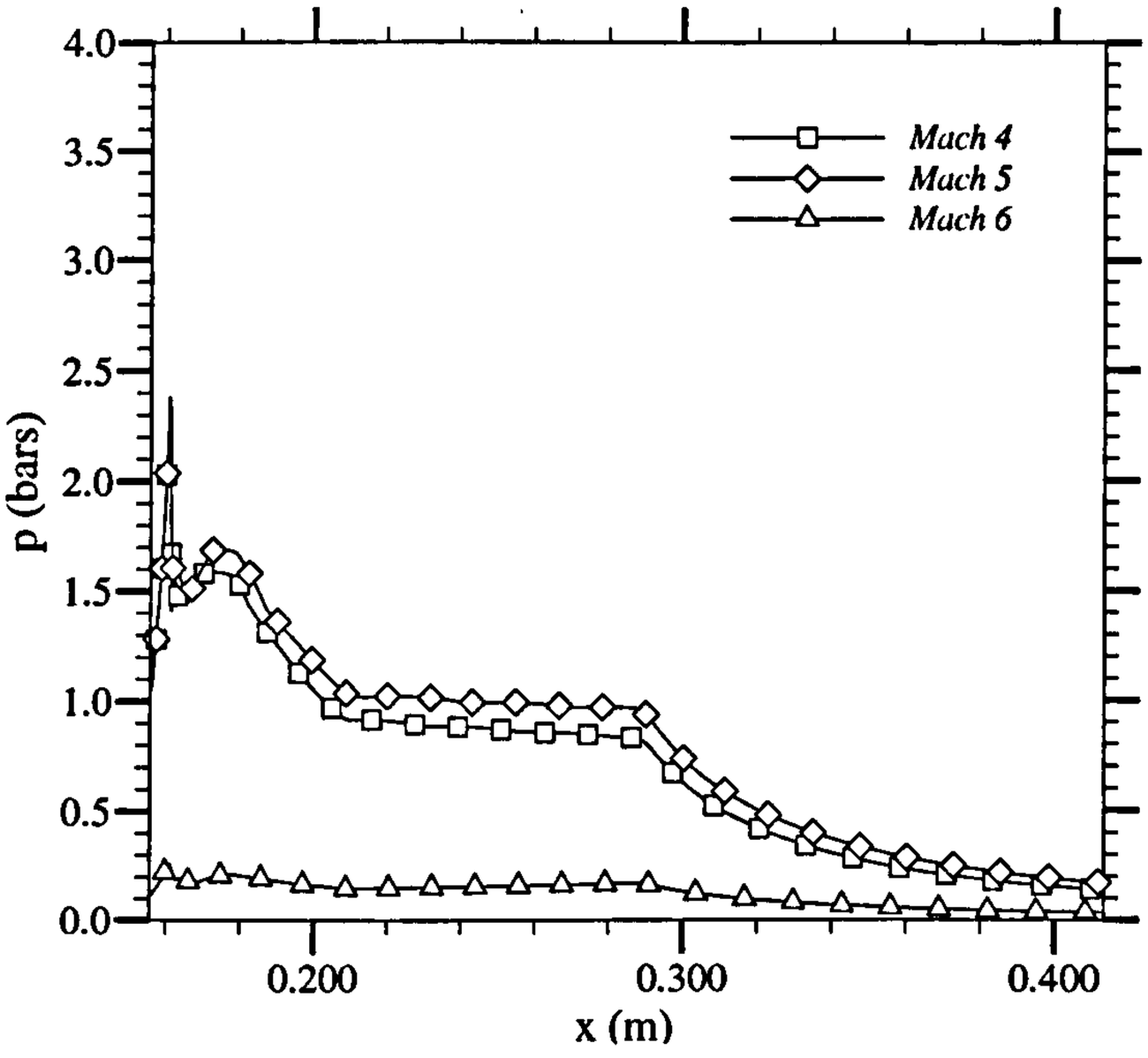


Figure 5.50: Average pressure in the intake duct versus x-distance for the i1530 intake with a backward-facing step at the three freestream conditions.

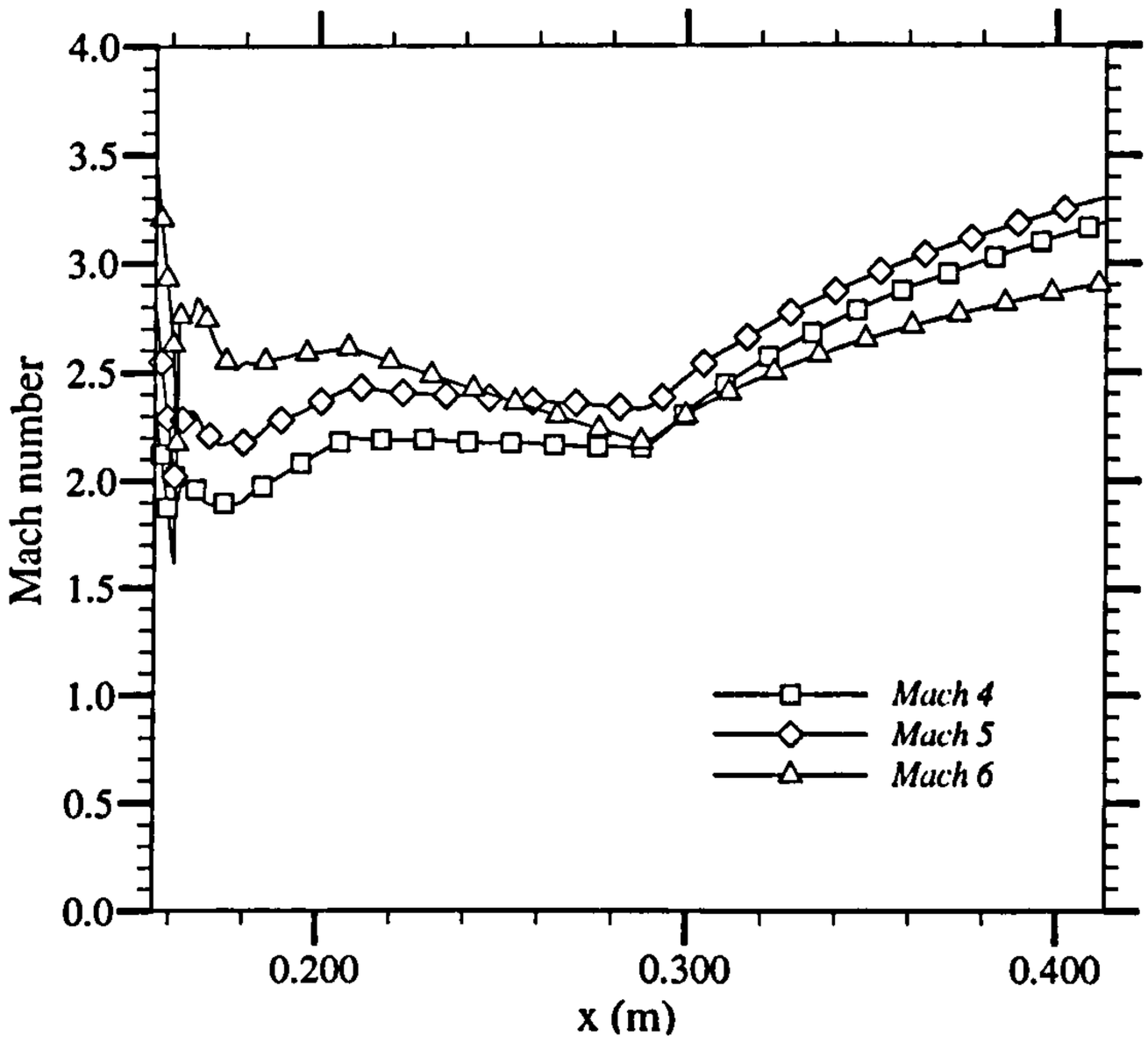


Figure 5.51: Average Mach number in the intake duct versus x-distance for the i1530 intake with a backward-facing step at the three freestream conditions.

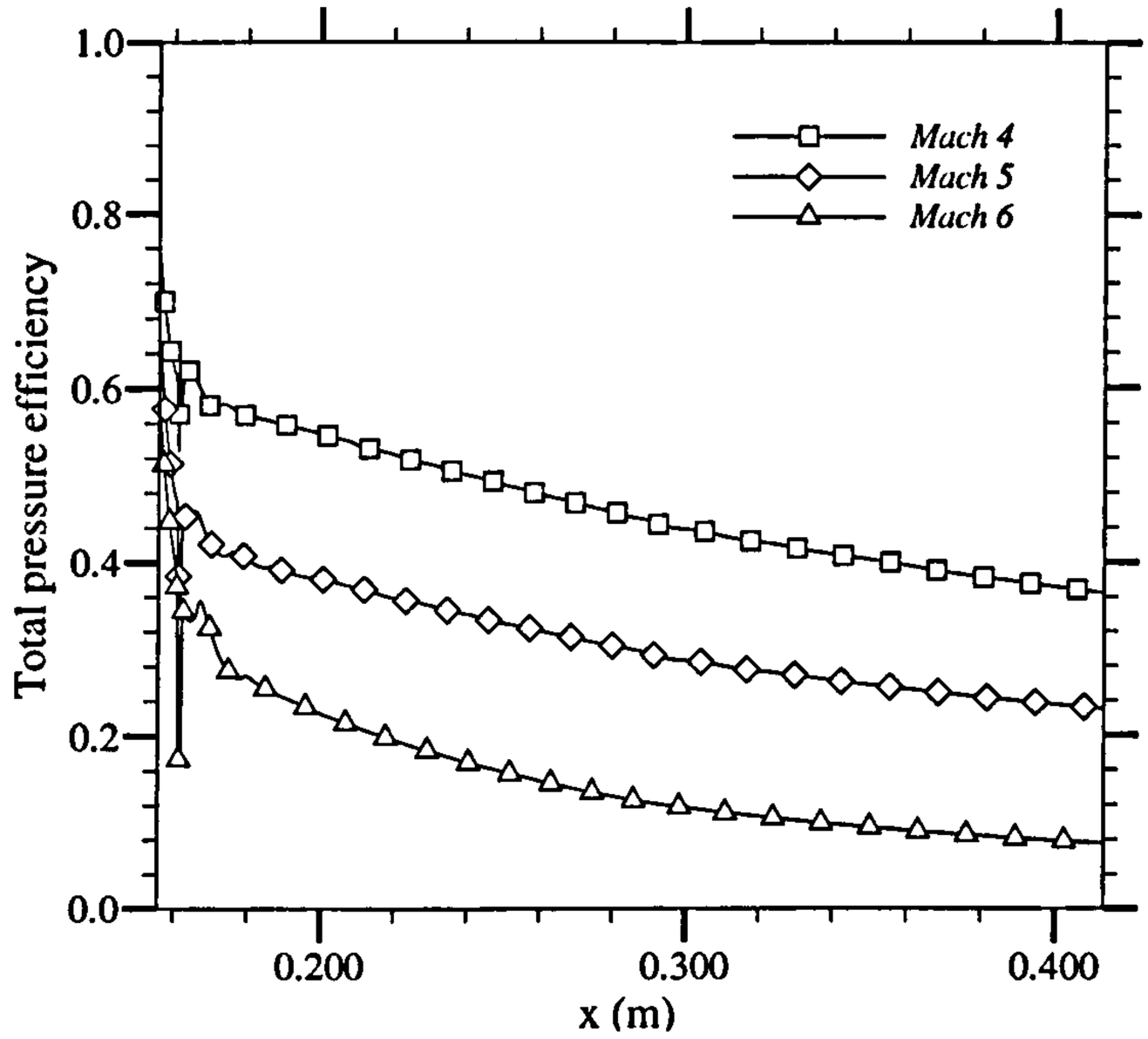


Figure 5.52: Total pressure efficiency in the intake duct versus x-distance for the i1530 intake with a backward-facing step at the three freestream conditions.

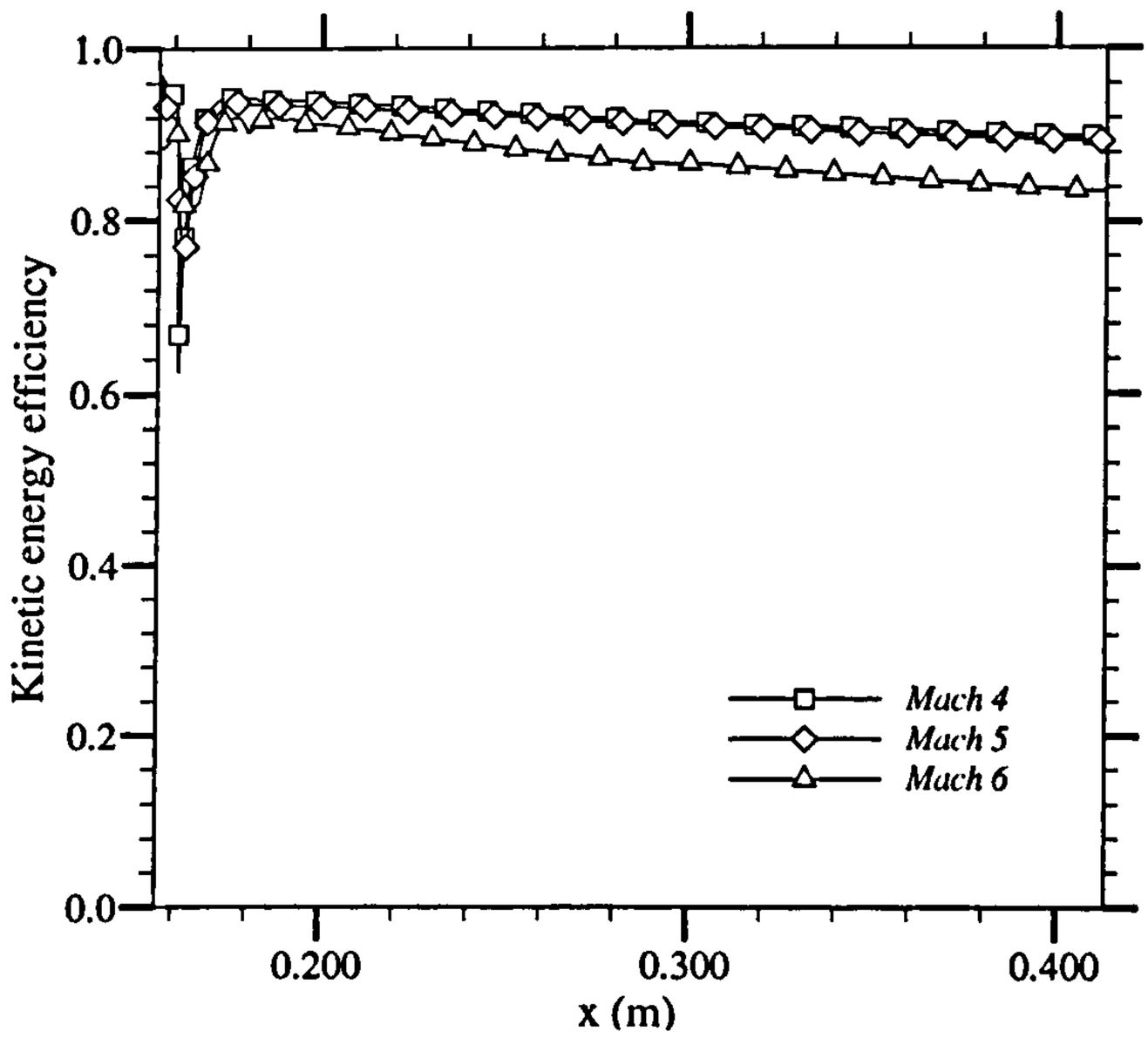


Figure 5.53: Kinetic energy efficiency in the intake duct versus x-distance for the i1530 intake with a backward-facing step at the three freestream conditions.

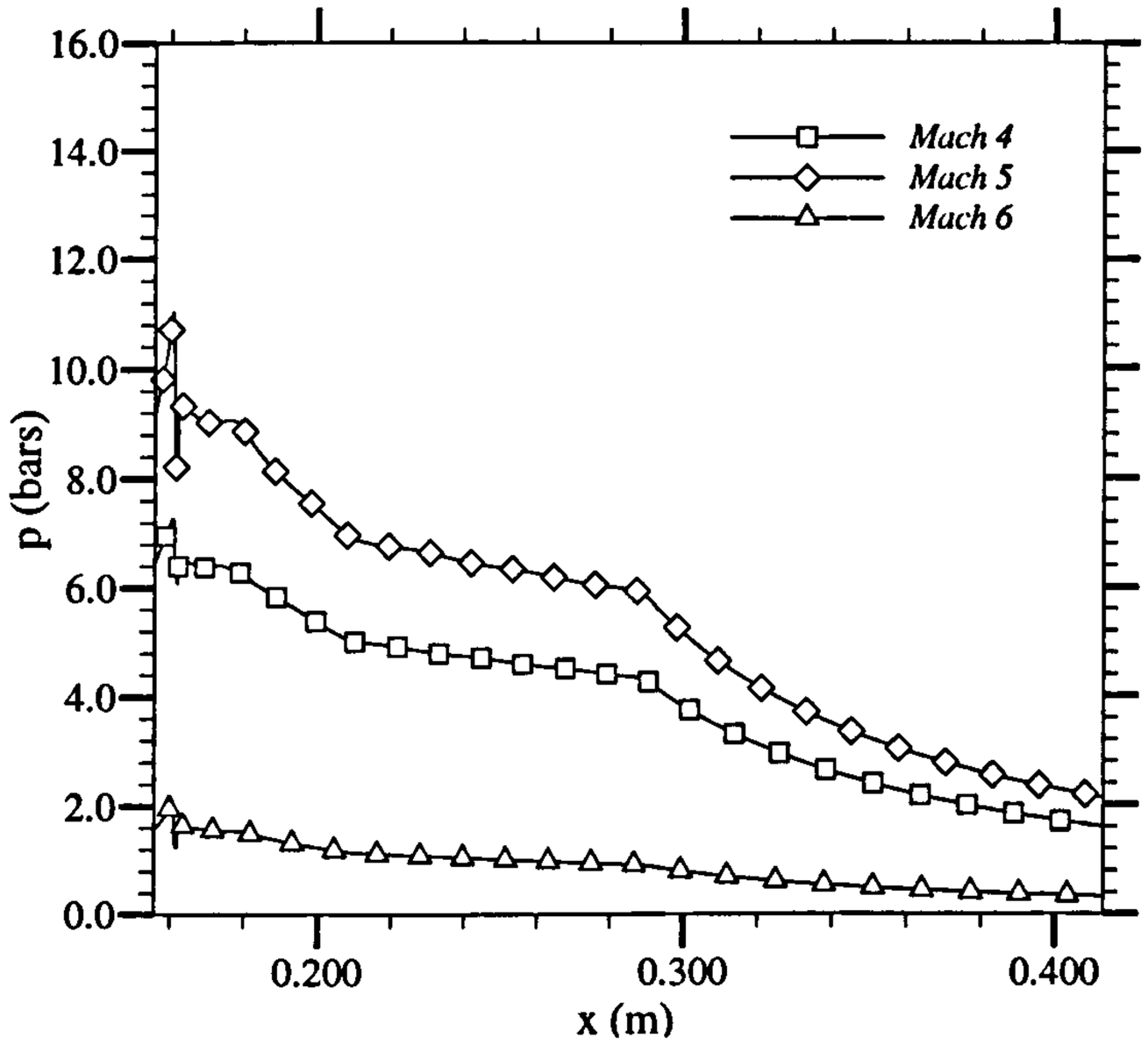


Figure 5.54: Pressure behind a normal shock in the duct versus x-distance for the i1530 intake with a backward-facing step at freestream conditions.

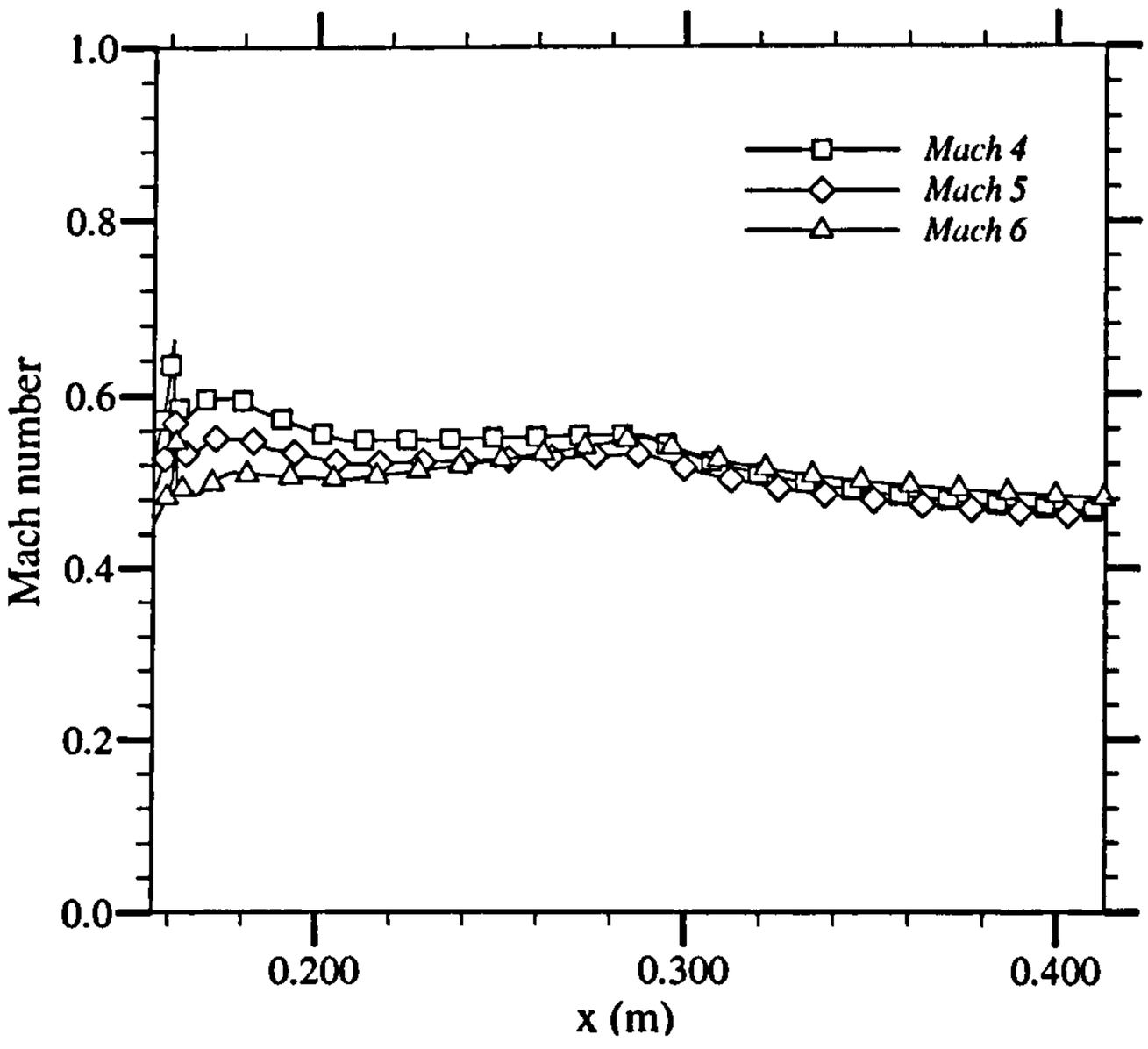


Figure 5.55: Mach number behind a normal shock in the duct versus x-distance for the i1530 intake with a backward-facing step at freestream conditions.

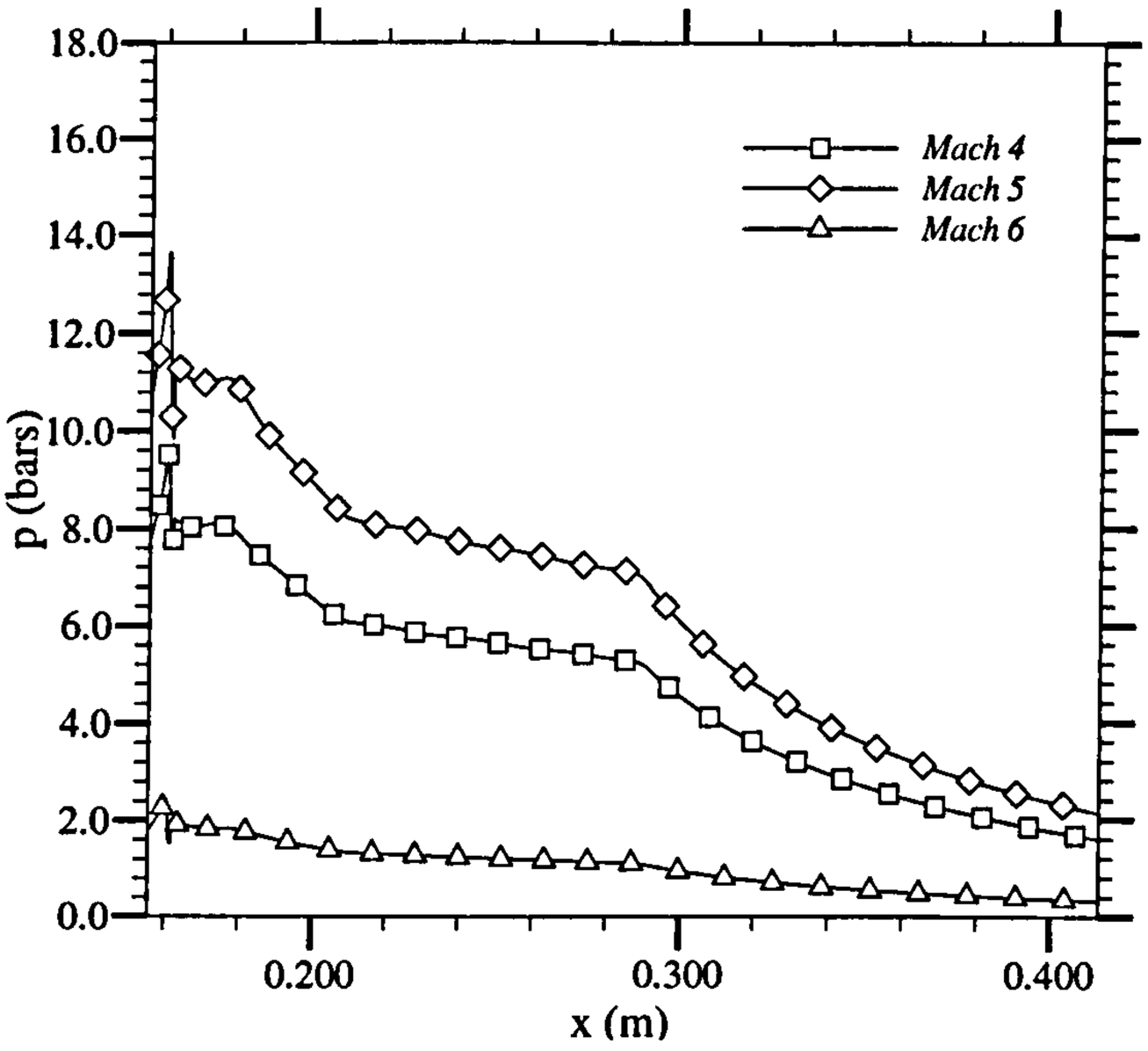


Figure 5.56: Exit pressure with a normal shock in the duct versus x-distance for the i1530 intake with a backward-facing step at freestream conditions.

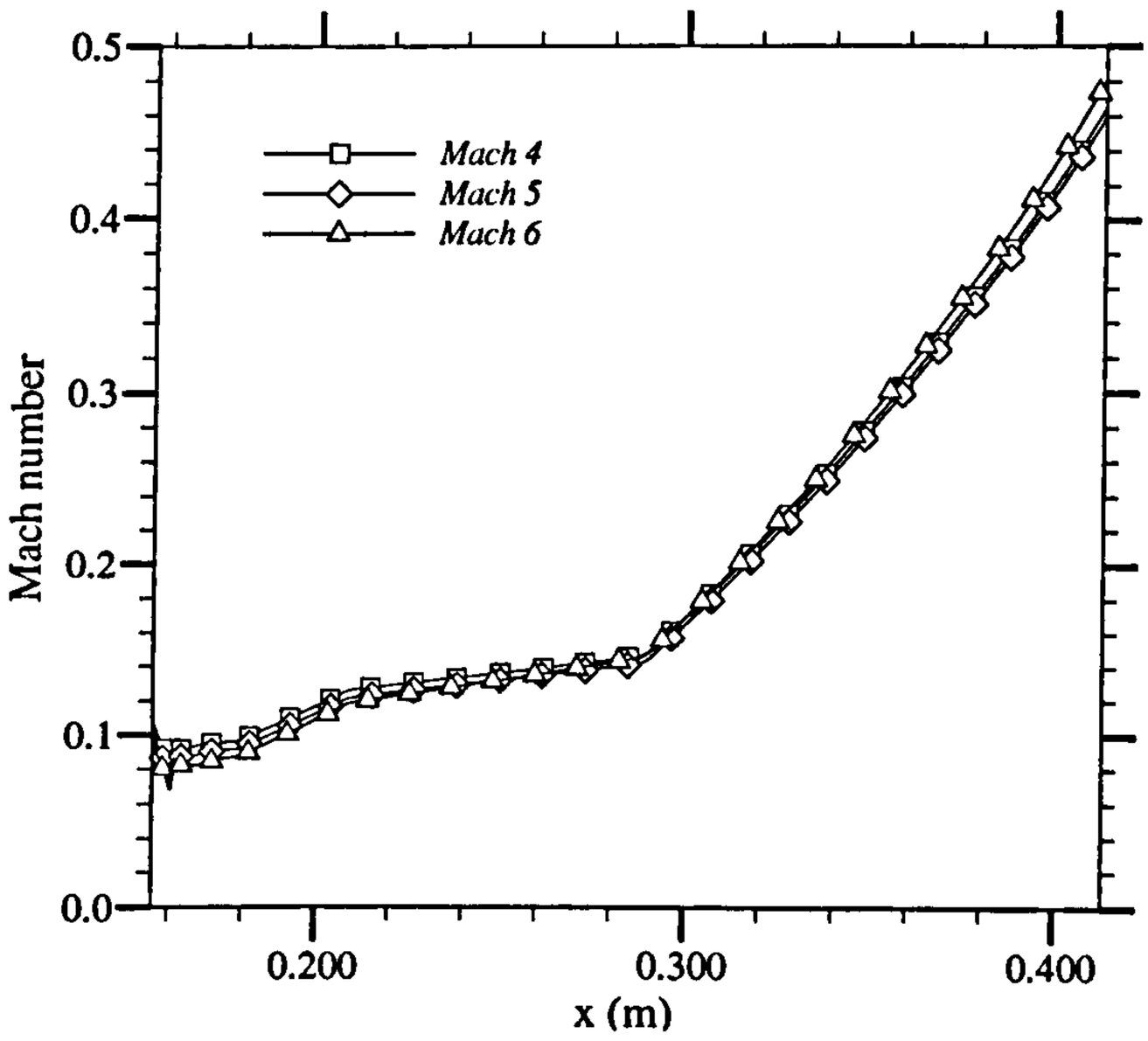


Figure 5.57: Exit Mach number with a normal shock in the duct versus x-distance for the i1530 intake with a backward-facing step at freestream conditions.

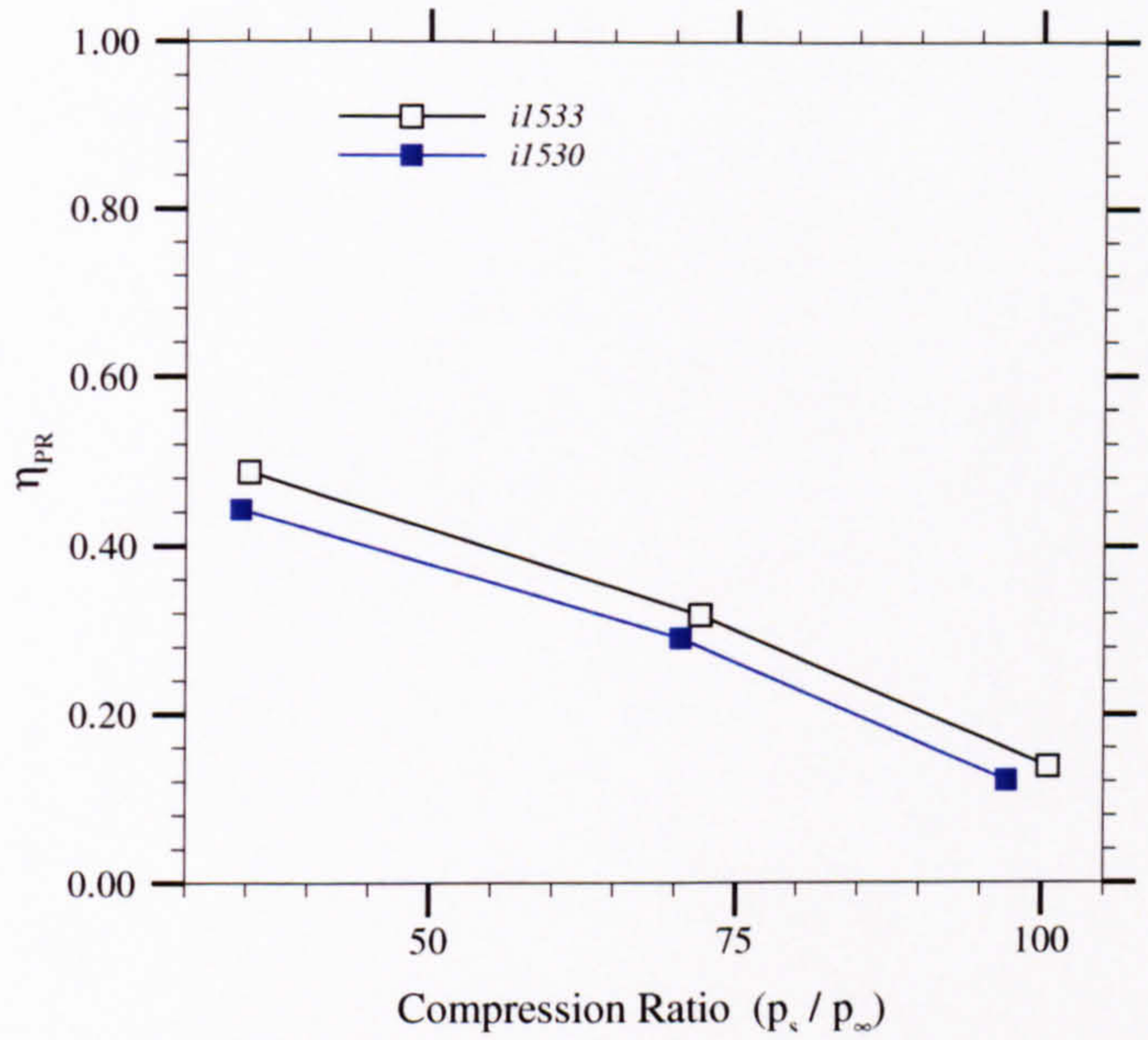


Figure 5.58: Performance map showing the compression ratio versus the total pressure efficiency for the i1533 and i1530 intakes at the three flight conditions (values taken at the start of the diffuser section).

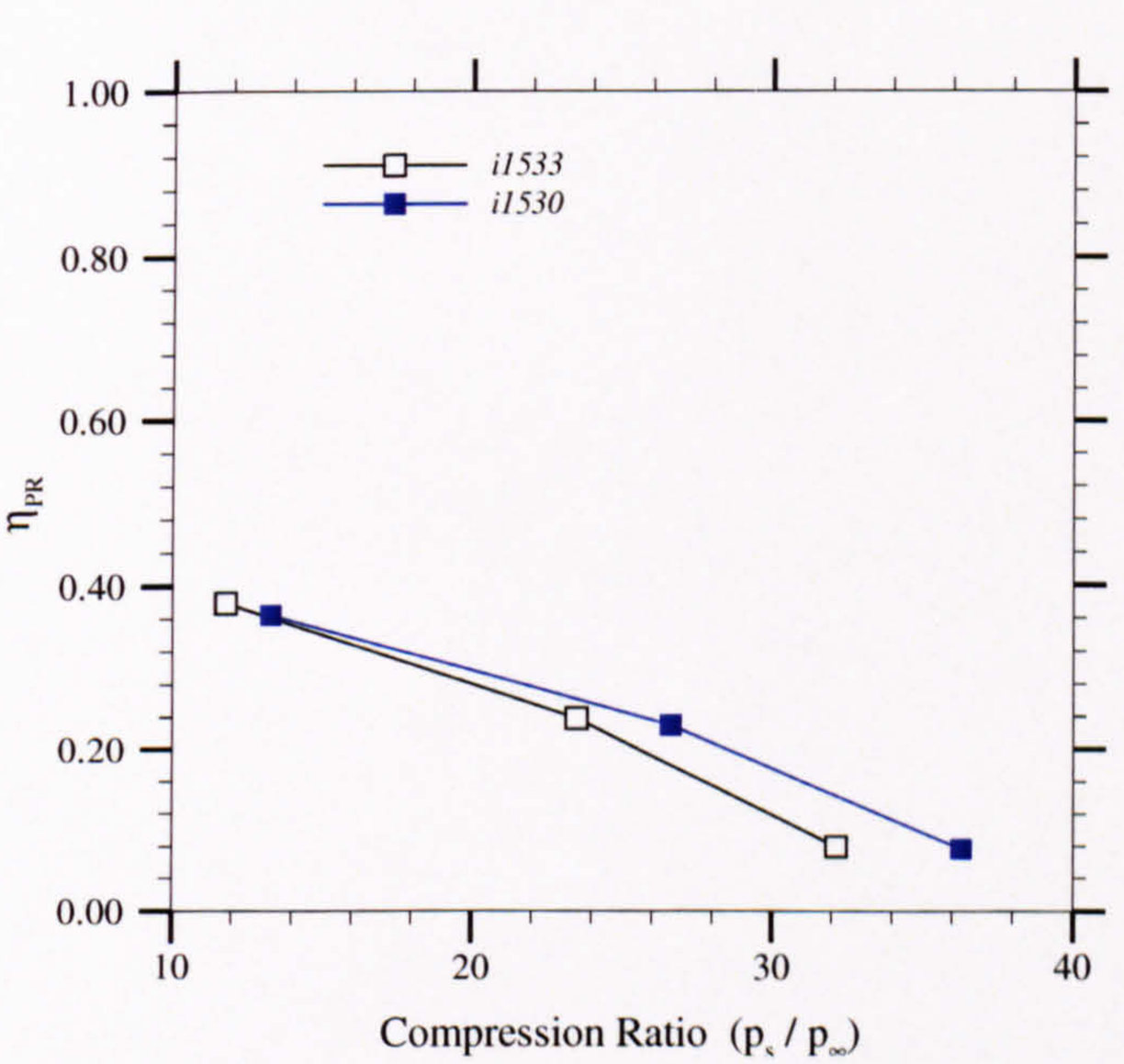


Figure 5.59: Performance map showing the compression ratio versus the total pressure efficiency for the i1533 and i1530 intakes at the three flight conditions (values taken at the end of the diffuser section).

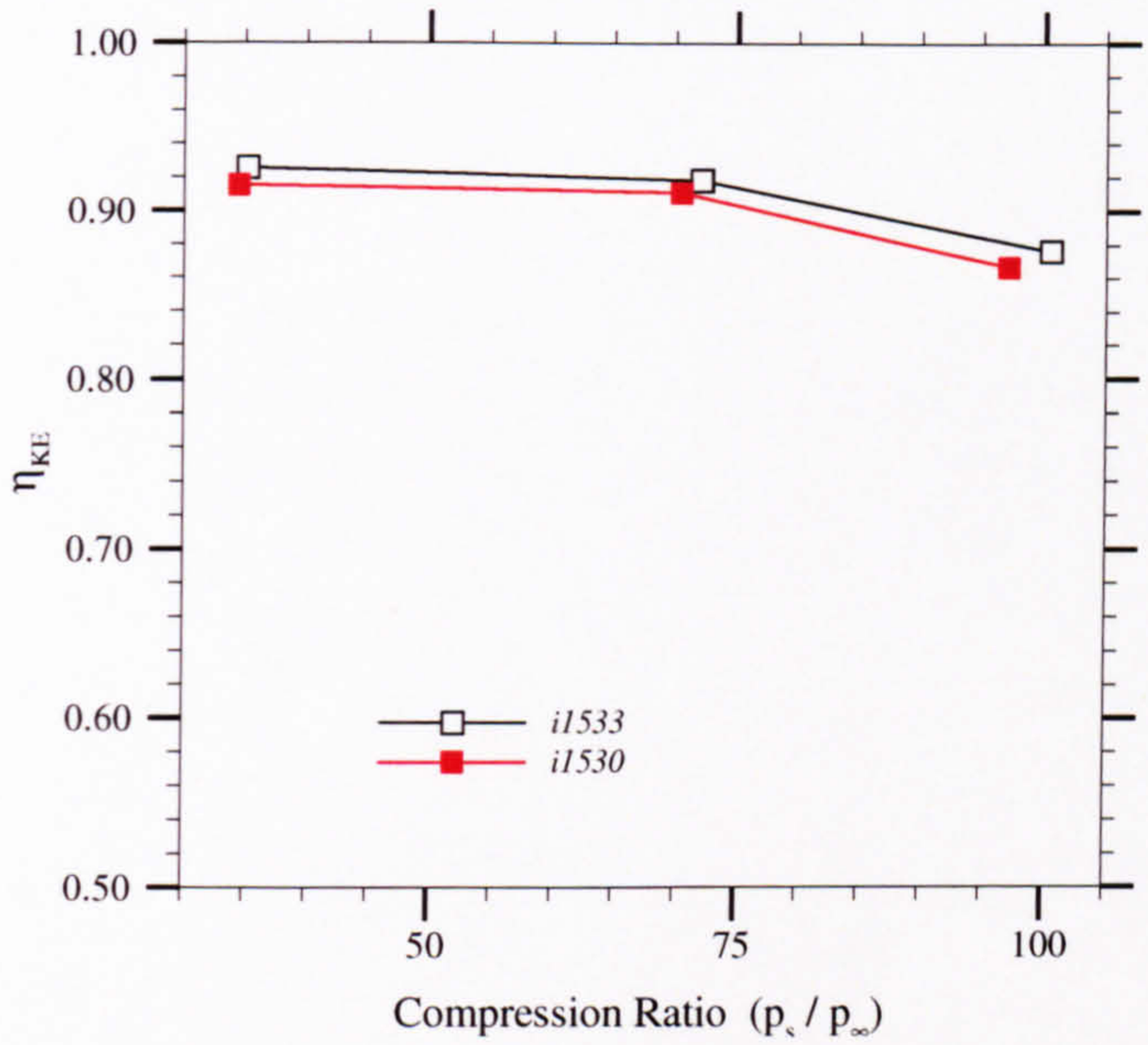


Figure 5.60: Performance map showing the compression ratio versus the kinetic energy efficiency for the i1533 and i1530 intakes at the three flight conditions (values taken at the start of the diffuser section).

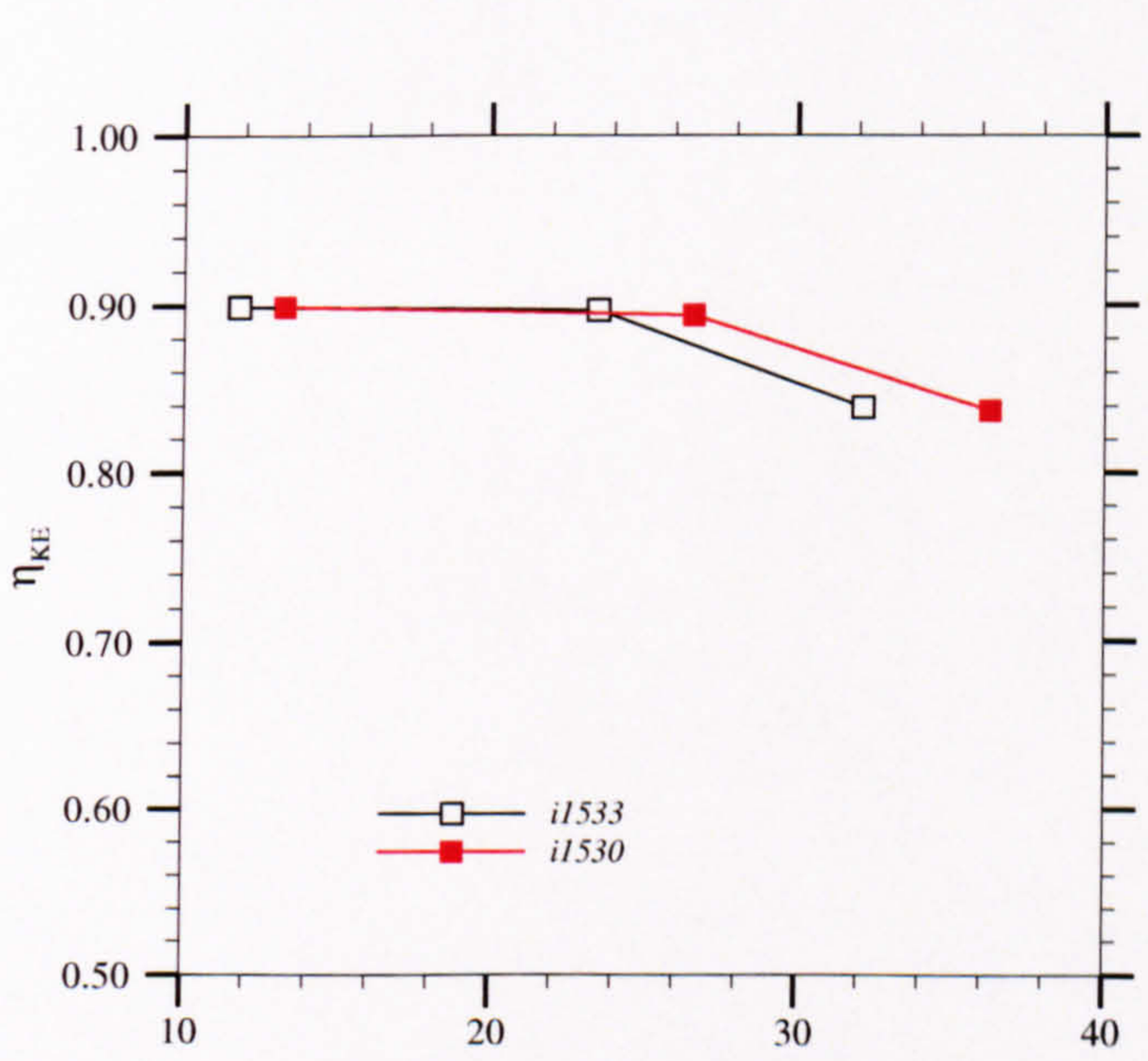


Figure 5.61: Performance map showing the compression ratio versus the kinetic energy efficiency for the i1533 and i1530 intakes at the three flight conditions (values taken at the end of the diffuser section).

Intake	M_∞	x_c , y_c (m)	θ_1 (deg)	δ_c (deg)	η_{pr}	η_{ke}	MCR	CR
i1533	4.0	0.1557, 0.0550	33	12	0.487	0.926	0.717	35.20
i1533	5.0	0.1557, 0.0550	33	12	0.318	0.918	0.947	72.10
i1533	6.0	0.1557, 0.0550	33	12	0.138	0.876	0.965	100.52
i1530	4.0	0.1844, 0.0500	30	6	0.443	0.915	0.719	34.55
i1530	5.0	0.1844, 0.0500	30	6	0.290	0.911	0.942	70.45
i1530	6.0	0.1844, 0.0500	30	6	0.121	0.867	0.963	97.13

Table 5.2: Intake performance (M_{sol}=5.5): Values of freestream Mach number, cowl position, spike termination angle, cowl angle, total pressure efficiency, kinetic energy efficiency, mass capture ratio and compression ratio for the i1533 and i1530 intakes. (values taken at the start of the diffuser section).

Intake	M_∞	x_c , y_c (m)	θ_1 (deg)	δ_c (deg)	η_{pr}	η_{ke}	CR
i1533	4.0	0.1557, 0.0550	33	12	0.379	0.899	11.795
i1533	5.0	0.1557, 0.0550	33	12	0.238	0.897	23.50
i1533	6.0	0.1557, 0.0550	33	12	0.079	0.839	32.157
i1530	4.0	0.1844, 0.0500	30	6	0.364	0.899	13.299
i1530	5.0	0.1844, 0.0500	30	6	0.230	0.894	26.60
i1530	6.0	0.1844, 0.0500	30	6	0.076	0.837	36.29

Table 5.3: Intake performance (M_{sol}=5.5): Values of freestream Mach number, cowl position, spike termination angle, cowl angle, total pressure efficiency, kinetic energy efficiency and compression ratio for the i1533 and i1530 intakes. (values taken at the end of the diffuser section).

Chapter 6

Intakes with applied back pressure

6.1 Flow characteristics in the isolator

The previous chapters focused on the intake with a supersonic flow throughout the engine. In conventional (or subsonic combustion) ramjet engines, a terminal shock system is required to be stabilised in the isolator to decelerate the flow from supersonic to subsonic conditions. CFD simulations presented in earlier chapters had shown that the inlet flows in hypersonic engines are primarily influenced by the shock systems that form at inlet. Multiple wave interactions and reflections can result in flow non-uniformities which can continue downstream into the isolator and can have an effect on the isolator performance and combustion stability of the hypersonic engine.

This chapter focuses on the interactions between the inlet and the isolator when the intake flow-field is modelled with a simulated combustion pressure rise. Figure 6.1 presents an image showing the configuration of the inlet and the isolator in the Shyfe vehicle. The isolator starts at the beginning of the parallel section after the centrebody shoulder and continues up to the combustor entry. The isolator consists of a parallel section which contains the shock train generated from the inlet shock system, and also consists of the diffuser section which extends from the parallel section up to the combustor entry. The main function of the isolator is to minimise any risk of disturbances caused by mixing and combustion from propagating upstream.

The isolator is also needed for decelerating the incoming supersonic flow to a subsonic condition and maximising recovery of the total pressure. With a back pressure applied at the combustor entry, a normal shock should stabilise in the diffuser section between the intake and combustion chamber, to diffuse the supersonic flow to a subsonic condition and maximise recovery of the total pressure in a ramjet engine.

Figure 6.2 shows a schematic of the inlet flow field after external compression. The isolator receives the supersonic stream from the inlet as a shock train, a series of either *normal* or *oblique* waves depending on the conditions at the isolator entrance.[31]

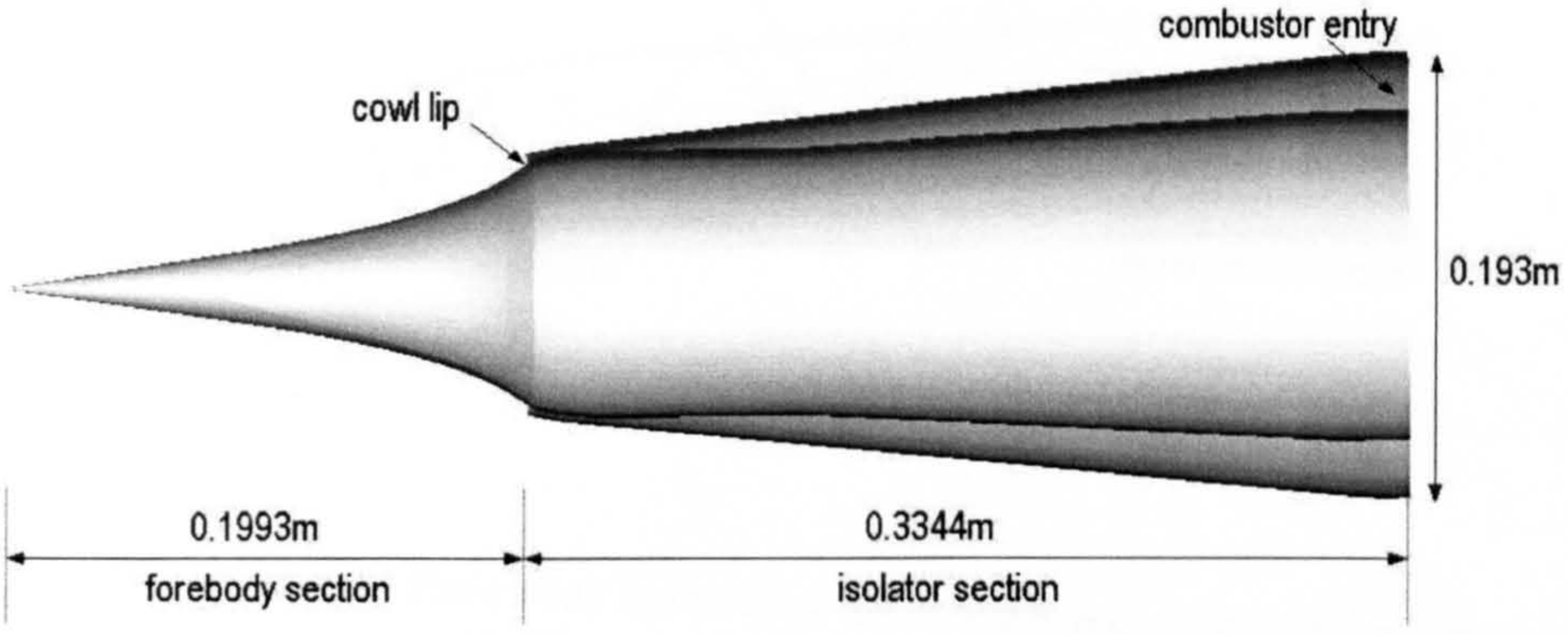


Figure 6.1: 3D View of the Shyfe intake.

Flow non-uniformities due to unfavourable inlet shock systems such as shock detachment or Mach reflection can lead to slip surfaces convecting into the duct. The turning of the compressed flow into the isolator and the impingement of the cowl shock onto the centrebody boundary-layer can result in the separation of the boundary-layer. This can lead to non-uniformities in the flow profile entering the duct. Boundary-layer separation can induce separation shocks and can cause further flow separations which can increase flow non-uniformity and lead to instabilities downstream. These flow non-uniformities can create problems in stabilising a terminal shock in the isolator. In a ramjet engine, the flow downstream in the isolator is subsonic. In supersonic flows, the downstream flows do not have an influence on the flow upstream, whereas in subsonic flow pressure waves can propagate upstream and cause disturbances. These disturbances can then propagate downstream and so on to develop an effective feedback loop. The interaction of the various inlet shock

waves as well as large inlet convergence can lead to flow separation and can increase the likelihood of an intake unstart. Excessive back pressuring due to combustion pressure rise can also push the shock train forwards within the isolator towards the inlet throat.[35] This indicates the maximum back pressure limit that the intake can withstand before the onset of unstart. The degree of maximum sustainable combustor pressure rise before the onset of unstart depends on inlet geometry, contraction ratio, isolator length,[35,75,91,104] and also on the flow profile in the isolator.

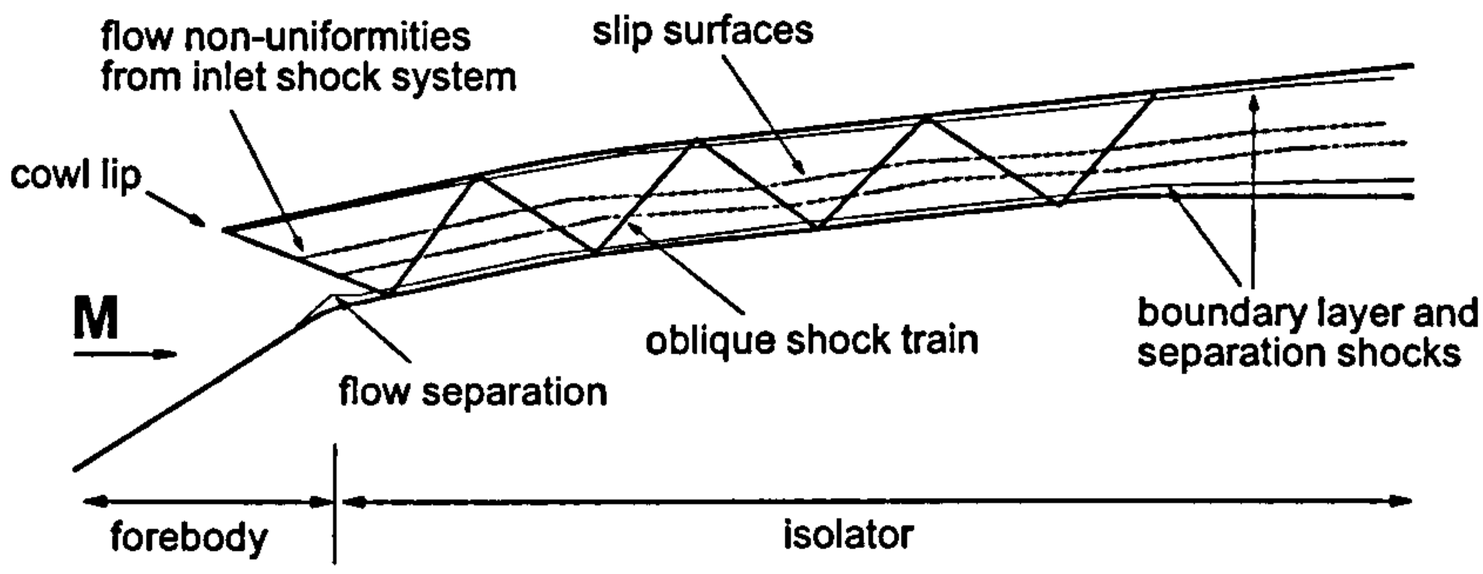


Figure 6.2: Schematic of hypersonic inlet flow after external compression showing the various flow-field characteristics present in the isolator section of the engine.

Limited literature is available on the effect of flow non-uniformity on the isolator performance. Most of the work documented in the literature has focused on the effect of the isolator geometry on overall performance. Due to the limitations in computational power available, a brief analysis of the effect of the flow profile on isolator performance is made in this chapter.

6.2 Method for applying a back pressure

The Shyfe intake with a thin-plate cowl in the geometry is used to carry out the following test cases. The intake shock-on-lip condition is at Mach 5.5. The spike terminates at an angle of 33 degrees and the flow is then turned into the parallel section of the isolator with a centrebody and cowl angle of 12 degrees. Table 6.1 presents the Mach number, freestream pressure, freestream temperature and required combustion pressure at the three flight conditions for the intake ($M_{sol} = 5.5$). The

intake is required to sustain the given combustion pressure for successful operation.

Several methods to simulate a combustion pressure rise were investigated. Initially, a characteristic boundary condition was used to apply a back pressure to the downstream exit boundary of the mesh. The pressure at this boundary was applied instantaneously and was held constant at a specified value of pressure. Several back pressure simulations carried out using this method revealed problems in the flow-field, namely the reversal of flow at the isolator exit. While investigating this method to apply a back pressure to the flow-field, computations were carried out by ramping the back pressure up slowly in time steps rather than introducing it instantaneously. A specified rise time was used to ramp the back pressure up in steps before reaching its final required value. The computations again showed an unacceptable reversal of flow at the isolator exit and almost always resulted in an intake unstart. An alternative method to simulate the back pressure using a *second throat* or *fictitious throat* was therefore tried. This involved extending the isolator geometry to incorporate a second throat whereby the choked flow would produce a terminal shock system in the diffuser which could propagate to the isolator.

Figure 6.3 presents CFD pressure contours of the extended isolator section to show the application of the back pressure via a second throat. For a given condition upstream of the second throat there is an area ratio that will create sonic conditions at the throat, i.e. a normal shock at the throat. Any reduction in this area ratio will lead to the shock strength increasing and thus the pressure ratio across the shock increasing, and hence will propagate the shock upstream due to the back pressure. The level of back pressure was controlled by the alteration of the throat area. This method required numerous modifications to the mesh as different throat areas were used to change the level of back pressure applied on the intake.

Mach Number	*Pressure*	*Temperature*	*Combustor Pressure*
4.0	12.0 KPa	217 K	8.7 bar
5.0	8.0 KPa	217 K	9.3 bar
6.0	0.89 KPa	228 K	1.2 bar

Table 6.1: Freestream conditions for the intake (shock-on-lip at Mach 5.5) at the three flight conditions showing the level of back pressure required in each case.

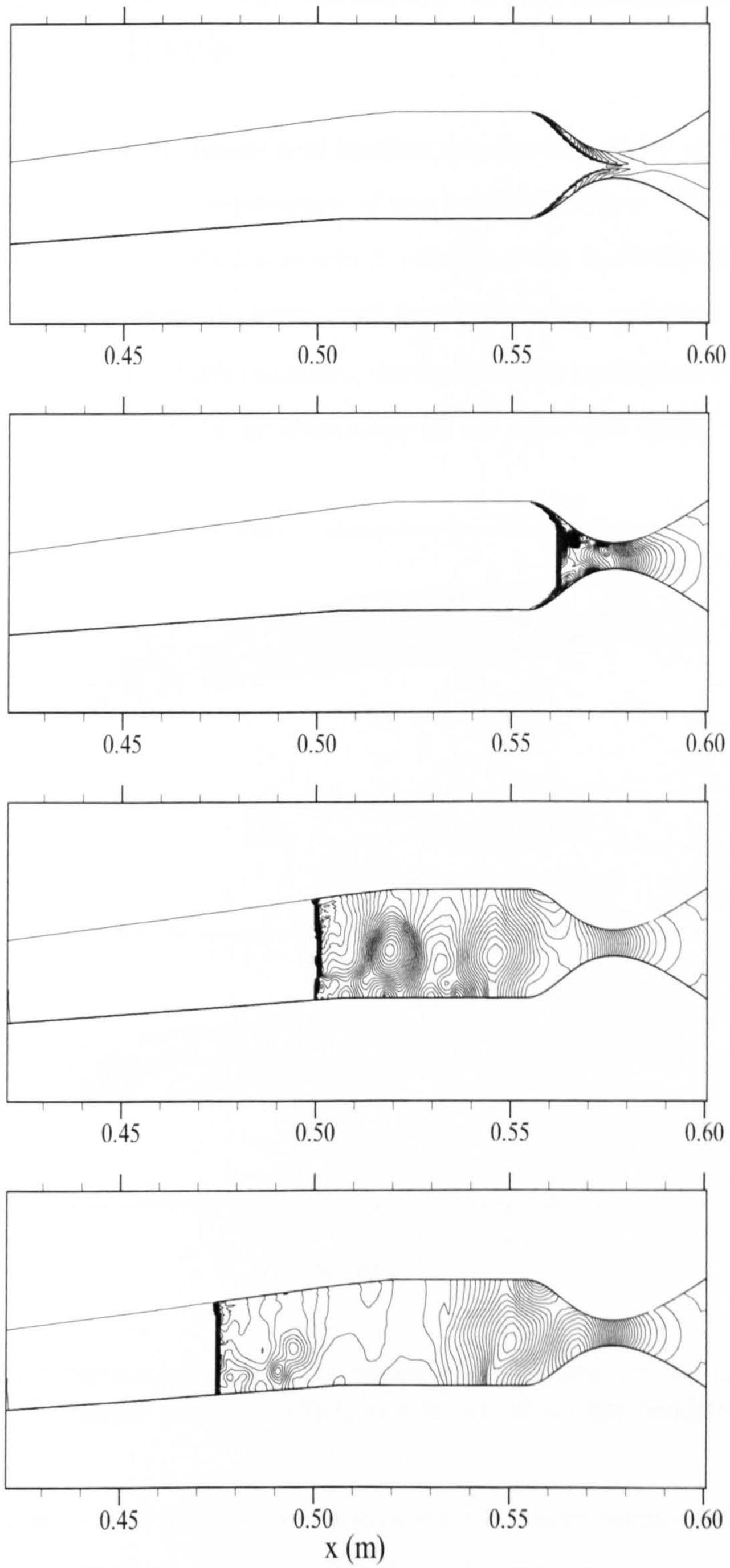


Figure 6.3: CFD Pressure contours to show the application of the back-pressure boundary condition on the intake to simulate combustion pressure rise; time-dependent contours from (top) to (bottom).

6.3 Effect of non-uniformity on sustainable back pressure levels

Flow non-uniformities in an intake and isolator can be caused by unfavourable off-design wave interactions and separation of the boundary-layer. The intake is designed for shock-on-lip at Mach 5.5 at which condition the forebody isentropic compression waves coalesce to meet at the cowl lip. This is the optimum configuration for the inlet. At off-design Mach numbers, the focus of the compression waves moves away from the cowl lip to cause imperfections in the inlet flow field.

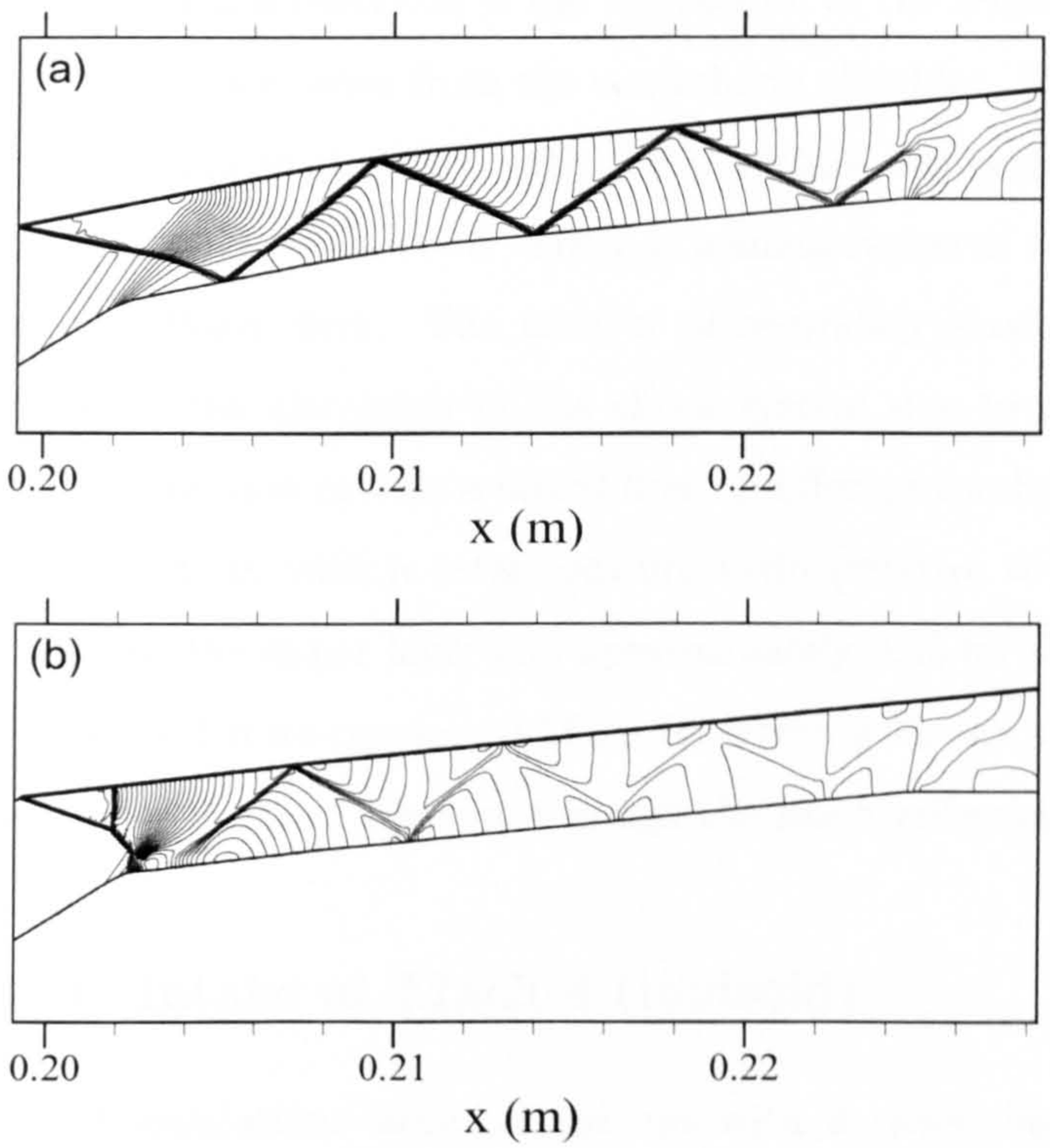


Figure 6.4: CFD Pressure contours from inviscid simulations of the intake ($M_{sol} = 5.5$) with a (a) 12 degrees and (b) 7 degrees cowl at off-design condition Mach 4.

Figure 6.4 (a) presents an inviscid simulation for the intake with a centrebody and cowl angle of 12 degrees at off-design Mach 4. In this case, no back pressure is imposed at the combustor entry and the flow throughout the intake is supersonic. The isentropic compression waves from the forebody coalesce to a point above the

cowl, to cause flow spillage. The reflected shock wave from the cowl lip reflects onto the centrebody as regular reflection and forms an oblique shock train in the parallel section of the duct. The solution shows near-uniform flow through the isolator with slight transverse variation in total pressure across the duct.

In testing several inlet configurations, it was found that reducing the cowl leading edge angle to 7 degrees, hence increasing the flow turning angle at inlet, results in the shock system from the cowl reflecting on to the centrebody as Mach reflection, Figure 6.4 (b). The centrebody angle after the shoulder is also reduced to 7 degrees to keep the centrebody and cowl inner surfaces parallel. The significant interaction here in producing the Mach reflection is the interaction of the reflected shock from the cowl with the expansion wave from the centrebody shoulder. The flow reflects as an oblique shock train in the duct with a slip surface convecting downstream from the triple point of the Mach stem. There is a small region of reverse subsonic flow just behind the Mach stem. The number of secondary shocks in the shock train increases due to the alteration in the shock system due to the presence of Mach reflection. The solution reveals a mixed flow of different total pressures above and below the slip surface, with a total pressure ratio (relative to freestream) of approximately 0.73 for the upper layer and approximately 0.55 for the layer below. The shock shifts forward from regular to Mach reflection with the surface pressure values indicating a rise in static pressure through the Mach reflection.

6.3.1 Case 1: Intake at Mach 4 (inviscid)

A series of inviscid simulations were carried out with a raised back pressure to simulate combustion pressure rise, and to test the stability of the terminal shock in the isolator for the two cases. Inviscid simulations allow for the focus of the flow problem on the inviscid interactions without the added complexities of boundary-layer separation. The first cases tested are at Mach 4 for the intake with a 12 and 7 degrees centrebody and cowl angle. For a back pressure ratio p_{comb}/p_{∞} of approximately 24, for the intake with a 12 degrees cowl angle, a normal shock system stabilises in the isolator at x=0.30m, Figure 6.5 (a). The shock is stable at

this position and the flow behind the shock wave is subsonic with the flow properties behind the shock wave showing no fluctuations. The inlet flow in this case had produced a regular reflection of the cowl shock on the centrebody, with near-uniform flow across the intake duct. The same level of back pressure is then applied to the intake with a 7 degrees cowl angle, where Mach reflection occurs.

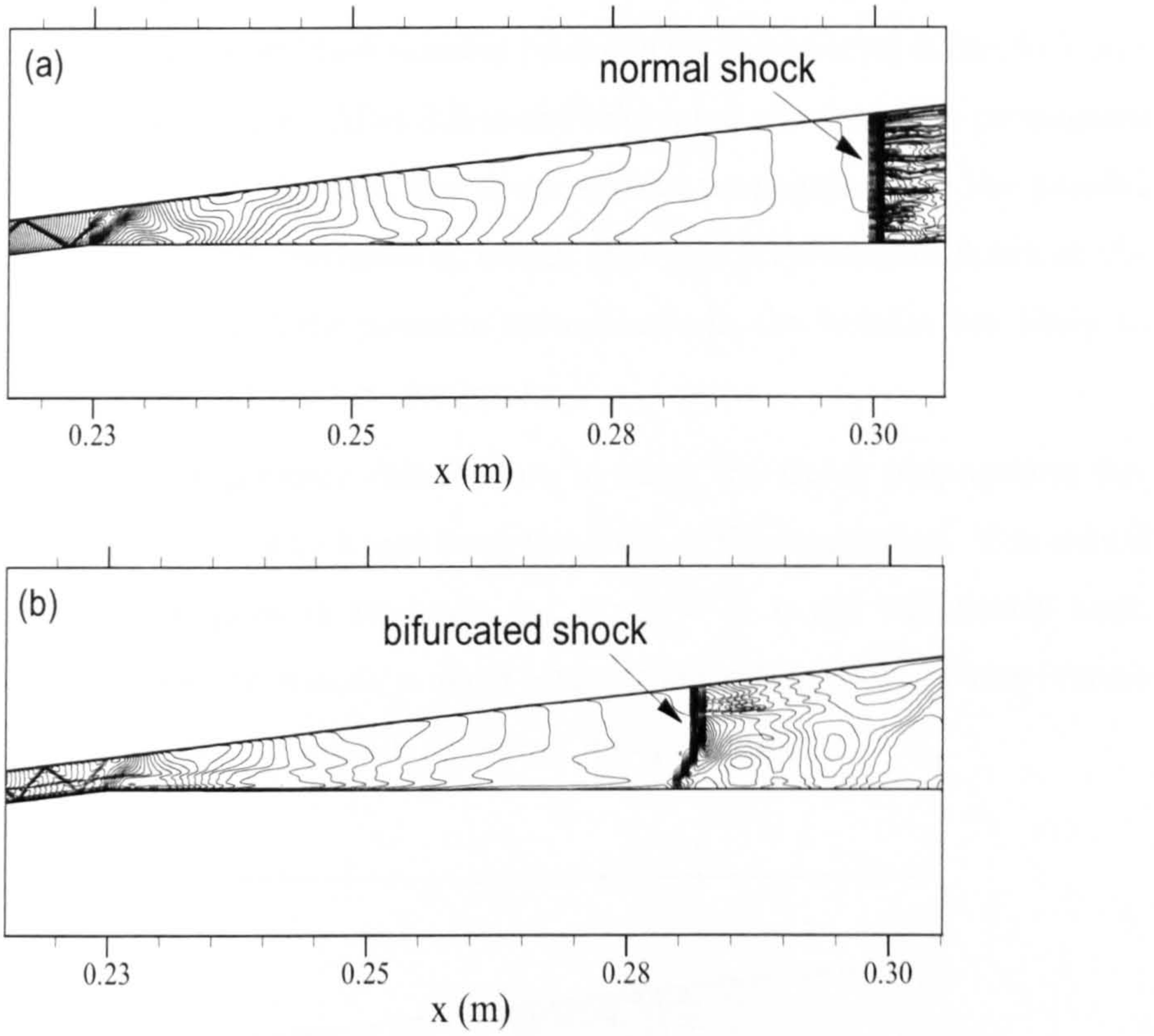


Figure 6.5: CFD Density contours from inviscid simulations of the intake (M_{sol} = 5.5) with a centrebody and cowl angle of (a) 12 degrees and (b) 7 degrees; at off-design condition Mach 4 with an applied back pressure p_{comb}/p_{∞} of approximately 24.

Figure 6.5 (b) presents Mach number contours from this simulation showing the shock system stabilising in the isolator further forwards at x=0.28m, in a bifurcated shock formation. The post-shock flow shows regions of mixed subsonic and supersonic flow regions. The solution shows oscillations in pressure, and the appearance of reverse flow regions. The back pressure is now increased to an approximate ratio of $p_{comb}/p_{\infty} = 41$. This results in the normal shock system in Figure 6.5 (a)

(12 degrees cowl case) propagating further upstream in the isolator to a position x=0.262m, Figure 6.6. The solution reveals that the normal shock oscillates slightly about this position but does not propagate into the parallel section of the duct.

The higher back pressure ratio $p_{comb}/p_{\infty} = 41$ is then applied to the intake with a 7 degrees centrebody/cowl angle. The duct flow profile in this case was non-uniform due to the Mach reflection at inlet, from which slip surfaces convect into the isolator. Figure 6.7 shows a sequence of Mach number contours for the interval 3.2ms to 5.5ms from the start of the simulation. After 3.2ms the bifurcated shock system propagates forwards towards x=0.25m. At 4ms, the shock system propagates into the parallel section, and reaches the inlet entrance at 5.5ms. The shock system stabilises at the inlet annulus, however any slight pressure disturbance in the isolator are likely to perturb the shock wave and unstart the intake.

Figure 6.11 plots surface pressure distribution to show the shock propagating forwards in the duct from 2.9ms to 5.5ms from the start of the simulation. The actual level of back pressure applied in this case, $p_{comb}/p_{\infty} = 41$ is not sufficiently high, and the intake would need to sustain a much higher combustion pressure rise (values for required pressure given in Table 6.1) during its operation.

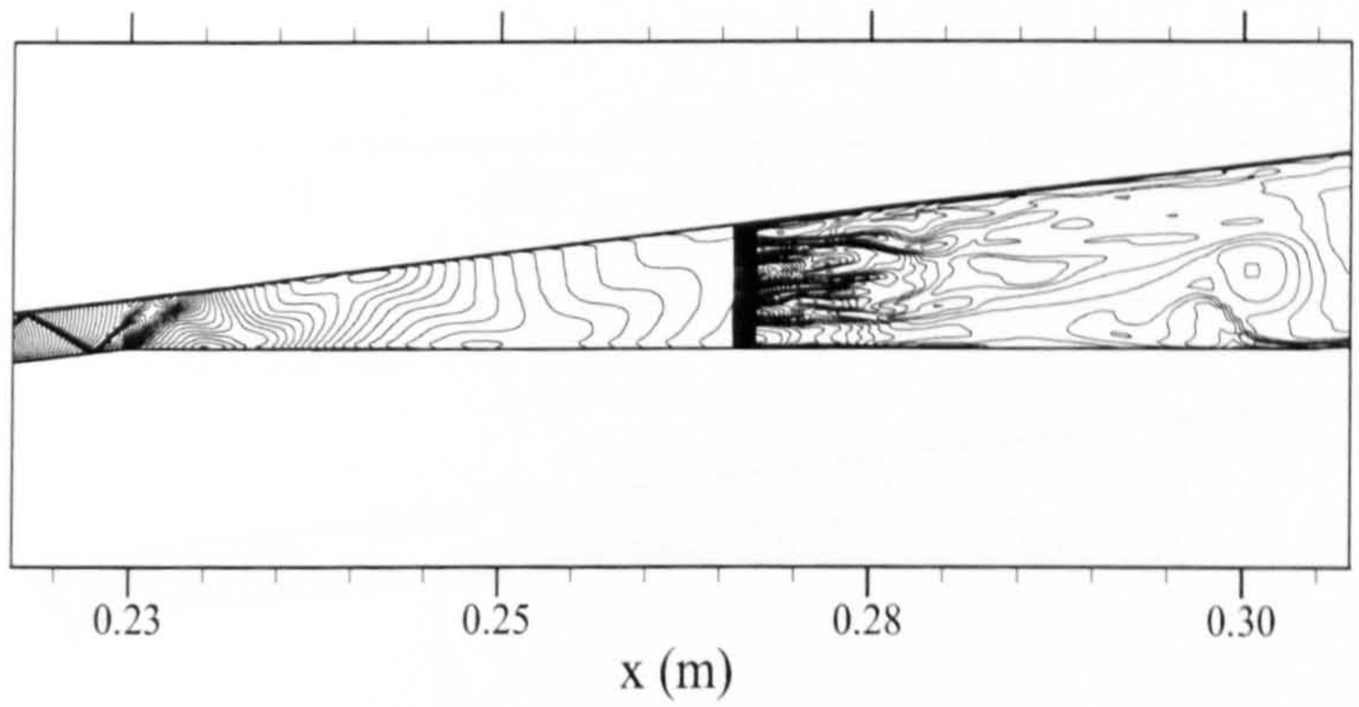


Figure 6.6: CFD Mach number contours from an inviscid simulation of the intake ($M_{sol} = 5.5$) with a centrebody and cowl angle of 12 degrees at off-design condition Mach 4 with an applied back pressure p_{comb}/p_{∞} of approximately 41; time=4ms.

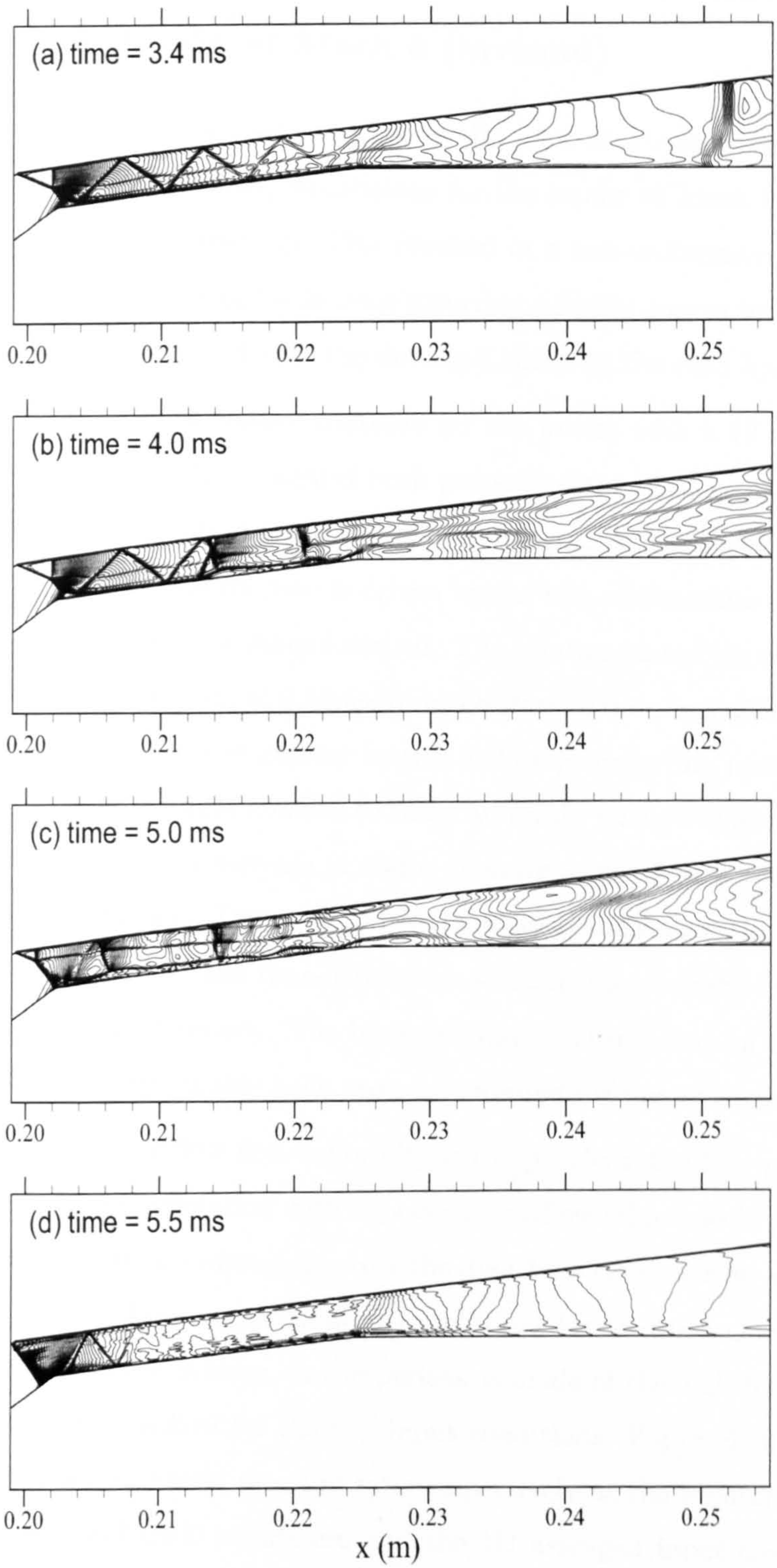


Figure 6.7: CFD Mach number contours from an inviscid simulation of the intake ($M_{sol} = 5.5$) with a centrebody and cowl angle of 7 degrees at off-design condition Mach 4 with an applied back pressure p_{comb}/p_{∞} of approximately 41; time=3.2 to 5.5ms.

6.3.2 Case 2: Intake at Mach 6 (inviscid)

The next test cases apply a back pressure to the inlet at above-design condition Mach 6. Inviscid (and turbulent) simulations for the intake at Mach 6 had shown a shock detachment at the cowl lip. This resulted in a non-uniformity in the duct flow, with upper layer of flow in the isolator incurring a higher loss in total pressure, approximately 65 percent loss due to the detached shock at the cowl lip.

Figure 6.8 shows a series of density contours for the intake with a 12 degree centrebody/cowl angle and with an applied back pressure ratio of $p_{comb}/p_{\infty} = 47.2$ at freestream Mach 6. The solution shows an oblique shaped terminal shock wave, seen in Figure 6.8 (a). In this case the flow is driven by the non-uniformities in the duct and hence the terminal shock is oblique shaped. The solution shows the shock propagating into the parallel section, at 0.32ms from the start of the simulation and then oscillating back and forth in the isolator section before propagating upstream and finally disgorging out of the inlet annulus to cause an *intake unstart.* The flow at the cowl lip experiences a sudden increase in static pressure as the flow is reversed out of the inlet to cause spillage. The detached shock wave stabilises on the forebody, as seen in Figure 6.8 (c) and the time-dependent solution shows slight oscillations of this shock wave on the forebody. The back pressure level imposed on the intake is again lower than the sustainable back pressure required for ramjet operation.

To assess whether the basic flow non-uniformity is the problem, the flow properties from the Mach 6 inviscid simulation with supersonic outflow (this case is presented in Chapter 4, Figure 4.20) are averaged across the duct by a conservation averaging method. This obtains a 1D averaged (uniform) conditions for the inlet which is then used as an input flow to the isolator. A comparison is made of the exit flow for the intake with a supersonic outflow for the two input conditions. Figure 6.10 (a) and (b) show Mach number and total pressure ratio respectively at the isolator exit for both the two-dimensional CFD simulation and the 1D averaged input conditions, and the highly non-uniform profile of the two-dimensional CFD case is evident.

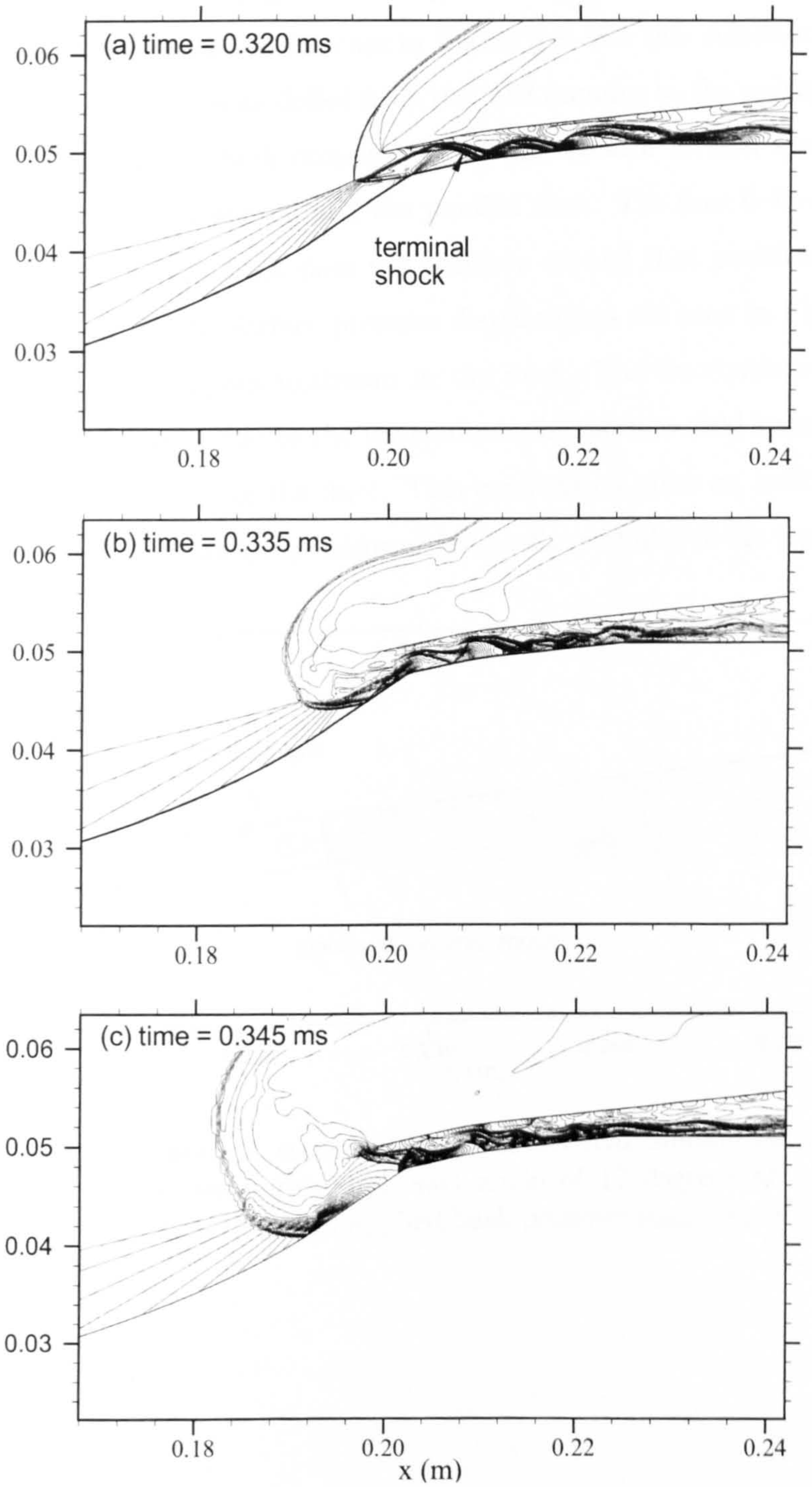


Figure 6.8: CFD Mach number contours from an inviscid simulation of the intake ($M_{sol} = 5.5$) with a centrebody and cowl angle of 12 degrees at off-design condition Mach 6 with an applied back pressure p_{comb}/p_{∞} of approximately 47.2; time=3.2 to 5.5ms.

Figure 6.9 shows the 1D averaged inlet properties case with a back pressure ratio of $p_{comb}/p_{\infty} = 47.2$ to compare to the case in Figure 6.8. For this simulation, only the duct portion of the intake is modelled from the inlet annulus to the isolator exit. The solution shows a normal shock propagating up the isolator section and stabilising just between the diffuser section and the parallel duct. The flow behind the shock wave is subsonic and the shock does not oscillate around that position, stabilising satisfactorily in the duct. Surface pressure distributions are seen in Figure 6.12 as the normal shock propagates upstream in the duct. The fluctuations in pressure behind the shock wave is due to the unsteadiness in the flow-field before the shock wave eventually stabilised in the duct. This comparison gives an indication of the effect of isolator flow profile (non-uniformities) on the stability of the terminal shock.

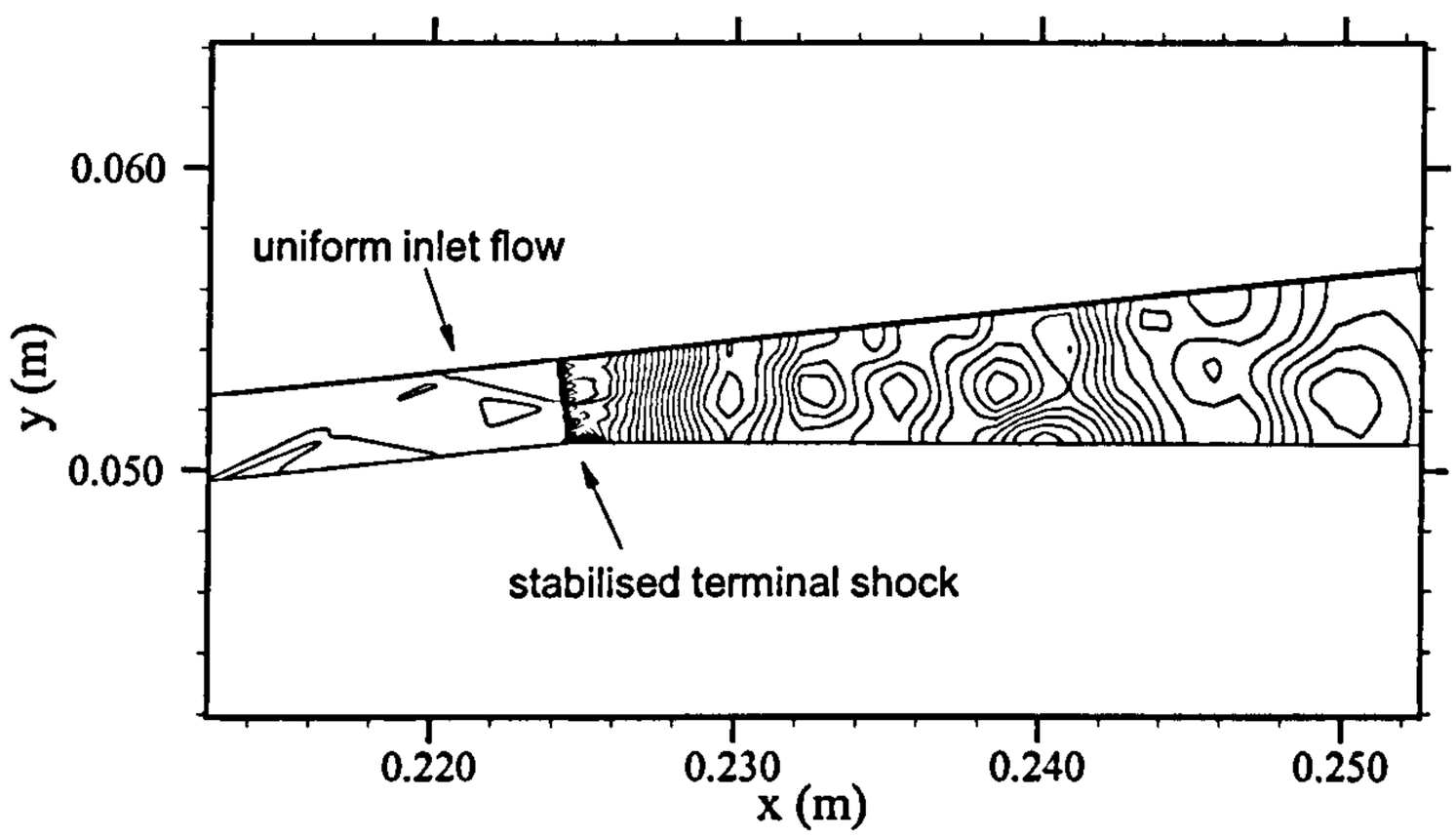


Figure 6.9: CFD Pressure contours from an inviscid simulation of the intake ($M_{sol} = 5.5$) with a centrebody and cowl angle of 12 degrees at Mach 6 (averaged inlet flow properties) with an applied back pressure p_{comb}/p_{∞} of approximately 47.2; time=5.5ms.

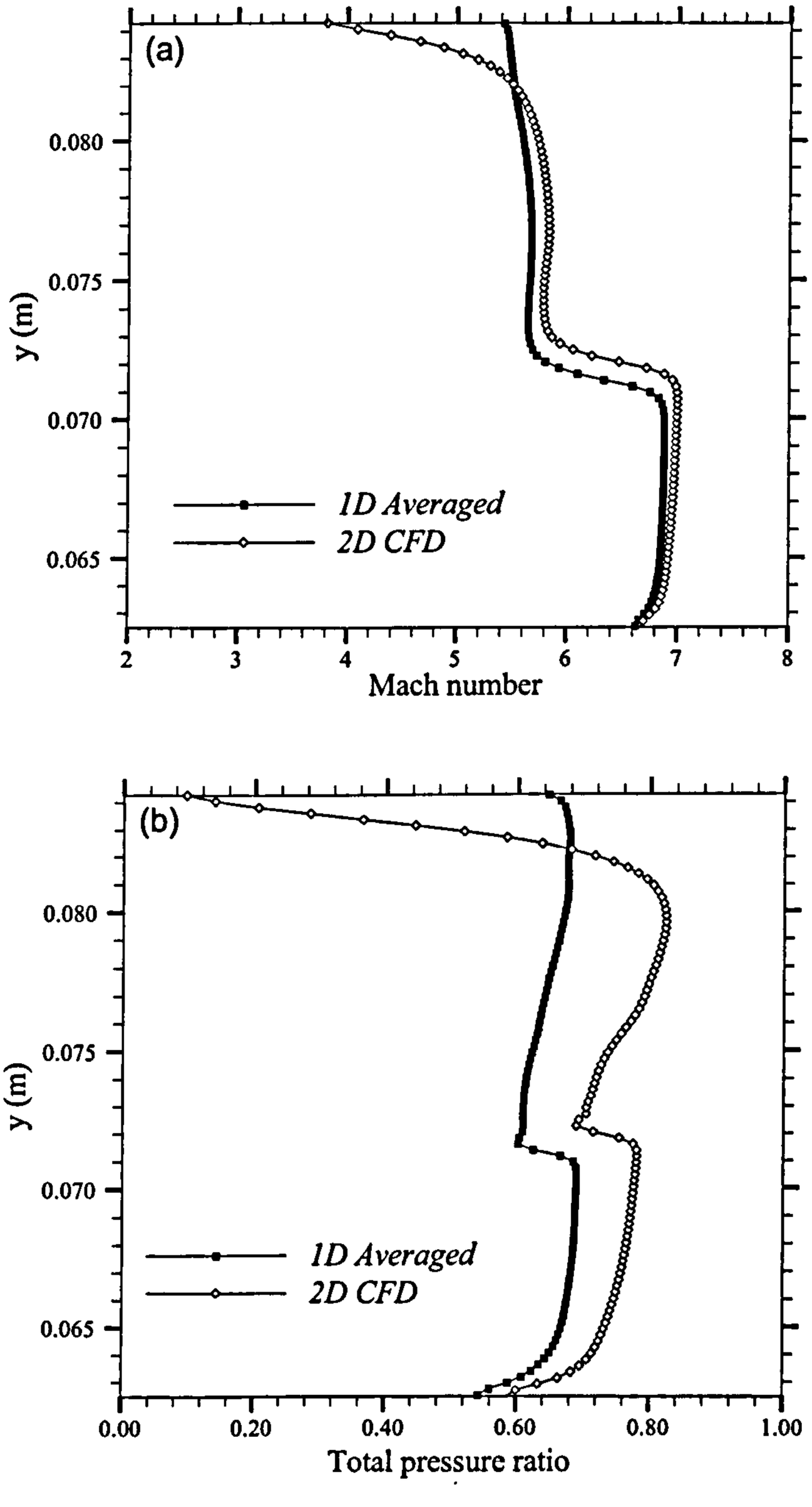


Figure 6.10: Comparison of the flow properties at the isolator exit for the intake ($M_{sol} = 5.5$) with a centrebody and cowl angle of 12 degrees at off-design condition Mach 6 with an applied back pressure p_{comb}/p_{∞} of approximately 47.2 for the 2D and averaged inlet flow properties case; (a) exit Mach number and (b) exit total pressure ratio.

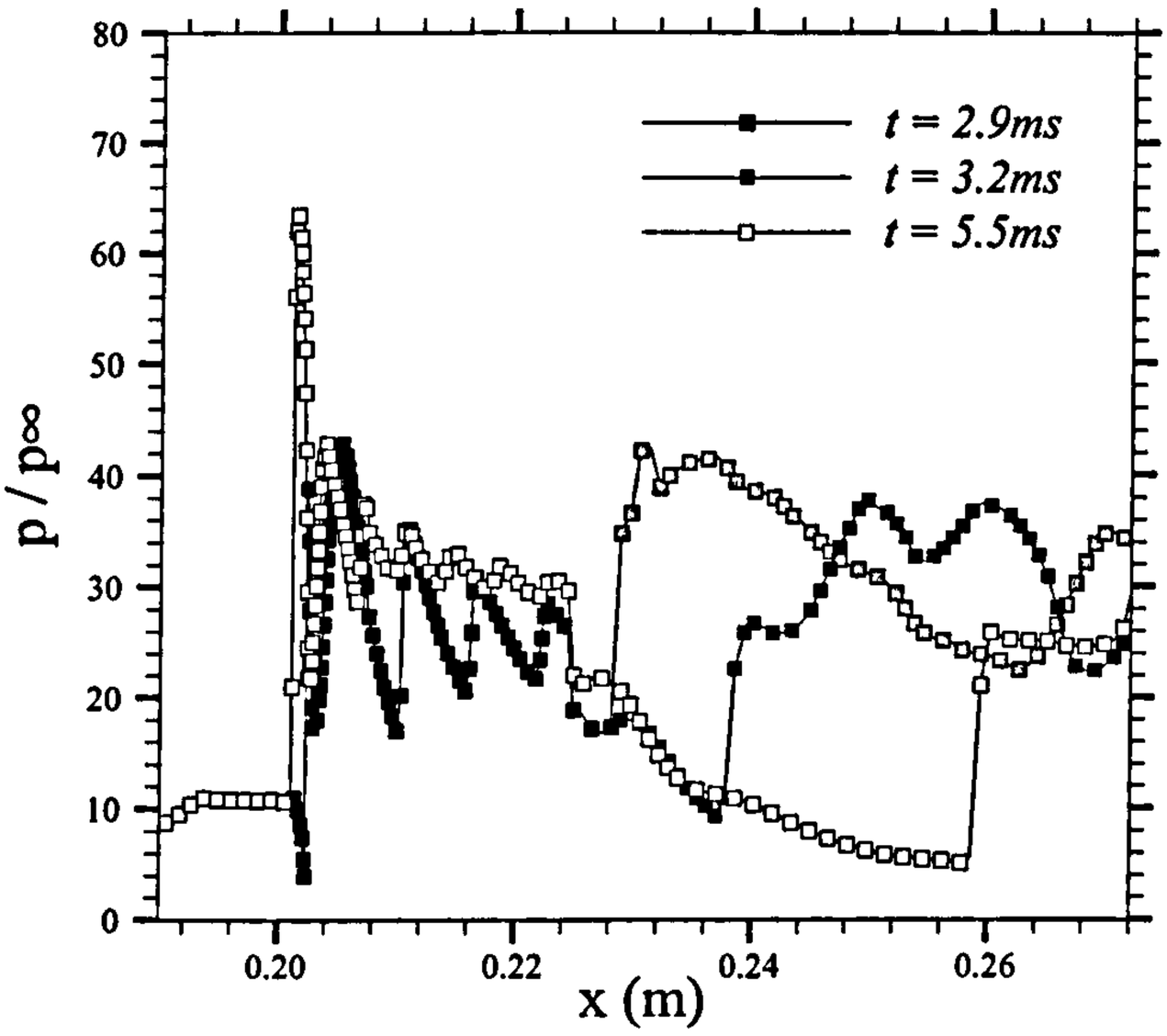


Figure 6.11: Surface pressure distribution for the intake ($M_{sol} = 5.5$) with a centrebody and cowl angle of 7 degrees at off-design Mach 4 with an applied back pressure p_{comb}/p_{∞} of approximately 41 at time intervals from time=2.9 to 5.5 ms.

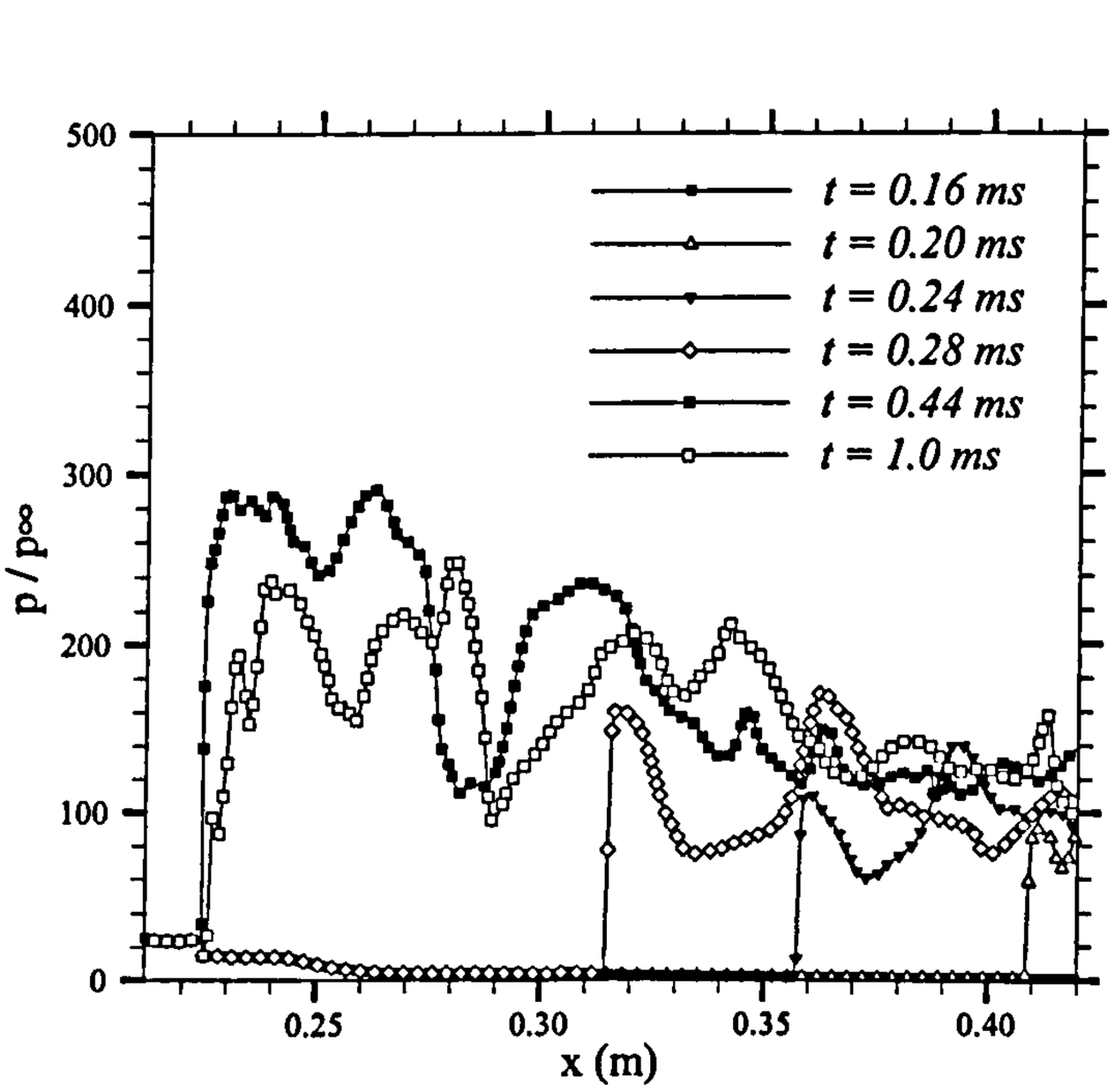


Figure 6.12: Surface pressure distribution for the intake ($M_{sol} = 5.5$) with a centrebody and cowl angle of 12 degrees at off-design Mach 6 with an applied back pressure p_{comb}/p_{∞} of approximately 47.2 at time intervals from time=0.16 to 1,0 ms.

6.3.3 Case 3: Viscous effects

Thus far all cases presented in this chapter have been modelled as an inviscid flow-field however for any realistic realistic assessment of the sustainable back pressure level of the intake, a turbulent simulation would be required. However, the simulation of a turbulent intake flow with an applied back pressure is a highly expensive computation and this analysis is beyond the scope of this present work.

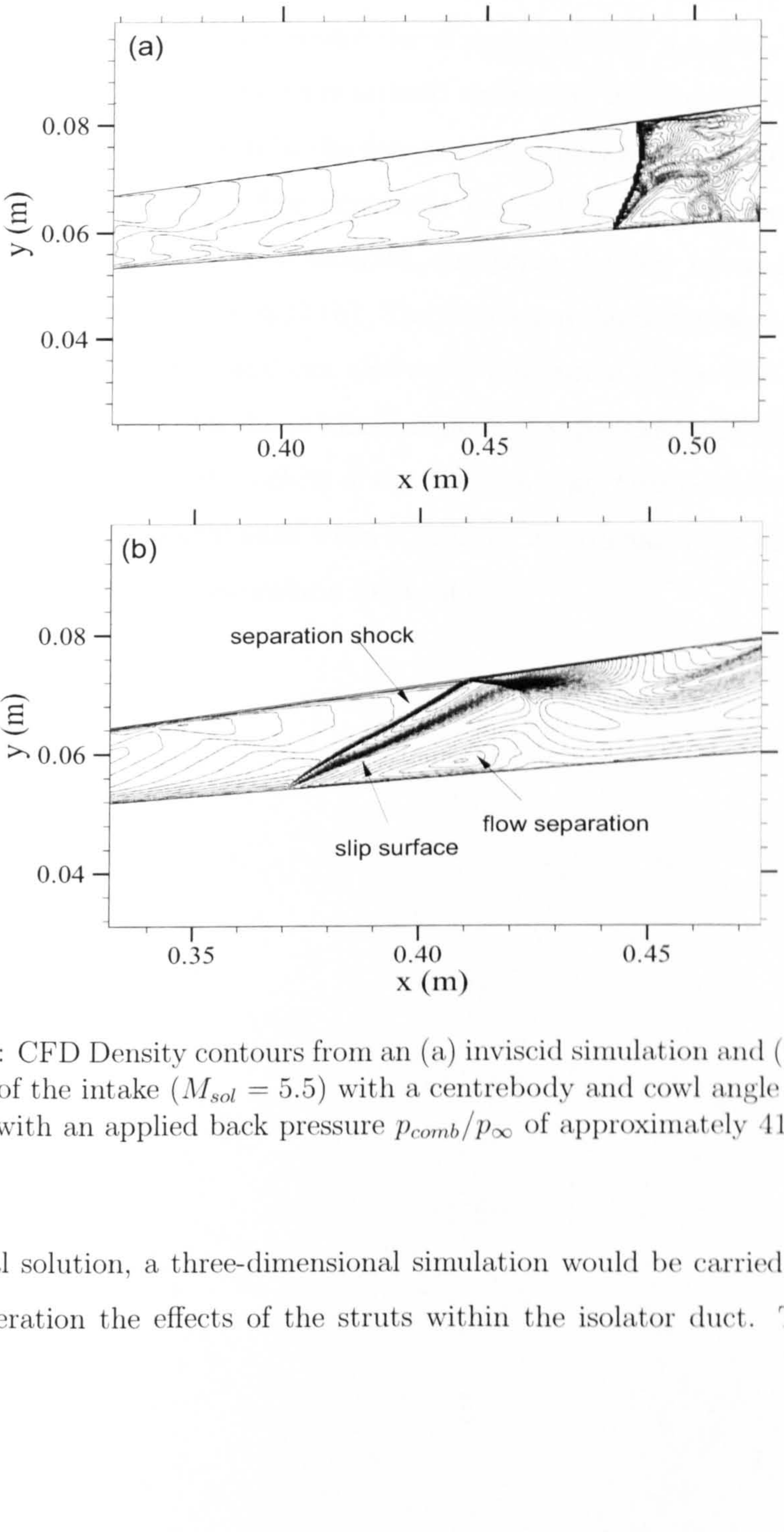


Figure 6.13: CFD Density contours from an (a) inviscid simulation and (b) turbulent simulation of the intake ($M_{sol} = 5.5$) with a centrebody and cowl angle of 7 degrees at Mach 4 with an applied back pressure p_{comb}/p_{∞} of approximately 41; time=0.30 ms.

For an ideal solution, a three-dimensional simulation would be carried out, taking into consideration the effects of the struts within the isolator duct. The inviscid

simulations presented for all the previous cases, do however, provide some correlation between inlet flow non-uniformity and the stability of the terminal shock system. Turbulent simulations of the intake with a back pressure were started but proved to be too computationally expensive for an extensive investigation.

This next result presents an indication of what the flow-field characteristics would encompass when including the effects of viscous and turbulence modelling. Figure 6.13 (b) presents a turbulent computation of the intake with a 7 degrees cowl at Mach 4 with a simulated combustion pressure rise of approximately $p_{comb}/p_{\infty} = 41$ at the combustor entry, to compare with the inviscid simulation in Figure 6.13 (a). In the inviscid case, the shock is driven by the flow non-uniformities at inlet. In the viscous case the flow is driven by the flow separation induced by the high back pressure. This causes the boundary-layer to separate, displacing the flow upwards to form a separation shock, seen in Figure 6.13 (b). The separation shock impinges on the cowl inner surface boundary-layer and can also cause separation of the cowl boundary-layer. The turbulent solution shows mixed regions of supersonic and subsonic flow behind the shock region, with pockets of reverse flow. This flow-field shows some of the complex flow features that arise when stabilising a terminal shock in the ramjet isolator in the presence of non-uniform intake flow.

Chapter 7

Conclusions and further work

7.1 Conclusions

This thesis has presented an analysis of the flow characteristics in the intake of a hypersonic vehicle. CFD simulations have been carried out on a fixed-geometry isentropic compression intake at speeds up to Mach 6, with both a supersonic flow throughout the engine and with a simulated combustion pressure rise. The CFD simulations have revealed complex internal flow structures which would otherwise have been difficult to determine from experiment. The findings from this work have given new insight into the flow phenomena in hypersonic intakes, particularly for the off-design conditions - and have led to an improvement in the design of a real intake configuration. The conclusions from this work are summarised as follows:

Inviscid CFD simulations were carried out for several intake configurations at Mach numbers from 4 to 6. Variations in inlet geometry and flight condition allowed for a parametric study of the intake flow-field which have given a wider understanding of the possible wave interactions that control the intake flow. Various off-design wave interactions have been examined and these have been found to depend on the position of the cowl and centrebody relative to the incoming shock system.

The interaction of the various waves at inlet can lead to either a shock attachment or detachment at the cowl lip. The cowl shock wave can reflect on the centrebody either as a regular reflection or a Mach reflection. The presence of either Mach

reflection or shock detachment in the intake flow has been found to affect the flow quality in the intake duct and significantly reduce intake performance. One of the critical interactions in this flow-field has been found to be the shock-wave/expansion-wave interaction of the cowl shock and the centrebody expansion fan which can lead to Mach reflection on the centrebody surface. Another critical point in this flow is when the focused shock (which radiates from the triple point) enters the inlet annulus and intends to reflect from the cowl inner surface. For the intake design tested, in no case can this lead to regular reflection, and so Mach reflection on the cowl interior surface will cause the shock system to propagate forwards to cause a shock detachment. This interaction is made worse when the cowl expansion fan affects the focused shock impingement onto the cowl inner surface. Results obtained from various simulations have also shown that allowing the triple point to fall below the cowl lip such that the shear layer enters the intake duct is clearly hazardous for successful intake operation and should be avoided at all cost.

Comparisons have also been made between flows with thin-plate cowls and blunted leading-edge cowls, and it has been found that the inlet flow is not specifically connected with the detail of the cowl leading edge. The wave systems at inlet were found to be similar for both thin-plate and blunted cowls.

The extensive computational effort required to run various well-resolved cases has led to a theoretical analysis of the intake flow-field which focuses on the essential details of the shock-wave and expansion-wave interactions in the flow, thus, enabling the prediction of the resultant wave system. Parameter studies have been carried out based on this analysis by varying the cowl and centrebody angles - and the results have been found to be in good agreement with the numerical simulations.

The findings have shown that the intake flow is highly sensitive to small changes in the cowl and centrebody geometry. They have also shown that the flow turning angle of the incoming flow is important in determining the shock systems at inlet. This led to studies of intake configurations with reduced spike termination angles (θ_1) and the results have shown that as this angle is reduced, the intake moves into a safer operating domain in terms of avoiding shock detachment and Mach reflection in the flow. This reduction in the spike termination angle however, results in reduced

intake compression ratios, and hence a reduced downstream performance.

Laminar simulation of the forebody flow showed boundary-layer separation. Imposing transition to turbulent flow led to an attached turbulent boundary-layer on the forebody indicating the need to operate at a high enough Reynolds number or to trigger transition early enough on the forebody.

Turbulent simulations of the intake flow indicated the severity of the centrebody boundary-layer separation problem which was primarily a consequence of the interaction of the cowl shock with the centrebody boundary-layer. The separation of the boundary-layer at inlet leads to total pressure losses, poor flow quality and non-uniformities which continue into the isolator and lead to a deterioration in performance. CFD studies have shown that the separation-induced shock wave which radiates onto the cowl inner surface and reflects back onto the centrebody boundary-layer acts as a sustaining mechanism in driving the separation to a greater degree. Reducing the spike termination angle - an hence reducing the flow turning angle at inlet was found to reduce boundary-layer separation at inlet.

Turbulent simulations have highlighted a critical aspect in the design - the ratio of the boundary-layer thickness to the annulus height. Shyfe is a small scale, low Reynolds number design, so that the forebody boundary-layer is thick compared to the cowl-centrebody annulus, so that it would be prone to this phenomenon. Higher Reynolds number - large scale designs would have a reduced ratio of 'δ_1' to 'H' so that this phenomenon might be avoided. The flow separation at inlet was successfully controlled by incorporating a backward-facing step on the centrebody. This resulted in an improved flow quality in the intake which is beneficial in improving the downstream performance.

Several intake variants of the Shyfe vehicle were tested during this research work. A performance analysis of two of the final variants of the Shyfe intake - the i1533 and the i1530 intake design, have been presented in the thesis. Due to the modelling of the flow in the intake section, with no information available on the rear half of the engine and propulsion - a drag analysis has not been carried out, hence the performance analysis focused on the internal flow quality of the intake.

The i1533 proved the best design with better total pressure efficiency and isolator performance - in terms of sustainable back pressure levels. The i1530 intake showed similar performance and the lower 6 degrees cowl angle (12 degrees for the i1533 intake) in this geometry would be beneficial in drag reduction.

CFD simulations have proven to be an invaluable design tool in the optimisation of the Shyfe intake. The CFD simulations and flow analysis carried out in this research work have uncovered and solved many of the flow problem areas in the intake which would have been difficult to solve by experimental methods. An understanding of the internal flow structure has enabled improvements in the design of the Shyfe intake and analysis of the internal flow-field has provided valuable information which will be useful in future optimisation work on the Shyfe engine. Further improvement in isolator design is however required if the intake is to sustain the levels of back pressure that are required for subsonic combustion operation.

Numerical simulations have also been carried out to investigate the effect of the flow non-uniformities in the intake duct on the stability of the terminal shock system - and on sustainable back pressure levels. Back pressure is applied to intakes with both a uniform and non-uniform duct flow. The findings have shown that the presence of non-uniformities at inlet make it increasingly difficult to stabilise a terminal shock system downstream in the isolator. Intakes with uniform flow were found to sustain a higher back pressure level than intakes with non-uniformities in the duct. The flow non-uniformities are primarily caused by the unfavourable off-design wave interactions which lead to shock detachment and Mach reflection in the duct. In addition, viscous effects, particularly shock/boundary-layer interactions, can cause separated flows adding further complexities in stabilising the terminal shock.

7.2 Further work

Further investigation of off-design wave interactions can be made from 3D CFD simulations. Studies can be carried out on the intake flow at angle-of-attack to determine the three-dimensional flow phenomena at inlet and the effect on off-design wave interactions - both for shock/shock and shock/expansion interactions, and also for shock/boundary-layer interactions in the intake flow-field.

Research into methods of controlling flow separation in the intake is an area which requires further research. Focused parameter studies on geometry modifications to control flow separation can aim to find improved methods of controlling the boundary-layer separation in the intake and in the isolator.

The design of the isolator is an important aspect of a hypersonic vehicle and further research can be carried out by varying isolator geometry to optimise downstream performance. One of the most important aspects of future work should be to explain the viscous isolator flow-field with applied back pressure. 3D analysis on the internal flow in the isolator should also be carried out for a deeper understanding in this area.

For improvements in the Shyfe intake design, studies should be carried out by further increasing the shock-on-lip Mach number to maintain the triple point system above the cowl. As mentioned before, allowing the triple point to fall below the cowl lip such that the shear layer generated from this point enters the intake duct is a critical point in this flow. This leads to complex wave systems in the intake and results in flow non-uniformities which significantly deteriorate intake performance and thus should be completely avoided. One method that could be explored is the continuation of the isentropic process internally on the cowl inner surface to reduce unfavourable off-design wave interactions when the focused shock enters the annulus.

7.3 Publications

Work from this thesis has been presented at four technical conferences:

1. Bachchan N. and Hillier R. *Hypersonic Inlet Flow Analysis at Off-Design Conditions.* American Institute of Aeronautics and Astronautics, AIAA Paper 2004-5380, 22nd AIAA Applied Aerodynamics Conference, USA, 2004.

2. Bachchan N. and Hillier R. *Effects of Hypersonic Inlet Flow Non-Uniformities on Stabilising Isolator Shock Systems.* American Institute of Aeronautics and Astronautics, AIAA Paper 2004-4716, AIAA Atmospheric Flight Mechanics Conference, USA, 2004.

3. Bachchan N. and Hillier R. *Shock-Expansion Interactions in Hypersonic Inlet Flow*, Royal Aeronautical Society: Aerospace Aerodynamics Research Conference, Session 2B: Paper 9, UK, 2004.

4. Bachchan N. and Hillier R. *Shock-wave/Expansion-wave Interactions and the Transition from Regular to Mach Reflection*, The 25th International Symposium on Shock Waves, ISSW25, Bangalore, India, July 2005.

Appendix A

Appendix

A.1 Shock-expansion interaction analysis

The interaction of a shock wave with an expansion wave is an important feature in the intake flow field. Analytical calculations have been carried out to determine the resulting shock system which occurs from the interaction of a shock wave with an expansion wave of the opposite family (presented in chapter 4). The shock-expansion interaction can result in a shock attachment or a shock detachment at inlet depending on the strength of the interaction. The interaction can also affect whether a cowl shock reflects as regular reflection or Mach reflection in the intake.

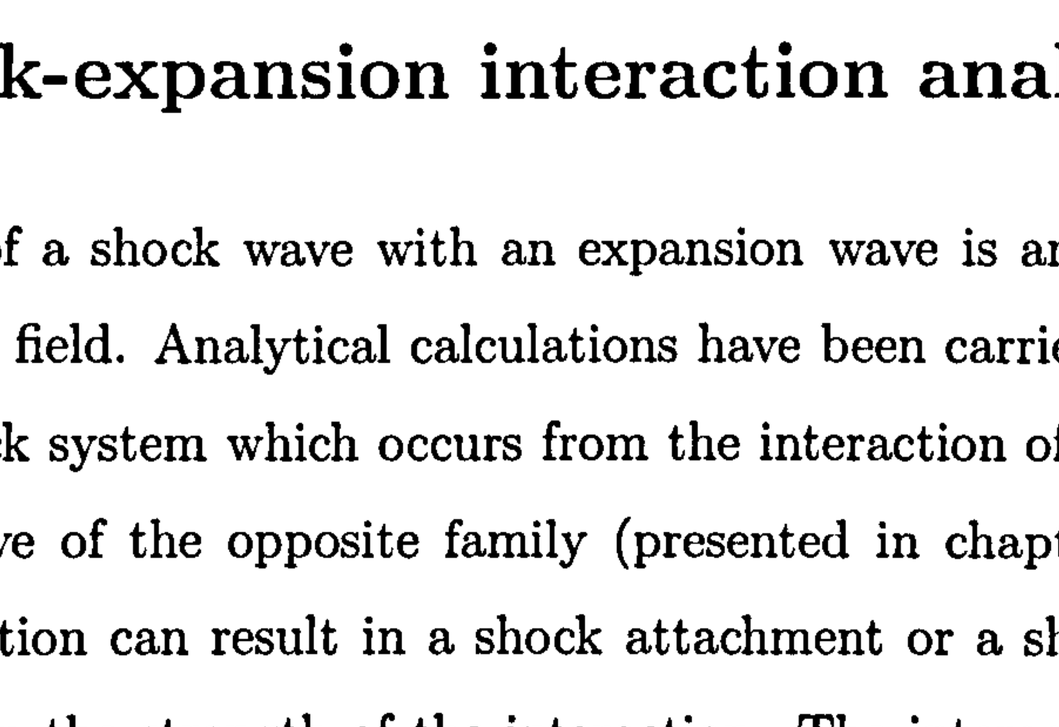


Figure A.1: Interaction of a shock wave with an expansion wave.

The basic system is shown in Figure A.1 where the incident expansion wave is transmitted through the shock system. The basic rotational characteristics calculation uses the element 1-2-3, where 2-3 is a C^+ characteristic and 1-3 is a C^-.

The basic difference equations are well known, expressed here for constant total enthalpy flow as:

$$\nu_3 - \delta_3 = \nu_2 - \delta_2 + sin(\bar{\mu})\frac{sin(\delta_2)}{\bar{r}}\Delta C^+_{2,3} - \frac{\sqrt{\bar{M}^2 - 1}}{\gamma \bar{M}^2} R(s_3 - s_2) \qquad \text{(A.1)}$$

$$\nu_3 + \delta_3 = \nu_2 + \delta_1 + sin(\bar{\mu})\frac{sin(\delta_1)}{\bar{r}}\Delta C^-_{1,3} - \frac{\sqrt{\bar{M}^2 - 1}}{\gamma \bar{M}^2} R(s_3 - s_1) \qquad \text{(A.2)}$$

where R is the gas constant, r is the distance from the axis of symmetry, ΔC represents the physical distance along the appropriate characteristic, an overbar on a variable means that the *best* value is used as an average along the appropriate characteristic segment. An iterative calculation is involved, including an iteration to determine the shock wave position and slope at the location where C^- characteristics terminate at the shock.

For the intake cases considered here, the distance $\bar{r}$ is so large compared with the intake annulus that, in a further simplification the term in ΔC can be ignored. The effect of entropy changes is also weak, so that only small errors are involved in computing the interaction using a single cell 1-2-3, where node 1 lies on the transmitted characteristic from the leading edge of the expansion wave and node 2 is the incident position on the shock wave for the final C^+ characteristic from the expansion wave. Although this is an apparently dramatic simplification, the prediction of critical angles is within 1 degree of the *exact* result. Exact or approximate, these calculations provide the flow deflection, and Mach number, of the flow downstream behind the transmitted expansion wave, as well as the transmitted shock strength and angle. Given the known centrebody angle it is straightforward to calculate whether shock reflection from the centrebody is regular or Mach reflection.

A.2 Intake geometry definition

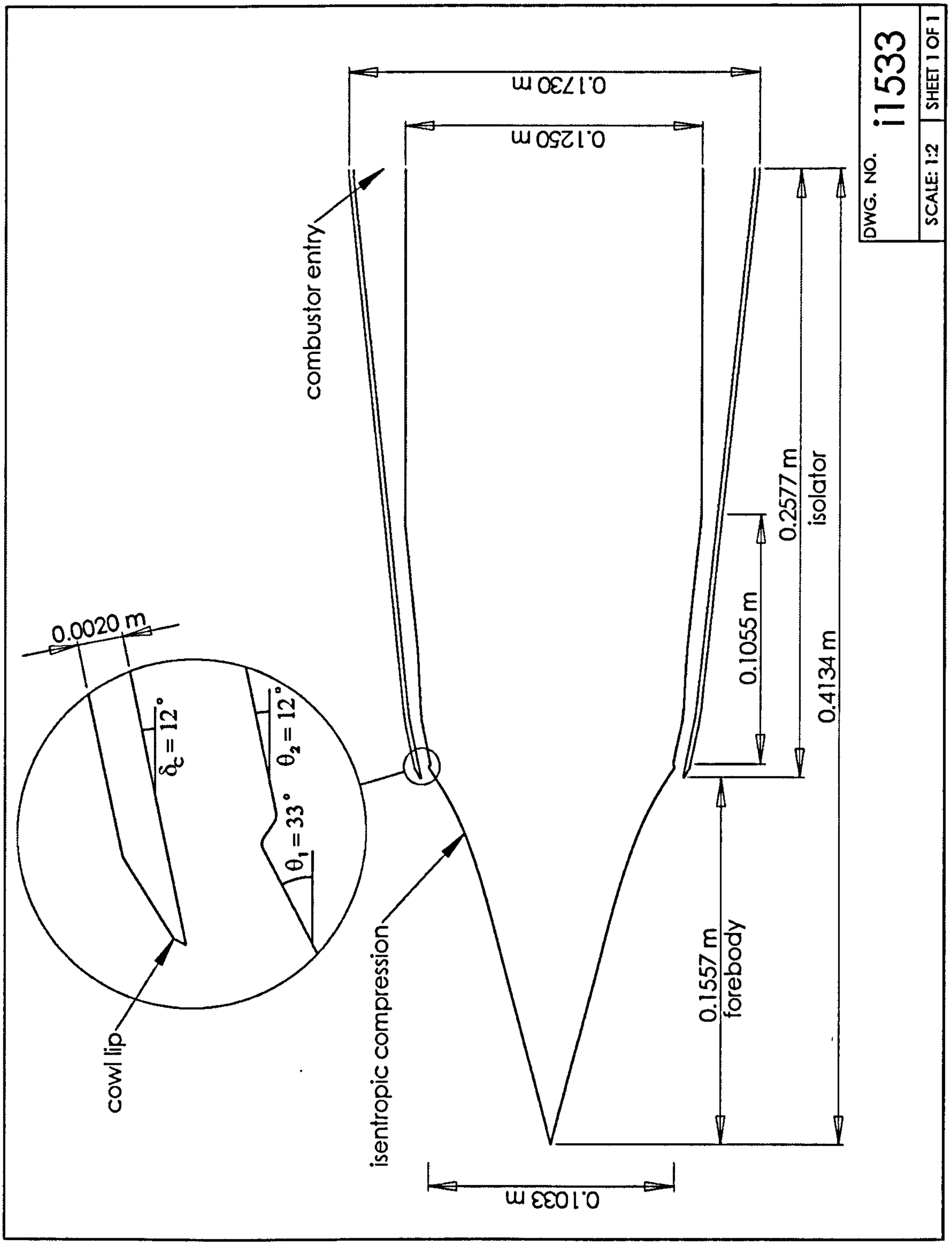


Figure A.2: 2D Drawing of the i1533 variant of the Shyfe intake from the apex to the combustor entry; and a close-up view of the blunted cowl geometry.

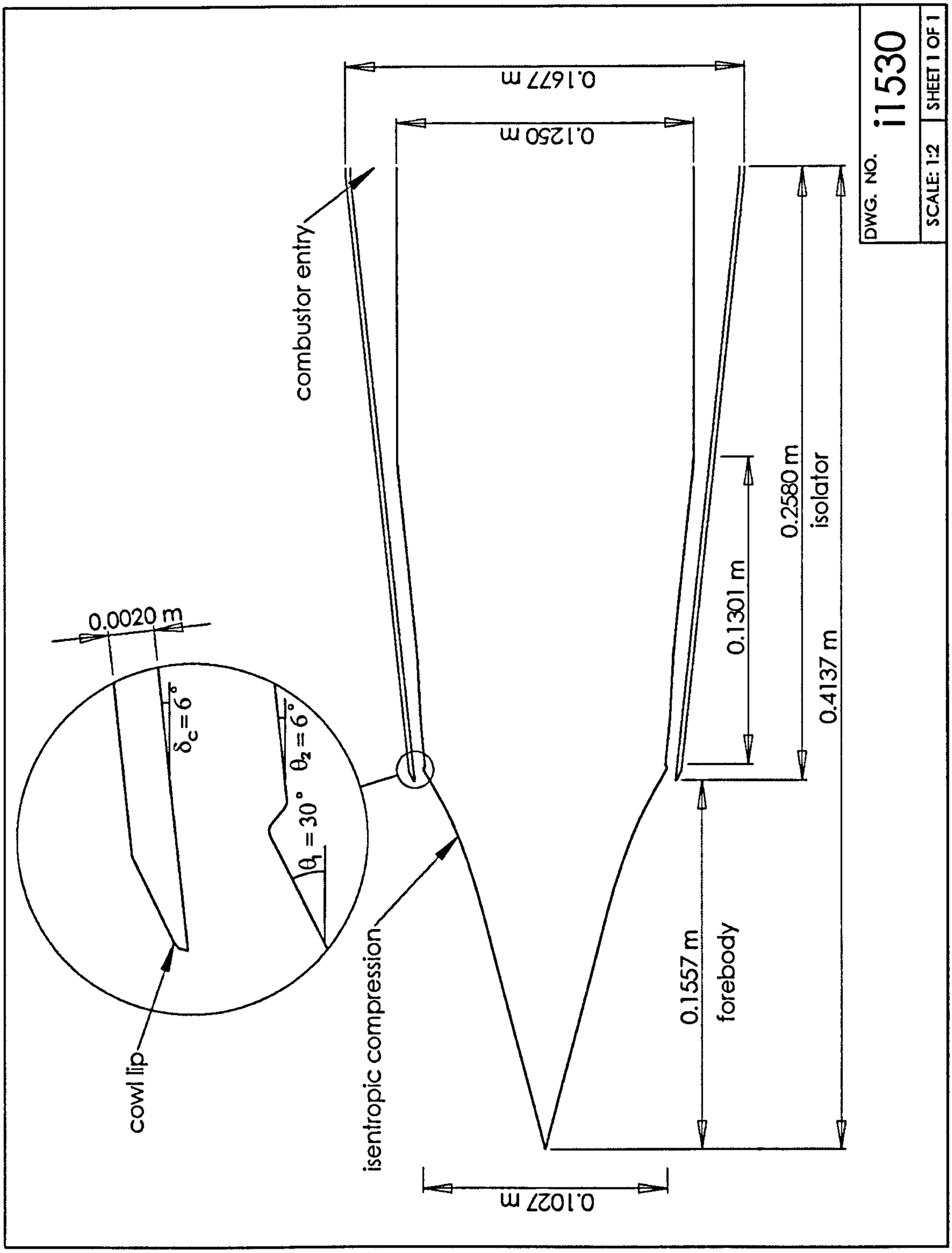


Figure A.3: 2D Drawing of the i1530 variant of the Shyfe intake from the apex to the combustor entry; and a close-up view of the blunted cowl geometry.

Bibliography

[1] Ferri A. **The Method of Characteristics for the Determination of Supersonic Flow over Bodies of Revolution at Small Angles of Attack.** *NACA Report TM-1809*, 1949.

[2] Ferri A. and Nucci L.M. **Theoretical and Experimental Analysis of Low-Drag Supersonic Inlets Having a Circular Cross Section and a Central Body at Mach Numbers of 3.30, 2.75 and 2.45.** *NACA Report RM-L8H13*, 1948.

[3] Kumar A. **Numerical Analysis of the Scramjet-Inlet Flow Field by using Two-Dimensional Navier-Stokes Equations.** *NASA Report TP-1940*, 1981.

[4] Paull A. **Hypersonic Airbreathing Propulsion.** *22nd International Symposium on Shock Waves, UK*, Paper 1620, 1999.

[5] Paull A. and Boyce R.R. **Intake Design of a Scramjet Flight Experiment.** *22nd International Symposium on Shock Waves, UK*, Paper 0190, 1999.

[6] Rudakov A. and Kopchenov V. **Russian Hypersonics Workshop.** *The Royal Institution of Great Britain, London*, pages February 24–27, 2003.

[7] SHAPIRO A.H. *The Dynamics and Thermodynamics of Compressible Fluid Flow.* Ronald Press Company, USA, 1954.

[8] Matthews A.J. *Scramjet Intakes.* PhD thesis, University of Oxford, UK, 2004.

[9] Anderson G.Y., McClinton C.R. and Weidner J.P. **Scramjet Performance.** *Scramjet Propulsion*, Chapter 6:369–446, 2001.

[10] Weiting A.R. and Holden M.S. Experimental study of shock wave interference heating on a cylindrical leading edge at Mach 6 and 8. Technical Report AIAA Paper 87-1511, AIAA, 1987.

[11] Arnette S.A., *et al.* **The Effects of Expansion on the Turbulence Structure of Compressible Boundary Layers.** *Journal of Fluid Mechanics*, 367:67–105, 1998.

[12] Duncan B. and Thomas S. Computational analysis of ramjet engine inlet interaction. Technical Report AIAA Paper 92-3102, AIAA, 1992.

[13] Edney B. **Anomalous Heat Transfer and Pressure Distributions on Blunt Bodies at Hypersonic Speeds in the Presence of an Impinging Shock.** *FFA The Aeronautical Research Institute of Sweden, Report 115*, 1968.

[14] Ben-Artzi M. and Falcovitz J. **A Second Order Godunov-Type Scheme for Compressible Fluid Dynamics.** *Journal of Computational Physics*, 55:1–32, 1984.

[15] Ben-Dor G., *et al.* **The Influence of the Downstream Pressure on the Shock Wave Reflection Phenomenon in Steady Flows.** *Journal of Fluid Mechanics*, 386:213–232, 1999.

[16] Glass C. **Numerical Simulation of Low-Density Shock-Wave Interactions.** *NASA Report TM-209358*, 1999.

[17] Herrmann C.D. and Koschel W.W. Experimental investigation of the internal compression of a hypersonic intake. Technical Report AIAA Paper 2002-4130, AIAA, 2002.

[18] Cockrell C.E. and Huebner L.D. Generic hypersonic inlet module analysis. Technical Report AIAA Paper 91-3209, AIAA, 1991.

[19] Rodriguez C.G. Asymmetry effects in numerical simulation of supersonic flows with upstream separated regions. Technical report, AIAA.

[20] Steffen C.J. and DeBonis J.R. Numerical analysis of the trailblazer inlet flowfield for hypersonic Mach numbers. Technical Report AIAA Paper 2000-0889, AIAA, 2000.

[21] Curran E.T., *et al.* **Fluid Phenomena in Scramjet Combustion Systems.** *Annual Review of Fluid Mechanics*, 28:323–360, 1996.

[22] KUCHEMANN D. and WEBER J. *Aerodynamics of Propulsion.* McGraw-Hill, USA, 1953.

[23] Sobel D. Cowl leading edge heat transfer in the presence of shock impingement. Technical Report AIAA Paper 90-5256, AIAA, 1990.

[24] WILCOX D.C. *Turbulence Modeling for CFD.* DCW, USA, 1998.

[25] Wyatt D.D. **A Review of Air Intake Problems.** *NACA Report*, 1958.

[26] Ding M., *et al.* Two-dimensional viscous simulation of a inlet-isolator flow at Mach number 4. Technical Report AIAA Paper 2001-3883, AIAA, 2001.

[27] Mee D.J. and Stalker R.J. Investigation of weak shock-shock and shock-expansion intersection in the presence of a turbulent boundary layer. Technical Report AIAA Paper 87-0549, AIAA, 1987.

[28] Van Wie D.M. and Ault D.A. Internal flowfield characteristics of a two-dimensional scramjet inlet at Mach 10. Technical Report AIAA Paper 94-0584, AIAA, 1994.

[29] Van Wie D.M. and Ault D.A. On the role of computational fluid dynamics in determining hypersonic inlet performance in ground test facilities. Technical Report AIAA-98-2782, AIAA, 1998.

[30] Dolling D.S. **Fifty Years of Shock-Wave/Boundary-Layer Interaction Research: What Next?** *AIAA Journal*, 39(8), 2001.

[31] Pratt D.T. and Heiser W.H. Isolator-combustor interaction in a dual-mode scramjet engine. Technical Report AIAA Paper 93-0358, AIAA, 1993.

[32] Mayer D.W. and Paynter G.C. Prediction of supersonic inlet unstart caused by freestream disturbances. Technical Report AIAA Paper 94-0580, AIAA, 1994.

[33] Chen C.P. *et al.* **Shock-Wave Oscillations in a Transonic Diffuser Flow.** *AIAA Journal*, 17(10), 1979.

[34] Chew Y.T. *et al.* **Shock Wave and Boundary Layer Interaction in the Presence of an Expansion Corner.** *Aeronautical Quarterly*, 30:506–527, 1979.

[35] Emami S. *et al.* **Experimental Investigation of Inlet-Combustor Isolators for a Dual-Mode Scramjet at a Mach Number of 4.** *NASA Report TP-3502*, 1995.

[36] Hillier R. *et al.* **Development of Some Hypersonic Benchmark Flows using CFD and Experiment.** *Shock Waves*, 13:375–384, 2003.

[37] Ivanov M.S. *et al.* **Transition Between Regular and Mach Reflection of Shock Waves: New Numerical and Experimental Results.** *Shock Waves 11*, pages 199–207, 2001.

[38] Kumar A. *et al.* Research in Hypersonic Airbreathing Propulsion at the NASA Langley Research Center. Technical Report ISABE-2001: Invited Lecture 4, ISABE, 2001.

[39] McLafferty G.H. *et al.* **Investigation of Turbojet Inlet Design Parameters.** *United Aircraft Corporation Report R-0790-13*, 1955.

[40] Moss J.N. *et al.* **DSMC Simulation of Shock/Shock Interaction: Emphasis on Type IV Interactions.** *NASA Report*, 1998.

[41] Talbot L. *et al.* **Hypersonic Viscous Flow over Slender Cones.** *NACA Report TN-4327*, 1958.

[42] Culick F.E.C. and Rogers T. **The Response of Normal Shocks in Diffusers.** *AIAA Journal*, 21(10), 1983.

[43] Lu F.K. and Chung K.M. Exploratory study of shock reflection near an expansion corner. Technical Report AIAA Paper 93-3132, AIAA, 1993.

[44] Wise G.A. and Sterbentz W.H. **Investigation of Shock-Boundary Layer Interaction on the Spike of a Conical-Spike Nose Inlet.** *NASA Report RM-E56I26a*, 1957.

[45] Paynter G.C. and Mayer D.W. Flow stability issues in supersonic inlet flow analyses. Technical Report AIAA Paper 93-0290, AIAA, 1993.

[46] Kobayashi H. Numerical and experimental study on precompression effect for hypersonic vehicle. Technical Report AAS-97-404, AIAA/ASME/SAE/ASEE, 1997.

[47] SCHLICHTING H. *Boundary-Layer Theory.* Springer-Verlag, Germany, 2000.

[48] Hornung H.G. **On The Stability of Steady-Flow Regular and Mach Reflection.** *Shock Waves 7*, pages 123–125, 1997.

[49] Kirk D. Hillier R. and Soltani S. **Navier-Stokes Computations of Hypersonic Flows.** *International Journal of Numerical Methods for Heat and Fluid Flow*, 5:195–211, 1995.

[50] Weinreich H.L. and Triesch K. Comparison of performances of different circular intakes. Technical report, DLR, Germany.

[51] Hsia Y.C., *et al.* Inviscid analysis of a dual mode scramjet inlet. Technical Report AIAA Paper 89-2681, AIAA, 1989.

[52] LIEPMANN H.W. and ROSHKO A. *Elements of Gas Dynamics.* Dover Publications, USA, 1957.

[53] Faro I. **Supersonic Inlets.** *AGARD-NATO Fluid Dynamics Panel AGARDograph 102*, 1965.

[54] Lipatov I.I. and Bogolepov V.V. Goertler vortices development in hypersonic flows. Technical Report AIAA Paper 97-2014, AIAA, 1997.

[55] Grotowsky I.M.G. and Ballmann J. **Numerical Investigation of Hypersonic Step-Flows.** *Shock Waves 10*, pages 57–72, 2000.

[56] Chung J. Numerical simulation of a mixed-compression supersonic inlet flow. Technical Report AIAA Paper 94-0583, AIAA, 1994.

[57] Fabri J. **Air Intake Problems in Supersonic Propulsion.** *AGARD-NATO Fluid Dynamics Panel AGARD-AG-27*, 1958.

[58] SEDDON J. and GOLDSMITH E.L. *Intake Aerodynamics.* Collins Professional and Technical Books, London, 1985.

[59] Schetz J.A. and Billig F.S. Studies of scramjet flowfields. Technical Report AIAA Paper 87-2161, AIAA, 1987.

[60] White J.A. and Rhie C.M. Numerical analysis of peak heat transfer rates for hypersonic flow over a cowl leading edge. Technical Report AIAA Paper 87-1895, AIAA, 1987.

[61] Jackson A.P., Hillier R. and Soltani S. **Experimental and Computational Study of Laminar Cavity Flows at Hypersonic Speeds.** *Journal of Fluid Mechanics*, 427:329–358, 2001.

[62] ANDERSON J.D. *Hypersonic and High Temperature Gas Dynamics.* McGraw-Hill Publishing Company, USA, 1989.

[63] ANDERSON J.D. *Modern Compressible Flow with Historical Perspective.* McGraw-Hill Publishing Company, USA, 1990.

[64] ANDERSON J.D. *Computational Fluid Dynamics.* McGraw-Hill Education, USA, 1995.

[65] BERTIN J.J. *Hypersonic Aerothermodynamics.* AIAA Education Series, Washington DC, 1994.

[66] MAHONEY J.J. *Inlets for Supersonic Missiles.* AIAA Education Series, USA, 1990.

[67] ZUCROW J.M. and HOFFMAN J.D. *Gas Dynamics Vol. 2 Multidimensional Flow.* Wiley, London, 1977.

[68] Oh J.Y. and Yang V. Interactions between shock and acoustic waves in a supersonic inlet. Technical Report AIAA Paper 94-2706, AIAA, 1994.

[69] Chung K. and Lu F. Hypersonic turbulent expansion-corner flow with shock impingement. Technical Report AIAA Paper 92-5101, AIAA, 1992.

[70] Kudryavtsev A.N., *et al.* Euler simulations of the flow over a hypersonic convergent inlet integrated with a forebody compression surface. Technical report, Institute of Theoretical and Applied Mechanics, Russian Academy of Sciences, 2000.

[71] Kudryavtsev A.N., *et al.* Numerical simulation of asymmetrical steady shock wave interactions. Technical report, Institute of Theoretical and Applied Mechanics, Russian Academy of Sciences, 2000.

[72] Hunter L.G. and Couch B.D. A CFD study of precombustion shock-trains from Mach 3-6. Technical Report AIAA Paper 90-2220, AIAA, 1990.

[73] Li H. and Ben-Dor G. **A Parametric Study of Mach Reflection in Steady Flows.** *Journal of Fluid Mechanics*, 341:101–125, 1997.

[74] Li H. and Ben-Dor G. **A Parametric Study of Mach Reflection in Steady Flows.** *Journal of Fluid Mechanics*, 341:101–125, 1997.

[75] Lin P., *et al.* Numerical analysis of normal shock train in a constant area isolator. Technical Report AIAA Paper 91-2162, AIAA, 1991.

[76] Lin P., *et al.* Numerical investigation on shock wave/boundary-layer interactions in a constant area diffuser at Mach 3. Technical Report AIAA Paper 91-1766, AIAA, 1991.

[77] Onofri M. and Nasuti F. **Theoretical Considerations on Shock Reflections and their Implications on the Evaluation of Air Intake Performance.** *Shock Waves 11*, pages 151–156, 2001.

[78] Smart M. and Trexler C.A. Mach 4 performance of a fixed-geometry hypersonic inlet with rectangular-to-elliptical shape transition. Technical Report AIAA Paper 2003-0012, AIAA, 2003.

[79] McClinton C.R., *et al.* Airbreathing hypersonic technology vision vehicles and development dreams. Technical Report AIAA Paper 99-4978, AIAA, 1999.

[80] White M.E. Expansion corner effects on hypersonic shock wave/turbulent boundary layer interactions. Technical Report AIAA Paper 96-4542, AIAA, 1996.

[81] White M.E. and Ault D.A. Hypersonic shock wave/turbulent boundary layer interactions in the vicinity of an expansion corner. Technical Report AIAA Paper 95-6125, AIAA, 1995.

[82] Menter F.R. **Eddy Viscosity Transport Equations and Their Relation to the $k-\epsilon$ Model.** *Transactions of the ASME*, 119:876–884, 1997.

[83] Messitt D., *et al.* Combined numerical and experimental investigation of a 2D scramjet inlet at Mach numbers from 10 to 25. Technical Report AIAA Paper 95-6020, AIAA, 1995.

[84] Messitt D.G., *et al.* NPARC simulation of scramjet inlet experiments at Mach numbers from 10-20. Technical Report AIAA Paper 96-4530, AIAA, 1996.

[85] Molder S., *et al.* **Performance of Three Hypersonic Air Inlets.** *22nd International Symposium on Shock Waves, UK*, Paper 1430, 1999.

[86] Bachchan N. and Hillier R. Shock-wave/Expansion-wave interactions and the transition from regular to Mach reflection. Technical report, 25th International Symposium on Shock Waves, 2005.

[87] Nair M.T., *et al.* Reynolds averaged Navier-Stokes based aerodynamic analysis of inlet for a hypersonic research vehicle. Technical Report AIAA Paper 2003-7067, AIAA, 2003.

[88] Osafune T., *et al.* **Experimental Study of an External Supersonic Compression Air Intake.** *22nd International Symposium on Shock Waves, UK*, Paper 4741, 1999.

[89] Waltrup P.J. and Billig F.S. **The Structure of Shock Waves in Cylindrical Ducts.** *AIAA Journal*, 11(10), 1973.

[90] Hillier R. Private communication. *Department of Aeronautics, Imperial College, UK*, 2003.

[91] Reinartz B., *et al.* Analysis of hypersonic inlet flows with internal compression. Technical Report AIAA Paper 2002-5230, AIAA, 2002.

[92] Reinartz B., *et al.* **Aerodynamic Performance Analysis of a Hypersonic Inlet Isolator Using Computation and Experiment.** *Journal of Propulsion and Power*, 19:868–875, 2003.

[93] Korkegi R.H. **Comparison of Shock-Induced Two- and Three-Dimensional Separation.** *AIAA Journal*, 13(4), 1975.

[94] Sandeman R.J. **A Simple Physical Theory of Weak Mach Reflection Over Plane Surfaces.** *Shock Waves 10*, pages 103–112, 2000.

[95] Weber R.J. and MacKay J.S. **An Analysis of Ramjet Engines using Supersonic Combustion.** *NACA Report TN-4386*, 1958.

[96] Trimpi R.L. **A Theory of Stability and Buzz Pulsation Amplitude in Ramjets and an Experimental Investigation Including Scale Effects.** *NACA Report 1265*, 1958.

[97] Cubbison R.W. and Samanich N.E. **Effect of Spike-Tip and Cowl-Lip Blunting on Inlet Performance of a Mach 3.0 External-Compression Inlet.** *NACA Report RM-E58G02a*, 1958.

[98] Creighton S. *Hypersonic Flow over Non-Rectangular Cavities.* PhD thesis, Department of Aeronautics, Imperial College, UK, 2004.

[99] Scortecci F., *et al.* Experimental investigation of shock-wave/boundary-layer interactions over an artificially heated model in hypersonic flow. Technical Report AIAA Paper 98-1571, AIAA, 1998.

[100] Holland S.D. Reynolds number and cowl position effects for a generic sidewall compression scramjet inlet at Mach 10: A computational and experimental investigation. Technical Report AIAA Paper 92-4026, AIAA, 1992.

[101] Holland S.D. **Internal Aerodynamics of a Generic Three-Dimensional Scramjet Inlet at Mach 10.** *NASA Report TP-3476*, 1995.

[102] Holland S.D. **Mach 10 Computational Study of a Three-Dimensional Scramjet Inlet Flow Field.** *NASA Report TM-4602*, 1995.

[103] Holland S.D. and Perkins J.N. Internal shock interactions in propulsion/airframe integrated three-dimensional sidewall compression scramjet inlets. Technical Report AIAA Paper 92-3099, AIAA, 1992.

[104] Cox-Stouffer S.K. and Hagenmaier M.A. The effect of aspect ratio on isolator performance. Technical Report AIAA Paper 001-0519, AIAA, 2001.

[105] Williams S.P. *Three-Dimensional Separation of a Hypersonic Boundary Layer.* PhD thesis, Department of Aeronautics, Imperial College, UK, 2004.

[106] Sullins G.A., *et al.* Investigation of surface temperature influence on Goertler vortices. Technical Report AIAA Paper 95-2297, AIAA, 1995.

[107] Cain T. and Walton C. Private communication. *QinetiQ, Farnborough*, 2003.

[108] Cain T. and Walton C. The Sustained Hypersonic Flight Experiment. Technical Report AIAA Paper 2003-7030, AIAA, 2003.

[109] Ito T. Effect of freestream noise on roughness-induced boundary-layer transition for a scramjet inlet. Technical Report AIAA Paper 2000-0284, AIAA, 2000.

[110] Tani K., *et al.* A geometrical approach for controlling pressure distributions in scramjet inlet and isolator. Technical Report AIAA Paper 2000-0620, AIAA, 2000.

[111] van Keuk J. and Ballmann J. Numerical simulation of hypersonic inlet flows. Technical Report AIAA Paper 98-1526, AIAA, 1998.

[112] Van Wie D.M. **Scramjet Inlets**. *Scramjet Propulsion*, Chapter 7:447–511, 2001.

[113] Bogolepov V.V. Investigation of surface temperature influence on Goertler vortices incipience. Technical Report AIAA Paper 95-2297, AIAA, 1995.

[114] Wang S., *et al.* Investigation on the entrance flow of a supersonic inlet. Technical Report AIAA Paper 97-7028, AIAA, 1997.

[115] HEISER W.H. and PRATT D.T. *Hypersonic Airbreathing Propulsion.* AIAA Education Series, Washington DC, 1994.

[116] Montazel X. and Sitbon D. Prediction of supersonic inlet performances with 3D Navier-Stokes calculations. Technical Report AIAA Paper 97-3147, AIAA, 1997.

[117] Burtschell Y. and Zeitoun D.K. **Shock/Shock and Shock/Boundary Layer Interactions in an Axisymmetric Steady Laminar Flow.** *Shock Waves 12*, pages 487–495, 2003.

[118] Yamamoto Y., *et al.* Numerical and experimental aerothermodynamics of strong hypersonic shock-shock interactions. Technical Report AIAA Paper 2002-2891, AIAA, 2002.

[119] Hsia Y.C. FNS analysis of an an axisymmetric scramjet inlet. Technical Report AIAA Paper 92-3100, AIAA, 1992.

[120] Chew Y.T. and Squire L.C. The boundary layer development downstream of a shock interaction at an expansion corner. Technical Report ARC Report and Memoranda No. 3839, Cambridge University Engineering Department, 1978.

[121] Zheltovodov A.A., *et al.* **Experimental and Computational Studies of Crossing-Shock-Wave/Turbulent-Boundary-Layer Interactions.** *Proceedings of International Conference RDAMM*, Volume 6, Pt 3, Special Issue, 2001.

